

JANUARY 2020

AJNR

VOLUME 41 • PP 1-189

AJNR

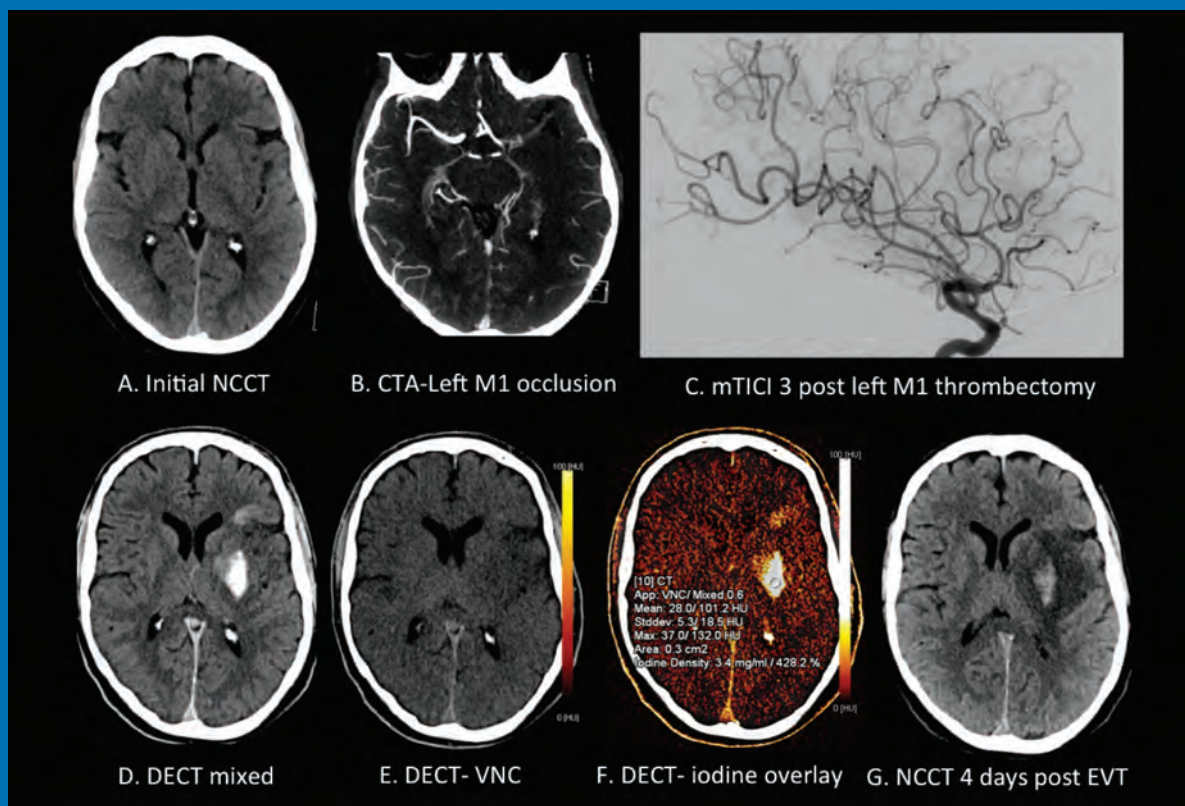
AMERICAN JOURNAL OF NEURORADIOLOGY

JANUARY 2020
VOLUME 41
NUMBER 1
WWW.AJNR.ORG

THE JOURNAL OF DIAGNOSTIC AND
INTERVENTIONAL NEURORADIOLOGY

Dual-energy CT in acute stroke
Lateral decubitus digital subtraction myelography
High-resolution MRI for evaluation of ventriculostomy tubes

Official Journal ASNR • ASFNR • ASHNR • ASPNR • ASSR





INDICATIONS FOR USE:

The WEB Aneurysm Embolization System is indicated for use at the middle cerebral artery (MCA) bifurcation, internal carotid artery (ICA) terminus, anterior communicating artery (AComm) complex, or basilar artery apex for the endovascular treatment of adult patients with saccular, wide neck bifurcation intracranial aneurysms with dome diameter from 3 mm to 10 mm and either neck size 4 mm or greater or the dome-to-neck ratio is greater than 1 and less than 2.

The WEB Aneurysm Embolization System is contraindicated for patients with known bacterial infection that may interfere with or negatively affect the implantation procedure and patients with known hypersensitivity to nickel. For complete indications, contraindications, potential complications, warnings, precautions, and instructions, see instructions for use (IFU provided with the device).

The VIA® Catheter is intended for the introduction of non-liquid interventional devices (such as stents/_ow diverters) and infusion of diagnostic (such as contrast media) or non-liquid therapeutic agents into the neuro, peripheral, and coronary vasculature. The VIA Catheter is contraindicated for use with liquid embolic materials, such as n-butyl 2-cyanoacrylate or ethylene vinyl alcohol & DMSO (dimethyl sulfoxide). The VIA Catheter is contraindicated for use in the pediatric population (<22 yrs of age).

Caution: Federal law restricts these devices to sale by or on the order of a physician.

WEB[®]

Aneurysm Embolization System

MicroVention[®] delivers the first intrasaccular solution for wide neck bifurcation aneurysms.

The **world leader**
and **first**
PMA - approved
device in an
important new
category of
intrasaccular
flow disruptors.

The WEB[®] System is a safe
and effective single-device
solution for treating wide
neck bifurcation aneurysms.



SL Device



SLS Device

Contact a MicroVention sales associate to learn more
about integrating the WEB[®] device into your practice.



MicroVention Worldwide
Innovation Center

35 Enterprise
Aliso Viejo, CA 92656 USA

MicroVention UK Limited

MicroVention Europe, S.A.R.L.

MicroVention Deutschland GmbH

microvention.com

PH +1.714.247.8000

PH +44 (0) 191 258 6777

PH +33 (1) 39 21 77 46

PH +49 211 210 798-0



Simplify the MOC Process



Manage your CME Credits Online **CMEgateway.org**

Available to Members of Participating Societies

American Board of Radiology (ABR)
American College of Radiology (ACR)
American Roentgen Ray Society (ARRS)
American Society of Neuroradiology (ASNR)
Commission on Accreditation of Medical
Physics Educational Programs, Inc. (CAMPEP)
Radiological Society of North America (RSNA)
Society of Interventional Radiology (SIR)
SNM
The Society for Pediatric Radiology (SPR)

It's Easy and Free!

Log on to CME Gateway to:

- View or print reports of your CME credits from multiple societies from a single access point.
- Print an aggregated report or certificate from each participating organization.
- Link to SAMs and other tools to help with maintenance of certification.

American Board of Radiology (ABR) participation!

By activating ABR in your organizational profile, your MOC-fulfilling CME and SAM credits can be transferred to your own personalized database on the ABR Web site.

Sign Up Today!

go to CMEgateway.org

We're Inside Every Great Neuroradiologist!

ASNR MEMBERS RECEIVE

American Journal of Neuroradiology (AJNR)

The leading neuroradiology research journal, published monthly

Neurographics

Bimonthly educational journal with CME for members

ASNR Annual Meeting

Discounts for members on the field's premier conference

eCME

Online collection of lectures and articles with SA-CME and Category 1 credit

Advocacy

Coding/reimbursement, quality standards and practice guidelines; demonstrating neuroradiology's value!

Networking

Access to 5,000 peers

... And More!

Join the leaders in neuroradiology today!

Learn more at www.asnr.org/join

ASNR

American Society of Neuroradiology

800 Enterprise Dr., Suite 205, Oak Brook, IL 60523 • (630)574-0220 • membership@asnr.org • www.asnr.org

AJNR

AMERICAN JOURNAL OF NEURORADIOLOGY

JANUARY 2020
VOLUME 41
NUMBER 1
WWW.AJNR.ORG

Publication Preview at www.ajnr.org features articles released in advance of print. Visit www.ajnrblog.org to comment on AJNR content and chat with colleagues and AJNR's News Digest at <http://ajnrndigest.org> to read the stories behind the latest research in neuroimaging.

1 PERSPECTIVES *N. Hainc*

REVIEW ARTICLES



2

Emerging Use of Ultra-High-Field 7T MRI in the Study of Intracranial Vascularity: State of the Field and Future Directions *J.W. Rutland, et al.*

ADULT BRAIN



10

Response Assessment in Neuro-Oncology Criteria for Gliomas: Practical Approach Using Conventional and Advanced Techniques *D.J. Leao, et al.*

ADULT BRAIN



21

Lateral Decubitus Digital Subtraction Myelography: Tips, Tricks, and Pitfalls *D.K. Kim, et al.*

SPINE

LEVEL 1 EVIDENCE-BASED MEDICINE



29

Does Increasing Packing Density Using Larger Caliber Coils Improve Angiographic Results of Embolization of Intracranial Aneurysms at 1 Year: A Randomized Trial *J. Raymond, et al.*

INTERVENTIONAL

PRACTICE PERSPECTIVES

35 **Redundant Neurovascular Imaging: Who Is to Blame and What Is the Value?** *E. Beheshtian, et al.*

GENERAL CONTENTS



40

Deep Transfer Learning and Radiomics Feature Prediction of Survival of Patients with High-Grade Gliomas *W. Han, et al.*

ADULT BRAIN
FUNCTIONAL



49

Dynamic Contrast-Enhanced MR Imaging of Nonenhancing T2 High-Signal-Intensity Lesions in Baseline and Posttreatment Glioblastoma: Temporal Change and Prognostic Value *I. Hwang, et al.*

ADULT BRAIN
FUNCTIONAL



57

High-Resolution MRI for Evaluation of Ventriculostomy Tubes: Assessment of Positioning and Proximal Patency *A.M. Blitz, et al.*

ADULT BRAIN



64

Prediction of Hemorrhage after Successful Recanalization in Patients with Acute Ischemic Stroke: Improved Risk Stratification Using Dual-Energy CT Parenchymal Iodine Concentration Ratio Relative to the Superior Sagittal Sinus *D. Byrne, et al.*

ADULT BRAIN

71 **Diffusion Properties of Normal-Appearing White Matter Microstructure and Severity of Motor Impairment in Acute Ischemic Stroke** *C. Ingo, et al.*


ADULT BRAIN
FUNCTIONAL

AJNR (Am J Neuroradiol ISSN 0195-6108) is a journal published monthly, owned and published by the American Society of Neuroradiology (ASNR), 800 Enterprise Drive, Suite 205, Oak Brook, IL 60523. Annual dues for the ASNR include approximately 21% for a journal subscription. The journal is printed by Cadmus Journal Services, 5457 Twin Knolls Road, Suite 200, Columbia, MD 21045; Periodicals postage paid at Oak Brook, IL and additional mailing offices. Printed in the U.S.A. POSTMASTER: Please send address changes to American Journal of Neuroradiology, P.O. Box 3000, Denville, NJ 07834, U.S.A. Subscription rates: nonmember \$410 (\$480 foreign) print and online, \$320 online only; institutions \$470 (\$540 foreign) print and basic online, \$935 (\$1000 foreign) print and extended online, \$380 online only (basic), extended online \$825; single copies are \$35 each (\$40 foreign). Indexed by PubMed/Medline, BIOSIS Previews, Current Contents (Clinical Medicine and Life Sciences), EMBASE, Google Scholar, HighWire Press, Q-Sensei, RefSeek, Science Citation Index, SCI Expanded, Meta/CZI, ReadCube, and Semantic Scholar. Copyright © American Society of Neuroradiology.

	79	Microstructural Integrity of Salvaged Penumbra after Mechanical Thrombectomy <i>M.T. Berndt, et al.</i>	ADULT BRAIN FUNCTIONAL
	86	Visualization of Nigrosome 1 from the Viewpoint of Anatomic Structure <i>N. Arai, et al.</i>	ADULT BRAIN
	92	Structural and Volumetric Brain MRI Findings in Mild Traumatic Brain Injury <i>J.B. Patel, et al.</i>	ADULT BRAIN FUNCTIONAL
	100	Vessel Wall Thickening and Enhancement in High-Resolution Intracranial Vessel Wall Imaging: A Predictor of Future Ischemic Events in Moyamoya Disease <i>A. Kathuveetil, et al.</i>	ADULT BRAIN
	106	Usefulness of Contrast-Enhanced 3D-FLAIR MR Imaging for Differentiating Rathke Cleft Cyst from Cystic Craniopharyngioma <i>M. Azuma, et al.</i>	ADULT BRAIN
	111	Decreased Subcortical T2 FLAIR Signal Associated with Seizures <i>P. Nicholson, et al.</i>	ADULT BRAIN
	115	Unilateral Nonvisualization of a Transverse Dural Sinus on Phase-Contrast MRV: Frequency and Differentiation from Sinus Thrombosis on Noncontrast MRI <i>Y.-M. Chang, et al.</i>	ADULT BRAIN
	122	Emergency Conversion to General Anesthesia Is a Tolerable Risk in Patients Undergoing Mechanical Thrombectomy <i>F. Flottmann, et al.</i>	INTERVENTIONAL
	129	Imaging Triage of Patients with Late-Window (6–24 Hours) Acute Ischemic Stroke: A Comparative Study Using Multiphase CT Angiography versus CT Perfusion <i>M.A. Almekhlafi, et al.</i>	INTERVENTIONAL ADULT BRAIN
	134	Flow-Diversion Treatment for Unruptured Nonsaccular Intracranial Aneurysms of the Posterior and Distal Anterior Circulation: A Meta-Analysis <i>F. Cagnazzo, et al.</i>	INTERVENTIONAL
	140	Reduced Activity of von Willebrand Factor after Flow-Diverting Stent Implantation for Intracranial Aneurysms: A Link to Acquired von Willebrand Disease? <i>I. Oran, et al.</i>	INTERVENTIONAL
	147	Lesion-Specific Language Network Alterations in Temporal Lobe Epilepsy <i>O. Foesleitner, et al.</i>	FUNCTIONAL
	155	CT and MRI Findings of Glomangiopericytoma in the Head and Neck: Case Series Study and Systematic Review <i>C.H. Suh, et al.</i>	HEAD & NECK
	160	Predicting Ischemic Risk Using Blood Oxygen Level–Dependent MRI in Children with Moyamoya <i>N. Dlamini, et al.</i>	PEDIATRICS FUNCTIONAL
	167	Acute Cortical Lesions in MELAS Syndrome: Anatomic Distribution, Symmetry, and Evolution <i>K.D. Bhatia, et al.</i>	PEDIATRICS
	174	Brain MR Imaging of Patients with Perinatal Chikungunya Virus Infection <i>D.G. Corrêa, et al.</i>	PEDIATRICS
	178	Number Needed to Treat with Vertebral Augmentation to Save a Life <i>J.A. Hirsch, et al.</i>	SPINE INTERVENTIONAL
	183	Simple Fluoroscopy-Guided Transforaminal Lumbar Puncture: Safety and Effectiveness of a Coaxial Curved-Needle Technique in Patients with Spinal Muscular Atrophy and Complex Spines <i>J.P. Jacobson, et al.</i>	SPINE INTERVENTIONAL
	189	35 YEARS AGO IN AJNR	

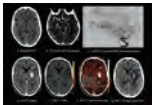
ONLINE FEATURES

LETTERS

- E1 Regarding “The Interpeduncular Angle: A Practical and Objective Marker for the Detection and Diagnosis of Intracranial Hypotension on Brain MRI” *J. Zhang, et al.*
- E2 **Reply** *D. Wang, et al.*
-  E3 **Manganese Uptake and Accumulation in the Human Brain** *V. Blomlie, et al.*

BOOK REVIEWS *R.M. Quencer, Section Editor*

Please visit www.ajnrblog.org to read and comment on Book Reviews.



Patient with preprocedural ASPECTS of 8 showing (A), left M1 occlusion (B), and angiogram showing modified TIC1 3 reperfusion (C). Postthrombectomy dual-energy CT demonstrates parenchymal hyperdensity (D), without hemorrhage on the virtual noncontrast dual-energy CT (E) shown to be contrast staining on the iodine overlay map (F), with maximum iodine concentration measuring 3.4 mg/mL and 428.2% relative to the superior sagittal sinus. NCCT performed 4 days postthrombectomy (G) shows evolving left MCA infarction with parenchymal hemorrhage involving the left lentiform nucleus.



Indicates Editor's Choices selection



Indicates Fellows' Journal Club selection



Indicates open access to non-subscribers at www.ajnr.org



Indicates article with supplemental on-line table



Indicates article with supplemental on-line photo



Indicates article with supplemental on-line video



Evidence-Based Medicine Level 1



Evidence-Based Medicine Level 2

EDITOR-IN-CHIEF

Jeffrey S. Ross, MD

Professor of Radiology, Department of Radiology,
Mayo Clinic College of Medicine, Phoenix, AZ

SENIOR EDITORS

Harry J. Cloft, MD, PhD

Professor of Radiology and Neurosurgery,
Department of Radiology, Mayo Clinic College of
Medicine, Rochester, MN

Christopher G. Filippi, MD

Professor and Vice Chair of Biomedical and
Translational Science,
Donald and Barbara Zucker School of Medicine at
Hofstra/Northwell,
Lenox Hill Hospital and Greenwich Village
Healthplex, New York, NY

Thierry A.G.M. Huisman, MD

Radiologist-in-Chief, Texas Children's Hospital,
Houston, TX

Yvonne W. Lui, MD

Associate Professor of Radiology,
Chief of Neuroradiology,
New York University School of Medicine,
New York, NY

C.D. Phillips, MD, FRCR

Professor of Radiology, Weill Cornell Medical
College, Director of Head and Neck Imaging,
New York-Presbyterian Hospital, New York, NY

Lubdhra M. Shah, MD, MS

Professor of Radiology and Director of Spine
Imaging, University of Utah Department of
Radiology and Imaging Sciences, Salt Lake City, UT

Charles M. Strother, MD

Professor of Radiology, Emeritus, University of
Wisconsin, Madison, WI

STATISTICAL SENIOR EDITOR

Bryan A. Comstock, MS

Senior Biostatistician,
Department of Biostatistics,
University of Washington, Seattle, WA

ARTIFICIAL INTELLIGENCE DEPUTY EDITOR

Peter D. Chang, MD

Assistant Professor-in-Residence,
Departments of Radiological Sciences,
Computer Sciences, and Pathology,
Director, Center for Artificial Intelligence in
Diagnostic Medicine (CAIDM),
University of California, Irvine, Irvine, CA

EDITORIAL BOARD

Ashley H. Aiken, Atlanta, GA
Lea M. Alhilali, Phoenix, AZ
Kubilay Aydin, Istanbul, Turkey
John D. Barr, Dallas, TX
Ari Blitz, Baltimore, MD
Barton F. Branstetter IV, Pittsburgh, PA
Jonathan L. Brisman, Lake Success, NY
Keith Cauley, Danville, PA
James Y. Chen, San Diego, CA
Asim F. Choudhri, Memphis, TN
Daniel Chow, Irvine, CA
J. Matthew Debnam, Houston, TX
Seena Dehkharghani, New York, NY
Yonghong Ding, Rochester, MN
Clifford J. Eskey, Hanover, NH
Saeed Fakhran, Phoenix, AZ
Massimo Filippi, Milan, Italy
Nils D. Forkert, Calgary, Alberta, Canada
Wende N. Gibbs, Hanover, AZ
Christine M. Glastonbury, San Francisco, CA
John L. Go, Los Angeles, CA
Philipp Göltz, Erlangen, Germany
Allison Grayev, Madison, WI
Brent Griffith, Detroit, MI
Ajay Gupta, New York, NY
Rakesh Kumar Gupta, Haryana, India
Lothi Hacein-Bey, Sacramento, CA
Christopher P. Hess, San Francisco, CA
Andrei Holodny, New York, NY
Benjamin Huang, Chapel Hill, NC
Mahesh V. Jayaraman, Providence, RI
Valerie Jewells, Chapel Hill, NC
Christof Karmonik, Houston, TX
Timothy J. Kaufmann, Rochester, MN
Hillary R. Kelly, Boston, MA
Toshitomi Kinoshita, Akita, Japan
Kenneth F. Layton, Dallas, TX
Alexander Lerner, Los Angeles, CA
Michael Lev, Boston, MA
Karl-Olof Lovblad, Geneva, Switzerland
Franklin A. Marden, Chicago, IL
Joseph C. McGowan, Merion Station, PA
Stephan Meckel, Freiburg, Germany
Christopher J. Moran, St. Louis, MO
Takahisa Mori, Kamakura City, Japan
Suresh Mukherji, Ann Arbor, MI
Alexander J. Nemeth, Chicago, IL
Renato Hoffmann Nunes, Sao Paulo, Brazil
Sasan Partovi, Cleveland, OH
Laurent Pierot, Reims, France
Jay J. Pillai, Baltimore, MD
Whitney B. Pope, Los Angeles, CA
Joana Ramalho, Lisbon, Portugal

Otto Rapalino, Boston, MA
Álex Rovira-Cañellas, Barcelona, Spain
Paul M. Ruggieri, Cleveland, OH
Amit M. Saindane, Atlanta, GA
Maksim Shapiro, New York, NY
Timothy Shepherd, New York, NY
Mark S. Shiroishi, Los Angeles, CA
Bruno P. Soares, Baltimore, MD
Maria Vittoria Spampinato, Charleston, SC
Khin Khin Tha, Sapporo, Hokkaido, Japan
Krishnamoorthy Thamburaj, Hershey, PA
Cheng Hong Toh, Taipei, Taiwan
Aquila S. Turk, Greenville, SC
Anja G. van der Kolk, Utrecht, the Netherlands
Willem Jan van Rooij, Tilburg, Netherlands
Arastoo Vossough, Philadelphia, PA
Elysa Widjaja, Toronto, Ontario, Canada
Max Wintermark, Stanford, CA
Ronald L. Wolf, Philadelphia, PA
Kei Yamada, Kyoto, Japan
Carlos Zamora, Chapel Hill, NC
Vahe M. Zohrabian, New Haven, CT

EDITORIAL FELLOW

Hediyeh Baradaran, Salt Lake City, UT

SPECIAL CONSULTANTS TO THE EDITOR

AJNR Blog Editor

Neil Lall, Denver, CO

Case of the Month Editor

Nicholas Stence, Aurora, CO

Case of the Week Editors

Juan Pablo Cruz, Santiago, Chile

Sapna Rawal, Toronto, Ontario, Canada

Classic Case Editor

Sandy Cheng-Yu Chen, Taipei, Taiwan

Health Care and Socioeconomics Editor

Pina C. Sanelli, New York, NY

Physics Editor

Greg Zaharchuk, Stanford, CA

Podcast Editor

Wende N. Gibbs, Phoenix, AZ

Twitter Editor

Roger Jordan, Houston, TX

Official Journal:

American Society of Neuroradiology
American Society of Functional Neuroradiology
American Society of Head and Neck Radiology
American Society of Pediatric Neuroradiology
American Society of Spine Radiology

Founding Editor
Juan M. Taveras

Editors Emeriti
Mauricio Castillo, Robert I. Grossman,
Michael S. Huckabee, Robert M. Quencer

Managing Editor
Karen Halm
Assistant Managing Editor
Laura Wilhelm
Editorial Assistant
Margaret B. Sabato
Executive Director, ASNR
Mary Beth Hepp



Title: Mount Everest. The world's highest mountain stands tall at 8848 m on the left. This photo was taken from Gokyo-Ri peak in Nepal at an altitude of 5357 m, where there is only 50% of the oxygen available at sea level. The trek is worth it, though, as you can see four of the world's highest mountains from this peak, namely Cho Oyo (sixth highest), Makalu (fifth highest), Lhotse (fourth highest), and Everest (highest). Lhotse is on the far right of the image and Nuptse can be seen in between. Notable records on the mountain include its first summit (Sir Edmund Hillary and Tenzing Norgay Sherpa, 1953), first summit without supplemental oxygen (Reinhold Messner and Peter Habeler, 1978), and most summits by one person (Kami Rita Sherpa, 24 summits).

Nicolin Hainc, MD, Attending Neuroradiologist, University Hospital of Zurich, Switzerland

Emerging Use of Ultra-High-Field 7T MRI in the Study of Intracranial Vascularity: State of the Field and Future Directions

J.W. Rutland, B.N. Delman, C.M. Gill, C. Zhu, R.K. Shrivastava, and P. Balchandani



ABSTRACT

SUMMARY: Cerebrovascular disease is a major source of mortality that commonly requires neurosurgical intervention. MR imaging is the preferred technique for imaging cerebrovascular structures, as well as regions of pathology that include microbleeds and ischemia. Advanced MR imaging sequences such as time-of-flight, susceptibility-weighted imaging, and 3D T2-weighted sequences have demonstrated excellent depiction of arterial and venous structures with and without contrast administration. While the advantages of 3T compared with 1.5T have been described, the role of ultra-high-field (7T) MR imaging in neurovascular imaging remains poorly understood. In the present review, we examine emerging neurosurgical applications of 7T MR imaging in vascular imaging of diverse conditions and discuss current limitations and future directions for this technique.

ABBREVIATION: UHF = ultra-high-field

MR imaging at 7T is particularly beneficial to vascular imaging techniques. TOF angiography benefits from increased SNR and lengthening T1s at higher field strengths, allowing more effective tagging of flowing spins.^{1,2} SWI also benefits from increased SNR as well as the enhanced sensitivity of susceptibility effects at 7T.^{3,4} Vessel wall imaging techniques benefit in the same way as other T2-weighted sequences from increased SNR, allowing depiction of smaller structures such as the thickness of the vessel wall. MPRAGE also benefits from increased SNR, permitting smaller voxel volumes and higher-resolution imaging. The benefits along with the limitations of 7T MR imaging, including increased B₀ and B₁ inhomogeneity artifacts, should be examined to clarify the role of this emerging technology in the field of cerebrovascular imaging.

Here, we focus on the vascular components of neurologic protocols at 7T and their value to better diagnose and plan surgery, predict prognosis, and monitor treatment. We cover current primary neurosurgical applications for 7T vascular imaging and discuss areas for future development.

CLINICAL APPLICATIONS

Intracranial Tumors

Glioma. High-grade gliomas are among the most vascularized malignant neoplasms, and angiogenesis is critical to their growth.^{5,6} There is interest in quantifying micro- and macrovascular properties of gliomas to predict tumor grade and better characterize microscopic infiltration (On-line Table 1). Moenninghoff et al⁷ found increasing microvasculature from low- to high-grade gliomas using 7T T2* MR imaging; 7T depicted susceptibility patterns that indicated microvasculature in 53% of patients compared with 33% using 1.5T MR imaging. While the authors attribute this difference to increased sensitivity of susceptibility contrast at 7T, there is a possibility that some of these findings could be false-positives due to increased conspicuity of imaging features imparted by a higher SNR at an ultra-high-field (UHF) strength. Differentiation of these potential false-positives from true clinical findings is an important area of future investigation.⁷ Paek et al⁸ also found that T2* 7T MR imaging provided superior depiction of glioma microvasculature compared with 1.5T MR imaging and reported gliomas with high intratumoral vasculature in 33.3% of cases at 7T compared with 12.5% at 1.5T. Christoforidis et al⁹ used UHF gradient-echo MR imaging to demonstrate that tumoral pseudoblood

Received August 23, 2019; accepted after revision October 15.

From the Translational and Molecular Imaging Institute (J.W.R., B.N.D., P.B.) and Departments of Neurosurgery (J.W.R., C.M.G., R.K.S.) and Diagnostic, Molecular, and Interventional Radiology (B.N.D.), Icahn School of Medicine at Mount Sinai, New York, New York; and Department of Radiology and Biomedical Imaging (C.Z.), University of California San Francisco, San Francisco, California.

This work was supported by National Institutes of Health R01 CA202911, Icahn School of Medicine Capital Campaign, and Translational and Molecular Imaging Institute and Department of Radiology, Icahn School of Medicine at Mount Sinai.

Please address correspondence to John Rutland, BA, Translational and Molecular Imaging Institute, Icahn School of Medicine at Mount Sinai, 1470 Madison Ave; Floor 1, New York, NY 10129; e-mail: jack.rutland@icahn.mssm.edu; @JohnRutland20

Indicates open access to non-subscribers at www.ajnr.org

Indicates article with supplemental on-line appendix and table.

Indicates article with supplemental on-line photos.

<http://dx.doi.org/10.3174/ajnr.A6344>

correlated histologically with foci of increased microvasculature and overall tumor grade. These studies suggest that 7T MR imaging may be useful in the noninvasive evaluation of tumor features that contribute to the World Health Organization grade, including microvasculature and necrosis, and could facilitate early stratification and risk assessment for patients with gliomas. However, multiple authors have also conceded that susceptibility artifacts near large air-tissue interfaces and the skull base could compromise the utility of 7T in some patients.^{8,10}

MR imaging at 7T may also assist in identifying parenchymal areas with an increased likelihood of microscopic high-grade glioma infiltration, which is challenging at clinical field strengths and important for determining resection margins.¹¹ Various imaging metrics, including those based on DWI, have been used to identify white matter infiltration by gliomas that cannot be resolved at lower field strengths. In addition, 7T SWI has proved superior in the delineation of venous structures.³ Grabner et al⁴ found that 7T SWI correctly predicted high-grade gliomas in 23.8% more cases than 3T SWI, suggesting that vasculature quantification at 7T may offer increased sensitivity for imaging glioblastoma multiforme preoperatively. These results concur with those of Moenninghoff et al,⁷ who also found higher tumor microvasculature in high-grade gliomas compared with low-grade lesions using 7T SWI.

Clinical applications of TOF angiography have been somewhat limited due to low spatial resolution attained at 1.5T and 3T; therefore, DSA remains the criterion standard angiographic technique. However, detectability of arterial structures using 7T TOF could be useful in noninvasive characterization of intratumoral vasculature. Advantages of TOF at 7T include increased SNR, longer T1 relaxation times augmenting vessel-tissue contrast, and inherently hyperintense arterial vasculature at higher field strengths overall.^{1,2} Radbruch et al¹² demonstrated the feasibility of 7T TOF in imaging intratumoral vessels, reporting excellent delineation of vasculature in all 12 patients, even though tortuous and highly permeable arteries in glioblastoma multiforme traditionally challenge delineation by TOF. Furthermore, because gliomas tend to display greater angiogenesis with increasing grade, 7T TOF may be useful in noninvasive grading of gliomas;¹³ 7T TOF angiography may also prove useful in monitoring the success of antiangiogenic agents in slowing tumor growth.¹⁴

Brain Metastases. Early detection and delineation of brain metastases is critical in optimizing treatment planning. Historical strategies at conventional strengths, including higher dose contrast and magnetization transfer contrast imaging, have increased the detectability of enhancing metastases.¹⁵ Exploitation of susceptibility is another method to identify subtle lesions. Just as 3T demonstrates superior sensitivity for brain metastases compared with 1.5T,¹⁶ 7T MR imaging demonstrates 20% more cerebral microhemorrhages on SWI compared with 1.5T, even though the quantity of brain metastases on T1-weighted MPRAGE is essentially equivalent.¹⁵ Because microscopic bleeding is common in brain metastases, 7T SWI may increase detection of very subtle metastatic disease. Direct comparison with 3T SWI is warranted. Increased susceptibility at higher field strengths may augment identification of metastatic brain foci over conventional techniques.

Skull Base Tumors. The skull base is anatomically complex. High-resolution imaging can contribute greatly to preoperative planning. de Rotte et al¹⁷ were the first to demonstrate the feasibility of pituitary adenoma imaging at 7T; however, their study did not report on vascular sequences. Barrett et al¹⁰ used a semiquantitative rating system to demonstrate superior visualization of internal carotid artery branches and vasculature within skull base tumors using 7T TOF, despite higher B₀ and B₁ inhomogeneity artifacts at 7T. It does appear that TOF could benefit surgical navigation to minimize vascular injury during endoscopic pituitary surgery (Fig 1). Additional limitations associated with 7T skull base imaging include artifacts from proximity to large air-tissue interfaces, such as the sphenoid sinus.¹⁷ Future technical development including advanced shimming and parallel transmit will be important to overcome local magnetic field inhomogeneity.

Most important, no study has directly compared noncontrast 7T TOF with contrast-enhanced 3T in the detection of intratumoral and adjacent vascular structures. Such an analysis is warranted because increased visibility of arterial structures at 7T may ultimately limit contrast administration for some patients.

In their study of a homogeneous series of meningiomas at 7T, Song et al¹⁸ reported increased peri- and intratumoral vasculature and enhanced delineation of the tumor-brain interface in 4 patients with supratentorial meningiomas. Although the current diagnostic utility of conventional MR imaging for meningioma is already high, increased spatial resolution and SNR make 7T well-positioned to improve vascular characterization among these tumors.

Treatment Monitoring for Tumors. Microhemorrhages are common sequelae following radiation therapy for intracranial neoplasms.¹⁹ Lupo et al²⁰ reported high rates of microbleeds on 7T SWI among patients with glioma 2 years after radiation. Another study of 7T SWI in 113 patients having undergone focal radiation found a 100% incidence of at least 1 microbleed 2 years following radiation.²¹ Belliveau et al¹⁹ further demonstrated the increased ability of 7T to detect radiation-related cerebral microbleeds using SWI, apparent transverse relaxation, and quantitative susceptibility mapping. Bian et al²³ found significantly more cerebral microbleeds in 7/10 patients with gliomas who underwent radiation therapy using 7T SWI compared with 3T SWI.²² However, when patients with 3 relatively inferior tumors were included, the effect between field strengths was not significant, suggesting that 7T SWI is more sensitive away from areas prone to inherent susceptibility artifacts.²³ SWI at 7T, combined with tumor location consideration, may offer additional diagnostic value in early detection of radiation-induced microvascular damage.

In addition to imaging vascular damage from radiation therapy, there is growing interest in leveraging 7T vascular imaging to monitor the efficacy of drug therapy for aggressive intracranial neoplasms.²⁴ Grabner et al²⁴ used 7T SWI to study longitudinal glioma microvasculature changes during antiangiogenic therapy, concluding that 7T SWI is useful for antiangiogenic therapy monitoring in patients with advanced disease. The feasibility of high-resolution imaging of intratumoral arteries has also been demonstrated with 7T TOF¹²; however, its utility in assessing antiangiogenic efficacy has not yet been defined.

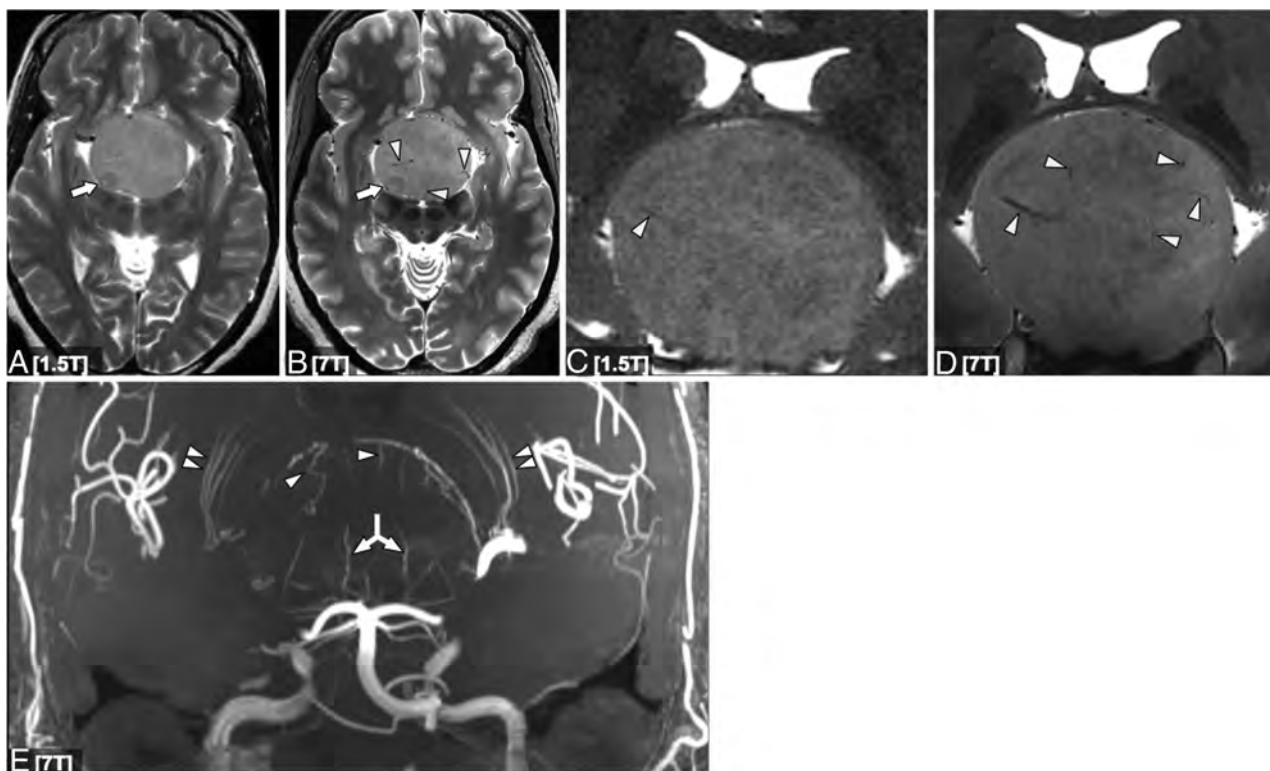


FIG 1. Axial (A and B) and coronal (C and D) T2-weighted 1.5T (A and C) and 7T (B and D) images in a patient with a giant pituitary macroadenoma. C and D, Magnified approximately 250% compared with A and B. Although lesion margins are conspicuous at 1.5T, the 7T image provides a better definition of the internal architecture, including intrinsic adenoma vasculature (white arrowheads in B, C, and D). Both strengths show a nodule of slightly lower signal posterolaterally (arrows in A and B), but internal architecture is again better seen at 7T. Coronal MIP projection of a 7T time-of-flight MRA in the same patient (E) shows striate artery displacement (double arrowheads), as well as a recruited posterior circulation supply inferiorly (double-headed arrow) and additional vessels arising from the anterior cerebral artery superiorly (arrowheads).

Dynamic contrast-enhanced imaging with 7T may also play an increasingly important role in the management of intracranial tumors and is a worthwhile area of technical development (On-line Appendix and On-line Fig 1).

Epilepsy

The benefits of 7T protocols for studying previously nonlesional epilepsy have recently been described.²⁵ Vascular imaging sequences, in conjunction with structural MR imaging, hold promise in localizing cryptogenic seizure-onset zones in the setting of vascular lesions. It is estimated that up to 70% of symptomatic cavernomas cause seizures, approximately 40% of which are drug-resistant.²⁶⁻²⁸ Seizure freedom following cavernoma surgery is dependent on complete resection of the vascular malformation and metabolic products in the surrounding hemosiderin ring, and approximately 25% of patients with cavernoma-related epilepsy fail to achieve postoperative seizure freedom.²⁹ The absence of an identifiable epileptogenic focus can disqualify certain patients from neurosurgery, necessitate invasive intracranial monitoring to localize seizure onset zone, and predispose patients who do progress to an operation to inferior postoperative outcomes.³⁰ Advanced imaging tools may help clarify epileptogenesis and guide neurosurgical therapy.

Schlamann et al³¹ found a greater number of cavernomas using T2*-weighted gradient-echo imaging at 7T compared with 1.5T, consistent with enhanced susceptibility that is known to

occur at higher fields. This finding is supported by a prior study that reported increased cavernoma detectability at 3T compared with 1.5T SWI.³² In a series of 37 patients with epilepsy with various etiologies who had negative findings on MR imaging at a lower field strength, small cavernomas were identified in 3 patients, 2 of which were likely related to epileptogenesis.³³ Developmental venous anomalies were detected in 4 other patients using 7T SWI, 2 of which coincided with regions of electrographic abnormality, suggesting possible occult cavernomas.³³ In another study of 11 patients with epilepsy with negative findings on MR imaging, 1 patient's diagnosis changed from suspected focal cortical dysplasia to cavernoma based on 7T SWI.³⁴ Examples of 7T SWI for polymicrogyria and cavernoma as epileptogenic foci are shown in Fig 2 and On-line Fig 2, respectively.

While these studies provide compelling evidence to support the use of 7T in vascular epilepsy imaging, no study has directly compared cavernoma detectability between 3T and 7T SWI. Comparison of Engel and quality-of-life scores between patients who underwent preoperative 7T versus conventional MR imaging may clarify the role of 7T imaging in treating cavernoma-related epilepsy. Although the importance of hemosiderin ring excision in cavernoma surgery is controversial,^{35,36} 7T MR imaging may facilitate a more precise definition of hemosiderin to optimize the resection of perilesional hemosiderin deposits.

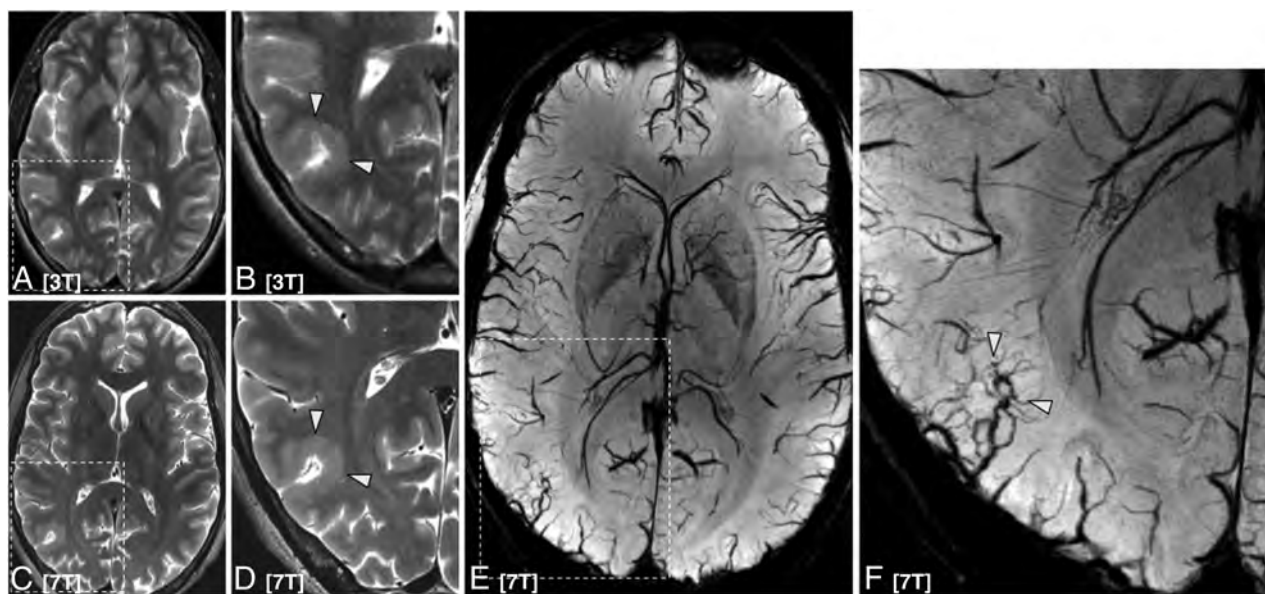


FIG 2. A patient with epilepsy with a subtle right-sided parieto-occipital polymicrogyria faintly seen on axial T2-weighted imaging at 3T (A, magnified *inset* B) with improved characterization at 7T (C, magnified *inset* D). Internal architecture and heterogeneity are also much better appreciated at 7T. SWI 7T minimum-intensity-projection demonstrates a cluster of venous structures (arrowheads) associated with the polymicrogyria (E, magnified *inset* F).

Neurovascular Pathology

Aneurysm. Intracranial aneurysms occur in approximately 3% of the general population. Rupture and subarachnoid hemorrhage are associated with considerable morbidity and mortality.³⁷ While neurosurgical treatment for intracranial aneurysms, including surgical clipping and endovascular coiling, are effective therapies, these procedures are not without risk. Therefore, identifying patients with aneurysms who are at high risk for rupture is critical in identifying appropriate candidates for preventative treatment. Advantages of 7T vessel wall imaging are increased SNR, higher spatial resolution, and greater CSF suppression compared with 3T.³⁸⁻⁴⁰ However, 7T imaging is limited by artifacts caused by increased transmit field (B_1) inhomogeneity. The superiority over lower-field MR imaging in vessel wall imaging remains inadequately understood.

Using gadolinium-enhanced MPRAGE 7T MR imaging, Sato et al⁴¹ reported 2 discrete aneurysm wall microstructures that are poorly resolved with lower-resolution MR imaging at lower field strengths: partial or complete enhancement of the inner wall (neovascularization) and outer wall (formation of the vasa vasorum). The latter pattern correlated histologically with vessel wall instability, suggesting that contrast-enhanced 7T MR imaging may be useful to characterize thrombosed intracranial aneurysms and could be a valuable clinical tool for determining rupture potential. Similarly, in comparing 1.5T and 7T TOF, Wrede et al² reported that detectability and characterization of unruptured intracranial aneurysms were increased at 7T. In another study, 7T TOF provided delineation of unruptured intracranial aneurysms comparable with DSA, which is the current criterion standard. Such evidence suggests that 7T MR imaging may obviate ionizing radiation and iodinated contrast agent administration in the future.⁴² In a study of 21 saccular and 11 fusiform intracranial aneurysms using 0.4-mm isotropic 7T contrast-enhanced black-blood MR imaging, fusiform aneurysms exhibited superior wall

enhancement due to increased resolution, image quality, and involvement of a larger surface than saccular aneurysms, reflecting differences in pathology.⁴³

Imaging hemodynamics and quantifying forces within vessels are another important component of predicting aneurysm rupture risk. Blankena et al⁴⁴ used a TSE-based vessel wall sequence and phase-contrast 7T MR imaging to demonstrate an inverse relationship between vessel wall thickness and wall shear stress. Other advanced imaging techniques, including volume pulsation quantification, rotational angiography, and 4D flow, have been explored as aneurysm-rupture risk predictors at lower-field MR imaging; however, their implementation at 7T remains limited. As a result of artifacts, UHF quantification of volume pulsation of unruptured cerebral aneurysms is not currently possible, even with the high spatial resolution of 7T data.⁴⁵ Additional applications of 7T TOF imaging have included differentiation between cerebral aneurysms and infundibula.⁴⁶

Despite these studies, it remains unclear whether 7T is more sensitive than lower-field MR imaging in detecting and characterizing cerebral aneurysms because there are relatively few direct comparison studies.

Atherosclerosis. Advanced high-resolution imaging methods may be useful in predicting atherosclerotic plaque rupture, embolization, and stroke (Fig 3).⁴⁷ Hartevelde et al,⁴⁸ who used 3D gadolinium-enhanced T1-weighted 7T MR imaging to quantify atherosclerotic lesion burden in patients with posterior cerebral ischemia, confirmed greater lesion burden in the posterior cerebral artery. These results suggest that 7T contrast-enhanced vessel wall imaging may aid in the association between intracranial vessel wall lesions and ischemic events. Direct comparison of vessel wall imaging in an elderly asymptomatic population confirmed greater vessel wall visibility and more lesions at 7T compared with 3T.⁴⁹ These authors suggested that the conspicuity of

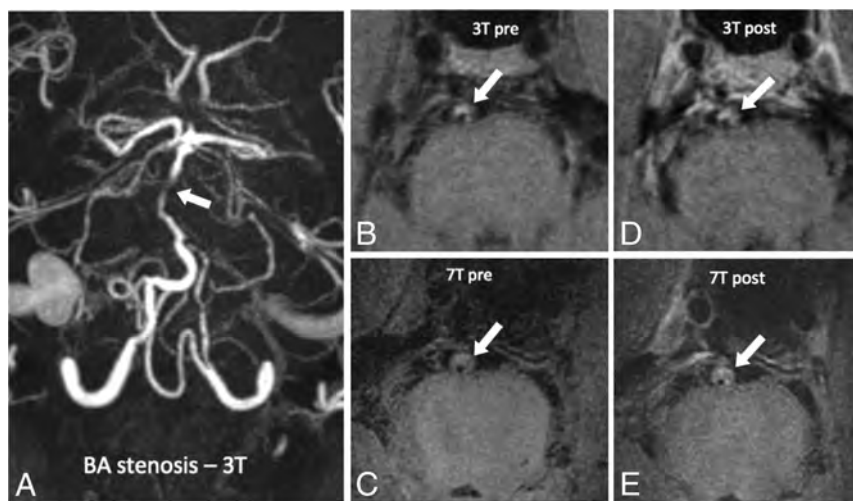


FIG 3. A 73-year-old man with a posterior circulation stroke, an occluded left vertebral artery, and stenosis of the basilar artery. TOF angiography at 3T of a patient with basilar artery stenosis (white arrow, A). Pre- and postcontrast vessel wall imaging at 3T (B and C) and 7T (D and E) in a patient with basilar artery atherosclerotic plaque (white arrows indicate areas of stenosis).

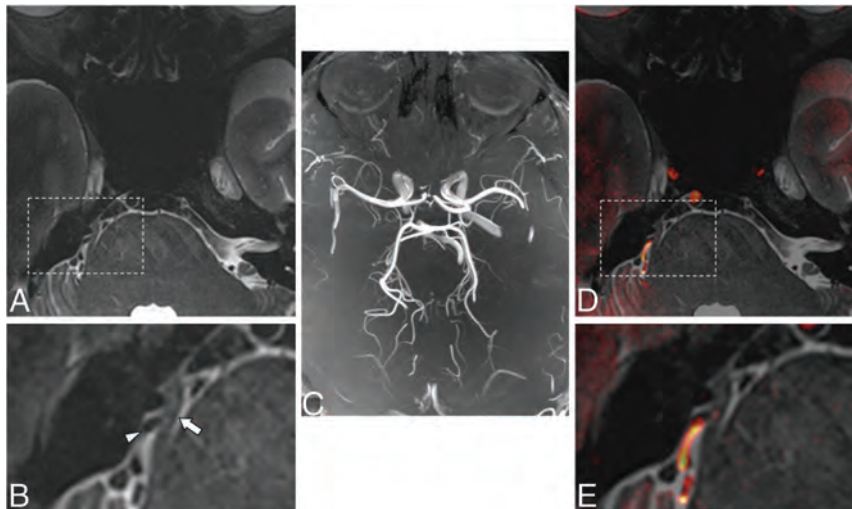


FIG 4. Axial T2-weighted image at 7T of a patient with classic trigeminal neuralgia and associated right-sided neurovascular compression (arrow indicates right trigeminal nerve; arrowhead indicates artery in A and magnified inset B). There may be subtle hyperintensity within the nerve itself. Whole-brain maximum intensity time-of-flight projection at 7T (C) and fused gray-scale T2 and color-encoded TOF (D and E, at same locations as A and B) show orientation of the vessels and nerve and resultant neurovascular compression.

vessel wall lesions in the proximal anterior cerebral and posterior cerebral arteries is optimally imaged with 7T MR imaging.⁵⁰ While 7T has been used to precisely measure circle of Willis vessel wall thickness in symptomatic and asymptomatic patients ex vivo,⁵⁰ a direct comparison between symptomatic and asymptomatic patients in vivo is required for more definitive clinical utility.

A report on a cohort with mixed pathologies, including cerebral atherosclerotic lesions and aneurysms, compared vessel wall imaging with 3T and 7T T1-weighted sampling perfection with application-optimized contrasts by using different flip angle evolution (SPACE sequence; Siemens,

Erlangen, Germany).⁵¹ MR imaging at 7T offered superior vessel wall characterization compared with 3T and greater visualization of the fibrous cap and lipid core among atherosclerotic plaques at 7T over 3T. Therefore, there may be a potential role of 7T MR imaging for diagnosis and risk stratification in intracranial vascular disease.⁵¹ By means of high-resolution 7T vessel wall imaging to determine the prevalence of vessel wall lesions, 96% of patients with vascular disease had at least 1 vessel wall lesion, nearly 3-fold the rate reported by the Atherosclerosis Risk in Communities Study at 3T.^{52,53} This discrepancy was attributed to differences in cohorts. Increased SNR at 7T MR imaging did contribute to higher detection of lesions. While these results suggest that 7T MR imaging may be useful in screening for intracranial vessel lesions and quantifying overall lesion burden, future studies are required to determine whether the smaller lesions detected only at UHF are clinically relevant.

Areas of wall thickening on imaging correspond to regions of advanced atherosclerosis with ex vivo 7T MR imaging.⁵⁴ Additionally, 7T signal heterogeneity permitted spatial differentiation of constituent plaque components, including macrophages and collagen.⁵⁴ Similar morphologic vessel wall properties at 3T and 7T, including vessel wall and luminal areas, were reported by others.⁵⁵ However, 7T exhibited a significantly higher vessel wall SNR and contrast-to-noise ratio for both T1- and T2-weighted sequences.⁵⁵ These results are similar to those of another carotid wall imaging study that reported sig-

nificantly higher SNR at 7T compared with 3T, suggesting that 7T may be superior in diagnosing carotid vessel wall pathology.⁵⁶ Majidi et al⁵⁷ correlated in vitro intravascular sonography and 7T MR imaging findings with histology, concluding that 7T MR imaging is a reliable method of detecting burden within intracranial arteries.

Stroke. MR imaging at 7T has been used to characterize infarct morphology.⁵⁸ When similar stroke protocols at 3T and 7T in patients with subacute and chronic stroke were compared, higher spatial resolution at 7T revealed more subtle features of ischemic lesions and infarct morphology compared with lower-field MR

imaging.⁵⁸ Prior studies have successfully used 7T MR imaging to image occlusive changes in lenticulostriate arteries in acute⁵⁹ and chronic⁶⁰ stroke. Lenticulostriate arteries are difficult to image with conventional modalities due to their small size, but advances in 7T imaging have permitted excellent visualization at improved resolution with both T2-weighted and TOF imaging (On-line Fig 3).^{59–61} However, a direct comparison between 7T and lower field strengths for visualization of lenticulostriate artery features such as occlusion has not yet been quantified.

Moyamoya Vasculopathy. MR imaging at 7T has been applied to Moyamoya vasculopathy.⁶² Because revascularization surgery is a common treatment, high-resolution arterial imaging by DSA or CT angiography is used to plan surgery. However, 7T imaging may obviate contrast and radiation techniques. If one compared DSA, 3T MRA, and 7T MRA, all 3 were of diagnostic value, but 7T TOF was superior to 3T for detecting disease-specific small-vessel pathology.⁶² Furthermore, 7T and DSA provided similar results, despite motion artifacts being observed at 7T.⁶² While there were no significant differences between ICA diameters or ivy sign scores between field strengths, 7T exhibited higher sensitivity and specificity than 3T for detecting flow voids and provided superior depiction of slow-flowing blood within peripheral arteries.⁶³ These preliminary studies using 7T MR imaging in characterizing abnormal vascular networks among patients with Moyamoya disease are promising and warrant further investigation.

Trigeminal Neuralgia. Trigeminal neuralgia is another pathology in which 7T MR imaging may find use. Vascular compression of the trigeminal nerve is the most common etiology; TOF plays an important role in diagnosing neurovascular conflict.⁶⁴ TOF at 7T facilitates increased visualization of first- and second-order arterial branches that are poorly depicted at 1.5T or 3T.⁶⁵ While trigeminal neuralgia can present without vascular compression,⁶⁴ some cases of MR imaging negative for trigeminal neuralgia may result from offending vessels that are too small to see by conventional imaging methods. Therefore, 7T TOF may be particularly useful for patients with trigeminal neuralgia in whom lower-field scanning fails to confirm vascular compression. Although studies have applied 7T MR imaging to trigeminal imaging,⁶⁶ no 7T study has coupled high-resolution TOF with structural or diffusion MR imaging to characterize neurovascular compression. Fusion of structural and high-resolution TOF imaging in trigeminal neuralgia is possible (Fig 4). Therefore, studies applying these techniques in patients with trigeminal neuralgia with nondiagnostic clinical MR imaging may clarify the value of 7T TOF in the diagnosis of neuropathic pain.

CONCLUSIONS

We described the emerging roles of vascular 7T MR imaging in neurosurgery and discussed current limitations of UHF neuroimaging. There has been considerable effort to apply vascular 7T MR imaging to conditions such as gliomas and vessel wall

imaging, yet many unexplored applications of vascular imaging remain. The superior resolution and SNR of 7T compared with lower-field MR imaging in certain brain regions, coupled with technical developments that minimize susceptibility artifacts, are expected to expand the increasingly important role of 7T in the work-up of various neurosurgical diseases.

Disclosures: Bradley N. Delman—UNRELATED: Consultancy: Bayer HealthCare; Payment for Lectures Including Service on Speakers Bureaus: Bayer HealthCare. Priti Balchandani—RELATED: Grant: National Institutes of Health*; UNRELATED: Employment: Icahn School of Medicine at Mount Sinai; Grants/Grants Pending: National Institutes of Health*; Patents (Planned, Pending or Issued): GE Healthcare, Siemens; Royalties: GE Healthcare, Siemens; OTHER RELATIONSHIPS: Dr Priti Balchandani (the Principal Investigator in this study) is a named inventor on patents relating to MRI and radiofrequency pulse design. The patents have been licensed to GE Healthcare, Siemens, and Philips International. Dr Balchandani receives royalty payments relating to these patents. Dr Balchandani is a named inventor on patents relating to Slice-Selective Adiabatic Magnetization T2-Preparation for efficient T2-weighted imaging at ultra-high-field strengths, Methods for Producing a Semi-Adiabatic Spectral-Spatial Spectroscopic Imaging Sequence and Devices Thereof, and Semi-Adiabatic Spectral-Spatial Spectroscopic Imaging. These patents have been filed through Mount Sinai Innovation Partners; they remain unlicensed, there is no discussion to license them in the near future, and there are, consequently, no royalties revolving around them. Raj Shrivastava—RELATED: Grant: National Institutes of Health R01 CA202911.* *Money paid to the institution.

REFERENCES

- Balchandani P, Naidich TP. **Ultra-high-field MR neuroimaging.** *AJNR Am J Neuroradiol* 2015;36:1204–15 CrossRef Medline
- Wrede KH, Dammann P, Mönninghoff C, et al. **Non-enhanced MR imaging of cerebral aneurysms: 7 Tesla versus 1.5 Tesla.** *PLoS One* 2014;9:e84562 CrossRef Medline
- Deistung A, Rauscher A, Sedlacik J, et al. **Susceptibility weighted imaging at ultra high magnetic field strengths: theoretical considerations and experimental results.** *Magn Reson Med* 2008;60:1155–68 CrossRef Medline
- Grabner G, Kiesel B, Wöhrer A, et al. **Local image variance of 7 Tesla SWI is a new technique for preoperative characterization of diffusely infiltrating gliomas: correlation with tumour grade and IDH1 mutational status.** *Eur Radiol* 2017;27:1556–67 CrossRef Medline
- Brat DJ, Van Meir EG. **Glomeruloid microvascular proliferation orchestrated by VPF/VEGF: a new world of angiogenesis research.** *Am J Pathol* 2001;158:789–96 CrossRef Medline
- Brem S. **The role of vascular proliferation in the growth of brain tumors.** *Clin Neurosurg* 1976;23:440–43 Medline
- Moenninghoff C, Maderwald S, Theysohn JM, et al. **Imaging of adult astrocytic brain tumours with 7T MRI: preliminary results.** *Eur Radiol* 2010;20:704–13 CrossRef Medline
- Paek SL, Chung YS, Paek SH, et al. **Early experience of pre- and post-contrast 7.0T MRI in brain tumors.** *J Korean Med Sci* 2013;28:1362–72 CrossRef Medline
- Christoforidis GA, Yang M, Abduljalil A, et al. **“Tumoral pseudo-blush” identified within gliomas at high-spatial-resolution ultra-high-field-strength gradient-echo MR imaging corresponds to microvasculature at stereotactic biopsy.** *Radiology* 2012;264:210–17 CrossRef Medline
- Barrett TF, Dyvorne HA, Padormo F, et al. **First application of 7-T magnetic resonance imaging in endoscopic endonasal surgery of skull base tumors.** *World Neurosurg* 2017;103:600–10 CrossRef Medline
- Regnery S, Knowles BR, Paech D, et al. **High-resolution FLAIR MRI at 7 Tesla for treatment planning in glioblastoma patients.** *Radiother Oncol* 2019;130:180–84 CrossRef Medline
- Radbruch A, Eidel O, Wiestler B, et al. **Quantification of tumor vessels in glioblastoma patients using time-of-flight angiography at 7 Tesla: a feasibility study.** *PLoS One* 2014;9:e110727 CrossRef Medline

13. Wen PY, Kesari S. **Malignant gliomas in adults.** *N Engl J Med* 2008;359:492–507 CrossRef Medline
14. Emblem KE, Mouridsen K, Bjørnerud A, et al. **Vessel architectural imaging identifies cancer patient responders to anti-angiogenic therapy.** *Nat Med* 2013;19:1178 CrossRef Medline
15. Monninghoff C, Maderwald S, Theysohn JM, et al. **Imaging of brain metastases of bronchial carcinomas with 7T MRI: initial results.** *Rofo* 2010;182:764–72 CrossRef Medline
16. Nobauer-Huhmann IM, Ba-Ssalamah A, Mlynarik V, et al. **Magnetic resonance imaging contrast enhancement of brain tumors at 3 Tesla versus 1.5 Tesla.** *Invest Radiol* 2002;37:114–19 CrossRef Medline
17. de Rotte AA, van der Kolk AG, Rutgers D, et al. **Feasibility of high-resolution pituitary MRI at 7.0 Tesla.** *Eur Radiol* 2014;24:2005–11 CrossRef Medline
18. Song SW, Son YD, Cho Z-H, et al. **Experience with 7.0 T MRI in patients with supratentorial meningiomas.** *J Korean Neurosurg Soc* 2016;59:405–09 CrossRef Medline
19. Belliveau JG, Bauman GS, Tay KY, et al. **Initial investigation into microbleeds and white matter signal changes following radiotherapy for low-grade and benign brain tumors using ultra-high-field MRI techniques.** *AJNR Am J Neuroradiol* 2017;38:2251–56 CrossRef Medline
20. Lupo JM, Chuang CF, Chang SM, et al. **7-Tesla susceptibility-weighted imaging to assess the effects of radiotherapy on normal-appearing brain in patients with glioma.** *Int J Radiat Oncol Biol Phys* 2012;82:e493–500 CrossRef Medline
21. Morrison MA, Hess CP, Clarke JL, et al. **Risk factors of radiotherapy-induced cerebral microbleeds and serial analysis of their size compared with white matter changes: a 7T MRI study in 113 adult patients with brain tumors.** *J Magn Reson Imaging* 2019;50:868–77 CrossRef Medline
22. Nandigam RN, Viswanathan A, Delgado P, et al. **MR imaging detection of cerebral microbleeds: effect of susceptibility-weighted imaging, section thickness, and field strength.** *AJNR Am J Neuroradiol* 2009;30:338–43 CrossRef Medline
23. Bian W, Hess CP, Chang SM, et al. **Susceptibility-weighted MR imaging of radiation therapy-induced cerebral microbleeds in patients with glioma: a comparison between 3T and 7T.** *Neuroradiology* 2014;56:91–96 CrossRef Medline
24. Grabner G, Nobauer I, Elandt K, et al. **Longitudinal brain imaging of five malignant glioma patients treated with bevacizumab using susceptibility-weighted magnetic resonance imaging at 7T.** *Magn Reson Imaging* 2012;30:139–47 CrossRef Medline
25. Rondinoni C, Magnun C, Vallota da Silva A, et al. **Epilepsy under the scope of ultra-high field MRI.** *Epilepsy Behav* 2019 Jul 10. [Epub ahead of print] CrossRef Medline
26. Bertalanffy H, Benes L, Miyazawa T, et al. **Cerebral cavernomas in the adult. Review of the literature and analysis of 72 surgically treated patients.** *Neurosurg Rev* 2002;25:1–53; discussion 54–55 Medline
27. Rosenow F, Alonso-Vanegas MA, Baumgartner C, et al. **Cavernoma-Related Epilepsy: Review and Recommendations for Management—Report of the Surgical Task Force of the ILAE Commission on Therapeutic Strategies.** *Epilepsia* 2013;54:2025–35 CrossRef Medline
28. Ryvlin P, Mauguère F, Sindou M, et al. **Interictal cerebral metabolism and epilepsy in cavernous angiomas.** *Brain* 1995;118:677–87 CrossRef Medline
29. Englot DJ, Han SJ, Lawton MT, et al. **Predictors of seizure freedom in the surgical treatment of supratentorial cavernous malformations.** *J Neurosurg* 2011;115:1169–74 CrossRef Medline
30. Leeman-Markowski B. **Review of MRI-negative epilepsy.** *JAMA Neurol* 2016;73:1377 CrossRef
31. Schlamann M, Maderwald S, Becker W, et al. **Cerebral cavernous hemangiomas at 7 Tesla: initial experience.** *Acad Radiology* 2010;17:3–6 CrossRef Medline
32. Pinker K, Stavrou I, Szomolanyi P, et al. **Improved preoperative evaluation of cerebral cavernomas by high-field, high-resolution susceptibility-weighted magnetic resonance imaging at 3 Tesla: comparison with standard (1.5 T) magnetic resonance imaging and correlation with histopathological findings: preliminary results.** *Invest Radiol* 2007;42:346–51 CrossRef Medline
33. Feldman RE, Delman BN, Pawha PS, et al. **7T MRI in epilepsy patients with previously normal clinical MRI exams compared against healthy controls.** *PLoS One* 2019;14:e0213642 CrossRef Medline
34. Colon AJ, van Osch MJ, Buijs M, et al. **Detection superiority of 7 T MRI protocol in patients with epilepsy and suspected focal cortical dysplasia.** *Acta Neurol Belg* 2016;116:259–69 CrossRef Medline
35. Baumann CR, Schuknecht B, Lo Russo G, et al. **Seizure outcome after resection of cavernous malformations is better when surrounding hemosiderin-stained brain also is removed.** *Epilepsia* 2006;47:563–66 CrossRef Medline
36. Yeon JY, Kim JS, Choi SJ, et al. **Supratentorial cavernous angiomas presenting with seizures: surgical outcomes in 60 consecutive patients.** *Seizure* 2009;18:14–20 CrossRef Medline
37. Vlak MH, Algra A, Brandenburg R, et al. **Prevalence of unruptured intracranial aneurysms, with emphasis on sex, age, comorbidity, country, and time period: a systematic review and meta-analysis.** *Lancet Neurol* 2011;10:626–36 CrossRef Medline
38. Umutlu L, Theysohn N, Maderwald S, et al. **7 Tesla MPRAGE imaging of the intracranial arterial vasculature: nonenhanced versus contrast-enhanced.** *Acad Radiol* 2013;20:628–34 CrossRef Medline
39. Vergouwen MDI, Backes D, van der Schaaf IC, et al. **Gadolinium enhancement of the aneurysm wall in unruptured intracranial aneurysms is associated with an increased risk of aneurysm instability: a follow-up study.** *AJNR Am J Neuroradiol* 2019;40:1112 CrossRef
40. van der Kolk AG, Hendrikse J, Brundel M, et al. **Multi-sequence whole-brain intracranial vessel wall imaging at 7.0 tesla.** *Eur Radiol* 2013;23:2996–3004 CrossRef Medline
41. Sato T, Matsushige T, Chen B, et al. **Wall contrast enhancement of thrombosed intracranial aneurysms at 7T MRI.** *AJNR Am J Neuroradiol* 2019;40:1106–11 CrossRef Medline
42. Wrede KH, Matsushige T, Goericke SL, et al. **Non-enhanced magnetic resonance imaging of unruptured intracranial aneurysms at 7 Tesla: comparison with digital subtraction angiography.** *Eur Radiol* 2017;27:354–64 CrossRef Medline
43. Liu X, Zhang Z, Zhu C, et al. **Wall enhancement of intracranial saccular and fusiform aneurysms may differ in intensity and extension: a pilot study using 7-T high-resolution black-blood MRI.** *Eur Radiol* 2019 Jun 19. [Epub ahead of print] CrossRef Medline
44. Blankena R, Kleinloog R, Verweij BH, et al. **Thinner regions of intracranial aneurysm wall correlate with regions of higher wall shear stress: a 7T MRI study.** *AJNR Am J Neuroradiol* 2016;37:1310–17 CrossRef Medline
45. Kleinloog R, Zwanenburg JJ, Schermers B, et al. **Quantification of intracranial aneurysm volume pulsation with 7T MRI.** *AJNR Am J Neuroradiol* 2018;39:713–19 CrossRef Medline
46. Wermer MJ, van Walderveen MA, Garpebring A, et al. **7 Tesla MRA for the differentiation between intracranial aneurysms and infundibula.** *Magn Reson Imaging* 2017;37:16–20 CrossRef Medline
47. Arenillas JF. **Intracranial atherosclerosis: current concepts.** *Stroke* 2011;42:(1 Suppl):S20–23 CrossRef Medline
48. Hartevelde AA, van der Kolk AG, van der Worp HB, et al. **Detecting intracranial vessel wall lesions with 7T-magnetic resonance imaging: patients with posterior circulation ischemia versus healthy controls.** *Stroke* 2017;48:2601–04 CrossRef Medline
49. Hartevelde AA, van der Kolk AG, van der Worp HB, et al. **High-resolution intracranial vessel wall MRI in an elderly asymptomatic population: comparison of 3T and 7T.** *Eur Radiol* 2017;27:1585–95 CrossRef Medline
50. Hartevelde AA, Denswil NP, Van Hecke W, et al. **Ex vivo vessel wall thickness measurements of the human circle of Willis using 7T MRI.** *Atherosclerosis* 2018;273:106–14 CrossRef Medline
51. Zhu C, Haraldsson H, Tian B, et al. **High resolution imaging of the intracranial vessel wall at 3 and 7 T using 3D fast spin echo MRI.** *MAGMA* 2016;29:559–70 CrossRef Medline

52. Zwartbol MH, van der Kolk AG, Ghaznawi R, et al. **Intracranial vessel wall lesions on 7T MRI (magnetic resonance imaging).** *Stroke* 2019;50:88–94 CrossRef Medline
53. Qiao Y, Suri FK, Zhang Y, et al. **Racial differences in prevalence and risk for intracranial atherosclerosis in a US community-based population.** *JAMA Cardiol* 2017;2:1341–48 CrossRef Medline
54. van der Kolk AG, Zwanenburg JJ, Denswil NP, et al. **Imaging the intracranial atherosclerotic vessel wall using 7T MRI: initial comparison with histopathology.** *AJNR Am J Neuroradiol* 2015;36:694–701 CrossRef Medline
55. Kroner ES, van Schinkel LD, Versluis MJ, et al. **Ultrahigh-field 7-T magnetic resonance carotid vessel wall imaging: initial experience in comparison with 3-T field strength.** *Invest Radiol* 2012;47:697–704 CrossRef Medline
56. Koning W, de Rotte AA, Bluemink JJ, et al. **MRI of the carotid artery at 7 Tesla: quantitative comparison with 3 Tesla.** *J Magn Reson Imaging* 2015;41:773–80 CrossRef Medline
57. Majidi S, Sein J, Watanabe M, et al. **Intracranial-derived atherosclerosis assessment: an in vitro comparison between virtual histology by intravascular ultrasonography, 7T MRI, and histopathologic findings.** *AJNR Am J Neuroradiol* 2013;34:2259–64 CrossRef Medline
58. Madai VI, von Samson-Himmelstjerna FC, Bauer M, et al. **Ultrahigh-field MRI in human ischemic stroke: a 7 Tesla study.** *PLoS One* 2012;7:e37631 CrossRef Medline
59. Miyazawa H, Natori T, Kameda H, et al. **Detecting lenticulostriate artery lesions in patients with acute ischemic stroke using high-resolution MRA at 7T.** *Int J Stroke* 2019;14:290–97 CrossRef Medline
60. Kang CK, Park CA, Park CW, et al. **Lenticulostriate arteries in chronic stroke patients visualised by 7T magnetic resonance angiography.** *Int J Stroke* 2010;5:374–80 CrossRef Medline
61. Cho ZH, Kang CK, Han JY, et al. **Observation of the lenticulostriate arteries in the human brain in vivo using 7.0T MR angiography.** *Stroke* 2008;39:1604–06 CrossRef Medline
62. Dengler NF, Madai VI, Wuerfel J, et al. **Moyamoya vessel pathology imaged by ultra-high-field magnetic resonance imaging at 7.0 T.** *J Stroke Cerebrovasc Dis* 2016;25:1544–51 CrossRef Medline
63. Oh BH, Moon HC, Baek HM, et al. **Comparison of 7T and 3T MRI in patients with Moyamoya disease.** *Magn Reson Imaging* 2017;37:134–38 CrossRef Medline
64. Lee A, McCartney S, Burbidge C, et al. **Trigeminal neuralgia occurs and recurs in the absence of neurovascular compression.** *J Neurosurg* 2014;120:1048–54 CrossRef Medline
65. Heverhagen JT, Bourekas E, Sammet S, et al. **Time-of-flight magnetic resonance angiography at 7 Tesla.** *Invest Radiol* 2008;43:568–73 CrossRef Medline
66. Moon HC, You ST, Baek HM, et al. **7.0 Tesla MRI tractography in patients with trigeminal neuralgia.** *Magn Reson Imaging* 2018;54:265–70 CrossRef Medline

Response Assessment in Neuro-Oncology Criteria for Gliomas: Practical Approach Using Conventional and Advanced Techniques

 D.J. Leao,  P.G. Craig,  L.F. Godoy,  C.C. Leite, and  B. Policeni



ABSTRACT

SUMMARY: The Response Assessment in Neuro-Oncology criteria were developed as an objective tool for radiologic assessment of treatment response in high-grade gliomas. Imaging plays a critical role in the management of the patient with glioma, from initial diagnosis to posttreatment follow-up, which can be particularly challenging for radiologists. Interpreting findings after surgery, radiation, and chemotherapy requires profound knowledge about the tumor biology, as well as the peculiar changes expected to ensue as a consequence of each treatment technique. In this article, we discuss the imaging findings associated with tumor progression, tumor response, pseudoprogression, and pseudoresponse according to the Response Assessment in Neuro-Oncology criteria for high-grade and lower-grade gliomas. We describe relevant practical issues when evaluating patients with glioma, such as the need for imaging in the first 48 hours, the radiation therapy planning and isodose curves, the significance of T2/FLAIR hyperintense lesions, the impact of the timing for the evaluation after radiation therapy, and the definition of progressive disease on the histologic specimen. We also illustrate the correlation among the findings on conventional MR imaging with advanced techniques, such as perfusion, diffusion-weighted imaging, spectroscopy, and amino acid PET. Because many of the new lesions represent a mixture of tumor cells and tissue with radiation injury, the radiologist aims to identify the predominant component of the lesion and categorize the findings according to Response Assessment in Neuro-Oncology criteria so that the patient can receive the best treatment.

ABBREVIATIONS: DCE = dynamic contrast-enhanced; GBM = glioblastoma; RANO = Response Assessment in Neuro-Oncology; rCBV = relative CBV; VEGF = vascular endothelial growth factor

Glioma tumors are the most common intra-axial primary tumors of the CNS, with an age-adjusted estimated incidence varying from 0.8 to 5.5 per 100,000, according to the reporting country/organization.^{1,2} The most common and aggressive histologic type is glioblastoma (GBM), which accounts for about 60% of the cases.¹ Despite decades of substantial advances in diagnostic radiology, surgery, radiation therapy, chemotherapy, and clinical management of oncology patients, the fatality rate for gliomas remains relentlessly high, especially for GBM. A recent study reported a 1-year survival rate after diagnosis of 41.4% and a 5-year survival rate of only

5.4% for GBM,³ after analysis of 150,631 patients. Similarly, the reported median survival time after tumor recurrence is about 6 months.⁴


Imaging plays a critical role in the management of the patient with glioma, from the initial diagnosis to the posttreatment follow-up, which can be particularly challenging for radiologists. Interpreting findings after an operation, radiation, and chemotherapy requires profound knowledge about the tumor biology, as well as the peculiar changes expected to ensue as a consequence of each treatment technique so that the patients with glioma can receive the best care and eventually improve their survival.

In this article, we discuss the imaging findings associated with tumor progression, tumor response, pseudoprogression, and pseudoresponse according to the Response Assessment in Neuro-Oncology (RANO) criteria for high-grade and lower-grade gliomas. We describe relevant practical issues when evaluating patients with glioma, such as the need for imaging in the first 48 hours, radiation therapy planning and isodose curves, the significance of T2/FLAIR hyperintense lesions, the impact of timing for the evaluation after radiation therapy and the definition of progressive disease on the histologic specimen. We also illustrate

Received August 7, 2019; accepted after revision October 29.

From the Cancer Hospital of Federal University of Uberlandia (D.J.L.), Uberlandia, Brazil; Department of Radiology, (P.G.C., B.P.), University of Iowa Hospitals and Clinics, Iowa City, Iowa; Department of Diagnostic Radiology (L.F.G.), Hospital Sirio-Libanes, Sao Paulo, Brazil; and Department of Neuroradiology (L.F.G., C.C.L.), Faculdade de Medicina Instituto de Radiologia, Universidade de Sao Paulo Neuroradiology, Sao Paulo, Brazil.

Please address correspondence to Diego J. Leao, MD, Cancer Hospital of Federal University of Uberlandia, Uberlandia, Brazil 38405-302; e-mail: diegojoseleao@yahoo.com.br

 Indicates open access to non-subscribers at www.ajnr.org

<http://dx.doi.org/10.3174/ajnr.A6358>

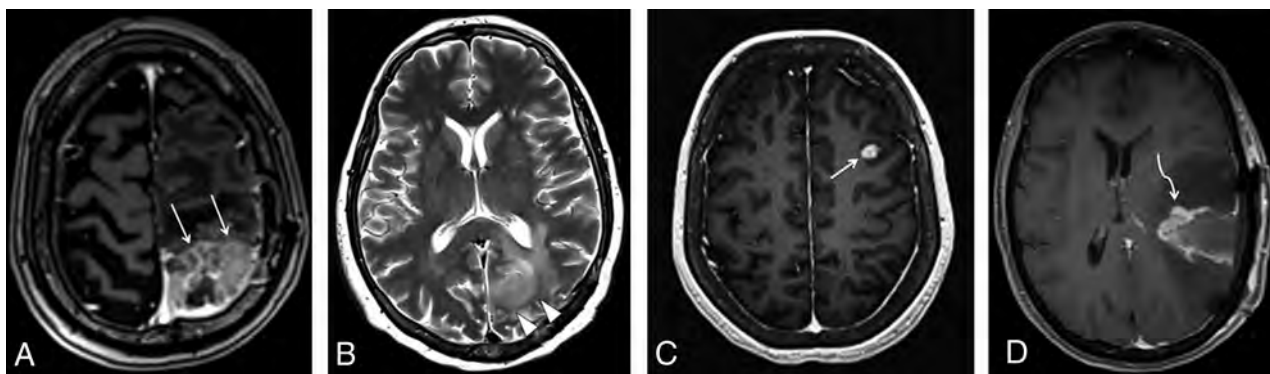


FIG 1. Examples of measurable and nonmeasurable disease, according to the RANO criteria. A, Axial contrast-enhanced T1-weighted image shows a heterogeneously enhancing lesion in the left parietal lobe (arrows), corresponding to recurrent GBM, with both perpendicular measurements of >10 mm, thus representing measurable disease. The more commonly seen examples of nonmeasurable disease are represented in the axial T2 image (B), depicting a hyperintense infiltrating lesion in the left parieto-occipital region (arrowheads) in a patient with anaplastic astrocytoma. The axial contrast-enhanced T1-weighted image (C) shows a subcortical enhancing nodule representing a recurrent GBM (arrow), in which perpendicular diameters are <10 mm. The axial contrast-enhanced T1-weighted image (D) shows residual tumor in the resection cavity of a partially resected GBM (curved arrow), which has poorly defined margins.

the correlation among the findings on conventional MR imaging with advanced techniques, such as perfusion, DWI, spectroscopy, and amino acid PET.

Management of Gliomas

The management of gliomas varies according to the histologic grade, location, resectability of the tumor, and the performance status of the patient. For the high-grade gliomas, it usually involves maximal safe resection, which can be defined as resection of the enhancing tumor as much as possible to improve survival, keeping the surgically induced deficit at an acceptable level.⁵ Resection with clear margins, a common concept in oncology, is virtually impossible for diffuse gliomas regardless of the grade because the neoplastic cells remain in the macroscopically normal-appearing brain tissue, given their highly infiltrative nature. After the initial operation, most patients undergo adjuvant treatment with radiation therapy and chemotherapy with temozolomide according to the Stupp protocol (also known as chemoradiation), which has been shown to improve survival significantly.⁶ Antiangiogenic agents, such as bevacizumab, an antibody against vascular endothelial growth factor (VEGF), are considered second-line agents with poor survival benefit,⁷ usually reserved for recurrent disease.

The term “lower-grade glioma” is generally used as a synonym for the 2 most common World Health Organization grade II diffuse gliomas: diffuse astrocytoma and oligodendroglioma. Because those tumors tend to have an indolent clinical course but are not curable and their natural history usually exhibits transformation to high-grade glioma in most patients, the treatment for those tumors is far more controversial. The timing and extent of surgery and radiation therapy, as well as adjunctive chemotherapy, should be individualized, weighing the survival benefits and adverse effects of those treatments. More recently, novel advances in immunotherapy with vaccines have shown promising results while treating patients with gliomas, as extensively described in a recent review by Lim et al.⁸ Although

the optimal immunotherapy treatment regimen and indications remain to be determined, as radiologists, we are expected to report an increasing number of examinations from patients under these therapies, either in clinical trials or in routine daily practice.

RANO Criteria: Standardized Definitions and Evaluation of Response

The Macdonald criteria were originally published in 1990,⁹ as the first objective tool for radiologic assessment of treatment response in high-grade gliomas. Such criteria were based primarily on evaluation of tumor enhancement through CT (and included information about steroid use and neurologic findings). In the following decades, MR imaging added fundamental information about the nonenhancing component of the tumor, depicted on T2-weighted/FLAIR sequences, and became the standard neuroimaging technique used to assess treatment response in high-grade gliomas, as updated by the same group in 2010 by publishing the RANO criteria.¹⁰ The most substantial difference in the RANO criteria was that contrast enhancement is not the only marker of tumor viability and that it may represent posttherapy changes instead of neoplastic tissue.

Similar to the Response Evaluation Criteria in Solid Tumors, the RANO criteria advocate standardization of imaging definitions so that the tumor-burden assessment can be accurate and reproducible. As shown in Fig 1, the RANO criteria define measurable disease as bidimensional contrast-enhancing lesions with clearly defined margins, with 2 perpendicular diameters of at least 10 mm, visible on ≥ 2 axial slices.¹⁰ The nonmeasurable disease is defined as either unidimensional measurable lesions, masses with margins not clearly defined as frequently noted in the surgical margins, or lesions with maximal perpendicular diameters of <10 mm.¹⁰ T2/FLAIR hyperintense lesions are also considered nonmeasurable and usually represent the most common imaging feature of lower-grade tumors. If there are multiple contrast-enhancing lesions, a minimum of 2 target lesions must be selected, which should be representative of the tumor burden,

Criteria for response assessment incorporating MR imaging and clinical factors^a

Response	Criteria
Complete response	Requires all of the following: complete disappearance of all enhancing, measurable and nonmeasurable disease sustained for at least 4 weeks; no new lesions; stable or improved nonenhancing (T2/FLAIR) lesions; patients must be off corticosteroids (or on physiologic replacement doses only) and stable or improved clinically; note that patients with nonmeasurable disease only cannot have a complete response; the best response possible is stable disease
Partial response	Requires all of the following: $\geq 50\%$ decrease compared with baseline in the sum of products of perpendicular diameters of all measurable enhancing lesions sustained for at least 4 weeks; no progression of nonmeasurable disease; no new lesions; stable or improved nonenhancing (T2/FLAIR) lesions on the same or lower dose of corticosteroids compared with baseline scan; the corticosteroid dose at the time of the scan evaluation should be no greater than the dose at time of baseline scan and stable or improved clinically; note that patients with nonmeasurable disease only cannot have a partial response; the best response possible is stable disease
Stable disease	Requires all of the following: does not qualify for complete response, partial response, or progression; stable nonenhancing (T2/FLAIR) lesions on the same or lower dose of corticosteroids compared with baseline scan; in the event that the corticosteroid dose was increased for new symptoms and signs without confirmation of disease progression on neuroimaging, and subsequent follow-up imaging shows that this increase in corticosteroids was required because of disease progression, the last scan considered to show stable disease will be the scan obtained when the corticosteroid dose was equivalent to the baseline dose
Progressive disease (≥ 12 weeks after radiation therapy completion)	Defined by any of the following: $\geq 25\%$ increase in sum of the products of perpendicular diameters of enhancing lesions compared with the smallest tumor measurement obtained either at baseline (if no decrease) or best response on stable or increasing doses of corticosteroids; significant increase in T2/FLAIR nonenhancing lesion on stable or increasing doses of corticosteroids compared with baseline scan or best response after initiation of therapy not caused by comorbid events (eg, radiation therapy, demyelination, ischemic injury, infection, seizures, postoperative changes, or other treatment effects); any new lesion; clear clinical deterioration not attributable to other causes apart from the tumor (eg, seizures, medication adverse effects, complications of therapy, cerebrovascular events, infection, and so on) or changes in corticosteroid dose; failure to return for evaluation as a result of death or deteriorating condition; or clear progression of nonmeasurable disease

^a Source: Wen et al.¹⁰

and the sum of the products of the perpendicular diameters of these lesions should be determined.¹⁰ The largest lesions are preferred, but the emphasis should also be placed on lesions that allow reproducible measurements.

In the follow-up assessment, the response of a patient with a high-grade glioma is usually classified into 4 categories: progressive disease, partial response, complete response, and stable disease, as summarized in Table. As will be discussed later, pseudoprogression and pseudoresponse are special situations in which the therapies (ie, radiation, temozolomide, and anti-VEGF agent) play a major role in the imaging appearance.

Complete Response. Complete response requires all of the following: complete disappearance of all enhancing measurable and nonmeasurable disease sustained for at least 4 weeks; no new lesions; and stable or improved nonenhancing (T2/FLAIR) lesions. Patients must be off corticosteroids (or on physiologic replacement doses only) and stable or improved clinically.¹⁰

Partial Response. Partial response requires all of the following: $\geq 50\%$ decrease, compared with baseline; the sum of products of perpendicular diameters of all measurable enhancing lesions sustained for at least 4 weeks; no progression of nonmeasurable disease; no new lesions; stable or improved nonenhancing (T2/FLAIR) lesions on the same or a lower dose of corticosteroids compared with baseline scan; and the patient being on a corticosteroid dose not greater than the dose at time of the baseline scan and stable or improved clinically.¹⁰

Stable Disease. Stable disease occurs if the patient does not qualify for complete response, partial response, or progression and requires the following: stable nonenhancing (T2/FLAIR) lesions on the same or lower dose of corticosteroids compared with baseline scan and clinically stable status.¹⁰

Progression. Progression is defined by any of the following: $\geq 25\%$ increase in the sum of the products of perpendicular diameters of enhancing lesions (compared with baseline if no decrease) on stable or increasing doses of corticosteroids; a significant increase in T2/FLAIR nonenhancing lesions on stable or increasing doses of corticosteroids compared with the baseline scan or the best response after initiation of therapy, not due to comorbid events; the appearance of any new lesions; clear progression of nonmeasurable lesions; or definite clinical deterioration not attributable to other causes apart from the tumor or to a decrease in the corticosteroid dose.¹⁰

RANO Criteria: Relevant Practical Issues

Need for Imaging in the First 48 Hours. It is of fundamental importance to obtain MR imaging within the first 48 hours after an operation to assess the extension of any residual lesion. Diffusion-weighted imaging can detect cytotoxic edema in the margins of the tumoral resection, which is considered to be a normal postoperative finding related to surgical manipulation. Similar to ischemic stroke, most of those areas of restricted diffusion eventually enhance beyond 48 hours, as depicted in Fig 2, as a sign of granulation tissue development. It is possible to differentiate residual tumor from contrast enhancement related to the

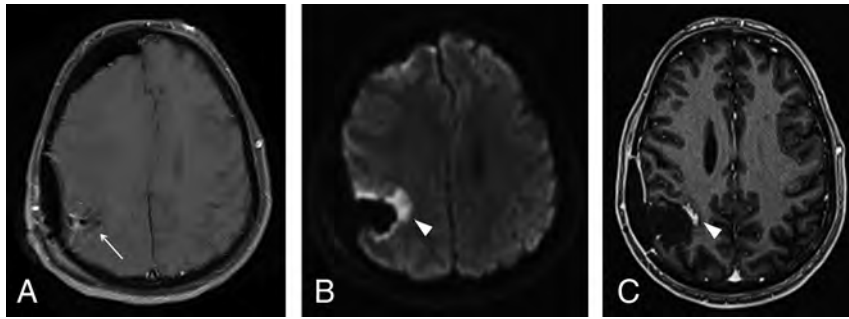


FIG 2. Postoperative findings after GBM resection in the right parietal lobe (not shown) in a 55-year-old man. *A*, Axial contrast-enhanced T1-weighted image in the immediate postoperative period demonstrates a fluid-filled surgical cavity (*arrow*) without any enhancing lesions, which is defined as gross total resection. *B*, An axial diffusion-weighted image shows marked restricted diffusion in the margins of the cavity (*arrowhead*), representing cytotoxic edema related to surgical manipulation. *C*, Axial contrast-enhanced T1-weighted image obtained 3 months after an operation shows the development of an enhancing focus in the surgical bed (*arrowhead*), corresponding to development of granulation tissue in the area of previously restricted diffusion, also a typical and predictable postoperative feature, which should not be misdiagnosed as recurrent or residual tumor.

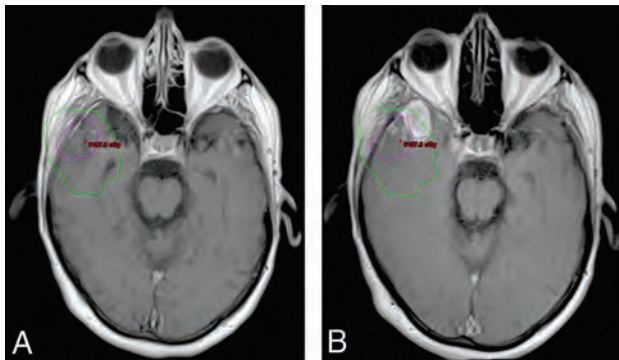


FIG 3. Delineation of the radiation therapy target for the treatment of a gross totally resected GBM in the right temporal lobe and its relation to tumor recurrence. *A*, Fused planning CT and axial contrast-enhanced T1-weighted postoperative image allow visualization of the radiation dose effectively delivered in the brain parenchyma adjacent to the surgical cavity (isodose chart). The high-dose region is defined as the area inside the *pink line*, corresponding to the 100% isodose line (60 Gy) plus the area between the *pink* and *green lines*, corresponding to the 80% isodose line (48 Gy). *B*, Fused planning CT and axial contrast-enhanced T1-weighted follow-up images demonstrate that a significant portion of the new enhancing lesion was located outside the high-dose radiation field (inside the *green line*), which is consistent with progressive disease.

normal postoperative period if imaging is obtained within 48 hours after an operation. On the other hand, if imaging is performed after 48 hours, contrast enhancement may be misinterpreted as residual tumor and impact future evaluations of tumor recurrence.

Understanding Radiation Therapy Planning and Isodose Curves. Current guidelines recommend the radiation therapy target volume to be delineated on the surgical cavity, encompassing any residual enhancement, with the addition of a 20-mm margin, which represents the most common site of recurrence.¹¹ A planning CT scan of the brain is obtained and fused with the postoperative MR imaging to accurately delineate the

radiation target.¹¹ The planning CT also provides fundamental information about the isodose curves, which can be defined as lines joining the points that receive the same percentage of radiation dose. As seen in Fig 3, those lines can be plotted in an isodose chart, which allows precise visualization of the radiation dose that a given region of the brain received. The isodose curves vary according to numerous factors, including field size, beam energy, depth in the patient, distance from the beam source, and external attenuators.¹² Although the isodose charts are not readily available in many centers, we strongly encourage radiologists to have access to and review them when reading post-treatment imaging to correctly assess the relation between any developing lesion and the high-dose region, as exemplified in Fig 3*B*.

Significance of T2/FLAIR Hyperintense Lesions. From the radiologic-pathologic correlation, it is well-established that the T2/FLAIR hyperintensity surrounding an enhancing tumor comprises not only vasogenic edema but also neoplastic infiltration. After an operation, radiation therapy, and temozolomide, these principles became less clear because of therapy-related inflammatory changes also present as T2/FLAIR hyperintensity. The more distinctive features of neoplastic infiltration are loss of gray matter–white matter differentiation and increased mass effect,¹³ as seen in Fig 4. These are in contrast to inflammatory and therapy-related changes, which typically spare the brain cortex. When in doubt about the presence of blurring of the gray-white junction, it is crucial to pay close attention to T2-weighted images because those findings may be subtle and the gray-white junction is better depicted on this sequence rather than on FLAIR.

Timing for Evaluation after Radiation Therapy. The time elapsed between the completion of the radiation therapy and the imaging acquisition should also be taken into account when interpreting posttreatment imaging. According to the RANO criteria, in the first 12 weeks after completion of chemoradiation, progressive disease can only be radiologically defined if there is new enhancement outside the radiation field (beyond the high-dose region or 80% isodose line)¹⁰ because of the high incidence of therapy-related changes in this period. If the area of new or increased enhancement occurs inside the radiation field, unequivocal evidence of viable tumor is required on histopathologic sampling.¹⁰

Defining Progressive Disease on Histologic Specimens. The diagnosis of tumor recurrence may be challenging despite histopathologic analysis due to the absence of standardized pathologic criteria. A recent report with 48 pathologists working at 30 cancer centers showed only marginal reproducibility when they were asked to provide a final diagnosis (active tumor, treatment effect, or unable to classify) in histologic sections from patients with

glioblastoma who underwent diagnostic surgery for suspected early recurrence. In this study, the κ coefficient was 0.228 (95% CI, 0.22–0.24), and the maximum agreement on the final diagnosis ranged from 36% to 68%.¹⁴ Such marginal reproducibility may be an explanation for the variable correlation between the pathologic diagnosis of tumor recurrence and patients' survival.¹⁵ These findings also impact the analysis of diagnostic accuracy of imaging because histopathology is the current criterion standard for diagnosing tumor recurrence. Further studies assessing radiologic-pathologic correlation and its relation to patient survival could be valuable for defining better pathologic criteria.

Pseudoprogression

The RANO criteria define pseudoprogression as new or increasing contrast enhancement that eventually subsides without any

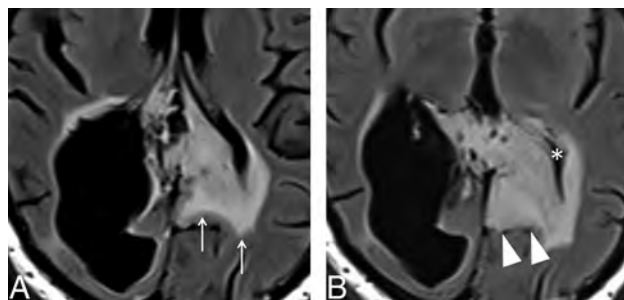


FIG 4. Imaging features of the nonenhancing component of glial tumors. A 36-year-old man underwent partial resection and adjuvant radiation therapy of an extensive diffuse astrocytoma (World Health Organization, grade II) involving both parietal lobes (not shown). A, Axial FLAIR image obtained 5 years after completion of radiation therapy demonstrates extensive hyperintensity crossing the midline through the splenium of the corpus callosum (arrows), probably representing a mixture of lower-grade tumor and radiation injury. B, Axial FLAIR image obtained 8 months later depicts blurring of the gray-white matter in the left parietal lobe (arrowheads), as well as effacement of the left lateral ventricle (asterisk), which is consistent with neoplastic infiltration (progressive disease).

change in therapy,¹⁰ as depicted in Fig 5. Using a broader definition in which stability of the enhancing lesion on follow-up images also represents pseudoprogression, a recent meta-analysis including 2603 patients with high-grade gliomas reported an incidence of pseudoprogression of around 36%.¹⁶ Of note, it can also occur in patients with lower-grade gliomas, with a reported incidence of 20%.¹⁷

Pseudoprogression likely results from transiently increased permeability of the tumor vasculature and inflammation induced by radiation therapy, which may be exacerbated by temozolomide. Histologic analysis of such lesions usually discloses features related to treatment effects like reactive gliosis and vascular hyalinization as well as foci of neoplastic cells.¹⁸ Progressive clinical signs and symptoms may accompany pseudoprogression (eg, altered mental status, hemiparesis),¹⁹ and it seems to be more frequent in patients with a methylated O⁶-methylguanine–DNA methyltransferase gene promoter, which is a marker of good prognosis.²⁰ Although the definitive diagnosis of pseudoprogression is retrospective, because it requires demonstration of decreased contrast enhancement in imaging follow-up, this pseudoprogression is conceivable if the lesion developed within the first 3–6 months after radiation therapy, if it is in the radiation field (inside the 80% isodose line), and especially if it presents as a pattern of enhancement related to radiation-induced necrosis, ie, “Swiss cheese” or “soap bubble” enhancement (Fig 5C).²¹

At this point, the term “pseudoprogression” is reserved for patients with gliomas who underwent chemoradiation, while radiation-induced necrosis, a frequently confused term, describes a focal lesion in the brain that may occur secondary to any technique of radiation therapy. Although both may share similar imaging presentations, pseudoprogression occurs predominantly within the first 6 months after chemoradiation completion, while radiation necrosis tends to occur later in the course, usually 1 year after radiation, and is not likely to subside. Furthermore, in histologic analysis, radiation-induced necrosis shows permanent

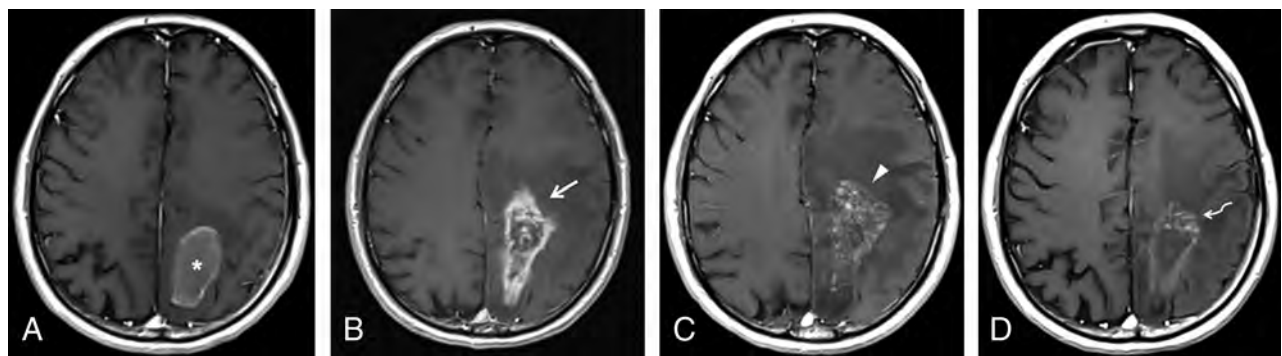


FIG 5. Pseudoprogression in a 56-year-old man who underwent chemoradiation after gross total resection of a GBM in the left parietal lobe. A, Axial contrast-enhanced T1-weighted image obtained 1 week after an operation shows thin ring enhancement in the surgical bed (asterisk), which was considered to represent granulation tissue, related to the operation. The study was not obtained within the first 48 hours due to hemodynamic instability of the patient. B, Soon after completion of radiation therapy, the patient developed marked enhancement in the margins of the surgical cavity (arrow), with effacement of the adjacent sulci. In the following 3 months, he presented with progressive altered mental status and right-side hemiparesis. C, At that time, axial contrast-enhanced T1-weighted imaging showed an increase in mass effect, midline shift, with a slight increase in enhancement extension, which turned to a soap bubble appearance (arrowhead), a pattern typically associated with radiation necrosis. D, The patient improved clinically, and after 4 months, a new image depicted fading of the enhancing lesion (curved arrow) and a marked decrease in mass effect, which is the classic course of pseudoprogression.

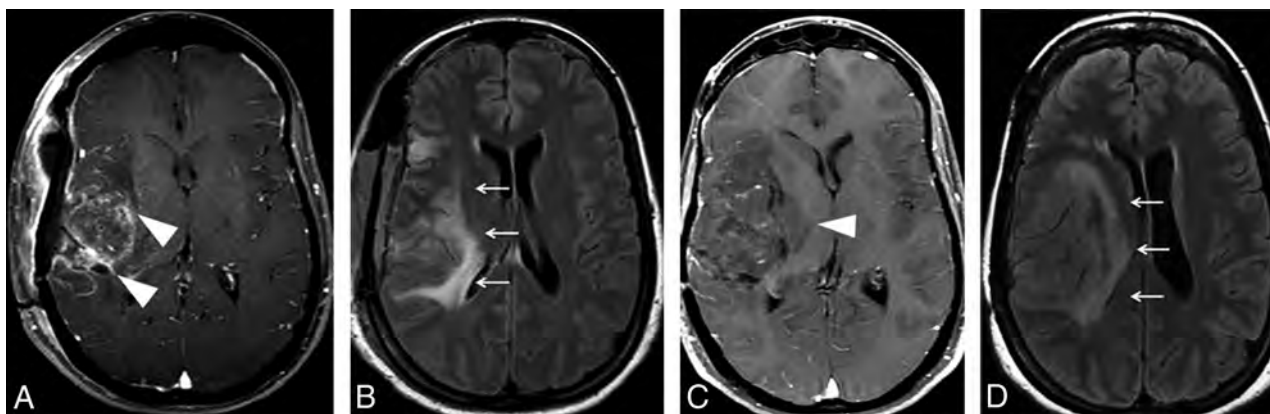


FIG 6. Pseudoresponse in a 36-year-old woman with a partially resected GBM in the right temporal lobe and insula. Axial contrast-enhanced T1-weighted (A) and FLAIR (B) images obtained in the immediate postoperative period show an extensive hyperintense FLAIR lesion (arrows) with multiple foci of contrast enhancement (arrowheads). C, An anti-VEGF agent was administered, and a follow-up axial contrast-enhanced T1-weighted image depicts a striking decrease of the enhancing component (arrowhead). D, However, there is also an increase of the nonenhancing infiltrative component, manifested as FLAIR hyperintensity in the right frontotemporal region and insula, with an expansive effect, blurring, and loss of the cortical-subcortical differentiation (arrows).

damage to the brain parenchyma, with extensive necrotic areas, vascular thrombosis, and fibrinoid necrosis.

The RANO Working Group also published guidelines addressing the evaluation of response in patients with glial tumors who underwent immunotherapy treatments: the Immunotherapy Response Assessment for Neuro-Oncology. Because boosting the immune response can also lead to development or increase in the extension of the enhancing lesion per se, according to the Immunotherapy Response Assessment for Neuro-Oncology, if the lesion developed within ≤ 6 months after starting immunotherapy and the patient has no new or substantially worsened neurologic deficits, disease progression requires confirmation on follow-up imaging, 3 months after initial radiographic progression.²²

Misdiagnosing progressive disease instead of pseudoprogression may have harmful consequences for the patient because it would eventually lead to discontinuation of a treatment that is working and/or an unnecessary operation. It also has significant implications in selecting appropriate patients for participation in clinical trials for recurrent gliomas because failure to exclude patients with pseudoprogression from these studies would result in an artificially higher response rate.

Pseudoresponse

Antiangiogenic agents, like bevacizumab, are designed to block the VEGF effect, which is overexpressed in high-grade glial tumors.²³ The mechanism of action may be related to decreased blood supply to the tumor and normalization of tumor vessels, which display increased permeability.²³ These agents are associated with high radiologic responses if we evaluate only the contrast enhancement. However, the infiltrative nonenhancing tumoral component does not seem to be affected and eventually increases in the follow-up imaging, as depicted in Fig 6, which characterizes the pseudoresponse. This increase may be an explanation for the poor survival benefits in trials with antiangiogenic agents.

RANO Criteria for Lower-Grade Gliomas

Lower-grade gliomas (ie, diffuse astrocytoma, oligodendroglioma, and anaplastic gliomas) tend to have an indolent clinical course, but their natural history usually demonstrates transformation to high-grade glioma in most patients. The measurement of tumor burden or response to therapy relies mainly on changes in T2-weighted and FLAIR images because most lower-grade gliomas do not demonstrate contrast enhancement. The radiologic assessment is further complicated by radiation therapy-induced local white matter changes, which also present as increasing areas of abnormal signal intensity on T2-weighted or FLAIR images. The typical findings for progressive lower-grade glioma are increased T2 or FLAIR nonenhancing lesions and development of contrast enhancement, indicating malignant transformation, as seen in Fig 7.²⁴

Role of Advanced Imaging Techniques

As we have demonstrated, an operation, radiation, and chemotherapy can lead to contrast-enhanced lesions and surrounding edema (hyperintense T2/FLAIR), similar to what is observed in cases of glioma progression. Most of the newly occurring lesions do not consist of only large areas of pure tumor or treatment-related changes; instead, they usually represent a mixture of both. Hence, our goal was to identify the predominant cause for the lesion, which allows the establishment of the prognosis and the best treatment for the patient.

Although not included in RANO criteria, advanced techniques such as perfusion MR imaging, MR spectroscopy, diffusion-weighted imaging, and amino acid PET/CT can provide valuable information for differentiating glioma recurrence and pseudoprogression.

Perfusion MR Imaging. Perfusion techniques are based on the fact that malignant gliomas have a compromised blood-brain barrier and increased angiogenesis, which will eventually affect tissue perfusion and/or vessel permeability.

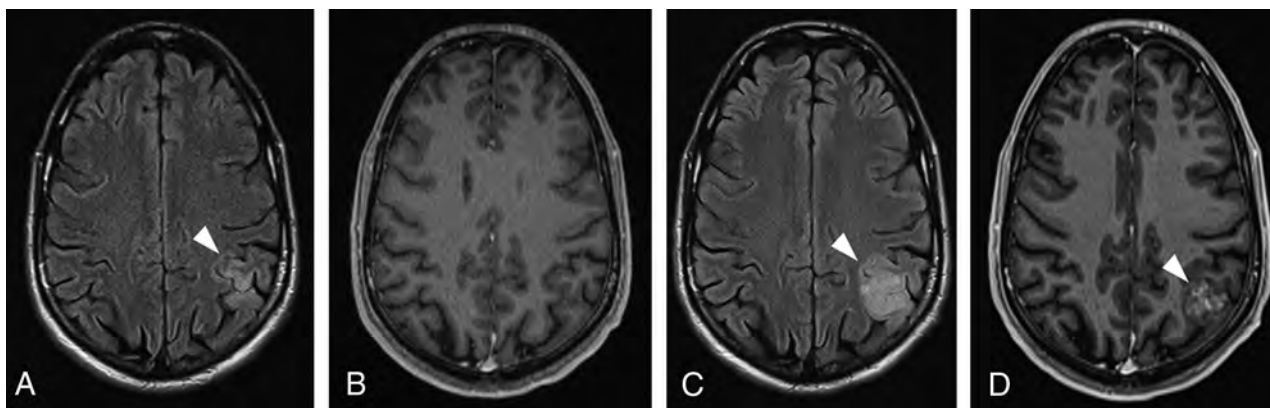


FIG 7. A progressive low-grade glioma in a 33-year-old man previously diagnosed with Li-Fraumeni syndrome. Initial axial FLAIR (A) and contrast-enhanced T1-weighted (B) images showed subtle cortical-subcortical FLAIR hyperintensity in the left inferior parietal lobule, with minimal expansive effect and no postcontrast enhancement, which was presumably considered to be a low-grade glial tumor (arrowhead). Two years later, axial FLAIR (C) and contrast-enhanced T1-weighted (D) images depict a marked increase in the expansive effect, with loss of gray-white matter differentiation and heterogeneous enhancement (arrowhead). Those findings are consistent with malignant transformation of a lower-grade glioma (progressive disease).

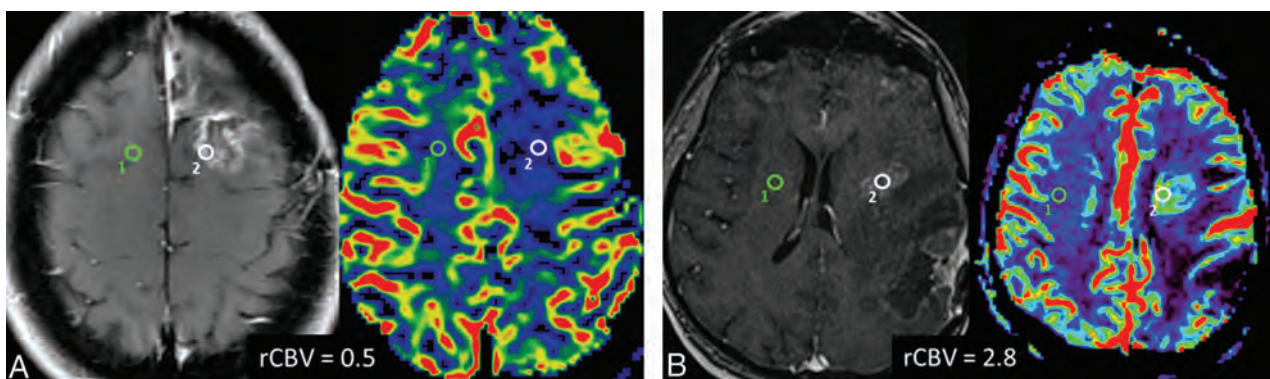


FIG 8. DSC perfusion in pseudoprogression and progressive disease. A, Axial contrast-enhanced T1-weighted and the corresponding rCBV map images show an enhancing lesion that developed after radiation therapy and temozolomide in a 46-year-old patient with multicentric GBM. The DSC perfusion of the enhancing lesion in the surgical bed (white ROI) shows decreased rCBV (0.5) in comparison with normal contralateral white matter (green ROI), which is consistent with predominance of radiation injury within the lesion (pseudoprogression). B, Axial contrast-enhanced T1-weighted and corresponding rCBV map images in a 60-year-old patient with a previously resected GBM show an enhancing lesion (white ROI) close to the margin of the radiation field. The DSC perfusion of the enhancing lesion in the surgical bed shows increased rCBV (2.8) in comparison with normal contralateral white matter (green ROI), indicating predominance of malignant cells within the lesion (progressive disease).

DSC T2*-weighted perfusion is based on tracking the passage of a contrast agent through the brain, which decreases the T2*-weighted signal, creating a susceptibility gradient between the tissue and the vasculature as a function of relative cerebral blood volume (rCBV). The analyzed ROIs within the brain should be small, adjusted as necessary to target the areas with the visually highest rCBV (on rCBV maps) and to avoid vessels or areas of magnetic susceptibility artifacts, especially blood, one of the major limitations of DSC. Another rCBV ROI is then obtained in the normal contralateral white matter as a reference, producing a ratio between lesion rCBV and normal white matter rCBV. High rCBV ratios are associated with tumor recurrence, whereas lower rCBV ratios usually represent therapy-related changes (ie, chemoradiation effects), as exemplified by Fig 8. Determining the optimal cutoff to confidently diagnose progressive disease (a high proportion of tumor in the lesion) may be troublesome because

thresholds vary significantly among the studies, with reported rCBV cutoff ratios ranging from 1.8 to 2.6.²⁵⁻²⁹ This issue was addressed by a recent meta-analysis of 28 studies that could not find clinically meaningful pooled PWI thresholds to reliably distinguish tumor from treatment effect.³⁰ As sources of heterogeneity, the authors listed variability in the postprocessing software, use of contrast preloading, the method of selection of ROIs (size, number, and location), and the evaluated DSC parameter (mean, maximum, or histogram-derived percentile).

Dynamic contrast-enhanced (DCE) T1-weighted perfusion, also known as permeability, estimates the rate of extravasation of contrast agent from the intravascular space into the extravascular extracellular space, plotted as a permeability curve. The greatest advantage of DCE perfusion over DSC is that it is less susceptible to magnetic artifacts because it is a T1-weighted imaging. However, in contrast to DSC perfusion, DCE requires disruption

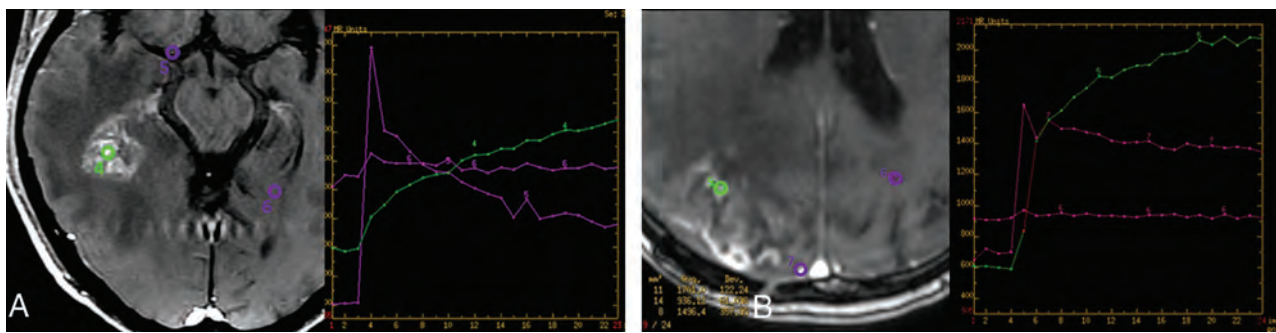


FIG 9. DCE perfusion in pseudoprogression and progressive disease. *A*, Axial contrast-enhanced T1-weighted image and the corresponding permeability curve show an enhancing lesion that developed after radiation therapy and temozolomide in a 46-year-old patient with multicentric GBM (same patient as presented previously). The DCE perfusion of the temporal lesion (*green ROI, 4*) shows slowly progressive accumulation of gadolinium in the extravascular space, as shown in the graphic (*green curve, 4*), which is consistent with predominance of radiation injury within the lesion (pseudoprogression). The ROIs in the vessel (*purple ROI, 5*) and in normal white matter (*purple ROI, 6*) are obtained for comparison. *B*, Axial contrast-enhanced T1-weighted imaging and the corresponding permeability curve show an enhancing lesion in a 65-year-old patient with a previously resected GBM, who developed an enhancing lesion in the surgical bed (*green ROI, 5*) after radiation therapy and temozolomide. DCE perfusion shows a fast ascension curve, which implies a highly vascular lesion (*green curve, 5*), indicating predominance of malignant cells within the lesion (progressive disease).

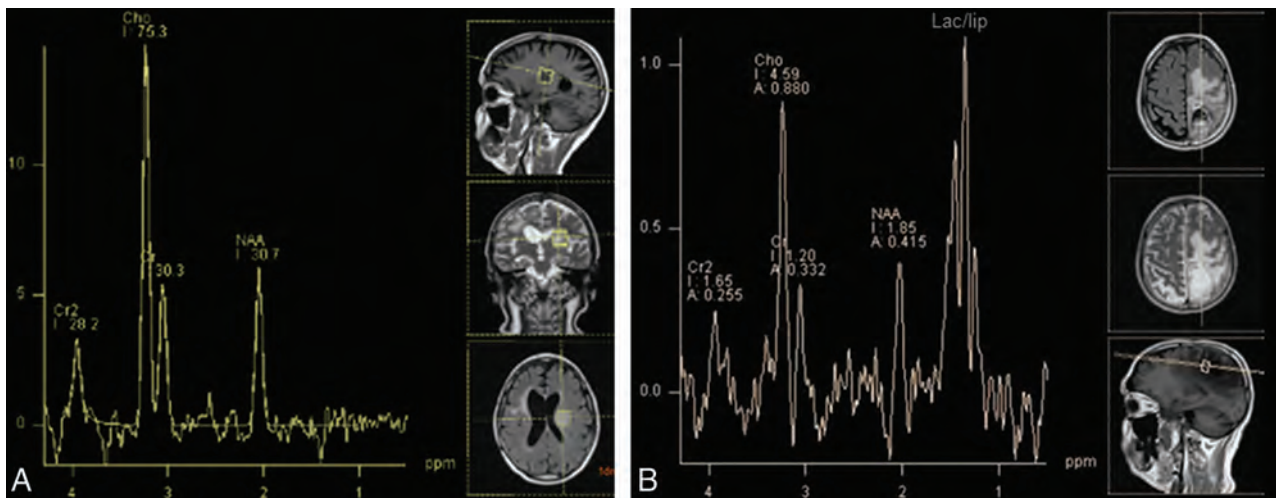


FIG 10. Characteristic findings of progressive disease and pseudoprogression on MR spectroscopy. *A*, A 54-year-old man presented with a ring-enhancing lesion in the left insula (not shown) distant from the radiation field after treatment of a right frontal lobe GBM. MR imaging spectroscopy shows marked elevation of the choline/NAA ratio (2.5), indicating high cellular turnover and diminished neuronal viability, typical for a malignant tumor and indicating progressive disease. *B*, A previously presented case of a 56-year-old man with pseudoprogression after treatment of a GBM in the left parietal lobe (Fig 5). MR imaging spectroscopy also shows elevation of choline/NAA ratio, but only slightly lower than that in the previous case (2.2 versus 2.5), which exemplifies the findings overlap between pseudoprogression and progressive disease on spectroscopy. The lipid/lactate peak is markedly elevated in patients with pseudoprogression but is also commonly present in GBM recurrence.

of the blood-brain barrier to analyze the intravascular-to-extravascular contrast flow, which makes this tool unsuitable to assess T2/FLAIR hyperintense nonenhancing lesions. As depicted by Fig 9, in the recurrent tumor, DCE perfusion demonstrates a very rapid initial increase in the vascular permeability curve, which is typical for a highly vascular and permeable tumor.³¹ In radiation-induced injury, the rate of enhancement is typically slow, as a result of radiation-induced occlusive vasculopathy. To obtain the permeability curve, the ROI should be set in the lesion, as well as in a vessel and the normal white matter for comparison. The numeric representation of those differences can be calculated through the time-dependent leakage constant (K^{trans}), which represents the volume transfer coefficient between blood plasma and

extravascular extracellular space. Although K^{trans} was demonstrated to be higher in true progressive disease in comparison with pseudoprogression,^{32,33} there is no established consensus about the exact cutoff, given the relatively fewer studies using DCE and, similar to DSC, the heterogeneity of techniques and postprocessing methods.

Arterial spin-labeling is another MR perfusion technique that can be useful in distinguishing early tumor progression from pseudoprogression, as seen in a study that reported that adjunctive arterial spin-labeling produced more accurate results than DSC perfusion MR imaging alone.³⁴ Arterial spin-labeling can quantitatively measure CBF using arterial water as a freely diffusible tracer,³⁵ instead of gadolinium.

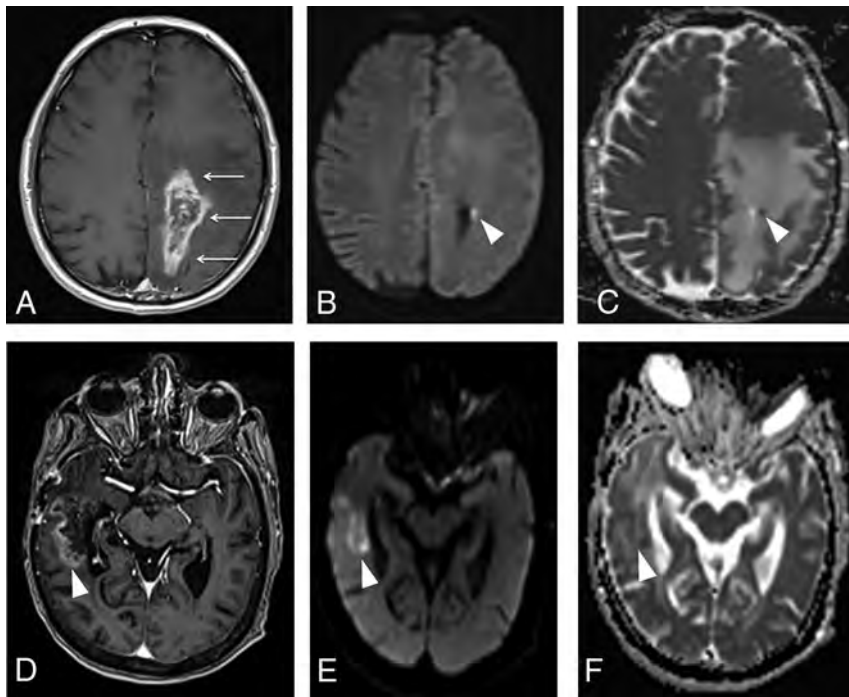


FIG 11. Typical features of pseudoprogression and progressive disease on diffusion-weighted imaging. A, Axial contrast-enhanced T1-weighted image from a previously presented case of a patient with pseudoprogression (Fig 5) after treatment of a GBM in the left parietal lobe shows an enhancing lesion with irregular margins in the surgical bed (arrows). Despite an axial DWI (B) and ADC map (C) showing a punctate focus of restricted diffusion in the lesion (arrowhead), with $ADC = 0.9 \times 10^{-6} \text{ mm}^2/\text{s}$, most of the enhancing lesion has no corresponding restricted diffusion, exhibiting ADC levels around $1.5\text{--}1.7 \times 10^{-6} \text{ mm}^2/\text{s}$, which is consistent with radiation injury. D, Axial contrast enhanced T1-weighted image shows a heterogeneously enhancing lesion in the right temporal lobe (arrowhead) in a patient with a resected GBM. Axial DWI (E) and an ADC map (F) show moderately restricted diffusion, with ADC values ranging from $1.0\text{--}1.1 \times 10^{-6} \text{ mm}^2/\text{s}$, consistent with predominance of malignant cells within the lesion (progressive disease). The ADC measurements were obtained by drawing a circular ROI in the visually lowest ADC areas on the ADC map.

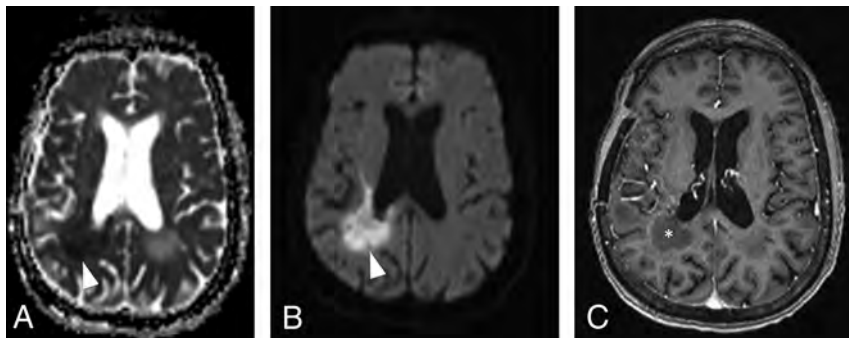


FIG 12. DWI changes after anti-VEGF agent administration in patients with GBM. Axial DWI (A) and an ADC map (B) show markedly restricted diffusion (lowest $ADC = 0.5 \times 10^{-6} \text{ mm}^2/\text{s}$) in the right periventricular white matter (arrowheads), soon after bevacizumab was started in a patient with recurrent GBM. C, Axial contrast-enhanced T1-weighted image shows only thin rim enhancement in the area of restricted diffusion (asterisk). Those findings most likely represent ischemic changes within the tumor and should not be confused with progressive disease. The ADC measurements were obtained by drawing a circular ROI in the visually lowest ADC areas on the ADC map.

MR Spectroscopy. MR spectroscopy evaluates the concentration of brain metabolites according to their precession frequency, which is influenced by the magnetic field generated by the number of hydrogen protons within a molecule.

As demonstrated by Fig 10, the major metabolites evaluated in differentiation of tumor recurrence and disease progression are choline, a membrane component and marker of increased cell proliferation, especially in tumors, and, to a lesser extent, in inflammation; and NAA, a marker of density and viability of neurons, which are decreased in both tumor and radiation injury. Although some studies reported promising findings with the use of the choline/NAA ratio, the result of a meta-analysis comprising a total sample size of 455 patients recommended against using spectroscopy alone to differentiate progressive disease from pseudoprogression.³⁶ A debate exists about the optimal cutoff for the choline/NAA ratio; however, a reasonable point may be 2.2. The major concern about spectroscopy is the lack of standardization of imaging acquisition among studies (eg, $1.5\text{T} \times 3\text{T}$, short TE \times long TE, single-voxel \times multivoxel), which may eventually affect their external validity. Spectroscopy may also be technically difficult while evaluating lesions located in the periphery of the brain hemispheres close to the calvaria or lesions with superimposed hemorrhagic foci because bone lipids and hemosiderin may cause severe artifacts in spectroscopic sequences.

DWI. DWI depicts changes in water movement through different tissues, according to the cell count, cell density over the extracellular matrix, and the nucleus-cytoplasm ratio. If these factors increase in a given tissue, the ability of water to move becomes more restricted. Hence, the high cellularity and high nucleus-cytoplasm ratio observed in malignant tumors are associated with decreased water diffusion, which can be quantitatively represented as low ADCs—ie, ADC is inversely associated with tumor predominance within the lesion (progressive disease), while higher ADCs are

noted in lesions with predominance of radiation injury, as shown in Fig 11. In DWI, most of the overlap between tumor recurrence and pseudoprogression relies on the intrinsic heterogeneity of GBM, with regions of high cellularity admixed with areas of

necrosis, edema, and microhemorrhage. These findings can also be seen in radiation-induced injury, which complicates the overall comparison.

Although the method to calculate ADC is controversial, it can be performed manually or through specific automated software with additional histogram analysis³⁷; the proposed ADC cutoff of most studies to differentiate progressive disease from pseudoprogression is about $1.3 \times 10^{-3} \text{ mm}^2/\text{s}$.^{38,39}

Some patients undergoing bevacizumab therapy can develop lesions with markedly high restricted diffusion (ADC levels under $0.7 \times 10^{-3} \text{ mm}^2/\text{s}$) within a few weeks to several months after drug initiation. These lesions usually appear near the ventricles and the corpus callosum,⁴⁰ as seen in Fig 12, and were demonstrated to be related to tissue ischemia and coagulative necrosis surrounded by a viable hypercellular tumor, instead of pure tumoral burden.⁴¹ Most important, if the areas of restricted diffusion remain stable for >3 months, they are associated with greater overall survival in comparison with the patients with no diffusion restriction and those with progressively growing restricted diffusion lesions.^{40,41}

Amino Acid PET. In 2019, neuro-oncology and nuclear medicine medical associations published practice guidelines and recommendations addressing the application of PET in the management of gliomas, from initial diagnosis to therapy monitoring.⁴² Glucose analog FDG-PET has shown only modest performance to diagnose tumor recurrence, mainly due to the intense intrinsic uptake of normal brain cortex, as well as hypermetabolism observed in inflammatory and therapy-related changes.⁴³ On the other hand, radiolabeled amino acids were reported to show promising results in glioma PET imaging, as demonstrated by numerous reviews and meta-analyses, especially ¹¹C-methionine (MET), [¹⁸F] fluoroethyl tyrosine, and [¹⁸F] dihydroxyphenylalanine.⁴³⁻⁴⁶ Their use is based on the increased amino acid use in glial tumors in the process of cell proliferation, in comparison with normal brain parenchyma and inflammatory conditions.

Similar to what we noticed in the perfusion MR imaging studies, there are several possible parameters to analyze, such as maximum standard uptake value, mean standard uptake value, mean tumor-to-background ratio, maximum tumor-to-background ratio, and the time-activity curve, leading to substantial heterogeneity among the studies, which, in turn, leads to difficulties in establishing optimal thresholds to detect tumor recurrence. Another major limitation to routine clinical use of those radio-tracers is their reduced availability—eg, MET-PET requires an on-site cyclotron and the ability to produce and perform ¹¹C radiochemistry, which has a half-life of 20 minutes.⁴⁴

CONCLUSIONS

The evaluation of treatment response is especially challenging in neuro-oncology because an operation, radiation, and chemotherapy can lead to the development of contrast-enhanced and T2/FLAIR hyperintense lesions that mimic glioma progression. Because many of the new lesions represent a mixture of tumor cells and tissue with radiation injury, the radiologist aims to identify the predominant component of the lesion and categorize the findings according to the RANO criteria so that the patient can

receive the best treatment. The advanced techniques can be extremely helpful, though standardization of the methods used for calculation of rCBV, ADC, spectroscopy peaks, and PET parameters is needed to optimize the evaluation of such patients and accurately compare the data from multicentric studies.

Disclosures: Bruno Policeni—UNRELATED: Expert Testimony; law firms, Comments: expert witness to review legal material, no deposition*; Payment for Lectures Including Service on Speakers Bureaus: University of Kansas, Comments: visiting professor. *Money paid to the institution.

REFERENCES

- Ostrom QT, Gittleman H, Truitt G, et al. **CBTRUS Statistical Report: Primary Brain and Other Central Nervous System Tumors Diagnosed in the United States in 2011–2015.** *Neuro Oncol* 2018;20:iv1–86 CrossRef Medline
- Ostrom QT, Gittleman H, Stetson L, et al. Epidemiology of intracranial gliomas. In: *Intracranial Gliomas: Part I-Surgery*. Vol 30. Basel: Karger Publishers; 2018:1–11
- Ostrom QT, Cote DJ, Ascha M, et al. **Adult glioma incidence and survival by race or ethnicity in the United States from 2000 to 2014.** *JAMA Oncol* 2018;4:1254–62 CrossRef Medline
- van Linde ME, Brahm CG, de Witt Hamer PC, et al. **Treatment outcome of patients with recurrent glioblastoma multiforme: a retrospective multicenter analysis.** *J Neurooncol* 2017;135:183–92 CrossRef Medline
- Lacroix M, Toms SA. **Maximum safe resection of glioblastoma multiforme.** *J Clin Oncol* 2014;32:727–28 CrossRef Medline
- Stupp R, Mason WP, van den Bent MJ, et al. **Radiotherapy plus concomitant and adjuvant temozolomide for glioblastoma.** *N Engl J Med* 2005;352:987–96 CrossRef Medline
- Wick W, Gorlia T, Bendszus M, et al. **Lomustine and bevacizumab in progressive glioblastoma.** *N Engl J Med* 2017;377:1954–63 CrossRef Medline
- Lim M, Xia Y, Bettgowda C, et al. **Current state of immunotherapy for glioblastoma.** *Nat Rev Clin Oncol* 2018;15:422–42 CrossRef Medline
- Macdonald DR, Cascino TL, Schold SC, et al. **Response criteria for Phase II studies of supratentorial malignant glioma.** *J Clin Oncol* 1990;8:1277–80 CrossRef Medline
- Wen PY, Macdonald DR, Reardon DA, et al. **Updated response assessment criteria for high-grade gliomas: Response Assessment in Neuro-Oncology Working Group.** *J Clin Oncol* 2010;28:1963–72 CrossRef Medline
- Cabrera AR, Kirkpatrick JP, Fiveash JB, et al. **Radiation therapy for glioblastoma: executive summary of an American Society for Radiation Oncology Evidence-Based Clinical Practice Guideline.** *Pract Radiat Oncol* 2016;6:217–25 CrossRef Medline
- Conway J, Bragg CM. Treatment planning and computer systems. In: Cherry P, Duxbury A. *Practical Radiotherapy Physics and Equipment*. London: Greenwich Medical Media; 1998:161–95
- Lasocki A, Gaillard F. **Non-contrast-enhancing tumor: a new frontier in glioblastoma research.** *AJNR Am J Neuroradiol* 2019;40:758–65 CrossRef Medline
- Holdhoff M, Ye X, Piotrowski AF, et al. **The consistency of neuropathological diagnoses in patients undergoing surgery for suspected recurrence of glioblastoma.** *J Neurooncol* 2019;141:347–54 CrossRef Medline
- Kim JH, Bae Kim Y, Han JH, et al. **Pathologic diagnosis of recurrent glioblastoma.** *Am J Surg Pathol* 2012;36:620–68 CrossRef Medline
- Abbasi AW, Westerlaan HE, Holtman GA, et al. **Incidence of tumour progression and pseudoprogression in high-grade gliomas: a systematic review and meta-analysis.** *Clin Neuroradiol* 2018;28:401–11 CrossRef Medline

17. van West SE, de Bruin HG, van de Langerijt B, et al. **Incidence of pseudoprogression in low-grade gliomas treated with radiotherapy.** *Neuro Oncol* 2017;19:719–25 CrossRef Medline
18. Melguizo-Gavilanes I, Bruner JM, Guha-Thakurta N, et al. **Characterization of pseudoprogression in patients with glioblastoma: is histology the gold standard?** *J Neurooncol* 2015;123:141–50 CrossRef Medline
19. Taal W, Brandsma D, de Bruin HG, et al. **The incidence of pseudoprogression in a cohort of malignant glioma patients treated with chemo-radiation with temozolomide.** *Cancer* 2008;113:405–10 CrossRef Medline
20. Brandes AA, Franceschi E, Tosoni A, et al. **MGMT promoter methylation status can predict the incidence and outcome of pseudoprogression after concomitant radiochemotherapy in newly diagnosed glioblastoma patients.** *J Clin Oncol* 2008;26:2192–97 CrossRef Medline
21. Kumar AJ, Leeds NE, Fuller GN, et al. **Malignant gliomas: MR imaging spectrum of radiation therapy- and chemotherapy-induced necrosis of the brain after treatment.** *Radiology* 2000;217:377–84 CrossRef Medline
22. Okada H, Weller M, Huang R, et al. **Immunotherapy response assessment in neuro-oncology: a report of the RANO Working Group.** *Lancet Oncol* 2015;16:e534–42 CrossRef Medline
23. Reardon DA, Wen PY, Desjardins A, et al. **Glioblastoma multiforme: an emerging paradigm of anti-VEGF therapy.** *Expert Opin Biol Ther* 2008;8:541–53 CrossRef Medline
24. van den Bent MJ, Wefel JS, Schiff D, et al. **Response assessment in neuro-oncology (a report of the RANO group): assessment of outcome in trials of diffuse low-grade gliomas.** *Lancet Oncol* 2011;12:583–93 CrossRef Medline
25. Hu LS, Baxter LC, Smith KA, et al. **Relative cerebral blood volume values to differentiate high-grade glioma recurrence from post-treatment radiation effect: direct correlation between image-guided tissue histopathology and localized dynamic susceptibility-weighted contrast-enhanced perfusion MR imaging measurements.** *AJNR Am J Neuroradiol* 2009;30:552–58 CrossRef Medline
26. Barajas RF, Chang JS, Segal MR, et al. **Differentiation of recurrent glioblastoma multiforme from radiation necrosis after external beam radiation therapy with dynamic susceptibility-weighted contrast-enhanced perfusion MR imaging.** *Radiology* 2009;253:486–96 CrossRef Medline
27. Xu JL, Shi DP, Dou S, et al. **Distinction between postoperative recurrent glioma and delayed radiation injury using MR perfusion weighted imaging.** *J Med Imaging Radiat Oncol* 2011;55:587–94 CrossRef Medline
28. Young RJ, Gupta A, Shah AD, et al. **MRI perfusion in determining pseudoprogression in patients with glioblastoma.** *Clin Imaging* 2013;37:41–49 CrossRef Medline
29. Blasel S, Zagorcic A, Jurcoane A, et al. **Perfusion MRI in the evaluation of suspected glioblastoma recurrence.** *J Neuroimaging* 2016;26:116–23 CrossRef Medline
30. Patel P, Baradaran H, Delgado D, et al. **MR perfusion-weighted imaging in the evaluation of high-grade gliomas after treatment: a systematic review and meta-analysis.** *Neuro Oncol* 2017;19:118–27 CrossRef Medline
31. Suh CH, Kim HS, Choi YJ, et al. **Prediction of pseudoprogression in patients with glioblastomas using the initial and final area under the curves ratio derived from dynamic contrast-enhanced T1-weighted perfusion MR imaging.** *AJNR Am J Neuroradiol* 2013;34:2278–86 CrossRef Medline
32. Thomas AA, Arevalo-Perez J, Kaley T, et al. **Dynamic contrast enhanced T1 MRI perfusion differentiates pseudoprogression from recurrent glioblastoma.** *J Neurooncol* 2015;125:183–90 CrossRef Medline
33. Yun TJ, Park CK, Kim TM, et al. **Glioblastoma treated with concurrent radiation therapy and temozolomide chemotherapy: differentiation of true progression from pseudoprogression with quantitative dynamic contrast-enhanced MR imaging.** *Radiology* 2015;274:830–40 CrossRef Medline
34. Choi YJ, Kim HS, Jahng G-H, et al. **Pseudoprogression in patients with glioblastoma: added value of arterial spin labeling to dynamic susceptibility contrast perfusion MR imaging.** *Acta Radiol* 2013;54:448–54 CrossRef Medline
35. Deibler AR, Pollock JM, Kraft RA, et al. **Arterial spin-labeling in routine clinical practice, Part 1: technique and artifacts.** *AJNR Am J Neuroradiol* 2008;29:1228–34 CrossRef Medline
36. Zhang H, Ma L, Wang Q, et al. **Role of magnetic resonance spectroscopy for the differentiation of recurrent glioma from radiation necrosis: a systematic review and meta-analysis.** *Eur J Radiol* 2014;83:2181–89 CrossRef Medline
37. Reimer C, Deike K, Graf M, et al. **Differentiation of pseudoprogression and real progression in glioblastoma using ADC parametric response maps.** *PLoS One* 2017;12:e0174620 CrossRef Medline
38. Kazda T, Bulik M, Pospisil P, et al. **Advanced MRI increases the diagnostic accuracy of recurrent glioblastoma: Single institution thresholds and validation of MR spectroscopy and diffusion weighted MR imaging.** *NeuroImage Clin* 2016;11:316–21 CrossRef Medline
39. Prager AJ, Martinez N, Beal K, et al. **Diffusion and perfusion MRI to differentiate treatment-related changes including pseudoprogression from recurrent tumors in high-grade gliomas with histopathologic evidence.** *AJNR Am J Neuroradiol* 2015;36:877–85 CrossRef Medline
40. Mong S, Ellingson BM, Nghiemphu PL, et al. **Persistent diffusion-restricted lesions in bevacizumab-treated malignant gliomas are associated with improved survival compared with matched controls.** *AJNR Am J Neuroradiol* 2012;33:1763–70 CrossRef Medline
41. Nguyen HS, Milbach N, Hurrell SL, et al. **Progressing bevacizumab-induced diffusion restriction is associated with coagulative necrosis surrounded by viable tumor and decreased overall survival in patients with recurrent glioblastoma.** *AJNR Am J Neuroradiol* 2016;37:2201–08 CrossRef Medline
42. Law I, Albert NL, Arbizu J, et al. **Joint EANM/EANO/RANO practice guidelines/SNMMI procedure standards for imaging of gliomas using PET with radiolabelled amino acids and [18F]FDG: version 1.0.** *Eur J Nucl Med Mol Imaging* 2019;46:540–57 CrossRef Medline
43. La Fougère C, Suchorska B, Bartenstein P, et al. **Molecular imaging of gliomas with PET: opportunities and limitations.** *Neuro Oncol* 2011;13:806–19 CrossRef Medline
44. Parent EE, Sharma A, Jain M. **Amino acid PET imaging of glioma.** *Curr Radiol Rep* 2019;7:14 CrossRef
45. Galldiks N, Law I, Pope WB, et al. **The use of amino acid PET and conventional MRI for monitoring of brain tumor therapy.** *Neuroimage Clin* 2016;13:386–94 CrossRef Medline
46. Nishihashi T, Dahabreh IJ, Terasawa T. **Diagnostic accuracy of PET for recurrent glioma diagnosis: a meta-analysis.** *AJNR Am J Neuroradiol* 2013;34:944–50 CrossRef Medline

Lateral Decubitus Digital Subtraction Myelography: Tips, Tricks, and Pitfalls

 D.K. Kim,  W. Brinjikji,  P.P. Morris,  F.E. Diehn,  V.T. Lehman,  G.B. Liebo,  J.M. Morris,  J.T. Verdoorn,  J.K. Cutsforth-Gregory,  R.I. Farb,  J.C. Benson, and  C.M. Carr



ABSTRACT

SUMMARY: Digital subtraction myelography is a valuable diagnostic technique to detect the exact location of CSF leaks in the spine to facilitate appropriate diagnosis and treatment of spontaneous spinal CSF leaks. Digital subtraction myelography is an excellent diagnostic tool for assessment of various types of CSF leaks, and lateral decubitus digital subtraction myelography is increasingly being used to diagnose CSF-venous fistulas. Lateral decubitus digital subtraction myelography differs from typical CT and fluoroscopy-guided myelograms in many ways, including equipment, supplies, and injection and image-acquisition techniques. Operators should be familiar with techniques, common pitfalls, and artifacts to improve diagnostic yield and prevent nondiagnostic examinations.

ABBREVIATIONS: DSM = digital subtraction myelography; SIH = spontaneous intracranial hypotension; SSCSFL = spontaneous spinal CSF leak

Digital subtraction myelography (DSM) is a valuable diagnostic technique to detect the exact location of CSF leaks in the spine to facilitate definitive treatment with surgery or targeted blood patch. Spontaneous spinal CSF leak (SSCSFL) stereotypically presents with daily orthostatic headaches and has also been called “spontaneous intracranial hypotension” (SIH) and “CSF hypovolemia.” This entity can be quite difficult to diagnose; thus, the prevalence is likely underestimated.¹ Although prone DSM has been used for several years to identify the exact focus of a CSF leak in patients with suspected fast ventral leaks in the setting of spinal extradural fluid collections,² the technique of lateral decubitus positioning has been introduced more recently to detect subtle CSF-venous fistulas and different types of leaks.^{3,4} At Mayo Clinic, we implemented this technique into our practice in 2018, and the advantages of DSM to identify CSF-venous fistulas compared with other techniques such as conventional, dynamic CT and positive pressure MR myelograms quickly became apparent, with continuously increasing demand

from the patients and referring clinicians to increase availability. As we have performed an increasing number of these procedures, we have encountered and refined numerous small but easily implemented procedural steps that can make the difference between a diagnostic and nondiagnostic examination. This article describes the equipment, supplies, technique, and common pitfalls for our current approach to lateral decubitus DSM.

Patient Selection


Patients who present with new persistent daily headache with orthostatic features, worse with upright posture and partial or incomplete relief with recumbency and/or exacerbation with Valsalva, have high clinical suspicion for SSCSFL. These patients first undergo brain and entire spine imaging. The spine MR imaging is used to assess extradural fluid collections, and the brain MR imaging is used to look for manifestations of CSF hypotension and to further stratify the pretest probability.^{4,5} At Mayo Clinic, patients are first evaluated in our CSF dynamics clinic by neurologists who specialize in headache disorders and intracranial hypotension, and if there is no extradural fluid collection in the spine MR imaging, we generally proceed with a conventional CT myelography with early and delayed images. If CT myelography findings are negative, lateral decubitus DSM is performed to look for CSF-venous fistulas or other slower CSF leaks. If the spine MR imaging demonstrates an extradural fluid collection, the leak is considered fast, and we proceed with dynamic CT myelography, given its high detection rate for the location of this type of CSF leak.⁶ A flow diagram for the SSCSFL diagnostic


Received August 5, 2019; accepted after revision October 29.

From the Departments of Radiology (D.K.K., W.B., P.P.M., F.E.D., V.T.L., G.B.L., J.M.M., J.T.V., J.C.B., C.M.C.) and Neurology (J.K.C.-G.), Mayo Clinic, Rochester, Minnesota; and Department of Medical Imaging (R.I.F.), Division of Neuroradiology, Toronto Western Hospital, Toronto, Ontario, Canada.

Please address correspondence to Dong Kun Kim, MD, Department of Radiology, Mayo Clinic, 200 First St SW, Rochester MN 55905 e-mail: kim.dongkun@mayo.edu

 Indicates open access to non-subscribers at www.ajnr.org

 Indicates article with supplemental on-line photo.

 Indicates article with supplemental on-line videos.

<http://dx.doi.org/10.3174/ajnr.A6368>

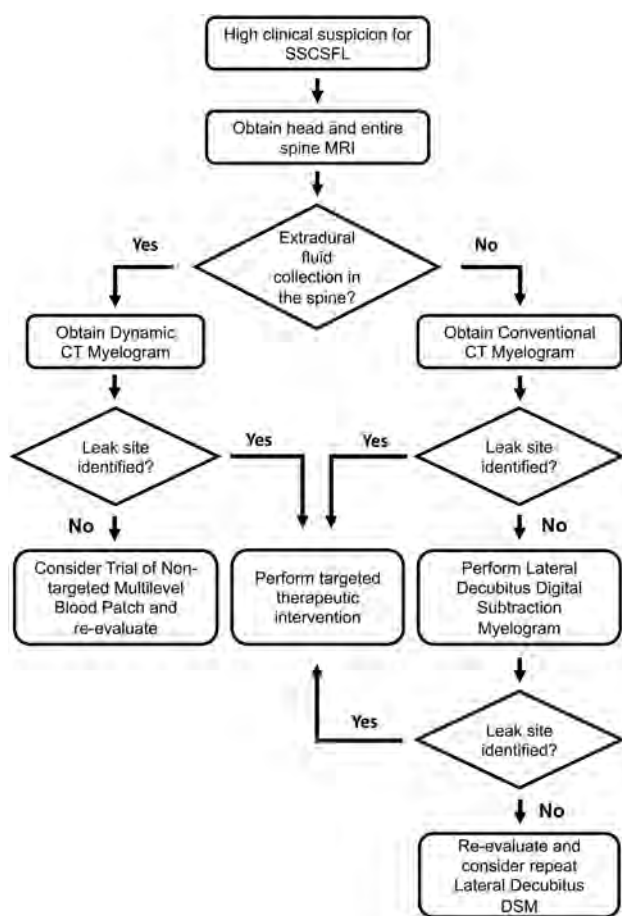


FIG 1. SSCSFL diagnostic imaging algorithm flow diagram.

imaging algorithm is presented in Fig 1. Our initial unpublished data suggested an approximately 50% rate of finding a CSF venous fistula in patients with negative CT myelography findings referred from our CSF dynamics clinic for high clinical suspicion.

Equipment and Supplies

DSM requires an x-ray system with a high-resolution flat panel detector and a high-power x-ray tube, similar to the ones used for cerebral and spinal angiography. We use Allura Xper FD 20/20 (Philips Healthcare, Best, the Netherlands) with spinal angiography set to 1 frame per 1–2 seconds. A tiltable table is preferred to adjust spine angling and control the contrast flow speed. Although it is not completely necessary, we have found that it is useful to have a wedge-shaped cushion to position a patient's hips more superiorly relative to the shoulders. Although our x-ray system is biplane, only a single plane is used for the procedure. We have used the MD Eleva system (Philips Healthcare) but were unable to get diagnostic images due to tube overheating. Although there may be other fluoroscopic units suitable for this examination, we have successfully acquired diagnostic-quality images using Axion Artis dTA ceiling mount (Siemens, Erlangen, Germany) and Allura Xper FD, and in our opinion, images from the Allura Xper FD are sharper and easier to interpret.

Our current setup for the DSM includes the following supplies (Fig 2) (manufacturer's information for our current setup

is included as a reference, but we recognize that there may be similar products just as suitable for this procedure): a 20-ga spinal needle (BD spinal needle; Becton Dickinson, Franklin Lakes, New Jersey), Omnipaque 300 contrast (GE Healthcare, Milwaukee, Wisconsin), sterile preservative-free normal saline, 3-way stopcock (Merit Medical Systems, South Jordan, Utah), 72-inch tubing (NAMIC pressure monitoring line; Navilyst Medical, Marlborough, Massachusetts), two 10-mL syringes, and two 30 mL syringes. The maximum recommended daily intrathecal dose of Omnipaque 300 is 10.2 mL. We have been using a total of 11 mL per day and dividing the contrast into two 10-mL syringes, 6 mL in one and 5 mL in the other. The 6-mL syringe is used for the upper thoracic run followed by 5 mL for the lower thoracic/upper lumbar region. Two 30-mL syringes are also filled with normal saline. The long tubing is 72 inches (183 cm) and holds approximately 3 mL of injectate. Typically, DuraPrep (3M, St. Paul, Minnesota) is used for skin preparation.

Procedure Technique

DSM is a 2-day procedure due to dose constraints of intrathecal Omnipaque 300. The patient receives 11 mL of intrathecal Omnipaque on the first day for DSM of one side and typically returns the following day for an additional 11 mL of intrathecal Omnipaque for DSM on the other side. We have performed >100 DSM runs in the past year without any major complications from intrathecal Omnipaque administration. Omnipaque 300 is the preferred concentration because we used Omnipaque 240 during our initial DSM experience and found it too dilute, and the ability to see subtle structures such as CSF-venous fistulas is compromised, even with the digital subtraction technique. Omnipaque 350 and 140 are contraindicated for intrathecal use.

DSM is performed with the patient in the lateral decubitus position on one side, and the patient returns the next day for the same procedure on the other side. For each side, 2 separate DSM runs are performed, typically, the first run with the FOV from the lower cervical-to-mid-/lower thoracic level, and the second run with the FOV mildly overlapping the mid-/lower thoracic level to the lumbar puncture level. A ruler or radiopaque markers are placed on the nondependent aspect of the spine to ensure appropriate vertebral counting between the 2 runs. Although the mid-to-upper cervical spine and lower lumbar spine are not routinely included (CSF-venous fistulas are thought to be rare in these locations), if needed, these levels can be assessed in the subsequent decubitus CT myelogram. DSM can be performed with the patient under general anesthesia or awake with or without moderate sedation, depending on the patient. Many patients develop headache or pressure when the contrast flows intracranially, similar to other myelograms. Given the need to minimize movement, it may be beneficial to give moderate sedation to awake patients to alleviate discomfort.

Patient Positioning. We use a custom-made wedge to position the hips higher than the shoulders to allow preferential cranial flow of contrast from the lumbar region by gravity (Fig 3). Although a custom-made wedge may be sufficient, a tiltable angiography table is preferred for maximum control of the contrast

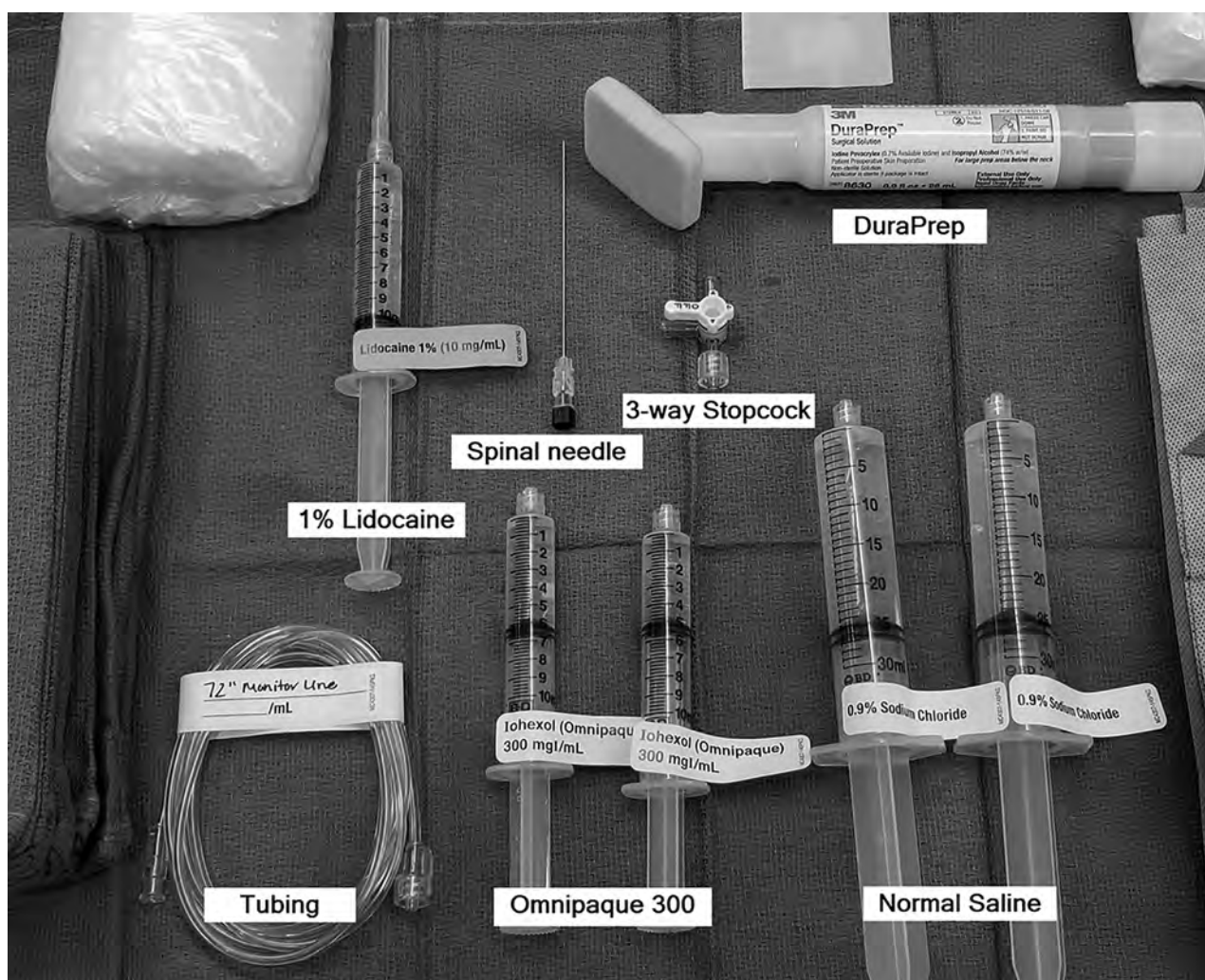


FIG 2. Supplies for DSM.

flow speed because the wedge may be too steep or not steep enough, depending on patient's body habitus. Patients need to be in as perfect a lateral decubitus position as possible to ensure that the neural foramina and nerve sheath diverticula have maximal exposure to the iodinated contrast and to increase the likelihood of optimally imaging potentially very subtle CSF-venous fistulas. Goals of positioning include moving all leads, IVs, tubing, clothing, and anything else physically located on the patient away from the midline so that they will not interfere with image quality during the DSM.

Positioning of the arms can be problematic, especially if the examination is performed with the patient under general anesthesia. The dependent arm typically can be tucked in close to the body and will be away from midline, as long as lateral positioning is maintained. If the patient begins to lean forward or backward, then the dependent arm may project across the midline. The superior arm can be positioned slightly to the front of the side and may need to be secured to maintain that position. It is not ideal for the superior arm to be positioned immediately along the side of the body. Positioning of lower extremities is not as important as long as the lumbar spine FOV is not obscured. During the placement of the needle into the thecal sac, it is advisable to move

the fluoroscopy unit into an anterior-posterior position with respect to the table to image the patient in the lateral view to avoid the needle puncturing the ventral dura. A ventral dural puncture can induce a temporary leak and has the potential to result in a nondiagnostic study. If the superior arm is along the side, it may interfere with clearly seeing the precise location of the needle tip during the needle placement.

Needle Positioning. Intrathecal access is obtained in a manner similar to a typical myelography.⁷ However, the combination of lateral decubitus positioning and CSF hypotension can make the needle positioning difficult at times. The needle is advanced slowly as the needle position is checked in anterior-posterior and lateral views, and once the needle position is confirmed to be in the center of the bony spinal canal, a small amount of iodinated contrast is injected while observing under fluoroscopy in the lateral view to confirm intrathecal positioning.

Injectate Preparation. The long tubing is connected to the 30-mL saline flush through the 3-way stopcock. Normal saline is flushed through the tubing while keeping the third port unflushed, thereby keeping air in the hub of the third port. The

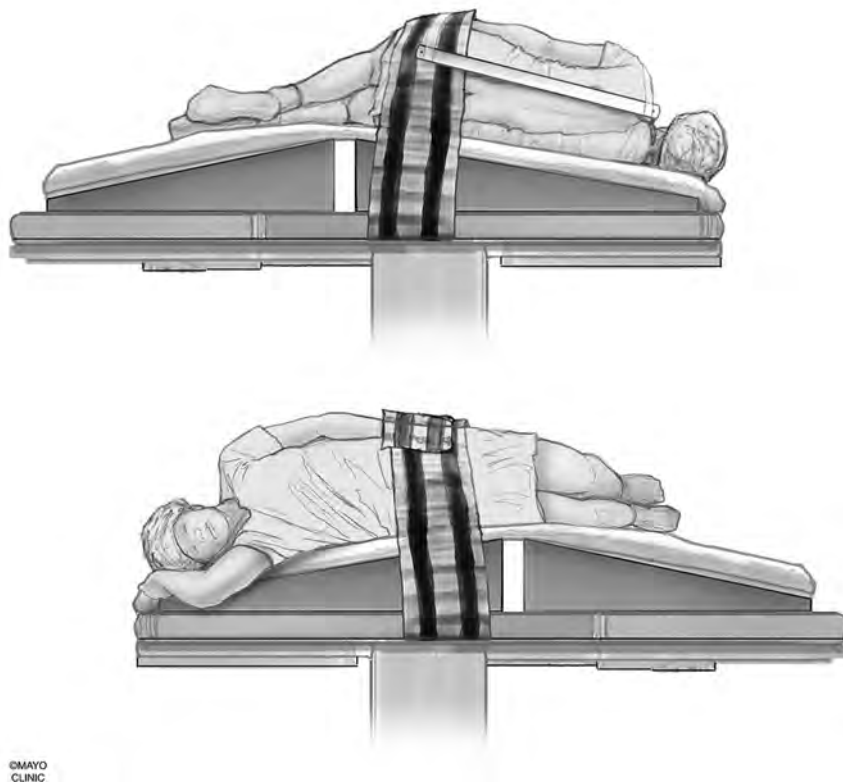


FIG 3. Patient positioning. A custom-made wedge is used to position the hips higher than the shoulders to create cranial flow of the contrast from the lumbar region by gravity. Reprinted with permission from the Mayo Foundation for Medical Education and Research. All rights reserved.

10-mL syringe with 6 mL of Omnipaque is then connected to the third port while maintaining an air bubble within that port. The other end of the long tubing is secured to the hub of the spinal needle, and 10–20 mL of sterile normal saline may be injected slowly to pressurize the thecal sac. Afterward, the 3-way stopcock is switched to open the tubing to the contrast, and the contrast is slowly injected through the tubing while following the air bubble that separates the contrast from the saline. Once the contrast column reaches the hub of the spinal needle, the injection is paused, the patient position is double-checked, possible causes of artifacts are corrected, and the patient (or the anesthesiologists/nurse anesthetists in general anesthesia cases) is coached on the importance of keeping still and breath-holding. The patient is coached about shallow/quiet breathing once he or she is no longer able to breath-hold.

Digital Subtraction Myelography Image Acquisition. The caudal-to-cranial tilt from the wedge will naturally cause contrast to flow cephalad. Due to differences in body habitus and boosting from pillows or blankets, the tilt angle of the table provided by the angiography unit is not representative of the actual degree of spine tilt with respect to the floor. The true angle of the spine with respect to the floor can be assessed by positioning the image

intensifier in a lateral position with respect to the table and the fluoroscopy unit vertical to the floor. A vertical line in the fluoroscopic image obtained this way will correspond to the horizontal axis with respect to the floor (Fig 4). Approximately 5°–7° of spine tilt with respect to this axis is optimal so that the contrast progresses cranially at about 1–2 vertebral segments per second.

The image intensifier is first positioned to span the lower cervical spine to mid-/lower thoracic level. The image is optimized by collimating the x-ray beam and using filters as necessary, focusing on the dependent side of the spine where the contrast will layer due to gravity. Because the imaged region is well above the lumbar puncture site, it takes usually 3–5 seconds for the contrast to reach the imaged region. Therefore, the proceduralist should start injecting the contrast first, wait about 2 seconds, then have the patient breath-hold while starting the digital subtraction image acquisition. Once all 6 mL of contrast is injected from the syringe, the 3-way stopcock is rapidly switched to open up the normal saline into the tubing and inject about 5 mL of normal saline to flush

the remaining contrast within the tubing and push the contrast lingering in the lumbar region cranially. Once contrast reaches the most superior level visible in the FOV, it is no longer necessary to continue flushing with normal saline. Diagnostic image acquisition should continue until the most superior nerve sheaths have had adequate time to be exposed to the contrast. We have found that image-acquisition length should be at least 45 seconds, though longer may be beneficial. The patient is instructed to resume quiet breathing if unable to breath-hold for the full duration of image acquisition because diagnostic-quality images can still be obtained with quiet breathing.

To prepare for the mid-/lower thoracic-to-lumbar region imaging, sterile normal saline is reloaded in the 30 mL syringe, and the empty 10-mL contrast syringe is disconnected. The 3-way stopcock from the saline port to the now-empty port is opened, the normal saline syringe is drawn back to recreate an air pocket, and then the 10-mL syringe filled with 5 mL of Omnipaque is connected to the air-filled hub of the 3-way stopcock. The table and image intensifier are positioned so that the needle tip is at the lower end of the image. If there is more than trace amount of residual contrast layering within the thecal sac, normal saline can be injected to push the contrast cranially. Afterward, in a similar manner, the contrast column in the



FIG 4. Defining the true horizontal axis and spine tilt on DSM. By placing the C-arm in a vertical position with respect to the floor (A, *dotted arrows*) while maintaining the long axis of the image intensifier orthogonal to the C-arm (B, *solid arrow*), the long axis of the image intensifier and the long axis of the image are aligned horizontally, parallel to the floor (B and C, *solid arrow*). The angle between this line and the line connecting the spinous processes (C, *dotted line*) defines the spine tilt with respect to the floor.

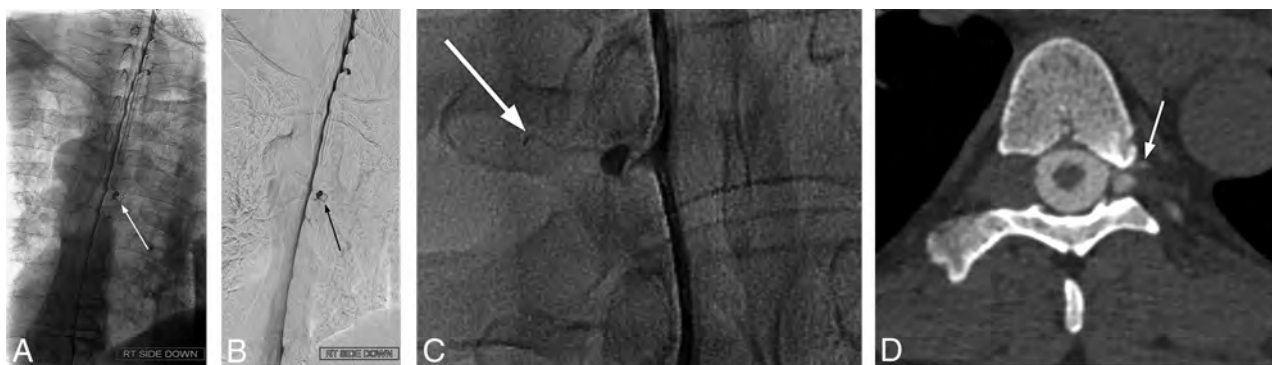


FIG 5. Examples of diagnostic DSM. Full-FOV DSM images from a lower cervical-to-mid-/lower thoracic run clearly delineate a CSF-venous fistula in the unsubtracted image (A) and subtracted image (B). A digitally magnified unsubtracted image from another patient shows a very subtle CSF-venous fistula (C), which is better seen in a subsequent CT myelogram (D).

tubing is advanced to the hub of the spinal needle by using the position of the bubble.

Because the needle is at the lower edge of the FOV, the contrast column will appear in the image almost immediately as contrast is injected. The patient should breath-hold, the digital subtraction acquisition is started, and then contrast is injected. Once all contrast in the syringe is injected, the stopcock is rapidly switched to open up the normal saline to the tubing and flush the remaining contrast in the tubing. Again, the goal is to image long enough so that each neural foramen is adequately exposed to contrast, at least ≥ 45 seconds if possible.

The tubing should be disconnected from the needle, the stylet reset, the spinal needle removed, and a sterile dressing placed. If

indicated, one may scan up and down the spine under fluoroscopy and take some magnified spot images.

Further Diagnostic Optimization Options

DSM can be performed with the patient under general anesthesia, moderate sedation, or without sedation depending on radiologist's preference and a variety of patient factors. General anesthesia is helpful to minimize motion artifacts, but there are other factors that can be problematic, such as positioning the patient in the lateral decubitus position under general anesthesia, artifacts from ventilation and monitoring equipment, and limitations of arm placement due to the risk of brachial plexus injury. For larger patients, we rarely perform

DSM with the patient under general anesthesia because the body habitus makes it difficult to place and maintain the patient in the lateral decubitus position. Moderate sedation can be effectively used in patients who are cooperative and have the ability to carefully follow breathing instructions. The area of interest is within the first 1–2 cm from the spinal canal overlying the vertebra and transverse processes, which is typically less degraded by respiratory motion. Correlating subtracted images with the unsubtracted images is helpful to clarify potential motion artifacts.

Another option to potentially increase the diagnostic yield is to perform a lateral decubitus CT myelography immediately following DSM, without repositioning the patient. Diagnostic yield for the additional CT study is yet to be determined and needs further evaluation. At this time, we perform lateral decubitus CT myelography on all patients with negative findings on DSM because we have seen a patient in whom a subtle fistula was missed in DSM, which was subsequently detected in a decubitus CT myelogram. We obtain the entire spine CT in a single pass in a dual-energy setting (100 kV and 140 kV) and create 50-keV monoenergetic reconstructions to maximize detection of subtle contrast leakage.^{8,9}

Image Interpretation. Both the subtracted and unsubtracted DSM images and, if available, subsequent decubitus CT myelograms, are scrutinized for CSF leaks and CSF-venous fistulas (Fig 5 and On-line Video Clip 1). In our experience, the decubitus CT myelogram often helps to problem-solve findings on the DSM and confirm the location of diverticula. To facilitate DSM image processing, we briefly review DSM images at the technologist's console to look for an obvious leak and to remask the images in case of gross patient motion. Obtained and processed images are then reviewed on the PACS. The 100-kV and 50-keV CT myelograms are reviewed in detail under multiplanar reconstructions.

Common Artifacts/Pitfalls. Due to the daily maximum intrathecal dose of Omnipaque 300, if the study is nondiagnostic, the patient needs to return on a different day for a repeat procedure. This is a major inconvenience, causes unnecessary additional radiation exposure to the patient, and is an inopportune use of medical resources. This section shows examples of common artifacts and pitfalls and ways to prevent or minimize their effects.

Patient Rotation. The ideal DSM position for detection of CSF-venous fistulas is to have the patient completely in a 90° lateral decubitus position and the x-ray beam horizontal to produce a straight contrast meniscus. If the patient is deviated from the 90° lateral decubitus position and the beam is horizontal, there will be foreshortening of the nerve root sheaths and the contrast within the thecal sac could potentially obscure the CSF-venous fistula (Fig 6). If the patient is tilted from true lateral decubitus position and the detector is also tilted to produce an anterior-posterior image, the contrast column will be slanted, making the contrast appear less dense, and less contrast will layer laterally to opacify the fistula.



FIG 6. Effect of patient rotation on the image. A, An unsubtracted image from a DSM study obtained with the patient in the true right lateral decubitus position and the image intensifier horizontal shows the contrast outlining the exiting nerve roots and filling small nerve sheath diverticula. B, An unsubtracted image from a DSM study from the same patient in the oblique left lateral decubitus position and the image intensifier horizontal shows partial obscuration of the contrast in the nerve sheaths due to an overlying contrast column within the thecal sac. Note the differences in the position of the spinous processes indicating the patient obliquity.

Suboptimal Contrast-Flow Speed. There needs to be an even and sufficient layer of contrast within thecal sac at all imaged levels to optimize opacification of a potential CSF-venous fistula. If the contrast flows too fast, not enough contrast column will be available to fill the fistula, and if contrast flow is too slow, not enough time will be available for the upper levels to fill the fistula before the patient needs to breathe. Straight spine alignment provides an even contrast flow, and spine tilt with respect to the floor determines the overall speed of the contrast. We have found that contrast progression of 1–2 levels per second provides an optimal contrast column (Fig 7).

Subdural Injection. The combination of CSF hypotension, lateral decubitus positioning, and forceful injection into the thecal sac make it relatively easy to perform a subdural injection. CSF hypotension causes tenting of the thecal sac, which makes intrathecal access difficult at times despite positioning the spinal needle tip in the middle of the bony spinal canal. Therefore, it is imperative that a test injection be performed to confirm the intrathecal needle position (Fig 8). Despite confirming intrathecal access and

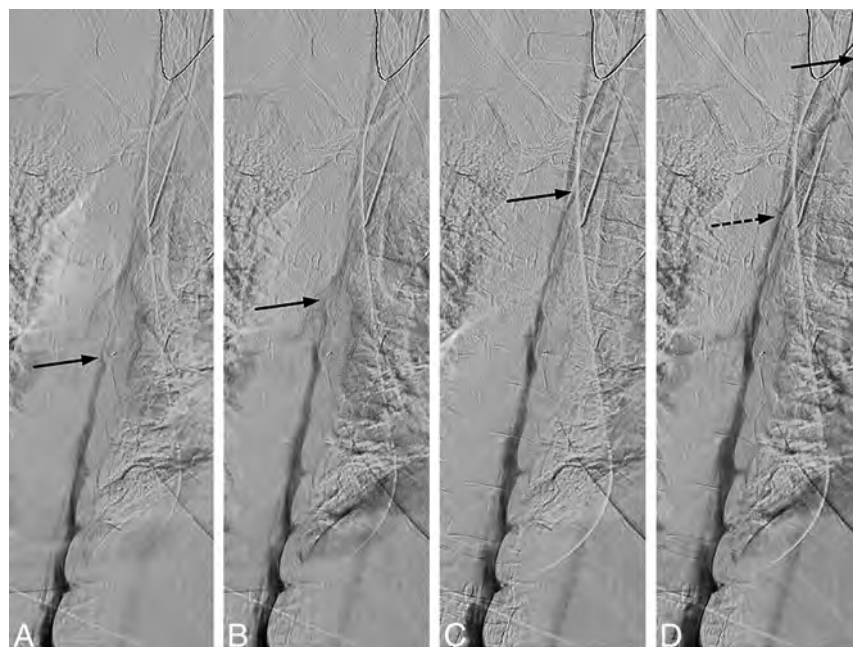


FIG 7. Uneven contrast flow. Consecutive DSM images at 1 frame per 2 seconds, with the leading edge of the contrast column denoted by the *solid arrows*. A and B, Initial optimal flow with 1-level progression per second, but subsequent images in C and D show contrast progressing more rapidly, 2–4 levels per second. Note that only a thin layer of contrast is visible at the convex aspect of the spine curvature and less contrast is available to opacify a potential CSF-venous fistula at this level (D, *dotted arrow*).

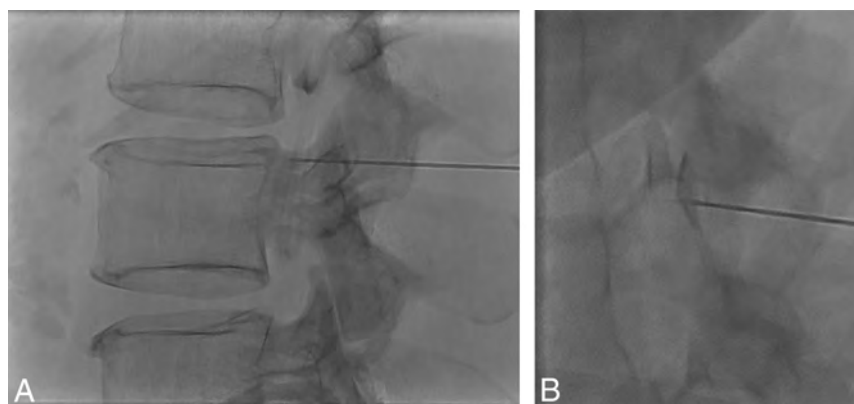


FIG 8. Tenting of the thecal sac and confirming intrathecal contrast flow. A, Lateral view spot image with a test injection shows contrast outlining the nerve roots, confirming intrathecal needle positioning. B, Lateral view spot image with a test injection in a different patient shows tenting of the thecal sac and subdural contrast despite the needle tip appearing to be well within the bony spinal canal.

keeping the needle still as the thecal sac is rapidly pressurized, the needle occasionally backs out and causes subdural injection (Fig 9). Although this issue usually results in partial subdural injection with enough intrathecal contrast for adequate diagnostic yield, we use a 20-ga needle instead of a smaller gauge needle to minimize the needle backing out due to the pressure. In addition, it is not necessary to have too strong an injection with the 20-ga needle because the optimal flow rate is a 1- to 2-level progression per second. The first indicator that an injection may be subdural is when contrast takes longer to arrive at the inferior part of the image on the first run. This is then followed by a masslike contrast collection, often in the middle of the spine rather than the

expected layering meniscus of contrast filling the nerve sheaths and nerve sheath diverticula. If this occurs, it is still worthwhile to continue if there is some intrathecal contrast flow because the source of the leak may still be found.

Artifacts from Superimposed Objects. Various objects overlying the patient can cause artifacts that can degrade the diagnostic quality of the DSM. This is especially problematic in patients under general anesthesia due to various monitoring leads and support material to keep the patient in the lateral decubitus position (On-line Figure). It is important to recognize these poten-

tial causes of artifacts before contrast injection and adjust as many overlying objects as possible to optimize image quality.

CONCLUSIONS

DSM is an excellent diagnostic tool for assessment of various types of CSF leaks, and lateral decubitus DSM is increasingly being used to diagnose subtle CSF-venous fistulas. Meticulous technique and attention to detail are critical for procedure optimization and interpretation. Neuroradiologists should be familiar with optimal techniques and common pitfalls and

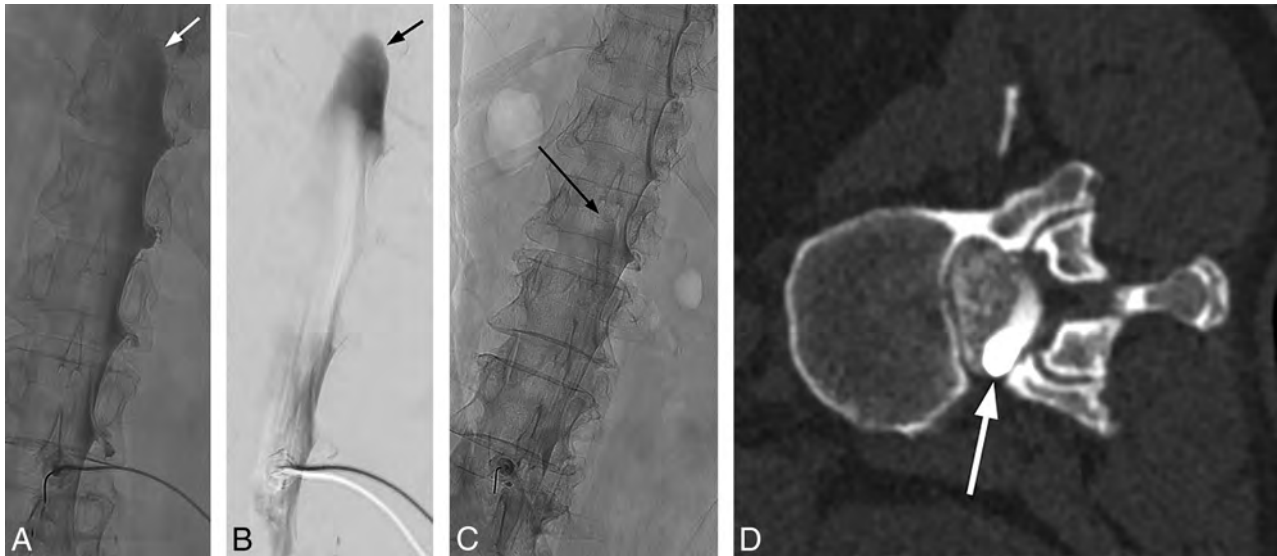


FIG 9. Mixed subdural and intrathecal injection. Unsubtracted (A) and subtracted (B) images from the DSM study demonstrate a subdural contrast injection superimposed on some intrathecal contrast. Note the masslike contrast extending cranially (arrows) rather than normal layering meniscus of intrathecal contrast. Unsubtracted image from the DSM study from another patient shows a small amount of masslike subdural contrast column extending cranially (C, arrow), which is confirmed on the subsequent decubitus CT myelogram (D, arrow).

artifacts to improve diagnostic yield and prevent nondiagnostic examinations.

Disclosures: Jeremy K. Cutsforth-Gregory—UNRELATED: Board Membership: Spinal CSF Leak Foundation Medical Advisory Board, Comments: This is a completely volunteer position, without financial or in-kind compensation; Royalties: textbook royalties from Oxford University Press, Comments: *Mayo Clinic Medical Neurosciences*. 6th ed.

ACKNOWLEDGMENTS

The authors acknowledge the assistance of Dr Sonia Watson in editing the manuscript.

REFERENCES

1. Schievink WI. Spontaneous spinal cerebrospinal fluid leaks and intracranial hypotension. *JAMA* 2006;295:2286–96 CrossRef Medline
2. Hoxworth JM, Trentman TL, Kotsenas AL, et al. The role of digital subtraction myelography in the diagnosis and localization of spontaneous spinal CSF leaks. *AJR Am J Roentgenol* 2012;199:649–53 CrossRef Medline
3. Schievink WI, Moser FG, Maya MM, et al. Digital subtraction myelography for the identification of spontaneous spinal CSF-venous fistulas. *J Neurosurg Spine* 2016;24:960–64 CrossRef Medline
4. Farb RI, Nicholson PJ, Peng PW, et al. Spontaneous intracranial hypotension: a systematic imaging approach for CSF leak localization and management based on MRI and digital subtraction myelography. *AJNR Am J Neuroradiol* 2019;40:745–53 CrossRef Medline
5. Dobrocky T, Grunder L, Breiding PS, et al. Assessing spinal cerebrospinal fluid leaks in spontaneous intracranial hypotension with a scoring system based on brain magnetic resonance imaging findings. *JAMA Neurol* 2019;76:580–87 CrossRef Medline
6. Luetmer PH, Schwartz KM, Eckel LJ, et al. When should I do dynamic CT myelography? Predicting fast spinal CSF leaks in patients with spontaneous intracranial hypotension. *AJNR Am J Neuroradiol* 2012;33:690–94 CrossRef Medline
7. Hudgins PA, Fountain AJ, Chapman PR, et al. Difficult lumbar puncture: pitfalls and tips from the trenches. *AJNR Am J Neuroradiol* 2017;38:1276–83 CrossRef Medline
8. Postma AA, Das M, Stadler AA, et al. Dual-energy CT: what the neuroradiologist should know. *Curr Radiol Rep* 2015;3:16 CrossRef Medline
9. Shuman WP, Chan KT, Busey JM, et al. Dual-energy CT aortography with 50% reduced iodine dose versus single-energy CT aortography with standard iodine dose. *Acad Radiol* 2016;23:611–18 CrossRef Medline

Does Increasing Packing Density Using Larger Caliber Coils Improve Angiographic Results of Embolization of Intracranial Aneurysms at 1 Year: A Randomized Trial

J. Raymond, J. Ghostine, B.A. van Adel, J.J.S. Shankar, D. Iancu, A.P. Mitha, P. Kvamme, R.D. Turner, A. Turk, V. Mendes-Pereira, J.S. Carpenter, S. Boo, A. Evans, H.H. Woo, D. Fiorella, A. Alaraj, D. Roy, A. Weill, P. Lavoie, M. Chagnon, T.N. Nguyen, J.L. Rempel, and T.E. Darsaut



ABSTRACT

BACKGROUND AND PURPOSE: The impact of increased aneurysm packing density on angiographic outcomes has not been studied in a randomized trial. We sought to determine the potential for larger caliber coils to achieve higher packing densities and to improve the angiographic results of embolization of intracranial aneurysms at 1 year.

MATERIALS AND METHODS: Does Embolization with Larger Coils Lead to Better Treatment of Aneurysms (DELTA) was an investigator-initiated multicenter prospective, parallel, randomized, controlled clinical trial. Patients had 4- to 12-mm unruptured aneurysms. Treatment allocation to either 15- (experimental) or 10-caliber coils (control group) was randomized 1:1 using a Web-based platform. The primary efficacy outcome was a major recurrence or a residual aneurysm at follow-up angiography at 12 ± 2 months adjudicated by an independent core lab blinded to the treatment allocation. Secondary outcomes included indices of treatment success and standard safety outcomes. Recruitment of 564 patients was judged necessary to show a decrease in poor outcomes from 33% to 20% with 15-caliber coils.

RESULTS: Funding was interrupted and the trial was stopped after 210 patients were recruited between November 2013 and June 2017. On an intent-to-treat analysis, the primary outcome was reached in 37 patients allocated to 15-caliber coils and 36 patients allocated to 10-caliber coils (OR = 0.931; 95% CI, 0.528–1.644; $P = .885$). Safety and other clinical outcomes were similar. The 15-caliber coil group had a higher mean packing density (37.0% versus 26.9%, $P = .0001$). Packing density had no effect on the primary outcome when adjusted for initial angiographic results (OR = 1.001; 95% CI, 0.981–1.022; $P = .879$).

CONCLUSIONS: Coiling of aneurysms randomized to 15-caliber coils achieved higher packing densities compared with 10-caliber coils, but this had no impact on the angiographic outcomes at 1 year, which were primarily driven by aneurysm size and initial angiographic results.

Endovascular embolization of intracranial aneurysms with platinum coils has been shown to be effective for preventing rebleeding in aneurysmal SAH and is a widely offered treatment

Received October 16, 2019; accepted after revision November 6.

From the Department of Radiology (J.R., J.G., D.R., A.W.), Service of Interventional Neuroradiology, Centre Hospitalier de l'Université de Montréal, Montreal, Quebec, Canada; Department of Surgery/Medicine (B.A.v.A.), McMaster University, Hamilton, Ontario, Canada; Division of Neuroradiology (J.J.S.), Department of Radiology, Dalhousie University, Halifax, Nova Scotia, Canada; Department of Radiology (J.J.S.), University of Manitoba, Winnipeg, Manitoba, Canada; Department of Radiology, Service of Interventional Neuroradiology (D.I.), University of Ottawa Hospitals, Civic Campus, Ottawa, Ontario, Canada; Department of Clinical Neurosciences (A.P.M.), University of Calgary, Calgary, Alberta, Canada; Department of Radiology (P.K.), University of Tennessee Medical Center, Knoxville, Tennessee; Department of Neurosurgery (R.D.T., A.T.), Prisma Health—Upstate, Greenville, South Carolina; Division of Neuroradiology (V.M.-P.), Department of Medical Imaging, Toronto Western Hospital, University Health Network, Toronto, Ontario, Canada; Department of Neuroradiology (J.S.C., S.B.), West Virginia University, Rockefeller Neuroscience Institute, Morgantown, West Virginia; Department of Interventional Neuroradiology (A.E.), University of Virginia Medical Center, Charlottesville, Virginia; Departments of Neurosurgery and Radiology, Northwell Health System (H.H.W., D.F.), Manhasset, New York; Department of Neurosurgery (A.A.), University of Illinois Hospital and Health Sciences System, Chicago, Illinois; Department of Neurosurgery (P.L.), Hôpital Enfant-Jésus, Quebec City, Quebec, Canada; Department of Mathematics and Statistics (M.C.), University of Montreal, Montreal, Quebec, Canada; Departments of Neurology, Neurosurgery, and Radiology (T.N.N.), Boston Medical Center, Boston, Massachusetts; and Department of Radiology and Diagnostic Imaging (J.L.R.) and Division of Neurosurgery (T.E.D.), Department of Surgery, Mackenzie Health Sciences Centre, University of Alberta Hospital, Edmonton, Alberta, Canada.

for the primary prevention of SAH from unruptured aneurysms.^{1,2} However, aneurysm recurrence following initial treatment is not infrequent, leading to long-term angiographic surveillance and retreatment when aneurysms recur.³ A multicenter registry has reported up to 15% retreatment rates at 2 years after coiling of ruptured aneurysms, but a yearly rerupture rate of only 0.2% after the first year.⁴ Recurrence has been linked to several factors, including rupture status, aneurysm size, neck width, initial angiographic results of treatment, and packing density.^{5,6} Large-caliber platinum coiling systems (15-caliber coils) have been introduced for use in relatively small aneurysms. The aim was to more completely fill the aneurysm sac with embolic material.⁷ We sought to determine the potential for those larger caliber

Unrestricted research grant from DePuy Synthes, part of Johnson & Johnson Medical Products, a division of Johnson & Johnson Inc; and Cerenovus, Part of DePuy Synthes Products Inc (study No. C55-CNV-14-006).

Please address correspondence to Jean Raymond, MD, Department of Radiology, Service of Interventional Neuroradiology, Centre Hospitalier de l'Université de Montréal, 1000 Saint-Denis St, Room D03-5462B, Montreal, QC H2X 0C1 Quebec, Canada; e-mail: jean.raymond@umontreal.ca

Indicates open access to non-subscribers at www.ajnr.org

Indicates article with supplemental on-line tables.

<http://dx.doi.org/10.3174/ajnr.A6362>

coils to achieve higher packing densities in 4- to 12-mm aneurysms and ultimately to decrease the rate of poor angiographic outcomes at 1 year. The Does Embolization with Larger Coils Lead to Better Treatment of Aneurysms (DELTA) trial was initiated to examine the safety and efficacy of endovascular coil embolization with 15-caliber coils (DELTAMAXX Microcoil; DePuy Synthes, Codman for Neuro, Raynham, Massachusetts) compared with embolization with 10-caliber coils in patients with small-to-medium-sized aneurysms. The prespecified pilot phase reporting the capacity for 15-caliber coils to increase packing density compared with 10-caliber coils has been previously published.⁸ The hypothesis of the pivotal study was a decrease in the rate of residual aneurysm and recurrence at 1 year from 33% with 10-caliber to 20% with 15-caliber coils, necessitating the recruitment of 564 patients (α , 5%; β error, 10%). Recruitment was stopped on December 5, 2108, because financial support was interrupted despite the recommendation of the trial Data Safety and Monitoring Committee (DSMC) to pursue the trial. We report here the final results of the DELTA trial.

MATERIALS AND METHODS

Trial Design

DELTA was an investigator-initiated multicenter prospective, parallel, randomized, controlled, single-blind clinical trial. The study is registered and summarized on <https://clinicaltrials.gov/>, NCT01943591, and the full protocol can be found at <http://bit.ly/2DZcTot>. There were no changes to the protocol during the conduct of the trial.

Eligibility Criteria

The trial had wide inclusion criteria: adult patients with at least 2 years of life expectancy, having a ruptured (World Federation of Neurosurgical Societies grades I–III SAH) or unruptured 4- to 12-mm intracranial aneurysm, considered for endovascular coil embolization and amenable for treatment with either 15- or 10-caliber coils. There were few exclusion criteria: patients with planned treatment of an associated cerebral arteriovenous malformation and those for whom parent vessel occlusion was the primary intent of the procedure.

Participating Centers

The trial was to be conducted in approximately 20 neurovascular centers with experience in endovascular treatment of aneurysms (at least 100 patients previously treated).

Interventions

Patients allocated to the 15-caliber coiling group were preferably to receive as many 15-caliber platinum coils as safely achievable, but the procedure could be completed with 10-caliber filling or finishing coils, to optimize complete occlusion. Patients allocated to the 10-caliber coiling group were to receive only platinum coils of the latter size. Operators had the technical freedom to use any adjunctive technique, such as balloon-assisted or stent-assisted coil embolization. The study did not require any additional testing or procedure other than routine practice at the participating center.

To explore some explanatory analyses in case of nonconclusive intent-to-treat analyses, we prespecified a coiling protocol deviation to occur in the 15-caliber coil group when <30% of coil length was 15-caliber coils; in the 10-caliber coil group, any use of 15-caliber coils was considered a coiling protocol deviation. Coiling protocol deviations were included in their allocated coil group in intent-to-treat analyses but were removed from their allocated coil group (ie, not considered as crossovers) in the per-protocol analyses.

Randomization

Randomized (1:1) allocation of treatment groups was concealed using a Web-based platform, and the rupture status and previous treatment of the aneurysm were used as minimization criteria.

Outcomes

The primary efficacy outcome measure was a composite end point consisting mostly of the occurrence of a major recurrence or a residual aneurysm at the time of follow-up angiography at 12 ± 2 months, as adjudicated by an independent core lab blinded to the treatment allocation. The degree of aneurysm occlusion was adjudicated according to the Montreal scale (complete occlusion, residual neck, or residual aneurysm).⁵ In the absence of follow-up imaging, other components of the composite primary end point were adjudicated by an independent committee according to the following prespecified criteria of treatment failures (expected to be infrequent): initial treatment failure, when no coils were deployed; hemorrhage during the follow-up period; retreatment of the same lesion by endovascular or surgical means during the follow-up period; occurrence or progression of mass effect in relation to the treated aneurysm; or treatment-related morbidity and mortality precluding follow-up angiography.

Secondary outcomes included indices of immediate treatment success, individual components of the composite primary outcome, and standard safety outcomes: initial technical success of the coiling strategy; use of adjunctive devices; number and total length of coils implanted for each type; packing density; time of fluoroscopic exposure (the addition of the time, in minutes, for both detectors of the biplane angiography unit); immediate angiographic results according to the Montreal scale; major recurrence on follow-up angiography; procedure-related serious adverse events; any adverse event; length of hospital stay; discharge destination; mRS at discharge and at 1-year follow-up; and morbidity and mortality that precluded angiographic follow-up.

Packing Density

Packing density or volume embolization ratio is the volume of inserted coils divided by the aneurysm volume. Coil volume was calculated using the following formula: $V = \pi(c/2)^2L$, where c is coil caliber and L is coil length for coils entered in the procedural case report forms. Aneurysm volumes were determined using a simple mathematic model: $V = 4/3 \pi ab(a+b)/2$, where a and b are half of the long and short axes of the aneurysm, as entered on the procedural case report forms.

Analyses

Descriptive statistics were obtained on demographic variables and aneurysm characteristics to compare the 2 groups at baseline.

Means, SDs, and range are presented for quantitative variables, and frequency tables, for categorical variables. Comparability of the groups was assessed through an independent Student *t* test (quantitative data) or exact χ^2 tests (categorical data). The primary outcome, recurrence rates (for both intent-to-treat and per-protocol groups), was compared between groups through χ^2 tests and odds ratios with 95% confidence intervals. Logistic regression was used to examine an association between packing density and primary outcome. Secondary outcomes and safety data were compared between groups through independent Student *t* tests (quantitative variables) or exact χ^2 statistics (categorical data). Finally, logistic regression was used to find variables capable of predicting recurrences. The variables were selected using the stepwise forward approach based on likelihood using $\alpha < .05$ for inclusion. Possible predictors included the type of aneurysm, size of the aneurysm, size of the neck, immediate angiographic results, and packing density. Analyses were performed using SPSS, Version 25 (IBM, Armonk, New York) and a significance level of 5%.

Trial Conduct

The trial was sponsored by the Center Hospitalier de l'Université de Montréal and funded by Johnson & Johnson Medical Products, a division of Johnson & Johnson and DePuy Synthes. The sponsor and funder had no role in study design, data collection, analysis, or reporting and had no direct or indirect access to the data or source documents. The Steering Committee bears the sole responsibility for all aspects of the trial.

RESULTS

Between November 2013 and June 2017, two hundred ten patients were recruited in 12 North American centers: One hundred four patients were allocated to the 15-caliber group versus 106 to the 10-caliber group. The trial profile is shown in Fig 1. The baseline patient and aneurysm characteristics of the 2 groups were similar (Table 1).

The primary outcome could be adjudicated in 201 patients (96%). Results are summarized in Table 2. In the intent-to-treat analysis, the primary outcome was reached in 37 patients allocated to 15-caliber coils compared with 36 patients allocated to 10-caliber coils (OR = 0.931; 95% CI, 0.528–1.644; *P* = .885). Including the “not attributed” cases in the “primary outcome met” category or repeating analyses using per-protocol definitions did not change the results.

There was no significant difference in the use of adjunctive devices between the 2 groups. Stents were used in 19 of 101 or 19% of patients in the 10-caliber group compared with 23 of 102 or 23% of patients in the 15-caliber group (*P* = .458). For patients treated with stent-assisted coiling, the primary outcome was met in 4 of 19 patients in the 10-caliber group compared with 7 of 23 patients in the 15-caliber group (*P* = .726).

Safety and other clinical outcomes were similar for the 2 groups (On-line Table 1). Fluoroscopy times were similar (71 ± 45 versus 64 ± 38 minutes, *P* = .232). Serious adverse events (Table 3) occurred in 25 patients, 7 in the 15-caliber group and 18 in the 10-caliber group, including 9 deaths, 2 in the 15-caliber and 7 in the 10-caliber group (*P* = .053). Other secondary outcomes were similar, except for the mean number of coils, which

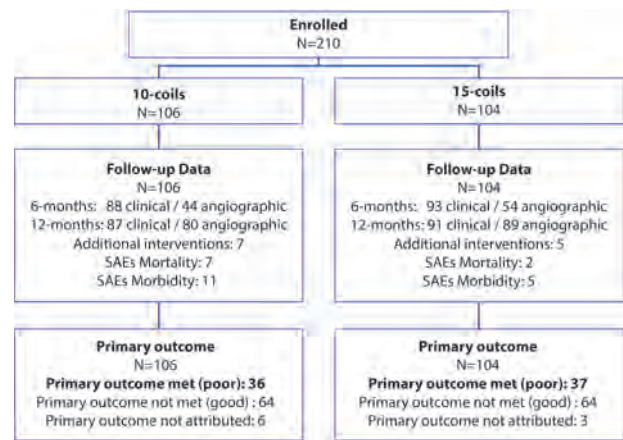


FIG 1. Trial profile. SAEs indicates severe adverse events.

Table 1: Patient demographics and aneurysm characteristics^a

	10-Caliber Coils (n = 106)	15-Caliber Coils (n = 104)
Female sex	81 (76.4%)	82 (78.8%)
Age (mean) (SD) (yr)	57 (11)	58 (10)
mRS at baseline >2	2 (1.9%)	3 (2.9%)
Multiple aneurysms (No.) (%)	29 (27.4%)	29 (27.9%)
Ruptured aneurysms		
(No.) (%) of treatment group	35 (33.0%)	36 (34.6%)
(No.) (%) recurrence	0	1 (1.0%)
Unruptured aneurysms		
(No.) (%) of treatment group	71 (67.0%)	68 (65.4%)
(No.) (%) recurrence	4 (3.8%)	3 (2.9%)
(No.) (%) symptomatic	7 (6.6%)	5 (4.8%)
Aneurysm size (maximal dimension)		
Mean (SD) (mm)	7.7 (2.6)	7.8 (2.3)
Aneurysm neck		
Mean (SD) (mm)	3.2 (1.1)	3.3 (1.3)
Neck ≥ 4.0 (mm)	39 (36.8%)	31 (29.8%)
Aneurysm location, anterior (No.) (%)	81 (76.4%)	88 (84.6%)
Internal carotid	36 (34.0%)	42 (40.4%)
Anterior cerebral	32 (30.2%)	31 (29.8%)
Middle cerebral	13 (12.3%)	15 (14.4%)
Aneurysm location, posterior (No.) (%)	25 (23.6%)	16 (15.4%)
Basilar	18 (17.0%)	12 (11.5%)
Other posterior	7 (6.6%)	4 (3.8%)

^a No significant difference was found between groups on any of the parameters.

Table 2: Primary outcome^a

	10-Caliber Coils (n = 106)	15-Caliber Coils (n = 104)
Primary outcome met	36 (34.0%)	37 (35.6%)
Major recurrence	20 (18.9%)	26 (25.0%)
Retreatment	4 (3.8%)	4 (3.8%)
Initial treatment failure	6 (5.7%)	4 (3.8%)
SAH	1 (0.9%)	0
Related mortality	5 (4.7%)	2 (1.9%)
Related morbidity	0	1 (1.0%)
Good outcome	64 (60.4%)	64 (61.5%)
Not attributed	6 (5.7%)	3 (2.9%)
Lost to follow-up	4 (3.8%)	3 (2.9%)
Unrelated mortality	2 (1.9%)	0

^a No significant difference between groups was found in the primary outcome. Data are (No.) (%).

was significantly smaller for 15-caliber coils (On-line Table 2). The 15-caliber coil group had a higher mean packing density (37.0% versus 26.9%, $P = .001$, 2-tailed t test; excluding cases in which coils could not be deployed). Exploratory per-protocol analyses excluded all coiling protocol violations ($n = 21$; 4 in the 10-caliber group, 17 in the 15-caliber group), initial treatment

failures ($n = 11$), and patients with no 12-month follow-up ($n = 17$). In those exploratory analyses, the most important predictor of long-term results was the immediate angiographic result. Other predictors were aneurysm size and rupture status of the aneurysm. Packing density was a significant predictor in univariate analysis, but packing density had no effect on the primary outcome when adjusted for initial angiographic results (OR = 1.001; 95% CI, 0.981–1.022; $P = .897$).

Table 3: Serious adverse events

	10-Caliber Coils ($n = 106$)	15-Caliber Coils ($n = 104$)
Mortality, total (No.) (%)	7 (6.6%)	2 (1.9%)
Aneurysm rupture during procedure	2 (1.9%)	1 (1.0%)
Stroke, periprocedural	2 (1.9%)	0
Stroke, related to SAH at presentation	1 (0.9%)	0
Related to SAH during follow-up	0	1 (1.0%)
Unrelated to aneurysm or its treatment	2 (1.9%)	0
Morbidity, total (No.) (%)	11 (10.4%)	5 (4.8%)
Aneurysm rupture during procedure	4 (3.8%)	3 (2.9%)
Stroke	6 (5.7%)	2 (1.9%)
SAH during follow-up	1 (0.9%)	0

DISCUSSION

Packing density has been conceived as an estimate of the extent to which an aneurysm is filled with embolic coiling material.^{9–11} It has been thought to play a role in objectively estimating the success of the initial endovascular treatment, at least compared with other, more subjective end points such as angiographic results.¹² Inferior packing density has been associated with an increased risk of angiographic recurrences in some observational follow-up angiographic studies,^{13–15} but randomized evidence had not been available before the DELTA study. Even though packing density can be calculated with relative ease, its value in predicting inferior follow-up angiographic results remains controversial.^{16,17} Packing density, though objective because based on mathematical calculations, can be predictive of long-term

angiographic outcome only after treatment. Packing density is not independent of other risk factors for recurrences that can be determined before treatment, such as aneurysm size, neck width, and the ruptured or unruptured nature of the aneurysm.^{5,6,14,15,18} In addition, if there is an association between packing density and immediate angiographic results, there are intuitive and empiric reasons to believe that immediate angiographic results are causally more pertinent to treatment success, in the long term, than packing density (Fig 2).

It would not be possible to under-treat or overtreat aneurysms in a deliberate, prospective, and randomized fashion, using the same platinum coil technology, keeping all other variables similar, to experimentally study the effects of packing density on long-term results. However, comparing 2 groups of patients with relatively small aneurysms randomly allocated to the exclusive use of 10-caliber platinum coils, considered the control group, or to as many 15-caliber coils as possible, considered the experimental group, keeping all other treatment variables the same, allowed us to examine the potential effects of packing density isolated from all other causal factors.

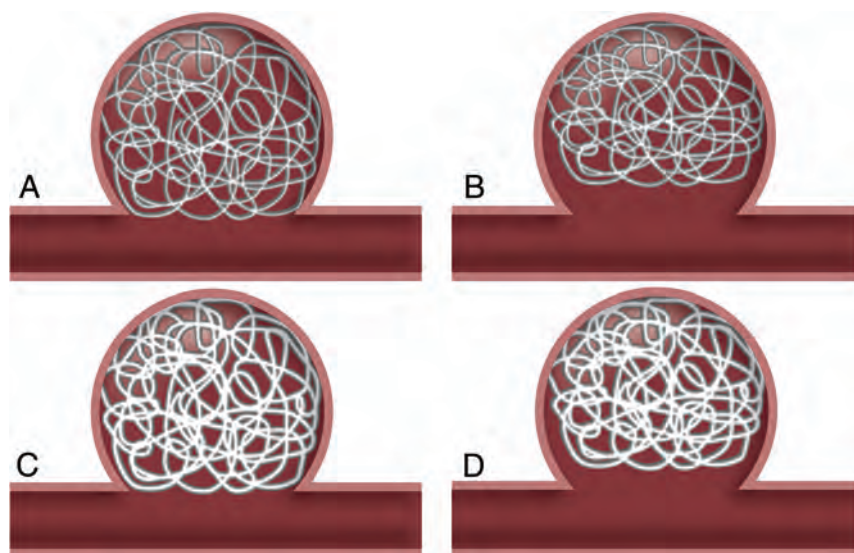


FIG 2. Effect of packing density and immediate angiographic results. From left to right, decreasing packing density has an impact, but it depends on inferior immediate angiographic results. From upper to lower rows, increasing packing density, given the same initial angiographic results, has no impact on long-term angiographic results.

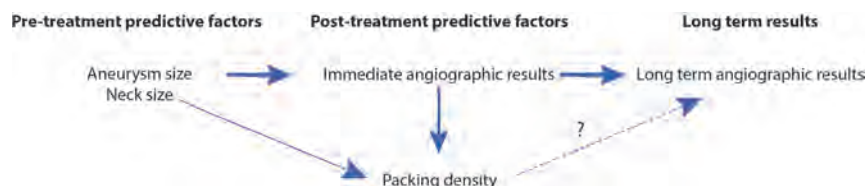


FIG 3. Effect of packing density and immediate angiographic results. Packing density is better thought of as an index compounding many causal factors, such as aneurysm and neck sizes and immediate angiographic results, rather than a true causal factor in long-term angiographic results.

Packing density is not an end in itself, but it was used as an end point of the pilot phase because it was thought that if the use of larger caliber coils (the only difference between the 2 platinum coil treatment groups) could not impact packing density, it would be unlikely to change the treatment substantially enough to impact long-term angiographic results.

The use of larger caliber coils did succeed in increasing packing density,⁸ but this had no impact on the primary outcome of the trial, the 1-year angiographic results. We must, of course, remember that the trial was interrupted prematurely. Nevertheless, our exploratory per-protocol data provide experimental evidence supporting an explanation regarding the potentially misleading idea that increasing packing density by itself improves the long-term results of coil embolization (Fig 2). While univariate analyses reveal a significant association between packing density and long-term results, there are also strong associations between aneurysm and neck sizes (predictive factors before treatment) and packing density. In addition, when adjusted for immediate angiographic results, packing density had no influence on results. In other words, packing density is more correctly an indicator rather than a true causal factor in recurrences (Fig 3).

Some authors have argued that packing density is not such an important factor when aneurysms are stented.^{19,20} The subgroup of stented aneurysms in DELTA was too small to draw any conclusions.

Our study has several limitations. The trial was interrupted before the target number of patients had been recruited. The resulting study cannot provide definitive conclusions. The follow-up period was relatively short. The method used to calculate aneurysm volumes is not as accurate as more exact experimental methods,^{6,21} but it is simple, immediately available, and in common clinical usage. Similar methods have been used in most published trials.²² This method likely results in an overestimation of aneurysm volumes and an underestimation of packing densities, but it is unlikely to introduce bias in the comparison because of random allocation and because measurement errors are expected to be the same for both groups.

CONCLUSIONS

Coiling of aneurysms randomized to 15-caliber coils achieved higher packing densities compared with 10-caliber coils, but this finding had no impact on the angiographic outcomes at 1 year, which were primarily driven by aneurysm size and initial angiographic results.

Disclosures: Jimmy Ghostine—RELATED: Grant: Johnson & Johnson, Comments: unrestricted grant, UNRELATED: Consultancy: Johnson & Johnson, Comments: short-term consultancy, January 2014, Codman for Neuro, invited speaker at Johnson & Johnson National Sales Meeting; 1-time honorarium of 2500\$ plus travel from Montreal to Toronto and 1-night lodging. Alim P. Mitha—UNRELATED: Consultancy: Cerus Endovascular, Stock/Stock Options: Fluid Biotech Inc, Comments: cofounder. Miguel Chagnon—UNRELATED: Consulting Fee or Honorarium: University of Montreal.* Raymond Turner—UNRELATED: Consultancy: J&J/Cerenovus, Siemens, Q'APEL, Rebound Tx, Corindus Vascular Robotics; Patents (planned, pending or issued): Medical University of South Carolina; Royalties: Medical University of South Carolina; Stock/stock options: Corindus Vascular Robotics, Rebound Tx, Endostream, Echovate, Synchron. Thanh Nguyen—David Fiorella—RELATED: Grant: Medtronic, MicroVention, Penumbra, Siemens*; Consulting Fee or Honorarium: Medtronic, MicroVention, Penumbra, Balt; Support for Travel to Meetings for the Study or Other Purposes: Medtronic, MicroVention, Penumbra, Balt; UNRELATED: Board Membership: Vascular Simulation; Consultancy: Medtronic, MicroVention, Penumbra, Siemens, Balt; Expert

Testimony: None; Grants/Grants Pending: Balt, MicroVention, Siemens, Penumbra*; Payment for Lectures Including Service on Speakers Bureaus: Medtronic, MicroVention, Penumbra, Siemens, Stryker, Balt; Patents (Planned, Pending or Issued): Cerenovus, Vascular Simulations; Royalties: Cerenovus; Payment for Development of Educational Presentations: Medtronic; Stock/Stock Options: Neurogami Medical, Marblehead Medical; Travel/Accommodations/Meeting Expenses Unrelated To Activities Listed: MicroVention, Stryker, Balt, Medtronic. Ali Alaraj—UNRELATED: Consultancy: Cerenovus; Grants/Grants Pending: National Institutes of Health.* A. Turk—UNRELATED: Board Membership: Blinktbi; Expert Testimony: Corindus Vascular Robotics, Imperative Care (Corindus Vascular Robotics)*; Patents (Planned, Pending or Issued): Navecap*; Stock/Stock Options: Travel/Accommodations/Meeting Expenses Unrelated to Activities Listed: Hemo China. Sohyun Boo—UNRELATED: Consultancy: Stryker, Microvention, Comments: Education/training. *Money paid to the institution.

ACKNOWLEDGMENT

The principal acknowledgment must go to the patients, the investigators and the staff who participated in this trial. We also wish to acknowledge the coordination and management team of the study: Guylaine Gevry, Suzanne Nolet, and Ruby Klink.

REFERENCES

1. Molyneux A, Kerr R, Stratton I, et al. **International Subarachnoid Aneurysm Trial (ISAT) of neurosurgical clipping versus endovascular coiling in 2143 patients with ruptured intracranial aneurysms: a randomized trial.** *Lancet* 2002;360:1267–74 CrossRef Medline
2. Raymond J, Darsaut TE, Molyneux AJ, TEAM Collaborative Group. **A trial on unruptured intracranial aneurysms (the TEAM trial): results, lessons from a failure and the necessity for clinical care trials.** *Trials* 2011;12:64 CrossRef Medline
3. Leclerc A, Raymond J, Rodriguez-Régent C, et al. **Intracranial Aneurysms: Recurrences More than 10 Years after Endovascular Treatment—A Prospective Cohort Study, Systematic Review, and Meta-Analysis.** *Radiology* 2015;277(1):173–80 CrossRef Medline
4. CARAT Investigators. **Rates of delayed rebleeding from intracranial aneurysms are low after surgical and endovascular treatment.** *Stroke* 2006;37:1437–42 Medline
5. Raymond J, Guilbert F, Weill A, et al. **Long-term angiographic recurrences after selective endovascular treatment of aneurysms with detachable coils.** *Stroke* 2003;34:1398–1403 CrossRef Medline
6. Sluzewski M, van Rooij WJ, Slob MJ, et al. **Relation between aneurysm volume, packing, and compaction in 145 cerebral aneurysms treated with coils.** *Radiology* 2004;231:653–58 CrossRef Medline
7. Quasar Grunwald I, Molyneux A, Kuhn AL, et al. **Influence of coil geometry on intra-aneurysmal packing density: evaluation of a new primary wind technology.** *Vasc Endovascular Surg* 2010;44:289–93 CrossRef Medline
8. Cloutier F, Khoury N, Ghostine J, et al. **Embolization with larger-caliber coils can increase packing density: evidence from the pilot phase of a randomized trial.** *Interv Neuroradiol* 2017;23:14–17 CrossRef Medline
9. Reul J, Spetzger U, Weis J, et al. **Endovascular occlusion of experimental aneurysms with detachable coils: influence of packing density and perioperative anticoagulation.** *Neurosurgery* 1997;41:1160–65; discussion 1165–68 Medline
10. Piotin M, Mandai S, Murphy KJ, et al. **Dense packing of cerebral aneurysms: an in vitro study with detachable platinum coils.** *AJNR Am J Neuroradiol* 2000;21:757–60 Medline
11. Uchiyama N, Kida S, Nomura M, et al. **Significance of volume embolization ratio as a predictor of recanalization on endovascular treatment of cerebral aneurysms with Guglielmi detachable coils.** *Interv Neuroradiol* 2000;6(Suppl 1):59–63 CrossRef Medline
12. Tollard E, Darsaut TE, Bing F, et al. **Outcomes of endovascular treatments of aneurysms: observer variability and implications for interpreting case series and planning randomized trials.** *AJNR Am J Neuroradiol* 2012;33:626–31 CrossRef Medline
13. Knap D, Gruszczynska K, Partyka R, et al. **Results of endovascular treatment of aneurysms depending on their size, volume and coil**

- packing density. *Neurol Neurochir Pol* 2013;47:467–75 CrossRef Medline
14. Leng B, Zheng Y, Ren J, et al. **Endovascular treatment of intracranial aneurysms with detachable coils: correlation between aneurysm volume, packing, and angiographic recurrence.** *J Neurointerv Surg* 2014;6:595–99 CrossRef Medline
 15. Mascitelli JR, Oermann EK, De Leacy RA, et al. **Predictors of treatment failure following coil embolization of intracranial aneurysms.** *J Clin Neurosci* 2015;22:1275–81 CrossRef Medline
 16. Pötin M, Spelle L, Mounayer C, et al. **Intracranial aneurysms: treatment with bare platinum coils—aneurysm packing, complex coils, and angiographic recurrence.** *Radiology* 2007;243:5000–8 CrossRef Medline
 17. Goddard JK, Moran CJ, Cross DT, 3rd, et al. **Absent relationship between the coil-embolization ratio in small aneurysms treated with a single detachable coil and outcomes.** *AJNR Am J Neuroradiol* 2005;26:1916–20 Medline
 18. Sadato A, Adachi K, Hayakawa M, et al. **Effects of anatomic characteristics of aneurysms on packing density in endovascular coil embolization: analysis of a single center's experience.** *Neurosurg Rev* 2016;39:109–14; discussion 114 CrossRef Medline
 19. Chalouhi N, Dumont AS, Hasan D, et al. **Is packing density important in stent-assisted coiling?** *Neurosurgery* 2012;71:381–86 CrossRef Medline
 20. Park YK, Bae HJ, Cho DY, et al. **Risk factors for recurrence and retreatment after endovascular treatment of intracranial saccular aneurysm larger than 8 mm.** *Acta Neurochir (Wien)* 2019;161:939–46 CrossRef Medline
 21. Mascitelli JR, Patel AB, Polykarpou MF, et al. **Analysis of early angiographic outcome using unique large diameter coils in comparison with standard coils in the embolization of cerebral aneurysms: a retrospective review.** *J Neurointerv Surg* 2015;7:126–30 CrossRef Medline
 22. White PM, Lewis SC, Gholkar A, et al. **Hydrogel-coated coils versus bare platinum coils for the endovascular treatment of intracranial aneurysms (HELPS): a randomised controlled trial.** *Lancet* 2011;377:1655–62 CrossRef Medline

Redundant Neurovascular Imaging: Who Is to Blame and What Is the Value?

 E. Beheshtian,  S. Emamzadehfard,  S. Sahraian,  R. Jalilianhasanpour, and  D.M. Yousem

ABSTRACT

BACKGROUND AND PURPOSE: Excessive use of neurovascular imaging studies such as Doppler ultrasound, CTA, MRA, and DSA adds cost to the evaluation of patients with new neurologic deficits. We sought to determine to what extent redundant neurovascular imaging is generated by radiologists' recommendations and the agreement rates among modalities in this setting.

MATERIALS AND METHODS: The radiology reports of 300 consecutive patients admitted for acute stroke to determine the frequency of the following: 1) >1 neurovascular study performed, 2) recommendation for another study, 3) recommendation made by the radiologist, and 4) agreement rates among these redundant neurovascular imaging studies.

RESULTS: Among the 300 consecutive patients, 125 had redundant neurovascular imaging, accounting for 144 redundant studies. These included 75/125 redundant neurovascular imaging studies after MRA, 48/125 after CTA, and 2/125 after Doppler ultrasound. The radiologist recommended another vascular study in 22/125 (17.6%) patients; the rest of the recommendations were made by clinicians. The second study agreed with the first in 54.6% (12/22) of cases recommended by radiologists and 73.8% (76/103) recommended by clinicians (P value = .06). CTA agreed with MRA, carotid Doppler ultrasound, and DSA in 66.7%, 66.7%, and 55.6%, respectively. MRA agreed with Doppler ultrasound and DSA in 78.3% and 66.7%, respectively.

CONCLUSIONS: Of cases with redundant neurovascular imaging, most were generated by clinicians, but radiologists recommended redundant neurovascular imaging in 17.6% of patients; 81.8% occurred following MRA. Overall, most secondary studies (68.8%) confirmed the findings of the first study. Such low-value, same-result redundant neurovascular imaging was more common when clinicians ordered the studies (73.8%) than when radiologists ordered them (54.6%).

ABBREVIATIONS: DUS = Doppler ultrasound; RNI = redundant neurovascular imaging

The diagnostic work-up and clinical decision-making in the setting of acute stroke depends on the use of accurate imaging modalities. Noninvasive vascular imaging is recommended in the American College of Radiology Practice Guideline for new neurologic deficits, and multiple choices of modalities are available, including CTA, MRA, and Doppler ultrasound (DUS). In the clinical setting in which the initial noninvasive test is non-diagnostic or inconclusive, a second noninvasive test may be corroborative or provide more definitive information. Such

noninvasive studies may serve as screening examinations before or instead of a definitive invasive test such as DSA.¹⁻³

However, for most cooperative patients, a single noninvasive neurovascular imaging test should be sufficient to determine future risk of stroke based on the degree of vascular stenosis in the neck or head. This is predicated, in part, on the NASCET study which, to this day, remains the basis for assessing vascular stenosis for surgical intervention.⁴ Recently, a study that compared potential drivers of health care spending in the United States with those of 10 of the highest income countries showed that the United States spends approximately twice as much as other nations despite comparable numbers of hospital beds (2.8 per 1000). The United States had the second highest use of MR imaging (118 per 1000) and the third highest CT use (245 per 1000) versus other countries.⁵

The performance of multiple redundant imaging modalities is potentially a low-yield, high-cost endeavor and results in transfer delay, unnecessary morbidity, and increased resource use.⁶ Recent studies have shown that, from 1994 through 2015, neuro-

Received September 6, 2019; accepted after revision October 2.

From the Russell H. Morgan Department of Radiology and Radiological Science (E.B., S.S., R.J., D.M.Y.), Johns Hopkins Medical Institution, Baltimore, Maryland; and Department of Radiology (S.E.), University of Texas Health Science Center, San Antonio, Texas.

E. Beheshtian and S. Emamzadehfard are co-first authors with equal contributions.

Please address correspondence to David M. Yousem, MD, MBA, 600 N Wolfe St, Phipps B1100F, Baltimore, MD 21287; e-mail: dyousem1@jhu.edu; @dyousem1; @EBeheshtian

<http://dx.doi.org/10.3174/ajnr.A6329>

Table 1: Baseline characteristics of patients with stroke

Characteristics	
Sex (No.) (%)	
Male	162/300 (54)
Female	138/300 (46)
Age (mean) (yr)	63.3 ± 13.9
Ethnicity (No.) (%)	
African American	198/300 (66)
White	65/300 (21.7)
Other	37/300 (12.3)
MRA (No.) (%)	248/300 (82.7)
CTA (No.) (%)	146/300 (48.7)
Diagnostic DSA (No.) (%)	15/300 (5.0)
DUS (No.) (%)	34/300 (11.3)

imaging use rates per 1000 emergency department visits increased 660% overall. From 2001 to 2015, rates increased 14,600% and 17,781% for head and neck CTA, respectively, and 525% and 667% for head and neck MRA, respectively.⁷ Increasingly, patients with stroke are undergoing ≥2 neuroimaging (CT and MR imaging) and neurovascular (CTA, MRA, DUS, and DSA unrelated to intravascular treatment) studies. Although some patients certainly merit careful evaluation, unnecessary duplicative vascular imaging observed in patients with stroke/TIA may lead to high-cost, low-value care.⁸

Such redundancy may result in between-study discrepancies, forcing yet a third imaging technique to adjudicate the 2, thereby potentially further increasing radiation, contrast exposure, false-positives, cost, and inconvenience. This compounds the wasteful health care expense and also leads to inefficiencies for patients and health care providers. In the setting of stroke, radiologists often blame the clinical service for ordering redundant neurovascular studies. Radiologists fail to recognize that their nondefinitive interpretations of reports may lead to additional testing or that they themselves recommend corroborative examinations that lead to added costs. We sought to assess the incidence of redundant neurovascular imaging (RNI) studies and determine the sources and referrers of such repetitive imaging, the reason for these duplicative examinations, the agreement rate when performing >1 imaging study on the same vascular anatomy, and guidance to reduce unnecessary repetitive imaging.

We hypothesized the following: 1) Such redundancy would occur in <10% of cases, 2) the clinical services (as opposed to radiologists) would be responsible for >90% of these cases, and 3) that MRA and CTA findings would be interchangeable. Therefore, ordering both studies would have low added value.

MATERIALS AND METHODS

This Health Insurance Portability and Accountability Act-compliant study was approved by the institutional review board at Johns Hopkins Medical Institution (approval No. 00102719).

This retrospective study was conducted using a maintained data base of patients with new-onset stroke admitted to our tertiary care academic medical institution. Informed consent requirements were waived due to the retrospective nature of the study. The data base was queried to identify 300 consecutive patients who presented to the emergency department and were subsequently admitted to the neurology stroke service for the 30 months between

February 2015 and August 2017. Only redundant studies from the same hospital admission/emergency department visit were included. Patients transferred from nearby community hospitals were not included to allow accurate inferences to be made about imaging ordering patterns, and patients who underwent interventional procedures such as thrombectomy were excluded from study.

The patients' electronic health records (Epic; 1979 Milky Way, Verona, Wisconsin) were reviewed to acquire demographics, risk factors, and different types of neuroimaging. Since the incidence of vascular stenosis is different based on their race/ethnicity, the ethnicity of patients extracted from their medical records. We specifically queried regarding incidences of carotid DUS, CTA, diagnostic DSA, and MRA occurring within the same admission. We looked at the individual official reports to identify recommendations and to ascertain whether the recommendation wording included the character string "recommend" such as "Consider CTA/MRA" or "Further evaluation with CTA/MRA, if clinically indicated." The reports were reviewed to determine the following: 1) the frequency of redundant studies, 2) the reasons specified for ordering the second neurovascular study, and 3) the rate at which radiologists recommended the additional studies in the reports.

We used the NASCET criteria to measure vascular stenoses in the neck and measured intracranial disease based on the narrowest segment diameter versus the closest normal segment diameters using electronic calipers. When studies showed >50% stenosis in any vessel in the neck or brain, the findings were positive. This was determined at a study level, not individual vessels, because the treatment outcome for the stenoses in the neck or brain was likely the same whether ≥1 vessel showed atherosclerotic narrowing. The 50% value is the threshold at our institution for the initiation of antiplatelet drugs and/or surgical consideration (>70% stenosis). We used the TOAST (Trial of Org 10172 in Acute Stroke Treatment) criteria to classify stroke etiology. This was based on the stroke neurology team assessment and final imaging findings.⁹

Statistical analyses were conducted using STATA software (Version 12; StataCorp, College Station, Texas).

RESULTS

The baseline characteristics of patients with and without RNI and studies performed are reported in Table 1.

Of the 300 patients admitted to our institution for ischemic stroke during February 2015 to August 2017, one hundred twenty-five (41.7%) had multiple vascular studies ordered, and among these 125 patients, 144 duplicative neurovascular studies were performed. On average, patients with stroke had a mean of 1.5 neurovascular imaging studies during the admission/emergency department visit. The time lapse between studies in patients with duplicative imaging is reported in the Figure.

In 17.6% (22/125) of patients with redundant imaging, the RNI was performed on the basis of a recommendation by the radiologist placed in the impression section of the report (7.3% of total patients with stroke). When radiologists recommended additional radiologic studies, 18/22 (81.8%) occurred following an MRA and 4/22 (18.2%) occurred after CTA. On the other hand, clinicians ordered additional imaging following MRA in 57 cases and after CTA in 44 cases (*P* value = .027).

Of the instances in which the radiologist recommended a second study, that second study confirmed the first study in 54.6% (12/22) of cases and disagreed with the first study in 45.4% (10/22). Of the 103 patients with redundant studies generated by clinicians, 73.8% (76/103) of the subsequent studies agreed with the first study and 26.2% (27/103) were discrepant. The difference between report discrepancy rates of RNI ordered by radiologists (45.4%) and clinicians (26.2%) approached significance (P value = .07).

The frequency of neurovascular imaging is reported in Table 2.

In 39/125 (31.2%) patients, the report of the first and second neurovascular studies did not agree as to the presence of $\geq 50\%$ stenosis in the head or neck. Of these 39 cases, a third study was ordered in 7 (17.9%) patients and agreed with the first study in

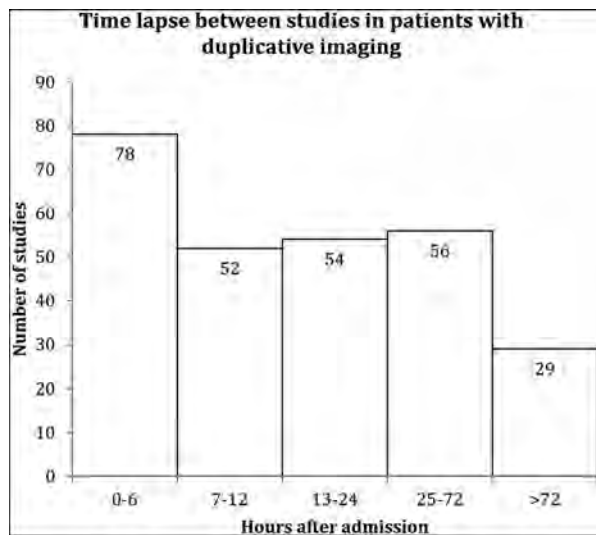


FIGURE. The time lapse between studies in patients with duplicative imaging.

Table 2: Type of neurovascular imaging ordered by clinicians and radiologists

Type of Imaging	No. (%)
CTA and MRA	77 (61.6)
CTA and DUS	4 (3.2)
CTA and DSA	5 (4)
MRA and DUS	19 (15.2)
MRA and DSA	3 (2.4)
CTA, MRA, DUS	9 (7.2)
CTA, MRA, DSA	6 (4.8)
MRA, CTA, CTA, DSA	1 (0.8)
MRA/CTA/MRA/DUS	1 (0.8)
Total	125 (100)

14.3% of the cases and the second study in 85.7% of the cases. Of 86 cases in which the 2 studies agreed, a third study was ordered in 10 (11.6%) cases.

Among the 125 patients with RNI, 40 (32%) had a second imaging test after positive findings of $>50\%$ vascular stenosis. In 85 (68%) cases, the second RNI was performed after negative ($<50\%$ stenosis) or inconclusive findings on the first imaging.

The source and discrepancy rates between modalities are reported in Table 3.

From a total of 75 MRAs and 48 CTAs performed as the first study, 51 and 33 study reports, respectively, confirmed the first study (P value = .9). Among all, CTA agreed with MRA, Doppler ultrasound, and DSA in 60/90 (66.7%), 8/12 (66.7%), and 5/9 (55.6%) imaging studies, respectively. MRA agreed with DUS and DSA in 18/23 (78.3%) and 4/6 (66.7%) patients, respectively. The CTA-MRA, CTA-ultrasound, and MRA-ultrasound disagreement rates were 33.3%, 33.3%, and 21.7%, respectively.

Indications for the second study are reported in Table 4.

DISCUSSION

Our findings show that acquiring multiple vascular imaging modalities in patients diagnosed with ischemic stroke is common (125/300 = 41.7%). Of cases of RNI, most are generated by clinicians (82.4%), with radiologists recommending additional imaging in 17.6% of patients. What is curious is that the rate of ordering a second neurovascular study occurred 2 times more frequently (68% versus 32%) after a study negative for vascular stenosis than a study positive for it. Furthermore, we showed that the likelihood that the second study would be discrepant with the first study was nearly half the rate if the clinician versus the radiologist ordered it (45.4% versus 26.2%).

Gupta et al¹⁰ found that 58% of transferred patients with trauma underwent duplicative CT studies, with head CT primarily repeated for follow-up of trauma, and body CT primarily, because of inadequate availability or quality from the referring institution. In our series of cases, duplicative imaging studies ordered by radiologists were mostly due to uncertainty about findings and motion artifacts. Lee et al¹¹ found that radiologists' recommendations accounted for only a small proportion (5.3%) of outpatient CT, MR imaging, and PET examinations performed. They showed that pulmonary nodule follow-up was the most common cause of radiologist-generated high-cost imaging and was driven by pre-existing practice guidelines intended for early detection of lung cancer.¹¹

When radiologists at our institution recommended additional studies for acute ischemic stroke evaluation, 18.2% occurred following CTA and 81.8% after MRA. This outcome may be explained by

Table 3: Source of duplicate imaging and agreement rates between modalities during the same admission

First Study Ordered	Source of Second Imaging		Agreement Rates between Modalities			
	Radiologist	Clinician	Agreed (%)	First Study Overestimated	First Study Underestimated	Total
				Disease (%)	Disease (%)	
CTA	4	44	33 (68.7)	11 (22.9)	4 (8.3)	48
MRA	18	57	51 (68)	4 (5.3)	20 (26.7)	75
DUS	0	2	2 (100)	0 (0)	0 (0)	2
Total	22	103	86 (68.8)	15 (11.0)	24 (19.2)	125

Table 4: Indications for second study^a

Indication	Radiologist	Clinician	Total
Patient motion	6	9	15
Technical artifact	3	5	8
Inadequate FOV	3	Unknown	Unknown
Uncertainty about findings	7	4	11
Other	3	Unknown	Unknown

^a Other causes include ruling out dissection or aneurysm, follow-up, and so forth.

the higher spatial resolution, lower rate of motion artifacts, less frequent metal/air artifacts, and more reliable image quality of CTA compared with MRA. One way to reduce redundant neurovascular imaging in patients with stroke would be to use CT/CTA as the initial stroke work-up. Although there was a propensity for the second study to confirm the findings of the first study (68.8%), the 31.2% rate of discordance suggests that the reason for ordering a corroborative RNI may have been justified. It reversed the initial finding in nearly one-third of cases. By contrast, the clinicians' RNIs showed a reversal rate of nearly half that of the radiologists (26.2% versus 45.4%).

Increased imaging use could be due to the increased availability and capacity of scanners during the past decades. While imaging use represents a growing proportion of health care expenditures, the influence of radiologists' self-referral on high-cost imaging volume is small. Hence, efforts to alter the radiologist's behavioral patterns in making recommendations for additional studies are unlikely to result in a substantial decrease in national health care costs. Additionally, based on a study by Siström et al,¹² the odds of radiologists making a recommendation for additional imaging in their reports decreased with experience by approximately 15% per decade.

Another study from Lee et al¹³ showed that self-referral by a radiologist through recommendations for redundant imaging in examination reports contributes very little to the overall volume of high-cost imaging; only 8% of studies are performed after a radiologist's recommendation for a repeat study (compared with our 22/300 [7.3%] rate for stroke patients). In their study, certain examinations with relatively higher repeat rates, such as chest CT (15%) and pelvic ultrasound (8%), represent specific situations in which imaging follow-up is one of the recognized methods for patient care. The authors recommended defining scenarios in which high-cost imaging studies have the maximal medical effect and developing consensus multidisciplinary recommendations for high-cost examination use in those clinical situations.¹³

Limitations of Our Study

Our study has some limitations that impact its conclusions. This study was a single-institution review with a modest sample size and is limited to the evaluation of neurovascular imaging modalities chosen because of the multiple modalities (CTA, MRA, DUS, and DSA) available for clinicians to order. The other limitation of our study was that we cannot always assess from the medical record the rationale, in a retrospective study, of clinicians when they order redundant modalities and we cannot reconstruct conversations that may have occurred between health care providers that may have led to ordering studies. Additionally, among our patient sample, we had some combinations of modalities (ie, DSA/DUS) with so few incidents that we cannot make

conclusions about accuracy rates. We also understand that there is some blurring of distinction between redundant imaging (implying little potential added value) versus repeat imaging (because of a changing clinical situation). Certain scenarios warrant close follow-up neurovascular imaging such as the following: 1) a patient who comes in with acute stroke due to dissection or nonocclusive intravascular thrombus who has new symptoms suggestive of an acute occlusion that might be treatable with thrombectomy; 2) a patient with dissection in whom a vessel is suggested to be occluded on 1 technique but confirmation is requested before sending the patient home on aspirin instead of anticoagulation; and 3) the patient with borderline NASCET criteria with fluctuating neurologic examination findings. Finally, our study is impacted by our institutional bias in favor of MR imaging/MRA for acute stroke evaluation and the availability for scheduling these emergently, given that we have an MR imaging scanner in our emergency department. This scenario may differ with the practice patterns of other radiology groups. We recommend a global assessment of the impact of RNI, which can lead to recommended practice parameters by national organizations.

Implications/Recommendations

During hand-offs between services, miscommunication can occur, leading to potential redundancies. One wonders whether there would be value in electronic reminders to clinicians that a previous neurovascular study had been performed, as part of the order-entry process of the physician. This would be an easy radiology information system/EMR (Electronic Medical Record) intervention. Such a feedback loop alerting the ordering physician ("You are aware that the patient had a DUS earlier today") may help avoid inadvertent, unintended RNIs. If radiologists who are unsure consult with colleagues before recommending additional tests due to uncertainty about findings, it may reduce RNIs. If clinicians discuss their concerns about studies with radiologists before ordering another technique, it may decrease redundant imaging. In the end, communication among practitioners may help address these problems.

CONCLUSIONS










Our hypothesis that radiologists would account for <10% of redundant neurovascular studies in the setting of stroke was incorrect. Radiologists recommended another technique in 17.6% of patients with RNI and 7.3% of all patients with stroke. The concordance rate of the 2 RNI modalities was much higher when those studies were clinician-driven; therefore, it implies limited second-study benefit. Such redundancy should be discouraged. Duplicative neurovascular studies on the same patient occur frequently, often agree, and are a source of added cost. Because clinicians and radiologists contribute to RNI, both specialties should be circumspect in their ordering habits. RNI should be addressed at a national level to reduce health care costs, and its use could benefit from order-entry feedback loops.

Disclosures: David M. Yousem—UNRELATED: Expert Testimony: expert witness testimony; Payment for Lectures Including Service on Speakers Bureaus: American College of Radiology Education Center speaker, mronline.com; Royalties: Elsevier for 5 books, Analytical Informatics.

REFERENCES

1. Nederkoorn PJ, van der Graaf Y, Hunink M. **Duplex ultrasound and magnetic resonance angiography compared with digital subtraction angiography in carotid artery stenosis: a systematic review.** *Stroke* 2003;34:1324–32 CrossRef Medline
2. Hassan AE, Rostambeigi N, Chaudhry SA, et al. **Combination of noninvasive neurovascular imaging modalities in stroke patients: patterns of use and impact on need for digital subtraction angiography.** *J Stroke Cerebrovasc Dis* 2013;22:e53–58 CrossRef Medline
3. Adla T, Adlova R. **Multimodality imaging of carotid stenosis.** *Int J Angiol* 2015;24:179–84 CrossRef Medline
4. Barnett HJ, Taylor DW, Haynes RB, et al; North American Symptomatic Carotid Endarterectomy Trial Collaborators. **Beneficial effect of carotid endarterectomy in symptomatic patients with high-grade carotid stenosis.** *N Engl J Med* 1991;325:445–53 CrossRef Medline
5. Papanicolaou I, Woskie LR, Jha AK. **Health care spending in the United States and other high-income countries.** *JAMA* 2018;319:1024–39 CrossRef Medline
6. Haley T, Ghaemmaghami V, Loftus T, et al. **Trauma: the impact of repeat imaging.** *Am J Surg* 2009;198:858–62 CrossRef Medline
7. Prabhakar AM, Gottumukkala RV, Hemingway J, et al. **Increasing utilization of emergency department neuroimaging in Medicare beneficiaries from 1994 to 2015.** *Am J Emerg Med* 2018;36:680–83 CrossRef Medline
8. Levine DA, Burke JF. **Stroke imaging: quantity, but is there quality?** *Med Care* 2016;54:423–25 CrossRef Medline
9. Adams HP, Bendixen BH, Kappelle LJ, et al. **Classification of subtype of acute ischemic stroke. Definitions for use in a multicenter clinical trial. TOAST. Trial of Org 10172 in Acute Stroke Treatment.** *Stroke* 1993;24:35–41 CrossRef Medline
10. Gupta R, Greer SE, Martin ED. **Inefficiencies in a rural trauma system: the burden of repeat imaging in interfacility transfers.** *J Trauma* 2010;69:253–55 CrossRef Medline
11. Lee SI, Krishnaraj A, Chatterji M, et al. **When does a radiologist's recommendation for follow-up result in high-cost imaging?** *Radiology* 2012;262:544–49 CrossRef Medline
12. Siström CL, Dreyer KJ, Dang PP, et al. **Recommendations for additional imaging in radiology reports: multifactorial analysis of 5.9 million examinations.** *Radiology* 2009;253:453–61 CrossRef Medline
13. Lee SI, Saokar A, Dreyer KJ, et al. **Does radiologist recommendation for follow-up with the same imaging modality contribute substantially to high-cost imaging volume?** *Radiology* 2007;242:857–64 CrossRef Medline

Deep Transfer Learning and Radiomics Feature Prediction of Survival of Patients with High-Grade Gliomas

 W. Han,  L. Qin,  C. Bay,  X. Chen,  K.-H. Yu,  N. Miskin,  A. Li,  X. Xu, and  G. Young



ABSTRACT

BACKGROUND AND PURPOSE: Patient survival in high-grade glioma remains poor, despite the recent developments in cancer treatment. As new chemo-, targeted molecular, and immune therapies emerge and show promising results in clinical trials, image-based methods for early prediction of treatment response are needed. Deep learning models that incorporate radiomics features promise to extract information from brain MR imaging that correlates with response and prognosis. We report initial production of a combined deep learning and radiomics model to predict overall survival in a clinically heterogeneous cohort of patients with high-grade gliomas.

MATERIALS AND METHODS: Fifty patients with high-grade gliomas from our hospital and 128 patients with high-grade glioma from The Cancer Genome Atlas were included. For each patient, we calculated 348 hand-crafted radiomics features and 8192 deep features generated by a pretrained convolutional neural network. We then applied feature selection and Elastic Net-Cox modeling to differentiate patients into long- and short-term survivors.

RESULTS: In the 50 patients with high-grade gliomas from our institution, the combined feature analysis framework classified the patients into long- and short-term survivor groups with a log-rank test P value $< .001$. In the 128 patients from The Cancer Genome Atlas, the framework classified patients into long- and short-term survivors with a log-rank test P value of .014. For the mixed cohort of 50 patients from our institution and 58 patients from The Cancer Genome Atlas, it yielded a log-rank test P value of .035.

CONCLUSIONS: A deep learning model combining deep and radiomics features can dichotomize patients with high-grade gliomas into long- and short-term survivors.

ABBREVIATIONS: C-indices = concordance indices; CNN = convolutional neural network; GBM = glioblastoma multiforme; HGG = high-grade glioma; OS = overall survival; SE = spin-echo; TCGA = the Cancer Genome Atlas

Glioblastoma multiforme (GBM), the largest diagnostic subcategory of high-grade glioma (HGG) and the most common malignant adult brain tumor, afflicts 12,000–13,000 new patients annually in the United States. GBM, comprising a genetically and phenotypically heterogeneous category of tumors, has a

very poor prognosis and a low rate of treatment response. The standard combined treatment of surgery, temozolomide, and chemoradiation has improved the median overall survival (OS) of GBM to roughly 2 years. Presently, there is no method to reliably predict the OS of patients with GBM as a response to treatment. The absence of such reliable prediction is a barrier in designing clinical trials and selecting optimal treatments for patients.

In the existing literature, MR imaging features of a brain tumor, including its volume, intensity, shape, and texture of contrast enhancement and evidence of tumor necrosis, diffusivity, infiltration, and blood volume, have been demonstrated to correlate with the OS of HGG.^{1–6} A large number of these features were included for radiomics, techniques that leverage the wealth of information in images by extracting semiquantitative or quantitative predefined image features to derive a relationship between the features and clinical outcomes of interest.

Radiomics feature analysis has been shown to correlate with molecular and histologic tissue types and outcomes,

Received July 13, 2019; accepted after revision October 25.

From the Department of Radiology (W.H., C.B., X.C., N.M., A.L., X.X., G.Y.), Brigham and Women's Hospital, Boston, Massachusetts; Department of Imaging (L.Q., G.Y.), Dana-Farber Cancer Institute, Boston, Massachusetts; Harvard Medical School (W.H., L.Q., C.B., K.-H.Y., N.M., X.X., G.Y.), Boston, Massachusetts; and Department of Radiology (X.C.), Guangzhou First People's Hospital, School of Medicine, South China University of Technology, Guangzhou, Guangdong, China.

W. Han and L. Qin are co-first authors.

This work was supported by National Institutes of Health award R01LM012434 and Harvard Data Science Fellowship.

Please address correspondence to Geoffrey Young, MD, Department of Radiology, Brigham and Women's Hospital, 75 Francis St., Boston MA 02115 USA; e-mail: geyoung@bwh.harvard.edu

 Indicates open access to non-subscribers at www.ajnr.org

<http://dx.doi.org/10.3174/ajnr.A6365>

Datasets

This study was approved by our institutional review board. We retrospectively retrieved 2 patient cohorts for this study. The first cohort is 50 patients with World Health Organization IV GBM, with known OS information, who had brain MRIs at the Brigham and Women's Hospital between 2006 and 2011. Brain MR imaging after maximal surgical resection and before radiation therapy was retrieved for each patient. Only the gadolinium-enhanced T1-weighted spin-echo sequences acquired on 1.5T and 3T scanners from GE Healthcare (Milwaukee, Wisconsin) were used. The parameters for these axial contrast-enhanced T1-weighted images were as follows: TR = 416–566 ms, TE = 8–22 ms, FOV = 200–240 mm, matrix size = 256×256 or 512×512 , section thickness = 5–6 mm. The second cohort set is 128 patients with World Health Organization IV GBM brain MR imaging retrieved from gadolinium-based contrast-enhanced T1-weighted images from The Cancer Genome Atlas (TCGA) (<http://cancergenome.nih.gov>), publicly available, and The Cancer Image Archive (<http://cancerimagingarchive.net/>) with known OS information. The MRIs were acquired on 1.5T and 3T scanners from GE Healthcare (Milwaukee, Wisconsin), Siemens (Erlangen, Germany), Philips Healthcare (Best, the Netherlands) between 1995 and 2008. For the acquisition of the axial contrast-enhanced T1-weighted images, there were 58 2D spin-echo (SE), 49 3D gradient recalled-echo, and 21 other sequences. Scan parameters for SE sequences were as followings: TR = 409–809 ms, TE = 8–20 ms, FOV = 200–280 mm, matrix size = 488×683 or 421×683 , section thickness = 1–6 mm. For gradient recalled-echo sequences, 28 were acquired using echo-spoiled gradient echo with TR = 25–250 ms, TE = 2.48–13.8 ms, flip angle = 25° – 70° , FOV = 200–260 mm, matrix = 536×634 or 421×634 , section thickness = 1–4 mm. Others were acquired using an MPRAGE sequence, with TR = 1160–2160 ms, TE = 2.75–4.24 ms, TI = 600–1100 ms, flip angle = 9° – 15° , matrix = 561×624 or 421×624 , section thickness = 0.9–5 mm.

From the 2 cohorts, we constituted 3 data groups. The first group is the 50 patients from Brigham and Women's Hospital. Scans for this group were all acquired using the SE sequence. The second group is the 128 patients from TCGA, and scans were acquired using SE or gradient recalled-echo sequences. The third group comprised the 50 SE scans from Brigham and Women's Hospital and the 58 selected SE scans from TCGA.

Tumor Segmentation and Image Preprocessing

For both patient cohorts, ROIs were manually traced by a radiologist on the section with the largest tumor area.

Before the extraction of quantitative features, several preprocessing techniques were applied to improve texture discriminations. First, intensity normalization was performed in a nonlinear way to convert MR images into standardized intensity ranges for all subjects.¹⁶ Second, to improve the computational performance and the signal-to-noise ratio of the texture outcome, we used gray-level quantization, which maps the full intensity range of the tumor region to different levels of gray.¹⁷ Two gray-level quantization algorithms (equal-probability quantization, uniform quantization) and 2 numbers of

gray levels (16 and 32) were adopted. Finally, all images were resampled to an isotropic pixel size using bilinear interpolation. Scale values of 1 mm (pixel size = $1 \times 1 \text{ mm}^3$) and initial in-plane resolution were both tested.

For deep features, we cropped the MR images by finding a rectangular ROI that enclosed the outlined tumor. Then we resized the tumor patch to a 224×224 square to fulfill the requirement for the input size of the pretrained CNN model that we used. Also considering that the CNN model that we used was pretrained on natural images with a color range of 0–255, we normalized the intensity of tumor patch images to the same color range.

Feature Extraction

Two types of features were extracted. The first type is hand-crafted features that were manually extracted from an ROI. Hand-crafted features were divided into 3 groups: 1) nontexture features, including volume, size, and intensity features (such as solidity, eccentricity); 2) first-order histogram-based texture features, including skewness, kurtosis, variance, and others; and 3) second-order texture features, including features from the gray-level co-occurrence matrix, gray-level run length matrix, gray-level size zone matrix, and neighborhood gray-tone difference matrix. In total, we calculated 348 radiomics features for each ROI.

The second type of features were deep features. We chose the VGG-19,¹⁸ which was pretrained on the natural image dataset ImageNet (<http://www.image-net.org/>),¹⁹ which contains >1.2 million images as our CNN. VGG-19 has 19 layers with weights, formed by 16 convolutional layers and 3 fully connected layers. All the convolutional layers are built with a fixed kernel size of 3×3 , and the stride and padding are fixed at 1. The network has 5 max-pooling layers with a window size of 2×2 and uses rectified linear units as the nonlinear activation function. The first 2 fully connected layers have 4096 features each, while the last FC layer has 1000 features with SoftMax activation (<https://www.moleculardevices.com/products/microplate-readers/acquisition-and-analysis-software/softmax-pro-software>) (Fig 1B). After we ran the front propagation of the VGG-19 model with pretrained weights as the initialization, a total number of 8192 deep features were extracted from the first 2 fully connected layers. All features were normalized by transforming the data into z scores with a mean of 0 and an SD of 1.

Feature Reduction

Feature reduction is a critical step because with 8192 deep features and 348 radiomics features, the number of features may result in overfitting in OS prediction. In addition, some features may have zero variance, have high correlations with other features, or have little relevance to the goal of OS prediction. Thus, the number of features needs to be reduced. We adopted 3 steps for feature reduction, namely, median absolute deviation, concordance indices (C-indices), and the Pearson coefficient correlation, to improve the generalizability and interpretability of our model.

Statistical Analysis

For censored survival data, we used the Elastic Net-Cox proportional hazards model²⁰ to analyze the OS of patients with HGG. We denoted the sample size as N . To maximize the use of the limited data, we applied leave-one-out cross validation N times as the outer loop to split the data into training and test sets. Each pair of training and test sets was examined independently. The model was fit on the basis of the training set by maximizing the penalized partial log-likelihood function for the Cox model with a penalty term. In this model, the penalty parameter λ was optimized within the 10-fold cross-validation loop; α , which was used to determine the influence of the L1 penalty on the L2 penalty was set to be 0.1. After optimization, the model output a survival score for each patient in the training and test sets. We used the median of survival scores in each training set as the threshold to classify each patient in the test set into either a longer term or a shorter term survivor cohort. Finally, Kaplan-Meier analysis was used to estimate survival probabilities of each cohort,²¹ and a log-rank test was implemented to test the hypothesis that the survival curves differed statistically significantly between the 2 cohorts. A P value representing the statistical significance of the curve separation was used as an index to model predictive performance. For all analyses, a P value $< .05$ was indicative of statistical significance. All testing was 2-tailed.

Hardware and Software

The ROI was manually labeled using Hermes on DICOM images (<https://hermes-router.github.io/>). Radiomics features were computed using the Radiomics Matlab package (<https://www.mathworks.com/matlabcentral/fileexchange/51948-radiomics>).³ Pretrained CNN models were run using Keras with Tensorflow

backend (<https://keras.io/applications/#vgg19>) on servers equipped with Xeon CPU and Tesla K80 GPU. Elastic Net-Cox model was built using R package 'glmnet' (<https://cran.r-project.org/web/packages/glmnet/index.html>).

RESULTS

Clinical Characteristics of Patients

The demographic and clinical characteristics of patients in all 3 datasets are shown on Table 1. The median and mean OS were 503 days and 690 days for the patients in group one, 352 days and 449 days for patients in group 2, and 490 days and 642 days for group 3.

Feature Extraction

An example of a contrast-enhanced T1-weighted MR image of a longer term survivor and that of a shorter term survivor are shown in Fig 2A, -C. With different quantization algorithms, different numbers of gray-levels, and different scales for isotropic pixel resampling, we collected 348 hand-crafted quantitative radiomics features: 4 nontexture features, 24 first-order histogram-based texture features, 72 second-order texture features from the gray-level co-occurrence matrix, 104 second-order texture features from the gray-level run length matrix, 104 second-order texture features from the gray-level size zone matrix, and 40 second-order texture features from neighborhood gray-tone difference matrix. Table 2 summarizes the radiomics features described in Chmelik et al.⁹ Meanwhile, we generated and pre-processed the tumor patch images (Fig 2B, -D) as the input for the deep CNN architecture. Then we extracted 8192 features from the first 2 fully connected layers of the pretrained CNN model. Finally, a set of 8540 features was generated for each ROI.

Table 1: Demographic and clinical characteristics of patients in all 3 datasets

Demographics	DATA 1 (n = 50)	DATA 2 (n = 128)	DATA 3 (n = 108)
Sex			
Female (No.) (%)	23 (46%)	46 (35.9%)	43 (39.8%)
Male (No.) (%)	27 (54%)	82 (64.1%)	65 (60.2%)
Mean	0.46 \pm 0.50	0.35 \pm 0.48	0.39 \pm 0.49
Age (yr)			
Range	23–87	17–86	23–87
Mean	57 \pm 13	58 \pm 14	56 \pm 12
OS (days)			
Range	149–3156	7–1638	7–3156
Mean	690.34 \pm 625.31	449.30 \pm 352.93	642.1 \pm 519.30

Feature Reduction and Multivariate Statistical Analysis

Feature reduction was performed on the training set of each leave-one-out 10-fold cross-validation loop. We noticed that the deep feature matrix is relatively sparse and there are many uninformative deep features with zero variance. We set zero as the threshold of median absolute deviation to reduce about 60% of the total features, which were all from deep

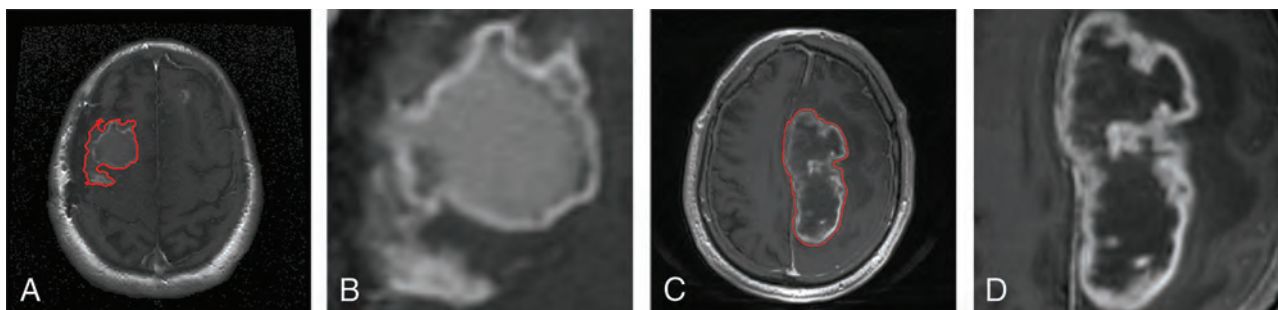


FIG 2. Example of contrast-enhanced T1-weighted MR images of longer term survivors (A and B) with an overall survival of 1405 days and shorter term survivors (C and D) with an overall survival of 447 days. A and C, Contrast-enhanced T1-weighted MR images with tumor contours in red. B and D, Tumor patches segmented from A and C, respectively.

Table 2: List of radiomics features in this study

Method	Quant. algo.	N _g	NS	Features	NF
Non-textures				Volume, size, solidity, eccentricity	4
Histogram	Equal probability, uniform	16 32	2	Variance, skewness, and kurtosis	24
GLCM	Equal probability, uniform	16 32	2	Energy, Contrast, Correlation, Homogeneity, Variance, Sum Average, Entropy, Dissimilarity and Autocorrelation	72
GLRLM	Equal probability, uniform	16 32	2	Short Run Emphasis (SRE), Long Run Emphasis (LRE), Gray-level Non-uniformity (GLN), Run-Length Non-uniformity (RLN), Run Percentage (RP), Low Gray-level Run Emphasis (LGRE), High Gray-level Run Emphasis (HGRE), Short Run Low Gray-level Emphasis (SRLGE), Short Run High Gray-level Emphasis (SRHGE), Long Run Low Gray-level Emphasis (LRLGE), Long Run High Gray-level Emphasis (LRHGE), Gray-level Variance (GLV) and Run-Length Variance (RLV)	104
GLSZM	Equal probability, uniform	16 32	2	Small Zone Emphasis (SZE), Large Zone Emphasis (LZE), Gray-level Non-uniformity (GLN), Zone-Size Non-uniformity (ZSN), Zone Percentage (ZP), Low Gray-level Zone Emphasis (LGZE), High Gray-level Zone Emphasis (HGZE), Small Zone Low Gray-level Emphasis (SZLGE), Small Zone High Gray-level Emphasis (SZHGE), Large Zone Low Gray-level Emphasis (LZLGE), Large Zone High Gray-level Emphasis (LZHGE), Gray-level Variance (GLV) and Zone-Size Variance (ZSV)	104
NGTDM	Equal probability, uniform	16 32	2	Coarseness, Contrast, Busyness, Complexity and Strength	40

Note:—Quant. algo. indicates quantization algorithm; N_g, number of gray levels; NS, number of scales; NF, number of features; GLCM, gray-level co-occurrence matrix; GLRLM, gray-level run length matrix; GLSZM, gray-level size zone matrix; NGTDM, neighborhood gray-tone difference matrix.

features. The remaining deep features are less noisy, and some of them have high C-indices. The ranges of C-indices among the 3 datasets vary, so the threshold of C-indices was slightly different. Because the distribution of C-indices for groups 2 and 3 was similar, the threshold of C-indices for these 2 datasets were the same at 0.66. The C-indices in the group 1 dataset were relatively higher at 0.685. The threshold for the Pearson coefficient correlation was set at 0.85 for all 3 datasets. Because the feature reduction was performed within each cross-validation loop and was based only on the subselected training set for the loop, the number of surviving features and the names of those features vary among the different training loops. In all loops, the number of surviving features was less than 100 and most of the surviving features were deep features.

In this study, individuals who were lost to follow-up or were still alive at the end of the study were right-censored. The ratio of noncensored-to-censored data in the 3 datasets was 45:5 for DATA 1, 97:31 for DATA 2, and 90:18 for DATA 3. The Elastic Net-Cox proportional hazards model was used as the multivariate statistical model to generate survival scores for each patient. On the basis of the survival scores, we were able to dichotomize patients into 2 groups: predicted long-term and short-term survivors. In Fig 3, we demonstrate the overall performance of our method in the group 1 dataset (Fig 3A) with a log-rank test P value $< .001$ (hazard ratio = 3.26; 95% CI, 1.7–6.0), group 2 dataset (Fig 3B) with a log-rank test P value = .014 (hazard ratio = 1.65; 95% CI, 1.1–2.4), and the group 3 dataset (Fig 3C) with a log-rank test P value = .035 (hazard ratio = 1.71; 95% CI, 1.0–2.3). The ratio of shorter term-to-longer term survivors and the percentage of shorter term survivors was 22:28 (44%) for DATA 1, 63:65 (49%) for DATA 2, and 57:51 (53%) for DATA 3.

DISCUSSION

In this study, we demonstrated that machine learning-based statistical analysis of an image feature set comprising both radiomics and deep learning features extracted from gadolinium-enhanced brain MR imaging of patients with GBM can be used to distinguish longer term from shorter term survivors. The model was proved efficient to analyze anonymized brain MR imaging data from both publicly available sources and our hospital.

Previous literature on quantitative image-based prediction of OS has suggested that deep features play a complementary role to radiomics features.^{12,14,22,23} Our study demonstrates that this remains true when using deep features extracted by VGG-19, an advanced model with documented excellent performance in image classification. Deep features are not limited to previously identified image attributes or even to those understandable by humans. This is an advantage because it leads to the possibility of discovering information in medical images that is not observable to human readers, which, in turn, raises the rational hope of adding diagnostic value beyond simple quantification of information already accessible in MR images. The abstract “features” represented in the weights of the deep CNN have a number of limitations. The meaning of individual features is not easy for humans to clearly understand. Also, it remains uncertain how reproducible the deep feature output is from the current CNN operating with available dataset sizes and processing power. As such, radiomics features were integrated to the pipeline, which were well-defined and selected a priori to comprise image attributes known or rationally expected by human experts to contain predictive information. At least in the near-term, we believe that the combination of radiomics and deep features may be rationally expected to provide greater value than deep feature-based analyses alone.

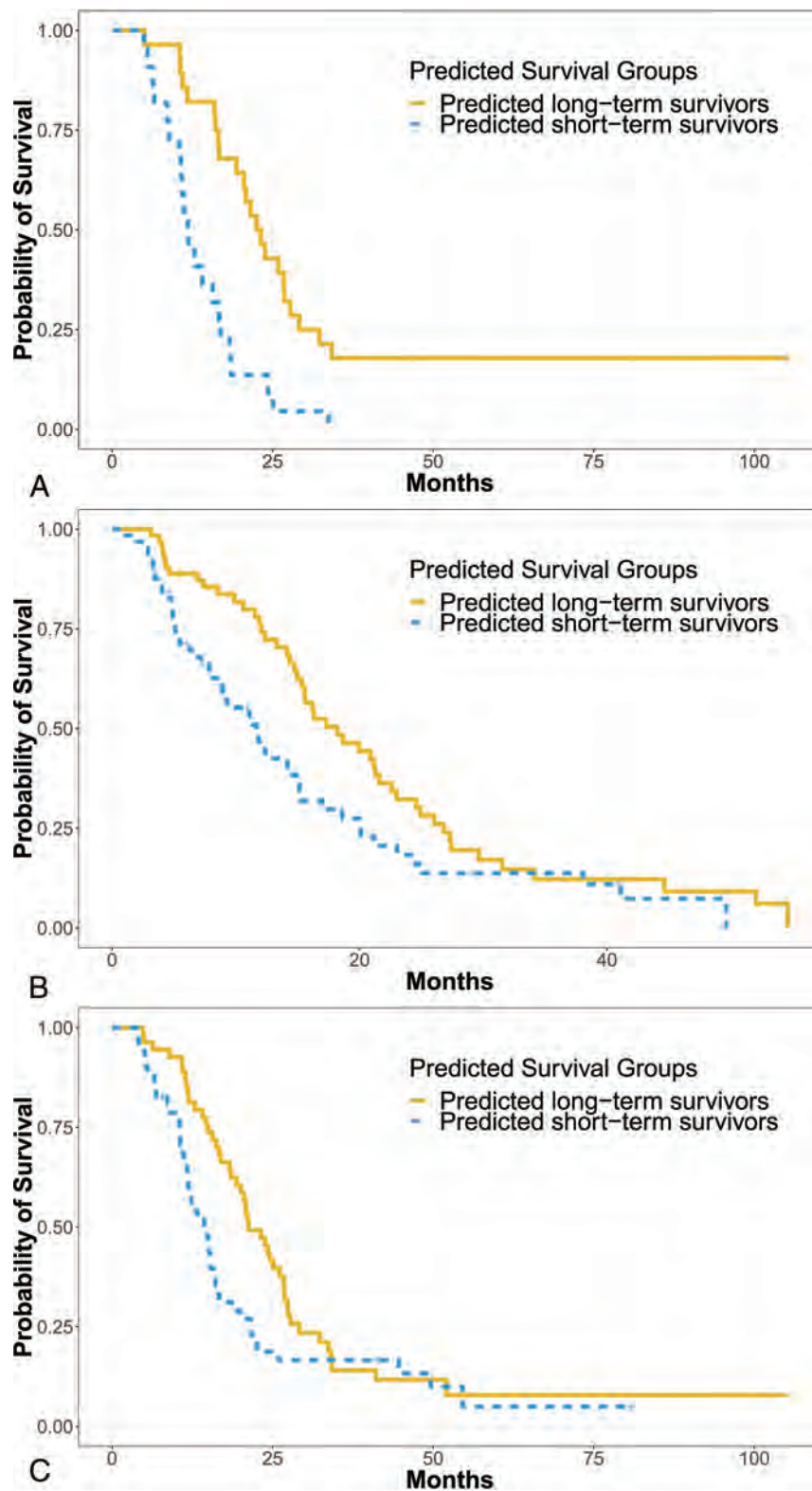


FIG 3. Kaplan-Meier curve of predicted longer term and shorter term survival in a dataset (A) with 50 patients with HGG from Brigham and Women's Hospital, a dataset (B) with 128 patients with HGG from the TCGA, and a dataset (C) with 108 patients with HGG from Brigham and Women's Hospital and the TCGA.

Besides deep features and radiomics features, we also investigated the effect of demographic features by adding sex and age information into the feature set of the TCGA dataset. This

investigation did not change the performance substantially, likely because the areas under the curve of sex and age were both so low (area under the curve of sex = 0.53; area under the curve of

age = 0.62) that these features were eliminated during feature reduction. We chose to include a deliberately heterogeneous cohort treated with a wide range of therapies to make the training set and model more readily generalizable to the heterogeneous patient mixture encountered in the clinic. Most of the patients received a standard treatment protocol of chemoradiation with temozolomide. Many received bevacizumab. Additional patients received a range of investigational therapies, including chemotherapies, targeted molecular therapies, and a few immunotherapies. Tumor genomics such as *Isocitrate dehydrogenase 1 (IDH-1)* mutation, *MGMT* methylation, and epidermal growth factor receptor application are powerful tumor markers that merit inclusion in future models. Because, unfortunately, tumor genomic data were unavailable for many patients in our cohort, we did not attempt to include this in our modeling. Twelve of 50 patients in our institutional dataset were *IDH-1* wild-type, but *IDH-1* status was not assessed in the remainder. Similarly, 11 of 50 were epidermal growth factor receptor-amplified, 20 of 50 were epidermal growth factor receptor not highly amplified, and 19 were unknown.

Like any statistical correlation approach, the CNN depends on the comprehensiveness of the training dataset, which is a statistically robust subset of the whole dataset. In general, the CNN model performance improves with increasing size of the dataset. Unfortunately, in the field of medical imaging and particularly in HGG brain MR imaging, annotating a large number of medical images remains challenging and time-consuming. While 50–150 fully annotated GBM datasets with known patient data represent a large amount of data to acquire, it is a small dataset from the perspective of the CNN training set and may result in overfitting. Under this circumstance, the transfer learning technique is introduced to apply CNN models from one field to another. For example, Paul et al^{14,22} generated deep features from a pretrained CNN model to improve survival prediction accuracy for patients with lung cancer. Lao et al¹² adopted the pretrained CNN_S model for prediction of survival in GBM. Ahmed et al²³ chose a pretrained CNN_F model in predicting the survival time of patients with brain tumor. Choi et al²⁴ used a pretrained VGG-19 model to classify retinal images. On the other hand, transfer learning can reduce the number of training sets used by several orders of magnitude, but it introduces certain bias into the resulting CNN in the form of the pretrained parameters. It is likely that the success of the transferred model depends, in large part, on which CNN is selected, but to date, there is no systematic way to know which of the large number of available pretrained neural networks is best suited to a given task, which layers are optimal for choosing the features, or which pretrained dataset should be used. We chose VGG-19 to generate deep features for this study because it was trained on a large image data base and validated to provide excellent accuracy in the many applications; and it has been successfully applied to many medically related problems. In future work, it may be important to compare our results with the performance of other models such as VGG-16 (<https://neurohive.io/en/popular-networks/vgg16/>)¹⁸ or ResNet-50 (<https://neurohive.io/en/popular-networks/resnet/>).²⁵

Transfer learning is not a fail-proof solution to the overfitting problem because overfitting may also occur in the retraining of the transferred CNN. Our initial output data matrix was very

unbalanced and sparse, with only several dozen patients but 8540 output features. Our applied feature-reduction method eliminated roughly 99% of features and reduced the probability of divergence and computational cost. Reducing the number of features is essential to avoid overfitting in such small datasets, but feature reduction remains complicated and somewhat controversial.^{26,27} A number of methods exist. We chose not to use principal component analysis, a well-established method, because it complicates further the interpretability problems intrinsic to radiomics and deep learning models by generating new features in a new coordinate system, yet 1 more step removed from the original image.

In our experiments, we found that there were more downstream features left in DATA 1 than in DATA 2 and DATA 3. One reason could be the data homogeneity, ie, some predictors in the homogeneous dataset may lead to an overfitting problem because they may not be very predictive in a heterogeneous dataset. In fact, in our data, DATA 1 was the most homogeneous one of all 3 datasets because it included only SE MR images and the data were acquired from a single institution only. In addition, the hazard ratio in DATA 1 was found to be higher than in the second and third datasets, suggesting that data homogeneity may affect the performance of a machine learning model in some way.

On a large-scale and high-throughput data mining field, especially medical imaging analysis, machine learning-based statistical analysis techniques are widely used. For example, de Carvalho Filho et al²⁸ used the support vector machine algorithm for lung nodule classification. Lao et al¹² used the lasso Cox regression model to find a useful subset of reduced features, then constructed radiomics signatures to predict the OS of patients with GBM. Yin et al²⁷ compared 3 feature-selection methods and 3 classification methods for differentiation of sacral chordoma and sacral giant-cell tumor. Yu et al²⁹ used an Elastic Net-Cox hazard ratio model to predict survival of patients with squamous cell carcinoma and stage I adenocarcinoma. In our study, we did not model OS as a binomial classification problem because binary classifiers do not consider censored information and are highly dependent on the manually determined survival threshold. Instead we chose Cox regression, a time-to-event model that is better suited to handle censored data and model a continuous range of the survival probabilities. Because the traditional Cox model does not work well on high-dimensional data in which a number of covariates are much larger than the sample size, we selected the Elastic Net-Cox hazard ratio model for statistical analysis. This penalized Cox model has been proved able to handle high-dimensional data and obtain reliable survival prediction.²⁹ It is possible that other statistical approaches may improve our ability to detect correlations in the data. This is an area that will benefit from future study.

Because postcontrast T1-weighted images are the critical mainstay of routine clinical brain tumor imaging,³⁰ we chose these as the initial image type around which to build our pipeline. Addition of more sequences (precontrast T1, T2, FLAIR T2, SWI, DWI, PWI) with independent image contrast can be expected to improve model performance and is planned for future work.

Other factors that may affect the final model performance include interoperator variation in ROI selection. To investigate, we had our 2 radiologists label our largest TCGA dataset independently. The intraclass correlation coefficient on the downstream features yielded a median of 0.76. Most individual-feature intraclass correlation coefficients were >0.7 . This high reproducibility implies that inter-operator variation in ROI selection had little effect on our dataset. We also performed a supplemental analysis to test the effect of normal tissue in the training set input. In the patients in the TCGA, we removed normal voxels from inside the bounding box and retrained the deep learning model. The result was similar to the performance with the normal tissue voxels retained in the bounding box, with a P value of .016. It remains unknown whether this result would be true using larger bounding boxes comprising more normal tissue. These analyses suggest that our model performance was robust to at least some variation in preprocessing. More investigation is needed with more heterogeneous and independent datasets to determine whether this is generally true.

CONCLUSIONS

We report successful production and initial validation of a deep transfer learning model combining radiomics and deep features to predict OS of patients with GBM from postcontrast T1-weighted brain MR images. Further optimization of these results will require systematic attention to each of the critical components of the pipeline, including choice and modification of the model, optimization of feature-reduction method, selection of statistical correlation strategy, incorporation of additional MR imaging data types, and inclusion of tumor genomics data. Necessary future steps before clinical translation will need to include interpretability analysis to determine the clinical significance of the surviving features in the model and testing in a dichotomized design that allows assessment or prediction performance on an individual patient basis.

Disclosures: Wei Han—RELATED: Grant: National Institutes of Health award R01LM012434.* Lei Qin—UNRELATED: Payment for Lectures Including Service on Speakers Bureaus: Purdue University, Biomedical Engineering Department. Comments: I gave a lecture to the Biomedical Engineering department about radiomics and machine learning. Kun-Hsing Yu—RELATED: Grant: Harvard Data Science Initiative. Comments: I received a fellowship from the Harvard Data Science Initiative*. UNRELATED: Patents (Planned, Pending or Issued): Harvard Medical School. Comments: Harvard Medical School submitted a nonprovisional patent on my work on digital pathology profiling (US Patent Application 16/179,101). Xiaoyin Xu—RELATED: Grant: National Institutes of Health. Comments: R01LM012434.* Geoffrey Young—RELATED: Grant: National Institutes of Health*. Support for Travel to Meetings for the Study or Other Purposes: National Institutes of Health*. UNRELATED: Expert Testimony: Risk Management Foundation; Grants/Grants Pending: Siemens. Comments: postprocessing software*. Payment for Lectures Including Service on Speakers Bureaus: Ray-Plus. Comments: honorarium for lecture; Travel/Accommodations/Meeting Expenses Unrelated to Activities Listed: Ray-Plus. Comments: travel expenses related to the lecture mentioned above; Other: collaborating institutions in China. Comments: support for visiting research fellows who participated in my lab as part of a research training program and participated in the work of the group. In the past 36 months, this has included fully externally supported MD fellows from the Henan Cancer Hospital, the Guangzhou First People's Hospital, and the Peking Union Medical College Hospital.* *Money paid to institution.

REFERENCES

1. Pope WB, Sayre J, Perlina A, et al. **MR imaging correlates of survival in patients with high-grade gliomas.** *AJNR Am J Neuroradiol* 2005;26:2466–74 Medline
2. Zhou M, Scott J, Chaudhury B, et al. **Radiomics in brain tumor: image assessment, quantitative feature descriptors, and machine-learning approaches.** *AJNR Am J Neuroradiol* 2018;39:208–16 CrossRef Medline
3. Vallieres M, Freeman CR, Skamene SR, et al. **A radiomics model from joint FDG-PET and MRI texture features for the prediction of lung metastases in soft-tissue sarcomas of the extremities.** *Phys Med Biol* 2015;60:5471–96 CrossRef Medline
4. Aerts HJ, Velazquez ER, Leijenaar RT, et al. **Decoding tumour phenotype by noninvasive imaging using a quantitative radiomics approach.** *Nat Commun* 2014;5:4006 CrossRef Medline
5. Qu J, Qin L, Cheng S, et al. **Residual low ADC and high FA at the resection margin correlate with poor chemoradiation response and overall survival in high-grade glioma patients.** *Eur J Radiol* 2016;85:657–64 CrossRef Medline
6. Qin L, Li A, Qu J, et al. **Normalization of ADC does not improve correlation with overall survival in patients with high-grade glioma (HGG).** *J Neurooncol* 2018;137:313–19 CrossRef Medline
7. Akkus Z, Galimzianova A, Hoogi A, et al. **Deep learning for brain MRI segmentation: state of the art and future directions.** *J Digit Imaging* 2017;30:449–59 CrossRef Medline
8. Zhou X, Takayama R, Wang S, et al. **Deep learning of the sectional appearances of 3D CT images for anatomical structure segmentation based on an FCN voting method.** *Med Phys* 2017;44:5221–33 CrossRef Medline
9. Chmelik J, Jakubicek R, Walek P, et al. **Deep convolutional neural network-based segmentation and classification of difficult to define metastatic spinal lesions in 3D CT data.** *Med Image Anal* 2018;49:76–88 CrossRef Medline
10. Acharya UR, Oh SL, Hagiwara Y, et al. **A deep convolutional neural network model to classify heartbeats.** *Comput Biol Med* 2017;89:389–96 CrossRef Medline
11. Burlina P, Pacheco KD, Joshi N, et al. **Comparing humans and deep learning performance for grading AMD: a study in using universal deep features and transfer learning for automated AMD analysis.** *Comput Biol Med* 2017;82:80–86 CrossRef Medline
12. Lao J, Chen Y, Li ZC, et al. **A deep learning-based radiomics model for prediction of survival in glioblastoma multiforme.** *Sci Rep* 2017;7:1035 CrossRef Medline
13. Nie D, Zhang H, Adeli E, et al. **3D deep learning for multi-modal imaging-guided survival time prediction of brain tumor patients.** *Med Image Comput Comput Assist Interv* 2016;9901:212–20 CrossRef Medline
14. Paul R, Hawkins SH, Balagurunathan Y, et al. **Deep feature transfer learning in combination with traditional features predicts survival among patients with lung adenocarcinoma.** *Tomography* 2016;2:388–95 CrossRef Medline
15. Zhen X, Chen J, Zhong Z, et al. **Deep convolutional neural network with transfer learning for rectum toxicity prediction in cervical cancer radiotherapy: a feasibility study.** *Phys Med Biol* 2017;62:8246–63 CrossRef Medline
16. Collewet G, Strzelecki M, Mariette F. **Influence of MRI acquisition protocols and image intensity normalization methods on texture classification.** *Magn Reson Imaging* 2004;22:81–91 CrossRef Medline
17. Gibbs P, Turnbull LW. **Textural analysis of contrast-enhanced MR images of the breast.** *Magn Reson Med* 2003;50:92–98 CrossRef Medline
18. Simonyan K, Zisserman A. **Very deep convolutional networks for large-scale image recognition.** *Computer Vision and Pattern Recognition* 2014;arXiv:1409.1556
19. Krizhevsky A, Sutskever I, Hinton GE. **ImageNet classification with deep convolutional neural networks.** *J Commun. ACM* 2017;60:84–90
20. Simon N, Friedman J, Hastie T, et al. **Regularization paths for Cox's proportional hazards model via coordinate descent.** *J Stat Softw* 2011;39:1–13 Medline

21. Feinstein AR. *Clinical Epidemiology: The Architecture of Clinical Research*. Philadelphia: W.B. Saunders; 1985:xii
22. Paul R, Hawkins SH, Hall LO, et al. **Combining deep neural network and traditional image features to improve survival prediction accuracy for lung cancer patients from diagnostic CT.** In: *Proceedings of the IEEE International Conference on Systems, Man, and Cybernetics*, Budapest, Hungary. October 9–12, 2016 CrossRef
23. Ahmed KB, Hall LO, Goldgof DB, et al. **Fine-tuning convolutional deep features for MRI based brain tumor classification.** In: *Proceedings of Medical Imaging 2017: Computer-Aided Diagnosis*, Orlando, Florida. February 11–16, 2017
24. Choi JY, Yoo TK, Seo JG, et al. **Multi-categorical deep learning neural network to classify retinal images: a pilot study employing small database.** *PLoS One* 2017;12:e0187336 CrossRef Medline
25. Kaiming H, Zhang X, Shaoqing R, Jian S. **Deep residual learning for image recognition.** In: *Proceedings of the IEEE Conference on Computer Vision and Pattern Recognition*, Las Vegas, Nevada. June 26 to July 1, 2016
26. Parmar C, Grossmann P, Bussink J, et al. **Machine learning methods for quantitative radiomic biomarkers.** *Sci Rep* 2015;5:13087 CrossRef Medline
27. Yin P, Mao N, Zhao C, et al. **Comparison of radiomics machine-learning classifiers and feature selection for differentiation of sacral chordoma and sacral giant cell tumour based on 3D computed tomography features.** *Eur Radiol* 2019;29:1841–47 CrossRef Medline
28. de Carvalho Filho AO, Silva AC, de Paiva AC, et al. **Lung-nodule classification based on computed tomography using taxonomic diversity indexes and an SVM.** *J Signal Process Syst* 2017;87:179–96 CrossRef
29. Yu KH, Zhang C, Berry GJ, et al. **Predicting non-small cell lung cancer prognosis by fully automated microscopic pathology image features.** *Nat Commun* 2016;7:12474 CrossRef Medline
30. Cha S. **CNS tumors: monitoring therapeutic response and outcome prediction.** *Top Magn Reson Imaging* 2006;17:63–68 CrossRef Medline

Dynamic Contrast-Enhanced MR Imaging of Nonenhancing T2 High-Signal-Intensity Lesions in Baseline and Posttreatment Glioblastoma: Temporal Change and Prognostic Value

I. Hwang, S.H. Choi, C.-K. Park, T.M. Kim, S.-H. Park, J.K. Won, I.H. Kim, S.-T. Lee, R.-E. Yoo, K.M. Kang, T.J. Yun, J.-H. Kim, and C.-H. Sohn



ABSTRACT

BACKGROUND AND PURPOSE: The prognostic value of dynamic contrast-enhanced MR imaging on nonenhancing T2 high-signal-intensity lesions in patients with glioblastoma has not been thoroughly elucidated to date. We evaluated the temporal change and prognostic value for progression-free survival of dynamic contrast-enhanced MR imaging–derived pharmacokinetic parameters on nonenhancing T2 high-signal-intensity lesions in patients with glioblastoma before and after standard treatment, including gross total surgical resection.

MATERIALS AND METHODS: This retrospective study included 33 patients who were newly diagnosed with glioblastoma and treated with gross total surgical resection followed by concurrent chemoradiation therapy and adjuvant chemotherapy with temozolomide in a single institution. All patients underwent dynamic contrast-enhanced MR imaging before surgery as a baseline and after completion of maximal surgical resection and concurrent chemoradiation therapy. On the whole nonenhancing T2 high-signal-intensity lesion, dynamic contrast-enhanced MR imaging–derived pharmacokinetic parameters (volume transfer constant [K^{trans}], volume of extravascular extracellular space [v_e], and blood plasma volume [v_p]) were calculated. The Cox proportional hazards regression model analysis was performed to determine the histogram features or percentage changes of pharmacokinetic parameters related to progression-free survival.

RESULTS: Baseline median K^{trans} , baseline first quartile K^{trans} , and posttreatment median K^{trans} were significant independent variables, as determined by univariate analysis ($P < .05$). By multivariate Cox regression analysis including methylation status of O⁶-methylguanine-DNA methyltransferase, baseline median K^{trans} was determined to be the significant independent variable and was negatively related to progression-free survival (hazard ratio = 1.48, $P = .003$).

CONCLUSIONS: Baseline median K^{trans} from nonenhancing T2 high-signal-intensity lesions could be a potential prognostic imaging biomarker in patients undergoing gross total surgical resection followed by standard therapy for glioblastoma.

ABBREVIATIONS: CCRT = concurrent chemoradiation therapy; DCE = dynamic contrast-enhanced; K^{trans} = volume transfer constant; MGMT = O⁶-methylguanine-DNA methyltransferase; PFS = progression-free survival; TMZ = temozolomide; v_e = volume of extravascular extracellular space; v_p = blood plasma volume

The standard treatment of glioblastoma is a multimodality strategy including maximal safe surgical resection and

radiation therapy with concomitant and adjuvant temozolomide (TMZ).^{1,2} Glioblastoma is a diffusely infiltrating and widespread malignant neoplasm. The main target for surgical resection to improve survival is a contrast-enhancing, high-grade portion of the tumor with a leaky BBB.^{3,4} However, certain nonenhancing infiltrative tumor cells may remain after surgical resection and

Received July 1, 2019; accepted after revision October 2.

From the Department of Radiology (I.H., S.H.C., R.-E.Y., K.M.K., T.J.Y., J.-H.K., C.-H.S.), Center for Nanoparticle Research; Institute for Basic Science, and School of Chemical and Biological Engineering (S.H.C.); Department of Neurosurgery and Biomedical Research Institute (P.C.-K.); Department of Internal Medicine and Cancer Research Institute (T.M.K.); Department of Pathology (S.-H.P., J.K.W.), Department of Radiation Oncology and Cancer Research Institute (I.H.K.); and Department of Neurology (S.-T.L.), Seoul National University Hospital, Seoul, Korea.

This study was supported by grants from the Korea Healthcare Technology R&D Projects, Ministry for Health, Welfare & Family Affairs (H16C1111); the Brain Research Program through the National Research Foundation of Korea funded by the Ministry of Science, ICT & Future Planning (2016M3C7A1914002); the Basic Science Research Program through the National Research Foundation of Korea funded by the Ministry of Science, ICT & Future Planning (2017RIA2B2006526); the Creative-Pioneering Researchers Program through Seoul National University, and Project Code (IBS-R006-D1).

Please address correspondence to Seung Hong Choi, MD, PhD, Department of Radiology, Seoul National University Hospital, 101 Daehak-ro, Jongno-gu, Seoul, 03080, Korea; e-mail: verocay@snuh.org

Indicates open access to non-subscribers at www.ajnr.org

Indicates article with supplemental on-line table.

Indicates article with supplemental on-line photo.

<http://dx.doi.org/10.3174/ajnr.A6323>

intermingle with peritumoral edema. Unfortunately, those lesions are difficult to distinguish because they are similarly presenting as high-signal-intensity lesions on T2-weighted or FLAIR images. The biologic nature of nonenhancing T2 high-signal-intensity lesions could be more important for the prognosis than that of the contrast-enhancing high-grade tumor portion, which would be removed by maximal safe surgical resection.

Dynamic contrast-enhanced (DCE) MR imaging could provide information on permeability and angiogenesis by quantitative pharmacokinetic parameters.^{5,6} Previous studies with DCE-MR imaging in gliomas have already demonstrated the capability of predicting histologic grading, differentiating pseudoprogression from progression, and predicting the progression of persistent enhancing nodules after standard treatment.⁷⁻⁹ A recent histopathologic study suggested that nonenhancing tumor contains a comparable amount of infiltrative tumor to enhancing tumor in glioblastomas.¹⁰ We hypothesized that a variable proportion of peritumoral edema, low-grade infiltrative tumor, or even nonenhancing high-grade tumors might coexist in the nonenhancing T2 high-signal-intensity lesions. As the tumor grade increases, it tends to have a large portion of immature vasculature. Therefore, DCE-MR imaging–derived pharmacokinetic parameters might have the potential to predict the biologic behavior of those lesions. Meanwhile, the permeability of the BBB may affect the delivery of the chemotherapeutic drug to brain tissue. Although brain tumors are different from other tumors due to their unique BBB structure, previous studies of malignant tumors outside the brain, such as cervical cancer, colorectal cancer, and lung cancer, have demonstrated that increased permeability or angiogenesis was related to a favorable tumor response.¹¹⁻¹³ Therefore, there is a possibility that increased permeability at certain time points might be related to a favorable treatment response.

Some studies have focused on the perfusion characteristics of nonenhancing T2 high-signal-intensity lesions in glioblastoma to predict prognosis.¹⁴⁻¹⁶ However, there have been few investigations of the DCE-MR imaging–derived pharmacokinetic parameters of nonenhancing T2 high-signal-intensity lesions of glioblastoma at the time of baseline and post concurrent chemoradiation therapy (CCRT) and their temporal change.

Therefore, the purpose of this study was to evaluate the temporal change and prognostic value for progression-free survival (PFS) of DCE-MR imaging–derived pharmacokinetic parameters on nonenhancing T2 high-signal-intensity lesions in patients with glioblastoma before and after standard treatment, including gross total surgical resection.

MATERIALS AND METHODS

Study Population

The institutional review board of our institution approved this single-center, retrospective study, and informed consent was waived. By means of a data base search between January 2010 and December 2017, two hundred eighty-nine consecutive patients were confirmed to have glioblastoma by histopathologic diagnosis. Two neuropathologists performed the histopathologic diagnosis at our institution (S.-H.P. and J.K.W. with 32 and 17 years of experience in pathology, respectively). Among the

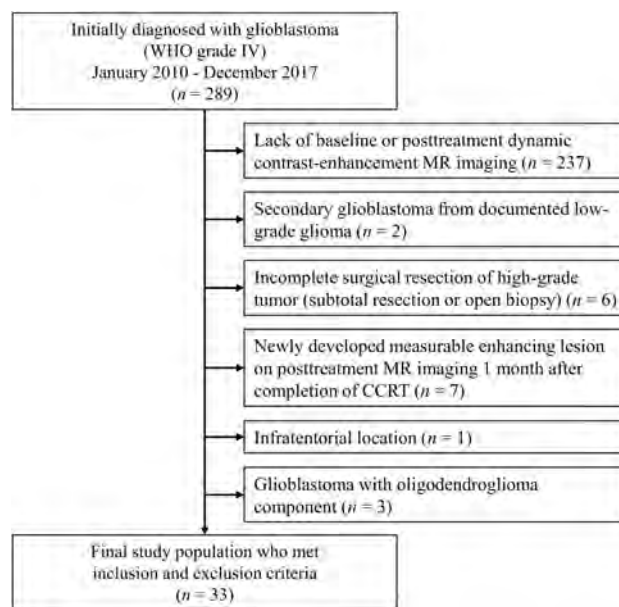


FIG 1. Flow chart for patient selection.

patients, the eligible study population was defined by the following inclusion criteria: The patient had a histopathologic diagnosis of supratentorial glioblastoma, underwent baseline DCE-MR imaging 24–48 hours before the operation, underwent maximal surgical resection (near-total or gross-total resection) followed by CCRT with TMZ administration, and underwent posttreatment DCE-MR imaging within 1 month after completion of CCRT. Ultimately, 33 patients met the inclusion criteria and were included in our study (Fig 1). All patients except 2 had 6 cycles of adjuvant TMZ administration 1 month after the completion of CCRT. One patient stopped adjuvant TMZ after 4 cycles because of disease progression and switched to second-line chemotherapy; another patient was discontinued after 2 cycles of TMZ administration due to severe skin eruption.

Calculation of PFS Time

All patients routinely visited the outpatient clinic and underwent follow-up brain MR imaging with a brain tumor evaluation protocol at our institution every 3 months for the first 2 years. Then the follow-up period was extended to 6 months if the patient had no clinical or radiologic evidence of progression. Clinicians and radiologists assessed the patient's response to treatment using the Response Assessment in Neuro-Oncology criteria.¹⁷ If the patient met at least 1 of the following criteria at each visit, the patient was diagnosed with disease progression: 1) >25% increase in the sum of the products of the perpendicular diameters of enhancing lesions, compared with the smallest tumor measurement obtained either at baseline or best response; 2) substantial increase in T2/FLAIR nonenhancing lesion; 3) any new lesion; 4) evident clinical deterioration not attributable to other causes apart from the tumor; and 5) clear progression of nonmeasurable disease. If there was imaging evidence of an increasingly enhancing lesion that did not meet the criteria of progression, short-term follow-up imaging was performed in 1–2 months. Then, the progression of disease was confirmed by subsequent

imaging or by histopathologic diagnosis. In case of changing the treatment plan due to disease progression, as decided by the multidisciplinary clinic in our institution, it was also regarded as a disease progression. The PFS was calculated between the date of initial imaging diagnosis and the date assessed as disease progression or the last follow-up date if the patient had no evidence of disease at the last follow-up visit.

Image Acquisition

All patients underwent brain MR imaging using a 3T MR imaging scanner (Magnetom Verio or Skyra; Siemens, Erlangen, Germany) with a 32-channel head coil. Our institution's routine brain MR imaging protocol for brain tumor evaluation included pre- and postcontrast 3D T1-weighted MPRAGE sequences (TR, 558 ms; TE, 1.9 ms; flip angle, 9°; matrix, 256 × 232; FOV, 220 × 250 mm; section thickness, 1 mm; and NEX, 1), a transverse T2 FLAIR sequence (TR, 9000 ms; TE, 97 ms; TI, 2500 ms; flip angle, 130°; matrix, 384 × 348; FOV, 199 × 220 mm; section thickness, 5 mm; and NEX, 1), and transverse T2WI with a TSE sequence (TR, 5160 ms; TE, 91 ms; flip angle, 124°–130°; matrix, 640 × 510–580; FOV, 175–199 × 220 mm; section thickness, 5 mm; NEX, 1).

DCE-MR images were obtained using a transverse T1-weighted spoiled gradient-echo sequence (TR, 2.8 ms; TE, 1.0 ms; flip angle, 10°; matrix, 192 × 192; FOV, 240 × 240; and section thickness, 3 mm) after intravenous administration of gadobutrol (Gadovist; Bayer Schering Pharma, Berlin, Germany) at a dose of 0.1 mmol/kg of body weight and at a rate of 4 mL/s followed by a 30-mL saline chaser using a power injector (Spectris; MedRad, Indianola, Pennsylvania). Sixty dynamic scans with a time resolution of 4.97 seconds were acquired with 40 slices of transverse plane images; the total acquisition time was 5 minutes 8 seconds.

Image Analysis

DCE-MR images were transferred to dedicated workstations, and postprocessing was performed with commercial software (nordicICE 4.0.6; NordicNeuroLab, Bergen, Norway).

We performed coregistration of FLAIR and DCE-MR imaging on postcontrast 3D T1WI as structural imaging achieved automatically by an algorithm that found an optimal rigid transformation based on the geometric information.¹⁸ If there was geometric distortion due to postsurgical changes, manual correction was performed for the best match of nonenhancing T2 high-signal-intensity lesions. After the motion correction of DCE-MR imaging volume, deconvolution with the arterial input function was performed in the pharmacokinetic model. After the ROI was positioned in the superior sagittal sinus at the level of the lateral ventricles, the average arterial input function curve from 3 to 5 pixels of the best arterial input function candidate was semiautomatically determined. The baseline T1 value was fixed at 1000 ms in this study because it would give more reliable results.^{19,20} Subsequently, DCE-MR imaging–derived pharmacokinetic parametric maps were generated by the extended Tofts model²¹; volume transfer constant map (K^{trans} , minute⁻¹), extravascular extracellular space per unit volume of tissue map (v_e , percentage), and blood plasma volume per unit volume of tissue map (v_p , percentage) were calculated on a pixel-by-pixel basis.

Two investigators (I.H. and S.H.C., with 8 and 17 years of experience in neuroradiology) carefully determined the VOI by consensus in every section of nonenhancing T2 high-signal-intensity lesions on FLAIR images. Enhancing areas on the post-contrast T1-weighted images and cystic/necrotic areas or macrovessels were carefully avoided. The pharmacokinetic parameters on K^{trans} , v_e , and v_p maps were measured at baseline and on the posttreatment study. The On-line Figure illustrates the representative image-analysis process. For further quantitative analysis, we performed histogram analysis from the total voxel values; the mean, SD, skewness, kurtosis, median, first and third quartile values, fifth and 95th percentile values of each pharmacokinetic parameter, as well as the mask volume of VOIs were calculated. We included the voxels in which each DCE pharmacokinetic parameter value was >0. Furthermore, the percentage change between posttreatment and baseline values of each pharmacokinetic parameter was calculated in each subject as follows:

$$\text{Percentage Change} = (\text{Posttreatment} - \text{Baseline}) / \text{Baseline} \times 100.$$

Other Clinical and Genetic Parameters

In addition to demographic characteristics, the Karnofsky Performance Status score before the operation and the radiation dose of CCRT were investigated to evaluate the prognostic value. Furthermore, the following genetic alterations were investigated in this study: mutation of *isocitrate dehydrogenase (IDH)* and promoter methylation of O⁶-methylguanine-DNA methyltransferase (MGMT).

Statistical Analysis

All statistical analyses were performed by open-source statistical language (R for Windows, Version 3.5.1) with the survival analysis package (survival).²² In all statistical tests, a *P* value < .05 was considered a significance level. Descriptive statistics summarized clinical and genetic characteristics. A univariate Cox proportional hazards regression model was used to investigate differentiating clinical, genetic, and pharmacokinetic parameters for PFS. A variance inflation factor was calculated for the significant pharmacokinetic parameters by univariate analysis, and variables with >10 were sequentially excluded to exclude variables having multicollinearity. Finally, multivariate Cox proportional hazard model analyses were performed to identify independent pharmacokinetic parameters for differentiating PFS. The optimal cutoff value was calculated by the published method using the R language.²³ After that step, the Kaplan-Meier survival curve was plotted, and the log-rank test was performed.

RESULTS

Clinical and Genetic Characteristics

Clinical and genetic characteristics are summarized in Table 1. The median PFS of our study population was 22.6 months (689 days). Twenty-six patients were diagnosed with tumor progression during the follow-up period. The prevalence of an *IDH* mutation was 6.1%, and the promoter methylation of MGMT was 66.7% (Table 1).

The patients with promoter methylation of MGMT of the tumor showed significantly better survival with a hazard ratio of 0.256 (*P* = .001). Otherwise, none of the clinical or genetic

Table 1: Clinical and genetic characteristics of our study population and prognostic value by univariate Cox regression test

	Mean (SD) or No. (%)	Hazard Ratio (95% CI)	P Value
Age (years)	55.5 (13.4)	1.02 (0.990–1.06)	.172
Sex			
Men	21 (63.6%)	0.887 (0.393–2.00)	.772
Women	12 (36.4%)		
Radiation dose			
Hypofractionated (45 Gy in 15 fractions)	6 (18.2%)	1.51 (0.593–3.84)	.388
Conventional long course (>60 Gy)	27 (81.8%)		
Karnofsky Performance Status score			
<70	3 (9.1%)	0.820 (0.193–3.50)	.789
≥70	30 (90.9%)		
IDH1 or 2 mutation			
Present	2 (6.1%)	0.324 (0.0432–2.436)	.274
Absent	31 (93.9%)		
MGMT promoter methylation			
Methylated	22 (66.7%)	0.256 (0.113–0.577)	.001
Unmethylated	11 (33.3%)		
Baseline T2 high-signal-intensity volume (mL)	59.5 (29.0)	0.996 (0.982–1.01)	.573
Posttreatment T2 high-signal-intensity volume (mL)	16.6 (24.8)	0.996 (0.978–1.01)	.668
Percentage change T2 high-signal-intensity volume	–64.3% (44.8%)	1.04 (0.412–2.63)	.934

Table 2: Significant variables by univariate Cox proportional hazards model analysis of pharmacokinetic parameters

	Hazard Ratio (95% CI) ^a	P Value
Baseline first quartile K^{trans}	1.51 (1.08–2.12)	.016
Baseline median K^{trans}	1.26 (1.01–1.57)	.038
Posttreatment median K^{trans}	1.22 (1.03–1.45)	.024

^a Hazard ratios for K^{trans} are adjusted for a unit change of 0.001 min^{-1} .

characteristics, the volume of VOI, or its percentage change showed statistical significance by univariate Cox regression (Table 1).

Univariate Cox Proportional Hazards Regression Model for DCE-MR Imaging–Derived Pharmacokinetic Parameters

The univariate Cox regression model of each histogram feature of DCE-MR imaging–derived pharmacokinetic parameters from baseline and posttreatment T2 high-signal-intensity lesions was performed and is described in the On-line Table. The variables with P values < .05 by the Wald test were baseline median K^{trans} , baseline first quartile K^{trans} , and posttreatment median K^{trans} (Table 2). Although the percentage change of kurtosis K^{trans} was marginally insignificant ($P = .066$), the percentage change of the pharmacokinetic parameter was not determined to be a significant variable.

Multivariate Cox Proportional Hazards Regression Model for DCE-MR Imaging–Derived Pharmacokinetic Parameters

Both the baseline median and first quartile K^{trans} showed significance on univariate analysis. We selected the median value, rather than the first quartile, for further analysis because of the better interpretability of this parameter. After that step, we performed a multivariate Cox regression test with baseline and posttreatment median K^{trans} . The Cox regression model with both baseline and posttreatment median K^{trans} showed that neither variable was significant (Table 3). However, after adding the methylation status

of MGMT as a clinical variable in the model, the multivariate Cox regression test revealed that the baseline median K^{trans} and the methylation status of MGMT were significant independent variables (Table 3). Finally, we performed a multivariate Cox regression test with a stepwise variable selection method including these variables: baseline median K^{trans} , posttreatment median K^{trans} , percentage change of kurtosis K^{trans} , and the methylation status of MGMT. The stepwise method selected the variables of baseline median K^{trans} and the methylation status of MGMT as significant independent variables ($P = .003$ and $P < .001$, respectively). The percentage change of kurtosis K^{trans} was included in the model, but it was not a significant variable ($P = .108$). The posttreatment median K^{trans} was excluded from the model by stepwise variable selection.

Comparison of Survival Curves by the Binary Representation of Differentiating Variables

Kaplan-Meier survival plots were compared by the binary representation of the baseline median K^{trans} (Fig 2). The calculated optimal cutoff value for baseline median K^{trans} was 0.00470 min^{-1} . By means of the log-rank test, baseline median K^{trans} from T2 high-signal-intensity lesions showed a significant difference in the survival curve ($P = .030$). In subgroup analysis grouped by the methylation status of MGMT, the significant difference of the survival curve by baseline median K^{trans} was seen only in patients with MGMT methylated ($n = 22$, $P = .029$), while it did not reach statistical significance in patients with unmethylated MGMT ($n = 11$, $P = .256$). However, the survival curves showed the consistent trend of the higher value group of baseline median K^{trans} being related to poor survival. Representative cases are illustrated in Fig 3.

DISCUSSION

Our results demonstrate that increased baseline median K^{trans} from nonenhancing T2 high-signal-intensity lesions was associated with poor survival by multivariate Cox regression analysis. However, there was no statistically significant pharmacokinetic parameter from the posttreatment study or its percentage change between baseline and posttreatment.

Our study intended to evaluate nonenhancing T2 high-signal-intensity lesions of glioblastoma. These lesions have been regarded as a mixture of peritumoral edema and infiltrative tumor cells, even including postsurgical changes and radiation effects after treatment. However, in cases in which a sufficient extent of tumor resection was achieved, some patients eventually had tumor recurrence from the near-resection margin.²⁴ Therefore, we postulated that the character of the remaining nonenhancing T2 high-signal-intensity lesions would be more critical to predict patient survival in cases of gross total resection. A few studies have investigated DCE-MR imaging-derived pharmacokinetic parameters for the prognostic value of T2 high-signal-intensity lesions in high-grade gliomas. Jensen et al²⁵ revealed, from a small study group, that a higher v_e value of peritumoral edema was associated with favorable overall survival. A recent prospective study extensively investigated perfusion characteristics at multiple time points, including baseline, during CCRT with TMZ, and during 6 cycles of adjuvant TMZ.²⁶ Their results

supported the higher K^{trans} of enhancing tumors at the fifth week during CCRT being associated with worse PFS, though baseline relative CBV and CBF in the edema region were marginally statistically insignificant.

In contrast to previous studies, our study evaluated the prognostic value of baseline and posttreatment, in particular post-CCRT DCE-MR imaging-derived pharmacokinetic parameters and their temporal changes with histogram analysis. In addition, our study included patients who underwent gross surgical resection and had no remaining measurable enhancing lesions on follow-up MR imaging. Therefore, the study population was more homogeneous than previous studies, and we could evaluate the true nature of T2 high-signal-intensity lesions at the posttreatment period. Our results were consistent with the findings of a previous study by Kim et al,¹⁶ agreeing that baseline K^{trans} of T2 high-signal-intensity lesions has potential prognostic value. K^{trans} is the most representative marker of permeability in the DCE-MR imaging parameter.²⁷ K^{trans} has been reported to be able to

predict the grade of glioma because aggressive tumor cells exhibit a higher portion of immature vessels, resulting in leaky vasculature.⁷ Therefore, a higher baseline K^{trans} value might reflect the aggressiveness of infiltrating tumor cells in nonenhancing T2 high-signal-intensity lesions and is probably related to worse PFS.

Unfortunately, our study did not obtain a statistically significant prognostic value of posttreatment DCE-MR imaging-derived pharmacokinetic parameters and their temporal change. The median K^{trans} from nonenhancing T2 high-signal-intensity lesions in the posttreatment study showed significance by univariate analysis. However, multivariate analysis revealed that it was not statistically significant for PFS. According to a published study, the

Table 3: Multivariate Cox proportional hazard model analysis of pharmacokinetic parameters^a

	Hazard Ratio (95% CI) ^a	P-value
Model 1: without MGMT methylation status		
Baseline median K^{trans}	1.19 (0.934–1.52)	.158
Posttreatment median K^{trans}	1.16 (0.958–1.40)	.129
Model 2: with MGMT methylation status		
Baseline median K^{trans}	1.48 (1.12–1.93)	.005
Posttreatment median K^{trans}	1.01 (0.840–1.21)	.935
Presence of MGMT methylation	0.150 (0.0541–0.417)	<.001
Model 3: by stepwise variable selection ^b		
Baseline median K^{trans}	1.49 (1.15–1.92)	.003
Posttreatment median K^{trans}		
Percentage change of kurtosis K^{trans}	1.26 (0.951–1.66)	.108
Presence of MGMT methylation	0.143 (0.0541–0.375)	<.001

^a Hazard ratios for K^{trans} were adjusted for a unit change of 0.001 min^{-1} .

^b A stepwise variable selection including baseline median K^{trans} , posttreatment median K^{trans} , the percentage change of kurtosis K^{trans} , and the methylation status of MGMT.

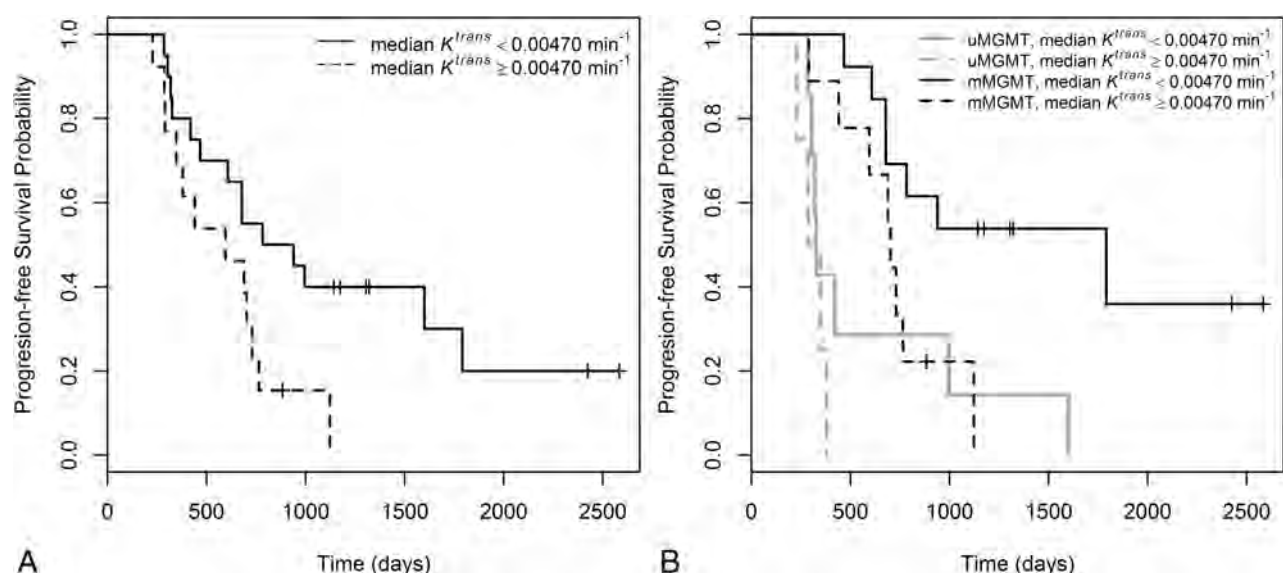


FIG 2. Kaplan-Meier curves of baseline median K^{trans} from a T2 high-signal-intensity lesion (A) and subgroup curves grouped by the methylation status of MGMT (B). mMGMT indicates methylated O⁶-methylguanine-DNA methyltransferase; uMGMT, unmethylated MGMT.

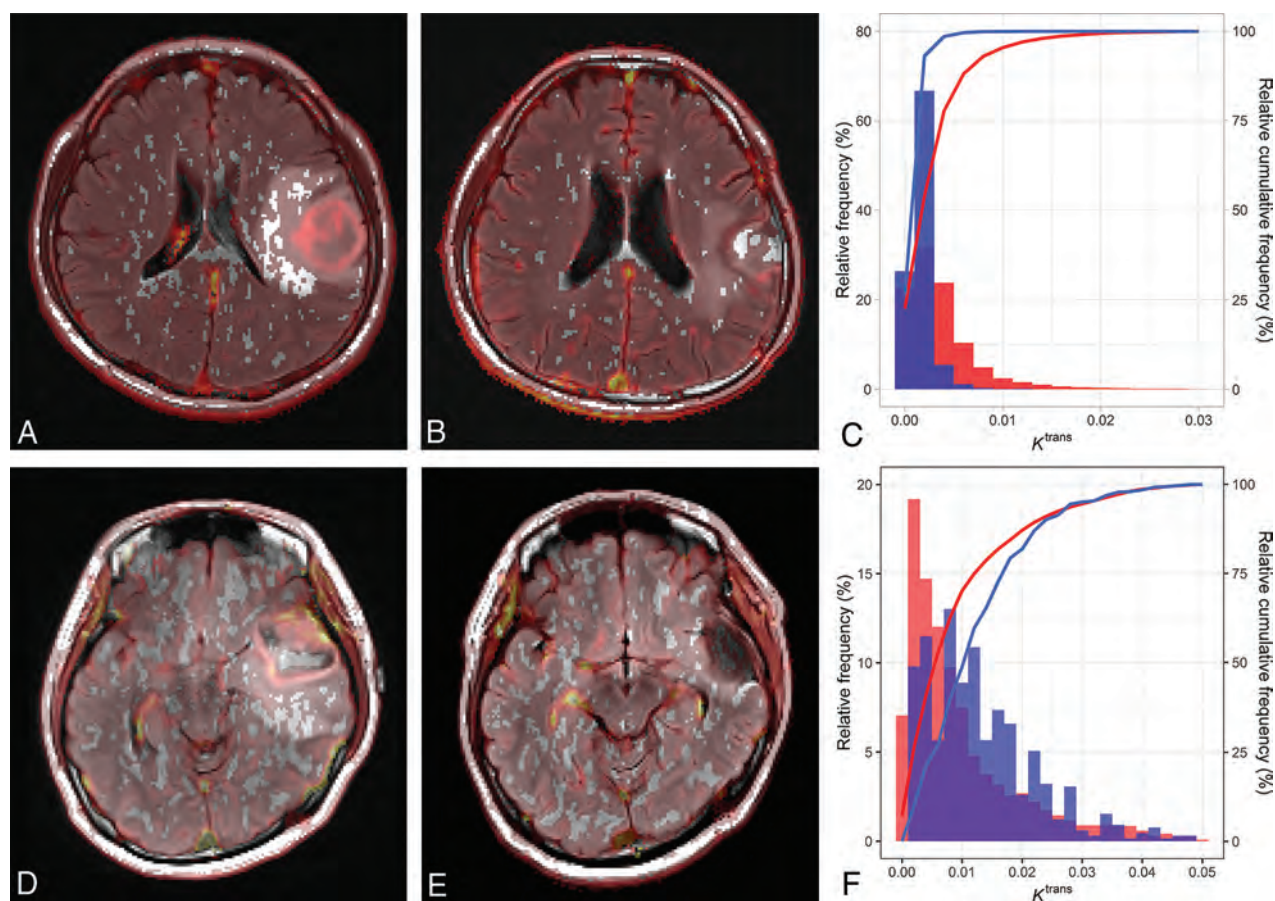


FIG 3. Representative cases. A 54-year-old man who was diagnosed with glioblastoma *IDH* wild-type in the left frontal lobe. Nonenhancing T2 high-signal-intensity lesions around the enhancing mass (postcontrast images are not shown) are noted on baseline FLAIR images with an overlay of the K^{trans} map (A). Posttreatment FLAIR images with an overlay K^{trans} map show residual T2 high-signal-intensity lesions around the surgical margin (B). A cumulative histogram is shown in C. The red bar and line indicate the distribution of the baseline K^{trans} of nonenhancing T2 high-signal-intensity lesions, while the blue bar and line show the distribution of the posttreatment K^{trans} values. The baseline median K^{trans} of nonenhancing T2 high-signal-intensity lesions was 0.00258 min^{-1} . The patient survived 1600 days after the diagnosis without progression. A 42-year-old woman was diagnosed with glioblastoma *IDH* wild-type in the left temporal lobe. Baseline (D) and posttreatment (E) FLAIR images with an overlay of the K^{trans} map show T2 high-signal-intensity lesions around the enhancing tumor (postcontrast images are not shown), partially removed by an operation, but remnant T2 high-signal-intensity lesions are noted. A cumulative histogram is shown in F. The baseline median K^{trans} is 0.00670 min^{-1} . The progression-free survival was 347 days, and the recurrent enhancing tumor developed along the superior-posterior surgical margin on subsequent follow-up MR imaging.

initial increase and subsequent overall decrease of K^{trans} of enhancing tumors were observed in nonresponders during CCRT in glioblastoma.²⁸ The study by these researchers also did not find prognostic value by multivariate Cox regression analysis, except for interval change of K^{trans} between the pre- and midtreatment scanning during CCRT. A possible explanation of our finding is that the subsequent change in DCE parameters after CCRT could reduce differences between better and worse PFS groups. In addition, some areas of nonenhancing T2 high-signal-intensity lesions were removed by an operation, and the nature of nonenhancing T2 high-signal-intensity lesions might not be the same between baseline and posttreatment examinations.

Most interesting, the prognostic value of baseline K^{trans} of nonenhancing T2 high-signal-intensity lesions was independent of the methylation status of the MGMT promoter. Methylation of the MGMT promoter is associated with favorable survival for patients with glioblastoma who are treated with CCRT with

TMZ.²⁹ The baseline DCE-MR imaging-derived pharmacokinetic parameters may reflect a different aspect of tumor biology than the methylation status of the MGMT promoter. In contrast, the posttreatment K^{trans} was not significant after adding the methylation status of the MGMT promoter. There is a possibility that the posttreatment K^{trans} has a relationship to the methylation status of the MGMT promoter. However, that would be beyond the scope of our study, and further studies are warranted.

In our study, only voxels with values greater than zero in the DCE parameter map were used for further histogram analysis. A previous study²⁸ used the DCE parameter >0 as the criterion of successfully fitted pixels. However, our study measured nonenhancing T2 high-signal-intensity lesions. In the edema portion where the BBB is intact, the K^{trans} would be near zero. By means of DCE curve fitting, a particular part of those areas would yield zero or even negative K^{trans} values; therefore, it would not necessarily be a fitting failure. Although particular voxels affected by motion artifacts also yielded nonphysiologic K^{trans} values due to

fitting failure, we believe that such a portion would not be substantial because we performed motion correction. However, we performed analysis with the positive DCE parameter voxel value for the comparability with previous studies and to maintain physiologic meaning.

The present study had a few limitations. First, the retrospective study design had potential selection bias. To minimize the selection bias, we attempted to include all consecutive patients diagnosed with glioblastoma and meeting the inclusion criteria. Second, we used 2D-FLAIR images to draw VOI masks. Therefore, there was a potential risk of spatial mismatch between FLAIR-based VOIs and DCE parametric maps due to the partial volume effect, though we coregistered image volumes. Furthermore, due to the intrinsic infiltrative nature of tumors, the margin of T2 high-signal-intensity lesions did not have a clear border, which may limit the reproducibility of determining the margin of the lesion on FLAIR images. Acquisition of the 3D-FLAIR images and use of automatic or semi-automatic segmentation techniques may improve reproducibility for the lesion. Third, a small sample size limits our ability to derive generalized conclusions from our results. However, to evaluate the nature of nonenhancing T2 high-signal-intensity lesions after the gross total resection of enhancing tumors, we had to exclude a large number of patients who had remnant measurable enhancing tumors immediately after surgical resection. Therefore, there is a limitation to generalizing our results to all patients with glioblastoma. Moreover, our study excluded subjects who demonstrated measurable enhancing lesions in the posttreatment study. For that reason, we could not evaluate pseudoprogression, which shows newly developed enhancing lesions during CCRT, but it might be related to favorable survival, though this is still controversial.^{30,31} In addition, our results showed no statistical survival difference by the presence of the *IDH* mutation. It was possibly due to a small number of patients with *IDH* mutation with glioblastoma in our study population, which had insufficient statistical power. Finally, we investigated only PFS, not overall survival. However, the PFS is known to be a surrogate marker of overall survival in glioblastoma.³²

CONCLUSIONS

Baseline median K^{trans} from nonenhancing T2 high-signal-intensity lesions could be a potential prognostic imaging biomarker in patients undergoing gross total surgical resection followed by standard therapy for glioblastoma. Our results suggest that DCE pharmacokinetic parameters derived from baseline nonenhancing T2 high-signal-intensity lesions have prognostic value; in contrast, those derived during the posttreatment period or percentage change values appear to have little prognostic value.

Disclosures: Seung Hong Choi—RELATED: Grant: government fund.* Tae Min Kim—UNRELATED: Grants/Grants Pending: AstraZeneca—Korea Health Industry Development Institute. *Money paid to the institution.

REFERENCES

1. Stupp R, Mason WP, van den Bent MJ, et al. **Radiotherapy plus concomitant and adjuvant temozolomide for glioblastoma.** *N Engl J Med* 2005;352:987–96 CrossRef Medline
2. Stupp R, Hegi ME, Mason WP, et al; European Organisation for Research and Treatment of Cancer Brain Tumour and Radiation Oncology Groups; National Cancer Institute of Canada Clinical Trials Group. **Effects of radiotherapy with concomitant and adjuvant temozolomide versus radiotherapy alone on survival in glioblastoma in a randomised phase III study: 5-year analysis of the EORTC-NCIC trial.** *Lancet Oncol* 2009;10:459–66 CrossRef Medline
3. Tate MC, Aghi MK. **Biology of angiogenesis and invasion in glioma.** *Neurotherapeutics* 2009;6:447–57 CrossRef Medline
4. Smets T, Lawson TM, Grandin C, et al. **Immediate post-operative MRI suggestive of the site and timing of glioblastoma recurrence after gross total resection: a retrospective longitudinal preliminary study.** *Eur Radiol* 2013;23:1467–77 CrossRef Medline
5. Tofts PS, Brix G, Buckley DL, et al. **Estimating kinetic parameters from dynamic contrast-enhanced T(1)-weighted MRI of a diffusible tracer: standardized quantities and symbols.** *J Magn Reson Imaging* 1999;10:223–32 CrossRef Medline
6. Harrer JU, Parker GJ, Haroon HA, et al. **Comparative study of methods for determining vascular permeability and blood volume in human gliomas.** *J Magn Reson Imaging* 2004;20:748–57 CrossRef Medline
7. Jung SC, Yeom JA, Kim JH, et al. **Glioma: application of histogram analysis of pharmacokinetic parameters from T1-weighted dynamic contrast-enhanced MR imaging to tumor grading.** *AJNR Am J Neuroradiol* 2014;35:1103–10 CrossRef Medline
8. Yun TJ, Park CK, Kim TM, et al. **Glioblastoma treated with concurrent radiation therapy and temozolomide chemotherapy: differentiation of true progression from pseudoprogression with quantitative dynamic contrast-enhanced MR imaging.** *Radiology* 2015;274:830–40 CrossRef Medline
9. Yoo RE, Choi SH, Kim TM, et al. **Dynamic contrast-enhanced MR imaging in predicting progression of enhancing lesions persisting after standard treatment in patients with glioblastoma: a prospective study.** *Eur Radiol* 2017;27:3156–66 CrossRef Medline
10. Eidel O, Burth S, Neumann JO, et al. **Tumor infiltration in enhancing and non-enhancing parts of glioblastoma: a correlation with histopathology.** *PLoS One* 2017;12:e0169292 CrossRef Medline
11. Zahra MA, Tan LT, Priest AN, et al. **Semiquantitative and quantitative dynamic contrast-enhanced magnetic resonance imaging measurements predict radiation response in cervix cancer.** *Int J Radiat Oncol Biol Phys* 2009;74:766–73 CrossRef Medline
12. Kim H, Hartman YE, Zhai G, et al. **Dynamic contrast-enhanced MRI evaluates the early response of human head and neck tumor xenografts following anti-EMMPRIN therapy with cisplatin or irradiation.** *J Magn Reson Imaging* 2015;42:936–45 CrossRef Medline
13. Tao X, Wang L, Hui Z, et al. **DCE-MRI perfusion and permeability parameters as predictors of tumor response to CCRT in patients with locally advanced NSCLC.** *Sci Rep* 2016;6:35569 CrossRef Medline
14. Artzi M, Bokstein F, Blumenthal DT, et al. **Differentiation between vasogenic-edema versus tumor-infiltrative area in patients with glioblastoma during bevacizumab therapy: a longitudinal MRI study.** *Eur J Radiol* 2014;83:1250–56 CrossRef Medline
15. Bag AK, Cezayirli PC, Davenport JJ, et al. **Survival analysis in patients with newly diagnosed primary glioblastoma multiforme using pre- and post-treatment peritumoral perfusion imaging parameters.** *J Neurooncol* 2014;120:361–70 CrossRef Medline
16. Kim R, Choi SH, Yun TJ, et al. **Prognosis prediction of non-enhancing T2 high signal intensity lesions in patients with glioblastoma after standard treatment: application of dynamic contrast-enhanced MR imaging.** *Eur Radiol* 2017;27:1176–85 CrossRef Medline
17. Wen PY, Macdonald DR, Reardon DA, et al. **Updated response assessment criteria for high-grade gliomas: response assessment in neuro-oncology working group.** *J Clin Oncol* 2010;28:1963–72 CrossRef Medline
18. Pluim JP, Maintz JB, Viergever MA. **Mutual-information-based registration of medical images: a survey.** *IEEE Trans Med Imaging* 2003;22:986–1004 CrossRef Medline

19. Haacke EM, Filletti CL, Gattu R, et al. **New algorithm for quantifying vascular changes in dynamic contrast-enhanced MRI independent of absolute T1 values.** *Magn Reson Med* 2007;58:463–72 CrossRef Medline
20. Nam JG, Kang KM, Choi SH, et al. **Comparison between the prebolus T1 measurement and the fixed T1 value in dynamic contrast-enhanced MR imaging for the differentiation of true progression from pseudoprogession in glioblastoma treated with concurrent radiation therapy and temozolomide chemotherapy.** *AJNR Am J Neuroradiol* 2017;38:2243–50 CrossRef Medline
21. Tofts PS, Kermode AG. **Measurement of the blood-brain-barrier permeability and leakage space using dynamic MR imaging, I: fundamental-concepts.** *Magn Reson Med* 1991;17:357–67 CrossRef Medline
22. R Core Team. **R: A Language and Environment for Statistical Computing.** <https://www.r-project.org/>. Accessed May 4, 2019
23. Chang C, Hsieh MK, Chang WY, et al. **Determining the optimal number and location of cutoff points with application to data of cervical cancer.** *PLoS One* 2017;12:e0176231 CrossRef Medline
24. Gaspar LE, Fisher BJ, Macdonald DR, et al. **Supratentorial malignant glioma: patterns of recurrence and implications for external beam local treatment.** *Int J Radiat Oncol Biol Phys* 1992;24:55–57 CrossRef Medline
25. Jensen RL, Mumert ML, Gillespie DL, et al. **Preoperative dynamic contrast-enhanced MRI correlates with molecular markers of hypoxia and vascularity in specific areas of intratumoral microenvironment and is predictive of patient outcome.** *Neuro Oncol* 2014;16:280–91 CrossRef Medline
26. Ly KI, Vakulenko-Lagun B, Emblem KE, et al. **Probing tumor microenvironment in patients with newly diagnosed glioblastoma during chemoradiation and adjuvant temozolomide with functional MRI.** *Sci Rep* 2018;8:17062 CrossRef Medline
27. Koh TS, Bisdas S, Koh DM, et al. **Fundamentals of tracer kinetics for dynamic contrast-enhanced MRI.** *J Magn Reson Imaging* 2011;34:1262–76 CrossRef Medline
28. Bisdas S, Smrdel U, Bajrovic FF, et al. **Assessment of progression-free-survival in glioblastomas by intratreatment dynamic contrast-enhanced MRI.** *Clin Neuroradiol* 2016;26:39–45 CrossRef Medline
29. Weller M, Felsberg J, Hartmann C, et al. **Molecular predictors of progression-free and overall survival in patients with newly diagnosed glioblastoma: a prospective translational study of the German Glioma Network.** *J Clin Oncol* 2009;27:5743–50 CrossRef Medline
30. Gunjur A, Lau E, Taouk Y, et al. **Early post-treatment pseudo-progression amongst glioblastoma multiforme patients treated with radiotherapy and temozolomide: a retrospective analysis.** *J Med Imaging Radiat Oncol* 2011;55:603–10 CrossRef Medline
31. Balana C, Capellades J, Pineda E, et al. **Pseudoprogession as an adverse event of glioblastoma therapy.** *Cancer Med* 2017;6:2858–66 CrossRef Medline
32. Ballman KV, Buckner JC, Brown PD, et al. **The relationship between six-month progression-free survival and 12-month overall survival end points for Phase II trials in patients with glioblastoma multiforme.** *Neuro Oncol* 2007;9:29–38 CrossRef Medline

High-Resolution MRI for Evaluation of Ventriculostomy Tubes: Assessment of Positioning and Proximal Patency

 A.M. Blitz,  P.P. Huynh,  L.W. Bonham,  S.K. Gujar,  D.E. Sorte,  A. Moghekar,  M.G. Luciano, and  D. Rigamonti



ABSTRACT

BACKGROUND AND PURPOSE: Imaging evaluation of ventriculostomy tubes, despite the frequency of malfunction, has remained inadequate due to the absence of a systematic way of assessing the catheter itself. In this retrospective review, we assessed the utility of high-resolution 3D MR imaging techniques, including CISS and volumetric interpolated breath-hold examination sequences, in the evaluation of ventriculostomy catheters.

MATERIALS AND METHODS: We performed a retrospective review of 23 clinical MR imaging cases of shunted hydrocephalus spanning a 3-year period, all depicting ventriculostomy catheters. The MR imaging examinations included isotropic CISS and volumetric interpolated breath-hold examination sequences performed with and without contrast. These were independently evaluated by 2 neuroradiologists with respect to the catheter course, side hole position, relationship of the side holes to the ventricles, patency, and the presence or absence of intraluminal debris.

RESULTS: The catheter tip was best seen on isotropic CISS sequences reformatted in an oblique plane, and side holes were visualized as CSF signal defects along the catheter wall in 10/23 (43%) cases. The relationship of the catheter side holes to the ventricles was seen in 47% of cases and was best visualized on the coronal CISS sequences. Catheter patency was confirmed in 12/23 (52%) cases, while the other 48% were notable for T2 hypointense filling defects compatible with luminal obstruction. Enhancement of some of these filling defects on imaging is suggestive of choroid plexus ingrowth rather than debris.

CONCLUSIONS: High-resolution 3D MR imaging using isotropic CISS sequences allows systematic evaluation of catheter positioning, patency, and potential etiologic differentiation of filling defects when shunt dysfunction is suspected.

ABBREVIATION: VIBE = volumetric interpolated breath-hold examination

Ventriculostomy tube placement has been performed for CSF diversion since the early 1960s¹ and is one of the most commonly performed neurosurgical procedures, accounting for approximately \$1 billion in health care costs per year in the United States.² CSF shunt dysfunction is an extremely common

clinical problem, with failure rates as high as 40% in the first year and 50% after 2 years,³ with about 50% of patients requiring at least 1 shunt revision during their lifetime.^{4,5} Although some of these failures relate to infection and overdrainage (3.6% and 7.6%, respectively)⁶ and are readily diagnosed clinically, mechanical failures, despite apparent adequate anatomic placement, also contribute to the overall failure rate. When shunt failure is suspected clinically, the site of obstruction may be proximal to the shunt valve (or reservoir) or in the distal tubing.

Despite the prevalence of shunt failure, conventional imaging studies are often inadequate to provide a diagnosis if they find no signs of obstruction.⁷⁻¹⁰ The radiographic “shunt series” identifies a cause of shunt malfunction in <10% of pediatric cases and even less frequently in adults, suggesting the low diagnostic utility of this technique.^{11,12} CT, while more sensitive in assessing ventricular size and grossly determining intracranial catheter position, does raise concerns for radiation exposure, especially in pediatric patients,^{13,14} who may require repeat imaging during

Received March 5, 2019; accepted after revision October 2.

From the Department of Radiology (A.M.B.), University Hospitals, Case Western Reserve University; Departments of Radiology and Radiological Sciences (A.M.B., P.P.H., L.W.B., S.E.G.), Neurology (A.M.), and Neurosurgery (A.M.B., M.G.L., D.R.), Johns Hopkins Medical Institutions, Baltimore, Maryland; and Department of Radiology (D.E.S.), University of New Mexico, Albuquerque, New Mexico.

Drs Blitz and Rigamonti have previously (>24 months prior) received research funding from Aesculab (Dr Rigamonti was the Principal Investigator). Dr Blitz receives research support (unrelated) via AVERT, FAIRN U01DC013778 (Newman-Toker is the Principal Investigator).

Please address correspondence to Ari M. Blitz, MD, University Hospitals, Case Western Reserve University, Diagnostic Radiology, Division of Neuroradiology, 11100 Euclid Ave., BSH 5056, Cleveland, OH 44106; e-mail: ari.blitz@uhhospitals.org



Indicates article with supplemental on-line video.

<http://dx.doi.org/10.3174/ajnr.A6320>

their lifetimes. Nuclear medicine radionuclide studies can also be used but require shunt access and entail radiation exposure as well.

MR imaging is not typically performed in the evaluation of shunted hydrocephalus in children, given its lengthy imaging time and potential need for sedation.¹⁵ Moreover, even when MR imaging is performed in a patient with shunted hydrocephalus,

the catheter patency, side hole position, and entire intracranial course may not be systematically evaluated by conventional sequences.

MR phase-contrast imaging can be performed to determine shunt flow,¹⁶⁻¹⁹ but it is technically challenging and does not define the anatomic position of the catheter or allow assessment of the catheter lumen itself when flow is not detected. High-resolution techniques, including CISS and volumetric interpolated breath-hold examination (VIBE) sequences, are used for evaluation of small structures such as cranial nerves, given their high spatial resolution.²⁰⁻²³ These techniques can also be used in the MR imaging of hydrocephalus.^{24,25}

At our center, dedicated imaging protocols for the evaluation of patients with hydrocephalus include high-resolution imaging. Such imaging is typically through the cerebral aqueduct, though imaging tailored to the evaluation of the ventriculostomy tubes is also available to the clinician. In the current study, we retrospectively analyzed the position and patency of ventriculostomy catheters on clinical MR imaging studies. We reviewed clinical MR imaging examinations performed for hydrocephalus to determine the value of MR imaging in the assessment of the ventriculostomy catheter itself. We hypothesized that detailed information about the ventriculostomy catheter could be gleaned from high-resolution, specialized MR imaging techniques.

MATERIALS AND METHODS

Approval for this study was obtained from the Johns Hopkins Institutional Review Board. A retrospective sample of convenience, including all available clinical cases spanning a 3-year period at our institution, was identified. Data were collected in adherence with the applicable Health Insurance Portability and

Accountability Act regulations. Twenty-three clinical MR imaging examinations were selected from clinical cases featuring ventriculostomy catheters due to concern for hydrocephalus or shunt complications, following placement in a variety of disorders including hydrocephalus and pseudotumor cerebri. Baseline patient data are shown in the Table.

The MR imaging examinations included routine brain imaging sequences and high-resolution isotropic CISS and VIBE sequences with and without contrast and were typically performed on a 3T Trio or Verio scanner (Siemens, Erlangen, Germany). Cases were excluded if CISS and VIBE sequences were not performed. A typical examination included standard sequences (sagittal MPRAGE/T1, axial T2, axial FLAIR, postcontrast T1) plus isotropic CISS sequences (TR, 5.88 ms; TE, 2.7 ms; FOV, 16 cm; matrix size, 320 × 320) without or before and after intravenous

Baseline patient demographic data

Demographic	Statistic (No.) (%)
Age (mean) (range) (yr)	47.9 (32–74)
Sex	
Male	10 (43.5)
Female	13 (56.5)
Indication for VP shunting	
Obstructive hydrocephalus	11 (47.8)
Congenital hydrocephalus	7 (30.4)
Communicating hydrocephalus	3 (13.0)
Pseudotumor cerebri	2 (8.7)
Indication for imaging	
Concern for shunt malfunction	11 (47.8)
Alarming neurologic symptoms	6 (26.1)
Routine follow-up	6 (26.1)
Type or brand of shunt (per chart review)	
Programmable shunts	8 (34.7)
Strata ^a	6 (26.1)
Unspecified	2 (8.7)
Nonprogrammable shunts	7 (30.4)
Codman	1 (4.3)
Raimondi	1 (4.3)
Unspecified	5 (21.7)
Unspecified/no information found	8 (34.7)

Note:—VP indicates ventriculoperitoneal.

^a Medtronic, Minneapolis, Minnesota.

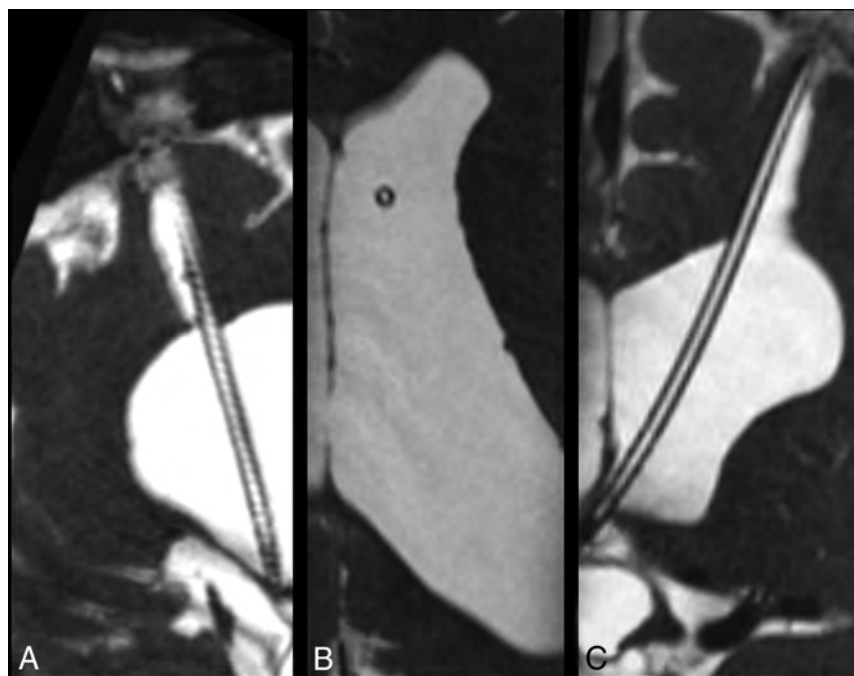


FIG 1. 3D high-resolution isotropic CISS MR imaging sequence acquired in the sagittal plane demonstrates CSF signal throughout a patent ventriculostomy tube. Images were reconstructed post hoc in the sagittal oblique (A), axial (B), and coronal (C) planes.

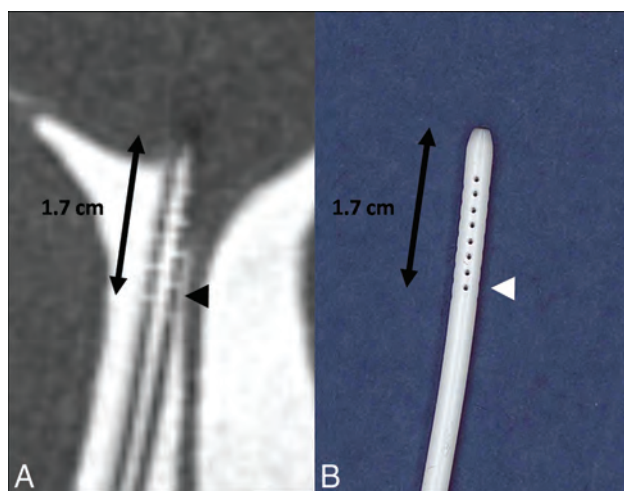


FIG 2. A, Isotropic CISS demonstrates a right-parietal-approach catheter with the tip extending just beyond the frontal horn of the right lateral ventricle. The side holes are seen as fluid-filled defects in the proximal aspect of the catheter extending to 1.7 cm from the tip (arrowhead). B, A photograph of a corresponding ventriculostomy catheter sample depicts the same relationship of side holes to the tip of the catheter.



FIG 3. Coronal isotropic CISS demonstrates the tip of the ventriculostomy catheter passing beyond the left lateral ventricle. The lumen is fluid-filled.

gabdobenate dimeglumine (MultiHance; Bracco Diagnostics, Princeton, New Jersey; 0.1 mmol/kg) or gadopentetate dimeglumine (Magnevist; Bayer HealthCare Pharmaceuticals, Wayne, New Jersey; 0.1 mg/kg), and isotropic T1 VIBE out-of-phase sequences with fat saturation after intravenous contrast (TR, 11.6 ms; TE, 4.3 ms; FOV, 16.9 × 21 cm; matrix size, 288 × 232). The voxel size was typically 0.5 mm except in 2 cases in which the voxel sizes were 0.6 and 0.7 mm. Seven of 23 examinations were requested specifically for ventriculostomy tube evaluation and included dedicated phase-contrast imaging through the catheter lumen (TR, 69.6 ms; TE, 10.8 ms; FOV,

8 cm; matrix, 320 × 256) in addition to high-resolution imaging along the intracranial course of the catheter. The visualized portion of the catheter was assessed on the remainder of the examinations. With these imaging modalities it is possible to view, when captured, the side hole location, tip location, and catheter patency as well as the content of the catheter lumen.

Two neuroradiologists (1 fellow [D.E.S.] and 1 Certificate of Added Qualification–certified neuroradiologist [A.M.B.] with 10 years of experience) retrospectively evaluated the MR imaging examinations with respect to 3 factors: proximal (tip) position/catheter course, side hole position, and the relationship of the side holes to the ventricular lumen; the catheter reservoir if visible, and the presence or absence of debris in the catheter lumen. The visibility of the side holes was rated as 0 for nonvisualization, 1 for partial visualization, and 2 for complete visualization. The neuroradiologists evaluated the patency of the catheter lumina. Patency was defined as fluid filling the catheter without obstruction. Additionally, the presence or absence of internal debris was documented. Each examination was reformatted in various obliquities to best demonstrate the catheter position. Disagreements were resolved by consensus.

RESULTS

Catheter Visualization

The catheter tip was visualized in all selected patients. The relationship of the catheter tip to anatomic structures was best visualized on isotropic CISS sequences reformatted in an oblique plane (Fig 1).

Catheter Position: Side Holes

Despite their small size, the side holes of the catheter were visualized completely (a score of 2) in 9/23 cases (39.1%). The side holes are seen as CSF signal defects along the proximal portion of the ventriculostomy catheter, extending 1.7 cm from the tip (Fig 2). The side holes of the catheter were partially visualized (a score of 1) in 1/23 cases (4.3%). In both the completely and partially visualized side holes, their relationship to the ventricles was well seen (47% of cases). When the side holes were not visualized this was usually due to the proximal portion of the catheter not being included in the FOV or, in 1 case, due to the larger voxel size.

Of the 7 cases in which a catheter evaluation was specifically requested, 4 (57.1%) were found to have radiographic findings concerning for malfunction, which was confirmed in the operative note. Of the other 3 cases in which tube evaluation was requested, 2 were for routine monitoring, whereas 1 showed no evidence of shunt malfunction. Catheter side holes were visualized in 4 of the 7 cases.

Catheter Position: Relation to the Ventricles

The relationship of the proximal catheter side holes and ventricular structures was subjectively best visualized on coronal CISS images (Fig 3). Catheter side holes were often seen in the frontal horns of the lateral ventricles. The relationship of the catheter tip to the foramen of Monro, septum pellucidum, and corpus callosum was depicted on coronal CISS images (Fig 4).

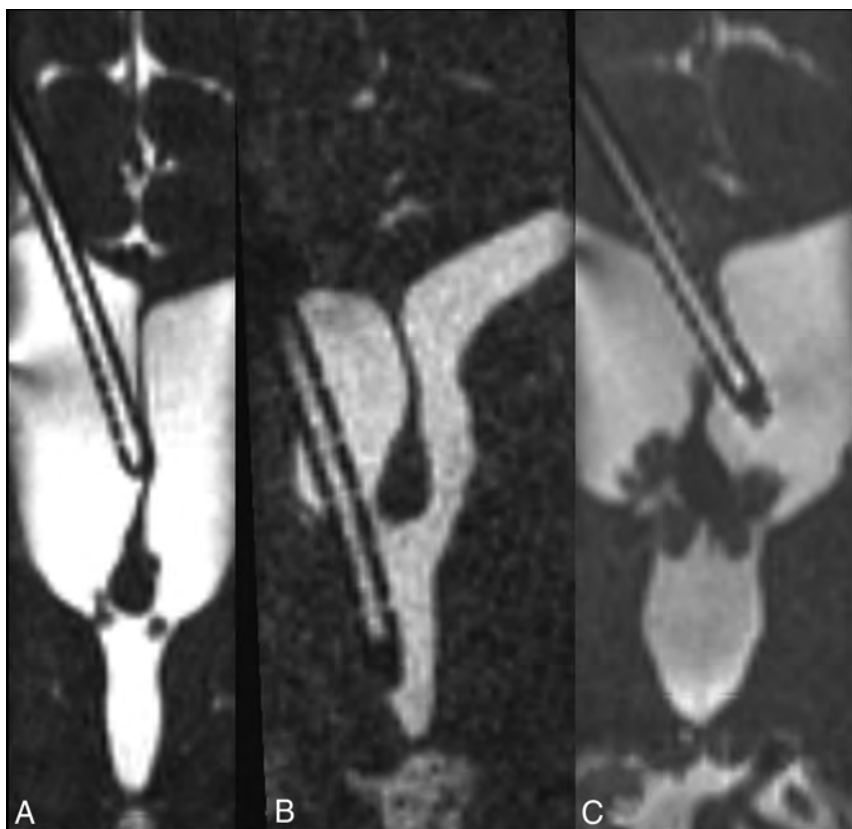


FIG 4. Coronal CISS images from 3 patients demonstrate the position of the catheter tip with precision with respect to the surrounding structures. A, The ventriculostomy catheter abuts the septum pellucidum. B, The ventriculostomy catheter traverses the foramen of Monro to terminate in the third ventricle. C, The ventriculostomy catheter pierces the septum pellucidum, crossing the midline, in a third patient.

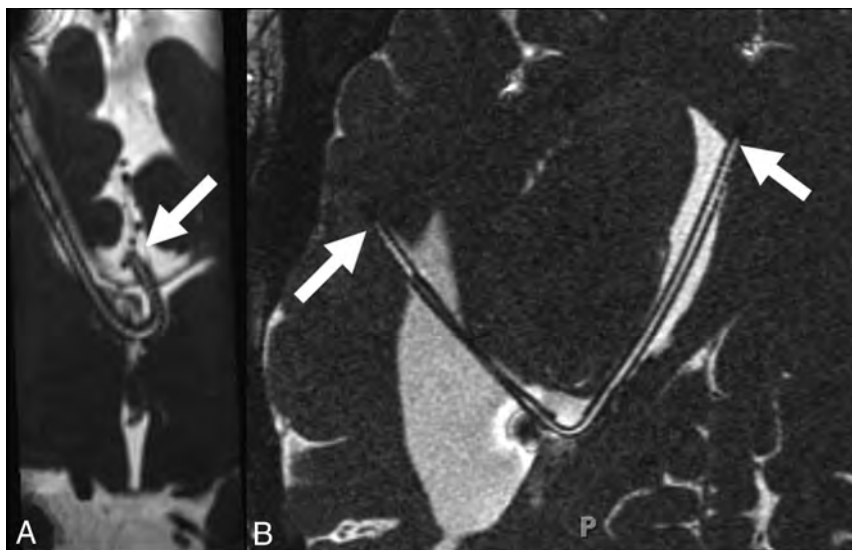


FIG 5. A, Coronal CISS in a patient with callosal dysgenesis demonstrates the curvilinear path of the ventriculostomy catheter with the tip in the interhemispheric fissure. B, Axial oblique CISS in a patient with previous obstruction at the posterior body of the lateral ventricle demonstrates tubing extending from the right frontal horn (*left-pointing arrow*) into the temporal horn of the lateral ventricle to terminate in the periventricular region (*right-pointing arrow*).

Catheter Configurations

Some catheters had unusual configurations and required additional post-processing to be adequately visualized on MR imaging (Fig 5). Reconstruction of isotropically acquired images at the workstation by the radiologist allowed depiction of most or the entirety of the intracranial portion of the catheter course. The catheter reservoir was also seen in 14/23 patients (60.9%). The detailed internal structure of the reservoir and its connection to the catheter were also seen on high-resolution imaging (Fig 6).

Catheter Patency: Presence of Debris or Choroid Plexus Ingrowth

The catheter lumina were determined to be patent in 12/23 ventriculostomy tubes (52%) by identification of CSF signal intensity throughout the lumen. The remaining catheters (11/23, 48%) demonstrated T2-hypointense filling defects within the lumen, compatible with internal obstruction, which varied widely in volume and distribution. Of these filling defects, postcontrast CISS and MPRAGE imaging allowed differentiation between debris, which showed no enhancement, and choroid plexus ingrowth, which demonstrated enhancement (Figs 7 and 8).

Global Characterization of Shunt Function

To better evaluate the sensitivity of imaging for shunt dysfunction, we reviewed each patient's operative note (if available) after shunt insertion. Of the 23 cases, 11 went to the operating room and were found to have nonfunctioning shunts. Notably, of the 11 cases clinically suspected of having shunt malfunction, 8 had radiographic findings supportive of the diagnoses, with the other 3 cases were found to have hydrocephalus despite a patent shunt.

DISCUSSION

To our knowledge, high-resolution MR imaging studies have never been reported as a tool to specifically evaluate the ventriculostomy catheter. This study demonstrates that high-resolution MR imaging can visualize, with

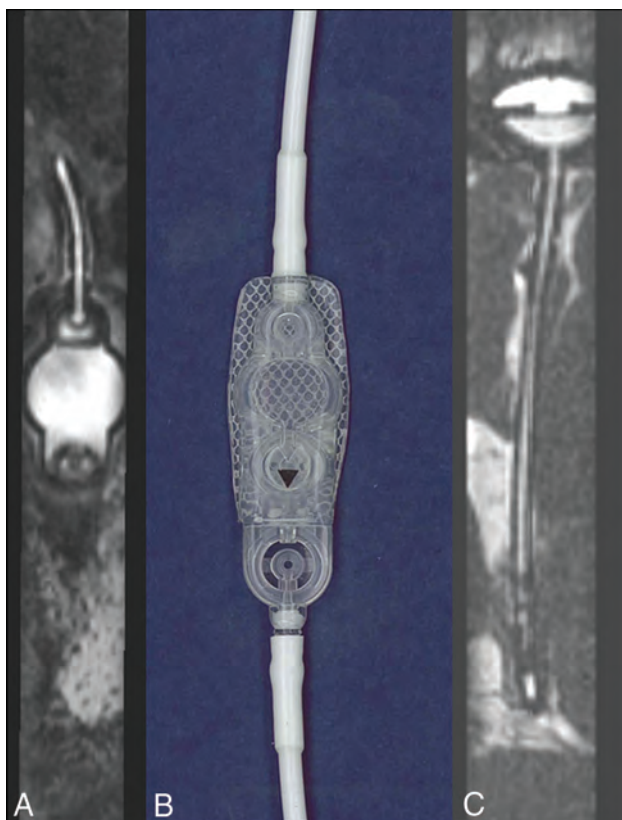


FIG 6. The detailed structure of the ventriculostomy tube and shunt reservoir can be evaluated in detail, particularly when the device does not contain metallic components. A, Sagittal oblique CISS through the extracranial component of the shunt device demonstrates the fluid-filled shunt reservoir corresponding to the sample (B) provided by the manufacturer Strata, Medtronic (Minneapolis, Minnesota). In another patient, the intracranial extent of the ventriculostomy tubing is seen extending to the shunt reservoir, of which the internal structures are visible.

precision, the placement of implanted tubes and can sometimes demonstrate the location of the side holes, potentially of use when it is not clear whether the tube is in actuality draining the intended cavity. From this retrospective review, we found that using high-resolution isotropic CISS sequences in the MR imaging assessment of hydrocephalus allowed visualization of the catheter tip, catheter course, side holes, the relationship of the side holes to the ventricles, and the presence or absence of debris within the lumen. The catheter course, though sometimes unusual (Fig 5), was viewed using post hoc reconstruction of isotropically acquired images in various obliquities. Additionally, we report that filling defects within the proximal catheter may be visualized and potentially characterized with high-resolution MR imaging when shunting dysfunction is suspected or when revision is contemplated.

One of the primary reasons for long-term shunt failure has been reported to be choroid plexus ingrowth. At the time of shunt removal, massive intraventricular hemorrhage can occur due to traction of the ingrown choroid plexus.²⁶ Chambi and Hendrick²⁷ first described a neurosurgical technique for shunt revision consisting of inserting a metal cannula into the ventriculostomy tube followed by unipolar diathermy to the distal end, believed to

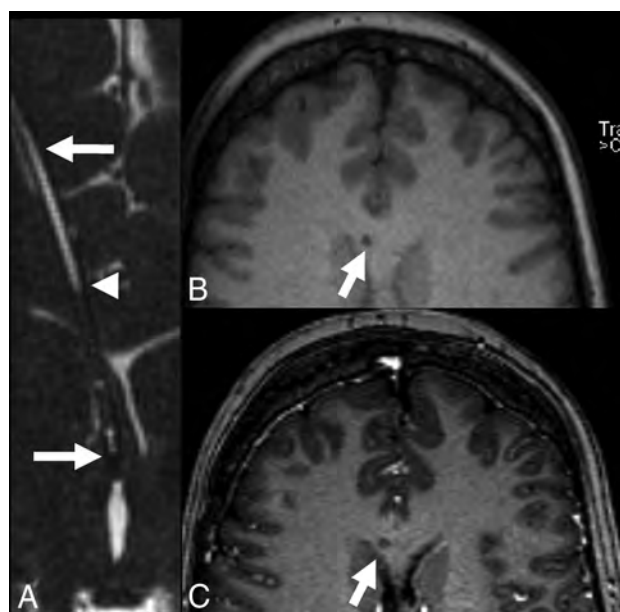


FIG 7. Shunt failure. While this case does not feature hydrocephalus, patients may have ventriculoperitoneal shunt placement for a variety of indications, including pseudotumor cerebri, where ventricles are narrowed rather than dilated, as well as cases involving multiple catheters, in which the development of obstructive hydrocephalus is impeded even if 1 of the shunts is partially occluded by debris. A, Axial oblique reconstructed CISS demonstrates the tip of the ventriculostomy tube (right-pointing arrow) extending peripherally through the frontal lobe (left-pointing arrow). CSF is not seen in the proximal catheter (compare with Fig 3) to the point marked with an arrowhead. B, Axial precontrast MPRAGE demonstrates the catheter extending through the corpus callosum. C, Axial post-contrast MPRAGE demonstrates no change in intensity, suggesting debris.

lyse adhesions to the ventricular ependyma or choroid plexus. Multiple variations of this technique have subsequently been described. However, this technique is not without its complications, as described by Handler,²⁸ because charring of the catheter (with potential injury to the adjoining brain) has been reported.

Prior techniques for imaging evaluation of ventriculostomy tube patency have largely come from the field of nuclear medicine (eg, a tracer is injected followed by serial imaging over the site of injection and along the expected track of the catheter to document the flow of the radiotracer). In some cases, the task of evaluation of tube patency is further complicated by lack of accessibility. This is the case with tubes that drain directly from 1 portion of the ventricular system or subarachnoid space such as ventriculo-ventricular catheters (Fig 5). In such cases, assessment of luminal patency by MR imaging may afford the only noninvasive means of postoperative results if symptoms persist or recur. Furthermore, contrast-enhanced imaging may help differentiate debris and choroid plexus ingrowth in the setting of contemplated removal of a ventriculostomy tube, potentially allowing appropriate surgical planning and application of preemptive electrocautery through the catheter lumen.

Delayed intracranial hemorrhage at the site of catheter placement is an uncommon-but-severe complication of

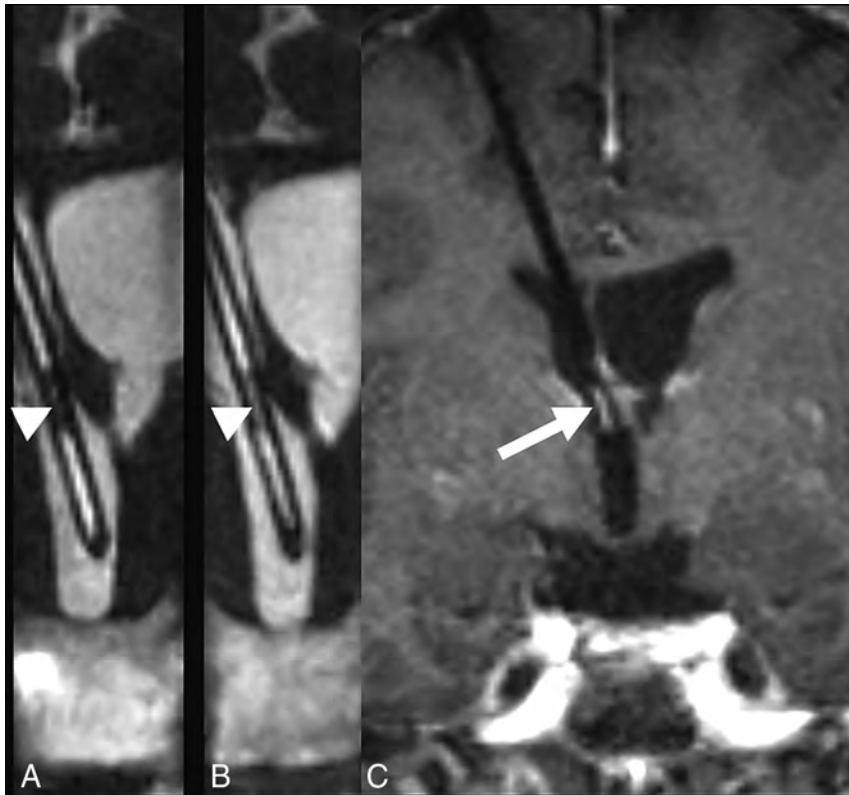


FIG 8. The ingrowth of the choroid plexus into the shunt catheter may significantly increase the risk of hemorrhage during shunt removal. *A*, Precontrast coronal CISS demonstrates a filling defect within the ventriculostomy tube. *B*, Postcontrast CISS demonstrates an increase in intensity due to enhancement of material filling the midportion of the catheter, suggesting choroid plexus ingrowth. *C*, Coronal postcontrast MPRAGE demonstrates corresponding hyperintensity, though the relationship to the catheter lumen is not as clear.

ventriculoperitoneal shunt placement and is associated with predisposing factors, including degenerative vascular change and puncture of the choroid plexus.²⁹ Similarly, intracranial hemorrhage and intraventricular hemorrhage have long been documented as potential complications of shunt removal and are commonly attributed to the disruption of the choroid plexus that has grown around and into the catheter.^{30–33} A retrospective review of 35 pediatric patients with a total of 52 shunt revisions found that 25% of the revisions resulted in intraventricular hemorrhage, though only 2% of such revisions were deemed clinically relevant, resulting in >5 mL of blood.³⁴ Given the risk of intraventricular hemorrhage and the time to subsequent shunt revision,^{31,34} it may be helpful for surgeons to visualize the presence of choroid plexus ingrowth to assess the risk of hemorrhage following shunt removal and to guide surgery.

We acknowledge that this study has limitations. Given the small sample size of 23 cases, larger studies are needed to verify and generalize our findings. With a limited sample size and heterogeneous comparison images (a mix of alternative MR imaging protocols and CT), calculation of sensitivities and specificities for detecting features such as the catheter lumen or tip is of limited clinical and scientific value. Additionally, in this initial retrospective review, we analyzed data available without respect to

manufacturer, tube caliber, or size of the side holes. The side hole position varies by catheter type, and not all devices were placed at our hospital, making inference of the overall position by side hole positioning difficult. It is possible that future prospective work on this topic that controls for these shunt characteristics may allow clarification of which factors, including side hole size and catheter position, are most important for visualization.

Furthermore, our initial work on the nature of filling defects in the catheter lumina is limited because histopathologic proof is not available for our cases of explanted catheters. Histologic confirmation is not easily achievable because withdrawing such catheters carries a substantial risk of intracranial hemorrhage. Thus, neurosurgeons often cauterize off the catheter lumen when choroid plexus ingrowth is suspected. If high-resolution MR imaging sequences can help differentiate choroid plexus ingrowth from intraluminal debris, we believe these findings can help guide the neurosurgeon's decisions in shunt-revision procedures. If this proves true, histologic characterization of intraluminal debris will be possible, but the ability to characterize choroid plexus ingrowth

will likely be precluded by the routine application of cautery to prevent intracranial hemorrhage. Finally, the clinical significance of intraluminal debris remains unknown. We suspect that there is a continuum of luminal obstruction that results in a spectrum of clinical manifestations for the patient, but this hypothesis will require further research in larger cohorts to better study its potential clinical consequences.

Future research should include determination of the sensitivity and specificity for these techniques in detecting the sites of clinical shunt malfunction. Additionally, it would be worthwhile to compare MR imaging results and operative findings to better evaluate the utility of this technique in differentiating debris and choroid plexus ingrowth. Incorporating these high-resolution sequences has the potential to aid in neurosurgical planning. Because the treatment of catheter obstruction or malpositioning is surgical revision, greater diagnostic accuracy in imaging evaluation can guide the surgeon in evaluating the best approach. Whether high-resolution visualization of the catheter tip proves to be of additional value compared with a lower resolution technique such as CT remains to be determined. Nevertheless, these techniques could be particularly useful in the setting of a clinical presentation of shunt dysfunction with multiple intracranial catheters. As shown in the On-line Video, high-resolution MR imaging sequences provide additional detail beyond that of standard head CT, which may equip both radiologists and their

clinical colleagues with useful information when assessing shunt function.

CONCLUSIONS

High-resolution 3D MR imaging using isotropic CISS sequences allows systematic evaluation of ventriculoperitoneal catheter positioning and patency and differentiation of filling defects when shunt dysfunction is suspected. Systematic evaluation of the catheter, in turn, may allow improved diagnosis of shunt failure and, potentially, assessment for hemorrhage risk following shunt removal, thereby guiding surgical effort.

REFERENCES

- Aschoff A, Kremer P, Hashemi B, et al. **The scientific history of hydrocephalus and its treatment.** *Neurosurg Rev* 1999;22:67–93; discussion 94–95 CrossRef Medline
- Patwardhan RV, Nanda A. **Implanted ventricular shunts in the United States: the billion-dollar-a-year cost of hydrocephalus treatment.** *Neurosurgery* 2005;56:139–44; discussion 144–45 CrossRef Medline
- Browd SR, Ragel BT, Gottfried ON, et al. **Failure of cerebrospinal fluid shunts, Part I: obstruction and mechanical failure.** *Pediatr Neurol* 2006;34:83–92 CrossRef Medline
- Lehnert BE, Rahbar H, Relyea-Chew A, et al. **Detection of ventricular shunt malfunction in the ED: relative utility of radiography, CT, and nuclear imaging.** *Emerg Radiol* 2011;18:299–305 CrossRef Medline
- Paulsen AH, Lunder T, Lindegaard KF. **Twenty-year outcome in young adults with childhood hydrocephalus: assessment of surgical outcome, work participation, and health-related quality of life.** *J Neurosurg Pediatr* 2010;6:527–35 CrossRef Medline
- Reddy GK. **Ventriculoperitoneal shunt surgery and the incidence of shunt revision in adult patients with hemorrhage-related hydrocephalus.** *Clin Neurol Neurosurg* 2012;114:1211–16 CrossRef Medline
- Goeser CD, McLeary MS, Young LW. **Diagnostic imaging of ventriculoperitoneal shunt malfunctions and complications.** *Radiographics* 1998;18:635–51 CrossRef Medline
- Madsen MA. **Emergency department management of ventriculoperitoneal cerebrospinal fluid shunts.** *Ann Emerg Med* 1986;15:1330–43 CrossRef Medline
- McNatt SA, Kim A, Hohuan D, et al. **Pediatric shunt malfunction without ventricular dilatation.** *Pediatr Neurosurg* 2008;44:128–32 CrossRef Medline
- Zhang H, Peng J, Hao X, et al. **A simple and reliable method for the diagnosis of ventriculoperitoneal shunt malfunction.** *World Neurosurg* 2017;103:355–59 CrossRef Medline
- Desai KR, Babb JS, Amodio JB. **The utility of the plain radiograph “shunt series” in the evaluation of suspected ventriculoperitoneal shunt failure in pediatric patients.** *Pediatr Radiol* 2007;37:452–56 CrossRef Medline
- Griffey RT, Ledbetter S, Khorasani R. **Yield and utility of radiographic “shunt series” in the evaluation of ventriculo-peritoneal shunt malfunction in adult emergency patients.** *Emerg Radiol* 2007;13:307–11 CrossRef Medline
- Berrington de Gonzalez A, Mahesh M, Kim KP, et al. **Projected cancer risks from computed tomographic scans performed in the United States in 2007.** *Arch Intern Med* 2009;169:2071–77 CrossRef Medline
- Pearce MS, Salotti JA, Little MP, et al. **Radiation exposure from CT scans in childhood and subsequent risk of leukaemia and brain tumours: a retrospective cohort study.** *Lancet* 2012;380:499–505 CrossRef
- Boyle TP, Paldino MJ, Kimia AA, et al. **Comparison of rapid cranial MRI to CT for ventricular shunt malfunction.** *Pediatrics* 2014;134:e47–54 CrossRef Medline
- Algin O, Hakyemez B, Parlak M. **The efficiency of PC-MRI in diagnosis of normal pressure hydrocephalus and prediction of shunt response.** *Acad Radiol* 2010;17:181–87 CrossRef Medline
- Dixon GR, Friedman JA, Luetmer PH, et al. **Use of cerebrospinal fluid flow rates measured by phase-contrast MR to predict outcome of ventriculoperitoneal shunting for idiopathic normal-pressure hydrocephalus.** *Mayo Clin Proc* 2002;77:509–14 CrossRef Medline
- Alperin N, Lee S, Macedo L, et al. **Direct visualization and quantitation of CSF flow in shunts.** *Proc Intl Soc Mag Reson Med* 2010;18
- Zhang H, Zhang J, Peng J, et al. **The diagnosis of ventriculoperitoneal shunt malfunction by using phase-contrast cine magnetic resonance imaging.** *J Clin Neurosci* 2019;64:141–44 CrossRef Medline
- Algin O, Hakyemez B, Parlak M. **Phase-contrast MRI and 3D-CISS versus contrast-enhanced MR cisternography for the detection of spontaneous third ventriculostomy.** *J Neuroradiol* 2011;38:98–104 CrossRef Medline
- Casselman JW, Kuhweide R, Ampe W, et al. **Pathology of the membranous labyrinth: comparison of T1- and T2-weighted and gadolinium-enhanced spin-echo and 3DFT-CISS imaging.** *AJNR Am J Neuroradiol* 1993;14:59–69 Medline
- Yousry I, Camelio S, Schmid U, et al. **Visualization of cranial nerves I–XII: value of 3D CISS and T2-weighted FSE sequences.** *Eur Radiol* 2000;10:1061–67 CrossRef Medline
- Blitz AM, Choudhri AF, Chonka ZD, et al. **Anatomic considerations, nomenclature, and advanced cross-sectional imaging techniques for visualization of the cranial nerve segments by MR imaging.** *Neuroimaging Clin* 2014;24:1–15 CrossRef Medline
- Doll A, Christmann D, Kehrli P, et al. **Contribution of 3D CISS MRI for pre- and post-therapeutic monitoring of obstructive hydrocephalus.** *J Neuroradiol* 2000;27:218–225 Medline
- Elkafrawy F, Reda I, Elsarafy M, et al. **Three-dimensional constructive interference in steady state sequences and phase-contrast magnetic resonance imaging of arrested hydrocephalus.** *World Neurosurg* 2017;98:296–302 CrossRef Medline
- Whitfield PC, Guazzo EP, Pickard JD. **Safe removal of retained ventricular catheters using intraluminal choroid plexus coagulation.** *J Neurosurg* 1995;83:1101–02 CrossRef Medline
- Chambi I, Hendrick EB. **A technique for removal of an adherent ventricular catheter.** *Pediatr Neurosci* 1988;14:216–17 CrossRef Medline
- Handler MH. **A complication in removing a retained ventricular catheter using electrocautery.** *Pediatr Neurosurg* 1996;25:276 CrossRef Medline
- Mavridis IN, Mitropoulos A, Mantas C, et al. **Delayed intraventricular hemorrhage following a ventriculoperitoneal shunt placement: exploring the surgical anatomy of a rare complication.** *Case Rep Med* 2017;2017:3953248 CrossRef Medline
- Becker DP, Nulsen FE. **Control of hydrocephalus by valve-regulated venous shunt: avoidance of complications in prolonged shunt maintenance.** *J Neurosurg* 1968;28:215–26 CrossRef Medline
- Brownlee RD, Dold ON, Myles ST. **Intraventricular hemorrhage complicating ventricular catheter revision: incidence and effect on shunt survival.** *Pediatr Neurosurg* 1995;22:315–20 CrossRef Medline
- Collins P, Hockley AD, Woollam DH. **Surface ultrastructure of tissues occluding ventricular catheters.** *J Neurosurg* 1978;48:609–13 CrossRef Medline
- Singh D, Saxena A, Jagetia A, et al. **Endoscopic observations of blocked ventriculoperitoneal (VP) shunt: a step toward better understanding of shunt obstruction and its removal.** *Br J Neurosurg* 2012;26:747–53 CrossRef Medline
- Calayag M, Paul AR, Adamo MA. **Intraventricular hemorrhage after ventriculoperitoneal shunt revision: a retrospective review.** *PED* 2015;16:42–45 CrossRef Medline

Prediction of Hemorrhage after Successful Recanalization in Patients with Acute Ischemic Stroke: Improved Risk Stratification Using Dual-Energy CT Parenchymal Iodine Concentration Ratio Relative to the Superior Sagittal Sinus

 D. Byrne,  J.P. Walsh,  H. Schmiedeskamp,  F. Settecasse,  M.K.S. Heran,  B. Niu,  A.K. Salmeen,  B. Rohr,  T.S. Field,  N. Murray, and  A. Rohr



ABSTRACT

BACKGROUND AND PURPOSE: Brain parenchymal hyperdensity on postthrombectomy CT in patients with acute stroke can be due to hemorrhage and/or contrast staining. We aimed to determine whether iodine concentration within contrast-stained parenchyma compared with an internal reference in the superior sagittal sinus on dual-energy CT could predict subsequent intracerebral hemorrhage.

MATERIALS AND METHODS: Seventy-one patients with small infarct cores (ASPECTS ≥ 7) and good endovascular recanalization (modified TIC1 2b or 3) for anterior circulation large-vessel occlusion were included. Brain parenchymal iodine concentration as per dual-energy CT and the percentage of contrast staining relative to the superior sagittal sinus were recorded and correlated with the development of intracerebral hemorrhage using Mann-Whitney *U* and Fisher exact tests.

RESULTS: Forty-three of 71 patients had parenchymal hyperdensity on initial dual-energy CT. The median relative iodine concentration compared with the superior sagittal sinus was significantly higher in those with subsequent intracerebral hemorrhage (137.9% versus 109.2%, $P = .007$). By means of receiver operating characteristic analysis, a cutoff value of 100% (iodine concentration relative to the superior sagittal sinus) enabled identification of patients going on to develop intracerebral hemorrhage with 94.75% sensitivity, 43.4% specificity, and a likelihood ratio of 1.71.

CONCLUSIONS: Within our cohort of patients, the relative percentage of iodine concentration at dual-energy CT compared with the superior sagittal sinus was a reliable predictor of intracerebral hemorrhage development and may be a useful imaging biomarker for risk stratification after endovascular treatment.

ABBREVIATIONS: DECT = dual-energy CT; ICH = intracerebral hemorrhage; SSS = superior sagittal sinus


Despite advances in patient selection for reperfusion therapy for acute ischemic stroke, intracerebral hemorrhage (ICH) remains a serious potential complication.^{1,2} Clinical outcome post-thrombectomy is multifactorial. Despite good preprocedural ASPECTS, successful reperfusion post-thrombectomy does not

always predict good clinical outcome. Immediately following endovascular treatment, parenchymal high density on NCCT is often seen, caused by disruption of the blood-brain barrier with secondary contrast staining³ and/or hemorrhage.⁴ It is difficult to differentiate contrast staining from hemorrhage at single-kilovolt (peak) energy CT because both abnormalities appear hyperdense.^{5,6} Dual-energy CT (DECT) has been shown effective in accurately differentiating parenchymal hemorrhage from contrast staining.^{3,7-9} The presence of parenchymal contrast staining on DECT immediately post-thrombectomy is associated with the development of ICH.^{3,7} A retrospective study by Bonatti et al⁷ of 85 patients undergoing mechanical thrombectomy showed that the presence of parenchymal hyperdensity with a maximum absolute iodine concentration of >1.35 mg/mL may identify patients developing intracerebral hemorrhage with 100% sensitivity and 67.6% specificity. Absolute iodine concentration, however, varies with patient height, weight, cardiac output, and renal function, as

Received August 14, 2019; accepted after revision October 8.

From the Division of Neuroradiology (D.B., F.S., M.K.S.H., A.R.), Department of Emergency Radiology (J.P.W., N.M.), and Vancouver Imaging (B.N.), Vancouver General Hospital, Vancouver, British Columbia, Canada; Siemens Medical Solutions USA (H.S.), Malvern, Pennsylvania; Division of Neurology (A.K.S., T.S.F.), Department of Medicine, Vancouver Stroke Program, Brain Research Center, University of British Columbia, Vancouver, British Columbia, Canada; and University of British Columbia (D.B., J.P.W., F.S., M.K.S.H., B.R., T.S.F., N.M., A.R.), Vancouver, British Columbia, Canada.

Please address correspondence to Danielle Byrne, FFR (RCSI), Department of Neuroradiology, 899 W 12th Ave, Vancouver, BC V5Z 1M9, Canada; e-mail: dbyrne.radiology@gmail.com

 Indicates article with supplemental on-line table.

<http://dx.doi.org/10.3174/ajnr.A6345>

well as contrast medium factors, including concentration and volume of contrast administered and scan technique.¹⁰ A recent study demonstrated that normalization of iodine quantification to the aorta resulted in better separation of vascular and nonvascular renal lesions.¹¹ We hypothesized that normalization of iodine concentration of brain parenchymal contrast staining on postthrombectomy DECT using the superior sagittal sinus (SSS) would reduce the variability in iodine quantification related to systematic differences in the timing/volume of contrast medium injection, as well as procedural and patient factors,^{12,13} and improve prediction of the presence of ICH on follow-up CT compared with absolute iodine concentration.

Previous studies investigating the value of brain parenchymal contrast staining on postthrombectomy CT to predict subsequent ICH have focused on relatively heterogeneous cohorts of patients with varying degrees of infarction and reperfusion.^{7,14-17} It is known that patients with larger infarct cores are more likely to develop ICH.^{18,19} In patients with small infarct cores and good reperfusion, development of ICH may be less predictable. We therefore wanted to examine a more homogeneous cohort of patients and included only patients with small preprocedural infarcts (ASPECTS ≥ 7) and good endovascular recanalization (modified TICI score 2b or 3) to identify an imaging biomarker for ICH risk stratification that could aid antithrombotic and blood pressure strategy in the early posttreatment period in patients in whom development of ICH may otherwise be unexpected.²⁰

MATERIALS AND METHODS

Patient Population

Approval was obtained from the institutional review board at Vancouver General Hospital, and the need for informed consent was waived for this retrospective study. Consecutive thrombectomy cases, scanned for anterior circulation large-vessel (distal ICA, MCA, and anterior cerebral artery) occlusion between January 2016 and June 2018 were reviewed. Inclusion criteria comprised endovascular treatment for anterior circulation large-vessel occlusion, preprocedural imaging with NCCT and CTA, small preprocedural infarct volume (ASPECTS ≥ 7), good endovascular recanalization (modified TICI 2b or 3), DECT performed within 1 hour after thrombectomy, and follow-up NCCT performed at 24 hours post-thrombectomy or earlier according to clinical necessity. Exclusion criteria were concomitant proximal ICA/common carotid artery occlusion and dissection, direct common carotid artery access, and poor image quality on DECT studies.

Imaging and Endovascular Treatment Protocols

Endovascular thrombectomy was performed on a biplane x-ray system, Allura Xper FD20/10 (Phillips Healthcare, Best, the Netherlands), by 1 of 5 interventional neuroradiologists/neurosurgeons with 10–20 years of experience in interventional neuro-radiology. As per local procedures, endovascular treatment consisted of first-attempt aspiration with a 5MAX/ACE64/ACE68 reperfusion catheter (Penumbra, Alameda, California), second-line mechanical thrombectomy with a Solitaire Flow

Restoration stent retriever (Covidien, Irvine, California),²¹⁻²⁴ or a combination technique.

Noncontrast DECT head studies were performed on 1 of 2 dual-source CT scanners (Somatom Definition Flash and Somatom Force; Siemens, Erlangen, Germany) at 80 kV/Sn 140kV and 90 kV/Sn 150kV, respectively. Preoperative and follow-up CT head studies were performed at 120 kV on both scanners. See the On-line Table for additional scan parameters.

Image Analysis

Preprocedural NCCT head and CTA studies were evaluated by 2 radiologists with subspecialty training (D.B. and J.P.W.). The ASPECTS²⁵ was recorded, and collateral status was assessed using the scoring system of Miteff et al.²⁶

Endovascular procedural imaging was reviewed by an interventional neuroradiologist (A.R.) with >10 years of experience, and the modified TICI score was recorded for each case.

DECT studies were evaluated by the 2 readers (D.B. and J.P.W.). We used 3-mm-thick multiplanar reconstructions. Simulated 120-kV images representing a weighted average of the original low-kilovolt and high-kilovolt images were provided, and virtual noncontrast images and generated iodine overlay maps using a 3-material decomposition algorithm with commercially available software (syngo.via, Dual Energy CT brain hemorrhage application, Version VB20; Siemens) were generated.

A small (0.1 cm²) ROI was placed on the SSS near the torcula to normalize the contrast. A 0.3-cm² ROI was then placed subjectively in the area of most dense contrast staining (Fig 1). Iodine concentration (milligrams/milliliter) and percentage in relation to the SSS were recorded (Fig 1). The mean of the values recorded by the 2 readers was used for statistical analysis. The presence and location (parenchymal, subarachnoid, intraventricular) of hemorrhage and contrast staining were recorded on the virtual noncontrast and iodine overlay maps, respectively. Follow-up NCCT studies were evaluated for the development of intracerebral hemorrhage and recorded according to the European Cooperative Acute Stroke Study classification²⁷ into hemorrhagic infarction and parenchymal hematoma.

Clinical and Radiologic Data Collection

Patient data including sex, age, NIHSS score at admission, site of vessel occlusion at preoperative CTA, preprocedural intravenous tPA administration (alteplase), number of passes, intra-arterial tPA administration, arterial stent delivery, puncture-to-recanalization time, time to recanalization, and oral antiplatelet/anticoagulation use before the procedure were recorded.

Statistical Analysis

The values of continuous variables are presented as mean or median with range as appropriate. Interobserver agreement was calculated according to intraclass correlation coefficient: A value below 0.50 indicates poor; between 0.5 and 0.75, moderate; between 0.75 and 0.90, good; and above 0.90, excellent reliability. Comparison between subgroups for continuous variables was performed using the Mann-Whitney *U* test. Categorical data were compared using the χ^2 or Fisher exact tests as appropriate. The

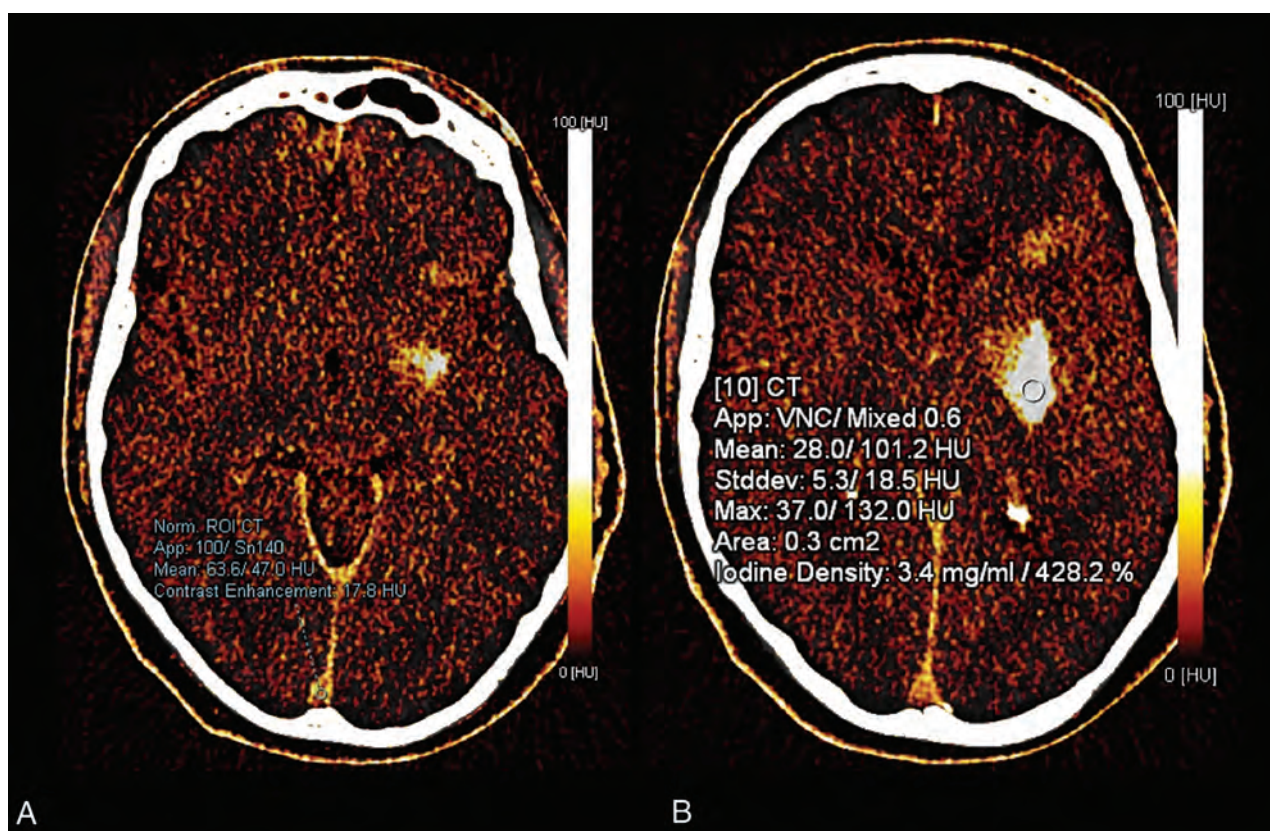


FIG 1. A, A small (0.1 cm²) ROI was placed in the superior sagittal sinus for normalization of contrast. B, In this case, the absolute maximum iodine concentration is 3.4 mg/mL and the relative concentration to the superior sagittal sinus is 428.2%.

Table 1: Findings on initial postprocedural DECT and follow-up

DECT Findings	Follow-Up CT (1–7 days)			Hemorrhage Grade	
	Overall (%)	No Hemorrhage (%)	Hemorrhage (%)	1–2 (%)	3–4 (%)
No hyperdensity	28 (39.4)	28 (39.4)	0 (0)	0 (0)	0 (0)
Staining only	39 (54.9)	22 (30.9)	17 (23.9)	11 (15.5)	6 (8.5)
Staining and hemorrhage	4 (5.6)	1 (1.4)	3 (4.2)	0 (0)	3 (4.2)
Total	71 (100.0)	51 (71.8)	20 (28.2)	11 (15.5)	9 (12.7)

correlation between absolute iodine density and relative iodine concentrations was assessed using the Spearman rank correlation coefficient. A *P* value < .05 was considered statistically significant. Statistical analysis was performed using SPSS, Version 25.0 (IBM, Armonk, New York).

RESULTS

Patient Population

We identified 130 patients who received thrombectomy for acute anterior circulation stroke (76 men and 54 women) with a median age of 70 years (range, 18–97 years). Seventy-one of 130 patients with small preprocedural infarct volumes (ASPECTS \geq 7) and good endovascular recanalization (modified TIC1 score 2b or 3) met the inclusion criteria (41 men and 30 women) with a median age of 70 years (range, 18–97 years). Patients with proximal ICA/common carotid artery occlusion (8/130) and dissection

(11/130) and direct common carotid artery access and poor image quality on DECT studies (2/130) were excluded.

Pre- and Periprocedural Data

Patients had a baseline median NIHSS score of 17 (range, 6–29). Of the cases meeting the inclusion criteria, the median ASPECTS on initial preprocedural NCCT was 8 (range, 7–10).

Intravenous tPA was administered to 45/71 (63.4%) patients. During endovascular treatment, 48 patients (67.6%) were treated with aspiration (a direct aspiration first pass technique) only; 2 (2.8%), with stent retriever only; and 21 (29.6%), with aspiration followed by stent retriever thrombectomy. The median number of aspiration attempts was 1 (range, 1–7). A carotid artery stent was placed in 2 patients. The final modified TIC1 score was 2b in 30 patients and 3 in 41 patients.

Image Analysis

ICH Development: Imaging Findings. Of the 28 patients with no hyperdensity on initial postthrombectomy DECT, none had ICH on follow-up CT. The remaining 43 patients demonstrated parenchymal hyperdensity, due to a combination of contrast staining and hemorrhage in 4/43 (9.3%) patients and due to

contrast staining alone in 39/43 (90.7%) patients, according to virtual noncontrast image analysis. Of the latter, 17/39 (44%) developed subsequent ICH, with grade 1 or 2 ICH identified in 11/17 (65%) and grade 3 or 4 ICH identified in 6/17 (35%). Of those with contrast staining, 22/39 (56%) demonstrated resolution of hyperdensity without ICH on follow-up CT. Table 1 shows data on the correlation between DECT findings and ICH on follow-up imaging.

Absolute and Relative Iodine Concentration on DECT. Of the 39 patients with initial contrast staining, the median iodine concentration was 1.20 mg/mL (range, 0.6–8.90 mg/mL) in those with ICH on follow-up imaging and 0.90 mg/mL (range, 0.40–2.10 mg/mL) in those without ICH. Differences did not reach statistical significance ($P = .183$). The median iodine concentration

in the brain parenchyma relative to the SSS was significantly higher in those who developed ICH (137.9%; range, 92.5%–1197.0%) compared with those who did not (109.2%; range, 25.4%–200.8%; $P = .007$) (Table 2). For iodine concentration relative to the SSS, a cutoff value of 100% enabled identification with 94.7% sensitivity and 43.4% specificity, with a likelihood ratio of 1.71. Significant correlation between the maximum absolute iodine concentration and relative iodine concentration was observed (Spearman $\rho = 0.761$; 95% CI, 0.644–0.842).

Examples of cases are provided in Figs 2 and 3.

ICH Development: Clinical Parameters. On preprocedural CT, the median ASPECTS was 8 in patients with ICH on follow-up imaging, and 8 in those without. There was no significant correlation between patient characteristics and subsequent ICH development: sex, age, site of vessel occlusion, revascularization technique, number of aspiration attempts, or number of stent retriever thrombectomy attempts.

The measured values of absolute iodine concentration and relative

Table 2: Iodine staining values in cohorts without and with subsequent ICH

Iodine Measurement Parameter	Follow-Up CT (Median) (IQR)		
	No ICH	ICH	P Value
Absolute iodine concentration (mg/mL)	0.90 (0.72)	1.20 (1.00)	.183 (NS)
Relative iodine concentration compared with SSS (%)	109.2 (97.1)	137.9 (99.1)	.007

Note:—IQR indicates interquartile range; NS, not significant.

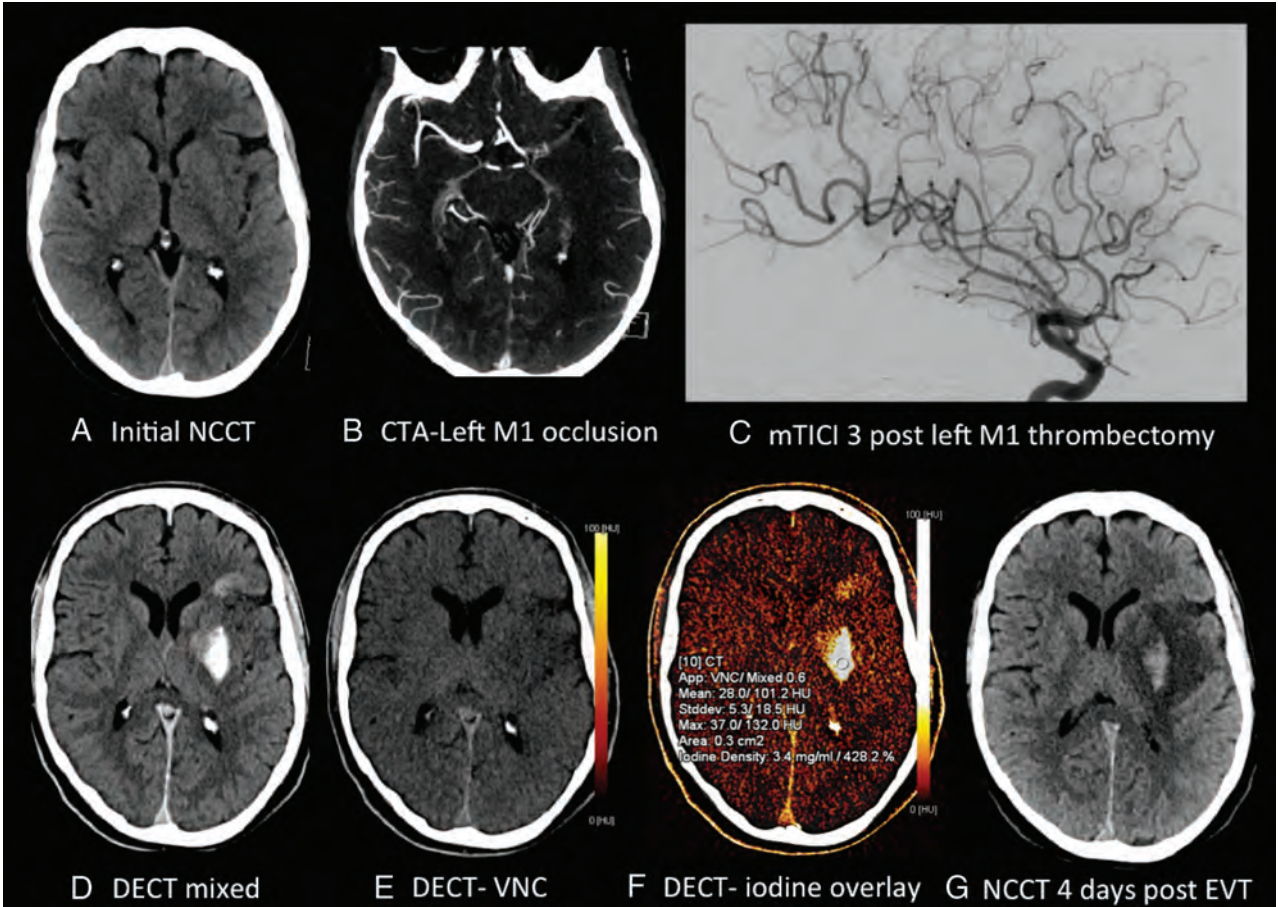


FIG 2. A 59-year-old man with a preprocedural ASPECTS of 8 (A), left M1 occlusion (B), and modified TICI 3 reperfusion (C). Postthrombectomy DECT demonstrates parenchymal hyperdensity in the left basal ganglia and frontal lobe (D), without hemorrhage on the virtual noncontrast DECT (E) and consistent with contrast staining on the iodine overlay map (F), with maximum iodine concentration measuring 3.4 mg/mL and 428.2% relative to the SSS. NCCT performed 4 days postthrombectomy (G) demonstrates evolving left MCA infarction with development of grade 3 ICH involving the left lentiform nucleus.

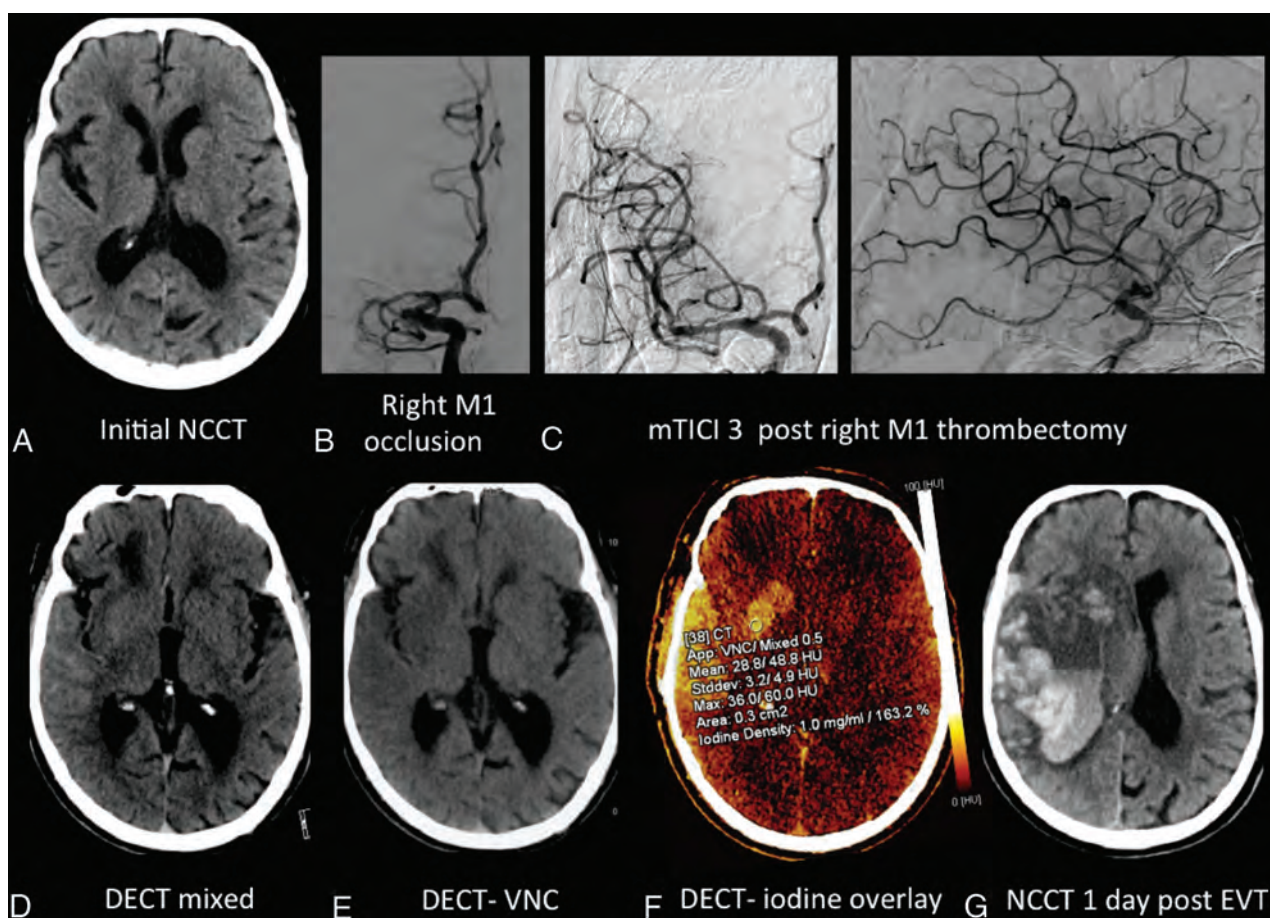


FIG 3. An 86-year-old man with a preprocedural ASPECTS of 7 (A), right M1 occlusion (B), and modified TICI 3 reperfusion (C). Postthrombectomy DECT demonstrates parenchymal hyperdensity in the right basal ganglia and frontal and temporal lobes (D), without hemorrhage on the virtual noncontrast DECT (E) and consistent with contrast staining on the iodine overlay map (F), with maximum iodine concentration measuring 1.0 mg/mL and 163.2% relative to the SSS. NCCT performed 1 day post-thrombectomy (G) demonstrates frank hemorrhagic transformation with marked mass effect.

iodine concentration showed excellent agreement between the 2 readers; the intraclass correlation coefficient for absolute iodine concentration was 0.993 ($P < .001$), while the intraclass correlation coefficient for relative iodine concentration was 0.994 ($P < .001$).

DISCUSSION

ICH can be a devastating complication of revascularization treatment for acute ischemic stroke. The incidence of symptomatic ICH was 4.4% in the recent endovascular treatment randomized controlled trials.²⁸ The presence and degree of brain parenchymal hyperdensity on head CTs obtained immediately after endovascular thrombectomy might predict which patients are at risk of developing ICH. Parenchymal hyperdensity is a common finding on postprocedural CT and may be due to hemorrhage and/or contrast staining due to breakdown of the blood-brain barrier at the site of ischemia,³ for which DECT allows differentiation. Contrast staining has also been previously shown to correlate moderately with final infarct volume and distribution.²⁹

It was previously reported that a maximum iodine concentration of >1.35 mg/mL within the area of brain parenchymal

contrast staining predicts development of ICH with 100% sensitivity and 67.5% specificity.⁷ In our dataset, there was no statistically significant difference in absolute iodine concentration between the cohort that developed ICH and the cohort that did not. This study shows that the relative iodine concentration compared with the SSS may be a better predictor of ICH development. In our study population, if iodine concentration in hyperdense brain areas was equal to or higher than the SSS, subsequent ICH development was predicted with 94.7% sensitivity and 43.4% specificity. Because parenchymal contrast staining resolved at 24 hours in most patients (22/39) with initial contrast staining, a cutoff value of 100% is associated with this relatively low specificity. However, having a high sensitivity for the prediction of ICH development is of more clinical importance in the early postprocedural phase. The ability to reliably predict ICH development in patients post-thrombectomy has clinical implications with regard to blood pressure control and antithrombotic strategy.^{20,30}

During ischemia, endothelial impairment with disruption of the BBB occurs, allowing contrast to leak into the brain interstitium.³ The degree of endothelial damage likely correlates with the severity and duration of ischemia. Patients with the most

profound endothelial damage are likely at risk of subsequent hemorrhage. While leakage of contrast/iodine staining is a surrogate marker of endothelial damage, the amount of contrast accumulating in ischemic brain tissue also depends on the concentration of iodine in the blood at the time of the CT scan, which varies according to the amount of contrast given before and during the intervention, blood volume, renal function, and so forth, which can be difficult to determine. Using the ratio of iodine in parenchyma versus blood in the SSS accounts for these interindividual differences and may explain why the relative value of iodine concentration in brain tissue may be a better predictor than absolute values. We chose the SSS because this is an easily identifiable constant anatomic structure that allows reproducible measurements of blood density.

This study has limitations due to its retrospective nature with a potential source for bias, because only patients with small infarcts and good reperfusion were included. Postprocedural DECT studies were performed on 2 different scanners. A recent phantom study demonstrated that iodine measurements are largely similar using different scanners and tube voltage pair combinations.³¹ However, slight differences might be possible and were not accounted for in our study. In addition, follow-up MR imaging was not routinely performed, and cases of petechial hemorrhage below the resolution of CT that could potentially be identified on MR imaging may have been missed and not included in the ICH cohort. ROIs within contrast-stained tissue were drawn subjectively and may not have reflected actual maximum iodine concentration; however, there was a high concordance among the 3 readers.

CONCLUSIONS

In this study, we sought an imaging biomarker of postthrombectomy ICH development in patients with acute stroke with small preprocedural infarcts and good recanalization. At dual-energy CT performed within 1 hour following thrombectomy, we found that the relative iodine concentration within contrast-stained brain parenchyma compared with that in the superior sagittal sinus was a more reliable predictor of ICH compared with the absolute maximum iodine concentration. A better understanding of risk for postprocedural hemorrhage can inform antithrombotic strategy, monitoring needs, and prognosis.

Disclosures: Heiko Schmiedeskamp—UNRELATED: Employment: Siemens, Thalia Field—UNRELATED: Grants/Grants Pending: Canadian Institutes of Health Research, Bayer Canada, Comments: site payments for recruitment (Canadian Institutes of Health Research) and in-kind study medication (Bayer Canada)*; Payment for Lectures Including Service on Speakers Bureaus: Servier Canada; Other: Michael Smith Foundation for Health Research, Vancouver Coastal Health Research Institute, Heart and Stroke Foundation of Canada, Comments: salary support awards.* * Money paid to the institution.

REFERENCES

- Fiorelli M, Bastianello S, von Kummer R, et al. Hemorrhagic transformation within 36 hours of a cerebral infarct: relationships with early clinical deterioration and 3-month outcome in the European Cooperative Acute Stroke Study I (ECASS I) cohort. *Stroke* 1999; 30:2280–84 CrossRef Medline
- Khatri P, Wechsler LR, Broderick JP. Intracranial hemorrhage associated with revascularization therapies. *Stroke* 2007;38:431–40 CrossRef Medline
- Renu A, Amaro S, Laredo C, et al. Relevance of blood-brain barrier disruption after endovascular treatment of ischemic stroke: dual-energy computed tomographic study. *Stroke* 2015;46:673–79 CrossRef Medline
- Yedavalli V, Sammet S. Contrast extravasation versus hemorrhage after thrombectomy in patients with acute stroke. *J Neuroimaging* 2017;27:570–76 CrossRef Medline
- Jang YM, Lee DH, Kim HS, et al. The fate of high-density lesions on the non-contrast CT obtained immediately after intra-arterial thrombolysis in ischemic stroke patients. *Korean J Radiol* 2006; 7:221–28 CrossRef Medline
- Tijssen MP, Hofman PA, Stadler AA, et al. The role of dual energy CT in differentiating between brain haemorrhage and contrast medium after mechanical revascularisation in acute ischaemic stroke. *Eur Radiol* 2014;24:834–40 CrossRef Medline
- Bonatti M, Lombardo F, Zamboni GA, et al. Iodine extravasation quantification on dual-energy CT of the brain performed after mechanical thrombectomy for acute ischemic stroke can predict hemorrhagic complications. *AJNR Am J Neuroradiol* 2018;39:441–47 CrossRef Medline
- Hu R, Padole A, Gupta R. Dual-energy computed tomographic applications for differentiation of intracranial hemorrhage, calcium, and iodine. *Neuroimaging Clin N Am* 2017;27:401–09 CrossRef Medline
- Van Hedent S, Hokamp NG, Laukamp KR, et al. Differentiation of hemorrhage from iodine using spectral detector CT: a phantom study. *AJNR Am J Neuroradiol* 2018;39:2205–10 CrossRef Medline
- Bae KT. Intravenous contrast medium administration and scan timing at CT: considerations and approaches. *Radiology* 2010; 256:32–61 CrossRef Medline
- Patel BN, Vernuccio F, Meyer M, et al. Dual-energy CT material density iodine quantification for distinguishing vascular from nonvascular renal lesions: normalization reduces intermanufacturer threshold variability. *AJR Am J Roentgenol* 2019;212:366–76 CrossRef Medline
- Li X, Meng X, Ye Z. Iodine quantification to characterize primary lesions, metastatic and non-metastatic lymph nodes in lung cancers by dual energy computed tomography: an initial experience. *Eur J Radiol* 2016;85:1219–23 CrossRef Medline
- Liang P, Ren XC, Gao JB, et al. Iodine concentration in spectral CT: assessment of prognostic determinants in patients with gastric adenocarcinoma. *AJR Am J Roentgenol* 2017;209:1033–38 CrossRef Medline
- Parrilla G, Garcia-Villalba B, Espinosa de Rueda M, et al. Hemorrhage/contrast staining areas after mechanical intra-arterial thrombectomy in acute ischemic stroke: imaging findings and clinical significance. *AJNR Am J Neuroradiol* 2012;33:1791–96 CrossRef Medline
- Xu C, Zhou Y, Zhang R, et al. Metallic hyperdensity sign on non-contrast CT immediately after mechanical thrombectomy predicts parenchymal hemorrhage in patients with acute large-artery occlusion. *AJNR Am J Neuroradiol* 2019;40:661–67 CrossRef Medline
- Gupta R, Phan CM, Leidecker C, et al. Evaluation of dual-energy CT for differentiating intracerebral hemorrhage from iodinated contrast material staining. *Radiology* 2010;257:205–11 CrossRef Medline
- Phan CM, Yoo AJ, Hirsch JA, et al. Differentiation of hemorrhage from iodinated contrast in different intracranial compartments using dual-energy head CT. *AJNR Am J Neuroradiol* 2012;33:1088–94 CrossRef Medline
- Tan S, Wang D, Liu M, et al. Frequency and predictors of spontaneous hemorrhagic transformation in ischemic stroke and its association with prognosis. *J Neurol* 2014;261:905–12 CrossRef Medline
- Terruso V, D'Amelio M, Di Benedetto N, et al. Frequency and determinants for hemorrhagic transformation of cerebral infarction. *Neuroepidemiology* 2009;33:261–65 CrossRef Medline
- Jadhav AP, Molyneaux BJ, Hill MD, et al. Care of the post-thrombectomy patient. *Stroke* 2018;49:2801–07 CrossRef Medline

21. Lapergue B, Blanc R, Guedin P, et al. **A direct aspiration, first pass technique (ADAPT) versus stent retrievers for acute stroke therapy: an observational comparative study.** *AJNR Am J Neuroradiol* 2016;37:1860–65 CrossRef Medline
22. Massari F, Henninger N, Lozano JD, et al. **ARTS (aspiration-retriever technique for stroke): initial clinical experience.** *Interv Neuroradiol* 2016;22:325–32 CrossRef Medline
23. Romano DG, Cioni S, Leonini S, et al. **Manual thromboaspiration technique as a first approach for endovascular stroke treatment: a single-center experience.** *Interv Neuroradiol* 2016;22:529–34 CrossRef Medline
24. Romano DG, Cioni S, Vinci SL, et al. **Thromboaspiration technique as first approach for endovascular treatment of acute ischemic stroke: initial experience at nine Italian stroke centers.** *J Neurointerv Surg* 2017;9:6–10 CrossRef Medline
25. Barber PA, Demchuk AM, Zhang J, et al. **Validity and reliability of a quantitative computed tomography score in predicting outcome of hyperacute stroke before thrombolytic therapy: ASPECTS Study Group—Alberta Stroke Programme Early CT Score.** *Lancet* 2000;355:1670–74
26. Miteff F, Levi CR, Bateman GA, et al. **The independent predictive utility of computed tomography angiographic collateral status in acute ischaemic stroke.** *Brain* 2009;132:2231–38 CrossRef Medline
27. Hacke W, Kaste M, Fieschi C, et al. **Randomised double-blind placebo-controlled trial of thrombolytic therapy with intravenous alteplase in acute ischaemic stroke (ECASS II): Second European-Australasian Acute Stroke Study Investigators.** *Lancet* 1998;352:1245–51 CrossRef Medline
28. Goyal M, Menon BK, van Zwam WH, et al. **Endovascular thrombectomy after large-vessel ischaemic stroke: a meta-analysis of individual patient data from five randomised trials.** *Lancet* 2016;387:1723–31 CrossRef
29. Djurdjevic T, Rehwald R, Knoflach M, et al. **Prediction of infarction development after endovascular stroke therapy with dual-energy computed tomography.** *Eur Radiol* 2017;27:907–17 CrossRef Medline
30. Vitt JR, Trillanes M, Hemphill JC 3rd. **Management of blood pressure during and after recanalization therapy for acute ischemic stroke.** *Front Neurol* 2019;10:138 CrossRef Medline
31. Jacobsen MC, Schellingerhout D, Wood CA, et al. **Intermanufacturer comparison of dual-energy CT iodine quantification and monochromatic attenuation: a phantom study.** *Radiology* 2018;287:224–34 CrossRef Medline

Diffusion Properties of Normal-Appearing White Matter Microstructure and Severity of Motor Impairment in Acute Ischemic Stroke

C. Ingo, C. Lin, J. Higgins, Y.A. Arevalo, and S. Prabhakaran

ABSTRACT

BACKGROUND AND PURPOSE: The effect of white matter hyperintensities as measured by FLAIR MR imaging on functional impairment and recovery after ischemic stroke has been investigated thoroughly. However, there has been growing interest in investigating normal-appearing white matter microstructural integrity following ischemic stroke onset with techniques such as DTI.

MATERIALS AND METHODS: Fifty-two patients with acute ischemic stroke and 36 without stroke were evaluated with a DTI and FLAIR imaging protocol and clinically assessed for the severity of motor impairment using the Motricity Index within 72 hours of suspected symptom onset.

RESULTS: There were widespread decreases in fractional anisotropy and increases in mean diffusivity and radial diffusivity for the acute stroke group compared with the nonstroke group. There was a significant positive association between fractional anisotropy and motor function and a significant negative association between mean diffusivity/radial diffusivity and motor function. The normal-appearing white matter ROIs that were most sensitive to the Motricity Index were the anterior/posterior limb of the internal capsule in the infarcted hemisphere and the splenium of the corpus callosum, external capsule, posterior limb/retrolenticular part of the internal capsule, superior longitudinal fasciculus, and cingulum (hippocampus) of the intrahemisphere/contralateral hemisphere.

CONCLUSIONS: The microstructural integrity of normal-appearing white matter is a significant parameter to identify neural differences not only between those individuals with and without acute ischemic stroke but also correlated with the severity of acute motor impairment.

ABBREVIATIONS: AD = axial diffusivity; ADC = apparent diffusion coefficient; DTI = diffusion tensor imaging; DWI = diffusion-weighted imaging; FA = fractional anisotropy; InfHem = infarcted hemisphere; IQR = interquartile range; NAWM = normal-appearing white matter; MD = mean diffusivity; RD = radial diffusivity; WMH = white matter hyperintensities

The effect of white matter hyperintensities (WMH) as measured by FLAIR MR imaging on functional impairment and recovery after ischemic stroke has been investigated thoroughly.^{1–7} However, there has been growing interest to investigate normal-appearing white matter (NAWM) microstructural integrity,^{8,9} that is neither classified as infarct/edema/lesion tissue^{10,11} in diffusion-weighted imaging (DWI) nor WMH via FLAIR.^{1,4} Recently, DTI

of NAWM in patients with acute ischemic stroke has been used to determine the relationship between decreased whole-brain fractional anisotropy (FA) in NAWM and functional outcomes after ischemic stroke.^{12,13} There have been other studies that have investigated DTI measures 10–15 days¹⁴ and 30+ days¹⁵ following stroke. In this study, we performed a region of interest (ROI) DTI analysis of NAWM to determine the relationship between diffusivity metrics and the severity of motor impairment in the acute stages (within 72 hours of symptom onset) in patients with confirmed acute ischemic stroke compared with controls suspected of having ischemic stroke but without acute infarct.

MATERIALS AND METHODS

Participants and Clinical Assessment

The Northwestern University institutional review board approved the study. Patients older than 18 years of age with a confirmed

Received July 30, 2019; accepted after revision October 30.

From the Departments of Neurology (C.I., Y.A.A.), Physical Therapy and Human Movement Sciences (C.L.), and Radiology (J.H.), Northwestern University, Chicago, Illinois; Department of Neurology (C.L.), University of Alabama at Birmingham, Birmingham, Alabama; and Department of Neurology (S.P.), University of Chicago Medical Center, Chicago, Illinois.

This study was funded through the Eleanor Wood Prince Grants Initiative of the Woman's Board of Northwestern University and the Davee Foundation.

Please address correspondence to Carson Ingo, PhD, Northwestern University, 645 N. Michigan Ave, Suite 850, Room 856, Chicago, IL 60611; e-mail: carson.ingo@northwestern.edu

<http://dx.doi.org/10.3174/ajnr.A6357>

Table 1: Demographics, clinical outcome measures, stroke risk factors, and acute infarct characteristics among those diagnosed with an acute ischemic stroke and those who were suspected of having an acute stroke but did not have an infarct (non-stroke)

	Acute Stroke (n = 52)	Nonstroke (n = 36)	P
Demographics			
Age (mean) (SD) (yr)	69.2 (17.4)	62.2 (17.7)	.068
Women (No.) (%)	28 (54.0%)	19 (52.8%)	.907
Black (No.) (%)	17 (32.7%)	13 (36.1%)	.715
Clinical outcome measures			
Motricity Index (median) (IQR)	77 (44–92)	NA	–
NIH Stroke Scale (median) (IQR)	4 (2–13)	NA	–
Stroke risk factors			
Diabetes mellitus	14 (26.9%)	7 (19.4%)	.394
Hypertension	40 (76.9%)	24 (66.7%)	.309
Atrial fibrillation/flutter	13 (32.5%)	8 (22.2%)	.595
Dyslipidemia	27 (51.9%)	17 (47.2%)	.652
Cardiomyopathy	14 (26.9%)	7 (19.4%)	.271
Smoking history	17 (32.7%)	8 (22.2%)	.612
Infarct characteristics			
Median infarct volume (IQR) (mL)	1.1 (0.3–9.2)	NA	–
Infarct overlap with corticospinal tract (No.) (%)	36 (69.2%)	NA	–
Side of infarct, right (No.) (%)	31 (59.6%)	NA	–
Median white matter hyperintensity volume (IQR) (mL)	11.7 (2.2–35.2)	10.1 (1.93–26.7)	.143
Stroke subtype			
Cardioembolic	12 (23.1%)	NA	–
Small artery disease	11 (21.2%)	NA	–
Large atherosclerosis	13 (25.0%)	NA	–
Cryptogenic	14 (26.9%)	NA	–
Other	2 (3.8%)	NA	–
IV-tPA cases	10 (19.2%)	NA	–
Thrombectomy rate	5 (9.6%)	NA	–

Note:—NA indicates not applicable; IV-tPA, intravenous tissue-type plasminogen activator; NIH, National Institutes of Health.

acute ischemic stroke or suspected of having an acute stroke were enrolled. Written informed consent was obtained from the patient or his or her legally authorized representative for all participants. Patients with an acute stroke were defined as those with MR imaging evidence of acute infarct as identified on diffusion-weighted and apparent diffusion coefficient (ADC) images. Patients without an acute stroke (non-stroke) were defined as those who underwent MR imaging to rule out stroke if they had presented with any neurologic symptom within the 72 hours of medical center admission. The non-stroke patients did not have a diagnosis of an acute infarct, TIA, or history of stroke (ischemic or hemorrhagic) or TIA. Diagnosis was made by a board-certified vascular neurologist in each case. It was confirmed that participants did not have demyelinating disease or a prior stroke diagnosis before inclusion in this study. Clinical assessments with the Motricity Index (range, 0–100, 100 = no motor impairment),¹⁶ NIHSS (range, 0–42, 0 = no stroke symptoms),¹⁷ and MR imaging data were acquired in the participants within 72 hours of symptom onset. Patient demographics, premorbid characteristics, risk factors, and comorbidities were also collected as shown in Table 1.

DWI

Axial diffusion-weighted images were acquired with the following parameters on a 3T MAGNETOM Skyra (Siemen, Erlangen, Germany) scanner: TE = 95 ms, TR = 10,000 ms, flip angle = 90°,

matrix size = 122 × 122, FOV = 220 × 220 mm², section thickness = 2 mm, voxel resolution = 1.8 × 1.8 × 2mm³, slices = 74, b = 0 s/mm² images = 3, diffusion gradient directions = 30, diffusion-weighting = 1000 s/mm².

FLAIR Imaging

Axial turbo spin-echo FLAIR images were acquired with the following parameters: TE = 81 ms, TR = 9000 ms, TI = 2500 ms, flip angle = 150°, matrix size = 320 × 320, FOV = 220 × 220 mm², section thickness = 4 mm, voxel resolution = 0.7 × 0.7 × 4.0 mm³, slices = 30.

DWI Preprocessing and Tensor Fitting

The diffusion-weighted images were first brain-extracted using the FSL Brain Extraction Tool.¹⁸ The data were then denoised using an estimate of the noise variance in the CSF signal intensity of the right ventricle. The data were corrected for motion and eddy currents by coregistering diffusion-weighted images to the image acquired with b = 0 s/mm² using the FMRIB Linear Image Registration Tool (<https://fsl.fmrib.ox.ac.uk/fsl/fslwiki/FLIRT>). The motion-correc-

tion transformation matrix was applied to the diffusion gradient directions to rotate them according to the registration algorithm. The preprocessed diffusion-weighted data were fitted to a tensor on a voxelwise basis using dtfit in the FSL Diffusion Toolbox to produce estimates of FA, mean diffusivity (MD), radial diffusivity (RD), and axial diffusivity (AD).

White Matter Hyperintensity and Infarct Segmentation

FLAIR images were skull-stripped, denoised using a nonlocal means filter,¹⁹ and corrected for intensity nonuniformity. Cleaned images were input to the lesion prediction algorithm of the Lesion Segmentation Toolbox in SPM12 (<https://www.applied-statistics.de/1st.html>). Lesion probability maps were thresholded at greater than zero percentage probability to form initial masks and corrected using FreeSurfer and approved by a neurologist (C.L.). The brain-extracted FLAIR images were affine registered to the b=0 s/mm² diffusion scan (3dAllineate; Analysis of Functional Neuro Images [AFNI]), and the resultant transform was applied to the corrected mask with nearest-neighbor interpolation to obtain diffusion-space WMH masks. The FLAIR images were brain-extracted and affine-registered to the b=0 s/mm² diffusion scan using FLIRT in FSL. The same transformations were applied to the WMH mask images.

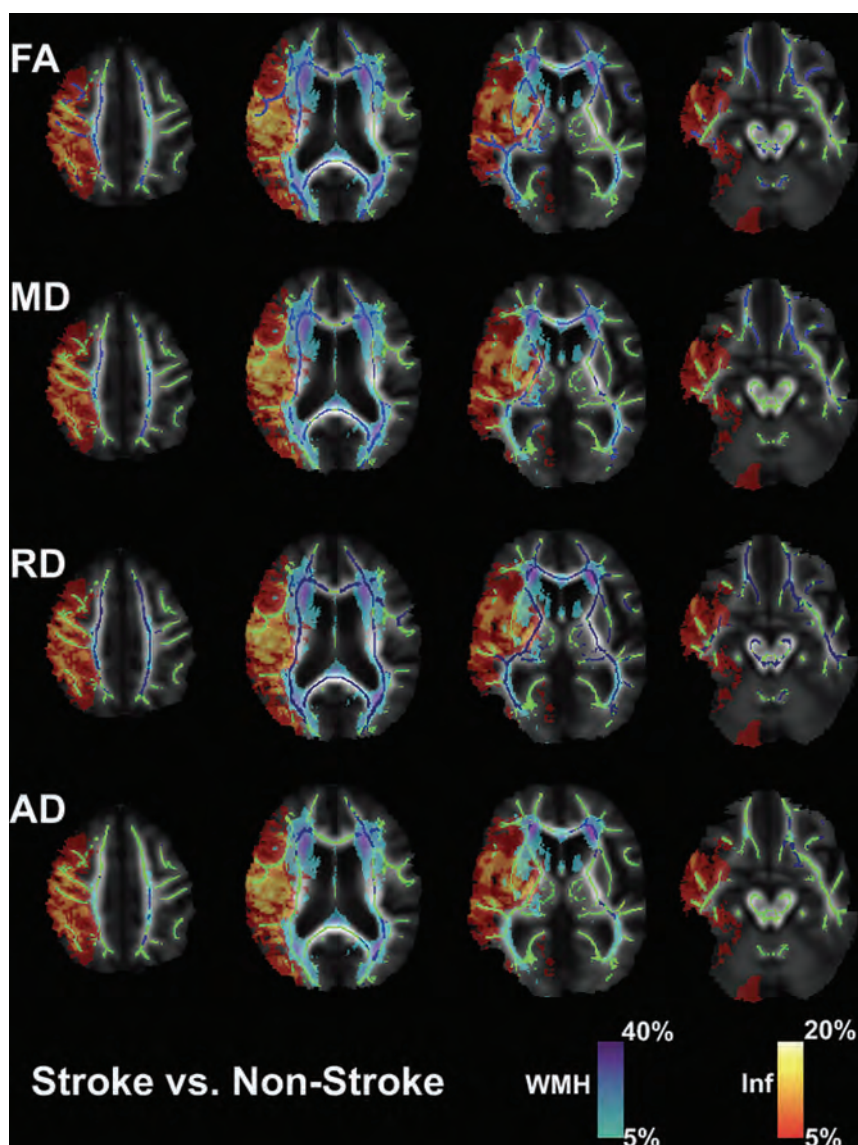


FIG 1. Group analysis for those diagnosed with an acute ischemic stroke and those who were suspected of having an acute stroke but did not have an infarct (non-stroke). Green represents the white matter skeleton for the group comparison. Blue represents significantly changed voxels ($P < .05$) for FA, MD, RD, and AD: stroke FA < non-stroke FA, stroke MD > non-stroke MD, stroke RD > non-stroke RD, and stroke AD > non-stroke AD. The cool map represents the WMH probability map from FLAIR images. The heat map represents the infarct (Inf) probability map from MD images. Statistical analyses were adjusted for age as a covariate and corrected for multiple comparisons using permutation-based testing.

The infarct voxels were segmented using a threshold approach in which values were less than $0.68 \times 10^{-3} \text{ mm}^2/\text{s}$ from the MD images to produce the infarct masks.²⁰ These were manually corrected using FreeSurfer and approved by a neurologist (C.L.).

Statistical Analysis

Tract-Based Spatial Statistics (TBSS) was performed in FSL.²¹ For those individuals with infarcts in the left hemisphere, FA maps were flipped so that all subjects had infarcts in the right hemisphere. FA maps were first linearly and then nonlinearly registered to the FMRIB58_FA in the standard space of the Montreal Neurological Institute. A mean FA image was then created from

all individual FA images and was used to generate a common group skeleton. A threshold was applied at 0.2 to minimize potential white matter/gray matter partial volume effects. Each FA image was projected onto the common group skeleton for subsequent statistical analysis. For those individuals with infarcts in the left hemisphere, MD, RD, AD, infarct, and WMH maps were flipped so that all subjects had infarcts in the right hemisphere. The same transformations that were applied to the FA maps were also applied to the MD, RD, AD, infarct, and WMH maps. The infarct (heat) and WMH (cool) maps are shown in Figs 1 and 2 and are presented as a percentage of those individuals who had instances of infarct or white matter hyperintensity voxels with respect to the total acute stroke group. The Johns Hopkins University ICBM-DTI-81 white matter labels and tractography atlases were used to identify the white matter ROIs that contained the significantly changed voxels.²²⁻²⁴

Test 1. To investigate potential differences in diffusivity metrics in those diagnosed with an acute ischemic stroke and those who were suspected of having an acute stroke but did not have an infarct (non-stroke), a 2-group unpaired t test was performed with age as a covariate. In order to correct for multiple comparisons, permutation testing ($n = 500$) was performed using the *randomise* and threshold-free cluster enhancement (TFCE) functions in FSL.²⁵

Test 2. To test for possible significant interactions between the diffusivity

metrics and each individual risk factor (diabetes mellitus, hypertension, atrial fibrillation/flutter, dyslipidemia, cardiomyopathy, and smoking history) for those who were diagnosed with an acute stroke, a partial correlation analysis was performed with age as a covariate. In order to correct for multiple comparisons, permutation testing ($n = 500$) was performed.²⁵

Test 3. To investigate potential associations between the diffusivity metrics and the Motricity Index for those who were diagnosed with an acute stroke, a partial correlation analysis was performed with age, total infarct volume, and infarct volume overlap with the corticospinal tract as covariates. In order to correct for multiple comparisons, permutation testing ($n = 500$) was performed.²⁵

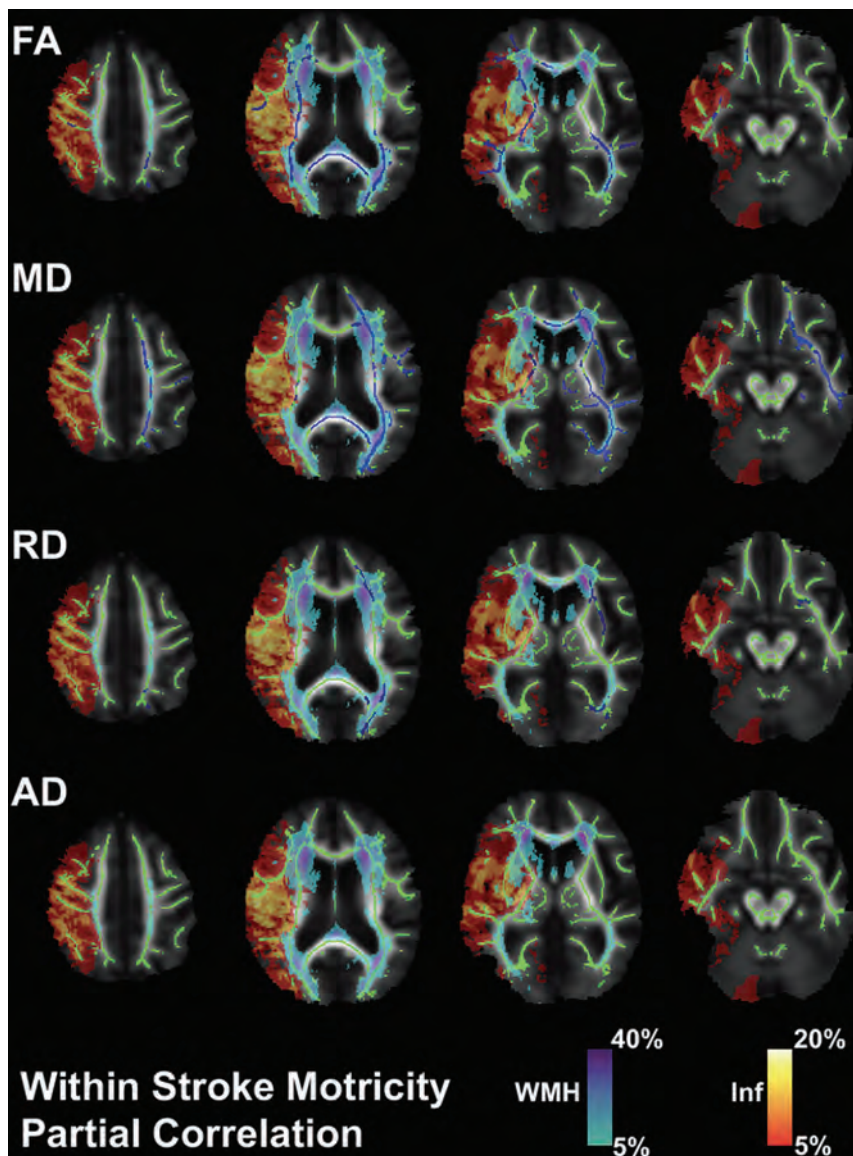


FIG 2. Partial correlation analysis for those diagnosed with an acute ischemic stroke. Green represents the white matter skeleton for the imaging measures versus the Motricity Index (MI) correlation. Blue represents significantly changed voxels ($P < .05$) for FA, MD, RD, and AD: FA positively associated with MI, MD negatively associated with MI, RD negatively associated with MI, and AD not significantly associated with MI. The cool map represents the WMH probability map from FLAIR images. The heat map represents the infarct (Inf) probability map from MD images. Statistical analyses were adjusted for covariates of age, total infarct volume, and infarct volume overlap with the corticospinal tract and then were corrected for multiple comparisons using permutation-based testing.

RESULTS

As shown in Table 1, the final analysis included 52 patients with acute ischemic stroke and 36 without stroke (non-stroke group) who were enrolled consecutively. In the patients with stroke, the mean age was 69.2 ± 17.4 years, 28 were women (54%), and 17 were black (32.7%). There were no statistical differences in these baseline characteristics between the stroke and non-stroke groups. Within the stroke group, the median Motricity Index was 77 (interquartile range [IQR], 44–92) and the median NIHSS score was 4 (IQR, 2–13). The median infarct volume in the stroke group was 1.1 mL (IQR, 0.3–9.2 mL) with

predominance in the right hemisphere in 31 (59.6%), and 36 infarcts (69.2%) had overlap with the corticospinal tract.

Acute Ischemic Stroke versus Non-stroke Controls

As shown in Fig 1, the NAWM voxels (green) that exclude infarct (heat map) and white matter hyperintensity (cool map) probability masks were tested for group differences in FA, MD, RD, and AD between the acute stroke group and the non-stroke group. There were widespread decreases in FA (blue, panel 1) and increases in MD and RD (blue, panels 2 and 3) for the acute stroke group compared with the nonstroke group. There were minimal increases in AD (blue, panel 4) for the acute stroke group compared with the non-stroke group; however, most of these voxels overlapped with the WMH probability map.

Acute Stroke Risk Factor Testing

Each individual risk factor (diabetes mellitus, hypertension, atrial fibrillation/flutter, dyslipidemia, cardiomyopathy, and smoking history) for those who were diagnosed with an acute stroke was tested for significant interactions with FA, MD, RD, and AD. None of the risk factors had any significant interaction with the diffusivity metric voxels. Additionally, potential asymmetry effects²⁶ in the diffusion metrics between hemispheres were investigated. The individuals who were flipped were compared with the non-flipped individuals in a 2-group unpaired t test with Motricity Index, age, total infarct volume, and infarct volume overlap with the corticospinal tract

as covariates to isolate potential effects of asymmetry. There were no significant voxels.

Acute Stroke Testing for Motor Impairment Measured by the Acute Motricity Index

As shown in Fig 2, in stroke, for the NAWM voxels tested for partial correlation with the Motricity Index, 12.1% FA, 28.9% MD, and 3.8% RD voxels were significant (blue) with respect to the NAWM TBSS skeleton (green). There was a positive association between FA and the Motricity Index and a negative association between MD/RD and the Motricity Index. There were no

Table 2: FA versus the Motricity Index adjusted for covariates of age, total infarct volume, and infarct volume overlap with the corticospinal tract^a

	No. of Significant Voxels	Significant Voxels (%)	<i>r</i>	<i>P</i>
Anterior corona radiata, R	69	4.4%	0.379	.027
Anterior limb of internal capsule, R	383	55.1%	0.396	.025
Body of corpus callosum	23	2.4%	0.275	.032
Cerebral peduncle, R	47	10.1%	0.285	.030
Cingulum (cingulate gyrus), L	22	3.8%	0.252	.032
Cingulum (cingulate gyrus), R	41	6.8%	0.297	.032
External capsule, L	86	11.0%	0.311	.030
External capsule, R	129	19.5%	0.392	.033
Genu of corpus callosum	17	5.6%	0.237	.039
Posterior limb of internal capsule, R	419	73.6%	0.434	.023
Posterior thalamic radiation, L	22	4.0%	0.296	.035
Retrolenticular part of internal capsule, L	20	14.0%	0.269	.036
Retrolenticular part of internal capsule, R	87	31.3%	0.398	.027
Sagittal stratum, L	131	37.6%	0.345	.031
Sagittal stratum, R	128	29.6%	0.361	.031
Splenium of corpus callosum	1068	65.2%	0.443	.023
Superior corona radiata, L	40	3.1%	0.371	.034
Superior corona radiata, R	188	13.8%	0.563	.021
Superior longitudinal fasciculus, L	126	8.7%	0.307	.039
Superior longitudinal fasciculus, R	68	5.0%	0.536	.033
Uncinate fasciculus, R	23	30.3%	0.451	.033

Note:—L indicates left; R, right.

^a The reported *P* value is corrected for multiple comparisons using permutation-based testing. Voxels are reported from NAWM ROIs that exclude infarcts and white matter hyperintensities visible from FLAIR images. The right hemisphere represents the infarcted hemisphere.

significant AD voxels. The right hemisphere represents the infarcted hemisphere (InfHem).

Table 2 shows the ROI breakdown of the significantly changed voxel overlay with the Johns Hopkins University ICBM-DTI-81 white matter labels for the FA-Motricity Index partial correlation. The splenium of the corpus callosum (1068, $r = 0.443$, $P = .023$) had the most significant number of voxels, followed by the right (InfHem) posterior limb of the internal capsule (419, $r = 0.434$, $P = .023$), the right (InfHem) anterior limb of the internal capsule (383, $r = 0.396$, $P = .025$), the right (InfHem) superior corona radiata (188, $r = 0.563$, $P = .021$), and the left/right sagittal stratum (131, $r = 0.345$, $P = .031$ /128, $r = 0.361$, $P = .031$). The right (InfHem) posterior limb of the internal capsule (73.6%, $r = 0.434$, $P = .023$) had the largest percentage of significant ROI voxels, followed by the splenium of the corpus callosum (65.2%, $r = 0.443$, $P = .023$), the right (InfHem) anterior limb of the internal capsule (55.1%, $r = 0.396$, $P = .025$), the left/right sagittal stratum (37.6%, $r = 0.345$, $P = .031$ /29.6%, $r = 0.361$, $P = .031$), the right (InfHem) retrolenticular part of the internal capsule (31.3%, $r = 0.398$, $P = .027$), and the right (InfHem) uncinate fasciculus (30.3%, $r = 0.451$, $P = .033$).

Table 3 shows the ROI breakdown of the significantly changed voxel overlay with the Johns Hopkins University white matter labels for the MD-Motricity Index partial correlation. The splenium of the corpus callosum (947, $r = -0.450$, $P = .012$) had the most significant number of voxels, followed by the left superior longitudinal fasciculus (561, $r = -0.448$, $P = .021$), the left external capsule (544, $r = -0.492$, $P = .017$), the right (InfHem) anterior limb of internal capsule (282, $r = -0.481$, $P = .047$), the

left posterior limb of the internal capsule (274, $r = -0.400$, $P = .014$), and the left sagittal stratum (220, $r = -0.457$, $P = .015$). The left cingulum (hippocampus) (91.2%, $r = -0.385$, $P = .021$) had the largest percentage of significant ROI voxels, followed by the left retrolenticular part of internal capsule (87.4%, $r = -0.368$, $P = .014$), the left posterior limb of the internal capsule (74.7%, $r = -0.400$, $P = .014$), the left external capsule (69.6%, $r = -0.492$, $P = .017$), the left uncinate fasciculus (65.0%, $r = -0.428$, $P = .011$), the left sagittal stratum (63.2%, $r = -0.457$, $P = .015$), and the splenium of the corpus callosum (57.8%, $r = -0.450$, $P = .012$).

Table 4 shows the ROI breakdown of the significantly changed voxel overlay with the Johns Hopkins University white matter labels for the RD-Motricity Index partial correlation. The left external capsule (155, $r = -0.409$, $P = .018$) had the most significant number of voxels, followed by the left posterior thalamic radiation (56, $r = -0.298$, $P = .029$), and the splenium of the corpus callosum (44, $r = -0.273$, $P = .032$).

The left external capsule (19.8%, $r = -0.409$, $P = .018$) had the largest percentage of significant ROI voxels, followed by the left posterior thalamic radiation (10.1%, $r = -0.298$, $P = .029$).

There were no significantly changed voxels for the AD-Motricity Index partial correlation.

DISCUSSION

Occurrence of Acute Stroke in Relation to Normal-Appearing White Matter Integrity

As evidenced by the FA, MD, and RD results for the group test between acute ischemic stroke and non-stroke participants, there appears to be a decrease in integrity for normal-appearing white matter surrounding not only the infarcted hemisphere, which was predominately the MCA territory, but also in the contralateral hemisphere. Previous work has shown that whole-brain integrity of normal-appearing white matter is associated with functional motor outcomes following ischemic acute stroke.^{12,13} A recent DTI study analyzed cognitive impairment 10–14 days following stroke in comparison with a control group, but there were no delineations between abnormal and normal-appearing white matter.¹⁴ However, there has been a lack of investigations into the baseline NAWM integrity in those who have been imaged within 72 hours of stroke onset compared with those without stroke. The new evidence presented in this study suggests that baseline normal-appearing white matter microstructural integrity in the infarcted hemisphere, intrahemisphere, and contralateral hemisphere may potentially be an additional risk factor that determines the susceptibility to stroke occurrence, which

Table 3: MD versus the Motricity Index adjusted for covariates of age, total infarct volume, and infarct volume overlap with the corticospinal tract^a

	No. of Significant Voxels	Significant Voxels (%)	<i>r</i>	<i>P</i>
Anterior corona radiata, L	29	2.1%	−0.390	.021
Anterior limb of internal capsule, R	282	40.6%	−0.481	.047
Body of corpus callosum	21	2.2%	−0.259	.031
Cerebral peduncle, L	136	26.7%	−0.388	.020
Cerebral peduncle, R	69	14.8%	−0.378	.047
Cingulum (cingulate gyrus), L	19	3.3%	−0.313	.030
Cingulum (hippocampus), L	124	91.2%	−0.385	.021
External capsule, L	544	69.6%	−0.492	.017
External capsule, R	21	3.2%	−0.390	.048
Genu of corpus callosum	106	34.6%	−0.336	.037
Posterior limb of internal capsule, L	274	74.7%	−0.400	.014
Posterior limb of internal capsule, R	158	27.8%	−0.412	.048
Posterior thalamic radiation, L	183	33.1%	−0.465	.010
Retrolenticular part of internal capsule, L	125	87.4%	−0.368	.014
Retrolenticular part of internal capsule, R	21	7.6%	−0.353	.048
Sagittal stratum, L	220	63.2%	−0.457	.015
Splenium of corpus callosum	947	57.8%	−0.450	.012
Superior corona radiata, L	194	15.1%	−0.350	.017
Superior longitudinal fasciculus, L	561	38.6%	−0.448	.021
Uncinate fasciculus, L	39	65.0%	−0.428	.011

Note:—L indicates left; R, right.

^a The reported *P* value is corrected for multiple comparisons using permutation-based testing. Voxels are reported from NAWM ROIs that exclude infarcts and white matter hyperintensities visible from FLAIR images.

Table 4: RD versus Motricity Index adjusted for covariates of age, total infarct volume, and infarct volume overlap with the corticospinal tract^a

	Total No. of Significant Voxels	Total Percentage of Significant Voxels	<i>r</i>	<i>P</i>
Cerebral peduncle, L	17	3.3%	−0.269	.030
External capsule, L	155	19.8%	−0.409	.018
Posterior limb of internal capsule, L	19	5.2%	−0.315	.028
Posterior thalamic radiation, L	56	10.1%	−0.298	.029
Splenium of corpus callosum	44	2.7%	−0.273	.032

Note:—L indicates left.

^a The reported *P* value is corrected for multiple comparisons using permutation-based testing. Voxels are reported from NAWM ROIs that exclude infarcts and white matter hyperintensities visible from FLAIR images.

builds on previous reports of overt WMH as a risk factor.²⁷ However, it is still possible that widespread changes in NAWM diffusivity metrics in patients with acute ischemic stroke compared with non-stroke are sequelae of the acute infarct.

Severity of Initial Motor Impairment Due to Acute Stroke and Infarcted Hemisphere Normal-Appearing White Matter Integrity

As evidenced by the FA and MD results for the ipsilateral anterior/posterior limb of the internal capsule with the partial correlation to the initial Motricity Index score for motor impairment, there appears to be a decrease in integrity for normal-appearing white matter in the infarcted hemisphere, which relates to the initial severity of the injury.

Severity of Initial Motor Impairment Due to Acute Stroke and Intrahemisphere/Contralateral Hemisphere Normal-Appearing White Matter Microstructural Integrity

As evidenced by the FA and MD results for the splenium of the corpus callosum and the contralateral external capsule, posterior

limb/retrolenticular part of the internal capsule, superior longitudinal fasciculus, and cingulum (hippocampus) with the partial correlation to initial Motricity Index score for motor impairment, there appears to be a decrease in integrity for normal-appearing white matter in the intrahemisphere and contralateral hemisphere that relates to the initial severity of the injury.

Relationship of Normal-Appearing White Matter Microstructural Integrity and Traditional Imaging Markers

This study considered both the functional locations and volumes of traditional markers of neural injury and burden via infarcted and WMH tissue as covariates to isolate, as well as possible, the relationship between NAWM microstructural integrity and the severity of motor impairment in acute ischemic stroke. Because there were statistically significant correlations, particularly with FA/MD and the Motricity Index, in motor ROIs in each of the infarcted hemispheres, intrahemisphere, and contralateral hemisphere, these results suggest that the health of NAWM is an additional important variable along with traditional metrics of infarct volume, infarct location, and WMH burden¹⁻⁷ to better understand the severity and extent of functional impairment.

Significant MD Results and Relationship to the Apparent Diffusion Coefficient (ADC)

Because the MD (28.9% of voxels) results showed more significance in the statistical testing of the white matter skeleton in comparison with FA (12.1% of voxels), this study is optimistic for larger studies being leveraged using typical clinical stroke MR imaging protocol DWI scans that sample only 3 diffusion directions instead of the 30 directions used in this study. MD is a metric akin to what is typically referred to as the ADC, which is calculated from a 3-diffusion-direction DWI scan.²⁸ Because a minimum of 6 diffusion directions are needed to compute the diffusion tensor,²⁹ it is not possible to calculate, for example, FA. However, because MD and ADC are both average diffusivity measures, it is possible that a 3-direction DWI scan could provide similar insight into NAWM following acute ischemic stroke.

Clinical Implications and Impact

The results presented in the current study provide the clinical potential to improve on previous attempts to develop multimodal algorithms and models³⁰ to predict the likelihood and capacity

for recovery following stroke. One study has shown that the ability to detect the preservation of the cortical spinal tract based on early DTI measures is an important parameter that predicts motor recovery and those who would benefit from targeted intervention and therapy strategies.³⁰ It is possible that not only early estimates of available motor resources in the infarcted hemisphere are important, but early estimates of intrahemisphere and contralateral hemisphere normal-appearing white matter, as evidenced in the current study, are also relevant to better understand the potential for extent of motor recovery. These results may lead to further inquiries as to whether changes in normal-appearing white matter are present before or are a result of the acute injury and whether the decreased integrity in the intrahemisphere and contralateral hemisphere is chronic in nature.

Limitations

The Johns Hopkins University white matter label atlas^{22–24} covers only a subset of the white matter skeleton used for statistical analysis in this study. Therefore, significant voxels are not represented in the ROI analysis presented in Tables 2–4. Because this study is focused on both the acute imaging analysis and clinical assessment of motor function in ischemic stroke within 72 hours of symptom onset, future work is needed to perform follow-up imaging analysis and clinical assessment at 3–6 months to determine the possibility of long-term motor recovery with respect to the viability of the NAWM microstructure. Vascular neurologists in this study did not record further clinical diagnosis of the etiology of neurologic symptoms for the nonstroke patient group once they were determined to not have strokes. While the present study focused on milder cases of stroke, it has been shown from a public health standpoint that those with minor strokes (NIHSS < 3) are the most commonly reported group of patients with strokes in the United States³¹ which further emphasizes that there are meaningful acute imaging parameters associated with motor impairment, even in patients with relatively mild severity. While potential asymmetry effects have been reported previously in the diffusion metrics between hemispheres²⁶ and they were found in this study to not produce significant results between flipped versus non-flipped images, it is possible that potential hemispheric asymmetry could contribute to the imaging results shown in Figs 1 and 2.

CONCLUSIONS

The microstructural integrity of NAWM, as measured by diffusion tensor parameters, is a significant parameter to not only identify microstructural differences between those individuals with acute ischemic stroke compared with those who did not have an infarct but also to correlate with the severity of acute motor impairment. In this study, the NAWM ROIs that were most sensitive to the Motricity Index were the anterior/posterior limb of the internal capsule in the infarcted hemisphere and the splenium of the corpus callosum, external capsule, posterior limb/retrolenticular part of the internal capsule, superior longitudinal fasciculus, and cingulum (hippocampus) of the intrahemisphere/contralateral hemisphere. Future studies could include the 3- to 6-month follow-up of the morphology of these imaging measures in relation to clinical assessment, recovery, and rehabilitation of motor function.

Disclosures: Carson Ingo—RELATED: Grant: The data collection of this study was funded through the Eleanor Wood Prince Grants Initiative of the Woman's Board of Northwestern University and the Davee Foundation.* Chen Lin—RELATED: Grant: Woman's Board of Northwestern Memorial Hospital, Comments: covered imaging scans.* Yurany A. Arevalo—RELATED: Grant: the Eleanor Wood Prince Grants Initiative of the Woman's Board of Northwestern University and the Davee Foundation.* Shyam Prabhakaran—RELATED: Grant: Women's Board Foundation Grant*; UNRELATED: Grants/Grants Pending: National Institutes of Health/National Institute of Neurological Disorders and Stroke, Agency for Healthcare Research and Quality*; Royalties: UpToDate.* *Money paid to institution.

REFERENCES

- Henninger N, Lin E, Haussen DC, et al. **Leukoaraiosis and sex predict the hyperacute ischemic core volume.** *Stroke* 2013;44:61–67 CrossRef Medline
- Ay H, Arsava EM, Rosand J, et al. **Severity of leukoaraiosis and susceptibility to infarct growth in acute stroke.** *Stroke* 2008;39:1409–13 CrossRef Medline
- Arsava EM, Rahman R, Rosand J, et al. **Severity of leukoaraiosis correlates with clinical outcome after ischemic stroke.** *Neurology* 2009;72:1403–10 CrossRef Medline
- Henninger N, Lin E, Baker SP, et al. **Leukoaraiosis predicts poor 90-day outcome after acute large cerebral artery occlusion.** *Cerebrovasc Dis* 2012;33:525–31 CrossRef Medline
- Kissela B, Lindsell CJ, Kleindorfer D, et al. **Clinical prediction of functional outcome after ischemic stroke: the surprising importance of periventricular white matter disease and race.** *Stroke* 2009;40:530–56 CrossRef Medline
- Schirmer MD, Dalca AV, Sridharan R, et al. **White matter hyperintensity quantification in large-scale clinical acute ischemic stroke cohorts: the MRI-GENIE study.** *Neuroimage Clin* 2019;23:101884 CrossRef Medline
- Khan M, Heiser H, Bernicchi N, et al. **Leukoaraiosis predicts short-term cognitive but not motor recovery in ischemic stroke patients during rehabilitation.** *J Stroke Cerebrovasc Dis* 2019;28:1597–603 CrossRef Medline
- de Groot M, Verhaaren BFJ, de Boer R, et al. **Changes in normal-appearing white matter precede development of white matter lesions.** *Stroke* 2013;44:1037–42 CrossRef Medline
- Vernooij MW, Ikram MA, Vrooman HA, et al. **White matter microstructural integrity and cognitive function in a general elderly population.** *Arch Gen Psychiatry* 2009;66:545–53 CrossRef Medline
- Sorensen AG, Wu O, Copen WA, et al. **Human acute cerebral ischemia: detection of changes in water diffusion anisotropy by using MR imaging.** *Radiology* 1999;212:785–92 CrossRef Medline
- Dacosta-Aguayo R, Graña M, Fernández-Andújar M, et al. **Structural integrity of the contralesional hemisphere predicts cognitive impairment in ischemic stroke at three months.** *PLoS One* 2014;9:e86119 CrossRef Medline
- Etherton MR, Wu O, Cougo P, et al. **Integrity of normal-appearing white matter and functional outcomes after acute ischemic stroke.** *Neurology* 2017;88:1701–08 CrossRef Medline
- Etherton MR, Wu O, Giese AK, et al. **White matter integrity and early outcomes after acute ischemic stroke.** *Transl Stroke Res* 2019;10:630–38 CrossRef Medline
- Zuo LJ, Li ZX, Zhu RY, et al. **The relationship between cerebral white matter integrity and cognitive function in mild stroke with basal ganglia region infarcts.** *Sci Rep* 2018;8:8422 CrossRef Medline
- Zamboni G, Griffanti L, Mazziucco S, et al. **Age-dependent association of white matter abnormality with cognition after TIA or minor stroke.** *Neurology* 2019;93:e272–82 CrossRef Medline
- Demeurisse G, Demol O, Robaye E. **Motor evaluation in vascular hemiplegia.** *Eur Neurol* 1980;19:382–89 CrossRef Medline
- Brott T, Adams HP Jr, Olinger CP, et al. **Measurements of acute cerebral infarction: a clinical examination scale.** *Stroke* 1989;20:864–70 CrossRef Medline

18. Smith SM, Jenkinson M, Woolrich MW, et al. **Advances in functional and structural MR image analysis and implementation as FSL.** *Neuroimage* 2004;23: S208–19 CrossRef Medline
19. Manjon JV, Coupé P, Martí-Bonmatí L, et al. **Adaptive non-local means denoising of MR images with spatially varying noise levels.** *J Magn Reson Imaging* 2010;31:192–203 CrossRef Medline
20. Lin C, Sangha R, Lee J, et al. **Infarct location is associated with quality of life after mild ischemic stroke.** *Stroke* 2018;13:824–31 CrossRef Medline
21. Smith SM, Jenkinson M, Johansen-Berg H, et al. **Tract-based spatial statistics: voxelwise analysis of multi-subject diffusion data.** *Neuroimage* 2006;31:1487–505 CrossRef Medline
22. Mori S, Oishi K, Jiang H, et al. **Stereotaxic white matter atlas based on diffusion tensor imaging in an ICBM template.** *Neuroimage* 2008;40:570–82 CrossRef Medline
23. Oishi K, Zilles K, Amunts K, et al. **Human brain white matter atlas: identification and assignment of common anatomical structures in superficial white matter.** *Neuroimage* 2008;43:447–57 CrossRef Medline
24. Hua K, Zhang J, Wakana S, et al. **Tract probability maps in stereotaxic spaces: analyses of white matter anatomy and tract-specific quantification.** *Neuroimage* 2008;39:336–47 CrossRef Medline
25. Smith SM, Nichols TE. **Threshold-free cluster enhancement: addressing problems of smoothing, threshold dependence and localisation in cluster inference.** *Neuroimage* 2009;44:83–98 CrossRef Medline
26. Gong G, Jiang T, Zhu C, et al. **Asymmetry analysis of cingulum based on scale-invariant parameterization by diffusion tensor imaging.** *Hum Brain Mapp* 2005;24:92–98 CrossRef Medline
27. Debette S, Markus HS. **The clinical importance of white matter hyperintensities on brain magnetic resonance imaging: systematic review and meta-analysis.** *BMJ* 2010;341:c3666 CrossRef Medline
28. Basser PJ, Mattiello J, LeBihan D. **Estimation of the effective self-diffusion tensor from the NMR spin echo.** *J Magn Reson B* 1994; 103:247–54 CrossRef Medline
29. Basser PJ, Mattiello J, LeBihan D. **MR diffusion tensor spectroscopy and imaging.** *Biophys J* 1994;66:259–67 CrossRef Medline
30. Stinear CM, Byblow WD, Ackerley SJ, et al. **A biomarker-based algorithm for predicting upper limb function after stroke.** *Ann Clin Transl Neurol* 2017;4:811–20 CrossRef Medline
31. Reeves M, Khoury J, Alwell K, et al. **Distribution of National Institutes of Health stroke scale in the Cincinnati/Northern Kentucky stroke study.** *Stroke* 2013;44: 3211–13 CrossRef Medline

Microstructural Integrity of Salvaged Penumbra after Mechanical Thrombectomy

M.T. Berndt, C. Maegerlein, T. Boeckh-Behrens, S. Wunderlich, C. Zimmer, S. Wirth, F.G. Mück, S. Mönch, B. Friedrich, and J. Kaesmacher



ABSTRACT

BACKGROUND AND PURPOSE: There are sparse data on the microstructural integrity of salvaged penumbral tissue after mechanical thrombectomy of large-vessel occlusions. The aim of the study was to analyze possible microstructural alteration in the penumbra and their association with clinical symptoms as well as angiographic reperfusion success in patients undergoing mechanical thrombectomy.

MATERIALS AND METHODS: All patients who underwent mechanical thrombectomy for large-vessel occlusions in the anterior circulation and who received an admission CT perfusion together with postinterventional DTIs were included ($n = 65$). Angiographic reperfusion success by means of modified Thrombolysis in Cerebral Infarction (mTICI) scale and clinical outcome were recorded. Microstructural integrity was assessed by DTI evaluating the mean diffusivity index within the salvaged gray matter of the former penumbra.

RESULTS: The mean diffusivity index was higher in completely recanalized patients (mTICI 3: -0.001 ± 0.034 versus mTICI <3 : -0.030 ± 0.055 , $P = .03$). There was a positive correlation between the mean diffusivity index and NIHSS score improvement ($r = 0.49$, $P = .003$) and the mean diffusivity index was associated with midterm functional outcome ($r = -0.37$, $P = .04$) after adjustment for confounders. In mediation analysis, the mean diffusivity index and infarction growth mediated the association between reperfusion success and clinical outcomes.

CONCLUSIONS: The macroscopic salvaged penumbra included areas of microstructural integrity changes, most likely related to the initial hypoperfusion. These abnormalities were found early after mechanical thrombectomy, were dependent on angiographic results, and correlated with the clinical outcome. When confirmed, these findings prompt the evaluation of therapies for protection of the penumbral tissue integrity.

ABBREVIATIONS: IQR = interquartile range; LVO = large-vessel occlusion; MD = mean diffusivity; MT = mechanical thrombectomy; SD = standard deviation; mTICI = modified Thrombolysis in Cerebral Infarction; mRS = modified Rankin Scale; NIHSS = National Institutes of Health Stroke Scale

Mechanical thrombectomy (MT) has emerged as the standard of care for patients who present with anterior circulation large-vessel occlusions (LVO).¹⁻⁷ MT is associated with high reperfusion rates and reduces the final infarct volume as opposed to medical treatment alone. However, the benefit of MT may not be fully explained by a mere reduction of the final infarct volume. Previous analyses have suggested that microstructural alterations also occur in hypoperfused areas, which do not undergo final

infarction, as evidenced by conventional macrostructural DWI ("salvaged penumbra").⁸⁻¹⁰ If microstructural changes of the salvaged penumbra occur after MT is currently unknown. The aim of this analysis was to assess the occurrence of microstructural changes in the salvaged gray matter in patients undergoing MT by using postinterventional DTI. Secondary aims included the assessment of a potential relationship between microstructural changes, angiographic reperfusion success, and clinical outcomes.

Received July 10, 2019; accepted after revision October 24.

From the Departments of Neuroradiology (M.T.B., C.M., T.B.-B., C.Z., S.M., B.F.), and Neurology (S.W.), Klinikum rechts der Isar, School of Medicine, Technical University of Munich, Munich, Germany; Department of Radiology (S.W., F.G.M.), Donauis Hospital, Deggendorf, Germany; and Department of Neuroradiology (J.K.), Inselspital, University Hospital Bern, University Bern, Bern, Switzerland.

*B. Friedrich and J. Kaesmacher contributed equally to this work.

Work originated from Department of Neuroradiology, Klinikum rechts der Isar, School of Medicine, Technical University of Munich, Munich, Germany.

Please address correspondence to Maria Berndt, MD, Department of Neuroradiology, Klinikum rechts der Isar, School of Medicine, Technical University of Munich, Ismaninger Str. 22, 81675 Munich, Germany; e-mail: maria.berndt@tum.de.



Indicates article with supplemental on-line appendix.

<http://dx.doi.org/10.3174/ajnr.A6364>

MATERIALS AND METHODS

Sample and Patient Description

All patients included in a prospective stroke registry of a single comprehensive stroke center and treated with MT between April 2016 and December 2018 were reviewed. Four-hundred-thirty-nine patients with ischemic stroke presented with an LVO of the anterior circulation (MCA or carotid-T). Patients were included if they had postinterventional MR imaging, including DTI and structural 3D T1WI ($n = 192$). Patients with motion artifacts ($n = 20$) or space-occupying malignant infarction were excluded ($n = 7$). From the remaining 165 patients, 65 patients received quality-sufficient CT perfusion imaging on admission. Prospectively collected baseline demographic, clinical, and interventional data were extracted from the registry. Board-certified neurologists assessed NIHSS scores on admission and at the time of MR imaging acquisition. The functional outcome was evaluated by applying the modified Rankin Scale (mRS) 90 days after admission, either on a routinely scheduled clinical visit or by a structured telephone interview. This study was approved by the local ethics committee, and the need for patient consent was waived.

Angiographic Data

The modified Thrombolysis in Cerebral Infarction (mTICI) score¹¹ was determined by 2 experienced neuro-interventionalists in consensus (C.M., B.F.). Complete reperfusion was defined as mTICI 3. The time of groin puncture, time of reperfusion, and corresponding procedure times were extracted from the data base. The time elapsed between groin puncture to reperfusion is referred to as reperfusion time. If no successful recanalization was achieved (mTICI < 2b), then the control series after the last maneuver was used as the time point of procedure termination.

Assessment of the Penumbra in Admission CT Imaging

Standard nonhelical cerebral CT was performed on a 64-row CT scanner equipped with a 40-mm detector (Brilliance 64, Philips Healthcare, Best, the Netherlands). The scanner was calibrated weekly by air calibration and regularly by using phantom scans (CT calibration phantom; Mindways Software, Austin, Texas). Besides noncontrast images and CT angiography, a perfusion image was acquired by using the following parameters: 120 kV, 400 mAs, with 5-mm section thickness. A dual-head power injector (Medrad, Indianola, Pennsylvania) with an 18-gauge IV access was used for contrast injection. A delay of 5 seconds was applied after injecting 40 mL Imeron (400 mg I/mL Imeron 350, iomeprol; Bracco, Milan, Italy) at a flow rate of 6 mL/s, followed by 90 mL NaCl. For postprocessing of the acquired CT perfusion images, RAPID (iSchemaView, Stanford, California) was used. This software is an operator-independent fully automated image processing and visualization tool, and allows on-line estimation of perfusion maps and mismatch masks.¹² These maps were verified by a neuroradiologist (M.T.B.) with 3 years of experience. For assessing penumbral tissue, the individual hypoperfusion mask was extracted. With this, the hypoperfused tissue was estimated at threshold values

of Tmax delay of >6 seconds and the admission infarct core was estimated at threshold values of relative CBF < 30%.¹²⁻¹⁴

Assessment of Microstructural Changes Within the Penumbra

For analyses of microstructural tissue integrity within the above-identified penumbral tissue, an MR imaging examination was acquired in the acute poststroke phase, including DTI and structural T1WI. These data were postprocessed, coaligned with admission CT perfusion imaging, and analyzed with respect to microstructural tissue alterations within the salvaged penumbra by using the mean diffusivity (MD) index for gray matter. The salvaged penumbra was defined as formerly hypoperfused tissue in CT perfusion imaging, which, in the end, did not show visible infarction, which was semiautomatically segmented in MR imaging (Fig 1). A detailed methodologic description is found in the On-line Appendix.

Statistical Analysis

The mean value comparison of the MD index and infarction growth was performed by means of a 2-sample *t*-test for independent samples. Wilcoxon rank sum tests were used for comparison of the NIHSS scores and mRS values between the different reperfusion groups.

To test the association of the MD index and infarction growth with the NIHSS score (at the MR imaging date and the percentage improvement compared with admission) as well as with midterm functional outcome (mRS after 90 days), the following statistical procedures were applied. After performing linear regression to get residuals of the MD index/infarction growth (corrected for age, sex, time between recanalization and MR imaging scan, reperfusion time, admission infarct core), the Spearman rank bivariate correlation was performed between residuals of the MD index/infarction growth and the NIHSS score at the time of MR imaging as well as percentage improvement of the NIHSS score between admission and time of MR imaging and mRS at 90 days. In a second analysis, new residuals of the MD index that additionally control for infarction growth were calculated and used for Spearman rank bivariate correlation analyses with clinical outcome parameters.

In a mediation model, reperfusion success, measured by the mTICI score and dichotomized into complete and incomplete, was entered as the causal variable; percentage improvement of the NIHSS score between admission and the time of MR imaging as the outcome variable; and infarction growth and the MD index as mediator variables. The analysis was corrected for age, sex, and the time between recanalization and MR imaging by calculating residuals of infarction growth and the MD index by using linear regression. Path coefficients were estimated by using unstandardized regression coefficients of multiple regression analyses. Statistical significance of the indirect pathway, which reflects the impact of mediation, was evaluated by using a nonparametric bootstrap approach with 10,000 replication samples to obtain a 95% CI.^{15,16} All statistical analyses were performed by using SPSS Statistics, version 25 (IBM, Armonk, New York).

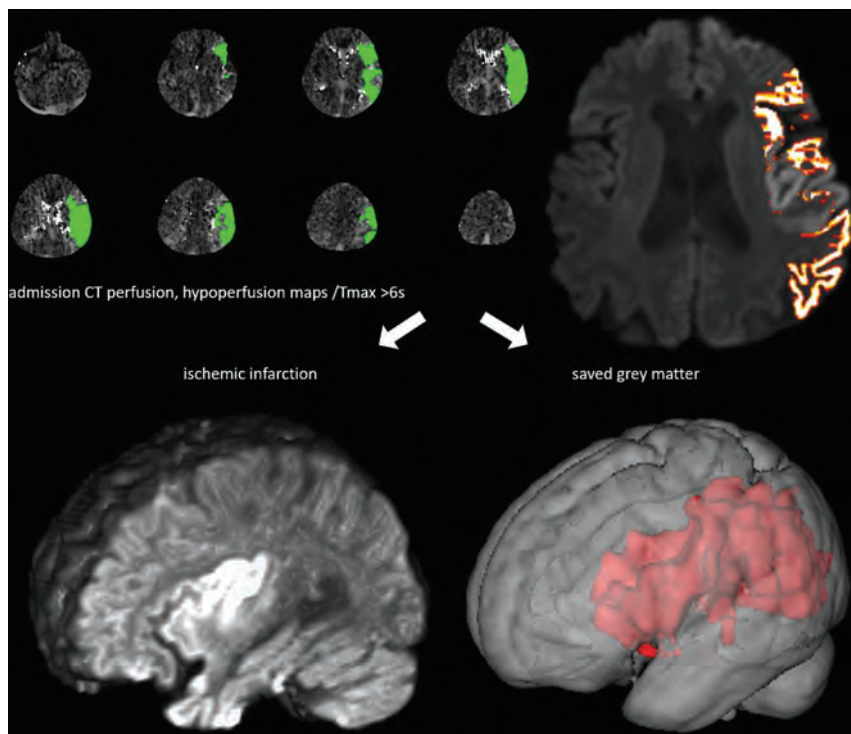


FIG 1. The tissue at risk (penumbra) in admission CT perfusion imaging (maps generated by RAPID software) was co-registered to MR imaging, including the DTI sequence, within 3 days after MT of acute occlusions of the anterior circulation. Penumbra was classified in ischemic infarction, segmented in DWI, and salvaged gray matter, which was further analyzed in respect to microstructural changes by calculation of the MD index in DTI (illustrations made by Mango [ric.uthscsa.edu/mango] and 3DSlicer [slicer.org]) (Reproduced with permission from Springer Nature <https://doi.org/10.1007/s00062-019-00826-9>).

Basic demographic, clinical, and interventional data as well as the volume of infarction, admission infarct core, and infarction growth of the final study cohort

Patient Characteristics	N = 65
Age, median (IQR), y	75 (63–83)
Males/females, n (%)	31 (48)/34 (52)
Interventional parameters (time), median (IQR)	
Groin puncture to recanalization, min	26 (20–41)
Symptom onset to recanalization, min	199 (144–310)
No. maneuvers	1 (1–2.5)
mTICI score, n	
0	2
2a	2
2b	22
3	39
Additional IV thrombolysis, n	27
NIHSS score, median (IQR)	
Pretreatment	12 (6–17)
Time of MR imaging acquisition	2 (0–5)
Percentage improvement pretreatment to time of MR imaging	0.8 (0.49–1)
Modified Rankin Scale (after 90 days) (n = 52)	
0–2	33
>2	19
Time between recanalization and MR imaging acquisition, median (IQR), days	3 (3–4)
Volume of infarction, mean \pm SD, mL	28.8 \pm 48.8
Admission infarct core, mean \pm SD, mL	14.3 \pm 24.9
Infarction growth, mean \pm SD, mL	16.9 \pm 34.6

RESULTS

Patient Characteristics

Sixty-five patients were included (median age, 75 years; 52% female). Patients presented with severe symptoms (median [interquartile range {IQR}] NIHSS score, 12 [6–17]) and postinterventional MR imaging was scheduled at a median (IQR) of 3 days (3–4 days) after reperfusion. Most of the patients ($n = 39/65$, 60%) had complete reperfusion (mTICI 3), whereas only 4 patients (6.2%) were unsuccessfully recanalized (mTICI < 2b). Further details can be found in the Table.

Microstructural Changes of the Salvaged Penumbra

For the whole study cohort, the MD index of the salvaged penumbra showed mainly negative values (mean \pm standard deviation [SD], -0.013 ± 0.046). The MD index was higher in patients with complete reperfusion (mean \pm SD, -0.001 ± 0.034 versus -0.030 ± 0.055 , $P = .03$ for mTICI 3 versus mTICI 0–2b). A higher MD index means a smaller decrease of MD values within the salvaged gray matter in comparison with the contralateral side.

Association of Micro- and Macrostructural Changes to the Clinical Outcome

The following analyses showed the association of studied microstructural changes in the salvaged penumbra as well as infarction growth with clinical parameters: a significant negative correlation was found between the MD index and the NIHSS score at the time of MR imaging ($r = -0.43$, $P = .01$) and mRS after 90 days ($r = -0.37$, $P = .04$). A significant positive correlation was found between the MD index and percentage improvement of the NIHSS score between admission and the time of MR imaging ($r = 0.49$, $P = .003$). A significant positive correlation was found between infarction growth and the NIHSS score at the time of MR imaging ($r = 0.34$, $P = .05$) and mRS after 90 days ($r = 0.43$, $P = .02$). A significant negative correlation was found between the infarction growth and the percentage improvement of NIHSS scores between admission and the time of MR imaging ($r = -0.409$, $P = .02$).

After controlling for infarction growth, the MD index was negatively correlated with the NIHSS score at the time of MR imaging ($r = -0.28$, $P = .11$) and mRS after 90 days ($r = -0.35$, $P = .05$) and positively correlated with percentage improvement of the NIHSS score between admission and the time of MR imaging ($r = 0.37$, $P = .03$). All analyses were corrected for the above-mentioned covariates under the precondition of complete

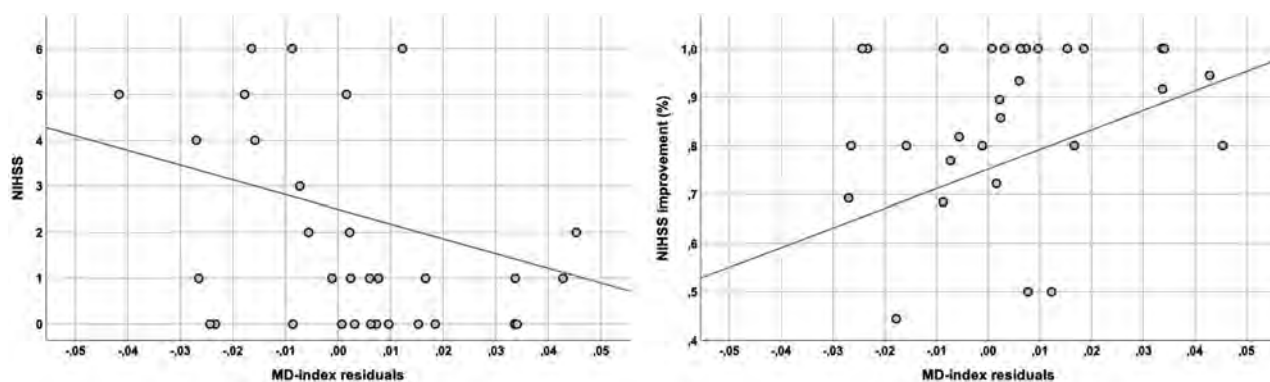


FIG 2. Graphs show the association of microstructural changes (measured by the MD index) with clinical outcome for all the patients who were completely recanalized. The MD index residuals (corrected for age, sex, time between recanalization and MR imaging, reperfusion time, admission infarct core) are negatively correlated to the NIHSS score at the time of MR imaging and positively correlated to percentage improvement of the NIHSS score between admission and the time of MR imaging.

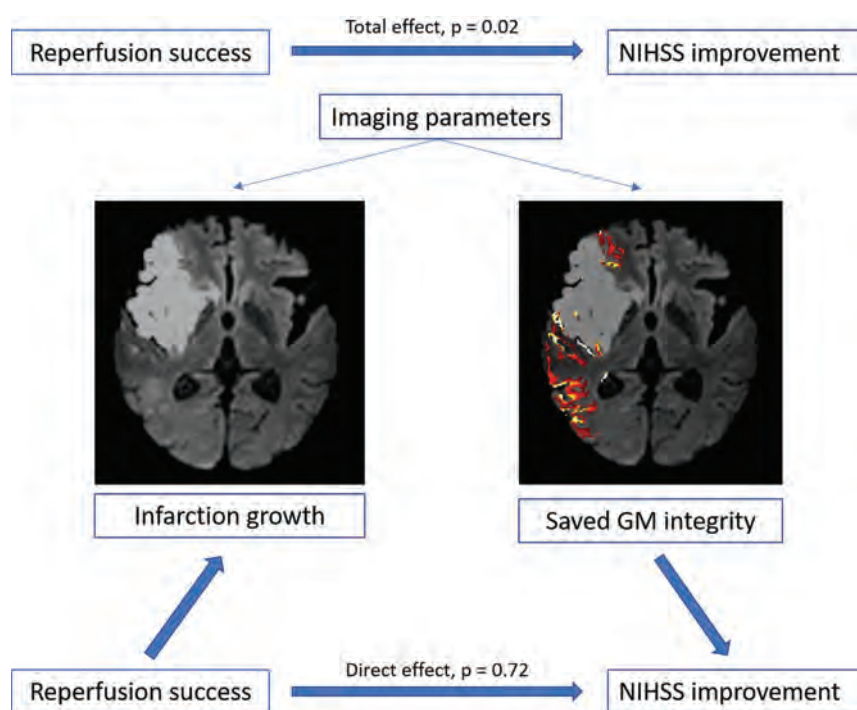


FIG 3. Imaging parameters, such as infarction growth and gray matter integrity of the saved tissue (measured by the MD index of the DTI within 3 days after MT of acute occlusions of the anterior circulation), significantly mediate the effect of reperfusion success (measured by mTICI) on the clinical presentation (measured by percentage improvement of the NIHSS score); the covariates age, sex, and time between recanalization and MR imaging showed no significant influence in the analysis (Reproduced with permission from Springer Nature <https://doi.org/10.1007/s00062-019-00826-9>).

reperfusion. The association between the MD index and the NIHSS score as well as NIHSS score improvement are shown in Fig 2.

Impact of Tissue Integrity on the Relationship between Complete Reperfusion and Clinical Outcome

The percentage improvement of the NIHSS scores between admission and the time of MR imaging differed significantly between the subgroups of complete reperfusion (mTICI 3: median [IQR] 0.9 [0.7–1]) and incomplete reperfusion (mTICI 0–2:

median [IQR] 0.47 [0.24–0.87], $P = .02$). In addition, an association between reperfusion success and imaging parameters, for example, the MD index, was found ($P = .03$) (see the section Results: Microstructural Changes of the Salvaged Penumbra). The mean \pm SD volume of infarction growth also showed significantly different values, depending on the reperfusion success (28.4 ± 48.9 mL for incomplete and 9.24 ± 17.0 mL for complete reperfusion, $P = .03$).

In a mediation analysis (Fig 3), the effect of reperfusion success (measured by mTICI) on the clinical presentation (measured by percentage improvement of the NIHSS score between admission and the time of MR imaging) (total effect $c = 0.22$, $SE = 0.09$, $P = .02$) was absent when controlling for imaging parameters such as infarction growth and the MD index (direct effect $c' = 0.03$, $SE = 0.08$, $P = .72$); critically, the bootstrapped 95% CI for the indirect effect (ie, mediation: total – direct effect) was different from zero for the mediator variable infarction growth (95% CI, 0.04–0.22) as well as for the MD

index (95% CI, 0.004–0.19) under consideration of the covariates, which indicated that both imaging parameters significantly mediated the relationship between reperfusion success and clinical improvement.

DISCUSSION

The present study shows that the macroscopic salvaged penumbra after MT includes areas of microstructural integrity changes related to the preceding hypoperfusion. The existence of

microstructural integrity alterations was evaluated by using tissue integrity measurements by assessing diffusion parameters, such as the MD in a sample of 65 patients early after MT of an LVO of the anterior circulation. Compared with the contralateral side, a relative decrease of gray matter MD values within the salvaged penumbra was found. There was an explicit dependency on reperfusion success, which suggests that incomplete reperfusion results in further tissue abnormalities beyond macrostructural ischemia. Microstructural changes in the salvaged penumbra were further associated with neurologic and functional deficits, underlining their potential clinical importance.

The salvaged penumbra was identified by applying a co-registration process between DTIs in the acute poststroke phase and admission CT perfusion images, which visualize the tissue at risk. This penumbral tissue was assessed via RAPID software, which has been used in numerous studies.^{2,3,17,18} Penumbral tissue, which did not undergo final infarction in poststroke DTIs, was defined as the salvaged penumbra. Previous analyses have suggested that microstructural alterations also occur in the salvaged penumbra,⁸⁻¹⁰ which was affirmed in the present structural imaging study.

The MD alterations found in the acute poststroke phase with lowered values in the gray matter suggest cytotoxic-like processes with a decrease of the MD but on the microstructural, not the apparent level.¹⁹ As a result of this, assessing the cortical MD asymmetry compared with the contralateral nonaffected hemisphere has the potential to detect changes of the molecular diffusion rate, which can be affected by subtle integrity alterations.²⁰ The asymmetry index was already used in several previous DTI studies, mostly in the context of FA (fractional anisotropy) calculations, and appeared as an accessible predictor variable.²¹⁻²³ MD loss within the salvaged penumbra that was temporarily undersupplied could either be a consequence of the primary ischemic processes when the tissue was at risk (eg, microembolization) or could arise out of ischemic reperfusion, which could exacerbate a primary ischemic injury. Results of studies with animal models found diffusion restriction early after stroke within the reversible penumbra similar to the findings in the present study in humans, and the studies discuss the phenomenon of reperfusion injury extensively.²⁴

The observed “secondary deterioration” of diffusivity could be explained by a secondary energy failure after reperfusion,^{25,26} but the pathophysiological mechanism and processes of reperfusion injury are not yet conclusively clarified in humans. Existing pathophysiologic concepts explain the loss of diffusivity by a decline in extracellular water induced by a water shift from extracellular to intracellular space. This shift comes from cell depolarization because of a failure of adenosine triphosphate (ATP)-dependent pumps, which ATP levels are deteriorated by the over-release of toxic intermediates in reperfusion injury.^{24,27-29} Despite the underlying processes that cause such an observed integrity change in the salvaged penumbra, these alterations may be substantial with concern for technical, procedural, or clinical aspects.

A theoretic attempted explanation of microstructural changes of the salvaged penumbra would relate to clot fragmentation and distal microemboli, which occur within previously unaffected

vascular territories as well as within the occlusion-dependent brain tissue during mechanical recanalization. Thus, the penumbral tissue would be less affected by lessening microembolic damage during recanalization. This explanation would fit the above-mentioned theory of primary ischemic processes as a reason for MD loss caused by microembolization into the penumbral tissue. It encourages the usage of proximal flow arrest during mechanical recanalization, which was recently recommended by reporting improved procedural, angiographic, and clinical outcomes.³⁰

The study results show a relationship between the MD values of the penumbral tissue and the clinical presentation at the time of MR imaging acquisition with a loss of MD correlated to a more significant concern measured by the NIHSS score. It is also associated with less percentage improvement of the NIHSS score between admission and the time of MR imaging and higher mRS after 90 days. Thus, MD loss has a negative association with the clinical presentation measured in the present study within the clinical workflow. Consequently, effort should be invested to minimize penumbral integrity changes within the therapeutic setting of an LVO.

A focus should be on gaining complete reperfusion because this is associated with a better clinical outcome as well as a reduced infarction growth and a better-preserved penumbral integrity as shown in the present study. By performing a mediation analysis on the relationship between reperfusion success and clinical outcome, imaging parameters of the acute poststroke phase, such as the infarction growth as well as the penumbral integrity, turned out to be significant mediators. By the disappearance of this known relationship, such imaging parameters gain importance because they can explain the impact of recanalization on clinical outcome, which again raises the meaningfulness of applying procedures with the aim of complete reperfusion and less macro- and microstructural tissue damage.

However, it is important to discuss that the observed microstructural integrity changes within the penumbra are measured at a single time within the acute poststroke phase. Reversibility of these abnormalities, which are well known even for macrostructural diffusion restrictions, was not proved. The results present microstructural diffusion restrictions within the penumbra, which is most probably based on the primary ischemic process and influenced by the therapeutic intervention (which was shown for reperfusion success). Follow-up imaging is required to examine reversibility, which was not the content of the present study. The first evidence of sustainable changes in terms of permanent damage could be derived from the existing association between microstructural penumbral changes and midterm functional outcome.

With regard to methodologic aspects, the analyses of tissue alterations were restricted to the gray matter and analyzing white matter integrity was not the content of the present study. By constructing the methodologies like this, the following aspects were considered: during ischemic processes, gray matter is more sensible to infarction, determined by the ischemic time, than white matter, which is secondarily dependent on the related gray matter in respect to processes like early disintegration. Thus, measuring the processes within the gray matter may reflect the ischemic processes more accurately and have an impact on further progressions, such as degeneration, which is important for the

clinical outcome. However, studying white matter integrity by using fiber-tracking should be considered in further studies, which would, additionally, gain importance by creating a longitudinal approach.

CONCLUSIONS

The macroscopic salvaged penumbra included areas of microstructural integrity changes early after MT of an LVO in the anterior circulation. Penumbra microstructural integrity seemed to be dependent on recanalization success and was associated with clinical outcome. If confirmed, it harbors another rationale for further development of procedural processes of MT, with the aim for complete reperfusion, less ischemic macro- and microstructural injury, and, as a result of this, a better clinical outcome. The method used in this work enables the early consideration of the outcome on the microstructural level beyond the classic clinical scores.

Disclosures: Johannes Kaesmacher—UNRELATED: Grants/Grants Pending: SAMW Bangerter Foundation*; Travel/Accommodations/Meeting Expenses Unrelated to Activities Listed: Stryker.* Benjamin Friedrich—UNRELATED: Consultancy: Stryker, Medtronic; Grants/Grants Pending: iSchemaView. Stefan Wirth—UNRELATED: Board Membership: Past president of the European Society of Emergency Radiology. Comments: money paid to individual. The ESER Board Membership did not influence the submitted manuscript in any way; Travel/Accommodations/Meeting Expenses Unrelated to Activities Listed: PPC meeting hotel costs, Comments: The European Society took over hotel costs that were related with a stay in Vienna to participate at the Programm Planning Committee for the ESR Congress 2020. Costs <1000 Euro. There is no connection to the submitted work. Claus Zimmer—UNRELATED: Board Membership: Scientific advisory boards for Philips and Bayer Schering; Grants/Grants Pending: Claus Zimmer disclosed no relevant relationships with regard to activities related to the present article. The institution has received research support and investigator fees for clinical studies from Biogen Idec, Quintiles, MSD Sharp and Dome, Boehringer Ingelheim, Inventive Health Clinical UK Ltd., Advance Cor, Brainsgate, Pfizer, Bayer-Schering, Novartis, Roche, Servier, Penumbra, WCT GmbH, Syngis, SSS International Clinical Research, PPD Germany GmbH, Worldwide Clinical Trials Ltd., Phenox, Covidien, Actelion, Medivation, Medtronic, Harrison Clinical Research, Concentric, Pharmtrace, Reverse Medical Corp., Premier Research Germany Ltd., Surpass Medical Ltd., GlaxoSmithKline, AXON Neuroscience, Bristol-Myers Squibb, Genentech, Acandis, Eisai, NeuroRx, Italfarmaco, Bioclinica, MIAC, and IXICO. No patents issued and pending*. Payment for Lectures, Including Service on Speakers Bureaus: Speaker honoraria from Bayer Schering and Philips. *Money paid to the institution.











REFERENCES

- Goyal M, Demchuk AM, Menon BK, et al. **Randomized assessment of rapid endovascular treatment of ischemic stroke.** *N Engl J Med* 2015;372:1019–30 CrossRef Medline
- Saver JL, Goyal M, Bonafe A, et al. **Stent-retriever thrombectomy after intravenous t-PA vs. t-PA alone in stroke.** *N Engl J Med* 2015;372:2285–95 CrossRef Medline
- Campbell BC, Mitchell PJ, Kleinig TJ, et al. **Endovascular therapy for ischemic stroke with perfusion-imaging selection.** *N Engl J Med* 2015;372:1009–18 CrossRef Medline
- Jovin TG, Chamorro A, Cobo E, et al. **Thrombectomy within 8 hours after symptom onset in ischemic stroke.** *N Engl J Med* 2015;372:2296–306 CrossRef Medline
- Berkhemer OA, Fransen PS, Beumer D, et al. **A randomized trial of intraarterial treatment for acute ischemic stroke.** *N Engl J Med* 2015;372:11–20 CrossRef Medline
- Muir KW, Ford GA, Messow CM, et al. **Endovascular therapy for acute ischaemic stroke: the Pragmatic Ischaemic Stroke Thrombectomy Evaluation (PISTE) randomised, controlled trial.** *J Neurol Neurosurg Psychiatry* 2017;88:38–44 CrossRef Medline
- Bracard S, Ducrocq X, Mas JL, et al. **Mechanical thrombectomy after intravenous alteplase versus alteplase alone after stroke**

- (THRACE): a randomised controlled trial. *Lancet Neurol* 2016;15:1138–47 CrossRef Medline
- del Zoppo GJ, Sharp FR, Heiss WD, et al. **Heterogeneity in the penumbra.** *J Cereb Blood Flow Metab* 2011;31:1836–51 CrossRef Medline
- Zhu LH, Zhang ZP, Wang FN, et al. **Diffusion kurtosis imaging of microstructural changes in brain tissue affected by acute ischemic stroke in different locations.** *Neural Regen Res* 2019;14:272–79 CrossRef Medline
- Baron CA, Kate M, Gioia L, et al. **Reduction of diffusion-weighted imaging contrast of acute ischemic stroke at short diffusion times.** *Stroke* 2015;46:2136–41 CrossRef Medline
- Zaidat OO, Yoo AJ, Khatri P, et al. **Recommendations on angiographic revascularization grading standards for acute ischemic stroke: a consensus statement.** *Stroke* 2013;44:2650–63 CrossRef Medline
- Straka M, Albers GW, Bammer R. **Real-time diffusion-perfusion mismatch analysis in acute stroke.** *J Magn Reson Imaging* 2010;32:1024–37 CrossRef Medline
- Dehkharghani S, Bammer R, Straka M, et al. **Performance and predictive value of a user-independent platform for CT perfusion analysis: threshold-derived automated systems outperform examiner-driven approaches in outcome prediction of acute ischemic stroke.** *AJNR Am J Neuroradiol* 2015;36:1419–25 CrossRef Medline
- Lansberg MG, Lee J, Christensen S, et al. **RAPID automated patient selection for reperfusion therapy: a pooled analysis of the Echoplanar Imaging Thrombolytic Evaluation Trial (EPITHE) and the Diffusion and Perfusion Imaging Evaluation for Understanding Stroke Evolution (DEFUSE) Study.** *Stroke* 2011;42:1608–14 CrossRef Medline
- Hayes AF, Rockwood NJ. **Regression-based statistical mediation and moderation analysis in clinical research: observations, recommendations, and implementation.** *Behav Res Ther* 2017;98:39–57 CrossRef Medline
- Preacher KJ, Hayes AF. **SPSS and SAS procedures for estimating indirect effects in simple mediation models.** *Behav Res Methods Instrum Comput* 2004;36:717–31 CrossRef Medline
- Nogueira RG, Jadhav AP, Haussen DC, et al. **Thrombectomy 6 to 24 hours after stroke with a mismatch between deficit and infarct.** *N Engl J Med* 2018;378:11–21 CrossRef Medline
- Albers GW, Marks MP, Kemp S, et al. **Thrombectomy for stroke at 6 to 16 hours with selection by perfusion imaging.** *N Engl J Med* 2018;378:708–18 CrossRef Medline
- van Gelderen P, de Vleeschouwer MH, DesPres D, et al. **Water diffusion and acute stroke.** *Magn Reson Med* 1994;31:154–63 CrossRef Medline
- Alexander AL, Lee JE, Lazar M, et al. **Diffusion tensor imaging of the brain.** *Neurotherapeutics* 2007;4:316–29 CrossRef Medline
- Doughty C, Wang J, Feng W, et al. **Detection and predictive value of fractional anisotropy changes of the corticospinal tract in the acute phase of a stroke.** *Stroke* 2016;47:1520–26 CrossRef Medline
- Puig J, Blasco G, Schlaug G, et al. **Diffusion tensor imaging as a prognostic biomarker for motor recovery and rehabilitation after stroke.** *Neuroradiology* 2017;59:343–51 CrossRef Medline
- Stinear CM, Barber PA, Petoe M, et al. **The PREP algorithm predicts potential for upper limb recovery after stroke.** *Brain* 2012;135:2527–35 CrossRef Medline
- Guo J, Zheng HB, Duan JC, et al. **Diffusion tensor MRI for the assessment of cerebral ischemia/reperfusion injury in the penumbra of non-human primate stroke model.** *Neurol Res* 2011;33:108–12 CrossRef Medline
- Olah L, Wecker S, Hoehn M. **Relation of apparent diffusion coefficient changes and metabolic disturbances after 1 hour of focal cerebral ischemia and at different reperfusion phases in rats.** *J Cereb Blood Flow Metab* 2001;21:430–39 CrossRef Medline
- Olah L, Wecker S, Hoehn M. **Secondary deterioration of apparent diffusion coefficient after 1-hour transient focal cerebral ischemia in rats.** *J Cereb Blood Flow Metab* 2000;20:1474–82 CrossRef Medline
- Harris NG, Zilkha E, Houseman J, et al. **The relationship between the apparent diffusion coefficient measured by**

- magnetic resonance imaging, anoxic depolarization, and glutamate efflux during experimental cerebral ischemia. *J Cereb Blood Flow Metab* 2000;20:28–36 CrossRef Medline
28. Wei J, Quast MJ. Effect of nitric oxide synthase inhibitor on a hyperglycemic rat model of reversible focal ischemia: detection of excitatory amino acids release and hydroxyl radical formation. *Brain Res* 1998;791:146–56 CrossRef Medline
 29. Rother J, de Crespigny AJ, D'Arceuil H, et al. Recovery of apparent diffusion coefficient after ischemia-induced spreading depression relates to cerebral perfusion gradient. *Stroke* 1996;27:980–86; discussion 986–87 CrossRef Medline
 30. Brinjikji W, Starke RM, Murad MH, et al. Impact of balloon guide catheter on technical and clinical outcomes: a systematic review and meta-analysis. *J Neurointerv Surg* 2018;10:335–39 CrossRef Medline

Visualization of Nigrosome 1 from the Viewpoint of Anatomic Structure

 N. Arai,  H. Kan,  M. Ogawa,  Y. Uchida,  M. Takizawa,  K. Omori,  T. Miyati,  H. Kasai,  H. Kunitomo, and  Y. Shibamoto

ABSTRACT

BACKGROUND AND PURPOSE: Parkinson disease is related to neurodegeneration and iron deposition in the substantia nigra pars compacta and nigrosome 1. However, visualization of nigrosome 1 via MR imaging is poor owing to the bilateral asymmetry, regardless of whether it is healthy. We focused on the magic angle and susceptibility effect and evaluated the anatomic slant structure of nigrosome 1 by tilting subjects' heads in the B_0 direction.

MATERIALS AND METHODS: To investigate the effectiveness of the magic angle, we tilted the volunteers' heads to the right and left in the B_0 direction or not at all for evaluating correlations between the degree of head tilting and visualization of the right nigrosome 1 and left nigrosome 1 using 3D spoiled gradient-echo sequences with multiecho acquisitions. We evaluated the susceptibility of nigrosome 1 and the local field using quantitative susceptibility mapping to assess static magnetic field inhomogeneity.

RESULTS: The heads tilted to the right and left showed significantly higher contrasts of nigrosome 1 and the substantia nigra pars compacta than the nontilted heads. No significant differences were observed in the visualization and susceptibility between the right nigrosome 1 and left nigrosome 1 for each head tilt. The effect of the magic angle was remarkable in the nontilted heads. This finding was supported by quantitative susceptibility mapping because the anatomic slant structure of nigrosome 1 was coherent between the axis of nigrosome 1 and the magic angle.

CONCLUSIONS: The asymmetric visualization of nigrosome 1 is affected by the magic angle and susceptibility. The anatomic slant structure of nigrosome 1 causes these challenges in visualization.

ABBREVIATIONS: PD = Parkinson disease; SNc = substantia nigra pars compacta

Parkinson disease (PD) is associated with major pathologic degeneration of dopaminergic neurons, mainly in the basal ganglia and especially in the substantia nigra pars compacta (SNc).¹ It has been reported that PD or other neurodegenerative disorders include iron accumulation in the SNc.^{2–6} In addition, normally, the iron load in the basal ganglia increases with age,^{7,8}

and the best indicators of physiologic aging are iron deposition in the putamen and microstructural damage and atrophy in the thalamus.¹

Increased SNc iron content generally indicates that there is dopaminergic neuronal loss. However, the degree of dopaminergic neuronal loss in PD is higher in the nigrosomes than in the other subregions of the substantia nigra with the maximum loss occurring in nigrosome 1.^{9,10} Recent studies have suggested that nigrosome 1 is the largest cluster of neurons within the nigrosomes and it is highly attenuated.¹¹ It is located in the caudal and mediolateral part of the SNc and is associated with PD.^{9,10,12–14}

From a neuroradiologic point of view, MR imaging shows nigral changes, and changes in T2* relaxation times seem to be associated with increased iron deposition in the SNc that occurs in some cases of PD. It is essential to determine which conditions affect iron deposition in nigrosome 1 because PD is closely related to neurodegeneration of the SNc and especially nigrosome 1. Nigrosome 1 has been evaluated by a combination of images obtained with a 3D spoiled gradient-echo technique and with a multiecho technique.^{11,15,16} As PD progresses, the MR imaging

Received June 29, 2019; accepted after revision October 10.

From the Department of Radiology (N.A., H. Kasai, H. Kunitomo), Nagoya City University Hospital, Nagoya, Japan; Radiological and Medical Laboratory Sciences (H. Kan), Nagoya University Graduate School of Medicine, Nagoya, Japan; Departments of Radiology (H. Kan, M.O., Y.S.), and Neurology (Y.U.), Nagoya City University Graduate School of Medical Sciences, Nagoya, Japan; Healthcare Business Unit (M.T., K.O.), Hitachi Ltd, Tokyo, Japan; and Division of Health Sciences, Graduate School of Medical Science (T.M.), Kanazawa University, Kanazawa, Japan.

The sponsor of this research is Hitachi Ltd.

Paper previously presented at: Annual Meeting of the European Congress of Radiology, March 1–5, 2017; Vienna, Austria (C-1756); and Annual Meeting of the Japanese Society of Radiological Technology, April 13–16, 2017; Yokohama, Japan.

Please address correspondence to Nobuyuki Arai, MS, Department of Radiology, Nagoya City University Hospital, 1-Kawasumi, Mizuho-cho Mizuho-ku, Nagoya, Aichi, 4678602, Japan; e-mail: rurai51@med.nagoya-cu.ac.jp

<http://dx.doi.org/10.3174/ajnr.A6338>

signals of nigrosome 1 commonly diminish; this feature reflects iron accumulation and neurodegeneration. However, the MR imaging visualization of nigrosome 1 is often poor because of the asymmetry of this cell cluster, regardless of whether nigrosome 1 is healthy. In addition, little attention has been paid to poor visualization due to asymmetry. This is important because poor visualization could result in misclassification of a healthy or abnormal nigrosome 1.

In this study, we explored the cause of nigrosome 1 being poorly visualized despite healthy conditions. We focused on the magic angle and the susceptibility effect, and we evaluated the anatomic slant structure (head tilt) of nigrosome 1 in the B₀ direction using combined multi-gradient-echo images and by tilting the subjects' heads in the B₀ direction.

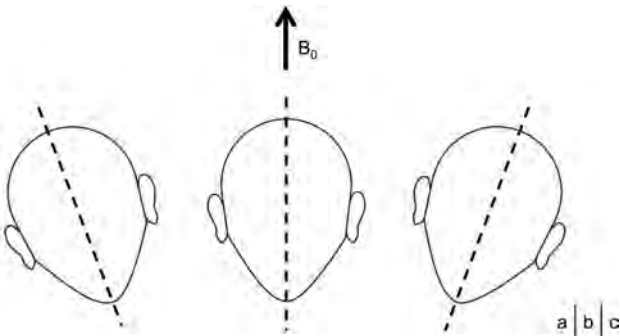


FIG 1. Volunteers' heads were held in 1 of 3 ways: tilted to the right (A), not tilted (B), and tilted to the left (C) in the B₀ direction.

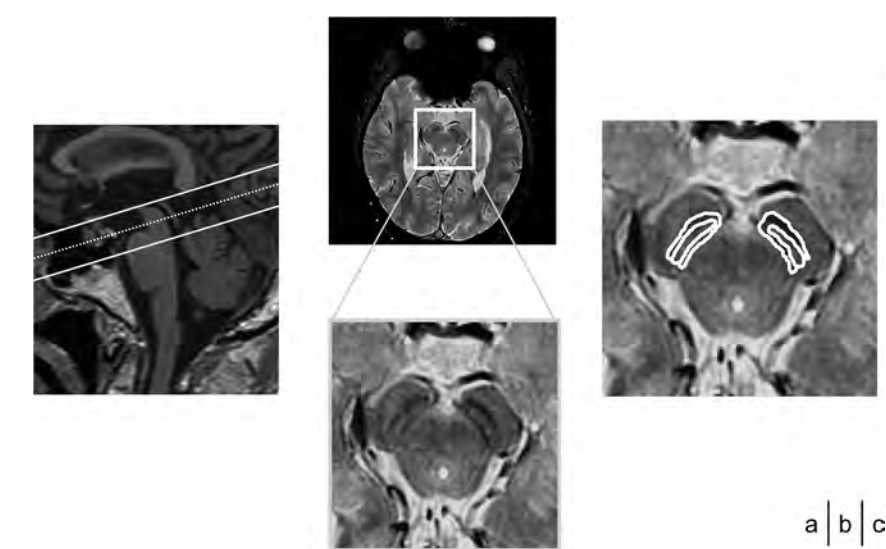


FIG 2. The 3D spoiled gradient-echo sequences with multiecho acquisitions are oriented orthogonally to the anterior midbrain (A), and nigrosome 1 is visualized in the caudal and mediolateral part of the substantia nigra pars compacta (B). When the subjects' heads were tilted to the right or left, the MR imaging signal intensities measured on the basis of the depicted ROI (C) differentiated nigrosome 1 and SNc.

MATERIALS AND METHODS

Subjects

Fourteen young healthy volunteers (3 women and 11 men; mean age, 25 years; ranging from 22 to 31 years) participated in the study. This study was approved by the institutional review board at Nagoya City University. The volunteers participated in the study of their own free will, and informed consent was obtained from all the participants.

Data Analysis

The volunteers' heads were tilted to the right (20.9° ± 5.8°) or left (18.9° ± 6.6°) in the B₀ direction or not at all, to investigate the effectiveness of the magic angle (Fig 1). The 3D spoiled gradient-echo sequences with multiecho acquisitions targeted the mid-brain and were oriented orthogonally across from the anterior midbrain (Fig 2A, -B). We evaluated the correlations between the degree of head tilting and visualization of the right nigrosome 1 and left nigrosome 1. To calculate the contrast of nigrosome 1 and the remaining SNc that was positioned around nigrosome 1 to assess its visualization, we used the following equation:

$$\text{Contrast} = \frac{SI_{n1} - SI_{\text{SNc}}}{SI_{n1} + SI_{\text{SNc}}},$$

where *SI*_{n1} and *SI*_{SNc} are the signal intensities of nigrosome 1 and SNc, respectively (Fig 2C). We calculated the SDs of the contrasts of the right nigrosome 1 and left nigrosome 1 and the SNc for each head tilt, to evaluate the reproducibility of contrast measurement. The contrast was measured 6 times in 1 volunteer using

right head tilting and left head tilting. We used ImageJ 1.48 image-processing software (National Institutes of Health, Bethesda, Maryland) to analyze the images.

In addition, we evaluated the susceptibility of nigrosome 1 and the local field using quantitative susceptibility mapping^{16,17} to assess the visualization of nigrosome 1 changed by the phase modulation due to the dipole effect.¹⁸⁻²⁰ To estimate the tissue-generated local field map and the susceptibility map, we used the multi-spoiled gradient-echo sequence in healthy volunteers. First, the local field map was estimated from the acquired multiphase images by means of sophisticated harmonic artifact reduction using the phase data method with variable kernel sizes from 0.75 at the boundary of the brain to 30 mm toward the

Table 1: Number of visualizations of discriminable nigrosome 1 when the subjects' heads were tilted in the B₀ direction (n = 14)

Tilting Head in B ₀ Direction Nigrosome 1	Right		None		Left	
	Right	Left	Right	Left	Right	Left
Discriminable nigrosome 1 (No.)	9	9	6	5	10	11

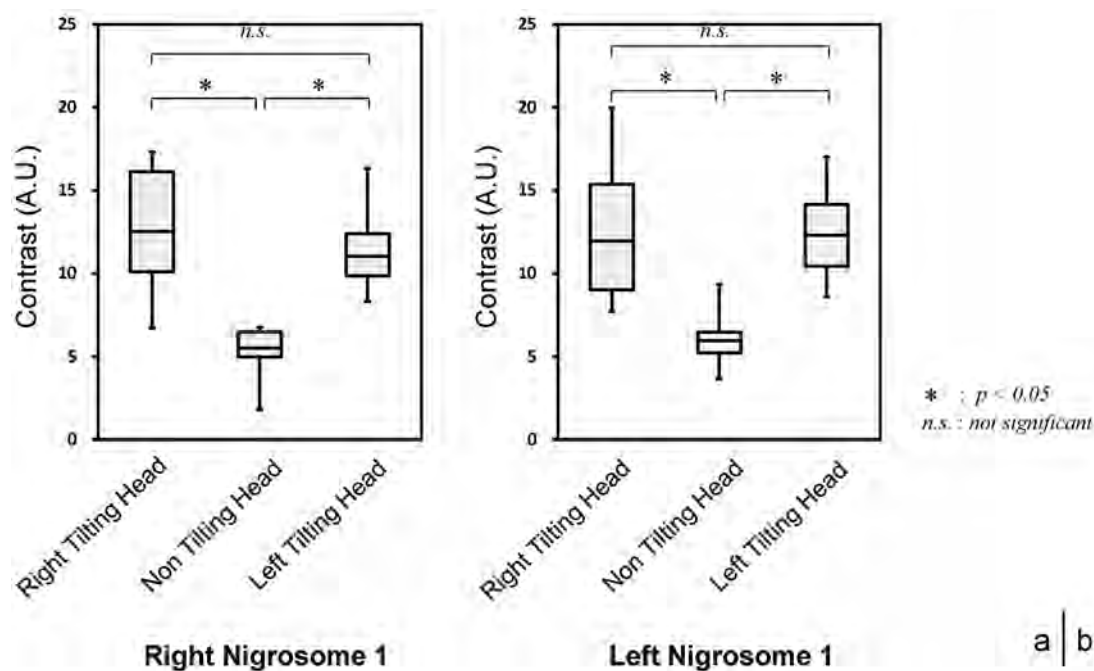


FIG 3. Visualization of the right (A) and left (B) nigrosome 1, in which the volunteers' heads were tilted to the right or left in the B_0 direction or not at all.

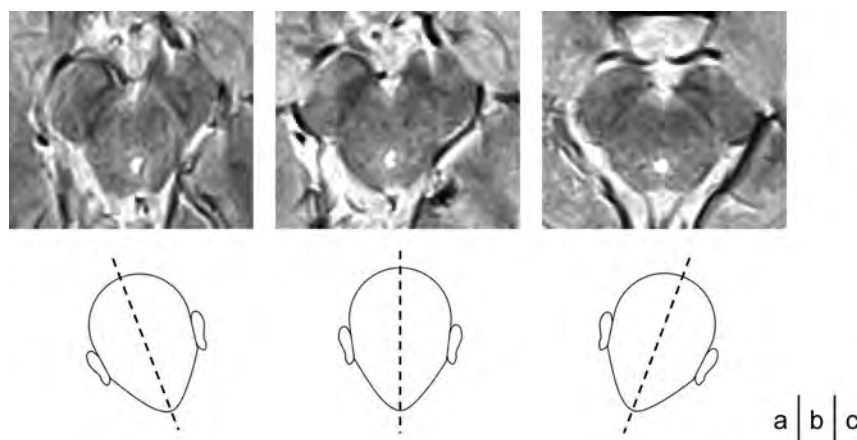


FIG 4. Examples of visualization of nigrosome 1 with a right head tilt (A), without a head tilt (B), and with a left head tilt (C) in the B_0 direction.

center of the brain.^{21,22} Then, the susceptibility map was reconstructed with an improved sparse linear equation and the least-squares algorithm.²³ All data were processed with the in-house Matlab R2018a (MathWorks, Natick, Massachusetts) program.

MR Imaging Acquisition

All examinations were performed on a 3T MR imaging system (Trillium Oval; Hitachi, Tokyo, Japan) with a 15- or 32-channel head matrix coil. The evaluation was based on a combination of 3D spoiled gradient-echo images with 9 echoes. To combine the 3D spoiled gradient-echo with each TE magnitude, we used the following parameters: TR, 83 ms; minimum and maximum TE, 18.5 and 55.3 ms, respectively (number of combined echoes, 9; echo spacing, 4.6 ms);

flip angle, 10°; section thickness, 1.5 mm; matrix, 300 × 300; FOV, 190 mm (in-plane resolution, 0.63 × 0.63 mm); parallel imaging factor, 1.1; number of signal averages, 1; receiver bandwidth, 210 kHz; and acquisition time, 4 minutes 53 seconds. The receiver bandwidth was fixed for each TE in the multiecho imaging technique. Quantitative susceptibility mapping was performed using the following parameters: TR, 34 ms; TE, 6–30 ms at 6-ms intervals; flip angle, 15°; section thickness, 1.0 mm; matrix, 192 × 192; FOV, 192 mm (in-plane resolution, 1.0 × 1.0 mm); parallel imaging factor, 1.9; number of signal averages, 1; receiver bandwidth, 77 kHz; and

acquisition time, 10 minutes 5 seconds.

Statistical Analysis

A Wilcoxon signed rank test with a Bonferroni correction for non-normally distributed data was performed to examine the relationship between the visualization of nigrosome 1 and the degree of head tilting to the right and left. Statistical analysis was performed using SPSS (IBM, Armonk, New York). $P < .05$ and $P < .017$ (.05/3 after Bonferroni correction based on 3 comparisons per task) were considered statistically significant.

RESULTS

The visualization of nigrosome 1 depends on the difference in the field strength; however, it should be visualized bilaterally,

Table 2: Results of contrast measurement repeated 6 times in 1 volunteer with right head tilting and left head tilting

Tilting Head in B_0 Direction Nigrosome 1 and SNc	Right		Left	
	Right	Left	Right	Left
Times				
1	12.0	11.8	10.6	12.6
2	12.1	11.4	11.0	12.3
3	12.3	11.4	10.6	13.0
4	11.9	11.9	10.4	12.4
5	12.5	11.0	10.5	12.6
6	12.3	11.4	10.9	12.4
SD	0.20	0.32	0.21	0.26

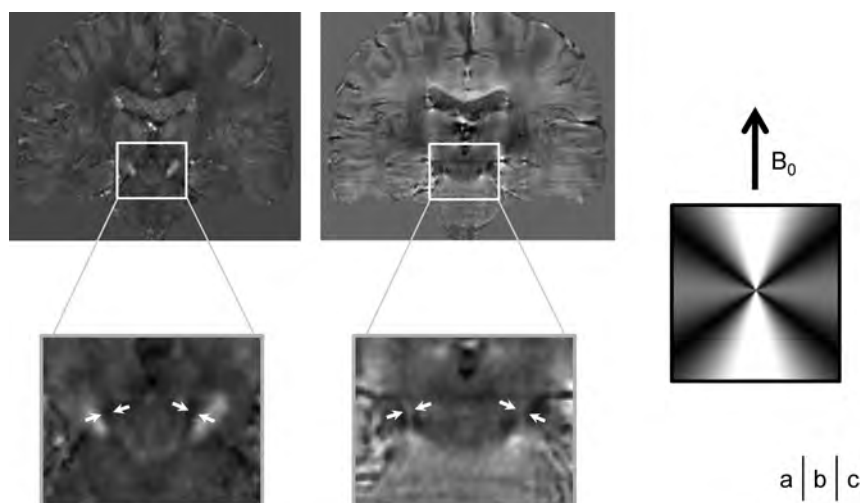


FIG 5. Coronal sections of the 3D susceptibility map (A) and the local field map (B). The anatomic slant structure of nigrosome 1 is coherent between the axis of nigrosome 1 (arrows) and the magic angle that occurs at approximately 54.7° in the B_0 direction by dipolar interaction (C).

especially when visualizing a healthy nigrosome 1. Poor visualization due to asymmetry of the bilateral nigrosome 1 was discovered, though all the subjects in this study were young and healthy and had no nucleus degeneration. Additionally, in some subjects, we were unable to find a discriminable nigrosome 1 (Table 1).

The heads tilted to the right and left showed a significantly higher contrast of nigrosome 1 and SNc than the nontilted heads (Fig 3). Figure 4 shows examples of the visualization of nigrosome 1 with a right head tilt (A), without a head tilt (B), and with a left head tilt (C). No significant differences were observed in the visualization and susceptibility between the right nigrosome 1 and left nigrosome 1 for each head tilt. The contrast of nigrosome 1 and SNc showed sufficient reproducibility among the 6 measurements (Table 2). However, the effect of the magic angle was remarkable in the nontilted heads and was also supported by quantitative susceptibility mapping. The boundary of nigrosome 1 and SNc is likely visible (Fig 5A, -B), because according to the anatomic slant structure of nigrosome 1 along the magic angle, the dipolar interaction has angular dependence (Fig 5C).

DISCUSSION

Conventional MR imaging characteristics of the substantia nigra in PD involve increased iron-related contrast enhancement, which reflects the sensitivity of the gradient-echo sequences to

the resulting changes in R_2^* relaxivity—that is, the signal intensity on a 3D spoiled gradient-echo is diminished specifically in the lateral portion of the SNc. Iron is the main source of susceptibility in the regions of the nucleus in the midbrain. In addition, a boundary is visible between nigrosome 1 and SNc on gradient-echo images because they naturally have different degrees of iron deposition. The important point here is that the degree of iron deposition is lower than that of neurodegeneration in the midbrain.

In principle, one would expect to visualize a healthy nigrosome 1 bilaterally on MR imaging, but the visualization is often poor because of its asymmetry. Furthermore, SNc is also asymmetric. Hence, a healthy nigrosome 1 and an abnormal nigrosome 1 might be misclassified. The problem that we have assessed here (ie, misclassification of a healthy nigrosome 1 and an abnormal nigrosome 1) has seldom been studied.

The differences in visualization were due to the way in which the subjects' heads were tilted (ie, to the right or left), which caused asymmetric visualization of nigrosome 1. In our study, we found that when the heads were tilted to the right or left, the contrast between nigrosome 1 and SNc on the images was significantly higher than that with the nontilted heads. Furthermore, the results in Fig 4 strongly suggest the reproducibility of contrast measurements by manually drawing the ROIs and measuring the signal intensities of nigrosome 1 and SNc. We focused on the magic angle in the B_0 direction. The magic angle that occurs at approximately 54.7° in the B_0 direction and so forth along the axis of the magic angle^{24,25} accounts for interference with this boundary in the nontilted heads. The relationship between the poor visualization of nigrosome 1 and the magic angle causes asymmetric visualization of nigrosome 1 (Table 1 and Fig 3).

We evaluated the anatomic slant structure of nigrosome 1 using quantitative susceptibility mapping, which enables quantitative investigations of the iron content in tissues.^{17,21,26-29} R_2^* increases exponentially with increasing age,^{7,8} but all the subjects included in this study were young and healthy without any nucleus degeneration. Hence, nigrosome 1 and the local field were

not assessed with susceptibility-weighted imaging and the T2* image technique; instead, quantitative susceptibility mapping, which is more sensitive, was used. The results indicated that the anatomic slant structure of nigrosome 1 was coherent between the axis of nigrosome 1 and the magic angle (Fig 5).

Quantitative susceptibility mapping can also be used for the detection and quantification of iron deposition, whereas the status of the nuclear regions of the midbrain is assessed through diffusion tensor imaging. The bulk tissue microstructure can be measured with this technique on the basis of the tissue microenvironment with mean diffusivity and fractional anisotropy. The mean diffusivity increases with microscopic barrier disruption and extracellular fluid accumulation, and fractional anisotropy provides information on the microstructural integrity of highly oriented microstructures (eg, myelin).^{30,31} MR diffusional kurtosis imaging has recently been proposed as a means of quantifying non-Gaussian water diffusion; in general, the regions of high fractional anisotropy are also characterized by increased mean kurtosis.

With regard to PD, previous diffusion tensor imaging studies on affected patients have demonstrated a decrease in fractional anisotropy in SNc compared with the fractional anisotropy in SNc obtained in studies conducted on healthy control subjects.^{32,33} Patients with PD exhibit significantly higher R_2^* values in the SNc, lower fractional anisotropy values in the SNc and thalamus, and higher mean diffusivity values in the thalamus than control subjects.¹ However, the appearance of artifacts, which are more common in diffusion MR imaging sequences, depends on the local magnetic field.³⁴ Inhomogeneities in the local magnetic field, such as those induced by iron deposition, lead to some artifacts in diffusion MR imaging sequences and have an effect on ADC. The sensitivity of the magnetic susceptibility changes because motion-probing gradients into echo-planar imaging are used in diffusion MR imaging sequences. Hence, it is possible that ADC is underestimated in the presence of iron depositions. Conversely, a 3D spoiled gradient-echo with a multi-echo technique is more robust for evaluating nigrosome 1 than a diffusion MR imaging sequence in local magnetic field inhomogeneities. However, as mentioned earlier, the problem with the magic angle in the B_0 direction affecting nigrosome 1 visualization became clear in this study.

There were some limitations to this study. The local field gradients by blood containing deoxyhemoglobin were paramagnetic.³⁵ In the future, we will be able to evaluate the magnetic susceptibility of each tissue with more focus. Moreover, the effect of aging needs to be examined in detail. It has been reported that the mean diffusivity and fractional anisotropy are highly influenced by physiologic aging.³⁶ Therefore, we will evaluate older subjects who are added to the study. The current MR imaging technique has made it possible to use appropriate parameters in this study (eg, the number or timing of combined echoes).

CONCLUSIONS

The visualization of nigrosome 1 is affected by the magic angle, thus causing asymmetric visualization. We observed that visualization was improved when the head was tilted to the right and

left in the B_0 direction. Furthermore, nigrosome 1 is affected by susceptibility. The cause of these problems in visualization is the anatomic slant structure of nigrosome 1; each anatomic slant structure individually has an effect on visualization.

Disclosures: Nobuyuki Arai—UNRELATED: Employment: Department of Radiology, Nagoya City University Hospital, Comments: The corresponding author had full access to all the data in the study and had final responsibility for the decision to submit for publication. Hirohito Kan—UNRELATED: Employment: Radiological and Medical Laboratory Sciences, Nagoya University Graduate School of Medicine, Comments: Assistant Professor. Masaki Ogawa—UNRELATED: Employment: Department of Radiology, Nagoya City University Graduate School of Medical Sciences. Yuto Uchida—UNRELATED: Employment: Department of Neurology, Nagoya City University Graduate School of Medical Sciences. Masahiro Takizawa—UNRELATED: Employment: Hitachi Ltd., Comments: The sponsor had no control over the interpretation, writing, or publication of this work. Kazuyoshi Omori—UNRELATED: Employment: Hitachi Healthcare Ltd., Comments: The sponsor had no control over the interpretation, writing, or publication of this work. Tosiaki Miyati—UNRELATED: Employment: Division of Health Sciences, Graduate School of Medical Science, Kanazawa University, Comments: Professor. Harumasa Kasai—UNRELATED: Employment: Department of Radiology, Nagoya City University Hospital. Hiroshi Kunitomo—UNRELATED: Employment: Department of Radiology, Nagoya City University Hospital. Yuta Shibamoto—UNRELATED: Employment: Department of Radiology, Nagoya City University Graduate School of Medical Sciences, Comments: Professor.

REFERENCES

1. Péran P, Cherubini A, Assogna F, et al. **Magnetic resonance imaging markers of Parkinson's disease nigrostriatal signature.** *Brain* 2010;133:3423–33 CrossRef Medline
2. Brass SD, Chen NK, Mulkern RV, et al. **Magnetic resonance imaging of iron deposition in neurological disorders.** *Top Magn Reson Imaging* 2006;17:31–40 CrossRef Medline
3. Berg D, Youdim MB. **Role of iron in neurodegenerative disorders.** *Top Magn Reson Imaging* 2006;17:5–17 CrossRef Medline
4. Griffiths PD, Dobson BR, Jones GR, et al. **Iron in the basal ganglia in Parkinson's disease: an in vitro study using extended x-ray absorption fine structure and cryo-electron microscopy.** *Brain* 1999;122:667–73 CrossRef Medline
5. Graham JM, Paley MN, Grünewald RA, et al. **Brain iron deposition in Parkinson's disease imaged using the PRIME magnetic resonance sequence.** *Brain* 2000;123 Pt 12:2423–31 CrossRef Medline
6. Griffiths PD, Crossman AR. **Distribution of iron in the basal ganglia and neocortex in postmortem tissue in Parkinson's disease and Alzheimer's disease.** *Dementia* 1993;4:61–65 CrossRef Medline
7. Sedlák J, Boelmans K, Lobel U, et al. **Reversible, irreversible and effective transverse relaxation rates in normal aging brain at 3T.** *Neuroimage* 2014;84:1032–41 CrossRef Medline
8. Aquino D, Bizzi A, Grisoli M, et al. **Age-related iron deposition in the basal ganglia: quantitative analysis in healthy subjects.** *Radiology* 2009;252:165–72 CrossRef Medline
9. Blazejewska AI, Schwarz ST, Pitiot A, et al. **Visualization of nigrosome 1 and its loss in PD: pathoanatomic correlation and in vivo 7 T MRI.** *Neurology* 2013;81:534–40 CrossRef Medline
10. Damier P, Hirsch EC, Agid Y, et al. **The substantia nigra of the human brain, II: patterns of loss of dopamine-containing neurons in Parkinson's disease.** *Brain* 1999;122:1437–48 CrossRef Medline
11. Cosottini M, Frosini D, Pesaresi I, et al. **Comparison of 3T and 7T susceptibility-weighted angiography of the substantia nigra in diagnosing Parkinson disease.** *AJNR Am J Neuroradiol* 2015;36:461–66 CrossRef Medline
12. Damier P, Hirsch EC, Agid Y, et al. **The substantia nigra of the human brain, I: nigrosomes and the nigral matrix, a compartmental organization based on calbindin D(28K) immunohistochemistry.** *Brain* 1999;122:1421–36 CrossRef Medline
13. Schwarz ST, Afzal M, Morgan PS, et al. **The 'swallow tail' appearance of the healthy nigrosome: a new accurate test of Parkinson's disease—a case-control and retrospective cross-sectional MRI study at 3T.** *PLoS One* 2014;9:e93814 CrossRef Medline

14. Wallis LI, Paley MN, Graham JM, et al. **MRI assessment of basal ganglia iron deposition in Parkinson's disease.** *J Magn Reson Imaging* 2008;28:1061–67 CrossRef Medline
15. Noh Y, Sung YH, Lee J, et al. **Nigrosome 1 detection at 3T MRI for the diagnosis of early-stage idiopathic Parkinson disease: assessment of diagnostic accuracy and agreement on imaging asymmetry and clinical laterality.** *AJNR Am J Neuroradiol* 2015;36:2010–06 CrossRef Medline
16. Nam Y, Gho SM, Kim DH, et al. **Imaging of nigrosome 1 in substantia nigra at 3T using multiecho susceptibility map-weighted imaging (SMWI).** *J Magn Reson Imaging* 2017;46:528–36 CrossRef Medline
17. Bilgic B, Pfefferbaum A, Rohlfing T, et al. **MRI estimates of brain iron concentration in normal aging using quantitative susceptibility mapping.** *Neuroimage* 2012;59:2625–35 CrossRef Medline
18. Lee J, Nam Y, Choi JY, et al. **Mechanisms of T2 * anisotropy and gradient echo myelin water imaging.** *NMR Biomed* 2017;30 [Epub 2016 Apr 7] CrossRef Medline
19. Puwal S, Roth BJ, Basser PJ. **Heterogeneous anisotropic magnetic susceptibility of the myelin-water layers causes local magnetic field perturbations in axons.** *NMR Biomed* 2017;30 CrossRef Medline
20. Aggarwal M, Kageyama Y, Li X, et al. **B₀-orientation dependent magnetic susceptibility-induced white matter contrast in the human brainstem at 11.7T.** *Magn Reson Med* 2016;75:2455–63 CrossRef Medline
21. Wu B, Li W, Guidon A, et al. **Whole brain susceptibility mapping using compressed sensing.** *Magn Reson Med* 2012;67:137–47 CrossRef Medline
22. Khabipova D, Wiaux Y, Gruetter R, et al. **A modulated closed form solution for quantitative susceptibility mapping: a thorough evaluation and comparison to iterative methods based on edge prior knowledge.** *Neuroimage* 2015;107:163–74 CrossRef Medline
23. Li W, Wang N, Yu F, et al. **A method for estimating and removing streaking artifacts in quantitative susceptibility mapping.** *Neuroimage* 2015;108:111–22 CrossRef Medline
24. Erickson SJ, Prost RW, Timins ME. **The “magic angle” effect: background physics and clinical relevance.** *Radiology* 1993;188:23–25 CrossRef Medline
25. Chappell KE, Robson MD, Stonebridge-Foster A, et al. **Magic angle effects in MR neurography.** *AJNR Am J Neuroradiol* 2004;25:431–40 Medline
26. Kan H, Arai N, Kasai H, et al. **Quantitative susceptibility mapping using principles of echo shifting with a train of observations sequence on 1.5T MRI.** *Magn Reson Imaging* 2017;42:37–42 CrossRef Medline
27. Wang Y, Liu T. **Quantitative susceptibility mapping (QSM): decoding MRI data for a tissue magnetic biomarker.** *Magn Reson Med* 2015;73:82–101 CrossRef Medline
28. Liu J, Liu T, de Rochefort L, et al. **Morphology enabled dipole inversion for quantitative susceptibility mapping using structural consistency between the magnitude image and the susceptibility map.** *Neuroimage* 2012;59:2560–68 CrossRef Medline
29. de Rochefort L, Liu T, Kressler B, et al. **Quantitative susceptibility map reconstruction from MR phase data using Bayesian regularization: validation and application to brain imaging.** *Magn Reson Med* 2010;63:194–206 CrossRef Medline
30. Abe O, Aoki S, Hayashi N, et al. **Normal aging in the central nervous system: quantitative MR diffusion-tensor analysis.** *Neurobiol Aging* 2002;23:433–41 CrossRef Medline
31. Le Bihan D, Mangin JF, Poupon C, et al. **Diffusion tensor imaging: concepts and applications.** *J Magn Reson Imaging* 2001;13:534–46 CrossRef Medline
32. Vaillancourt DE, Spraker MB, Prodoehl J, et al. **High-resolution diffusion tensor imaging in the substantia nigra of de novo Parkinson disease.** *Neurology* 2009;72:1378–84 CrossRef Medline
33. Yoshikawa K, Nakata Y, Yamada K, et al. **Early pathological changes in the parkinsonian brain demonstrated by diffusion tensor MRI.** *J Neurol Neurosurg Psychiatry* 2004;75:481–84 CrossRef Medline
34. Fujiwara S, Uhrig L, Amadon A, et al. **Quantification of iron in the non-human primate brain with diffusion-weighted magnetic resonance imaging.** *Neuroimage* 2014;102:789–97 CrossRef Medline
35. Ogawa S, Menon RS, Tank DW, et al. **Functional brain mapping by blood oxygenation level-dependent contrast magnetic resonance imaging: a comparison of signal characteristics with a biophysical model.** *Biophys J* 1993;64:803–12 CrossRef Medline
36. Cherubini A, Peran P, Hagberg GE, et al. **Characterization of white matter fiber bundles with T2* relaxometry and diffusion tensor imaging.** *Magn Reson Med* 2009;61:1066–72 CrossRef Medline

Structural and Volumetric Brain MRI Findings in Mild Traumatic Brain Injury

J.B. Patel, S.H. Wilson, T.R. Oakes, P. Santhanam, and L.K. Weaver



ABSTRACT

BACKGROUND AND PURPOSE: Routine MR imaging findings are frequently normal following mild traumatic brain injury and have a limited role in diagnosis and management. Advanced MR imaging can assist in detecting pathology and prognostication but is not readily available outside research settings. However, 3D isotropic sequences with $\sim 1\text{-mm}^3$ voxel size are available on community MR imaging scanners. Using such sequences, we compared radiologists' findings and quantified regional brain volumes between a mild traumatic brain injury cohort and non-brain-injured controls to describe structural imaging findings associated with mild traumatic brain injury.

MATERIALS AND METHODS: Seventy-one military personnel with persistent symptoms and 75 controls underwent 3T MR imaging. Three neuroradiologists interpreted the scans using common data elements. FreeSurfer was used to quantify regional gray and white matter volumes.

RESULTS: WM hyperintensities were seen in 81% of the brain-injured group versus 60% of healthy controls. The odds of ≥ 1 WM hyperintensity in the brain-injured group was about 3.5 times the odds for healthy controls (95% CI, 1.58–7.72; $P = .002$) after adjustment for age. A frontal lobe-only distribution of WM hyperintensities was more commonly seen in the mild traumatic brain injury cohort. Furthermore, 7 gray matter, 1 white matter, and 2 subcortical gray matter regions demonstrated decreased volumes in the brain-injured group after multiple-comparison correction. The mild traumatic brain injury cohort showed regional parenchymal volume loss.

CONCLUSIONS: White matter findings are nonspecific and therefore a clinical challenge. Our results suggest that prior trauma should be considered in the differential diagnosis of multifocal white matter abnormalities with a clinical history of mild traumatic brain injury, particularly when a frontal predilection is observed.

ABBREVIATIONS: DAI = diffuse axonal injury; mTBI = mild traumatic brain injury; TAI = traumatic axonal injury; TBI = traumatic brain injury; WMH = white matter hyperintensity

Many patients experiencing mild traumatic brain injury (mTBI) report symptom resolution and return to baseline function within 3 months. A subset (3%–53%) develop postconcussive symptoms that persist months to years postinjury,^{1–3}

including dizziness, headache, cognitive deficits, sleep disturbances, tinnitus, visual symptoms, and behavioral/affective changes.^{1,4} Because symptoms are nonspecific to mTBI and routine clinical neuroimaging findings are frequently normal, identifying imaging correlates and biomarkers of postconcussive syndrome is of clinical importance.

MR imaging is the appropriate technique for patients with subacute or chronic mTBI with cognitive or neurologic deficits,⁵ but routine clinical MR imaging may have limited utility for diagnosis and management.⁶ Advanced MR imaging sequences obtained at 3T field strength demonstrate changes not

Received August 21, 2019; accepted after revision October 16.

From Lovelace Biomedical Research (J.B.P., T.R.O., P.S.), Albuquerque, New Mexico; VA Maryland Health Care System (J.B.P.), Baltimore, Maryland; Emmes (S.H.W.), Rockville, Maryland; Division of Hyperbaric Medicine (L.K.W.), Intermountain Medical Center, Murray, Utah, and Intermountain LDS Hospital, Salt Lake City, Utah; University of Utah School of Medicine (L.K.W.), Salt Lake City, Utah; and University of Wisconsin-Madison (T.R.O.), Madison, Wisconsin.

This work was supported by the United States Army Medical Research and Materiel Command Contract No. W81XWH-15-D-0039-0003.

The views, opinions and/or findings contained in this report are those of the authors and should not be construed as an official Department of the Army, Veterans Affairs, or US government position, policy, or decision unless so designated by other documentation. In the conduct of research in which humans are the subjects, the investigators adhered to the policies regarding the protection of human subjects as prescribed by Code of Federal Regulations Title 45, Volume 1, Part 46; Title 32, Chapter 1, Part 219; and Title 21, Chapter 1, Part 50 (Protection of Human Subjects).

Please address correspondence to Lindell K. Weaver, MD, FACP, FCCP, FCCM, FUHM, Intermountain LDS Hospital Hyperbaric Medicine, 8th Ave and C St, Salt Lake City, UT 84143; e-mail: lindell.weaver@gmail.com

Indicates open access to non-subscribers at www.ajnr.org

Indicates article with supplemental on-line table.

<http://dx.doi.org/10.3174/ajnr.A6346>

typically observable in routine clinical MR imaging. DTI, MR spectroscopy, fMRI, and perfusion techniques assist in pathology detection and may provide improved diagnostic and prognostic indicators;⁶ however, postacquisition processing is required, group-based differences can be difficult to apply to individual patients, and such techniques are not readily available in community settings. High-resolution structural imaging (3D sequences with isotropic 1-mm³ voxels that can be reconstructed in all planes) can be acquired on routine clinical scanners without time-intensive postprocessing. High-resolution MR imaging scans, recommended by the Defense Centers of Excellence,⁷ are regarded as best practice for traumatic brain injury (TBI).

A challenge in the interpretation of such structural imaging is determining the importance of imaging findings identified more easily at higher resolution and field strengths.⁸ White matter hyperintensities (WMHs), dilated perivascular spaces, pineal gland cysts, and pituitary gland abnormalities have been identified in both mTBI and healthy cohorts,^{9,10} and the imaging manifestation of multifocal T2 and FLAIR hyperintensity is visible across conditions including demyelination, inflammation, chronic small vessel ischemia, normal aging, migraine headaches, and moderate/severe TBI. Recent studies in military populations have demonstrated similar rates of WMH in mTBI and non-head trauma groups (Tate et al,¹¹ 41% mTBI versus 49% orthopedically injured versus 29% posttraumatic stress disorder only; and Riedy et al,⁹ 51.8% mTBI versus 38.1% healthy controls).

Established software packages (eg, FreeSurfer; <http://surfer.nmr.mgh.harvard.edu>)¹² can quantify regional white matter and gray matter volumes, with longitudinal decreases in brain volumes following mTBI¹³ in the anterior cingulate white matter bilaterally, left cingulate gyrus isthmus white matter, and right precuneal gray matter. Many studies report group differences, but large between- and within-group variance limits interpretation for individual patient diagnosis.

In this article, we describe the clinical interpretation and volumetric analysis of MR imaging scans acquired during the BIMA (Brain Injury and Mechanisms of Action of HBO2 for Persistent Post-Concussive Symptoms After Mild Traumatic Brain Injury) study,¹⁴ a randomized, double-blind study of hyperbaric oxygen in US military personnel with persistent postconcussive symptoms after mTBI (clinicaltrials.gov: NCT01611194). A complementary observational study, NORMAL (Development of Normative Datasets for Assessments Planned for Use in Patients With Mild Traumatic Brain Injury),¹⁵ evaluated non-brain-injured volunteers using the same imaging protocol on the same scanner (clinicaltrials.gov: NCT01925963). We compare baseline structural imaging findings, WMH burden, and segmented white and gray matter volumes between mTBI and healthy control groups. We also test imaging findings for correlation with injury characteristics and clinical outcome and compare the results with those of other military mTBI cohorts.

MATERIALS AND METHODS

Study Populations

BIMA enrolled 71 military personnel (70 with MR imaging data are included in the analysis) with ≥ 3 persistent symptoms from active duty mTBI 3 months to 5 years before enrollment. Mild

TBI was assessed by structured interview¹⁶ and included loss of consciousness of ≤ 30 minutes, altered consciousness of ≤ 24 hours, or posttraumatic amnesia of ≤ 1 day. Seventy participants with complete MR imaging data are included in this report. NORMAL enrolled 75 participants; prior stroke, infection, therapeutic ionizing radiation exposure, neurologic disorder, chronic migraine headaches, drug/alcohol abuse, and diabetes mellitus were exclusionary. Primary study results are published elsewhere.^{14,15} The United States Army Medical Research and Materiel Command institutional review board approved the studies, and participants provided written informed consent.

MR Imaging Protocol

Participants underwent 3T structural MR imaging (Achieva, Software Release 3.2; Philips Healthcare, Best, the Netherlands; 32-channel sensitivity encoding head coil) without the use of gadolinium at Evans Army Community Hospital, a 92-bed community hospital. Three trained technologists performed the imaging protocol. Although there was no on-site MR imaging physicist, experienced MR imaging researchers made frequent visits for training and setup, quality control, and troubleshooting. The complete MR imaging acquisition protocol is provided elsewhere.¹⁷

Participants underwent an initial quick-scan protocol consisting of rapid T2 and FLAIR sequences, which were loaded onto the hospital PACS system and interpreted at the time of imaging by a hospital radiologist to screen for major abnormalities and document the MR imaging in the military medical record.

Structural sequences were acquired at a spatial resolution as high as possible while maintaining good signal quality. Anatomic images included isotropic 3D T1-weighted, T2-weighted, T2 FLAIR, and 2D T2*-weighted. The full MR imaging protocol required approximately 2 hours. Herein we report anatomic MR imaging and FreeSurfer results. DICOM files were conditioned by using the Radiological Society of North America Clinical Trials Processor and distributed to clinical specialists for processing (<https://www.rsna.org/research/imaging-research-tools>).

MR Imaging Clinical Interpretation

Each scan was assigned to 2 of 3 board-certified neuroradiologists for independent review. In the event of disagreement on any finding, all 3 reviewed and discussed the findings to arrive at a consensus on the final scoring. The radiologists viewed DICOM images via OsiriX Imaging Software (<http://www.osirix-viewer.com>),¹⁸ allowing real-time generation of MPR and MIP images and synchronizing the spatial location between series and across time points. These features were useful in evaluating small foci of white matter signal abnormality.

Interpretations were standardized using a Web-based case report form based on the National Institute of Neurological Disorders and Stroke neuroradiologic TBI common data elements (QuesGen Systems, Burlingame, California).¹⁹ The forms triggered external clinical referral in the event of critical findings.

Each neuroradiologist manually enumerated, annotated, and saved all relevant imaging findings using single-point ROIs and completed a series of electronic interpretation forms. We specifically evaluated and scored the following items: ventricular

enlargement, asymmetric ventricles, arachnoid cyst, possible diffuse axonal injury (DAI)/traumatic axonal injury (TAI), contusion, gliosis, microhemorrhage, intracerebral hemorrhage, brain atrophy, encephalomalacia, dilated perivascular spaces, cavum septum, pituitary abnormality, pineal cyst, sinus disease, mastoid fluid, lymphadenopathy, ischemia/infarction, intraventricular hemorrhage, epidural hematoma, subdural hematoma, subarachnoid hemorrhage, and edema.

The broad category of T2 and FLAIR white matter signal changes was classified as DAI/TAI when there was increased T2 and FLAIR white matter signal in a pattern and distribution that could be consistent with prior traumatic injury.^{9,20} Possible DAI/TAI lesions were typically identified in the subcortical white matter often involving the frontal or parietal lobes; however, we also included periventricular and deep white matter foci in this classification. Other definitions included the following:

- Encephalomalacia—focal cortical volume loss
- Dilated perivascular spaces—longitudinally oriented cystic spaces nearly isointense to CSF on the T1, T2, and FLAIR sequences
- Gliosis—an area of T2 FLAIR white matter signal exceeding 3 mm with morphology atypical for DAI/TAI or in an area of encephalomalacia.

The terms DAI/TAI, white matter T2 FLAIR hyperintensities, WMH, and white matter lesion burden are used interchangeably. For discrepant WMH counts, the larger number was reported.

Quantified Volumetric Analysis

Cortical and subcortical segmentation and volumetric quantification of the 3D T1-weighted sequence were performed using FreeSurfer (Version 5.3). Processing included removal of nonbrain tissue,²¹ automated Talairach transformation, segmenting of subcortical white matter and deep gray matter structures,^{12,22} intensity normalization,²³ gray matter/white matter boundary tessellation, automated topology correction,^{24,25} and surface deformation following intensity gradients along the gray/white and gray/CSF borders.^{26–28} Segmentations were checked to verify the automated reconstruction, and manual interventions corrected small processing defects and any segmentation inaccuracies due to the presence of lesions.

Statistical Analyses

Continuous outcomes are summarized using means and SDs, whereas discrete outcomes are summarized using counts and percentages. Statistical models include adjustment for age at study enrollment.

Baseline demographics are presented by study population with between-group differences tested using a Wilcoxon rank sum or χ^2 test. Baseline characteristics were tested in the mTBI cohort between those with zero versus ≥ 1 WMH using logistic regression.

Baseline MR imaging findings are presented when prevalence in either study group was $>3\%$. Total and regional WMH distributions are summarized by the number of WMHs and by the prevalence of ≥ 1 WMH with group differences, tested using logistic regression. Regional WMH

patterns are displayed graphically using bar charts and were tested using the Fisher exact test.

Given the potential effect of sex on WMH burden, lesion prevalence was analyzed by sex for a subset of the healthy controls, and a sensitivity analysis was performed testing between-study group WMH differences excluding women. We performed an exploratory analysis to try to understand more about participants with mTBI with outlier WMH counts (defined as any WMH count of >1.5 , with interquartile ranges above the third quartile) and the following characteristics: TBI symptom duration (3 months to 5 years versus 1–5 years postinjury), number of injuries (1 versus multiple), type of injuries (lifetime history of blast versus blunt force versus a combination), baseline posttraumatic stress disorder diagnosis, number of deployments, and military tenure. For characteristics in which visual inspection of summary statistics indicated a potential trend, logistic regression models were fit to model the probability of WMH outliers predicted by the characteristic and adjusted for age.

FreeSurfer regional volumes, expressed as a percentage of total intracranial volume, are presented by hemisphere, parcellation type (cortical gray matter, subcortical gray matter, white matter), and study group. ROI-specific between-group differences were tested using general linear models with *P* values adjusted using the Holm-Bonferroni²⁹ procedure applied within parcellation type. Heat maps display group differences by ROI.

The relationship between regional FreeSurfer volume and WMH burden, defined as total or frontal WMH of 0 vs ≥ 1 , was investigated by fitting general linear models of each regional volume with fixed effects of WMH burden and age. Models were fit separately for each study population and limited to those regions indicating a difference in volume between the mTBI and healthy control populations.

Analysis was performed using SAS 9.4 (SAS Institute, Cary, North Carolina), and statistical testing was performed at the $\alpha = .05$ level unadjusted for multiple comparisons unless otherwise noted.

RESULTS

BIMA participants were younger (BIMA mean age, 33 ± 7 years; range, 21–53 years; NORMAL mean age, 39 ± 13 years; range, 18–65 years; $P = .008$), and more participants were male than healthy control participants (BIMA, 99% male; NORMAL, 77% male; $P < .001$). BIMA recruited nearly all active duty military (97%) compared with NORMAL (1%). In BIMA, time since injury ranged from 4 to 60 months (mean, 25.6 ± 16.2 months), and injury types included a history of blast injuries (32%, $n = 23$), blunt force injuries (20%, $n = 14$), and a combination of blast/blunt force injuries (48%, $n = 34$).

Structural Findings

The most common findings in the mTBI study group were DAI/TAI, sinus disease, cavum septum, pineal cysts, dilated perivascular spaces, and brain atrophy (Table 1). Only DAI/TAI ($n = 56$, 80% BIMA versus $n = 45$, 61% NORMAL; OR = 3.06; 95% CI, 1.40–6.69; $P = .005$) and brain atrophy ($n = 22$, 31% BIMA versus $n = 10$, 14% NORMAL; OR = 3.00; 95% CI, 1.23–7.30; $P = .02$) differed between groups. Incidental findings referred for clinical

Table 1: Baseline findings of neuroradiologists

	BIMA (<i>n</i> = 70) (No.) (%)		NORMAL (<i>n</i> = 75) (No.) (%)		Odds Ratio (95% CI) ^a	<i>P</i> Value ^b
	N ^a	(No.) (%)	N ^a	(No.) (%)		
Arachnoid cysts	70	6 (8.6)	70	3 (4.3)	1.74 (0.41–7.37)	.45
Asymmetric ventricles	70	14 (20.0)	70	8 (11.4)	2.75 (0.94–8.03)	.06
Brain atrophy	70	22 (31.4)	71	10 (14.1)	3.00 (1.23–7.30)	.02 ^c
Cavum septum	70	34 (48.6)	70	32 (45.7)	1.32 (0.66–2.67)	.43
Developmental venous anomalies	70	3 (4.3)	71	4 (5.6)	0.72 (0.15–3.49)	.68
DAI/TAI	70	56 (80.0)	74	45 (60.8)	3.06 (1.40–6.69)	.005 ^c
Dilated perivascular spaces	70	33 (47.1)	72	34 (47.2)	1.06 (0.53–2.12)	.86
Lymph nodes	70	11 (15.7)	71	7 (9.9)	1.51 (0.50–4.55)	.47
Mastoid fluid	70	6 (8.6)	70	1 (1.4)	6.44 (0.70–59.08)	.10
Microhemorrhages	70	3 (4.3)	70	0 (0.0)	NA	NA
Pineal cysts	70	32 (45.7)	70	31 (44.3)	1.33 (0.65–2.71)	.43
Pituitary abnormalities	70	9 (12.9)	71	13 (18.3)	1.15 (0.40–3.33)	.80
Sinus disease	70	35 (50.0)	71	38 (53.5)	0.95 (0.48–1.89)	.89

Note:—NA indicates not applicable.

^a Number nonmissing for the denominator of the percentage calculation.

^b Results obtained from logistic regression models of the probability of MR imaging findings adjusted for age.

^c *P* < 0.05.

Table 2: Total and regional WMH distribution by study group

	BIMA (<i>n</i> = 70)			NORMAL (<i>n</i> = 75)			Odds Ratio (95% CI) ^a	<i>P</i> Value ^a
	No. (%) With ≥1 WMH	Mean WMH Count (SD)	Median WMH Count (Range)	No. (%) With ≥1 WMH	Mean WMH Count (SD)	Median WMH Count (Range)		
Total WMH	57 (81.4)	8.6 (17.9)	3 (0–108)	45 (60.0)	8.5 (18.0)	1 (0–83)	3.49 (1.58–7.72)	.002 ^b
Regional WMH								
Frontal	52 (74.3)	6.3 (13.0)	2 (0–69)	44 (58.7)	6.0 (13.3)	1 (0–74)	2.43 (1.16–5.08)	.02 ^b
Parietal	22 (31.4)	1.2 (3.9)	0 (0–29)	21 (28.0)	1.6 (4.5)	0 (0–29)	1.51 (0.70–3.28)	.30
Temporal	16 (22.9)	0.7 (1.9)	0 (0–10)	15 (20.0)	0.5 (1.2)	0 (0–6)	1.46 (0.62–3.45)	.39
Occipital	2 (2.9)	0.0 (0.2)	0 (0–1)	8 (10.7)	0.2 (0.5)	0 (0–2)	0.33 (0.06–1.77)	.20
Cerebellum	1 (1.4)	0.0 (0.1)	0 (0–1)	0 (0.0)	0.0 (0.0)	0 (0–0)	NA	NA
Corpus callosum genu	2 (2.9)	0.1 (0.4)	0 (0–3)	2 (2.7)	0.1 (0.3)	0 (0–2)	0.93 (0.12–6.93)	.94
Corpus callosum body	8 (11.4)	0.1 (0.4)	0 (0–2)	5 (6.7)	0.1 (0.5)	0 (0–3)	2.12 (0.6–7.51)	.25
Corpus callosum splenium	2 (2.9)	0.0 (0.2)	0 (0–1)	1 (1.3)	0.0 (0.1)	0 (0–1)	8.39 (0.29–242.91)	.22
Midbrain	1 (1.4)	0.0 (0.1)	0 (0–1)	0 (0.0)	0.0 (0.0)	0 (0–0)	NA	NA
Pons	0 (0.0)	0.0 (0.0)	0 (0–0)	1 (1.3)	0.0 (0.2)	0 (0–2)	NA	NA
Medulla	0 (0.0)	0.0 (0.0)	0 (0–0)	0 (0.0)	0.0 (0.0)	0 (0–0)	NA	NA

Note:—NA indicates not applicable.

^a Results obtained from logistic regression models of the probability of ≥1 WMH adjusted for age.

^b *P* < 0.05.

evaluation included the following: possible jugular foramen thrombus, maxillary bone lesion, pineal mass, possible demyelination, pituitary mass, and incidental intracranial aneurysms.

WMH Findings

We observed ≥1 WMH in 57 (81%) of the mTBI group versus 45 (60%) in the healthy controls (Table 2). Logistic regression models were fit to model the probability of lesion burden (defined as ≥1 WMH) and included an effect for study (BIMA versus NORMAL) to test differences in lesion burden between the mTBI and healthy controls populations and a covariate for age. The odds of ≥1 WMH in the mTBI group was about 3.5 times the odds for the healthy controls (95% CI, 1.58–7.72; *P* = .002) after adjustment for age (odds ratio without age = 2.92; 95% CI, 1.37–

6.25; *P* = .006). Similar findings were seen for frontal lobe WMH (OR = 2.43; 95% CI, 1.16–5.08; *P* = .02). Median total WMHs in the mTBI and healthy controls groups were 3 (range, 0–108) and 1 (range, 0–83), respectively. Increasing white matter lesion burden in the mTBI-versus-healthy controls cohort was not observed in other regions (Table 2).

The most common lobar involvement pattern in the mTBI group was frontal-only (*n* = 26, 37%) versus no WMH (*n* = 30, 40%) in the healthy controls (Fig 1). Differences in patterns approached but did not reach significance (*P* = .08).

Seventy-one percent (*n* = 12) of the female healthy controls had ≥1 WMH versus only 39% of the male subgroup (OR = 4.2; 95% CI, 0.96–18.42; *P* = .06). Results of this subanalysis should be interpreted with caution, given small within-group sample sizes.

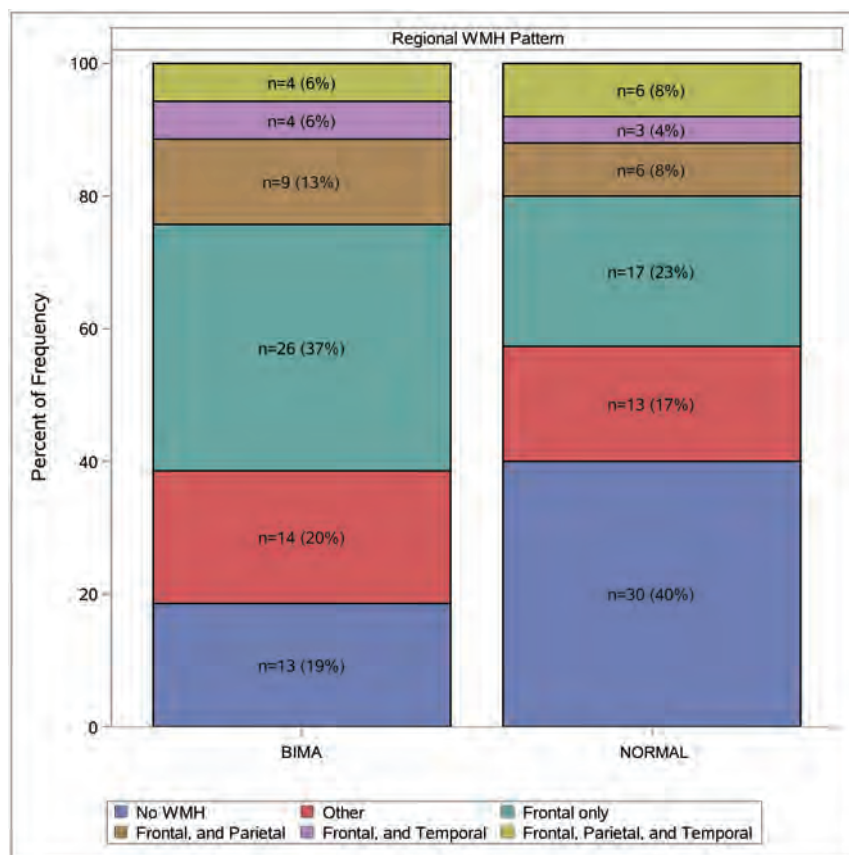


FIG 1. WMH pattern by study group. Distributions of regional WMH patterns are presented by study population. Patterns are classified by the presence of ≥ 1 WMH in each region (eg, in BIMA $n = 4$, 6% of participants were observed to have ≥ 1 WMH in the frontal, parietal, and temporal regions). The most commonly observed patterns are presented in this figure; less commonly observed patterns are classified as "Other."

Results of the sensitivity analysis of WMH prevalence excluding women were similar to primary analysis results; 1 difference was that the OR for ≥ 1 corpus callosum body WMH increased in magnitude and became significant (OR = 8.17; 95% CI, 1.07–62.44; $P = .04$; other data not shown).

No significant differences were detected between higher (≥ 1) versus lower (zero) WMH burden for any baseline characteristics in the mTBI cohort, including age, military tenure, number of deployments, history of blast injury, time from injury (duration of postconcussive symptoms), or baseline composite clinical outcome scores³⁰ (data not shown).

Exploratory analysis of participants with mTBI who had an outlier WMH count ($n = 7$) versus those without ($n = 63$) revealed a potential trend for longer military service (mean for WMH outliers = 16 years; 95% CI, 12–20 years; mean for WMH nonoutliers = 10 years; 95% CI, 9–12 years) and number of deployments (deployments for WMH outliers = 4.6; 95% CI, 2.8–6.3; for WMH nonoutliers = 2.7; 95% CI, 2.2–3.4). However, after adjusting for age, these associations were not statistically significant.

Volumetric Comparisons

Regional volumetric analysis revealed smaller mean volumes in the mTBI-versus-healthy controls cohorts. We identified significant (adjusted) between-group volume differences in the left insula,

rostral anterior cingulate cortex, and transverse temporal gyri, as well as the right lateral and medial orbitofrontal cortices and postcentral and precentral gyri of the 68 regional cortical gray matter comparisons, in the left transverse temporal gyrus of the 68 regional white matter comparisons, and in the left cerebellum cortical and right thalamus regions of the 28 subcortical gray matter comparisons (Fig 2 and On-line Table).

In the mTBI population, mean regional FreeSurfer volumes for all regions investigated were smaller among those with ≥ 1 WMH versus those with no WMH. No clear pattern across regions was identified in the healthy controls population. However, in general linear models adjusted for age, the only significant finding was in the healthy controls population, in which an increase was observed in the right lateral orbitofrontal volume in those with ≥ 1 WMH (adjusted mean = 0.51; 95% CI, 0.45–0.50) compared with no WMH (adjusted mean = 0.4; 95% CI, 0.49–0.53) ($P = .04$). Similar findings were observed in an analysis of frontal WMH related to regional volumes.

DISCUSSION

In this study, brain atrophy and the presence of WMHs were more common in participants with TBI compared with healthy controls, but WMH burden was not associated with baseline TBI injury history, military tenure, and age or cognitive, functional, or symptom outcomes. Some regional brain volumes were significantly different between groups as well. Exploratory analyses suggest a potential relationship between the presence of WMH and lower volumes in some brain regions.

This work adds to the growing body of literature about structural MR imaging findings after mTBI, particularly for WMH, which was the most common imaging finding in both mTBI and healthy controls groups. These findings present a clinical challenge, given their nonspecific nature and diverse causative etiologies, including normal aging. We found a greater frequency of frontal lobe involvement in the mTBI group. While this approached significance, the pattern supports the hypothesis that WMH related to non-TBI causes such as chronic small vessel ischemia or normal aging may demonstrate a more widespread distribution.

The types of imaging findings we observed were similar to those of another large military cohort by Riedy et al.⁹ However, we identified WMH in 81.4% of our mTBI group, compared with 51.8% in that study, which also included individuals with moderate and severe TBI. We found a 4% prevalence of microhemorrhage versus 7% in that study. Methodologic differences could

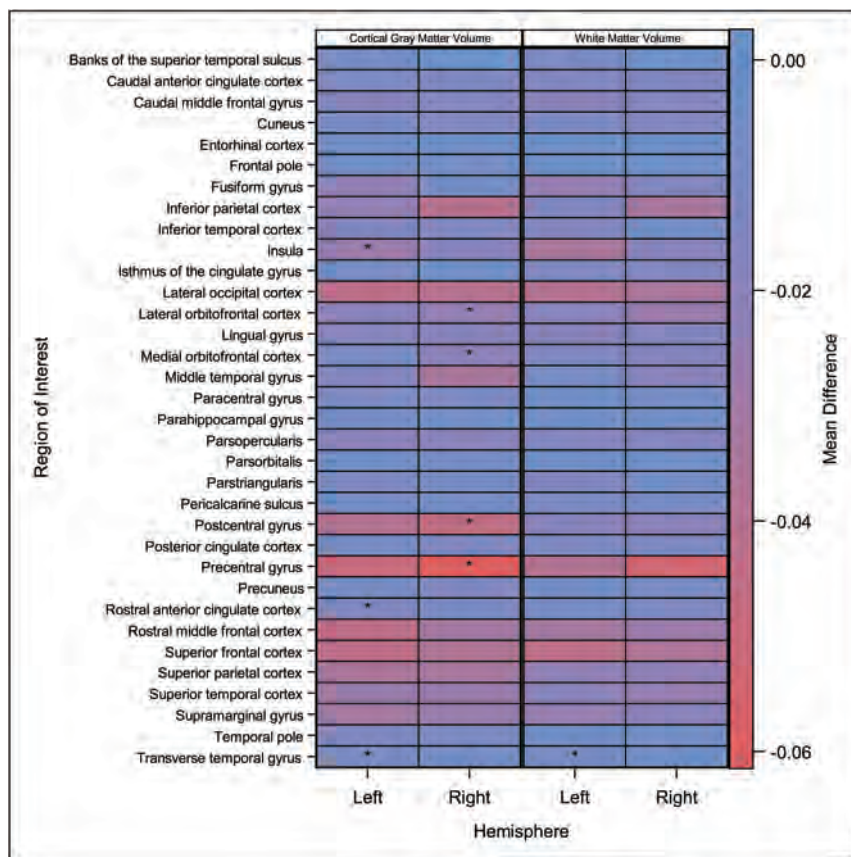


FIG 2. FreeSurfer regional volume differences between mTBI and healthy control cohorts. The heat map presents mean differences by study population (mTBI versus healthy control) in FreeSurfer regional volumes by region and hemisphere. Colors within each cell represent the magnitude of the mean difference: Blue represents no difference between groups, and red indicates a negative difference (ie, smaller mean volume in mTBI compared with the healthy control group). Asterisks within each cell indicate regions where a significant difference in volume (after Holm-Bonferroni correction) was identified between study groups according to general linear models adjusted for age.

explain these discrepancies. We used multiple readers and adjudicated interpretations in contrast to a single reader in Riedy et al. Our neuroradiologists reviewed a volumetric T2 FLAIR sequence with 1-mm³ voxels in 3 planes. The Riedy et al radiology reader reviewed a high-resolution sagittal T2 FLAIR sequence with 3-mm reconstructions in the axial and coronal planes. Differences in reconstruction parameters may have given our neuroradiologists greater confidence in identifying small lesions. Our decreased prevalence of microhemorrhage may be secondary to the type of hemosiderin-sensitive sequence used in our protocol (2D T2*-weighted) versus the SWI sequence of Reidy et al. SWI is a more sensitive sequence for small, chronic hemorrhages.³¹

Tate et al¹¹ performed SWI and FLAIR imaging in 77 military participants with mTBI comparable in age with our population, though their time from injury was shorter (mean = 10.1 versus 25.6 months). Tate et al found a 40.3% rate of FLAIR abnormalities, substantially less than the 80% rate of BIMA. The study of Tate et al analyzed 3-mm-thick routine FLAIR images in contrast to our volumetric acquisition described above. Furthermore, the study of Tate et al used multiple readers for only a small subset

(15 examinations) of their interpretations. The higher baseline WMH rate in our healthy control group (60%) versus the orthopedic injury (49%) and posttraumatic stress disorder (29%) groups of Tate et al further supports an underlying methodologic difference possibly accounting for the varying rates.

We also observed a high rate of pineal gland cysts in both mTBI (46%) and healthy control groups (44%). Review of the recent literature demonstrates a high prevalence of pineal cysts in both pediatric³² (57%) and adult populations³³ (35.1%). Given the similar rates we observed across study cohorts, we suspect that this finding may be due to improved visualization secondary to higher resolution.

Whole-brain and regional volume loss following moderate and severe TBI is well-documented, but volume loss following mTBI is not well-established. Small sample sizes typically limit such studies (Dean et al,³⁴ $n = 16$; Spitz et al,³⁵ $n = 8$; Zhou et al,¹³ $n = 28$; Burrowes et al,³⁶ $n = 50$). Our larger sample size allows our results to further substantiate the relationship between mTBI and regional volume loss, though region-level comparisons with other work are limited by heterogeneous definitions of mTBI, methodology, and varying time to injury.

Our cross-sectional analysis revealed 10 regions with significantly smaller volume in the mTBI versus healthy controls. Future work could explore mTBI symptoms based on the degrees of specific regional volume loss such as in a report by Epstein et al³⁷ ($n = 55$), who found increased symptoms of aggression, depression, and anxiety in subjects with chronic mTBI. They found cortical thinning of the right lateral orbitofrontal cortex; however, findings were not significant after multiple-comparison correction. We observed an analogous significant (adjusted) decrease in the cortical volume of the right lateral and medial orbitofrontal cortices.

Strengths of our study include a single, prospective, standardized imaging and interpretation protocol across mTBI and healthy control groups; and 3 independent neuroradiologists with a priori rules for adjudication and the use of a 3T scanner with a 32-channel head coil. We attempted to minimize interpretation variability and maximize sensitivity for the detection of small lesions using standardized interpretation forms, isotropic multiplanar reconstructions, adjudicated interpretations, and pre-established guidelines for classifying imaging findings. Despite our attempt to establish a robust control group, there were some differences in age and sex between the study cohorts.

We adjusted for age in statistical models testing between-group differences. Although we were unable to adjust for sex given that only 1 woman enrolled in the mTBI cohort, we conducted a sensitivity analysis excluding women and obtained similar results.

Our mTBI group also had variability in the time since injury and diverse injury types, and this heterogeneity in injury could mask imaging differences between study groups. Another limitation is the lack of preinjury or acute postinjury imaging in our participants, which limits our ability to understand the causative association between mTBI and WMH. Predeployment imaging in military populations may help characterize the chronicity of white matter changes following mTBI. In addition, MR imaging findings, including WMH, have not yet been associated with long-term clinical outcomes after mTBI. Our study supports WMH being more frequent in those with mTBI, but at least in our cohort, WMH burden could not be used to make statements about clinical outcome, which may require a much larger sample size.

CONCLUSIONS

Group analyses demonstrated statistically significant decreases in regional brain volumes. While group-based differences are of limited value to a radiologist interpreting an individual MR imaging, such findings motivate future effort in establishing volume-based biomarkers for prognostication. We identified structural findings in both mTBI and healthy control cohorts. Because high-resolution scans (3D sequences with isotropic 1-mm³ voxels) have become commonly performed for multiple brain-related problems such as traumatic brain injury, stroke, anoxia, inflammation, and dementia, understanding the frequency of imaging findings relative to control groups is crucial.

We found a higher prevalence of WMH burden than Riedy et al⁹ and Tate et al.¹¹ While methodologic differences could account for this prevalence, our results emphasize the importance of a dedicated mTBI imaging protocol such as the Defense Centers of Excellence for Psychological Health and Traumatic Brain Injury with high-resolution structural imaging (<https://health.mil/Reference-Center/Forms/2013/07/08/Neuroimaging-following-TBI-in-non-deployed-setting>).

While white matter findings are nonspecific and a clinical challenge, we observed a greater prevalence of ≥ 1 WMH in our mTBI-versus-healthy control groups after adjustment for age. A frontal-only distribution of WMH was observed more commonly in the mTBI group. Our results suggest that prior trauma should be considered in the differential diagnosis of multifocal white matter abnormalities with a clinical history suggesting even mTBI.

ACKNOWLEDGMENTS

The authors thank Thomas Perkins, PhD, for design/implementation of the MR imaging protocol; Pavel Krapiva, MD, for image interpretation (with author J.B.P.); Kayla Deru for manuscript review; and the BIMA/NORMAL study team who made this multidisciplinary effort possible. They also acknowledge the

instrumental contributions of William Orrison Jr, MD, for BIMA/NORMAL neuroimaging protocol design and image interpretation. Dr Orrison died on October 19, 2017.

Disclosures: Jigar B. Patel—**UNRELATED:** Other: Lovelace Biomedical Research, Albuquerque, New Mexico. **Comments:** For a portion of the study described in this article, I was a paid subject matter expert for a research firm that was a subcontractor to the “prime” awardee for this work. The remaining portion of the time, I worked as a volunteer. There is no conflict of interest with the subject matter, and this affiliation is listed on the title page of the article. Steffanie H. Wilson—**RELATED:** Fees for Participation on Review Activities Such as Data Monitoring Boards, Statistical Analysis, End Point Committees, and the Like: United States Army Medical Research and Materiel Command. **Comments:** This work was supported by the United States Army Medical Research and Materiel Command Contract No. W81XWH-15-D-0039-0003*. **Payment for Writing or Reviewing the Manuscript:** US Army Medical Research and Materiel Command. **Comments:** This work was supported by the United States Army Medical Research and Materiel Command Contract No. W81XWH-15-D-0039-0003*. Terrence R. Oakes—**UNRELATED:** Consulting Fee or Honorarium: Lovelace Respiratory Research Institute; **Payment for Writing or Reviewing the Manuscript:** Lovelace Respiratory Research Institute. Lindell K. Weaver—**RELATED:** Grant: United States Army Medical Research and Materiel Command. **Comments:** grant paid to my institution for all principal investigator activities associated with this work (protocol development, study oversight, travel, and manuscript writing and review). *Money paid to institution.

REFERENCES

1. Taylor CA, Bell JM, Breiding MJ, et al. **Traumatic Brain Injury-Related Emergency Department Visits, Hospitalizations, and Deaths: United States, 2007 and 2013.** *MMWR Surveill Summ* 2017; 66:1–16 CrossRef Medline
2. McMahon P, Hricik A, Yue JK, et al. **Symptomatology and functional outcome in mild traumatic brain injury: results from the prospective TRACK-TBI study.** *J Neurotrauma* 2014;31:26–33 CrossRef Medline
3. Nelson LD, Temkin NR, Dikmen S, et al. **Recovery after mild traumatic brain injury in patients presenting to US Level I trauma centers: A Transforming Research and Clinical Knowledge in Traumatic Brain Injury (TRACK-TBI) study.** *JAMA Neurol* 2019; Jun 3. [Epub ahead of print] CrossRef Medline
4. Management of Concussion-mild Traumatic Brain Injury Working Group. **VA/DoD Clinical Practice Guideline for Management of Concussion/Mild Traumatic Brain Injury.** Washington, DC: Department of Veterans Affairs, Department of Defense; 2016
5. Shetty VS, Reis MN, Aulino JM, et al. **ACR Appropriateness Criteria Head Trauma.** *J Am Coll Radiology* 2016;13:668–79 CrossRef Medline
6. Wu X, Kirov II, Gonen O, et al. **MR imaging applications in mild traumatic brain injury: an imaging update.** *Radiology* 2016;279:693–707 CrossRef Medline
7. DCoE Clinical Recommendation. **Neuroimaging following Mild Traumatic Brain Injury in the Non-Deployed Setting.** July 2013. <https://health.mil/Reference-Center/Forms/2013/07/08/Neuroimaging-following-TBI-in-non-deployed-setting>. Accessed March 25, 2019
8. Reneman L, de Win MM, Booi J, et al. **Incidental head and neck findings on MRI in young healthy volunteers: prevalence and clinical implications.** *AJNR Am J Neuroradiol* 2012;33:1971–74 CrossRef Medline
9. Riedy G, Senseney JS, Liu W, et al. **Findings from structural MR imaging in military traumatic brain injury.** *Radiology* 2016;279:207–15 CrossRef Medline
10. Orrison WW, Hanson EH, Alamo T, et al. **Traumatic brain injury: a review and high-field MRI findings in 100 unarmed combatants using a literature-based checklist approach.** *J Neurotrauma* 2009;26:689–701 CrossRef Medline
11. Tate DF, Gusman M, Kini J, et al. **Susceptibility weighted imaging and white matter abnormality findings in service members with**

- persistent cognitive symptoms following mild traumatic brain injury.** *Mil Med* 2017;182:e1651–58 CrossRef Medline
12. Fischl B, Salat DH, Busa E, et al. **Whole brain segmentation: automated labeling of neuroanatomical structures in the human brain.** *Neuron* 2002;33:341–55 CrossRef Medline
 13. Zhou Y, Kierans A, Kenul D, et al. **Mild traumatic brain injury: longitudinal regional brain volume changes.** *Radiology* 2013;267:880–90 CrossRef Medline
 14. Weaver LK, Wilson SH, Lindblad AS, et al. **Hyperbaric oxygen for post-concussive symptoms in United States military service members: a randomized clinical trial.** *Undersea Hyperb Med* 2018;45:129–56 Medline
 15. Weaver LK, Wilson SH, Lindblad AS, et al; NORMAL Study Team. **Comprehensive evaluation of healthy volunteers using multi-modality brain injury assessments: an exploratory, observational study.** *Front Neurol* 2018;9:1030 CrossRef Medline
 16. Corrigan JD, Bogner J. **Initial reliability and validity of the Ohio State University TBI Identification Method.** *J Head Trauma Rehabil* 2007;22:318–29 CrossRef Medline
 17. Weaver LK, Chhoeu AH, Lindblad AS, et al. **Hyperbaric oxygen for mild traumatic brain injury: design and baseline summary.** *Undersea Hyperb Med* 2016;43:489–508 Medline
 18. Rosset A, Spadola L, Ratib O. **OsiriX: an open-source software for navigating in multidimensional DICOM images.** *J Digit Imaging* 2004;17:205–16 CrossRef Medline
 19. Grinnon ST, Miller K, Marler JR, et al. **National Institute of Neurological Disorders and Stroke Common Data Element Project: approach and methods.** *Clin Trials* 2012;9:322–29 CrossRef Medline
 20. Brandstack N, Kurki T, Tenovuo O, et al. **MR imaging of head trauma: visibility of contusions and other intraparenchymal injuries in early and late stage.** *Brain Inj* 2006;20:409–16 CrossRef Medline
 21. Segonne F, Dale AM, Busa E, et al. **A hybrid approach to the skull stripping problem in MRI.** *Neuroimage* 2004;22:1060–75 CrossRef Medline
 22. Fischl B, Salat DH, van der Kouwe AJ, et al. **Sequence-independent segmentation of magnetic resonance images.** *Neuroimage* 2004;23 (Suppl 1):S69–84 CrossRef Medline
 23. Sled JG, Zijdenbos AP, Evans AC. **A nonparametric method for automatic correction of intensity nonuniformity in MRI data.** *IEEE Trans Med Imaging* 1998;17:87–97 CrossRef Medline
 24. Fischl B, Liu A, Dale AM. **Automated manifold surgery: constructing geometrically accurate and topologically correct models of the human cerebral cortex.** *IEEE Trans Med Imaging* 2001;20:70–80 CrossRef Medline
 25. Segonne F, Pacheco J, Fischl B. **Geometrically accurate topology-correction of cortical surfaces using nonseparating loops.** *IEEE Trans Med Imaging* 2007;26:518–29 CrossRef Medline
 26. Dale AM, Fischl B, Sereno MI. **Cortical surface-based analysis, I: segmentation and surface reconstruction.** *Neuroimage* 1999;9:179–94 CrossRef Medline
 27. Dale AM, Sereno MI. **Improved localization of cortical activity by combining EEG and MEG with MRI cortical surface reconstruction: a linear approach.** *J Cogn Neurosci* 1993;5:162–76 CrossRef Medline
 28. Fischl B, Dale AM. **Measuring the thickness of the human cerebral cortex from magnetic resonance images.** *Proc Natl Acad Sci U S A* 2000;97:11050–55 CrossRef Medline
 29. Holm S. **A simple sequentially rejective multiple test procedure.** *Scand J Stat* 1979;6:65–70
 30. Weaver LK, Churchill S, Wilson SH, et al. **A composite outcome for mild traumatic brain injury in trials of hyperbaric oxygen.** *Undersea Hyperb Med* 2019;46:341–52 Medline
 31. Akiyama Y, Miyata K, Harada K, et al. **Susceptibility-weighted magnetic resonance imaging for the detection of cerebral microhemorrhage in patients with traumatic brain injury.** *Neurol Med Chir (Tokyo)* 2009;49:97–99; discussion 99 CrossRef Medline
 32. Bumb JM, Brockmann MA, Groden C, et al. **TrueFISP of the pediatric pineal gland: volumetric and microstructural analysis.** *Clin Neuroradiol* 2012;22:69–77 CrossRef Medline
 33. Nolte I, Brockmann MA, Gerigk L, et al. **TrueFISP imaging of the pineal gland: more cysts and more abnormalities.** *Clin Neurol Neurosurg* 2010;112:204–08 CrossRef Medline
 34. Dean PJ, Sato JR, Vieira G, et al. **Long-term structural changes after mTBI and their relation to post-concussion symptoms.** *Brain Inj* 2015;29:1211–18 CrossRef Medline
 35. Spitz G, Bigler ED, Abildskov T, et al. **Regional cortical volume and cognitive functioning following traumatic brain injury.** *Brain Cogn* 2013;83:34–44 CrossRef Medline
 36. Burrowes SA, Rhodes CS, Meeker TJ, et al. **Decreased grey matter volume in mTBI patients with post-traumatic headache compared to headache-free mTBI patients and healthy controls: a longitudinal MRI study.** *Brain Imaging Behav* 2019 Apr 12. [Epub ahead of print] CrossRef Medline
 37. Epstein DJ, Legarreta M, Bueler E, et al. **Orbitofrontal cortical thinning and aggression in mild traumatic brain injury patients.** *Brain Behav* 2016;6:e00581 CrossRef Medline

Vessel Wall Thickening and Enhancement in High-Resolution Intracranial Vessel Wall Imaging: A Predictor of Future Ischemic Events in Moyamoya Disease

A. Kathuveetil, P.N. Sylaja, S. Senthilvelan, K. Chandrasekharan, M. Banerjee, and B. Jayanand Sudhir



ABSTRACT

BACKGROUND AND PURPOSE: Very few data are available with regard to high-resolution intracranial vessel wall imaging characteristics of Moyamoya disease and their relation to ischemic stroke risk. We investigated the high resolution imaging characteristics of MMD and its correlation with recent ischemic events.

MATERIALS AND METHODS: Patients with Moyamoya disease confirmed by DSA, including patients after revascularization, were enrolled. All the patients underwent high-resolution intracranial vessel wall imaging. Vessel wall thickening, enhancement, and the remodeling index of the bilateral distal ICA and proximal MCA were noted. The patients were followed up at 3 months and 6 months after high-resolution intracranial vessel wall imaging and the association of ischemic events with imaging characteristics was assessed.

RESULTS: Twenty-nine patients with Moyamoya disease were enrolled. The median age at symptom onset was 12 years (range, 1–51 years). A total of 166 steno-occlusive lesions were detected by high-resolution intracranial vessel wall imaging. Eleven lesions with concentric wall thickening (6.6%) were noted in 9 patients. Ten concentric contrast-enhancing lesions were observed in 8 patients, of which 3 patients (4 lesions) showed grade II enhancement. The presence of contrast enhancement ($P = .01$) and wall thickening ($P \leq .001$) showed a statistically significant association with ischemic events within 3 months before and after the vessel wall imaging. Grade II enhancement showed a statistically significant ($P = .02$) association with ischemic events within 4 weeks of high-resolution intracranial vessel wall imaging. The mean \pm standard deviation outer diameter of the distal ICA (right, -3.3 ± 0.68 mm; left, 3.4 ± 0.60 mm) and the remodeling index (right, 0.71 ± 0.13 ; left, 0.69 ± 0.13) were lower in Moyamoya disease.

CONCLUSIONS: High-resolution intracranial vessel wall imaging characteristics of concentric wall thickening and enhancement are relatively rare in our cohort of patients with Moyamoya disease. The presence of wall thickening and enhancement may predict future ischemic events in patients with Moyamoya disease.

ABBREVIATIONS: ACA = anterior cerebral artery; HRVWI = high-resolution intracranial vessel wall imaging; MMD = Moyamoya disease; PCA = posterior cerebral artery; SD = standard deviation

Moyamoya disease (MMD) is a rare cerebrovascular disease characterized by progressive steno-occlusive changes at the terminal portion of the ICA associated with the development of a fine basal collateral network.^{1–3} In the routine clinical practice,

particularly in the Asian population where both intracranial atherosclerotic disease and MMD are common and may present with similar angiographic features, clinicians face difficulties in differentiating them, which may delay the appropriate management. High-resolution intracranial vessel wall imaging (HRVWI) has recently been developed as a reliable tool to distinguish MMD from other intracranial vessel pathologies.^{2,4,5} There are few studies that describe concentric vessel wall enhancement that involves the distal ICA and proximal MCA in patients with symptomatic and patients with asymptomatic MMD.^{1,4} On the symptomatic side, concentric enhancement was observed in 82.1% of distal ICAs and 94.1% of proximal MCAs.¹ Also, concentric enhancement of bilateral distal ICAs was observed exclusively in MMD compared with intracranial atherosclerotic disease (53% versus 0%).¹ In addition, one recent study also observed a significant

Received September 12, 2019; accepted after revision October 27.

From the Comprehensive Stroke Care Program (A.K., P.N.S.), Department of Neurology; Departments of Radiology (S.S., K.C.) and Neurosurgery (B.J.S.), Rajiv Gandhi Centre for Biotechnology, Trivandrum, Kerala, India; and Sree Chitra Tirunal Institute for Medical Sciences and Technology (M.B.), Trivandrum, Kerala, India.

This study was funded by Wellcome Trust-Department of Biotechnology (DBT)/India Alliance as part of Research Training Fellowship.

Please address correspondence to P.N. Sylaja, MD, DM, Neurology Comprehensive Stroke, Care Program, Sree Chitra Tirunal Institute for Medical Sciences and Technology, Trivandrum, India 695011; e-mail: sylajapn@hotmail.com; @DrArunKNair

Indicates open access to non-subscribers at www.ajnr.org

<http://dx.doi.org/10.3174/ajnr.A6360>

association of vessel wall enhancement with cerebral ischemic events in patients with MMD, which suggests the role of inflammation and neovascularization.^{3,6,7} Little is known about the characteristic HRVWI findings and the clinical significance of those findings in MMD. This study sought to investigate the high-resolution imaging characteristics of MMD and their correlation with recent ischemic events in an Indian population.

MATERIALS AND METHODS

Patient Data

Patients with MMD who satisfied the diagnostic criteria were included in the study.⁸ The inclusion criteria were the following: 1) patients with MMD, including postrevascularization cases and those medically stable enough to be in the MR scanner for 30 to 90 minutes without general anesthesia and/or sedation, and 2) good quality images. The exclusion criteria were as follows: 1) potential sources of cardioaortic embolism, 2) $\geq 50\%$ extracranial stenosis, 3) vasculopathies, such as dissection, vasculitis, or Takayasu arteritis, 4) failure of renal function (glomerular filtration rate < 60 mL/min), or 5) contraindications to MR imaging. The criteria for selecting a patient for cerebral revascularization included 1) cerebral infarction or hemorrhage based on the patient's functional disability and 2) Suzuki stage II to IV in angiographic staging. The timing of the operation was at least 4–6 weeks in patients with stroke.

Surgery for a patient who is asymptomatic or has an asymptomatic hemisphere is rarely offered. All the patients provided informed consent, and the study was approved by the institutional ethics committee. The clinical features and demographics of the patients were collected, and the images were reviewed. After HRVWI, the patients were followed up at 3 months and 6 months. They were assessed clinically for new-onset strokes, TIA, and headaches, and for syncope. The association of acute ischemic events with HRVWI characteristics was noted. HRVWI characteristics of the patients who underwent surgical revascularization were noted and the association of imaging findings with ischemic events was analyzed.

HRVWI Protocol

The included subjects underwent pre- and postcontrast HRVWI after obtaining informed consent. HRVWI was performed as per previously published protocol from Sree Chitra Tirunal Institute for Medical sciences and technology, Trivandrum, India on a 3T Discovery system (GE Healthcare, Milwaukee, Wisconsin).⁹ Acquired sequences (corresponding voxel resolution before interpolation, after interpolation) are shown as follows: sagittal Cube (GE Healthcare) T1 ($0.8 \times 0.8 \times 1.4$ mm, $0.3 \times 0.3 \times 1.4$ mm), sagittal Cube T2 ($0.6 \times 0.6 \times 1.2$ mm, $0.3 \times 0.3 \times 1.2$ mm), sagittal Cube proton density ($0.6 \times 0.5 \times 1.2$ mm, $0.3 \times 0.3 \times 1.2$ mm). Interpolation was done by using zero-filling interpolation X 512 (matrix or in-plane) zero-filling interpolation X 2 (section or through-plane). Also, SWI and DWI sequences were also acquired. These sequences eventually resulted in the following scan time for each sequence: sagittal CUBE T1 fat suppressed, 6:49 minutes; sagittal Cube T2, 6:04 minutes; sagittal Cube proton density, 4:28 minutes; and postcontrast sagittal Cube T1 fat suppressed, 6:49 minutes. Postcontrast images were acquired after

30 seconds of intravenous administration of gadoterate meglumine (Dotarem; Guerbet, Aulnay-sous-Bois, France) Guerbet LLC, headquarters located in Princeton, US at a dose of 0.1 mmol/kg body weight.

Image Review

The conventional MR imaging, DSA-Digital subtraction angiography, and HRVWI were read by 1 neuroradiologist S. Senthilvelan and 1 neurologist K. Arun with 4 years of experience and were blinded to the clinical information. All the images were read in consensus. MR images were reviewed for the presence of acute and chronic infarcts, hemorrhages, the pattern of infarcts, and the presence of small-vessel ischemic changes. All patients underwent DSA by using a biplane angiography system (Philips Healthcare, Best, the Netherlands) in an interventional radiology angiography suite. Luminal images were evaluated for the presence of stenosis and/or occlusion that involved distal ICA, proximal MCA, anterior cerebral artery (ACA), posterior cerebral artery (PCA), and basilar artery, and for the type of collaterals. Collaterals were classified as superficial meningeal (leptomeningeal, durocortical) and deep parenchymal (subependymal anastomotic, inner thalamic) networks.¹⁰ The disease was staged in all the patients by using DSA based on the Suzuki staging: 1) narrowing of carotid bifurcation, 2) dilation of the ACA and MCA with initiation of Moyamoya, 3) partial disappearance of the ACA and MCA with intensification of ICA Moyamoya, 4) advanced steno-occlusive changes in the ICA with a small amount of ICA Moyamoya, 5) absence of the ACA and MCA with further reduction of ICA Moyamoya, and 6) complete disappearance of ICA Moyamoya.¹¹

HRVWI was reviewed for wall thickening and wall enhancement that involved the distal ICA, proximal MCA, ACA, PCA, and basilar artery. The remodeling index of only the distal ICA was assessed considering the large caliber and early involvement of distal ICA in MMD:

Wall Thickening. Wall thickening was classified as concentric, eccentric, or no wall thickening by using a precontrast T1 Cube sequence by visual inspection. Concentric wall thickening was defined as a circumferential and uniform thickening, with the width of the thinnest wall segment $\geq 50\%$ of the thickest segment. Eccentric wall thickening was defined as either limited to 1 side of the vessel wall, or, where circumferential enhancement was noted, the thinnest part of the wall enhancement was estimated to be $< 50\%$ of the thickest point.¹²

Contrast Enhancement. The degree of enhancement of vessels was qualitatively graded, depending on its signal intensity on postcontrast T1 images compared with corresponding precontrast images: grade 0, no enhancement; grade I, mild enhancement, the signal intensity of vessel wall is less than that of the pituitary infundibulum; and grade II, strong enhancement, the signal intensity of contrast-enhanced vessel wall is similar to or greater than that of the infundibulum.^{3,13} Enhancement was considered concentric if it was circumferential and uniform (defined specifically as the width of the thinnest wall segment of $\geq 50\%$ of the thickest segment). Eccentric enhancement was defined as

Table 1: Demographic and clinical characteristics (N = 29)

Patient Characteristics	Results
Sex, n (%)	
Males	17 (58.6)
Females	12 (41.6)
Age, n (%)	
<18 y	15 (51.7)
≥18 y	14 (48.3)
Age at first event ^a , median (IQR), y	−12 (6–36)
Initial clinical presentation, n (%)	
Ischemic stroke	10 (34.5)
Intracerebral bleed	5 (17.2)
TIA	7 (24.2)
Syncope	1 (3.4)
Seizure	6 (20.7)
Recurrent events, n (%)	22 (75.9)
Ischemic stroke	10 (34.5)
Intracranial bleed (intraventricular hemorrhage)	2 (6.9)
Positive family history of MMD, n (%)	2 (6.9)
NIHSS on admission, median (IQR)	1 (0–3)
mRS on admission, median (IQR)	1 (0–3)

Note:—IQR indicates interquartile range; mRS, modified Rankin scale.

^aThe mean ± SD interval between the first symptom and HRVWI was 64.7 ± 80.7 months.

either limited to 1 side of the vessel wall (eg, not 360° circumferential enhancement) or, where circumferential enhancement was noted, the thinnest part of the wall enhancement was estimated to be < 50% of the thickest point.^{1,12}

Remodeling Index. The outer diameter of the terminal portion of the ICA was measured by using sagittal T1 fat-suppressed images. The remodeling index was calculated as the outer diameter of a narrowed vessel (measurements between both outer diameters) divided by the caliber of the normal proximal reference vessel¹ (proximal ICA). If the ratio is > 1.05, then it was taken as positive remodeling, <0.95 was negative remodeling, and 0.95–1.05 was normal.¹⁴ The caliber of the vessel was calculated in the sagittal-oblique images perpendicular to the vessel in axial sections.

Statistical Analysis

Continuous-median (interquartile range) or mean standard deviation (SD) categorical variables-percentage (count), respectively. Data comparison of categorical variables was done by using the Fisher exact test. A *P* value of < .05 was considered statistically significant. The data were analyzed by using analytical software SPSS Statistics for Windows, version 21.0 (2012) (IBM, Armonk, New York).

Table 2: Imaging characteristics of patients with MMD

Characteristic	n (%) (n = 58 Hemispheres)	
A. MRI		
1. Pattern of infarct	Acute Infarcts	Chronic Infarcts
Watershed	9 (15.5)	15 (25.9)
Territorial	3 (5.2)	5 (8.6)
Cortical	2 (3.4)	3 (5.2)
Isolated subcortical	1 (1.7)	2 (3.4)
B. DSA		
1. Laterality (n = 29)		
Bilateral	27 (93.1)	
Unilateral	2 (6.9)	
2. Vessels involved (n = 166 vessels)	Narrowed	Occluded
Distal ICA	19 (11.4)	37 (22.2)
Proximal MCA	12 (7.2)	39 (23.5)
Proximal ACA	17 (10.2)	25 (15.0)
PCA	8 (4.8)	1 (0.6)
Basilar artery (29 vessels)	1 (0.6)	0 (0)
3. Suzuki stage	Right	Left
I	2 (7.1)	2 (7.1)
II	0 (0)	1 (3.6)
III	5 (17.9)	2 (7.1)
IV	4 (14.3)	10 (35.7)
V	16 (57.1)	13 (46.4)
VI	1 (3.6)	0 (0)
4. Collaterals (n = 58 hemispheres)		
Superficial meningeal		
Leptomeningeal		
Anterior	27 (46.6)	24 (41.4)
Posterior	21 (36.2)	20 (34.5)
Durocortical		
Anterior	21 (36.2)	18 (31.1)
Posterior	3 (5.2)	5 (8.6)
Deep parenchymal		
Subependymal anastomotic		
Anterior	6 (10.3)	6 (10.3)
Posterior	5 (8.6)	5 (8.6)
Inner thalamic		
Anterior	8 (13.8)	6 (10.3)
Posterior	8 (13.8)	7 (12.1)

RESULTS

Twenty-nine patients with MMD, confirmed by DSA, were enrolled in the study. Of them, 15 patients had undergone surgical revascularization. Seventeen (58.6%) were males and 12 (41.4%) were females (male-to-female ratio, 1.4) and 51.7% were <18 years old. The median age at symptom onset was 12 years (range, 1–51 years), with ischemic stroke (34.5%) being the most common initial clinical presentation, followed by TIA (24.1%), seizures (20.7%), intracranial hemorrhage (17.2%), headache (6.8%), and syncope (3.4%). Seizures and hemorrhage as initial presentation occurred predominantly in children <10 years old (*P* = .03) and in adults >30 years old (*P* = .04), respectively. Recurrence of neurologic events was observed in 75.9% of the patients (Table 1). A total of 58 hemispheres, including 2 cases of unilateral MMD, were analyzed by using MR imaging, which showed 9 watershed, 3 territorial, 2 cortical, and 1 subcortical infarct in the MCA territory. DSA showed predominantly occlusive lesions that involved the distal ICA, proximal MCA, ACA, and PCA (Table 2) and collaterals, predominantly originating from the superficial meningeal network, which was reinforced by the deep parenchymal network (Table 2).

HRVWI was performed in 29 patients. A total of 166 steno-occlusive lesions were

detected (56 distal ICA, 51 proximal MCA, 49 proximal ACA, 9 PCA, and 1 basilar artery). Among them, 11 lesions (6.6%) with concentric wall thickening (Figure) were noted in 9 patients (31.03%), of which 9 lesions (81.8%) involved the distal ICAs and 2 proximal MCAs (18.2%). Ten concentric contrast-enhancing lesions (6.02%) were noted in 8 patients (27.6%), of whom 3 patients (4 lesions) showed lesions with grade II enhancement. Grade I enhancement involved 4 distal ICAs and 2 proximal MCAs. Grade II enhancement (Figure) was observed in 3 distal ICAs and 1 proximal MCA on the symptomatic side. None of the

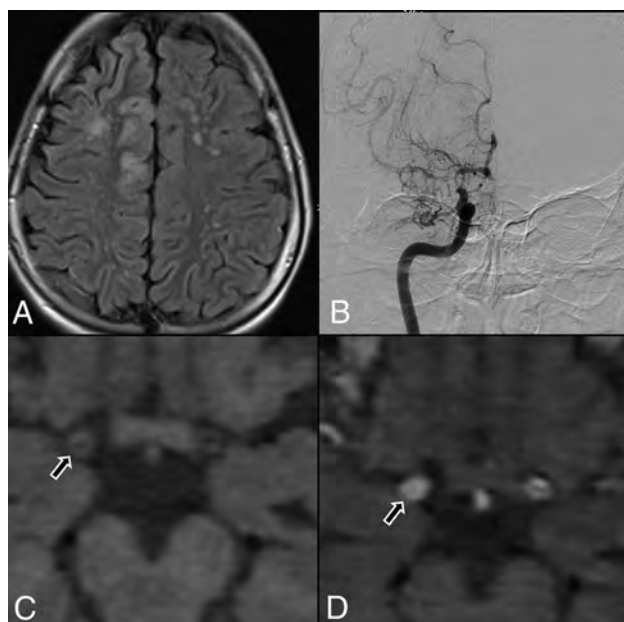


FIGURE. A, Flair axial section showing right ACA and MCA territory cortical infarct and multiple discrete MCA-ACA watershed infarct on the left side. B, DSA, showing tight stenosis of the distal ICA, with concomitant narrowing of proximal MCA and ACA, with leptomeningeal collaterals. C, Axial T1 noncontrast, HRVWI, showing circumferential wall thickening (arrow) and narrowing of the lumen of right distal ICA. D, Axial T1 contrast-enhanced, HRVWI, showing circumferential grade II enhancement (arrow) of a right distal ICA (Note:—Enhancement is graded by comparing with pituitary infundibulum).

ACA, PCA, and basilar artery MMD lesions revealed wall thickening or enhancement.

The mean age at the initial presentation of patients with wall thickening and enhancement was 22.4 and 27.3 years, respectively. The mean \pm SD interval between the first symptom and HRVWI was 64.7 ± 80.7 months, which showed a statistically insignificant inverse relationship with T1 contrast enhancement (mean \pm SD, 55.6 ± 49.6 versus 68.1 ± 90.6 , $P = .44$). The mean \pm SD follow-up period after the vessel wall imaging was 6.9 ± 3.4 months. The presence of contrast enhancement (50%, $P = .01$) and wall thickening (64.3%, $P \leq .001$) showed a statistically significant association with the ischemic events within 3 months before and after vessel wall imaging. Grade II contrast enhancement showed a statistically significant ($P = .02$) association with events within 4 weeks of HRVWI. The mean \pm SD outer diameter of the distal ICA (right, 3.3 ± 0.68 mm; left, 3.4 ± 0.60 mm) and mean \pm SD remodeling index (right, 0.71 ± 0.13 ; left, 0.69 ± 0.13) were lower in MMD (Table 3).

Among the 15 patients (51.7%) who underwent revascularization, 11 (73.3%) underwent unilateral revascularization and 4 (26.7%) underwent bilateral revascularization. HRVWI revealed contrast enhancement in only 1 patient who underwent bilateral revascularization and in 2 patients who underwent unilateral revascularization. Wall thickening was noted in 1 patient who underwent bilateral revascularization and 4 patients with unilateral revascularization. None of these patients developed ischemic events that corresponded to the arterial territory of wall thickening or enhancement during the follow-up period.

DISCUSSION

We analyzed the characteristic HRVWI findings in MMD and their possible role in predicting the risk of recent ischemic events. In our cohort of 29 patients with MMD, only 6.02% MMD lesions showed contrast enhancement and 6.6% MMD lesions showed wall thickening. Among them, wall thickening and enhancement were mostly observed in distal ICA and proximal MCA. The ACA, PCA, and basilar artery did not reveal such changes in HRVWI. A smaller outer diameter of the involved vessel with negative remodeling was also observed. Also, the

Table 3: HRVWI characteristics of MMD

HRVWI Characteristics	Contrast Enhancement (8 Patients, 10 Lesions)	T1 Wall Thickening (9 Patients, 11 Lesions)
Pattern, <i>n</i> (%)		
Concentric	10 (100)	11 (100)
Eccentric	0 (0)	0 (0)
Vessel involved, <i>n</i> (%)		
Distal ICA	8 (80)	9 (81.8)
Proximal MCA	2 (20)	2 (18.2)
Events within 3 mo before and after the imaging, <i>n</i> (%)	7 (87.5) ($P = .01$)	9 (100) ($P \leq .001$)
Recent events (DWI positive) within 4 wk of imaging, <i>n</i> (%)		4 (44.4) ($P = .20$)
Grade I contrast enhancement	0 (0)	
Grade II contrast enhancement	3 (100) ($P = .02$)	
Suzuki stage	Grade 2 enhancement (4 lesions)	Wall thickening (11 lesions)
I	1 (25)	1 (9.1)
II	1 (25)	2 (18.2)
III	0	4 (36.4)
IV	2 (50)	4 (36.4)
Remodeling index, mean \pm SD	Right, 0.71 ± 0.13	Left, 0.69 ± 0.13

presence of wall thickening and enhancement showed a statistically significant association with ischemic events.

We observed concentric wall enhancement in 27.6% of patients with MMD. Among the 166 steno-occlusive lesions detected by HRVWI, 6.02% of lesions only showed contrast enhancement, which is lower in comparison with the previously published data, which accounted for 70%–93%.^{1,3,15,16} This may be related to the characteristics of the population under study or might be related to the small sample size. There is evidence that MMD is primarily a proliferative disease of the intima and smooth muscles that leads to vascular stenosis and that concentric enhancement may represent hyperproliferation of vessel components.¹⁷ It is well known that strong contrast enhancement of the arterial wall suggests an increase in the vascular supply and increased endothelial permeability, which promotes entry of the contrast agent into the extravascular space.¹⁸

Chmelova et al¹⁹ found a higher expression of both angiogenic factors in intima and vascular endothelial growth factor in the endothelium of Moyamoya-affected arteries than normal arteries. Nestin, a marker of newly formed endothelial cells was expressed in the Moyamoya-affected vessels.²⁰ Thus, it can be presumed that an active angiogenic milieu prevails in the enhanced vessels in patients with MMD.¹⁹ Similar to the atherosclerotic process in the extracranial vessels where concentric and circumferential wall enhancements suggest an inflammatory response due to increased macrophage infiltration and neovascularity, the enhancement in Moyamoya vessels may be considered to represent an active angiogenic process and inflammatory response.

Vessel wall thickening was observed in 31.03% of the patients with MMD. Among the 166 steno-occlusive lesions detected, 6.6% of lesions only showed vessel wall thickening, which was diffuse and concentric. Also, the outer diameter of the distal ICA was attenuated with negative remodeling in all the patients. Histopathologic studies of ICAs and MCAs in MMD demonstrated eccentric intimal fibrous thickening, which is often multilayered, with newly formed elastic lamina between the layers.²¹ The internal elastic lamina is markedly tortuous, with duplication and a decrease in the number of smooth-muscle cells in the media and these pathologic changes are seen predominantly in the distal ICA, proximal MCA, and ACA. The thinning of media and decreased flow as well as constriction of the internal elastic lamina, culminate in the decreased outer diameter of the vessels as well as the negative remodeling. It can also be postulated that diffuse wall thickening might be due to vessel wall edema and investigators have found that the wall edema has a correlation with inflammation²² associated with significantly greater plasma concentration of matrix metalloproteinase-9, monocyte chemoattractant protein-1, vascular endothelial growth factor, and other inflammatory cytokines.

Our study also observed steno-occlusive lesions, which predominantly involved the distal ICA, which supports the notion that stenosis in MMD begins first in the ICA and as the disease progress involves the MCA, followed by the ACA. The occlusive lesions in MMD predominantly involve the anterior circulation and the involvement of the vertebral and basilar arteries is relatively rare,²¹ which is also the same in our study. Our study could

not demonstrate thickening or enhancement of the ACA, PCA, and basilar artery. However, in 1 study, 19.6% of ACAs showed contrast enhancement.³

We also studied the role of HRVWI to possibly predict a future event based on its characteristic findings. It was observed that grade II enhancing lesions were significantly associated with ischemic events within 4 weeks of imaging. Besides, those lesions that showed either wall thickening or contrast enhancement were significantly associated with neurologic events within 3 months before or after vessel wall imaging. Wang et al³ reported that high-grade enhancement in the Moyamoya-affected vessel is associated with an increased risk of acute ischemic infarction. As with atherosclerotic plaque, in which higher-grade contrast enhancement represents plaque instability and identifies lesions responsible for ischemic events, higher-grade enhancement in MMD may reflect a proliferative neovascular change and activity of the lesion.³ These findings suggest that HRVWI might help to identify patients at risk of an early event and help the physician triage them for early revascularization. We also observed that the presence of wall thickening and enhancement did not correlate with subsequent events after revascularization, which suggests that these findings cannot be taken into consideration in predicting the risk of future events after revascularization.

The strength of our study is that, because all the patients underwent detailed evaluation for secondary etiology, the study population truly represents idiopathic MMD. The HRVWI was read by a neuroradiologist and a neurologist who were blinded to clinical data and, hence, the imaging data are homogeneous and unbiased. Because all these patients were on a regular follow-up schedule, the recurrent cerebral events could be carefully documented. The study was conducted in a single center and the sample size was small. Also, the HRVWI was done at varying time intervals from the symptom onset with a long interval in a few of the patients, which may explain the relatively few patients with wall enhancement compared with previous studies. A study with a large sample size that involves multiple centers is needed to validate the findings in our study.

CONCLUSIONS

The presence of concentric wall thickening and enhancement in HRVWI was relatively rare in our cohort of patients with MMD compared with the Japanese and Chinese populations. The presence of wall thickening, and enhancement may predict future ischemic events in patients with MMD.

Disclosures: K. Arun—RELATED: Grant: Wellcome Trust/DBT*; Support for travel to meetings for the study or other purposes: Wellcome Trust/DBT.* P.N. Sylaja—RELATED: Grant: Wellcome DBT project* UNRELATED: Employment: Sree Chitra Tirunal Institute for Medical Sciences and Technology. C. Kesavadas—RELATED: Grant: Wellcome DBT* UNRELATED: Employment: Grants/Grants Pending: DST India.* *Money paid to the institution.

REFERENCES

1. Ryoo S, Cha J, Kim SJ, et al. **High-resolution magnetic resonance wall imaging findings of moyamoya disease.** *Stroke* 2014;45:2457–60 CrossRef Medline
2. Han C, Li ML, Xu Y, et al. **Adult moyamoya-atherosclerosis syndrome: clinical and vessel wall imaging features.** *J Neurol Sci* 2016;369:181–84 CrossRef Medline

3. Wang M, Yang Y, Zhou F, et al. **The contrast enhancement of intracranial arterial wall on high-resolution MRI and its clinical relevance in patients with moyamoya vasculopathy.** *Sci Rep* 2017;7:44264 CrossRef Medline
4. Kim YJ, Lee DH, Kwon JY, et al. **High resolution MRI difference between moyamoya disease and intracranial atherosclerosis.** *Eur J Neurol* 2013;20:1311–18 CrossRef Medline
5. Kesav P, Krishnavadana B, Kesavadas C, et al. **Utility of intracranial high-resolution vessel wall magnetic resonance imaging in differentiating intracranial vasculopathic diseases causing ischemic stroke.** *Neuroradiology* 2019;61:389–96 CrossRef
6. Hatsukami TS, Yuan C. **MRI in the early identification and classification of high-risk atherosclerotic carotid plaques.** *Imaging Med* 2010;2:63–75 CrossRef Medline
7. Wasserman BA. **Advanced contrast-enhanced MRI for looking beyond the lumen to predict stroke: building a risk profile for carotid plaque.** *Stroke* 2010;41(Suppl):S12–S16 CrossRef Medline
8. Fukui M. **Guidelines for the diagnosis and treatment of spontaneous occlusion of the circle of Willis ('moyamoya' disease).** Research Committee on Spontaneous Occlusion of the Circle of Willis (Moyamoya Disease) of the Ministry of Health and Welfare. *Clin Neurol Neurosurg* 1997;99:S238–40 CrossRef
9. Adhithyan R, Kesav P, Thomas B, et al. **High-resolution magnetic resonance vessel wall imaging in cerebrovascular diseases.** *Neurol India* 2018;66:1124–32 CrossRef Medline
10. Baltasvias G, Khan N, Valavanis A. **The collateral circulation in pediatric moyamoya disease.** *Childs Nerv Syst* 2015;31:389–98 CrossRef Medline
11. Zhao M, Zhang D, Wang S, et al. **Posterior circulation involvement in pediatric and adult patients with moyamoya disease: a single center experience in 574 patients.** *Acta Neurol Belg* 2018;118:227–33 CrossRef Medline
12. Swartz RH, Bhuta SS, Farb RI, et al. **Intracranial arterial wall imaging using high-resolution 3-Tesla contrast-enhanced MRI.** *Neurology* 2009;72:627–34 CrossRef Medline
13. Qiao Y, Steinman DA, Qin Q, et al. **Intracranial arterial wall imaging using three-dimensional high isotropic resolution black blood MRI at 3.0 Tesla.** *J Magn Reson Imaging* 2011;34:22–30 CrossRef Medline
14. Yu LB, Zhang Q, Shi ZY, et al. **High-resolution magnetic resonance imaging of moyamoya disease.** *Chin Med J (Engl)* 2015;128:3231–37 CrossRef Medline
15. Yuan M, Liu ZQ, Wang ZQ, et al. **High-resolution MR imaging of the arterial wall in moyamoya disease.** *Neurosci Lett* 2015;584:77–82 CrossRef Medline
16. Mossa-Basha M, de Havenon A, Becker KJ, et al. **Added value of vessel wall magnetic resonance imaging in the differentiation of moyamoya vasculopathies in a non-Asian cohort.** *Stroke* 2016;47:1782–88 CrossRef Medline
17. Fukui M, Kono S, Sueishi K, et al. **Moyamoya disease.** *Neuropathology* 2000;20(Suppl):S61–64 CrossRef Medline
18. Millon A, Boussel L, Brevet M, et al. **Clinical and histological significance of gadolinium enhancement in carotid atherosclerotic plaque.** *Stroke* 2012;43:3023–28 CrossRef Medline
19. Chmelova J, Kolar Z, Prochazka V, et al. **Moyamoya disease is associated with endothelial activity detected by anti-nestin antibody.** *Biomed Pap Med Fac Univ Palacky Olomouc Czech Repub* 2010;154:159–62 Medline
20. Mokry J, Cizkova D, Filip S, et al. **Nestin expression by newly formed human blood vessels.** *Stem Cells Dev* 2004;13:658–64 CrossRef Medline
21. Kaku Y, Morioka M, Ohmori Y, et al. **Outer-diameter narrowing of the internal carotid and middle cerebral arteries in moyamoya disease detected on 3D constructive interference in steady-state MR image: is arterial constrictive remodeling a major pathogenesis?** *Acta Neurochir (Wien)* 2012;154:2151–57 CrossRef Medline
22. Chen X, Zhao H, Chen Z, et al. **Association between proximal internal carotid artery steno-occlusive disease and diffuse wall thickening in its petrous segment: a magnetic resonance vessel wall imaging study.** *Neuroradiology* 2017;59:485–90 CrossRef Medline

Usefulness of Contrast-Enhanced 3D-FLAIR MR Imaging for Differentiating Rathke Cleft Cyst from Cystic Craniopharyngioma

M. Azuma, Z.A. Khant, M. Kitajima, H. Uetani, T. Watanabe, K. Yokogami, H. Takeshima, and T. Hirai

ABSTRACT

BACKGROUND AND PURPOSE: Because it can be difficult to discriminate between a Rathke cleft cyst and cystic craniopharyngioma by conventional MR imaging alone, we investigated whether contrast-enhanced 3D T2-FLAIR MR imaging at 3T helps to distinguish a Rathke cleft cyst from a cystic craniopharyngioma.

MATERIALS AND METHODS: We evaluated pre- and postcontrast T1-weighted and 3D T2-FLAIR images of 17 patients with pathologically confirmed Rathke cleft cyst ($n=10$) or cystic craniopharyngioma ($n=7$). All underwent 3T MR imaging studies before surgery. Two neuroradiologists independently recorded the enhancement grade of the lesion wall as grade 2 (most of the wall enhanced), grade 1 (some of the wall enhanced), and grade 0 (none of the wall enhanced). One neuroradiologist performed a blinded reading study of conventional MR images with/without 3D T2-FLAIR images. Interobserver agreement was determined by calculating the κ coefficient. Statistical analyses, including receiver operating characteristic curve analysis were performed.

RESULTS: Interobserver agreement for postcontrast T1WI and 3D T2-FLAIR images was excellent ($\kappa = 0.824$ and $\kappa = 0.867$, respectively). Although the difference in the mean enhancement grade of Rathke cleft cysts and cystic craniopharyngiomas was not significant on postcontrast T1WIs, it was significant on postcontrast 3D T2-FLAIR images ($P=.0011$). The area under the receiver operating characteristic curve of the conventional MR alone and conventional MR with 3D T2-FLAIR readings was 0.879 and 1.0, respectively, though there was no significant difference in the area under the curve between the 2 readings.

CONCLUSIONS: Contrast-enhanced 3D T2-FLAIR imaging at 3T helps to distinguish a Rathke cleft cyst from cystic craniopharyngioma.

ABBREVIATIONS: CCP = cystic craniopharyngioma; CE = contrast-enhanced; RCC = Rathke cleft cyst

A Rathke cleft cyst (RCC) with mild symptoms can be managed conservatively because it may shrink or disappear spontaneously.¹ Severe symptoms are usually managed by surgical drainage with partial excision of the cyst wall.² Cystic craniopharyngioma (CCP), however, usually requires more extensive surgery and/or radiation therapy.³ Therefore, the differentiation between an RCC and a CCP is important.

The discrimination between RCC and CCP on CT and conventional MR imaging can be difficult.⁴ According to Hofmann et al,⁵ the size of the lesion (>2 cm), its suprasellar location, and

the presence of calcification were diagnostic for CCP. Choi et al⁶ reported that superior tumor lobulation, a large tumor volume, and compression of the third ventricle on MR imaging supported a diagnosis of CCP. However, Choudhry et al⁷ encountered an RCC with CCP features, that is, a large lesion size (6.5 cm), suprasellar location, calcification, superior tumor lobulation, and compression of the third ventricle. Hua et al⁴ suggested that cyst wall enhancement may help to differentiate neoplastic from non-neoplastic cystic lesions. However, many RCCs are surrounded by the enhancing normal pituitary gland and this mimics wall enhancement,⁸ which renders the differentiation between RCC and CCP difficult.

The contrast-enhanced (CE) 3D T2-FLAIR MR imaging sequence is more highly sensitive to low concentrations of gadolinium than T1WI^{9,10} and the signal intensity of vessels at a flow velocity that exceeds 1.0 cm/s is suppressed.¹¹ On CE 3D T2-FLAIR images, the anterior lobe of the pituitary gland is often unenhanced.¹² Therefore, we investigated whether differences in cyst wall enhancement on CE 3D T2-FLAIR MR imaging help to differentiate between an RCC and a CCP.

Received August 16, 2019; accepted after revision October 29.

From the Departments of Radiology (M.A., Z.A.K., T.H.) and Neurosurgery (T.W., K.Y., H.T.), Faculty of Medicine, University of Miyazaki, Miyazaki, Japan; and Department of Diagnostic Radiology (M.K., H.U.), Graduate School of Medical Science, Kumamoto University, Kumamoto, Japan.

This study was supported by a Grant-in-Aid for Clinical Research from Miyazaki University Hospital.

Please address correspondence to Minako Azuma, Department of Radiology, Faculty of Medicine, University of Miyazaki, 5200 Kihara, Kiyotake, Miyazaki 889-1692, Japan; e-mail: minako_azuma@med.miyazaki-u.ac.jp

<http://dx.doi.org/10.3174/ajnr.A6359>

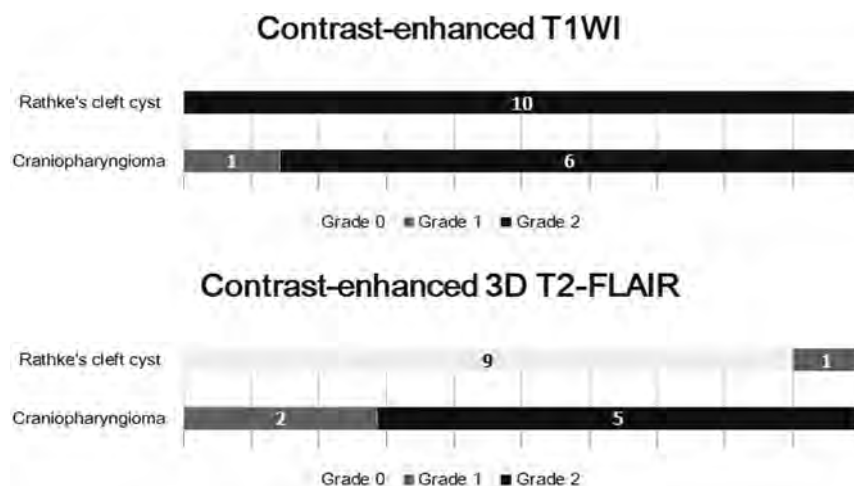


FIG 1. Distribution of the wall-enhancement grade of RCC and CCP on CE T1WI and 3D T2-FLAIR images.

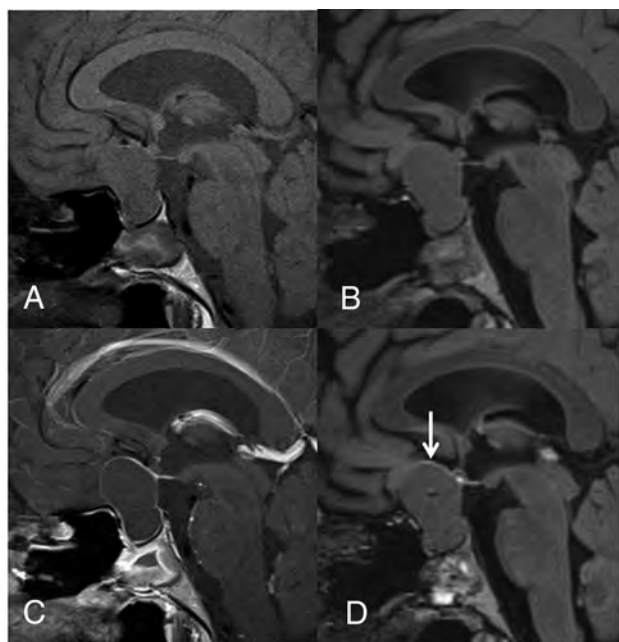


FIG 2. A 23-year-old woman with RCC. Compared with the precontrast T1WI (A), the postcontrast T1WI (C) demonstrates enhancement in most of the cyst wall (grade 2). Compared with the precontrast 3D T2-FLAIR image (B), the postcontrast 3D T2-FLAIR image (D) shows grade 1 enhancement of some of the cyst wall (arrow). In the blinded reading study, the confidence scale of this lesion was probably an RCC (scale 2) at both the first and second interpretation sessions.

MATERIALS AND METHODS

Study Population

Our retrospective study was approved by the institutional review board of the University of Miyazaki Hospital; informed consent was waived. Seventeen consecutive patients (9 men, 8 women; age range, 23–81 years; mean age, 51.6 years) were included: 10 had pathologically confirmed RCC, the other 7 had CCP. Before surgery, all had undergone conventional MR pre- and postcontrast T1WI and 3D T2-FLAIR imaging studies on a 3T unit.

MR Study Protocol

All studies were performed on a 3T MR imaging scanner (Magnetom Trio; Siemens, Erlangen, Germany); a 12-channel head coil was used. The scanning parameters for 3D T2-FLAIR were TR, 6000 ms; TE_{eff}, 420 ms; inversion time, 2000 ms; echo-train length, 142; imaging time, 4 min 26 s; field of view, 230 × 230 mm; matrix, 256 × 256; and 0.9-mm-thick sections. For T1WI, the parameters were TR, 560 ms; TE, 11 ms; section thickness, 3 mm; matrix, 256 × 218; field of view, 130 mm on coronal and sagittal planes.

The contrast agent was gadopentetate dimeglumine (Magnevist, Bayer HealthCare Pharmaceuticals, Wayne, New Jersey), injected at 0.1 mmol/kg body weight. To reduce the imaging time, we obtained sagittal 3D planes that covered the entire brain with each pulse sequence. CE MR studies were started approximately 60–120 s after contrast material injection; a T1-weighted sequence was the first sequence.

Image Evaluation

Two neuroradiologists with 6 and 8 years of reading experience who were blinded to the patient identity and the final diagnosis independently graded the degree of CE of the cyst wall on T1WI and 3D T2-FLAIR images on a PACS workstation by using a 3-point scoring system in which grade 2 represented most of the wall enhanced, grade 1 represented some of the wall enhanced, and grade 0 represented no wall enhancement. Final judgments were obtained by consensus of the 2 readers.

One experienced neuroradiologist with 28 years of reading experience performed a blinded reading study. Each case was subjected to 2 reading sessions on a PACS workstation. At the first session, the reader was provided with only the conventional MR images to diagnose the 2 types of pituitary lesions. Sagittal views of pre- and postcontrast T1WI, and T2WI were evaluated. The reader assessed the lesions by using a 5-point confidence scale: 1, definitely an RCC; 2, probably an RCC; 3, equivocal; 4, probably a CCP; and 5, definitely a CCP. After the first session, the reader performed a second interpretation in which sagittal views of pre- and postcontrast 3D T2-FLAIR images were added. The reader reassessed the lesion by using the same 5-point confidence scale. After the blinded study, the reader retrospectively identified the reason(s) for the incorrect image interpretation.

Statistical Analysis

All statistical analyses were performed with MedCalc version 19.0.7 (MedCalc Software, Mariakerke, Belgium). The statistical significance of scoring differences was analyzed by using the Mann-Whitney U test. Interobserver agreement was determined by calculating the κ coefficient in which $\kappa = 0.81$ –1.0 indicated

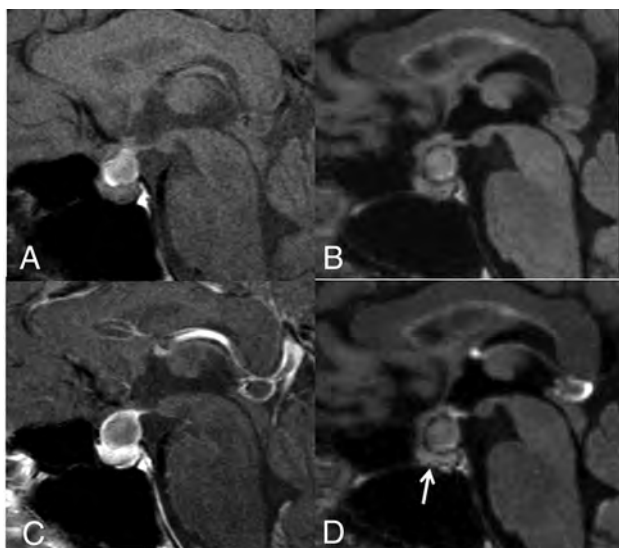


FIG 3. A 40-year-old woman with an RCC. On the postcontrast T1WI (C) compared with the precontrast T1WI (A), the cyst wall is enhanced (grade 2), as is the pituitary gland. Unlike the precontrast 3D T2-FLAIR image (B), the postcontrast image (D) shows no contrast enhancement (grade 0). Different from the postcontrast T1WI (C), the pituitary gland is not enhanced on the postcontrast 3D T2-FLAIR image (arrow in D). The observer judged this lesion as equivocal (scale 3) at the conventional MR interpretation, whereas the confidence level was changed to probably an RCC (scale 2) by the addition of 3D T2-FLAIR interpretation.

excellent agreement, 0.61–0.80 indicated good agreement, 0.41–0.60 indicated moderate agreement, 0.21–0.40 indicated fair agreement, and 0–0.20 indicated slight agreement.

Receiver operating characteristic analysis was performed to evaluate the diagnostic performance of conventional MR images with and without 3D T2-FLAIR images. Lesions with a confidence score of 3, 4, or 5 were considered to be CCPs and those with a score of 1 or 2 were considered to be RCCs. Pair-wise comparison of the receiver operating characteristic curves was also performed by using the area under the receiver operating characteristic curve. Differences of $P < .05$ were considered statistically significant.

RESULTS

Interobserver agreement for postcontrast T1WI and 3D T2-FLAIR images was excellent ($\kappa = 0.824$ and $\kappa = 0.867$, respectively). The distribution of the wall-enhancement grade of 10 RCCs and 7 CCPs on CE T1WI and CE 3D T2-FLAIR images is shown in Fig 1. On CE T1WI, all RCCs and CCPs were classified as grade 1 or 2 (Figs 2–5). The difference in the mean grade assigned to CCPs and RCCs was not significant. On CE 3D T2-FLAIR images, 1 RCC was classified as grade 1 (Fig 2) and the other 9 RCCs as grade 0 (Figs 3 and 4). Of the 7 CCPs, 5 were of enhancement grade 2 (Fig 5), the others were of grade 1. The difference in the mean grade assigned to RCCs and CCPs was significant ($P = .0011$). As shown in Fig 6, adding the 3D T2-FLAIR images at the first reading session resulted in achieving perfect diagnostic performance in the discrimination between an RCC and a CCP. The area under the curve of the first and second

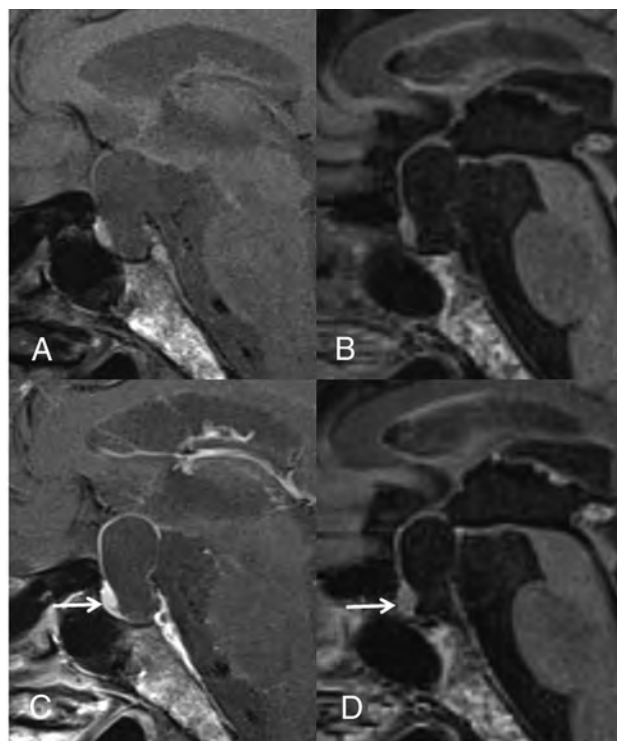


FIG 4. A 60-year-old man with RCC. On the postcontrast T1WI (C) compared with the precontrast T1WI (A), the cyst wall is enhanced (grade 2) and a solid enhanced area is seen (arrow). Unlike the precontrast 3D T2-FLAIR image (B), the postcontrast image (D) shows no contrast enhancement of the wall (grade 0) and the solid area (arrow). The observer judged this lesion as probably a CCP (scale 4) at the conventional MR interpretation, whereas the confidence level was changed to probably an RCC (scale 2) by the addition of 3D T2-FLAIR interpretation.

reading session was 0.879 and 1.0, respectively. There was no significant difference in the area under the curve between the first and second reading session ($P = .16$).

A retrospective review revealed the reasons for incorrect interpretation for 2 of 17 (11.8%) conventional MR readings (first interpretation session). In one patient with an RCC, the lesion determination on conventional MR interpretation was a false-positive result due to the presence of a solid component on CE T1WI (Fig 4), which was correctly interpreted as normal anterior pituitary gland by adding the 3D T2-FLAIR images (second interpretation session). In 1 patient with a CCP, the false-negative result of a conventional MR interpretation was attributed to a homogeneously enhanced cystic wall (Fig 5).

DISCUSSION

We found that cyst wall enhancement on CE 3D T2-FLAIR images was significantly different between an RCC and a CCP. In addition, adding CE 3D T2-FLAIR images to conventional MR images was useful for differentiating RCC from CCP. On CE T1WI, all RCCs and CCPs showed wall enhancement. On CE 3D T2-FLAIR images, however, the cyst wall enhanced in all the CCPs and in only 1 RCC. The difference in cyst wall enhancement must have contributed to our blinded interpretation results. To our knowledge, our study is the first documentation that CE

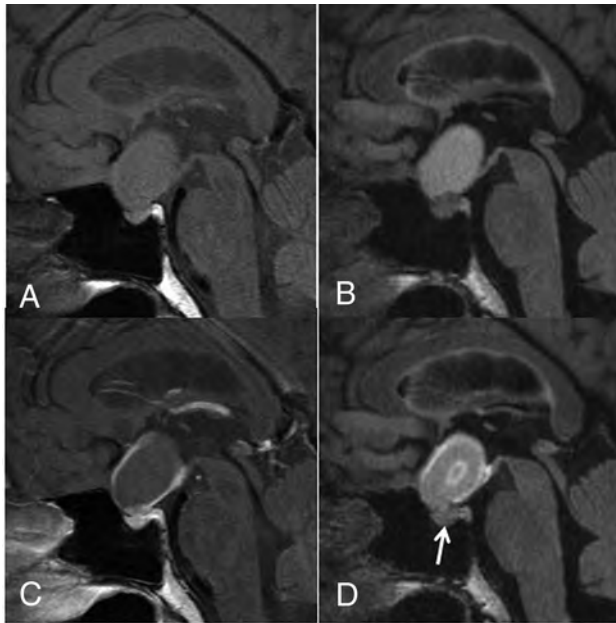


FIG 5. A 44-year-old woman with a CCP. A comparison of pre- (A) and postcontrast T1WI (C) shows that the cyst wall is enhanced on the postcontrast image (grade 2). A comparison of pre- (B) and postcontrast 3D T2-FLAIR images (D) reveals enhancement of the cyst wall (grade 2) and the lesion center on the postcontrast image (D). Different from the postcontrast T1WI (C), the pituitary gland is not intensely enhanced on the postcontrast 3D T2-FLAIR image (arrow in D). The observer judged this lesion as probably an RCC (scale 2) at the conventional MR interpretation, whereas the confidence level was changed to probably a CCP (scale 4) by the addition of 3D T2-FLAIR interpretation.

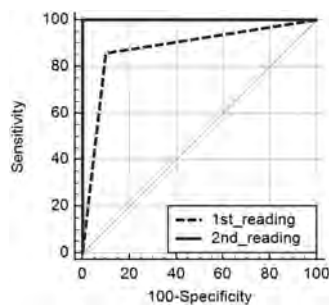


FIG 6. Comparison of the receiver operating characteristic (ROC) curves of the first (conventional MR alone) and second (conventional MR and 3D T2-FLAIR) reading session. The areas under the ROC curve (AUC) of the first and second reading sessions were 0.879 and 1.0, respectively. There was no significant difference in the AUC between the first and second reading session ($P = .16$).

3D T2-FLAIR imaging is useful for the differentiation between an RCC and a CCP.

RCCs are often surrounded by the enhancing normal pituitary gland and thus mimic wall enhancement on CE T1WI.⁸ On CE 3D T2-FLAIR images, the anterior lobe of the pituitary gland is often unenhanced. This may be attributable to T2 shortening due to a high gadolinium concentration or to the sequence's sensitivity to the flow in the hypophyseal portal system, which is composed of sinusoidal capillaries in the anterior pituitary gland.¹² Thus, the lack of wall enhancement of the anterior pituitary gland

on CE 3D T2-FLAIR images may render the differentiation of neoplastic and non-neoplastic cystic lesions possible.

CE in the CNS on T1-weighted sequences is the result of a combination of 2 primary processes, that is, intravascular (vascular) and interstitial (extravascular) enhancement.^{13,14} Enhancement on 3D-FLAIR sequences, however, is probably due to vessel permeability, which results from extravascular enhancement and suppression of the signal in the vessels.¹² The wall of all CCPs was enhanced on CE T1WI and CE 3D FLAIR scans. With respect to RCCs, the wall was enhanced on all T1WI, whereas only 1 lesion wall was enhanced on 3D T2-FLAIR images. We think that the permeability of the CCP wall is high, whereas the RCC wall is less permeable. Consequently, on CE 3D T2-FLAIR sequences, the differences in the wall permeability of RCCs and CCPs resulted in helping to differentiate between the 2 types of pituitary lesions. Azuma et al¹² reported enhancement of the pituitary stalk on CE 3D T2-FLAIR images. The partial enhancement of the RCC wall that we observed in 1 case on 3D T2-FLAIR images may have been due to displacement of the pituitary stalk. Another possible mechanism of the enhancement of the RCC wall may be related to inflammation or squamous metaplasia.¹⁵

The visual evaluation of sellar cystic lesions requires the acquisition of thin imaging slices. Because 3D T2-FLAIR imaging suppresses flow artifacts from CSF^{16,17} and yields 3D volume data with isotropic information, thinner section images can be acquired in any plane. This minimizes the partial volume effect between small lesions and surrounding tissue,^{18,19} and these advantages of CE 3D T2-FLAIR imaging were useful in our study.

Our study had some limitations. Although our study population was small, our findings were not unimportant and encourage clinical studies on larger populations. To decrease the influence of partial volume effects on our interpretation of the images, we used 0.9- and 3-mm isovoxel images in our assessment of 3D T2-FLAIR images and T1WI, respectively. Also, the time-dependence of gadolinium enhancement may have affected our results. The first CE sequence that we acquired in all instances was the conventional T1-weighted sequence; because the 3D sequence was obtained subsequently, we may have overestimated the added value of the 3D sequence.

CONCLUSIONS

On CE 3D FLAIR images, RCCs and CCPs showed significantly different wall enhancement; consequently, we suggest that CE 3D FLAIR images are useful for differentiating between RCC and CCP.

Disclosures: T. Hirai—RELATED: Grant: Grant-in-Aid for Clinical Research from the University of Miyazaki Hospital.

REFERENCES

1. Saeki N, Sunami K, Sugaya Y, et al. **MRI findings and clinical manifestations in Rathke's cleft cyst.** *Acta Neurochir (Wien)* 1999;141:1055–61 CrossRef Medline
2. Kim JE, Kim JH, Kim OL, et al. **Surgical treatment of symptomatic Rathke cleft cysts: clinical features and results with special attention to recurrence.** *J Neurosurg* 2004;100:33–40 CrossRef Medline

3. Müller HL. Risk-adapted, long-term management in childhood-onset craniopharyngioma. *Pituitary* 2017;20:267–81 CrossRef Medline
4. Hua F, Asato R, Miki Y, et al. Differentiation of suprasellar nonneoplastic cysts from cystic neoplasms by Gd-DTPA MRI. *J Comput Assist Tomogr* 1992;16:744–49 CrossRef Medline
5. Hofmann BM, Kreutzer J, Saeger W, et al. Nuclear beta-catenin accumulation as reliable marker for the differentiation between cystic craniopharyngiomas and Rathke cleft cysts: a clinico-pathologic approach. *Am J Surg Pathol* 2006;30:1595–603 CrossRef Medline
6. Choi SH, Kwon BJ, Na DG, et al. Pituitary adenoma, craniopharyngioma, and Rathke cleft cyst involving both intrasellar and suprasellar regions: differentiation using MRI. *Clin Radiol* 2007;62:453–62 CrossRef Medline
7. Choudhry OJ, Choudhry A, Patel SK, et al. Giant suprasellar Rathke's cleft cyst mimicking craniopharyngioma: implications for a spectrum of cystic epithelial lesions of ectodermal origin. *J Neurol Surg A Cent Eur Neurosurg* 2012;73:324–29 CrossRef Medline
8. Byun WM, Kim OL, Kim D. MR imaging findings of Rathke's cleft cysts: significance of intracystic nodules. *AJNR Am J Neuroradiol* 2000;21:485–88 CrossRef Medline
9. Deliganis AV, Fisher DJ, Lam AM, et al. Cerebrospinal fluid signal intensity increase on FLAIR MR images in patients under general anesthesia: the role of supplemental O₂. *Radiology* 2001;218:152–56 CrossRef Medline
10. Maeda M, Tsuchida C. "Ivy sign" on fluid-attenuated inversion-recovery images in childhood moyamoya disease. *AJNR Am J Neuroradiol* 1999;20:1836–38 Medline
11. Fukuoka H, Hirai T, Okuda T, et al. Comparison of the added value of contrast-enhanced 3D fluid-attenuated inversion recovery and magnetization-prepared rapid acquisition of gradient echo sequences in relation to conventional postcontrast T1-weighted images for the evaluation of leptomeningeal diseases at 3T. *AJNR Am J Neuroradiol* 2010;31:868–73 CrossRef Medline
12. Azuma M, Hirai T, Kadota Y, et al. Circumventricular organs of human brain visualized on post-contrast 3D fluid-attenuated inversion recovery imaging. *Neuroradiology* 2018;60:583–90 CrossRef Medline
13. Provenzale JM, Mukundan S, Dewhirst M. The role of blood-brain barrier permeability in brain tumor imaging and therapeutics. *AJR Am J Roentgenol* 2005;185:763–67 CrossRef Medline
14. Smirniotopoulos JG, Murphy FM, Rushing EJ, et al. Patterns of contrast enhancement in the brain and meninges. *Radiographics* 2007;27:525–51 CrossRef Medline
15. Wen L, Hu LB, Feng XY, et al. Rathke's cleft cyst: clinicopathological and MRI findings in 22 patients. *Clin Radiol* 2010;65:47–55 CrossRef Medline
16. Naganawa S, Koshikawa T, Nakamura T, et al. Comparison of flow artifacts between 2D-FLAIR and 3D-FLAIR sequences at 3 T. *Eur Radiol* 2004;14:1901–08 CrossRef Medline
17. Chagla GH, Busse RF, Sydnor R, et al. Three-dimensional fluid attenuated inversion recovery imaging with isotropic resolution and nonselective adiabatic inversion provides improved three-dimensional visualization and cerebrospinal fluid suppression compared to two-dimensional FLAIR at 3 Tesla. *Invest Radiol* 2008;43:547–51 CrossRef Medline
18. Kallmes DF, Hui FK, Mugler JP, III. Suppression of cerebrospinal fluid and blood flow artifacts in FLAIR MR imaging with a single-slab three-dimensional pulse sequence: initial experience. *Radiology* 2001;221:251–55 CrossRef Medline
19. Bink A, Schmitt M, Gaa J, et al. Detection of lesions in multiple sclerosis by 2D FLAIR and single-slab 3D FLAIR sequences at 3.0 T: initial results. *Eur Radiol* 2006;16:1104–10 CrossRef Medline

Decreased Subcortical T2 FLAIR Signal Associated with Seizures

 P. Nicholson,  S. Abdulla,  L. Alshafai,  D.M. Mandell, and  T. Krings



ABSTRACT

SUMMARY: Abnormally decreased T2/T2 FLAIR signal can be seen on brain imaging of patients who are experiencing clinical or subclinical seizures and can be associated with various intracranial pathologies. We identified 29 such patients. The abnormal signal was unilateral in 75.9% of patients. It affected various lobes of the brain, but only in the anterior circulation. In 28 patients (96.6%), there was corresponding decreased signal on DWI. The ADC was normal in all cases. In 26 patients (89.7%), there was corresponding low signal on SWI/gradient recalled-echo; 44.8% of patients underwent contrast-enhanced scans, and there was no abnormal enhancement. Twenty-two (75.9%) patients had documented clinical seizures on the day of imaging. The most frequent concomitant pathology was a subdural hematoma. Electroencephalograms obtained within 24 hours of imaging were available in 65.5%. Findings of all of these electroencephalograms were abnormal, and these electroencephalogram changes were either localized to the area of the abnormal MR imaging signal (where the signal was unilateral) or were bilateral (where the MR imaging changes were bilateral). In summary, decreased white matter T2/T2 FLAIR signal changes can be seen in patients with remarkably similar clinical findings (particularly seizures). These changes are often correlated with abnormal electroencephalogram activity localized to the involved lobes.

ABBREVIATIONS: EEG = electroencephalogram; GRE = gradient recalled-echo

Much has been published on the abnormal MR imaging appearances of the brain in patients experiencing acute seizures.¹ These articles have mainly focused on the more common descriptions of such changes, namely diffusion restriction and T2 hyperintensity in the gray matter and/or subcortical white matter.^{2,3} Transient cortical swelling or parenchymal enhancement or both have also been described.

Less attention has been paid to decreased signal in the subcortical white matter on T2-weighted and T2-weighted FLAIR sequences. These changes have been described in various conditions such as intracranial hypotension,⁴ head injury,⁵ encephalitis, meningitis, leptomenigeal disease,⁶ diffuse axonal injury, and cortical ischemia⁷ and in patients with seizures.⁸ We report a series of 29 patients with abnormally decreased T2 FLAIR signal

in the subcortical white matter. We describe their imaging appearances, clinical and EEG findings, and follow-up.

MATERIALS AND METHODS

Case Selection

Using a natural-language processing search engine (mPower; Nuance, Burlington, Massachusetts), we searched our radiology data base from 2013 to 2019 for variations of the terms “T2 hypointensity” and “FLAIR hypointensity.” This yielded >350 records; these reports were then read to identify those patients with confirmed abnormal T2 FLAIR low-signal changes. Patient records for each case were then retrospectively reviewed, and demographic, clinical, and EEG features were noted. Specific clinical features recorded included the primary CNS pathology (eg, subdural hematoma) and whether the patient was having active clinically evident seizures on the day of imaging.

Imaging Acquisition and Analysis

All images were obtained at our institution on either 1.5T or 3T scanners. Each study consisted of a minimum of a sagittal T1-weighted, axial T2 FSE, and axial T2-weighted FLAIR, DWI, and gradient recalled-echo (GRE)/SWI sequence (depending on the scanner). Two neuroradiologists reviewed all scans in a consensus analysis. The presence and location of abnormally decreased T2

Received August 7, 2019; accepted after revision October 2.

From the Division of Neuroradiology, Joint Department of Medical Imaging, Toronto Western Hospital, University of Toronto, Toronto, Ontario, Canada.

Please address correspondence to Patrick Nicholson, MD, Division of Neuroradiology, Joint Department of Medical Imaging, Toronto Western Hospital, University of Toronto, 399 Bathurst St, Toronto, ON M5T 2S8, Canada; e-mail: patrick.nicholson@uhn.ca; @paddynicholson



Indicates article with supplemental on-line table.

<http://dx.doi.org/10.3174/ajnr.A6328>

FLAIR signals were recorded, and the corresponding DWI and GRE/SWI signals were analyzed.

RESULTS

Demographic Findings

Patient demographics, imaging, and clinical findings for the cohort are summarized in the Table. Twenty-nine patients were

identified; 19 were men (65.5%). The median patient age was 49 years (range, 18–85 years).

Imaging Findings

Imaging findings are summarized in the Table. Hypointensity on T2 and T2 FLAIR images was present in the subcortical white matter in all cases, with sparing of the overlying cortex (Figs 1–3). The abnormal signal was bilateral in 7 cases (24.1%) and unilateral in 22 (75.9%). It was usually found in >1 lobe. In 6 cases (20.7%), it was confined to the frontal lobe only; in 1 case (2.1%), to just the parietal lobe; and in 1 case, to the occipital lobe alone. Overall, the frontal lobe was the most common lobe involved (19 cases, 65.5%), followed by the parietal (17%, 58.6%), temporal (16%, 55.2%), and occipital (14%, 48.3%) lobes. The signal pattern was not seen in the posterior fossa in any case. In 28 patients (96.6%), the areas of brain with low T2 signal showed corresponding decreased signal on DWI and increased DWI signal in none. The ADC findings were normal in all cases. In 26 patients (89.7%), there was also corresponding decreased signal on SWI/GRE sequences. Contrast was administered in 13 scans (44.8%); none of the T2 hypointense signal areas showed enhancement. There were no instances of T2 FLAIR hyperintense cortical signal.

Clinical Data

Twenty-seven patients were inpatients at the time of imaging (93.1%), while the remaining 2 were imaged as outpatients (6.9%). All clinical and imaging data are presented in the On-line Table. All the inpatient MR imaging studies were performed within 72 hours of the initial clinical presentation. Twenty-two patients (75.9%) had documented clinical seizures on the day of imaging. Of those patients with seizures, 18 seizures were generalized (81.8%), while the remaining 4 (18.2%) were focal. A further 3 patients had a documented alteration in the level of consciousness and were undergoing investigation for “possible seizures.” Of the remaining patients, 1 patient had asymptomatic signal changes adjacent to a meningioma, 2 patients developed a subdural hematoma following a meningioma resection but were also asymptomatic, and the remaining 2 patients had these signal changes underlying an acute subdural hematoma and were, similarly, clinically asymptomatic. The most frequent concomitant

Findings	
Demographics	
Patients	29
Sex (male)	19 (65.5%)
Age (yr)	49 (range, 18–85)
Clinical information	
Associated seizures	22 (75.9%)
Extrinsic compressive lesions	14 (48.3%)
Imaging findings	
Laterality	
Bilateral	7 (24.1%)
Unilateral	22 (75.9%)
Multiple lobes involved	21 (72.4%)
Frequency of involved lobes	
Frontal	19 (65.5%)
Parietal	17 (58.6%)
Temporal	16 (55.2%)
Occipital	14 (48.3%)
EEG findings	
Availability	19 (65.5%)
Laterality	
Unilateral	12/12 Cases with MRI T2 changes unilateral
Bilateral	7/7 Cases with MRI T2 changes bilateral
Follow-up imaging	
Availability	9 (31%)
Changes resolved	6 (66.6%)
Associated with compressive lesion	4/6
Nonresolved/gliosis	3 (33.3%)
Associated with compressive lesion	1/3

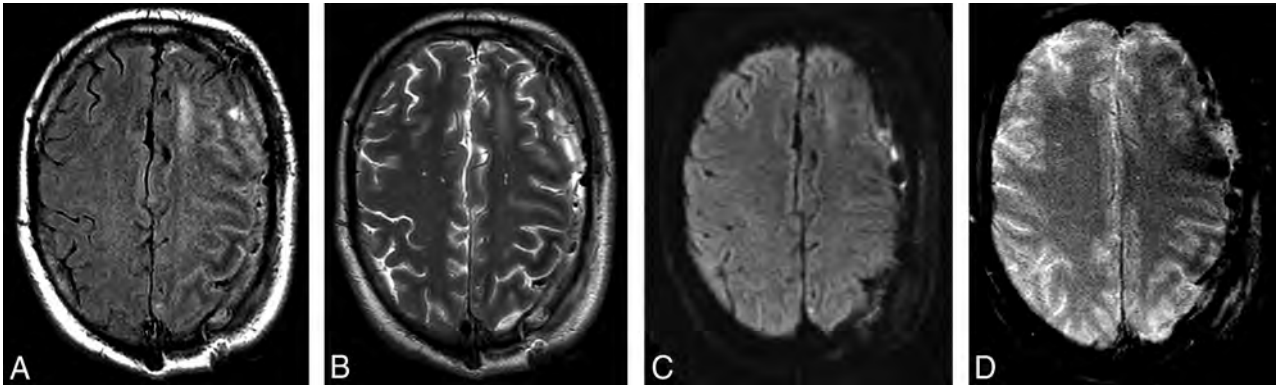


FIG 1. Patient admitted to the intensive care unit with persistent seizures 1 day after evacuation of a left-sided subdural hematoma. A, T2 FLAIR, B, FSE T2, C, DWI, and D, GRE-weighted images. Note the decreased T2-weighted signal in the subcortical white matter of the left frontal and parietal lobes on A and B, as well as the lack of corresponding diffusion restriction on C. D, GRE-weighted image shows there is subtle corresponding decreased subcortical white matter signal change.

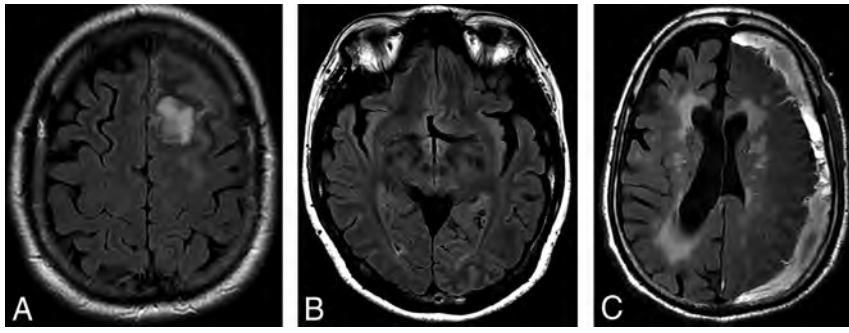


FIG 2. A, T2 FLAIR images from a 49-year-old male patient being followed for a left-frontal meningioma with asymptomatic low signal in the subcortical white matter adjacent to the meningioma. Nonspecific failure of suppression of CSF signal in the subjacent sulci was also noted. B, T2 FLAIR images showing low signal in the left occipital lobe in a 46-year-old patient who initially presented with visual seizures. C, T2 FLAIR images from a 48-year-old patient with a left convexity subdural hematoma and seizures. Subcortical low T2 signal is present in the compressed posterior frontal and parietal lobes.

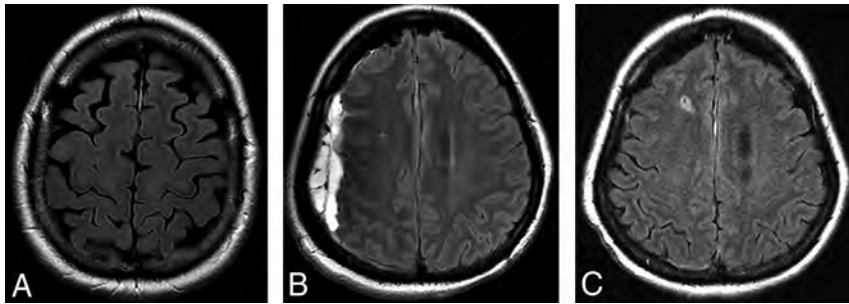


FIG 3. A, T2 FLAIR image in the same patient as in Fig 2A shows complete resolution of the white matter changes 2 years after resection of the lesion. B, T2 FLAIR image from a 53-year-old female patient with a spontaneous right-sided acute subdural hematoma. T2 hypointense signal changes are present in the subjacent white matter. C, Follow-up 5 months later shows resolution of both the hematoma and the white matter changes.

pathology was a subdural hematoma (12 patients, 41.8%), and the signal alterations were always found in the subjacent white matter. Similarly, the signal abnormality was always found in the white matter adjacent to compressed brain region in those cases of meningioma. Overall, an extrinsic compressive lesion (eg, meningioma, subdural hematoma) was present in 14/29 patients (48.3%).

Electroencephalograms (EEGs) obtained within 24 hours of the MR imaging were available in 19 of the total cohort (65.5%), including all patients who were having clinical seizures. In these patients, abnormal EEG signal was found in all cases, and these changes were localized to the side of the MR imaging abnormality in 12/12 cases in which the MR imaging signal was unilateral. The EEG showed bilateral abnormalities in the remaining 7 patients who had bilateral T2-hypointense changes. All inpatients were receiving antiseizure medication at the time of MR imaging. Two outpatients were taking antiseizure medication, while data were unavailable for the remainder.

Follow-Up

Imaging follow-up was available in 9 patients (31%), at a median of 18 months (range, 1.25–72 months). The changes had resolved in

6 of these patients (66.6% of this subgroup), while 2 patients had persistent decreased T2 FLAIR signal (at 18- and 5-month follow-ups, respectively). One patient had gliosis with volume loss on follow-up imaging (performed at 18 months). Of those patients in whom the changes resolved, 4/6 (66.6%) had an extra-axial compressive lesion, which had been removed or treated in the interval. Conversely, 1 of the 3 patients in whom the signal changes did not resolve or progressed to gliosis had a compressive lesion which was treated.

DISCUSSION

We have described a series of patients with remarkably similar imaging features: All had areas of decreased T2 FLAIR signal in the subcortical white matter, usually with corresponding decreased signal on GRE/SWI and without corresponding diffusion restriction or enhancement. This imaging pattern was most commonly unilateral and affected multiple lobes. In addition, many of these patients had strikingly similar clinical features: More than 80% had either clinical seizures or altered levels of consciousness at the time of imaging. We do not perform continuous EEG monitoring on all patients in our intensive care unit, so it is also possible that at least some of the remaining patients were experiencing some subclinical seizures during the course of their admission.

The causative factor was also quite similar in many cases; almost half (48%) had an extrinsic lesion (subdural hematoma, meningioma) with mass effect on the subjacent subcortical white matter.

The question still exists regarding the nature of these white matter signal alterations. It is not clear whether they are the result of the causative process that leads to the seizure activity or whether they represent imaging evidence of abnormal neuronal activity “spilling over” to the adjacent white matter—ie, a possible imaging biomarker of seizure activity. As mentioned in our introduction, there are a range of pathologies that can cause decreased T2 signal in white matter. For example, this pattern can be seen in patients with a primarily leptomeningeal process, such as meningitis or leptomeningeal metastasis. However, it can also be seen in patients with intracranial hypotension, which is not a primary “leptomeningeal” pathology per se but still could be considered an extra-axial issue that is having an effect on intra-axial tissues. In addition, these disparate diseases often cause generalized signal changes. In our cohort, we see a remarkable side concordance (and often lobe concordance) with both causative pathology (when such a cause was known) and with abnormal EEG activity.

Previously, some groups have attributed this signal change to accumulation of oxygen-free radicals in the white matter,⁹ but the evidence for this theory remains sparse at best. Free radicals are transient oxygen intermediates, with a supposed paramagnetic effect due to their unpaired electrons. However, recent laboratory work has shown that the paramagnetic effect of reactive oxygen-free radicals is mainly on T1 shortening, with a negligible effect on T2-relaxation times.¹⁰ If these transient free radicals are responsible for this decreased signal, we would not expect to see persistent changes many months later as we did in some patients in our cohort. Furthermore, in patients with seizures, free radicals are present in the cortex as well as in the subcortical white matter,¹¹ yet we do not see these signal changes in the cortex in our patients. On balance, it appears that there is not much proof to directly implicate free radicals as the cause of the described findings.

Some other possibilities remain. It is interesting that there was associated decreased signal on T2*-weighted sequences in our cohort. Decreased signal on such sequences has been associated with increased oxygen extraction (ie, an uncoupling between oxygen supply and demand). Cortical perfusion abnormalities are well-described in patients undergoing seizure activity¹² as well as with pathologies such as subdural hematomas,¹³ so perhaps the changes we are seeing are reflective of such increased oxygen extraction. Direct nonheme iron deposition in the tissues has also been suggested previously,^{7,9} and while this could account for the pattern we are seeing acutely, it would not be expected to resolve in most cases as it did in our cohort.

The neurochemical changes in the subcortical white matter in a patient group such as ours are undoubtedly complex. Various pathophysiologic mechanisms are likely at play, such as loss of autoregulation, changes in cellular permeability, regional perfusion changes, and neuronal excitotoxicity.¹⁴ Much has been written about these changes^{15,16} and about the danger of applying a single imaging label to what is surely multiple parallel processes.¹⁷ However, it appears clear that the MR imaging findings we describe indicate some abnormality in the subcortical white matter. They may also serve as a useful suggestion to the clinician to consider EEG monitoring in those patients in whom seizures cannot be clinically identified (eg, the intubated patients in the intensive care unit).

There are obvious limitations with this retrospective study, which was performed in an adult-only population. It is possible that the abnormal EEG activity could be related to the offending pathology in such cases as subdural hematomas; however, this EEG-imaging concordance was also maintained in those patients in whom such an extrinsic factor did not exist (eg, those patients with primary seizures or epilepsy). We did not perform advanced imaging techniques such as MR perfusion, which could potentially provide more information about the areas of signal alteration. It is also likely that these changes are also underreported, both in our center and in the literature more generally, so the prevalence of such changes is possibly higher than that seen here. Finally, most of our patients were inpatients (93.1%), so we are unable to comment on the prevalence of these findings in outpatients with chronic seizure disorders.

CONCLUSIONS

We have described a cohort of 29 patients with a similar clinical presentation (most had seizures/altered level of consciousness),

with strikingly similar imaging findings of decreased T2-weighted signal in the subcortical white matter, in whom EEG abnormalities were frequently localized to the area of the MR imaging changes. We emphasize that these changes are often correlated with a degree of seizure activity in the surrounding brain parenchyma. Whether the altered signal change is a cause or effect of seizure activity is still uncertain, as is the underlying pathophysiology causing the signal changes.

Disclosures: Timo Krings—UNRELATED: Consultancy: Stryker, Medtronic, Penumbra; Royalties: Thieme; Stock/Stock Options: Marblehead.

REFERENCES

1. Cianfoni A, Caulo M, Cerase A, et al. **Seizure-induced brain lesions: a wide spectrum of variably reversible MRI abnormalities.** *Eur J Radiol* 2013;82:1964–72 CrossRef Medline
2. Cartagena AM, Young GB, Lee DH, et al. **Reversible and irreversible cranial MRI findings associated with status epilepticus.** *Epilepsy Behav* 2014;33:24–30 CrossRef Medline
3. Giovannini G, Kuchukhidze G, McCoy MR, et al. **Neuroimaging alterations related to status epilepticus in an adult population: definition of MRI findings and clinical-EEG correlation.** *Epilepsia* 2018;59(Suppl 2):120–27 CrossRef Medline
4. Adachi M, Mugikura S, Shibata A, et al. **Relative decrease in signal intensity of subcortical white matter in spontaneous intracranial hypotension on fluid-attenuated inversion recovery images.** *AJNR Am J Neuroradiol* 2009;30:906–10 CrossRef Medline
5. Okanishi T, Saito Y, Fujii S, et al. **Low signal intensity and increased anisotropy on magnetic resonance imaging in the white matter lesion after head trauma: unrecognized findings of diffuse axonal injury.** *J Neurol Sci* 2007;263:218–22 CrossRef Medline
6. Lee JH, Na DG, Choi KH, et al. **Subcortical low intensity on MR images of meningitis, viral encephalitis, and leptomeningeal metastasis.** *AJNR Am J Neuroradiol* 2002;23:535–42 Medline
7. Ida M, Mizunuma K, Hata Y, et al. **Subcortical low intensity in early cortical ischemia.** *AJNR Am J Neuroradiol* 1994;15:1387–93 Medline
8. Raghavendra S, Ashalatha R, Thomas SV, et al. **Focal neuronal loss, reversible subcortical focal T2 hypointensity in seizures with a nonketotic hyperglycemic hyperosmolar state.** *Neuroradiology* 2007;49:299–305 CrossRef Medline
9. Cross PA, Atlas S, Grossman R. **MR evaluation of brain iron in children with cerebral infarction.** *AJNR Am J Neuroradiol* 1990;11:341–48 Medline
10. Tain RW, Scotti AM, Li W, et al. **Imaging short-lived reactive oxygen species (ROS) with endogenous contrast MRI.** *J Magn Reson Imaging* 2018;47:222–29 CrossRef Medline
11. Shin EJ, Jeong JH, Chung YH, et al. **Role of oxidative stress in epileptic seizures.** *Neurochem Int* 2011;59:122–37 CrossRef Medline
12. Newton MR, Berkovic SF, Austin MC, et al. **Postictal switch in blood flow distribution and temporal lobe seizures.** *J Neurol Neurosurg Psychiatry* 1992;55:891–94 CrossRef Medline
13. Brodersen P, Gjerris F. **Regional cerebral blood flow in patients with chronic subdural hematomas.** *Acta Neurol Scand* 1975;51:233–39 CrossRef Medline
14. Holmes GL. **Seizure-induced neuronal injury: animal data.** *Neurology* 2002;59:S3–6 CrossRef Medline
15. Cole AJ. **Status epilepticus and periictal imaging.** *Epilepsia* 2004;45(Suppl 4):72–77 CrossRef Medline
16. Briellmann RS, Wellard RM, Jackson GD. **Seizure-associated abnormalities in epilepsy: evidence from MR imaging.** *Epilepsia* 2005;46:760–66 CrossRef Medline
17. Grillo E. **Seizure-induced excitotoxicity: just considering it could be a fallacy—comment on: Cianfoni A, Caulo M, Cerase A. Seizure-induced brain lesions: a wide spectrum of variably reversible MRI abnormalities (in press).** *Eur J Radiology* 2013;82:e903–04 CrossRef Medline

Unilateral Nonvisualization of a Transverse Dural Sinus on Phase-Contrast MRV: Frequency and Differentiation from Sinus Thrombosis on Noncontrast MRI

Y.-M. Chang, A.L. Kuhn, N. Porbandarwala, R. Rojas, V. Ivanovic, and R.A. Bhadelia

ABSTRACT

BACKGROUND AND PURPOSE: Unilateral decreased/nonvisualization of a transverse dural sinus on MRV poses a diagnostic dilemma when gadolinium administration is contraindicated. We determined the frequency of unilateral decreased/nonvisualization of the transverse dural sinus and the performance of pregadolinium MR imaging sequences in diagnosing transverse sinus thrombosis in the presence of unilateral decreased/nonvisualization on phase-contrast MRV.

MATERIALS AND METHODS: We conducted a retrospective review of consecutive 3D phase-contrast MRV (VENC, 30 cm/s) and routine brain imaging (noncontrast sagittal T1, axial T2, FLAIR, DWI, GRE, and postgadolinium 3D-MPRAGE images) performed during a 3-year period for a total of 208 patients. Nonvisualization of a transverse dural sinus was defined as $\geq 50\%$ nonvisualization of the transverse sinus caliber versus the contralateral side on MRV. Noncontrast imaging findings were considered abnormal when hyperintense signal was present on T2, FLAIR, T1, and DWI, and there were T2* blooming artifacts on GRE and DWI. Postgadolinium 3D-MPRAGE was used to confirm the diagnosis of transverse sinus thrombosis.

RESULTS: Nonvisualization of a transverse dural sinus was observed in 72/208 (34.6%) patients on MRV; 56/72 (77.8%) were without transverse sinus thrombosis, and 16/72 (22.2%) patients had transverse dural sinus thrombosis. Nonvisualization of a transverse dural sinus was seen in 56/192 (29.2%) patients without transverse sinus thrombosis and 16/16 (100%) with transverse sinus thrombosis. Abnormal findings on DWI (transverse sinus hyperintense signal or T2* blooming artifact) are 93.8% sensitive and 100.0% specific for transverse sinus thrombosis. Other noncontrast MR imaging sequences ranged from 56.3%–68.8% sensitive and 91.1%–100.0% specific.

CONCLUSIONS: Nonvisualization of a transverse dural sinus is a frequent phenomenon on phase-contrast MRV. DWI can be effectively used to exclude sinus thrombosis when nonvisualization of a transverse dural sinus is a diagnostic conundrum on phase-contrast MRV and contrast-enhanced studies are contraindicated.

ABBREVIATIONS: CE = contrast-enhanced; CVT = cerebral venous thrombosis; DST = dural venous sinus thrombosis; MPRAGE+ = postgadolinium 3D-MPRAGE; MRI- = noncontrast MRI brain sequences; NV = unilateral decreased/nonvisualization; NVTS = nonvisualization of a transverse dural sinus; PC = phase-contrast; TS = transverse dural sinus; TST+ = transverse sinus thrombosis; TST- = no transverse sinus thrombosis

Dural venous sinus thrombosis (DST) and cerebral venous thrombosis (CVT) are reportedly uncommon, with an annual incidence of 3–4 per 1 million to 1.32 per 100,000 and represent approximately 0.5%–1.0% of all strokes.^{1–3} Young and middle-aged adults are disproportionately affected; within this age group, DST and CVT are 3 times more common in women.⁴ While the etiologies include infection, trauma, iatrogenic causes, and genetic

predisposition to hypercoagulability, this prominent sex predisposition is thought to be secondary to oral contraceptive use and, most important, pregnancy and peripartum states.⁴

Although rare, delayed diagnosis of DST and CVT could result in devastating clinical consequences, including venous infarct and intracranial hemorrhages, leading to high morbidity and mortality rates between 5% and 10%.^{3,5} There is a highly variable clinical presentation, ranging from asymptomatic, headache, focal neurologic deficits, intracranial hypertension, and seizures.⁴ Of DST and CVT, DST is more frequent, and of these, transverse dural sinus (TS) thrombosis is among the most common, with 44.8% involvement of the left TS and 41.3% of the right TS per 1 report and up to 70% (side not specified) in another series.^{2,6}

Given the variable and nonspecific clinical presentation of DST and the importance of rapid treatment, imaging is essential

Received June 20, 2019; accepted after revision October 11.

From the Division of Neuroradiology, Department of Radiology, Beth Israel Deaconess Medical Center, Boston, Massachusetts.

Please address correspondence to Yu-Ming Chang, MD, PhD, Department of Radiology, Beth Israel Deaconess Medical Center, WCB90, 330 Brookline Ave, Boston, MA 02115; e-mail: ychang2@bidmc.harvard.edu

<http://dx.doi.org/10.3174/ajnr.A6337>

Table 1: Patient demographics

	No Thrombosis		Thrombosis
	Normal TS	NVTS	
Total (No.)	136	56	16
Mean age (range) (yr)	42.9 (16–83)	48.6 (27–90)	42.3 (21–87)
Patients (No.)	136 (79.4% Female)	56 (58.9% Female)	16 (68.8% Female)

in its diagnosis.⁷ Contrast-enhanced MR imaging techniques, such as contrast-enhanced MRV (CE-MRV), followed by 3D T1-weighted imaging and CVT are now considered the criterion standard for imaging diagnosis of DST, demonstrating superiority over noncontrast MRV, MR imaging, and CT.^{7–12}

However, the use of gadolinium contrast may be contraindicated or relatively contraindicated in patients with renal failure and in pregnant patients, given the concerns for nephrogenic systemic fibrosis and teratogenic effects on the fetus, respectively. Most important, this concern limits the use of gadolinium in pregnant patients, a group with increased risk for the development of DST. CVT may also be refused by pregnant patients due concerns secondary to the use of ionizing radiation, despite negligible fetal exposure for head examinations.¹³ Furthermore, there has been increasing concern among the public regarding gadolinium deposition of entirely uncertain clinical significance in patients with normal renal function, particularly in deep brain structures.¹⁴ This has led many patients to refuse gadolinium out of concern for bodily harm.

In particular, diagnosis and subsequent appropriate treatment for transverse sinus thrombosis (TST+) can be challenging with noncontrast MRV. Well-established pitfalls includes false-positive diagnoses due to difficulty in distinguishing nonvisualization of a transverse dural sinus (NVTS) secondary to congenital hypoplasia, slow flow due to downstream compression of the brachiocephalic or internal jugular veins, direction of venous flow, as well as idiopathic intracranial hypertension from true thrombosis.^{15–19} While standard noncontrast MR imaging head sequences can be insensitive compared with CE-MRV and CVT for detection of DST,¹² we hypothesize that standard MR imaging head sequences may be highly sensitive and specific in differentiating thrombosis from other causes of NVTS when applied to equivocal noncontrast MRVs, significantly increasing the diagnostic confidence in clinical scenarios where contrast or ionizing radiation are contraindicated or refused. Our purpose was to determine the frequency of unilateral NVTS and the performance of pregadolinium MR imaging sequences in diagnosing TST+ in the setting of unilateral decreased/nonvisualization (NV) on phase-contrast MRV (PC-MRV).

MATERIALS AND METHODS

Patient Selection

Following institutional review board approval for this Health Insurance Portability and Accountability Act-compliant study, a retrospective review from 2014 to 2017 of our institutional imaging data base for noncontrast 3D-PC-MRV (VENC, 30 cm/s) with additional standard MR imaging brain sequences (spin-echo sagittal T1, axial T2, axial GRE, axial FLAIR, axial DWI, and postgadolinium 3D-MPRAGE [MPRAGE+]) performed within 24 hours

of each other was conducted. Exclusion criteria included known preexisting DST and CVT and a recent operation involving the cranium. At our institution, initial MR imaging assessment for suspected DST was made with PC-MRV because CE-MRV had not been implemented during the study period.

Standard MR imaging brain sequences (including MPRAGE+) were subsequently performed on patients whose clinical presentations required additional imaging to assess intracranial abnormalities including, but not limited to, infarct, hemorrhage, mass, infection/inflammation, or high suspicion for DST. Two hundred eight patients fitting the inclusion criteria were identified. MPRAGE+ served as the diagnostic criterion standard for TST+ versus NV of PC-MRV signal. Demographic characteristics of the patients are shown in Table 1.

Imaging Protocols

All MR imaging examinations were performed on either a 1.5T Signa HDx scanner (GE Healthcare, Milwaukee, Wisconsin) or a 1.5T Magnetom Espree scanner (Siemens, Erlangen, Germany) using standard 8- and 12-channel head coils, respectively.

The Signa HDx scanner imaging parameters (TR/TE/flip angle/section thickness/matrix) were the following: sagittal T1 (650/13 ms/90°/5 mm/256 × 192), axial T2 (4200/11 ms/90°/5 mm/320 × 224), axial GRE (550/9.1 ms/20°/5 mm/320 × 224), axial FLAIR (8600/80 ms/150°/5 mm/320 × 192), axial DWI (8000/96 ms/90°/5 mm/128 × 128), MPRAGE+ (7.7/3.3 ms/15°/1 mm/240 × 224), and 3D PC-MRV (9.83/4.3 ms/90°/1.8 mm/256 × 224).

Imaging parameters (TR/TE/flip angle/section thickness/matrix) for the Magnetom Espree scanner included the following: sagittal T1 (420/8.8 ms/90°/5 mm/256 × 100), axial T2 (4500/95 ms/150°/5 mm/384 × 88), axial GRE (835/26 ms/20°/5 mm/256 × 75), axial FLAIR (9000/84 ms/170°/5 mm/256 × 100), axial DWI (4600/103 ms/90°/5 mm/130 × 100), MPRAGE+ (2100/3.57 ms/15°/1 mm/256 × 100), and 3D PC-MRV (43.5/6.86 ms/15°/1.8 mm/256 × 88).

We administered 0.1 mmol/kg of gadobutrol (Gadavist; Bayer Schering Pharma, Berlin, Germany), with a maximum of 10 mL at a rate of 1.5 mL/s for postcontrast imaging.

Image Analysis

Two hundred eight PC-MRVs were reviewed for the presence of NVTS by 2 neuroradiologists separately, blinded to the final reported diagnosis and without access to MPRAGE+ or standard MR imaging brain sequences: A.L.K. (neuroradiology fellow) and R.A.B. (28 years of experience), with no disagreements. Before data analysis, A.L.K. was trained by R.A.B. using a series of 5 representative PC-MRVs with NVTS and 5 PC-MRVs with normal findings (as defined by R.A.B.) in association with corresponding MPRAGE images that were not obtained within the study date range. These representative examples were then used as a reference during the analysis period. The TS was categorized as normal or NV, with laterality recorded. TS was defined as NV on PC-MRV when the lack of flow-related signal was ≥50%

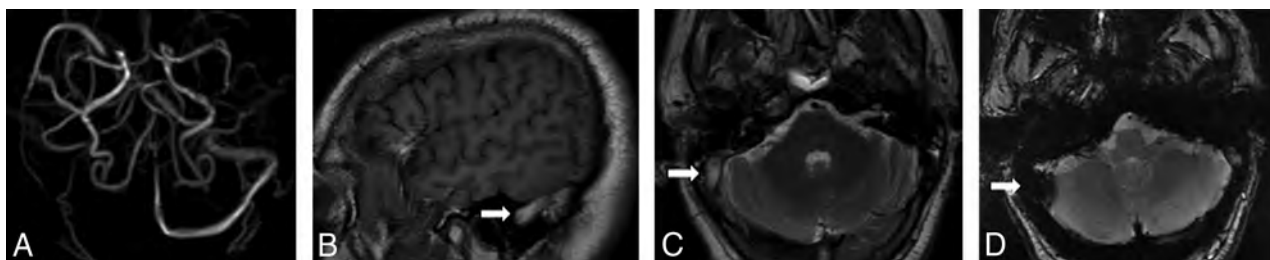


FIG 1. Absence of the right transverse and sigmoid sinuses on PC-MRV (A). Abnormal hyperintense signal in the right transverse and sigmoid sinuses on sagittal T1 (B, arrow) and axial T2 (C, arrow), with corresponding T2*-hypointense signal with blooming artifacts on axial GRE sequences (D, arrow).

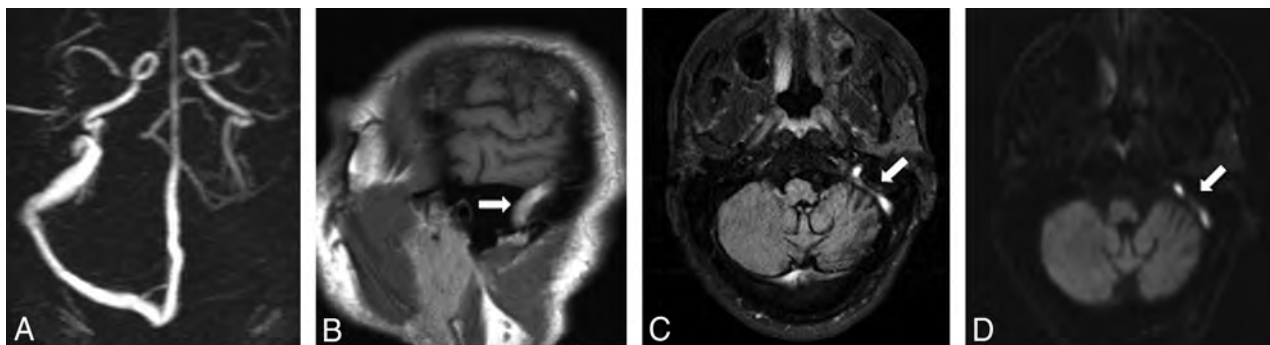


FIG 2. Absence of the left transverse and sigmoid sinuses on PC-MRV (A). Abnormal hyperintense signal in the left transverse and sigmoid sinuses on sagittal T1 (B, arrow) and axial FLAIR sequences (C, arrow) with corresponding high signal on DWI (D, arrow).

relative to contralateral TS.¹⁶ Nonocclusive short-segment and rounded filling defects in the TS were not considered abnormal because these findings are typically attributable to arachnoid granulations.^{18,20}

The presence or absence of TST+ was then confirmed in both groups with corresponding MPRAGE+ sequences by R.A.B. and A.L.K., separately, with no disagreements. A normal TS on PC-MRV was confirmed to be free of thrombosis.

For all patients with NVTS on PC-MRVs, the signal characteristics of the bilateral TS on pregadolinium images (sagittal T1, axial T2, axial GRE, axial FLAIR, and axial DWI) were further categorized as normal or abnormal by 2 neuroradiologists blinded to the results of PC-MRV analysis, for the presence or absence of TS thrombosis without access to MPRAGE+ images (R.R., with 20 years of experience and V.I. with 12 years of experience). R.R. and V.I. did not receive additional training before the analysis regarding thresholds for considering abnormal TS signal. Evaluation of abnormal TS signal on standard noncontrast MR imaging brain sequences (MRI-) was performed on only patients with NVTS on PC-MRV because those with a normal TS on PC-MRV had negative findings for TST+.

Pregadolinium imaging findings were considered normal if the TS signal was iso- to hypointense on T1, T2, and FLAIR and hyperintense on GRE to the cortex. TS signal isointense to CSF was considered a normal finding on DWI. Pregadolinium imaging findings were considered abnormal when hyperintense signal was present on T1, T2, FLAIR, and DWI and T2*-hypointense signal with blooming artifacts (T2* blooming artifacts) was present with expanded TS on GRE and DWI (Figs 1–4). NVTS on

PC-MRV was correlated to the anatomic size of the TS at the level of the sigmoid notch relative to the contralateral side on MPRAGE+. TS size measurements were performed by 1 neuro-radiologist (Y.-M.C.) with 4 years of experience.

Data Analysis

Interobserver reliability for the presence of NVTS, TST+ on MPRAGE+, and normal-versus-abnormal TS signal on noncontrast MRI brain sequences (MRI-) in patients with NVTS on PC-MRV was assessed with κ coefficients. The side of abnormal TS signal on MR imaging was recorded. Disagreements were resolved by consensus review, and the reconciled data were used for subsequent analysis.

The association between sizes of the TS and TST+ was calculated with a χ^2 test.

The frequency and laterality of abnormal MRI- TS signal were determined for NVTS without transverse sinus thrombosis (TST-) and NVTS with TST+. The sensitivity and specificity of abnormal MRI- TS signal for individual sequences in patients with NVTS and for all sequences combined excluding DWI (ie, if any sequence had abnormal findings) in confirming TST+ in the setting of NVTS on PC-MRV, were determined. Statistical significance was considered with $P \leq .05$.

RESULTS

By means of terminology established by Landis and Koch,²¹ there was perfect agreement between readers in detecting NVTS on PC-MRV and the presence of TST+ on MPRAGE+ ($\kappa = 1.0$, respectively). There was substantial agreement in detecting GRE

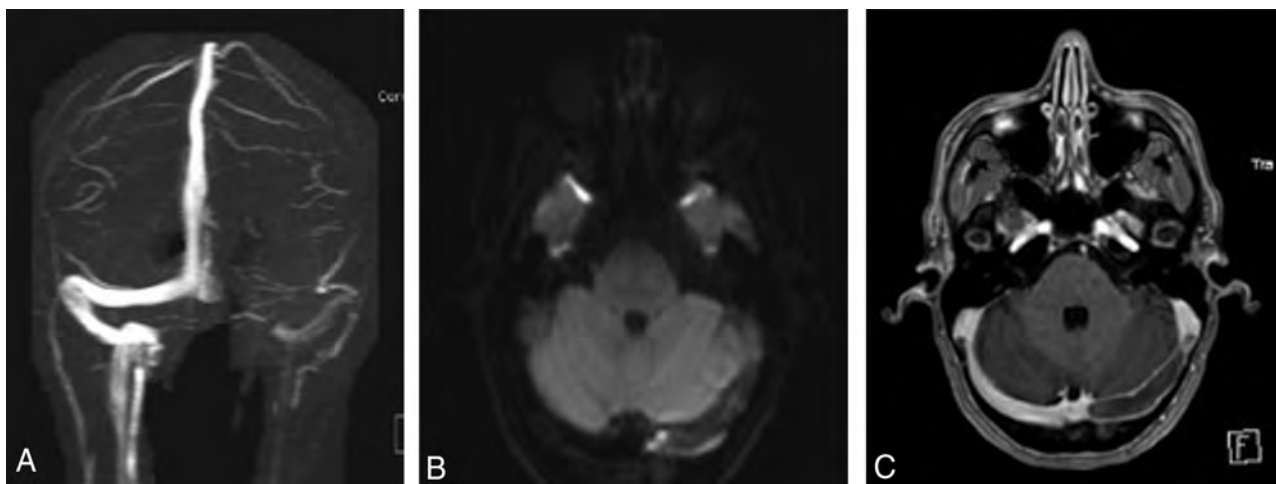


FIG 3. Representative images of a patient demonstrating T2*-hypointense signal with blooming artifacts on DWI. Absence of the left transverse sinus on PC-MRV (A) with associated T2*-hypointense signal with blooming artifacts on DWI (B), corresponding to a filling defect on axial MPRAGE (C).

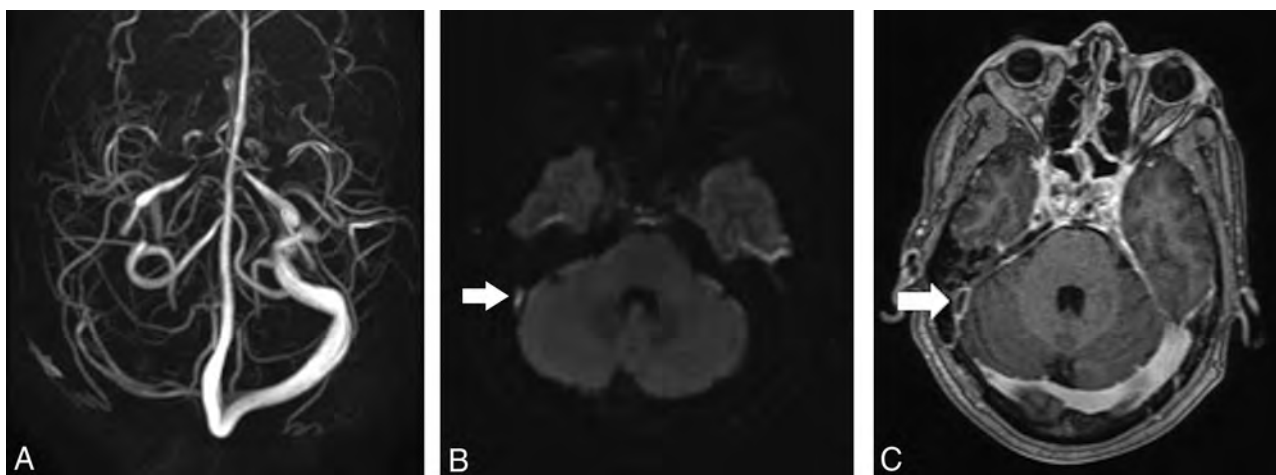


FIG 4. Representative images of a patient different from the one in Fig 3, demonstrating DWI hyperintense signal. Absence of the right transverse and sigmoid sinuses on PC-MRV (A), with associated hyperintense signal on DWI (B, arrow), corresponding to a filling defect on axial MPRAGE (C, arrow).

signal abnormality ($\kappa = 0.78$) and almost perfect agreement in detecting T1 ($\kappa = 0.85$), T2 ($\kappa = 0.95$), FLAIR ($\kappa = 0.97$), and DWI ($\kappa = 0.86$) signal abnormalities.

NVTS on PC-MRV was observed in 72/208 (34.6%) patients, and 16 of these 72 patients demonstrated TST+ on MPRAGE+. NVTS was seen in 56/192 (29.2%) patients with TST- and 16/16 (100%) with TST+.

In NVTS without transverse sinus thrombosis, 11 right TSs and 45 left TSs were not visualized. Relative size comparison of the TS at the level of the sigmoid notch on MPRAGE showed that the right TS was smaller than the left in 6 cases, the left TS was smaller than the right in 46 cases, with the right and left TSs were equal in 4 cases. Although 51/56 (91.1%) NVTSs with TST- were associated with a smaller size of the TS on MPRAGE+, 5/56 (8.9%) were not, suggesting other etiologies such as venous slow flow due to downstream effects.

In NVTS with transverse sinus thrombosis, 10 right TSs and 6 left TSs were not visualized secondary to thrombus. Relative size

comparison of the TSs showed that the right TS was smaller than the left in 3 cases, the left TS was smaller than the right in 8 cases, with the right and left TS equal in 5 cases. There was no association between the size of the TS and TST+ ($P = .42$).

Signal abnormality on standard MR imaging sequences in cases of NVTS on PC-MRV for TST+ versus TST- as well as sensitivity and specificity for the detection of TST+ on T1, T2, FLAIR, GRE, and DWI (hyperintense and T2* blooming artifacts combined) are noted on Table 2. DWI hyperintense signal alone is 43.8% sensitive (95% CI, 19.8%–70.1%) and 100.0% specific (95% CI, 93.6%–100.0%). DWI T2* blooming artifacts alone is 50.0% sensitive (95% CI, 24.7%–75.4%) and 100.00% specific (95% CI, 93.6%–100.00%). A combination of T1, T2, FLAIR, and GRE was 87.5% sensitive (95% CI, 61.7–98.5) and 92.9% specific (95% CI, 82.7–98.0) for TST+ in NV TS on PC-MRV. The combination of both signal abnormalities on DWI (DWI hyperintense signal and T2* blooming artifacts) is 93.8% sensitive (95% CI, 69.8%–99.8%) and 100.0% specific (95% CI, 93.6%–100.0%).

Table 2: TS signal abnormality on standard MR imaging sequences with NVTs on MRV with and without thrombosis

	TST+ on MPRAGE+ (n = 16)				TST- on MPRAGE+ (n = 56)				Sensitivity (95% CI) (%)	Specificity (95% CI) (%)
	Low/Iso	Hyper	T2*	Normal Signal	Low/Iso	Hyper	T2*	Normal Signal		
T1 sagittal	7	9	—	—	56	0	—	—	56.3 (29.9–80.3)	100 (93.6–100.0)
T2WI	6	10	—	—	55	1	—	—	62.5 (35.4–84.8)	98.2 (90.5–99.9)
FLAIR	5	11	—	—	51	5	—	—	68.8 (41.3–89.0)	91.1 (80.4–97.0)
GRE	—	8	8	—	—	56	0	—	50.0 (24.7–75.4)	100 (93.6–100.0)
DWI	—	7	8	1	—	0	0	56	93.8 ^a (69.8–99.8)	100 ^a (93.6–100.0)

Note:—Iso indicates isointensity; Hyper, hyperintensity; —, no data.

^a Combined DWI hyperintense and T2* hypointense signal with blooming artifacts.

DISCUSSION

To the best of our knowledge, for the first time, our results show that DWI signal abnormality, both T2* blooming artifacts and hyperintense signal, can be a powerful diagnostic tool for the clarification of equivocal findings of TST+ on noncontrast MRVs, with a sensitivity of 93.8% and a specificity of 100% and interrater reliability of $\kappa = 0.86$. While most prior work described much lower sensitivities for the detection of DST with DWI sequences, these studies did not assess T2* blooming artifacts on DWI.^{12,22} However, our results are supported in prior work by Yildiz et al²³ on cortical vein thrombosis, which demonstrated sensitivities of up to 84% on DWI if both hyperintense signal and T2* blooming artifacts were assessed. It is possible that our higher sensitivity for DWI is because the current study aims to clarify a specific diagnostic conundrum in a much larger anatomic structure (TS) on PC-MRV and due to our assessment of both DWI hyperintense signal and T2* blooming artifacts. Thus, in the setting of NVTs on PC-MRV, DWI signal abnormality is virtually diagnostic for TST+, with the interrater reliability ranging from substantial to almost perfect agreement in the acute-to-subacute setting. This may prove to be a powerful tool in overcoming the limitations of commonly used noncontrast MRV (such as 2D-TOF, 3D-TOF, and PC-MRV) when the use of gadolinium contrast is contraindicated for criterion standard CE-MRV techniques.

The fairly low sensitivity and variable specificity of individual T1, T2, FLAIR, and GRE sequences in the detection of DST has been previously documented, and our results support the earlier findings. For example, prior work in detecting DST in all major dural venous sinuses by Sadigh et al²² found that for 1 reviewer, the sensitivity and specificity, respectively, of T1 noncontrast was 55% and 55%; for T2, they were 58% and 97%; for FLAIR, they were 67% and 62%; for GRE, they were 67% and 62%; and for DWI (high signal only), they were 25% and 93%. The above sensitivities are similar to those reported in the current study focusing on the TS: For example, the sensitivity for the detection of TST+ is 62.5% for T2 and 68.8% for FLAIR. The much higher specificity in our cohort may be secondary to increased pretest probability for TST+, given that our analysis was limited to patients with abnormal findings on PC-MRV. As discussed above, the prominent difference between the current report and previously reported DWI sensitivities is presumed secondary to the inclusion of T2* blooming artifacts on DWI as abnormal in the current study.

A combination of all MRI- sequences (excluding DWI) results in an improved sensitivity of 87.5% and a decreased specificity of 92.9%, similar to that reported in a large series of

429 patients in which standard MR imaging sequences, including postcontrast sequences, had a combined sensitivity of 79.2% and specificity of 89.9% for the detection of DST (including the superior sagittal, sigmoid, and transverse sinuses).¹²

T1, T2, and FLAIR had false-negative rates up to 40%, thought to be likely secondary to previously described signal characteristics of acute thrombus, which can mimic normal flow voids, in the dural sinuses, reviewed by Bonneville²⁴ in 2014, and have been described as a factor underlying the false-negative results in noncontrast MRV-DST detection. We observed that GRE T2* blooming artifacts alone detected only 8/16 (50%) cases of TST+. This is also presumed to be due to changes in T2* signal during the evolution from the acute-to-subacute phase,²⁴ supporting T2* blooming artifacts being sensitive for acute thrombus but less so for subacute-to-chronic thrombi (as characterized by T1, T2, and FLAIR hyperintense TS signal). However, at least 2 prior studies have reported that GRE is highly sensitive to not only acute but also subacute thrombosis (also characterized by T1, T2, and FLAIR hyperintense signal), though not for chronic DST.^{25,26} Of note, Altinkaya et al²⁶ has demonstrated that the sensitivity of GRE for TST+ and sigmoid sinus thrombosis is decreased due to artifacts from the skull base, potentially explaining the discrepancy between the prior studies and the current study, which specifically focused on the TS.

Fifty-six of 192 (29.2%) PC-MRVs without TST+ demonstrated NVTs. Of these, the left TS was NV 23.4% of the time and was considered smaller versus the right TS in 24.0% of cases. The right TS was NV in 5.7% of cases and was considered smaller versus the left TS in 3.1% of cases. These findings are concordant with reports across multiple imaging modalities showing that the left and right TSs are hypoplastic in 39%–60% and 6%–14% of patients, respectively.^{27–29} The percentages reported in the current work are lower than of those previously reported, likely secondary to our strict criteria of NV as >50% nonvisualized relative to the contralateral side.

Our limited dataset demonstrates no association with hypoplastic TS and TST+, in disagreement with a recent case-control report correlating TS hypoplasia and increased relative risk for TST+.²⁸ However, an earlier study described the opposite finding that the dominant TS was more likely to thrombose, suggesting that more work will be needed in the future to elucidate whether there is a correlation between TST+ and TS size.³⁰

This study has several limitations. First, the study inclusion criteria of patients who had PC-MRV, noncontrast MR imaging, and MPRAGE+ performed within 24 hours of each other meant that not all patients with TST+ were selected. Thus, the true

prevalence of the disease, positive predictive value, negative predictive value, and accuracy could not be calculated, potentially decreasing the generalizability of the results and introducing unforeseen selection bias. Second, because the study was designed specifically to assess the utility of standard MR imaging sequences in the diagnosis of TS thrombosis in a subset of patients with presumed higher pretest probability based on abnormal noncontrast MRV findings, we did not perform an analysis of patients with normal MRV imaging findings. While it is known that conventional MR imaging sequences result in false-positive detection for DST (specificity of 14%–89.9%), a comparison of conventional MR imaging sequence performance in patients without NVTS for detection of TS thrombosis in the current study with prior work could have yielded information on population differences and selection biases.^{12,22}

Third, although MPRAGE+ is superior to PC-MRV and MRI– in the diagnosis of TST and is thus established as the diagnostic criterion standard for TST+ in this study, some authors have shown that MPRAGE+ demonstrates decreased sensitivity compared with CE-MRV.^{9,10} This lowered sensitivity has been theorized to be from the time delay following gadolinium administration to image acquisition, causing enhancement of subacute thrombus, thus resulting in false-negative findings. This outcome could result in underreporting of true TST+ in our study and decreases the sensitivity and specificity of noncontrast MR imaging sequences for thrombus detection. Future work using CE-MRV as the diagnostic criterion standard may be required. Fourth, because the diagnosis of DST of the superior sagittal sinus, internal cerebral veins, vein of Galen, and straight sinus is typically less of a diagnostic challenge on noncontrast MRV due to significantly fewer anatomic variations versus the TS, this study did not assess venous anatomy or MRI– signal on the remainder of the dural venous sinuses, limiting the generalizability of the results to DST other than TST+. Finally, our selection criteria excluded patients with known chronic TST+, and our current findings cannot necessarily be extended to the detection of chronic thrombosis. Future work is needed to assess the clinical utility of DWI for thrombi in the more chronic phase.

CONCLUSIONS

Unilateral NVTS on noncontrast MRV is a frequent phenomenon and presents a diagnostic challenge in determining whether the findings represent a TS anatomic variation, downstream venous effects, or technical artifacts versus true thrombosis. In patients in whom gadolinium contrast is contraindicated or refused, the DWI sequence can be effectively used to help exclude TST+ in the setting of an equivocal noncontrast MRV.

REFERENCES

1. Stam J. **Thrombosis of the cerebral veins and sinuses.** *N Engl J Med* 2005;352:1791–98 CrossRef Medline
2. Coutinho JM, Zuurbier SM, Aramideh M, et al. **The incidence of cerebral venous thrombosis: a cross-sectional study.** *Stroke* 2012;43:3375–77 CrossRef Medline
3. Konakondla S, Schirmer CM, Li F, et al. **New developments in the pathophysiology, workup, and diagnosis of dural venous sinus thrombosis (DVST) and a systematic review of endovascular treatments.** *Aging Dis* 2017;8:136–48 CrossRef Medline
4. Coutinho JM. **Cerebral venous thrombosis.** *J Thromb Haemost* 2015;13(Suppl 1):S238–44 CrossRef Medline
5. Coutinho JM, Zuurbier SM, Stam J. **Declining mortality in cerebral venous thrombosis: a systematic review.** *Stroke* 2014;45:1338–41 CrossRef Medline
6. Miranda B, Ferro JM, Canhão P, et al. **Venous thromboembolic events after cerebral vein thrombosis.** *Stroke* 2010;41:1901–06 CrossRef Medline
7. Dmytriw AA, Song JS, Yu E, et al. **Cerebral venous thrombosis: state of the art diagnosis and management.** *Neuroradiology* 2018;60:669–85 CrossRef Medline
8. Khandelwal N, Agarwal A, Kochhar R, et al. **Comparison of CT venography with MR venography in cerebral sinovenous thrombosis.** *AJR Am J Roentgenol* 2006;187:1637–43 CrossRef Medline
9. Saindane AM, Mitchell BC, Kang J, et al. **Performance of spin-echo and gradient-echo T1-weighted sequences for evaluation of dural venous sinus thrombosis and stenosis.** *AJR Am J Roentgenol* 2013;201:162–69 CrossRef Medline
10. Sari S, Verim S, Hamcan S, et al. **MRI diagnosis of dural sinus: cortical venous thrombosis: Immediate post-contrast 3D GRE T1-weighted imaging versus unenhanced MR venography and conventional MR sequences.** *Clin Neurol Neurosurg* 2015;134:44–54 CrossRef Medline
11. Liang L, Korogi Y, Sugahara T, et al. **Evaluation of the intracranial dural sinuses with a 3D contrast-enhanced MP-RAGE sequence: prospective comparison with 2D-TOF MR venography and digital subtraction angiography.** *AJNR Am J Neuroradiol* 2001;22:481–92 Medline
12. Patel D, Machnowska M, Symons S, et al. **Diagnostic performance of routine brain MRI sequences for dural venous sinus thrombosis.** *AJNR Am J Neuroradiol* 2016;37:2026–32 CrossRef Medline
13. McCollough CH, Schueler BA, Atwell TD, et al. **Radiation exposure and pregnancy: when should we be concerned?** *Radiographics* 2007;27:909–17; discussion 917–18 CrossRef Medline
14. Guo BJ, Yang ZL, Zhang LJ. **Gadolinium deposition in brain: current scientific evidence and future perspectives.** *Front Mol Neurosci* 2018;11:335 CrossRef Medline
15. Ayanzen RH, Bird CR, Keller PJ, et al. **Cerebral MR venography: normal anatomy and potential diagnostic pitfalls.** *AJNR Am J Neuroradiol* 2000;21:74–78 Medline
16. Han K, Chao AC, Chang FC, et al. **Diagnosis of transverse sinus hypoplasia in magnetic resonance venography: new insights based on magnetic resonance imaging in combined dataset of venous outflow impairment case-control studies: post hoc case-control study.** *Medicine (Baltimore)* 2016;95:e2862 CrossRef Medline
17. Chik Y, Gottesman RF, Zeiler SR, et al. **Differentiation of transverse sinus thrombosis from congenitally atretic cerebral transverse sinus with CT.** *Stroke* 2012;43:1968–70 CrossRef Medline
18. Provenzale JM, Kranz PG. **Dural sinus thrombosis: sources of error in image interpretation.** *AJR Am J Roentgenol* 2011;196:23–31 CrossRef Medline
19. Morris PP, Black DF, Port J, et al. **Transverse sinus stenosis is the most sensitive MR imaging correlate of idiopathic intracranial hypertension.** *AJNR Am J Neuroradiol* 2017;38:471–77 CrossRef Medline
20. Leach JL, Jones BV, Tomsick TA, et al. **Normal appearance of arachnoid granulations on contrast-enhanced CT and MR of the brain: differentiation from dural sinus disease.** *AJNR Am J Neuroradiol* 1996;17:1523–32 [Mismatch]Medline
21. Landis JR, Koch GG. **The measurement of observer agreement for categorical data.** *Biometrics* 1977;33:159–74 CrossRef Medline
22. Sadigh G, Mullins ME, Saindane AM. **Diagnostic performance of MRI sequences for evaluation of dural venous sinus thrombosis.** *AJR Am J Roentgenol* 2016;206:1298–306 CrossRef Medline
23. Yildiz ME, Ozcan UA, Turk A, et al. **Diffusion-weighted MR imaging findings of cortical vein thrombosis at 3 T.** *Clin Neuroradiol* 2015;25:249–56 CrossRef Medline
24. Bonneville F. **Imaging of cerebral venous thrombosis.** *Diagn Interv Imaging* 2014;95:1145–50 CrossRef Medline

25. Ihn YK, Jung WS, Hwang SS. **The value of T2*-weighted gradient-echo MRI for the diagnosis of cerebral venous sinus thrombosis.** *Clin Imaging* 2013;37:446–50 CrossRef Medline
26. Altinkaya N, Demir S, Alkan O, et al. **Diagnostic value of T2*-weighted gradient-echo MRI for segmental evaluation in cerebral venous sinus thrombosis.** *Clin Imaging* 2015;39:15–19 CrossRef Medline
27. Manara R, Mardari R, Ermani M, et al. **Transverse dural sinuses: incidence of anatomic variants and flow artifacts with 2D time-of-flight MR venography at 1 Tesla.** *Radiol Med* 2010;115:326–38 CrossRef Medline
28. Arauz A, Chavarria-Medina M, Patiño-Rodriguez HM, et al. **Association between transverse sinus hypoplasia and cerebral venous thrombosis: a case-control study.** *J Stroke Cerebrovasc Dis* 2018;27:432–37 CrossRef Medline
29. Matsuda W, Sonomura T, Honma S, et al. **Anatomical variations of the torcular Herophili: macroscopic study and clinical aspects.** *Anat Sci Int* 2018;93:464–68 CrossRef Medline
30. Glik A, Benkovich E, Kesler A, et al. **Lateral sinus thrombosis: the importance of the unaffected sinus.** *J Neuroimaging* 2016;26:599–604 CrossRef Medline

Emergency Conversion to General Anesthesia Is a Tolerable Risk in Patients Undergoing Mechanical Thrombectomy

F. Flottmann, H. Leischner, G. Broocks, T.D. Faizy, A. Aigner, M. Deb-Chatterji, G. Thomalla, J. Krauel, M. Issleib, J. Fiehler, and C. Brekenfeld



ABSTRACT

BACKGROUND AND PURPOSE: Mechanical thrombectomy for acute ischemic stroke is performed with the patient under local anesthesia, conscious sedation, or general anesthesia. According to recent trials, up to 16% of patients require emergency conversion to general anesthesia during mechanical thrombectomy. This study investigated the procedural and clinical outcomes after emergency conversion in comparison with local anesthesia, conscious sedation, and general anesthesia.

MATERIALS AND METHODS: This retrospective study included 254 patients undergoing mechanical thrombectomy for acute large-vessel occlusion. The procedure was started with the patient either under local anesthesia, conscious sedation, or general anesthesia. Emergency conversion was defined as induction of general anesthesia during mechanical thrombectomy. The primary outcomes were successful reperfusion (TICI 2b/3) and functional independence (mRS at 90 days, ≤ 2).

RESULTS: Twenty-five patients (9.8%) required emergency conversion to general anesthesia. The time from admission to flow restoration was increased under general anesthesia (median, 137 minutes) and emergency conversion (median, 138 minutes) compared with local anesthesia (median 110 minutes). After adjustment for confounders, emergency conversion to general anesthesia and primary general anesthesia had comparable chances of successful reperfusion (OR = 1.28; 95% CI, 0.31–5.25). Patients with emergency conversion had a tendency toward higher chances of functional independence (OR = 4.48; 95% CI, 0.49–40.86) compared with primary general anesthesia, but not compared with local anesthesia (OR = 0.86; 95% CI, 0.14–5.11) and conscious sedation (OR = 1.07; 95% CI, 0.17–6.53).

CONCLUSIONS: Patients with emergency conversion did not have lower chances of successful reperfusion or functional independence compared those with primary general anesthesia, and time to flow restoration was also similar. We found no evidence supporting the primary induction of general anesthesia in patients at risk for emergency conversion.

ABBREVIATIONS: CS = conscious sedation; GA = general anesthesia; MAP = mean arterial pressure

In acute ischemic stroke due to large-vessel occlusion, mechanical thrombectomy combined with standard treatment has been shown to be more effective than standard therapy alone and is now considered standard of care.^{1–6} However, the optimal anesthesia management during thrombectomy is still controversial.^{7–10}

Patients are usually allocated to either local anesthesia, conscious sedation (CS), or general anesthesia (GA) before initiation of mechanical thrombectomy. However, up to 16% of patients

who undergo thrombectomy under initial local anesthesia or CS require emergency conversion to GA during the procedure, often due to severe agitation or loss of airway-protective reflexes.^{11–13} The impact of conversion to GA on procedural and clinical outcomes is unknown.

We therefore conducted a retrospective study with the aim of comparing procedural and clinical outcomes of patients requiring emergency conversion to GA with those of patients undergoing treatment under either local anesthesia, CS, or GA for the entire intervention. Our hypotheses were that there are differences in the time from admission to flow restoration and in the numbers of successful reperfusions and/or good clinical outcomes between emergency conversion and the 3 groups with other anesthesia management.

MATERIALS AND METHODS

Patient Selection

Between June 2015 and January 2018, all patients older than 18 years of age who underwent endovascular treatment for acute

Received May 18, 2019; accepted after revision October 1.

From the Department of Diagnostic and Interventional Neuroradiology (F.F., H.L., G.B., T.D.F., J.F., C.B.), Institute of Medical Biometry and Epidemiology (A.A.), and Departments of Neurology (M.D.-C., G.T.) and Anaesthesiology (J.K., M.I.), University Medical Center Hamburg-Eppendorf, Hamburg, Germany; and Institute of Public Health (A.A.), Charité–Universitätsmedizin Berlin, Berlin, Germany.

Please address correspondence to Fabian Flottmann, MD, Department of Diagnostic and Interventional Neuroradiology, University Medical Center Hamburg-Eppendorf, Haus O22, Martinistr 52, 20246 Hamburg, Germany; e-mail: f.flottmann@uke.de



Indicates article with supplemental on-line table.

<http://dx.doi.org/10.3174/ajnr.A6321>

ischemic stroke of the anterior circulation at the University Medical Center Hamburg-Eppendorf were enrolled. During this time, local anesthesia with or without CS was the preferred anesthesia management. GA was induced before mechanical thrombectomy only if deemed necessary due to clinical conditions (coma, apnea, loss of airway protection, uncontrollable patient movement) or if patients arrived already intubated following transfer from another hospital.

Study procedures were conducted following the protocol of the German Stroke Registry in accordance with ethical guidelines (Ethics Committee of the Hamburg Chamber of Physicians, Hamburg, Germany) and in compliance with the Declaration of Helsinki. Informed consent was obtained from all capable patients or available legal representatives.

Intervention and Airway Management

All patients were under the supervision of an anesthesiologist during the entire procedure. Mechanical thrombectomy was initiated with the patient under either local anesthesia, CS, or GA. Local anesthesia or CS was the preferred protocol in nonagitated, compliant patients with patent airways. The decision to induce GA during mechanical thrombectomy was made by both the neurointerventionalist and the anesthesiologist in cases of excessive patient movement, complications, respiratory failure, or loss of airway-protective reflexes.

During CS and GA, the final combination and dosages of the administered anesthetics were left to the discretion of the attending anesthesiologist. Propofol was the preferred sedative, either fractionized or continuously administered (1–3 mg/kg/h). Remifentanyl, midazolam, and piritramide were used if propofol was deemed inappropriate or insufficient.

GA was induced following preoxygenation with an opioid for systemic anesthesia, a bolus of propofol for sedation, and rocuronium or suxamethonium for relaxation as a rapid sequence induction. Airway patency was maintained by endotracheal intubation and mechanical ventilation. Anesthesia was maintained with propofol (2–10 mg/kg/h) and an opioid.

Throughout the procedure, the patient's oxygenation, ventilation, and hemodynamics were continually monitored. Care was taken to avoid hypotension to maintain sufficient perfusion of penumbral tissue¹⁴ by the perfusor-controlled infusion of norepinephrine (titrated in steps of 0.05–0.1 µg/kg/min). After emergency conversion or GA, all patients were transferred to a neurointensive care unit without prior extubation in the neurointerventional suite.

Data Acquisition and Analysis

Baseline data were documented, as well as prehospital mRS and admission NIHSS. Procedural data included time intervals between symptom onset (if available), admission, imaging, groin puncture and reperfusion, and complications during and after mechanical thrombectomy. Anesthesiology protocols were reviewed for the type of anesthesia management, administered medication, and blood pressure records. A drop of blood pressure was defined as a >25% decrease of mean arterial blood pressure (MAP) during the intervention before achieving intracranial reperfusion. Clinical outcome parameters included NIHSS and mRS scores at 24 hours and

at discharge and the mRS score at 90 days. Functional independence was defined as mRS at 90 days ≤2.

Image Analysis

All image analyses were performed by an experienced neuroradiologist (>5 years of experience). Baseline ASPECTS was routinely assessed on preintervention nonenhanced CT scans or diffusion-weighted images.¹⁵ The collateral score was determined on admission CT angiography using the system of Maas et al.¹⁶ TICI scores were determined in a final angiographic series, and TICI 2b/3 was considered indicative of successful reperfusion, which was the primary procedural outcome.

Statistical Analysis

Categorical variables are reported as absolute and relative frequencies; continuous variables, as mean and SD when approximate normal distribution holds, and as median and first and third quartiles (Q1, Q3) otherwise. To better compare the median time from admission to flow restoration among groups, we estimated the 95% bootstrap confidence intervals of the differences in medians.^{17,18} We applied logistic regression to model the associations between the primary procedural and clinical outcomes and the 4 anesthesia groups (local anesthesia, CS, emergency conversion, GA), adjusting for relevant confounders: age, sex, admission NIHSS, prestroke mRS, comorbidities (systolic blood pressure on admission, arterial hypertension, diabetes, dyslipidemia, atrial fibrillation, active smoking), application of intravenous thrombolysis, location of vessel occlusion, and, additionally, for successful reperfusion and occurrence of a significant drop in blood pressure in the analysis of functional independence. On the basis of these models, we performed a likelihood-ratio χ^2 test to assess global differences in outcomes among the 4 groups as implemented in the R car package¹⁹ and derived OR estimates along with 95% CIs. Individual comparisons among the anesthesia groups were adjusted with the Tukey method, based on the R multcomp package,²⁰ visualized with the ggplot2 package.²¹

As a subset analysis, we performed the same models, additionally adjusting for collateral status and the time from symptom onset to reperfusion due to a high number of missing values in these variables. Instead of 238 observations with complete datasets, models were then based on 110 observations. Analyses were performed with the statistical software R.²²

RESULTS

Baseline Characteristics

Of the 307 patients treated with mechanical thrombectomy in the designated time period, 255 patients met the inclusion criteria. One patient had to be excluded due to missing anesthesia records. Of the 254 included patients, 53% were women, and the mean age was 72.1 ± 12.6 years. The median NIHSS score on admission was 15 (Q1–Q3, 12–19), and 15% of patients presented with a prestroke mRS of ≥2. The median ASPECTS on admission imaging was 7 (range, 6–9). GA was induced before endovascular treatment in 59 patients (23.2%). In 94 patients (37.0%), endovascular treatment was completed with the patient under local anesthesia, 76 patients (29.9%) had CS, and 25 patients (9.8%) required emergency conversion during the procedure (Table 1).

Table 1: Baseline characteristics

	Local Anesthesia Only (n = 94)	CS (n = 76)	Emergency Conversion to GA (n = 25)	GA (n = 59)
Age (mean) (SD) (yr)	74.3 (11.2)	71.7 (12.4)	67.8 (13.9)	71.0 (14.1)
Female sex (No.) (%)	55 (58.5%)	36 (47.4%)	12 (48.0%)	31 (52.5%)
Hypertension (No.) (%)	66 (70.2%)	54 (71.1%)	15 (60.0%)	37 (62.7%)
Diabetes mellitus (No.) (%)	15 (16.0%)	17 (22.4%)	4 (16.0%)	9 (15.3%)
Dyslipidemia (No.) (%)	11 (11.7%)	13 (17.1%)	2 (8.0%)	11 (18.6%)
Atrial fibrillation (No.) (%)	42 (44.7%)	27 (35.5%)	7 (28.0%)	24 (40.7%)
Active smoker (No.) (%)	11 (11.7%)	10 (13.2%)	2 (8.0%)	10 (16.9%)
Systolic blood pressure at admission (mean) (SD) (mm Hg)	154 (28.0)	162 (27.9)	166 (22.8)	156 (33.9)
Pre-Stroke mRS ≥ 2	14 (14.9%)	12 (15.8%)	2 (8.0%)	11 (18.6%)
Initial NIHSS (median) (Q1–Q3)	15.0 (11–18)	15.0 (11.0–18.0)	17.0 (13.0–19.0)	18.0 (15.0–20.5)
Initial ASPECTS (median) (Q1–Q3)	8 (7–9)	8 (6–8)	7 (5–9)	7 (6–8)
Collaterals on CTA ^a	2 (1–3)	2 (1–3)	2 (1–3)	2 (1–2)
Initial occlusion site (No.) (%)				
Left hemisphere	130 (51.2%)	46 (48.9%)	39 (51.3%)	13 (52.0%)
Tandem occlusion	11 (11.7%)	14 (18.4%)	3 (12.0%)	9 (15.3%)
ICA (non-terminal)	6 (6.38%)	4 (5.26%)	1 (4.00%)	3 (5.08%)
ICA (terminal segment)	9 (9.57%)	18 (23.7%)	3 (12.0%)	15 (25.4%)
M1 proximal	32 (34.0%)	19 (25.0%)	13 (52.0%)	22 (37.3%)
M1 distal	21 (22.3%)	13 (17.1%)	2 (8.00%)	7 (11.9%)
M2	15 (16.0%)	8 (10.5%)	3 (12.0%)	3 (5.08%)
Intravenous tPA (No.) (%)	57 (60.6%)	46 (60.5%)	17 (68.0%)	32 (54.2%)
Onset to admission (median) (Q1–Q3) (min) ^b	176 (115–226)	193 (124–236)	131 (65.0–176)	181 (139–239)

^a Available for 185 patients.^b Available for 153 patients.

Patients with emergency conversion had a higher median NIHSS at admission compared with patients treated under local anesthesia and CS, but a lower median NIHSS than patients treated under GA (emergency conversion: 17 versus local anesthesia and CS, 15, versus GA, 18). The median initial ASPECTS on imaging was lower in patients with emergency conversion and GA (emergency conversion and GA, 7, versus local anesthesia and CS, 8). Proximal M1 occlusions were more frequent in patients with emergency conversion compared with patients with GA (emergency conversion, 52.0%, versus GA, 37.3%).

Reasons for Emergency Conversion, Anesthesia Management, and Procedural Data

Before emergency conversion, 17/25 patients (68%) received sedative agents. Sedative agents used before emergency conversion were propofol ($n = 10$), remifentanyl ($n = 3$), propofol and pirritamide ($n = 2$), and midazolam ($n = 2$).

The median time from groin puncture to emergency conversion was 35 minutes (Q1–Q3, 25–60 minutes). The median number of passes before conversion to GA was 0 (Q1–Q3, 0–1). Reported reasons for emergency conversion were excessive patient movement ($n = 18$), neurologic deterioration ($n = 4$), periprocedural hemorrhage ($n = 1$), intention of stent placement in the intracranial ICA ($n = 1$), and emesis ($n = 1$).

None of the patients had a complication as a result of emergency conversion.

Time Intervals from Admission to Flow Restoration

Patients with emergency conversion had a shorter median time from admission to imaging than patients with primary GA (emergency conversion, 13.5 minutes, versus GA, 18 minutes)

and from imaging to groin puncture (emergency conversion, 50.5 minutes, versus GA, 77.5 minutes). However, in patients who required emergency conversion during mechanical thrombectomy, the time from groin puncture to flow restoration was longer compared with local anesthesia, CS, and GA (emergency conversion, 79 minutes, versus GA, 51.5 minutes; local anesthesia, 39 minutes; CS, 47 minutes).

Overall, the time from admission to flow restoration was longer in patients with emergency conversion compared with those receiving local anesthesia (emergency conversion [median], 138 minutes, versus local anesthesia, 110 minutes; difference of medians, 28 minutes; 95% CI, 4.5–54.5 minutes) but not longer than in those undergoing GA (emergency conversion, 138 minutes, versus GA, 137 minutes; difference of medians, 1 minute; 95% CI, –22–35.5 minutes).

Proportion of Successful Reperfusion

Overall, successful reperfusion (TICI 2b/3) was achieved in 69.1% of all patients, but proportions varied among the 4 groups (local anesthesia, 79.8%; CS, 69.7%, emergency conversion, 64.0%; GA, 54.2%; Table 2).

On the basis of the multivariable logistic regression, the chances of successful reperfusion differed significantly among the 4 anesthesia groups (P value = .002). However, there were no significant differences between emergency conversion and the other 3 groups, especially not between emergency conversion and GA (Fig 1; OR = 1.28; 95% CI, 0.31–5.25). There was a tendency toward lower chances of successful reperfusion after emergency conversion compared with local anesthesia (OR = 0.26; 95% CI, 0.06–1.06) and, to a lesser extent, compared with CS (OR = 0.55; 95% CI, 0.13–2.18).

Table 2: Procedural outcome

	Local Anesthesia	CS	Emergency Conversion to GA	GA
MR imaging before intervention (No.) (%)	20 (21.3%)	10 (13.2%)	3 (12.0%)	4 (6.78%)
Time from admission to imaging (median) (Q1–Q3)	16.0 (10.8–23.2)	13.5 (8–22.2)	13.5 (9.75–20.2)	18.0 (13.0–34.0)
Time from imaging to groin puncture (median) (Q1–Q3)	49.5 (40.0–65.5)	51.0 (41.0–73.2)	50.5 (37.0–61.5)	77.5 (56.5–94.2)
Time from groin puncture to flow restoration (median) (Q1–Q3)	39.0 (24.8–61.2)	47.0 (30.0–70.2)	79.0 (60.0–110)	51.5 (30.0–69.0)
Time from admission to flow restoration (median) (Q1–Q3)	110 (87.2–133)	118 (94.8–140)	138 (116–179)	137 (114–177)
Mechanical thrombectomy technique (No.) (%)				
Stent retriever only	41 (43.6%)	40 (52.6%)	16 (64.0%)	29 (49.2%)
Aspiration only	18 (19.1%)	7 (9.21%)	3 (12.0%)	8 (13.6%)
Both Stent retriever and aspiration	21 (22.3%)	24 (31.6%)	6 (24.0%)	15 (25.4%)
No endovascular treatment attempt (spontaneous reperfusion or failure of access)	14 (14.9%)	5 (6.58%)	0 (0%)	7 (11.9%)
Successful reperfusion (TICI 2b/3) (No.) (%)	75 (79.8%)	53 (69.7%)	16 (64.0%)	32 (54.2%)
Periprocedural complications (No.) (%)				
Dissections	5 (5.32%)	1 (1.32%)	1 (4.00%)	1 (1.69%)
Hypotonia (>25% drop of MAP)	2 (2.13%)	4 (5.26%)	7 (28.0%)	7 (11.9%)

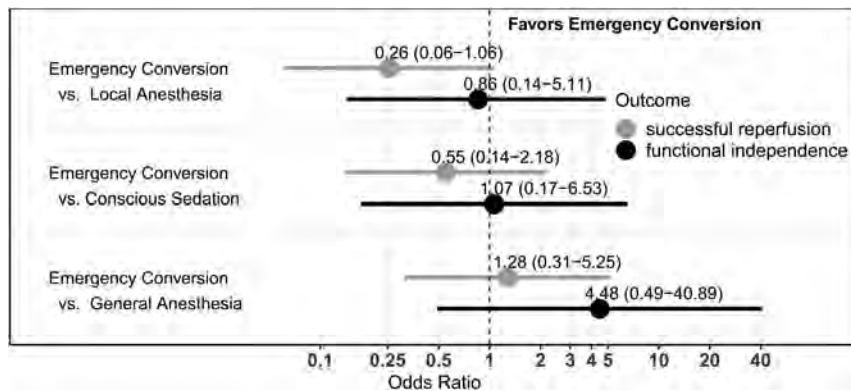


FIG 1. Adjusted odds ratio estimates with 95% confidence intervals comparing patients after emergency conversion with those who received local anesthesia, conscious sedation, and primary general anesthesia for successful reperfusion and functional independence. Successful reperfusion is TICI 2b/3 on the final angiogram, $P = .002$, for global differences across all groups (likelihood-ratio χ^2 test). Functional independence was mRS at 90 days ≤ 2 , $P = .12$, for global differences across all groups (likelihood-ratio χ^2 test). Results are derived from logistic regression models, adjusted for confounders (age, sex, admission NIHSS, prestroke mRS >1 , ASPECTS on admission imaging, comorbidities, application of IV thrombolysis, location of vessel occlusion and, additionally, TICI 2b/3 and occurrence of a drop of MAP in the analysis of functional independence) and based on 238 complete observations.

In the subset analysis extending the model with time from symptom onset and collateral score, there was no longer any significant difference among the 4 anesthesia groups (P value = .52). When we compared emergency conversion and GA in this subset analysis, emergency conversion showed a tendency toward lower odds of successful reperfusion (On-line Table; OR = 0.26; 95% CI, 0.01–5.04).

Clinical Outcomes

At 24 hours, at discharge, and at 90 days, patients after local anesthesia and CS had the lowest NIHSS and mRS scores, while emergency conversion and GA scores were comparable (Table 3). The proportion of functional independence was highest after local anesthesia (32.2%), followed by CS (29.2%), emergency conversion (28.0%), and GA (7.4%).

In the multivariable logistic regression, differences of functional independence among the groups were not statistically significant (P value = .12). In our cohort, patients with emergency conversion had higher odds of good outcome compared with those under GA (OR = 4.48; 95% CI, 0.49–40.89), but this effect was not statistically significant. Patients with emergency conversion had outcomes similar to those with local anesthesia (OR = 0.86; 95% CI, 0.14–5.1) and CS (OR = 1.07; 95% CI, 0.17–6.53).

In the subset analysis with time from symptom onset and collateral score, there was again no significant difference among the anesthesia groups (P value = .15). Again, emergency conversion had higher chances of functional independence than GA (OR = 14.34; 95% CI, 0.14–1448.78).

Blood Pressure during Intervention

In patients who underwent emergency conversion, an unwanted drop of blood pressure $>25\%$ of initial MAP occurred in 28.0% of patients, followed by GA (11.9%), CS (5.3%), and local anesthesia (2.1%). However, the occurrence of a drop of MAP was not significantly associated with functional independence in multivariable logistic regression (OR = 1.32; 95% CI, 0.29–5.78).

DISCUSSION

During mechanical thrombectomy, patients are treated under either local anesthesia, CS, or GA. In this retrospective study, 1 in 10 patients required emergency conversion to GA at some point during the intervention. The main finding of this study is that emergency conversion did not delay the time from admission to

Table 3: Clinical outcomes

	Local Anesthesia	CS	Emergency Conversion to GA	GA
Symptomatic intracranial hemorrhage (No.) (%)	3 (3.19%)	5 (6.58%)	1 (4.00%)	3 (5.08%)
NIHSS at 24 hr (median) (Q1–Q3)	9 (4–16.8)	12.5 (6–20.0)	19.0 (14.5–42.0)	21.0 (15.0–42.0)
Change in NIHSS at 24 hr (median) (Q1–Q3)	–3 (–9.75–0.00)	–1 (–8.00–4.00)	0 (–2.50–21.5)	3 (–1.00–9.50)
mRS at 24 hr (median) (Q1–Q3)	4 (3–5)	5 (3–5)	5 (5–5)	5 (5–5)
NIHSS at discharge (median) (Q1–Q3)	6 (2–11.0)	6 (2–13.0)	10.5 (6.50–18.2)	13.0 (10.0–18.0)
mRS at discharge (median) (Q1–Q3)	4 (2–5)	4 (2–5)	5 (3–5)	5 (4–5)
mRS at 90 days (median) (Q1–Q3) ^a	4 (1.50–5)	4 (2–6)	5 (2–5)	5 (4–6)
mRS 0–2 at 90 days (No.) (%) ^a	28 (32.2%)	21 (29.2%)	7 (28.0%)	4 (7.41%)

^a Data were available for 87/94 patients (local anesthesia), 72/76 patients (CS), 25/25 patients (emergency conversion), and 54/59 patients (GA).

reperfusion compared with primary GA, and emergency conversion did not cause deterioration of clinical outcome.

Both emergency conversion and primary GA resulted in a similar delay in the time from admission to flow restoration of 19–20 minutes compared with CS, and 27–28 minutes compared with local anesthesia. This result is in accordance with the times for primary GA induction reported in recently published randomized trials, which ranged from 10 to 27 minutes.^{11–13} Emergency conversion is performed under suboptimal conditions in comparison with primary GA (intubation on the angiography table versus the premedication room). However, emergency conversion was not associated with a loss of time compared with primary GA. Furthermore, no complications were reported as a result of emergency conversion to GA.

In approximately three-quarters of all patients, thrombectomy was initiated with the patient under local anesthesia or CS. Of these, 13% required emergency conversion. This number is comparable with the results of the SIESTA trial (14.3%, 11 of 77 patients under CS converted to GA)¹¹ and the AnStroke trial (15.6%, 7/45 patients),¹² while the GOLIATH trial reported a smaller proportion of emergency conversion (6.3%, 4/63 patients).¹³ Emergency conversion seems to be a common phenomenon during mechanical thrombectomy. In our study, we could not identify a clear pattern of anesthesia medication preceding emergency conversion to GA. Approximately one-third of patients received only local anesthesia without sedation, one-third received propofol only, and the remaining third was sedated with either benzodiazepines or opioids.

The main reason reported for emergency conversion during thrombectomy was excessive patient movement/agitation (72.0%, 18/25 patients), while 4 patients exhibited neurologic deterioration. In the SIESTA trial, the main reason for emergency conversion was also severe agitation (63.6%, 7/11 patients).¹¹ The AnStroke trial reported puncture of the common carotid artery as the main reason for conversion to GA (57.1%, 4/7 patients), while only 2 patients were intubated due to severe agitation.¹²

A drop of MAP during mechanical thrombectomy has been linked to unfavorable outcome.²³ We found a higher proportion of an unwanted drop of MAP in patients under emergency conversion (28%), followed by GA (12%). However, in the multivariable analysis conducted for the present study, the occurrence of an unwanted drop of MAP was not significantly associated with an unfavorable outcome.

With regard to clinical outcome after emergency conversion, there are 2 scenarios: First, one could hypothesize that emergency conversion is especially harmful compared with primary GA due

to the suboptimal conditions of GA induction (intubation in the angiography suite, less time for preparation, more frequent occurrence of a drop of blood pressure, and so forth.). In this case, all patients with even the slightest risk of emergency conversion, for example due to excessive movement on admission, should be intubated beforehand. Second, if emergency conversion is not especially harmful, one could initially perform local anesthesia/CS, even in these at-risk patients. To address this point, we compared all types of anesthesia in multivariable analysis for functional independence. Generally, we did not find any statistically significant differences between emergency conversion and the other types of anesthesia. We found a tendency toward higher chances of good clinical outcome after emergency conversion compared with primary GA, albeit it was not statistically significant. Therefore, CS-policy treatment centers should not hesitate to initiate treatment under local anesthesia/CS, even in patients at risk of emergency conversion.

The overall rate of successful perfusion in our patient cohort was similar to that in the HERMES meta-analysis of 5 randomized controlled trials (71% versus 69% in our patient cohort).²⁴ In our multivariable analysis, emergency conversion was not associated with decreased rates of successful reperfusion compared with GA. There was a tendency toward lower chances of successful reperfusion after emergency conversion compared with local anesthesia and CS. In the literature, the type of anesthesia seems to have little influence on the rate of successful reperfusion, as has been reported for CS and GA, both in a large meta-analysis of retrospective studies and in recent prospective trials.^{8,11–13}

In this single-center study, local anesthesia with or without CS was the method of choice. Primary GA was induced before thrombectomy only if necessary. Thus, patients with severe strokes more frequently received primary GA, as has been previously shown.^{25–27} Observational studies on the type of anesthesia in mechanical thrombectomy are subject to selection bias because primary GA is typically induced in more severely affected patients.⁸ Indeed, in this study, patients with emergency conversion fell between patients with CS and GA in terms of stroke severity and possibly had selection bias as well. However, we controlled for both symptom severity, prestroke mRS, successful reperfusion, and location of occlusion in the multivariable analysis and additionally for time from symptom onset to reperfusion and collateral score in a subset analysis.

Compared with larger randomized trials, patients in our study showed lower rates of functional independence: The HERMES meta-analysis of 5 randomized controlled trials²⁴ reported functional independence in 46% of patients in the intervention group

versus only 25% of patients in our cohort. This result is most likely because compared with the HERMES cohort, patients in our study were older (72 versus 68 years) and had lower ASPECTS at admission (median, 9 versus 7). Both factors were associated with poor outcome in the HERMES meta-analysis. Furthermore, a substantive proportion of our patients presented with prestroke mRS ≥ 2 (15%).

This study reflects cases from a single institution. Results could differ for emerging technical approaches of mechanical thrombectomy.²⁸ Furthermore, as in other retrospective studies on the type of anesthesia used in mechanical thrombectomy, selection bias is possible. The number of patients in the emergency conversion group was comparatively small, resulting in large confidence intervals, especially in the subset analysis, and results may differ for larger and/or multicenter patient cohorts. In addition, the reasons for induction of primary GA were not reported. The decision to administer sedation in patients with CS or to convert a patient under CS to GA was based on clinical indications and made individually by the attending neurointerventionalist and/or anesthesiologist.

CONCLUSIONS

In comparison with primary GA, emergency conversion to GA did not result in prolonged time to flow restoration, and chances of successful reperfusion and functional independence were not decreased. We found no evidence supporting the primary induction of GA in patients at risk for emergency conversion.

Disclosures: Annette Aigner—UNRELATED: Employment: University Medical Center Hamburg, Charité—Universitätsmedizin Berlin; Payment for Lectures Including Service on Speakers Bureaus: Hamburg University of Applied Sciences, Bernhard-Nocht Institute of Tropical Medicine, Roche Diagnostics, University of Salzburg, Charité—Universitätsmedizin Berlin, Studienstiftung des Deutschen Volkes, Hamburger Fern-Hochschule, Universität Heidelberg, Götz Thomalla—UNRELATED: Consultancy: Acandis, Stryker; Payment for Lectures Including Service on Speakers Bureaus: Bayer, Bristol Myers Squibb, Boehringer Ingelheim, Daiichi Sankyo, Jens Fiehler—UNRELATED: Consultancy: Acandis, Boehringer Ingelheim, Cerenovus, Covidien, Evasc Neurovascular, MD-Clinicals, Medtronic, Medina, MicroVention, Penumbra, Route 92 Medical, Stryker, Transverse Medical; Grants/Grants Pending: MicroVention, Medtronic, Stryker, Cerenovus.* Malte Issleib—UNRELATED: Employment: UKE—Center for Anesthesiology and Intensive Care. *Money paid to the institution.

ACKNOWLEDGMENT

We would like to thank Rosalie McDonough for reviewing the manuscript.

REFERENCES

- Berkhemer OA, Fransen PS, Beumer D, et al. **A randomized trial of intraarterial treatment for acute ischemic stroke.** *N Engl J Med* 2015;372:11–20 CrossRef Medline
- Saver JL, Goyal M, Bonafe A, et al. **Stent-retriever thrombectomy after intravenous t-PA vs. t-PA alone in stroke.** *N Engl J Med* 2015;372:2285–95 CrossRef Medline
- Campbell BC, Mitchell PJ, Kleinig TJ, et al. **Endovascular therapy for ischemic stroke with perfusion-imaging selection.** *N Engl J Med* 2015;372:1009–18 CrossRef Medline
- Jovin TG, Chamorro A, Cobo E, et al. **Thrombectomy within 8 hours after symptom onset in ischemic stroke.** *N Engl J Med* 2015;372:2296–2306 CrossRef Medline
- Goyal M, Demchuk AM, Menon BK, et al. **Randomized assessment of rapid endovascular treatment of ischemic stroke.** *N Engl J Med* 2015;372:1019–30 CrossRef Medline
- Bhogal P, Andersson T, Maus V, et al. **Mechanical thrombectomy—a brief review of a revolutionary new treatment for thromboembolic stroke.** *Clin Neuroradiol* 2018;28:313–26 CrossRef Medline
- Brinjikji W, Murad MH, Rabinstein AA, et al. **Conscious sedation versus general anesthesia during endovascular acute ischemic stroke treatment: a systematic review and meta-analysis.** *AJNR Am J Neuroradiol* 2015;36:525–29 CrossRef Medline
- Brinjikji W, Pasternak J, Murad MH, et al. **Anesthesia-related outcomes for endovascular stroke revascularization.** *Stroke* 2017;48:2784–91 CrossRef Medline
- Ilyas A, Chen CJ, Ding D, et al. **Endovascular mechanical thrombectomy for acute ischemic stroke under general anesthesia versus conscious sedation: a systematic review and meta-analysis.** *World Neurosurg* 2018;12:e355–67 CrossRef Medline
- Campbell BV, van Zwam WH, Goyal M, et al. **Effect of general anaesthesia on functional outcome in patients with anterior circulation ischaemic stroke having endovascular thrombectomy versus standard care: a meta-analysis of individual patient data.** *Lancet Neurol* 2018;17:47–53 CrossRef Medline
- Schönenberger S, Uhlmann L, Hacke W, et al. **Effect of conscious sedation vs general anesthesia on early neurological improvement among patients with ischemic stroke undergoing endovascular thrombectomy.** *JAMA* 2016;316:1986 CrossRef Medline
- Löwhagen Hendén P, Rentzos A, Karlsson JE, et al. **General anesthesia versus conscious sedation for endovascular treatment of acute ischemic stroke.** *Stroke* 2017;48:1601–07 CrossRef Medline
- Simonsen CZ, Yoo AJ, Sørensen LH, et al. **Effect of general anesthesia and conscious sedation during endovascular therapy on infarct growth and clinical outcomes in acute ischemic stroke.** *JAMA Neurol* 2018;75:470–77 CrossRef Medline
- Breckenfeld C, Mattle HP, Schroth G. **General is better than local anesthesia during endovascular procedures.** *Stroke* 2010;41:2716–17 CrossRef Medline
- Barber PA, Demchuk AM, Zhang J, et al. **Validity and reliability of a quantitative computed tomography score in predicting outcome of hyperacute stroke before thrombolytic therapy: ASPECTS Study Group—Alberta Stroke Programme Early CT Score.** *Lancet* 2000;355:1670–74 CrossRef Medline
- Maas MB, Lev MH, Ay H, et al. **Collateral vessels on CT angiography predict outcome in acute ischemic stroke.** *Stroke* 2009;40:3001–05 CrossRef Medline
- Canty A, Ripley BD. **Bootstrap R (S-Plus) Functions.** 2019. <https://astrostatistics.psu.edu/su07/R/html/boot/html/00Index.html>. Accessed ????????
- Davison AC, Hinkley DV. **Bootstrap Methods and Their Applications.** Cambridge: Cambridge University Press; 1997
- Fox J, Weisberg S. **An R Companion to Applied Regression.** Thousand Oaks: Sage Publication; 2011
- Hothorn T, Bretz F, Westfall P. **Simultaneous inference in general parametric models.** *Biom J* 2008;50:346–63 CrossRef Medline
- Wickham H. **Ggplot2 Elegant Graphics for Data Analysis.** New York: Springer-Verlag; 2016
- R Core Team. **R: A Language and Environment for Statistical Computing.** <https://cran.r-project.org/doc/manuals/fullrefman.pdf>. Accessed ?????
- Treurniet KM, Berkhemer OA, Immink RV, et al. **A decrease in blood pressure is associated with unfavorable outcome in patients undergoing thrombectomy under general anesthesia.** *J Neurointerv Surg* 2018;10:107–11 CrossRef Medline
- Goyal M, Menon BK, van Zwam WH, et al; HERMES collaborators. **Endovascular thrombectomy after large-vessel ischaemic stroke: a meta-analysis of individual patient data from five randomised trials.** *Lancet* 2016;387:1723–31 CrossRef Medline

25. Abou-Chebl A, Yeatts SD, Yan B, et al. **Impact of general anesthesia on safety and outcomes in the endovascular arm of Interventional Management of Stroke (IMS) III Trial.** *Stroke* 2015;46:2142–48 CrossRef Medline
26. van den Berg LA, Koelman DH, Berkhemer OA, et al. **Type of anesthesia and differences in clinical outcome after intra-arterial treatment for ischemic stroke.** *Stroke* 2015;46:1257–62 CrossRef Medline
27. Berkhemer OA, van den Berg LA, Fransen PSS, et al. **The effect of anesthetic management during intra-arterial therapy for acute stroke in MR CLEAN.** *Neurology* 2016;87:656–64 CrossRef Medline
28. Maegerlein C, Berndt MT, Mönch S, et al. **Further development of combined techniques using stent retrievers, aspiration catheters and BGC: the PROTECT^{PLUS} technique.** *Clin Neuroradiol* 2018; Nov 9. [Epub ahead of print] CrossRef Medline

Imaging Triage of Patients with Late-Window (6–24 Hours) Acute Ischemic Stroke: A Comparative Study Using Multiphase CT Angiography versus CT Perfusion

M.A. Almekhlafi, W.G. Kunz, R.A. McTaggart, M.V. Jayaraman, M. Najm, S.H. Ahn, E. Fainardi, M. Rubiera, A.V. Khaw, A. Zini, M.D. Hill, A.M. Demchuk, M. Goyal, and B.K. Menon

ABSTRACT

BACKGROUND AND PURPOSE: The role of collateral imaging in selecting patients for endovascular thrombectomy beyond 6 hours from onset has not been established. To assess the comparative utility of collateral imaging using multiphase CTA in selecting late window patients for EVT.

MATERIALS AND METHODS: We used data from a prospective multicenter observational study in which all patients underwent imaging with multiphase CT angiography as well as CTP. Two blinded reviewers evaluated patients' eligibility for endovascular thrombectomy using published collateral imaging (multiphase CTA) criteria compared with CTP using the selection criteria of the Clinical Mismatch in the Triage of Wake Up and Late Presenting Strokes Undergoing Neurointervention with Trevo (DAWN) and Endovascular Therapy Following Imaging Evaluation for Ischemic Stroke 3 (DEFUSE-3) trials. CTP images were processed using automated commercial software. The outcomes of patients eligible for endovascular thrombectomy according to multiphase CTA, DAWN, or DEFUSE-3 criteria were compared using multivariable logistic regression modeling. Model characteristics were compared using the C-statistic for the receiver operating characteristic curve, the Akaike information criterion, and the Bayesian information criterion.

RESULTS: Eighty-six patients presented beyond 6 hours from onset/last known well (median, 9.6 hours; interquartile range, 4.1 hours). Thirty-five patients (40.7%) received endovascular thrombectomy, of whom good functional outcome (90-day mRS, 0–2) was achieved in 16/35 (47%). Collateral-based imaging paradigms significantly modified the treatment effect of endovascular thrombectomy on 90-day mRS 0–2 ($P_{\text{interaction}} = .007$). The multiphase CTA-based regression model best fit the data for the 90-day outcome (C-statistic, 0.86; 95% CI, 0.77–0.94) and was associated with the least information loss (Akaike information criterion, 95.7; Bayesian information criterion, 114.9) compared with CTP-based models.

CONCLUSIONS: The collateral-based imaging paradigm using multiphase CTA compares well with CTP in selecting patients for endovascular thrombectomy in the late time window.

ABBREVIATIONS: AIC = Akaike information criterion; BIC = Bayesian information criterion; EVT = endovascular thrombectomy; IQR = interquartile range; LVO = large-vessel occlusion; mCTA = multiphase CTA

Endovascular thrombectomy (EVT) has become the standard of care in patients with acute ischemic stroke with large-vessel

occlusion (LVO) presenting within 6 hours from symptom onset.^{1,2} The treatment time window can be further extended to capture patients with salvageable tissue up to 24 hours from last known well. Two randomized trials have shown an overwhelming benefit of EVT over medical treatment in patients presenting up to 16 hours (Endovascular Therapy Following Imaging Evaluation for Ischemic Stroke 3 [DEFUSE-3])³ and 24 hours (Clinical Mismatch in the Triage of Wake Up and Late

Received July 30, 2019; accepted after revision October 1.

From the Department of Clinical Neurosciences (M.A.A., M.N., M.D.H., A.M.D., M.G., B.K.M.), Calgary Stroke Program, Department of Radiology (M.A.A., M.D.H., A.M.D., M.G., B.K.M.), Department of Community Health Sciences (M.A.A., M.D.H., B.K.M.), and Department of Medicine (M.D.H.), Hotchkiss Brain Institute, Cumming School of Medicine University of Calgary, Calgary, Alberta, Canada; Department of Radiology (W.G.K.), University Hospital, Ludwig Maximilian University of Munich, Munich, Germany; Departments of Neurology, Diagnostic Imaging, and Neurosurgery (R.A.M., M.V.J.), Warren Alpert Medical School of Brown University, Providence, Rhode Island; Department of Neurology (S.H.A.), Chosun University School of Medicine, Gwangju, South Korea; Department of Neurosciences and Rehabilitation (E.F.), University Hospital, Ferrara, Italy; Department of Neurology (M.R.), Hospital Vall d'Hebron, Passeig de la Vall d'Hebron, Barcelona, Spain; Department of Clinical Neurosciences (A.V.K.), University of Western Ontario, London, Ontario, Canada; and Department of Neurology and Stroke Center (A.Z.), Istituto Di Ricovero e Cura a Carattere Scientifico Istituto di Scienze Neurologiche di Bologna, Maggiore Hospital, Bologna, Italy.

Please address correspondence to Bijoy K. Menon, MBBS, MD, DM, MSc, FRCPC, Departments of Clinical Neurosciences, Radiology, and Community Health Sciences, Hotchkiss Brain Institute, Cumming School of Medicine, University of Calgary, 1403 29th St NW, Calgary, AB Canada T2N 2T9; e-mail: docbijoymenon@gmail.com; @AlmekhlafiMa; @mayank_G0; @bijoymenon; @HotchkissBrain; @DCNSNeuro; @mobilestroke4U; @MVJayaraman; @WolfgangGKunzMD
<http://dx.doi.org/10.3174/ajnr.A6327>

Presenting Strokes Undergoing Neurointervention with Trevo [DAWN]) from last known well.⁴ Both studies used CT perfusion imaging to identify patients with LVO with a limited-size-predicted infarct core or substantial salvageable brain tissue (target mismatch) for inclusion.

The Endovascular Treatment for Small Core and Proximal Occlusion Ischemic Stroke (ESCAPE) trial showed that an imaging paradigm based on measuring collateral status beyond target occlusion is capable of selecting patients with LVO who would benefit from EVT up to 12 hours from onset/last known well.^{5,6} Multiphase CTA (mCTA) is a reliable and well-validated tool for measuring collateral status beyond the target LVO.⁷⁻¹¹ Collateral assessments on mCTA, even at the brain region level, compare well with CTP-based blood flow measurements in predicting final tissue fate.⁷ Some of the shortcomings of CTP (eg, patient motion, limited brain coverage, larger radiation dose, additional contrast, time, and cost of image postprocessing software) are avoided using mCTA.^{12,13}

Recent studies have reported that patient selection using non-contrast CT and single-phase CTA^{14,15} or mCTA in the “late window” after stroke onset is an effective method of selecting patients for EVT.¹⁶ We compared patient selection using mCTA versus CTP in patients with late-window stroke with LVO using appropriate clinical treatment decisions and 90-day clinical outcomes to assess the comparative utility of each approach.

MATERIALS AND METHODS

Data are from the Precise and Rapid Assessment of Collaterals Using Multi-Phase CTA in the Triage of Patients with Acute Ischemic Stroke for IV or IA Therapy (PROVE-IT) study.^{7,8,17-19} This was a prospective, multicenter international observational study to assess the value of multimodal imaging in the triage of patients with acute ischemic stroke. All patients had noncontrast CT of the brain, CTA of the head and neck, mCTA, and CTP at baseline as described previously.⁸ For this analysis, only patients who presented ≥ 6 hours from stroke symptom onset/last known well time were included. Images were scored by consensus of 2 readers blinded to all clinical data (except the side of stroke), treatment allocation, and outcome data. In separate sessions and using random patient ordering, the same 2 readers scored the NCCT ASPECTS and then the collateral score on mCTA using a 6-point ordinal pial arterial filling scale as previously described.⁸ CT perfusion images were postprocessed using an automated commercial software.²⁰ Symptomatic intracranial hemorrhage was defined using the European Cooperative Acute Stroke Study III (ECASS) III criteria.²¹

For each imaging paradigm, readers assessed whether a patient would be a candidate for EVT (EVT eligibility) based on the following criteria:

1. NCCT and mCTA session: ASPECTS ≥ 5 and an mCTA-based collateral score of 4–6.⁸
2. DEFUSE-3 trial criteria: predicted core volume of <70 mL, predicted penumbra volume of ≥ 15 mL, and mismatch ratio of ≥ 1.8 .³
3. DAWN trial criteria: predicted core volume of <21 mL for patients older than 80 years of age 31–51 mL if younger than 80 years.⁴

We assessed the predictive validity of each imaging paradigm for functional outcomes by comparing logistic regression models generated using data regarding EVT eligibility from each of the above imaging paradigms. For each paradigm, a model was fitted for each of the following outcomes: early neurologic improvement (defined as $\geq 50\%$ drop in the NIHSS score during 24 hours) and 90-day functional independence (defined as mRS score of 0–2) using logistic regression and ordinal logistic regression with adjustment for key prognostic variables (age, sex, baseline NIHSS score, baseline ASPECTS, onset/last known well to imaging time, and treatment given). Modification of the effect of treatment (EVT versus no EVT) on clinical outcomes by the imaging paradigm was assessed using a multiplicative interaction term. The area under the curve of the receiver operating characteristic properties of the models was compared using the χ^2 test as described by Gönen.²² In addition, information content of the various models was compared using the Akaike information criterion (AIC) and the Bayesian information criterion (BIC).²³ These methods aim to identify the model that best approximates the outcome data (ie, the model that minimizes data/information loss) while applying a penalty for model complexity (ie, having too many variables). While the values of AIC or BIC do not have a simple interpretation, the model with the lowest values is the one that is better.

The PROVE-IT study was approved by the local ethics review committees. Analyses were performed using STATA 15 software (StataCorp, College Station, Texas).

RESULTS

Baseline Clinical Data

Among 614 patients in PROVE-IT, 86 patients were included in this analysis as patients with late-window stroke. The median age was 71 years (interquartile range [IQR], 14 years), and 48.8% were women, while the median baseline NIHSS score was 12 (IQR, 11). The median time from last known well/stroke symptom onset to baseline CT was 9.6 hours (IQR, 4.1 hours). Table 1 summarizes the baseline characteristics of this cohort according to the imaging paradigm and the treatment received.

Baseline Imaging Data

NCCT and mCTA were available in all patients; CTP, however, could not be processed in 6/86 patients (7%) due to acquisition- or patient motion-related technical limitations. These 6 patients were assumed to be ineligible for EVT using DAWN and DEFUSE-3 criteria. The median ASPECTS was 9 (IQR, 3). The distribution of the occlusion site was as follows: isolated intracranial ICA (11.6%), L- or T-type occlusions (12.8%), M1 MCA (33.7%), M2 MCA (22.1%), posterior cerebral artery (1/86, 1.2%), distal occlusions (9/86, 10.5%), and no occlusions (10/86, 11.6%). The mean and median baseline infarct volumes were 18.7 ± 28.2 mL and 8 mL (range, 0–162 mL), and penumbra volumes were 109.5 ± 10.7 mL and 94 mL (range, 0–753 mL), respectively.

Treatment and Outcome Data

Of 86 patients, 35 patients (40.7%) received EVT, while 51 (59.3%) were treated conservatively. Among EVT-treated patients, successful reperfusion (modified TICI 2b/3) was

Table 1: Baseline characteristics of the cohort according to actual treatment with endovascular therapy

	PROVE-IT Late-Window Cohort (n = 86)					
	Favorable mCTA Profile (n = 63)		Favorable DEFUSE Profile (n = 58)		Favorable DAWN Profile (n = 32)	
	EVT	No EVT	EVT	No EVT	EVT	No EVT
No.	33 (52.4%)	30 (47.6%)	28 (48.3%)	30 (51.7%)	18 (56.3%)	14 (43.7%)
Age ^a	75	72	75	72	75	77
NIHSS score ^a	18	12	18	14	19	18
ASPECTS ^a	9	9	9	8	9	9
Onset/LSN to imaging (min) ^a	578 (9.6 hr)	580 (9.7 hr)	559 (9.3 hr)	571 (9.5 hr)	608 (10.1 hr)	593 (9.9 hr)
Occlusion site						
Terminal ICA	12 (36.4%)	3 (10%)	10 (35.7%)	4 (13.3%)	7 (38.9%)	3 (21.4%)
M1	14 (42.4%)	13 (43.3%)	10 (35.7%)	13 (43.3%)	6 (33.3%)	5 (35.7%)
M2	6 (18.2%)	14 (46.7%)	7 (25%)	13 (43.3%)	4 (22.2%)	6 (42.9%)
M3 or distal	1 (3%)	0	1 (3.6%)	0	1 (5.6%)	0

Note:—LSN indicates last seen normal.

^a Denotes median.

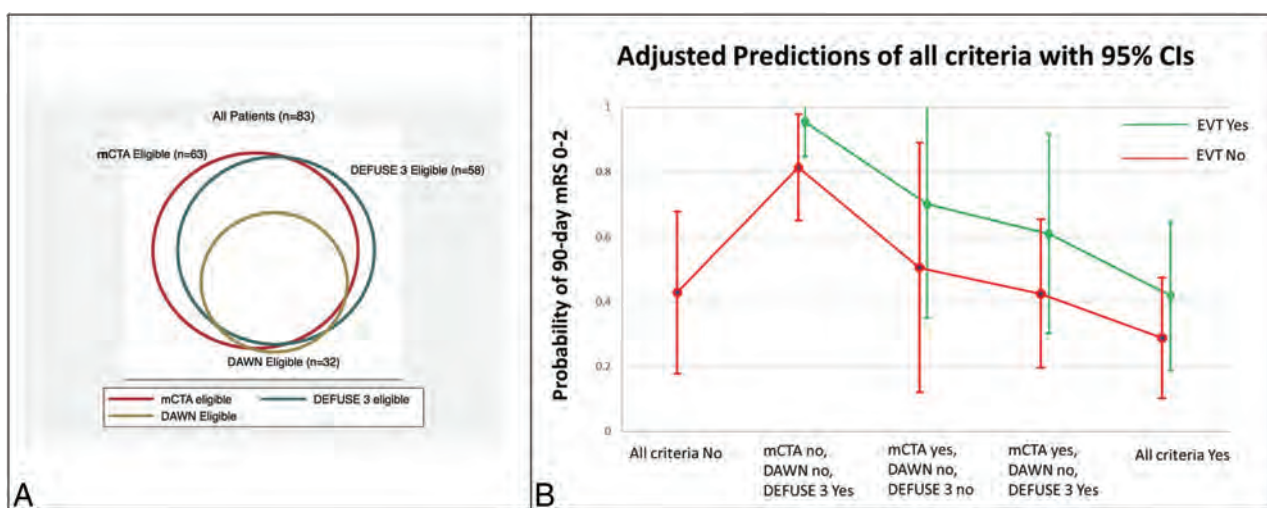


FIG 1. A, Proportion of patients eligible for EVT according to each imaging criterion. B, Adjusted predicted probability of achieving 90-day mRS score of 0–2 in those meeting none, some, or all the imaging criteria when treated with EVT (green) versus not (red).

achieved in 71.4% (25/35) patients. The median 24-hour NIHSS score in the overall cohort was 7 (IQR, 13). Early neurologic improvement was seen in 27/86 patients (31.4%) in the cohort overall and in 54.3% (19/35) of those treated with EVT (72%; 18/25 of those with successful reperfusion). Four of 86 patients (4.7%) had symptomatic intracranial hemorrhage; all received EVT (4/35, 11.4% of EVT-treated patients). Of the patients with symptomatic intracranial hemorrhage, all (4/4) met the DEFUSE-3 criteria for EVT, while 3/4 met the mCTA and DAWN criteria for EVT eligibility. Functional outcome data at 90 days were available for 83 of 86 patients (96.5%). Independent outcome (mRS, 0–2) was achieved in 47% (39/83) in the overall cohort and in 51.4% (18/35) of those treated with EVT (72%, 18/25 of those with successful reperfusion).

Eligibility for EVT and Predictive Validity of Imaging Paradigms

Of the 83 patients in this cohort with available 90-day outcomes, 63 patients (75.9%) were considered eligible for EVT according to the mCTA criteria, compared with 58 patients (69.9%)

according to the DEFUSE-3 criteria and only 32 patients (38.6%) according to DAWN criteria (Fig 1A). Among the 35 EVT-treated patients in our cohort, 33 patients (94.3%) were considered good EVT candidates according to the mCTA criteria compared with 28 patients (80%), according to DEFUSE-3 criteria, and only 18 patients (51.4%), according to DAWN criteria for EVT eligibility. Among EVT-treated patients, the proportion of patients with the highest early neurologic improvement and independent 90-day functional outcome were those who were good treatment candidates according to mCTA paradigm. Similarly, patients who were not EVT candidates according to mCTA paradigm had the lowest likelihood of having early neurologic improvement and an independent 90-day functional outcome.

The predictive validity of each imaging paradigm in determining prespecified clinical outcomes was assessed using logistic regression models (Table 2 and Fig 1B). All imaging paradigms performed well in predicting 90-day functional outcome versus early neurologic improvement. Patients who had a favorable mCTA imaging profile had significantly better 90-day functional

Table 2: Comparison of the ability of imaging paradigms in discriminating clinical outcomes using logistic regression modeling^a

Imaging Paradigm/Criteria	Comparison					
	No.	Odds Ratio (95% CI)	P Value	C-Statistic	AIC/BIC	AIC/BIC (o)
90-day mRS						
mCTA (>3 vs ≤3)	82	9.6 (1.9–48.8)	.001	0.86	95.7/114.9	300.6/331.9
DEFUSE-3 criteria	82	5.5 (1.2–25.3)	.028	0.84	99.0/118.3	
DAWN criteria	82	9.3 (0.9–98.8)	.065	0.83	99.3/118.6	303.1/334.4
Early neurologic improvement (≥50% drop in 24-hr NIHSS score from baseline)						
mCTA (>3 vs ≤3)	82	13.3 (2.9–61)	.001	0.80	98.2	117.5
DEFUSE-3 criteria	82	8.5 (1.9–37.5)	.005	0.74	105.9	125.1
DAWN criteria	82	5.6 (0.6–56.1)	.141	0.71	109.6	

^a Variables age, sex, baseline NIHSS score, baseline NCCT ASPECTS, onset/last known well to imaging time, EVT, and the interaction term imaging paradigm × EVT (yes versus no) were included in all models. C-statistic represents the area under a receiver operating characteristic curve. AIC and BIC are Bayesian information criteria methods to assess model fit in which the model with the lowest AIC or BIC is preferred. AIC/BIC (o) denotes the AIC and BIC for the ordinal regression models.

outcome when they were treated with EVT (mCTA/EVT, $P_{\text{interaction}} = .007$). This was also noted for the paradigm based on DEFUSE-3 criteria ($P_{\text{interaction}} = .028$) but not for the DAWN criteria ($P_{\text{interaction}} = .065$). The probability of 90-day independent functional outcome was highest among patients meeting DEFUSE-3 criteria both with and without EVT (Fig 1B).

For both outcomes, models using mCTA were not significantly better than the next-best model for clinical outcomes when comparing the C-statistic (χ^2 test for model comparisons, $P > .05$). For both outcomes however, models using the mCTA criteria minimized information loss (AIC and BIC values) better than either of the models that used CTP. For the 90-day mRS, after the mCTA model, the next-best model was the DEFUSE-3-based perfusion criteria (0.19 times as probable as the mCTA-based model to minimize information loss). For both outcomes, the next-best model was the perfusion imaging paradigm using the DEFUSE-3 criteria. Similarly, when using ordinal logistic regression for 90-day outcome, the model using the mCTA criteria best minimized information loss (lowest AIC and BIC values) compared with models that used CTP.

DISCUSSION

This analysis shows that collateral-based imaging paradigms using mCTA are at least as good as perfusion-based imaging paradigms in selecting patients presenting late for EVT. Models using mCTA had the highest likelihood of discriminating those who would have good clinical outcome when treated with EVT versus those who would not. Models using DEFUSE-3 selection criteria had better predictive validity in determining good clinical outcomes among EVT-treated patients than the DAWN paradigm. Models using mCTA or DEFUSE-3 criteria may result in more patients being offered EVT (Fig 1A).

In patients presenting within 6 hours from symptom onset/last known well, current guidelines recommend the use of NCCT and CTA in determining patient eligibility for EVT. The primary goal of imaging selection in these patients is to identify a patient with an ASPECTS of ≥ 6 and a proximal intracranial occlusion.¹ In patients presenting beyond 6 hours, current guidelines suggest identifying LVO using CTA and the DAWN or DEFUSE-3 eligibility criteria for patient selection. Most interesting, the American Heart Association guidelines suggest that the benefit with EVT was independently demonstrated for both the subgroup of

patients who met DAWN eligibility criteria and for the subgroup who did not.¹ This is important because the findings of DAWN and DEFUSE-3 trials do not rule out EVT benefits in patients who do not fit their imaging selection criteria.

Although perfusion imaging variability and interpretation have benefited from the use of automated software, challenges related to perfusion imaging such as time delays with acquisition, training of technologists, motion sensitivity, and the risks with extra radiation and contrast persist. In this analysis, 7% of patients' perfusion images could not be analyzed by postprocessing software. Moreover, a recent study suggests that perfusion-based selection criteria disqualified more patients from EVT compared with other selection paradigms, without improving outcomes.²⁴ While our analyses showed that patients meeting the DEFUSE-3 criteria had the highest predicted probability of functional independence, those patients did equally well with and without EVT. The treatment effect (ie, the difference in the proportion of good outcome when treated with EVT versus not having it) was higher in patients selected using the mCTA criteria alone rather than with other criteria (Fig 1B).

NCCT and CTA continue to be the workhorses of acute stroke diagnosis. Thus, using these modalities for determining eligibility, even in the extended time window, is a logical next step. Recent studies have shown that stroke centers that use an NCCT- and mCTA-based imaging paradigm to select patients for EVT in the extended time window achieve results that are comparable with those obtained in patients who received EVT in the DAWN and DEFUSE-3 trials.^{14–16} A post hoc analysis of the ESCAPE trial restricted to patients who presented late showed that patients receiving EVT had similar prospects of good clinical outcome (48.5%) versus those in the DAWN (49%) and DEFUSE-3 (45%) trials.⁶ Taken together, this analysis and other previous analyses provide more evidence to support the construct that an mCTA-based imaging paradigm is at least as good as current perfusion-based imaging paradigms in selecting patients presenting late for EVT.⁸ The adoption of NCCT-/mCTA-based imaging selection for the 6- to 24-hour time window would also have implications for stroke systems of care because this simplified imaging paradigm can be used at Primary Stroke Centers to triage patients for EVT without the need for implementing perfusion imaging.^{13,25}

Our study has limitations. First, a nonrandomized study of this nature is vulnerable to selection bias. Our inclusion of

patients who did not receive EVT is an attempt to mitigate any effects of bias related to selecting patients for EVT based on nonimaging factors (eg, age or stroke symptom severity). Second, this analysis did not differentiate between patients who had wake-up strokes from those with a witnessed onset that was 6 hours prior. Third, the images were read by 2 expert readers and not in real life. Automating collateral assessments and even NCCT ASPECTS interpretation using validated algorithms could be potential solutions to address this latter concern.

CONCLUSIONS

In this prospective study of patients presenting after 6 hours from onset/time last known well, an mCTA collateral-based paradigm is at least as good as guideline-approved perfusion imaging-based paradigms in selecting patients for EVT.

Disclosures: Mohammed Almekhlafi—UNRELATED: Employment: University of Calgary; Grants/Grants Pending: Canadian Institutes of Health Research.* Alexander V. Khaw—UNRELATED: Grants/Grants Pending: Lawson Health Research Institute, Comments: grant for investigator-initiated study.* Andrea Zini—UNRELATED: Board Membership: Stryker, Boehringer Ingelheim; Consultancy: Medtronic, Boehringer Ingelheim; Payment for Lectures Including Service on Speakers Bureaus: Medtronic, Cerenovus*; Travel/Accommodations/Meeting Expenses Unrelated to Activities Listed: Medtronic, Boehringer Ingelheim, Stryker.* Michael D. Hill—UNRELATED: Consultancy: Boehringer Ingelheim, Comments: COLUMBUS registry, involvement completed June 2019; Grants/Grants Pending: NoNO Inc, Medtronic, Stryker, Comments: ESCAPE-NAI trial, HERMES collaboration, UNMASK EVT study.* Andrew Demchuk—RELATED: Grant: CIHR*; Consulting fee or honorarium: Medtronic; UNRELATED: Employment: University of Calgary; Patents (planned, pending or issued): Circle NVI, Comments: Stroke imaging software. Mayank Goyal—UNRELATED: Consultancy: Medtronic, Stryker, Mentice, Micro-Vention, Comments: advice regarding acute stroke devices and procedures; Grants/Grants Pending: Stryker, Comments: unrestricted grant to University of Calgary concerning the UNMASK EVT study*; Other: GE Healthcare, Comments: licensing agreement related to Systems of Acute Stroke Diagnosis. Bijoy K. Menon—UNRELATED: Grant: PROVELT Canadian Institutes of Health Research.* *Money paid to the institution.

REFERENCES

1. Powers WJ, Rabinstein AA, Ackerson T, et al. **2018 Guidelines for the Early Management of Patients with Acute Ischemic Stroke: A Guideline for Healthcare Professionals from the American Heart Association/American Stroke Association.** *Stroke* 2018;49:e46–110 CrossRef Medline
2. Goyal M, Menon BK, van Zwam WH, et al. **Endovascular thrombectomy after large-vessel ischaemic stroke: a meta-analysis of individual patient data from five randomised trials.** *Lancet* 2016;387:1723–31 CrossRef Medline
3. Albers GW, Marks MP, Kemp S, et al. **Thrombectomy for stroke at 6 to 16 hours with selection by perfusion imaging.** *N Engl J Med* 2018;378:708–18 CrossRef Medline
4. Nogueira RG, Jadhav AP, Haussen DC, et al. **Thrombectomy 6 to 24 hours after stroke with a mismatch between deficit and infarct.** *N Engl J Med* 2018;378:11–21 CrossRef Medline
5. Goyal M, Demchuk AM, Menon BK, et al. **Randomized assessment of rapid endovascular treatment of ischemic stroke.** *N Engl J Med* 2015;372:1019–30 CrossRef Medline
6. Evans JW, Graham BR, Pordeli P, et al. **Time for a time window extension: insights from late presenters in the ESCAPE Trial.** *AJNR Am J Neuroradiol* 2018;39:102–06 CrossRef Medline
7. d'Este CD, Trivedi A, Pordeli P, et al. **Regional comparison of multiphase computed tomographic angiography and computed tomographic perfusion for prediction of tissue fate in ischemic stroke.** *Stroke* 2017;48:939–45 CrossRef Medline
8. Menon BK, d'Este CD, Qazi EM, et al. **Multiphase CT angiography: a new tool for the imaging triage of patients with acute ischemic stroke.** *Radiology* 2015;275:510–20 CrossRef Medline
9. García-Tornel A, Carvalho V, Boned S, et al. **Improving the evaluation of collateral circulation by multiphase computed tomography angiography in acute stroke patients treated with endovascular reperfusion therapies.** *Interv Neurol* 2016;5:209–17 CrossRef Medline
10. Di Giuliano F, Picchi E, Sallustio F, et al. **Accuracy of advanced CT imaging in prediction of functional outcome after endovascular treatment in patients with large-vessel occlusion.** *Neuroradiol J* 2019;32:62–70 CrossRef Medline
11. Uransilp N, Dharmasaroja PA, Watcharakorn A, et al. **Implementation of multiphase computed tomography angiography in management of patients with acute ischemic stroke in clinical practice.** *J Clin Neurosci* 2019;62:100–04 CrossRef Medline
12. Goyal M, Menon BK, Derdeyn CP. **Perfusion imaging in acute ischemic stroke: let us improve the science before changing clinical practice.** *Radiology* 2013;266:16–21 CrossRef Medline
13. Almekhlafi MA, Kunz WG, Menon BK, et al. **Imaging of patients with suspected large-vessel occlusion at primary stroke centers: available modalities and a suggested approach.** *AJNR Am J Neuroradiol* 2019;40:396–400 CrossRef Medline
14. Santos T, Carvalho A, Cunha AA, et al. **NCCT and CTA-based imaging protocol for endovascular treatment selection in late presenting or wake-up strokes.** *J Neurointerv Surg* 2019;11:200–03 CrossRef Medline
15. DiBisio E, Jayaraman M, Goyal M, et al. **Dismantling the ability of CT and MRI to identify the target mismatch profile in patients with anterior circulation large vessel occlusion beyond six hours from symptom onset.** *Emerg Radiol* 2019;26:401–08 CrossRef Medline
16. Motyer R, Thornton J, Power S, et al. **Endovascular thrombectomy beyond 12 hours of stroke onset: a stroke network's experience of late intervention.** *J Neurointerv Surg* 2018;10:1043–46 CrossRef Medline
17. Casault C, Al Sultan AS, Trivedi A, et al. **Collateral scoring on CT angiogram must evaluate phase and regional pattern.** *Can J Neurol Sci* 2017;44:503–07 CrossRef Medline
18. d'Este CD, Boesen ME, Ahn SH, et al. **Time-dependent computed tomographic perfusion thresholds for patients with acute ischemic stroke.** *Stroke* 2015;46:3390–97 CrossRef Medline
19. Ahn SH, d'Este CD, Qazi EM, et al. **Occult anterograde flow is an under-recognized but crucial predictor of early recanalization with intravenous tissue-type plasminogen activator.** *Stroke* 2015;46:968–75 CrossRef Medline
20. Campbell BC, Yassi N, Ma H, et al. **Imaging selection in ischemic stroke: feasibility of automated CT-perfusion analysis.** *Int J Stroke* 2015;10:51–54 CrossRef Medline
21. Hacke W, Kaste M, Bluhmki E, et al. **Thrombolysis with alteplase 3 to 4.5 hours after acute ischemic stroke.** *N Engl J Med* 2008;359:1317–29 CrossRef Medline
22. Gönen M. *Analyzing Receiver Operating Characteristic Curves with SAS.* SAS Institute, 2007
23. Burnham KP, Anderson DR. **Multimodel inference: understanding AIC and BIC in model selection.** *Sociol Methods Res* 2004;33:261–304 CrossRef
24. Bouslama M, Bowen MT, Haussen DC, et al. **Selection paradigms for large vessel occlusion acute ischemic stroke endovascular therapy.** *Cerebrovasc Dis* 2017;44:277–84 CrossRef Medline
25. McTaggart RA, Yaghi S, Cutting SM, et al. **Association of a primary stroke center protocol for suspected stroke by large-vessel occlusion with efficiency of care and patient outcomes.** *JAMA Neurol* 2017;74:793–800 CrossRef Medline

Flow-Diversion Treatment for Unruptured Nonsaccular Intracranial Aneurysms of the Posterior and Distal Anterior Circulation: A Meta-Analysis

F. Cagnazzo, P.-H. Lefevre, I. Derraz, C. Dargazanli, G. Gascou, D.T. di Carlo, P. Perrini, R. Ahmed, J.F. Hak, C. Riquelme, A. Bonafe, and V. Costalat



ABSTRACT

BACKGROUND: Treatment management and outcomes of unruptured nonsaccular aneurysms are different compared with their saccular counterparts.

PURPOSE: Our aim was to analyze the outcomes after flow diversion among nonsaccular unruptured lesions.

DATA SOURCES: A systematic search of 3 data bases (2005–2019) was performed according to Preferred Reporting Items for Systematic Reviews and Meta-Analyses (PRISMA) guidelines.

STUDY SELECTION: We included studies reporting flow diversion for nonsaccular unruptured aneurysms of the posterior and distal anterior circulations. Anterior circulation lesions were included if located distal to the petrocavernous and supraclinoid ICA (MCA, A1, anterior communicating artery, A2). Giant dolichoectatic holobasilar lesions were excluded because of their poor treatment outcomes.

DATA ANALYSIS: Aneurysm occlusion and complication rates were calculated (random effects meta-analysis).

DATA SYNTHESIS: We included 15 studies (213 aneurysms). The long-term adequate occlusion rate was 85.3% (137/168; 95% CI, 78.2%–92.4%; $I^2 = 42.3\%$). Treatment-related complications were 17.4% (41/213; 95% CI, 12.45%–22.4%; $I^2 = 0\%$). Overall, 15% (37/213; 95% CI, 10%–20%; $I^2 = 0\%$) were ischemic events. Procedure-related morbidity was 8% (20/213; 95% CI, 5%–12%; $I^2 = 0\%$). Fusiform or dissecting types had comparable adequate occlusion (116/146 = 83%; 95% CI, 74%–92%; $I^2 = 48\%$ versus 33/36 = 89%; 95% CI, 80%–98%; $I^2 = 0\%$; $P = .31$) and complication rates (35/162 = 17%; 95% CI, 10%–25%; $I^2 = 24\%$ versus 11/51 = 19%; 95% CI, 10%–31%; $I^2 = 0\%$; $P = .72$). Aneurysm size (>10 versus ≤ 10 mm) was independently associated with a higher rate of complications (OR = 6.6; 95% CI, 1.3–15; $P = .02$). The rate of ischemic events after discontinuation of the antiplatelet therapy was 5% (5/93; 95% CI, 2%–9%; $I^2 = 0\%$).

LIMITATIONS: Small and retrospective studies were available for this meta-analysis.

CONCLUSIONS: Unruptured nonsaccular aneurysms located in the posterior and distal anterior circulations can be effectively treated with flow diversion. Nevertheless, treatment-related complications are not negligible, with about 15% ischemic events and 8% morbidity. Larger size (>10 mm) significantly increases the risk of procedure-related adverse events.

ABBREVIATIONS: AC = anterior circulation; FD = flow diversion; IQR = interquartile range; PC = posterior circulation

Fusiform and dissecting aneurysms are defined as circumferential dilation of an intracranial artery, without a neck.¹ These lesions are uncommon compared with their saccular counterparts, presenting a different pathophysiology, natural history, and treatment management.² Accordingly, procedure-related outcomes after endovascular treatment of these lesions should be explored separately. When we investigated the literature, very few series focused on the flow diversion (FD) treatment of nonsaccular lesions, and most of the available results were

derived from a combination of saccular and nonsaccular aneurysms. Thus, the evidence surrounding treatment outcomes of FD among nonsaccular aneurysms requires further evaluation. We performed a meta-analysis exploring the angiographic and clinical outcomes of the off-label use of FD for nonsaccular posterior circulation lesions and nonsaccular

Please address correspondence to Federico Cagnazzo, MD, Neuroradiology Department, CHU Gui De Chauliac, 80 Ave Augustin Fliche, 34000 Montpellier, France; e-mail: f.cagnazzo86@gmail.com

Indicates article with supplemental on-line appendix and tables.

Indicates article with supplemental on-line photos.

<http://dx.doi.org/10.3174/ajnr.A6352>

Received August 28, 2019; accepted after revision October 14.

From the Neuroradiology Department (F.C., P.-H.L., I.D., C.D., G.G., R.A., J.F.H., C.R., A.B., V.C.), CHU Gui De Chauliac, Montpellier, France; and Department of Neurosurgery (D.T.d.C., P.P.), University of Pisa, Pisa, Italy.

anterior circulation aneurysms in distal locations (MCA, A1, anterior communicating artery, pericallosal segment).

MATERIALS AND METHODS

Literature Search

A comprehensive literature search of Scopus, PubMed, and Ovid EMBASE was performed for studies published from January 2005 to July 2019. The Preferred Reporting Items for Systematic Reviews and Meta-Analyses (PRISMA; <http://prisma-statement.org/>) guidelines were followed.³ The search strategy is described in On-line Table 1. The included studies are reported in On-line Table 2. The main inclusion criteria were the following: studies reporting series of FD treatment of unruptured nonsaccular aneurysms located in the anterior and posterior circulations. When reported in the article, nonsaccular aneurysms were classified as dissecting and fusiform aneurysms. Dissecting aneurysms were, in general, defined as lesions resulting from an injury to the arterial layers causing an irregular expansion of the vessel in a longitudinal fashion, whereas fusiform aneurysms incorporated the entire vessel circumferentially.^{2,4} In the anterior circulation (AC), nonsaccular aneurysms were included if located at the MCA, A1, anterior communicating artery, and distal anterior cerebral artery segments (at or beyond the A2 segment). We aimed to focus on AC aneurysms located distal to the circle of Willis because the indication for treatment with FD is still debated and is considered off-label. In fact, the efficacy of flow diverters in the ICA segment has already been reported,⁵ and the US Food and Drug Administration approved their use for unruptured saccular wide-neck or fusiform aneurysms in the ICA from the petrous segment to the terminus (https://www.accessdata.fda.gov/cdrh_docs/pdf17/P170024A.pdf). Accordingly, aneurysms arising from the petro-/cavernous and supraclinoid portions of the ICA (including the posterior communicating, anterior choroidal, and ophthalmic segments) were not included in this review.

Among the posterior circulation (PC), nonsaccular aneurysms were located at the vertebral, basilar, P1–P2, PICA, and AICA/superior cerebellar artery segments. Series reporting giant dolichoectatic aneurysms involving the entire vertebrobasilar artery (uniform dilation involving the entire vertebrobasilar system) were not included. Reasons behind the exclusion of these lesions are the following: 1) The natural history and treatment-related outcomes have been reported to be poor, and 2) indications for treatment still remain debatable.⁶

Other exclusion criteria were the following: 1) case reports, 2) review articles, 3) studies published in languages other than English, 4) in vitro studies and animal studies, and 5) series reporting saccular aneurysms. In cases of overlapping patient populations, we selected series with the largest number of subjects or with the most detailed data. The analysis was conducted by 2 independent readers. Articles were screened in their entirety to determine eligibility for inclusion. In addition, a third author solved potential discrepancies.

Data Collection

We extracted the following: 1) rate of aneurysm occlusion, 2) rate of complications, and 3) clinical outcomes.

Adequate aneurysm occlusion (complete/near-complete occlusion) was defined on the basis of the O'Kelly-Marotta grades C–D,⁷ the Raymond-Roy scale (class I–II),⁸ or when the terms “complete occlusion” or “neck remnant” were used in the study. Treatment-related complications were classified as following: 1) periprocedural (within 30 days after treatment) and delayed events (after 30 days); 2) transient complications (asymptomatic events or complete neurologic recovery) and permanent events (symptomatic complications with permanent deficits); and 3) hemorrhagic and ischemic complications. Aneurysms were classified as small and large lesions (<10 and ≥10 mm, respectively). Arteries covered by the stents were evaluated and classified as the following: 1) normal diameter, 2) arterial narrowing, and 3) arterial occlusion. Good outcome was defined as a modified Rankin Scale score of 0–2 or in the absence of adverse events.

Outcomes Analysis

The primary objectives of this meta-analysis study were to describe treatment-related complications (the safety of the treatment), the technical success rate, and occlusion during follow-up (efficacy of the treatment) after FD for nonsaccular aneurysms. The influence of aneurysm size, patient age, and treatment characteristics on the analyzed outcomes was also studied. This objective was achieved by performing a preplanned subgroups analysis as well as univariate and multivariate analyses on the available individual patient data. Individual patient data were extracted from each series (tables or on-line tables) when reported by the authors.

Quality Scoring

The Newcastle-Ottawa Scale⁹ was used to evaluate the quality of the included studies (details in On-line Table 3). Two authors independently performed the quality assessment, while a third author solved potential discrepancies.

Statistical Analysis

Meta-Analysis. Given the interstudy differences (patient population, aneurysm characteristics, and type of device used), random effects meta-analysis was adopted to report the studied outcomes because this model incorporates heterogeneity among studies. From each cohort, the cumulative prevalence and 95% confidence interval were calculated for each outcome. Heterogeneity was studied and was assessed by the Higgins index (I^2); subsequently, the DerSimonian and Laird random effects model was applied. The graphic representation was mostly performed by forest plot. In addition, we used subgroup analysis to estimate heterogeneity (aneurysm size, patient age, number of flow diverters, additional coils). To evaluate the risk of bias, we used a funnel plot followed by the Egger linear regression test. To verify the consistency of the meta-analysis outcome, we assessed the influence of each individual study by a sensitivity analysis (“leave-one-out” approach). Differences between subgroups of analyses were considered significant at $P < .05$. Meta-analysis was performed with ProMeta-2 (Internovi, Cesena, Italy) and OpenMeta [Analyst] (<http://www.cebm.brown.edu/openmeta/>).

Univariate and Multivariate Analysis. From the individual patient data, we extracted the following dependent variables: aneurysm occlusion (adequate-versus-incomplete occlusion) and treatment-

Table 1: Outcomes after flow-diversion treatment of unruptured nonsaccular intracranial aneurysms

Variables	Results of Systematic Review and Meta-Analysis	No. of Articles	Statistic (95% CI) (I ²)
Angiographic outcomes			
Rate of successful stent deployment	178/181 = 96%	11	(93–98) (I ² = 0%)
Long-term aneurysm adequate occlusion rate	137/168 = 85.3%	12	(78.2–92.4) (I ² = 42.3%)
Long-term aneurysm complete occlusion rate	128/168 = 78.8%	12	(72.8–84.8) (I ² = 0%)
Long-term adequate occlusion rate (fusiform aneurysms)	116/146 = 83%	11	(74–92) (I ² = 48%)
Long-term adequate occlusion rate (dissecting aneurysms)	33/36 = 89%	4	(80–98) (I ² = 0%)
Long-term occlusion rate among anterior circulation	51/61 = 87.5%	6	(79–95) (I ² = 0%)
Long-term occlusion rate among posterior circulation	86/107 = 83%	6	(71–95) (I ² = 60%)
Long-term adequate occlusion rate (PED)	118/149 = 82%	8	(75–90) (I ² = 25%)
Long-term adequate occlusion rate (other devices)	21/23 = 90%	3	(81–98) (I ² = 0%)
Treatment-related complications and clinical outcomes			
Overall treatment-related complications	41/213 = 17.4%	16	(12.5–22.4) (I ² = 0%)
Transient complications	21/213 = 9%	15	(5.6–13) (I ² = 0%)
Permanent complications	20/213 = 8%	15	(5–12) (I ² = 0%)
Ischemic complications	37/213 = 15%	15	(10–20) (I ² = 0%)
Hemorrhagic complications	4/213 = 3%	15	(1.2–6) (I ² = 0%)
Treatment-related complications (fusiform aneurysms)	35/162 = 17%	11	(10–25) (I ² = 24%)
Treatment-related complications (dissecting aneurysms)	11/51 = 19%	4	(10–31) (I ² = 0%)
Treatment-related complications among anterior circulation	13/81 = 14%	8	(7–22) (I ² = 0%)
Treatment-related complications among posterior circulation	28/132 = 20%	8	(3–13) (I ² = 0%)
Treatment-related complications (PED)	19/110 = 15%	9	(9–21) (I ² = 0%)
Treatment-related complications (other devices)	3/23 = 12%	3	(6–24) (I ² = 0%)
Periprocedural/early complications (within 30 days)	10/213 = 2.5%	15	(1–4) (I ² = 0%)
Delayed complications (after 30 days)	31/213 = 12%	15	(7–17) (I ² = 35%)
Premature discontinuation of AT and related ischemic events	5/93 = 5%	8	(2–9) (I ² = 0%)
Treatment-related mortality	1/213 = 2%	15	(0.2–3.5) (I ² = 0%)
Overall rate of good neurologic outcome	154/187 = 87%	10	(79–95) (I ² = 60%)
Occlusion of covered branches	5/72 = 7%	10	(2–13) (I ² = 0%)
Symptoms related to occlusion or impaired flow of covered branches	3/72 = 3%	10	(0.5–9) (I ² = 0%)

Note:—AT indicates antiplatelet therapy.

related complications (complications versus no complications). Individual patient data were selected from patients with nonsaccular aneurysms. The χ^2 test was used to evaluate qualitative factors associated with occlusion and complications (aneurysm location and size, type of stent, patient age, type of aneurysm). The independent variables significantly associated ($P \leq .1$ in the univariate analysis) with aneurysm complete occlusion or complications were analyzed together in a binary logistic regression (multivariate analysis) to assess the independent contribution of each factor. The results of the regression model were calculated by the Wald test and expressed using P values and the related odds ratios. All statistical analyses were performed with SPSS, Version 24 (IBM, Armonk, New York).

RESULTS

Literature Review

Studies included in our meta-analysis are summarized in On-line Table 2. The search flow diagram is shown in On-line Fig 1.

A total of 15 studies and 213 unruptured nonsaccular intracranial aneurysms treated with FD were included. We extracted 81 AC and 132 PC nonsaccular aneurysms treated with FD techniques.

Quality of Studies

Overall, 14 studies were retrospective series,^{4,10–22} whereas 1 study was a prospective multicenter trial.²³ On the basis of the Newcastle-Ottawa Quality Assessment Scale, 10 studies^{4,10,12–17,21,23} were rated as “high-quality” (On-line Table 3).

Patient Population and Aneurysm Characteristics

The mean age of patients was 52.5 years (range, 18–82 years), and the proportion of male patients was 42% (95% CI, 35%–49%) (On-line Table 4). The mean aneurysm size was 11 mm (median, 10 mm; range, 5–22 mm). The proportion of fusiform and dissecting aneurysms was 76% (162/213; 95% CI, 69%–81%) and 24% (51/213; 95% CI, 18%–30%), respectively. Aneurysms of the AC and PC were 38% (81/213; 95% CI, 31%–44%) and 62% (132/213; 95% CI, 55%–68%), respectively. Most aneurysms were located at the vertebrobasilar (97/213 = 45.5%; 95% CI, 38%–52%) and MCA segments (69/213 = 32.5%; 95% CI, 26%–38%). The most common device was the Pipeline Embolization Device (PED; Covidien, Irvine, California) (185/213 = 87%; 95% CI, 81%–90%).

The mean radiologic (DSA) follow-up was 13 months (range, 4–24 months; median, 12 months; interquartile range [IQR], 7–12 months), and the mean clinical follow-up was 14 months (range, 6–28 months; median, 12 months; IQR, 8–15 months).

Angiographic Outcomes

The technical success rate was 96% (178/181; 95% CI, 93%–98%; $I^2 = 0\%$) (Table 1). The rates of long-term adequate and complete occlusion were 85.3% (137/168; 95% CI, 78.2%–92.4%; $I^2 = 42.3\%$) and 78.8% (128/168; 95% CI, 72.8%–84.8%; $I^2 = 0\%$). Meta-regression showed a nonsignificant variation of the effect size ($P = .71$) during the analyzed period, and the funnel plot (Egger linear regression test) reasonably excluded publication bias ($P = .52$). The sensitivity analysis showed that no individual

Table 2: Univariate and multivariate analysis of predicting factors for aneurysm occlusion and treatment-related complications

	Univariate, <i>P</i> Value	Univariate, OR	Multivariate		
			Odds Ratio	95% CI	<i>P</i> Value
Independent variables for occlusion					
Type of FD (PED vs other)	0.22	1.2			
Patient age (younger than 60 vs older than 60 yr)	0.21	2.6			
Aneurysm size (large vs small) ^a	0.13	1.7	1.5	0.2–6.4	.81
Type of aneurysm (dissecting vs fusiform)	0.06	2.5	1.7	0.4–2.4	.35
Aneurysm location (AC vs PC)	0.11	3.1	0.5	0.2–0.7	.38
Independent variables for complications					
Type of FD (PED vs other)	0.94	1.1			
Patient age (younger than 60 vs older than 60 yr)	0.46	1.5			
Aneurysm size (large vs small) ^a	0.03	4.5	6.6	1.3–15	.02
Type of aneurysm (fusiform vs dissecting)	0.27	0.8			
Aneurysm location (AC vs PC)	0.04	0.7	0.3	0.6–1.8	.09

Note:—OR indicates odds ratio.

^aSmall aneurysms, ≤ 10 mm; large aneurysms, ≥ 10 mm.

study significantly influenced the combined aneurysm occlusion rate (On-line Fig 2).

The long-term adequate occlusion rate (O’Kelly-Marotta C–D) among fusiform lesions was 83% (116/146; 95% CI, 74%–92%; $I^2 = 48\%$), whereas among dissecting aneurysms, it was 89% (33/36; 95% CI, 80%–98%; $I^2 = 0\%$) ($P = .31$). Complete/near-complete occlusion among the AC and PC was 87.5% (51/61; 95% CI, 79%–95%; $I^2 = 0\%$) and 83% (86/107; 95% CI, 71%–95%; $I^2 = 60\%$) ($P = .45$), respectively. Long-term adequate occlusion was 82% (118/149; 95% CI, 75%–90%; $I^2 = 25\%$) and 90% (21/23; 95% CI, 81%–98%; $I^2 = 0\%$) ($P = .31$) after treatment with the PED and other stents, respectively.

Treatment-Related Complications

The overall complication rate was 17.4% (41/213; 95% CI, 12.45%–22.4%; $I^2 = 0\%$) (Table 1). Meta-regression showed a nonsignificant variation of the effect size ($P = .62$) over the analyzed period, and the funnel plot (the Egger linear regression test) reasonably excludes publication bias ($P = .24$). In addition, no individual study significantly influenced the treatment-related complication rate (On-line Fig 3).

Periprocedural/early complications were 2.5% (10/213; 95% CI, 1%–4%; $I^2 = 0\%$). Delayed complications were 12% (31/213; 95% CI, 7%–17%; $I^2 = 35\%$). Transient and permanent complications were 9% (21/213; 95% CI, 5.6%–13%; $I^2 = 0\%$) and 8% (20/213; 95% CI, 5%–12%; $I^2 = 0\%$), respectively (description of the adverse events is reported in On-line Table 2).

Overall, ischemic/thromboembolic and hemorrhagic events were 15% (37/213; 95% CI, 10%–20%; $I^2 = 0\%$) and 3% (4/213; 95% CI, 1.2%–6%; $I^2 = 0\%$), respectively. Treatment-related complications among fusiform and dissecting aneurysms were 17% (35/162; 95% CI, 10%–25%; $I^2 = 24\%$) and 19% (11/51; 95% CI, 10%–31%; $I^2 = 0\%$) ($P = .71$), respectively. PC lesions were associated with slightly higher rates of complications compared with AC lesions (28/132 = 20%; 95% CI, 3%–13%; $I^2 = 0\%$ versus 13/81 = 14%; 95% CI, 7%–22%; $I^2 = 0\%$) ($P = .22$). Treatment with the PED and other stents was associated with 15% (19/110; 95% CI, 9%–21%; $I^2 = 0\%$) and 12% (3/23; 95% CI, 6%–24%; $I^2 = 0\%$) rates of complications ($P = .76$), respectively.

The rate of ischemic events after discontinuation of the antiplatelet therapy was 5% (5/93; 95% CI, 2%–9%; $I^2 = 0\%$). There

were no cases of early or delayed rupture after treatment among the analyzed series.

Treatment-related mortality was 2% (1/213; 95% CI, 0.2%–3.5%; $I^2 = 0\%$), and the rate of good neurologic outcome was 87% (154/187; 95% CI, 79%–95%; $I^2 = 60\%$). Finally, the rate of occlusion of branches covered by flow diverters was 7% (5/72; 95% CI, 2%–13%; $I^2 = 0\%$), with 3% (3/72; 95% CI, 0.5%–9%; $I^2 = 0\%$) of symptoms related to the impaired flow on the covered vessel.

Subgroup Analysis: Factors Related to Aneurysm Occlusion and Complications

Occlusion and complication rates were compared between the following preplanned subgroups: FD alone versus FD + coils, single flow diverter versus multiple flow diverters, mean patient age, and small-versus-large aneurysms. The occlusion rate was comparable among all the studied subgroups. The complication rate was higher among large aneurysms (≥ 10 mm) compared with small (< 10 mm) lesions ($P = .04$) (On-line Table 5).

Overall, individual patient data were available for 80% of patients (Table 2). The following factors were tested in the univariate and multivariate analyses: type of FD (PED versus other), patient age (younger than 60 versus older than 60 years), aneurysm size (> 10 versus < 10 mm), fusiform versus dissecting, and aneurysm location (AC versus PC). In the multivariate analysis, none of the above-reported factors were independently associated with the occlusion rate, whereas the aneurysm size (> 10 versus < 10 mm) was independently associated with the complication rate (OR = 6.6; 95% CI, 1.3%–15%; $P = .02$).

Study Heterogeneity

Heterogeneity was low ($< 50\%$) for all the reported outcomes except for the following: the overall rate of good neurologic outcome and the mean difference of age among completely and incompletely occluded aneurysms.

DISCUSSION

After we pooled data from 15 studies and 213 aneurysms, our meta-analysis is the largest study investigating outcomes after FD for unruptured nonsaccular lesions. Particularly, this study aimed to improve the knowledge of angiographic and clinical outcomes

after FD for fusiform/dissecting lesions located both in the PC and in distal segments of the AC.

Angiographic Outcome

A very recent meta-analysis of 500 distal unruptured AC aneurysms demonstrated the efficacy of FD, reporting a rate of adequate occlusion close to 83%.²⁴ However, saccular and non-saccular aneurysms were pooled together, and fusiform/dissecting lesions were underrepresented in this review.²⁴ Kiyofuji et al²⁵ performed a meta-analysis of 131 nonsaccular PC aneurysms, reporting a 50% rate of complete/near-complete occlusion. This rate appears quite low compared with the general occlusion rate of 80% reported in others series and a meta-analysis of FD.²⁶ The lower occlusion rate in the review of Kiyofuji et al may reflect the inclusion of giant dolichoectatic aneurysms (involving all the vertebrobasilar system). These aneurysms remain one of the most formidable lesions to treat: Natural history is reported to be poor (mortality rates at 5 years are close to 30%), complication rates are quite high, and the indication for treatment is still debatable.⁶

Our meta-analysis, excluding dolichoectatic holobasilar lesions and aneurysms arising from the ICA segment, showed 85% of complete/near-complete occlusion (O'Kelly-Marotta C-D), with comparable rates in the anterior and posterior circulations. Although most of the included series classified nonsaccular aneurysms into fusiform and dissecting lesions, the diagnosis may not be correct in all cases because fusiform shape may represent a variety of different histopathologic pictures. Mizutani et al² classified 85 aneurysms unrelated to the branching zones into 4 types: Type 1 aneurysms were defined as "classic dissecting" lesions; type 2 indicated a fusiform segmental ectasia; and types 3 and 4 represented dolichoectatic and "blisterlike" aneurysms. In our review, unruptured dissecting aneurysms presented a slightly higher (89%) rate of occlusion compared with fusiform lesions (83%), though the meta-analysis was likely underpowered to highlight a statically significant difference. Griessenauer et al,⁴ in a series of 131 PC aneurysms, reported 83% and 64% complete occlusion after treatment with the PED of 29 dissecting and 53 fusiform lesions, respectively. Similarly, Lin et al¹⁰ described a series of 15 fusiform and 5 dissecting aneurysms of the MCA and anterior cerebral artery segments, reporting 73% and 100% complete occlusion after treatment with the PED, respectively.

In the univariate analysis, there was a trend toward higher occlusion rates in favor of dissecting aneurysms, though the multivariate logistic regression did not show any significant association among the occlusion rate and the analyzed factors.

Treatment-Related Complications

The overall rate of complications of 17% found in our meta-analysis appears quite high compared with series of flow diversion for saccular aneurysms. Brinjikji et al,¹⁶ in a post hoc analysis of the International Retrospective Study of the Pipeline Embolization Device (IntrePED), reported fusiform aneurysm configuration as the only variable independently associated with stroke (OR = 2.7, $P = .03$). In our study, complications were similar among fusiform and dissecting types and were mostly related to ischemic events (15%).

The anterior circulation was associated with an approximately 14% rate of adverse events. A recent meta-analysis and series of unruptured saccular anterior communicating artery and pericallosal aneurysms treated with flow diverters reported approximately 8% treatment-related complications.^{24,27,28} However, in our review, 90% of the nonsaccular AC aneurysms were located at the MCA. It has been reported that MCA location is associated with an approximately 18% rate of complications after FD.^{24,29} Accordingly, the relatively high rate of adverse events among AC fusiform/dissecting lesions found in our study can be partially influenced by the predominance of the MCA location.

Focusing on the PC, we report a 20% rate of complications after FD of nonsaccular aneurysms. This is in line with descriptions in the literature. Griessenauer et al⁴ reported roughly 25% and 23% adverse events among saccular and nonsaccular PC aneurysms treated with FD. In the IntrePED study, Kallmes et al³⁰ found higher rates of morbidity and mortality after FD in PC (16.5%) compared with AC lesions (5%–9%). In addition, Lopes et al,³¹ evaluating the morbidity among the subgroup of PC lesions of the IntrePED registry, showed a 19% neurologic morbidity among the fusiform group. In our study, the univariate analysis underlined PC and large aneurysms as factors associated with higher complications, though the size was the only variable independently associated with adverse events at the binary logistic regression (OR = 6.6, $P = .02$). Our meta-analysis is the first focusing on the factors associated with complications among a selected population of nonsaccular aneurysms. In the series of Griessenauer et al,⁴ small PC nonfusiform aneurysms presented with 17% complications, whereas large/giant lesions were associated with approximately 25% adverse events.

Finally, the 5% rate of ischemic complications after discontinuation of the antiplatelet therapy (1 in-stent occlusion, 2 cases of basilar perforators infarcts, and 2 thromboembolic events) indicates the importance of the antiplatelet regimen among nonsaccular lesions treated by flow diversion.

Limitations

Our study has limitations. Most of the series are small, retrospective studies. The included series classified aneurysms into fusiform and dissecting types; however, few studies reported a clear angiographic definition of fusiform and dissecting lesions. The antiplatelet regimen was quite comparable among the studies (On-line Table 2), but the influence of platelet inhibition was not evaluated. However, this review is the largest meta-analysis focusing on FD for nonsaccular aneurysms, providing updated data for the treatment management of these lesions.

CONCLUSIONS

Unruptured nonsaccular aneurysms located in the posterior and distal anterior circulations can be effectively treated with a flow-diversion strategy. Nevertheless, treatment-related complications are not negligible, with about 15% ischemic events and 8% morbidity. Larger size (>10 mm) significantly increases the risk of procedure-related adverse events among nonsaccular lesions.

Disclosures: Paolo Perrini—UNRELATED: Employment: Azienda Ospedaliero Universitaria Pisana. Alain Bonafe—UNRELATED: Consultancy: Stryker, Medtronic,

MicroVention. Vincent Costalat—UNRELATED: Consultancy: Medtronic, Cerenovus, MicroVention; Grants/Grants Pending: Medtronic, MicroVention, Stryker; Payment for Lectures Including Service on Speakers Bureaus: Stryker, MicroVention, Medtronic; Payment for Development of Educational Presentations: Medtronic, Stryker.* Pierre-Henri Lefevre—UNRELATED: Payment for development of educational presentations: Medtronic. *Money paid to the institution.

REFERENCES

- Awad AJ, Mascitelli JR, Haroun RR, et al. **Endovascular management of fusiform aneurysms in the posterior circulation: the era of flow diversion.** *Neurosurg Focus* 2017;42:E14 CrossRef Medline
- Mizutani T, Miki Y, Kojima H, et al. **Proposed classification of nonatherosclerotic cerebral fusiform and dissecting aneurysms.** *Neurosurgery* 1999;45:253–59; discussion 259–60 CrossRef Medline
- Moher D, Liberati A, Tetzlaff J, et al. **Preferred reporting items for systematic reviews and meta-analyses: the PRISMA statement.** *Int J Surg* 2010;8:336–41 CrossRef Medline
- Griessenauer CJ, Ogilvy CS, Adeeb N, et al. **Pipeline embolization of posterior circulation aneurysms: a multicenter study of 131 aneurysms.** *J Neurosurg* 2018;130:923–35 CrossRef Medline
- Becske T, Kallmes DF, Saatci I, et al. **Pipeline for uncoilable or failed aneurysms: results from a multicenter clinical trial.** *Radiology* 2013;267:858–68 CrossRef Medline
- Siddiqui AH, Abula AA, Kan P, et al. **Panacea or problem: flow diverters in the treatment of symptomatic large or giant fusiform vertebrobasilar aneurysms.** *J Neurosurg* 2012;116:1258–66 CrossRef Medline
- O'Kelly CJ, Krings T, Fiorella D, et al. **A novel grading scale for the angiographic assessment of intracranial aneurysms treated using flow diverting stents.** *Interv Neuroradiol* 2010;16:133–37 CrossRef Medline
- Roy D, Milot G, Raymond J. **Endovascular treatment of unruptured aneurysms.** *Stroke* 2001;32:1998–2004 CrossRef Medline
- Wells GS, O'Connell D. *The Newcastle-Ottawa Scale (NOS) for Assessing the Quality of Nonrandomized Studies in Meta-Analyses.* Ottawa: Ottawa Hospital Research Institute; 2011
- Lin N, Lanzino G, Lopes DK, et al. **Treatment of distal anterior circulation aneurysms with the Pipeline Embolization Device: a US multicenter experience.** *Neurosurgery* 2016;79:14–22 CrossRef Medline
- Lubicz B, Collignon L, Raphaeli G, et al. **Pipeline flow-diverter stent for endovascular treatment of intracranial aneurysms: preliminary experience in 20 patients with 27 aneurysms.** *World Neurosurg* 2011;76:114–19 CrossRef Medline
- Pistocchi S, Blanc R, Bartolini B, et al. **Flow diverters at and beyond the level of the circle of Willis for the treatment of intracranial aneurysms.** *Stroke* 2012;43:1032–38 CrossRef Medline
- Topcuoglu OM, Akgul E, Daglioglu E, et al. **Flow diversion in middle cerebral artery aneurysms: is it really an all-purpose treatment?** *World Neurosurg* 2016;87:317–27 CrossRef Medline
- Zanaty M, Chalouhi N, Tjoumakaris SI, et al. **Flow diversion for complex middle cerebral artery aneurysms.** *Neuroradiology* 2014;56:381–87 CrossRef Medline
- Bhagal P, Chudyk J, Bleise C, et al. **The use of flow diversion in vessels ≤ 2.5 mm in diameter: a single-center experience.** *World Neurosurg* 2018;118:e575–83 CrossRef Medline
- Brinjikji W, Lanzino G, Cloft HJ, et al. **Risk factors for ischemic complications following Pipeline Embolization Device treatment of intracranial aneurysms: results from the IntrePED study.** *AJNR Am J Neuroradiol* 2016;37:1673–78 CrossRef Medline
- Bender MT, Colby GP, Jiang B, et al. **Flow diversion of posterior circulation cerebral aneurysms: a single-institution series of 59 cases.** *Neurosurgery* 2019;84:206–16 CrossRef Medline
- Bhagal P, Perez MA, Ganslandt O, et al. **Treatment of posterior circulation non-saccular aneurysms with flow diverters: a single-center experience and review of 56 patients.** *J Neurointerv Surg* 2017;9:471–81 CrossRef Medline
- Munich SA, Tan LA, Keigher KM, et al. **The Pipeline Embolization Device for the treatment of posterior circulation fusiform aneurysms: lessons learned at a single institution.** *J Neurosurg* 2014;121:1077–84 CrossRef Medline
- Natarajan SK, Lin N, Sonig A, et al. **The safety of Pipeline flow diversion in fusiform vertebrobasilar aneurysms: a consecutive case series with longer-term follow-up from a single US center.** *J Neurosurg* 2016;125:111–19 CrossRef Medline
- Wallace AN, Grossberg JA, Almandoz JED, et al. **Endovascular treatment of posterior cerebral artery aneurysms with flow diversion: case series and systematic review.** *Neurosurgery* 2018;83:790–99 CrossRef Medline
- Wallace AN, Kamran M, Madaelil TP, et al. **Endovascular treatment of posterior inferior cerebellar artery aneurysms with flow diversion.** *World Neurosurg* 2018;114:e581–87 CrossRef Medline
- Mohlenbruch MA, Kizilkilic O, Killer-Oberpfalzer M, et al. **Multicenter experience with FRED Jr Flow Re-Direction Endoluminal Device for intracranial aneurysms in small arteries.** *AJNR Am J Neuroradiol* 2017;38:1959–65 CrossRef Medline
- Cagnazzo F, Perrini P, Dargazanli C, et al. **Treatment of unruptured distal anterior circulation aneurysms with flow-diverter stents: a meta-analysis.** *AJNR Am J Neuroradiol* 2019;40:687–93 CrossRef Medline
- Kiyofuji S, Graffeo CS, Perry A, et al. **Meta-analysis of treatment outcomes of posterior circulation non-saccular aneurysms by flow diverters.** *J Neurointerv Surg* 2018;10:493–49 CrossRef Medline
- Brinjikji W, Murad MH, Lanzino G, et al. **Endovascular treatment of intracranial aneurysms with flow diverters: a meta-analysis.** *Stroke* 2013;44:442–47 CrossRef Medline
- Cagnazzo F, Limbucci N, Nappini S, et al. **Flow-diversion treatment of unruptured saccular anterior communicating artery aneurysms: a systematic review and meta-analysis.** *AJNR Am J Neuroradiol* 2019;40:497–502 CrossRef Medline
- De Macedo Rodrigues K, Kuhn AL, Tamura T, et al. **Pipeline Embolization Device for pericallosal artery aneurysms: a retrospective single center safety and efficacy study.** *Oper Neurosurg (Hagerstown)* 2018;14:351–58 CrossRef Medline
- Cagnazzo F, Mantilla D, Lefevre PH, et al. **Treatment of middle cerebral artery aneurysms with flow-diverter stents: a systematic review and meta-analysis.** *AJNR Am J Neuroradiol* 2017;38:2289–94 CrossRef Medline
- Kallmes DF, Hanel R, Lopes D, et al. **International retrospective study of the Pipeline Embolization Device: a multicenter aneurysm treatment study.** *AJNR Am J Neuroradiol* 2015;36:108–15 CrossRef Medline
- Lopes DK, Jang DK, Cekirge S, et al. **Morbidity and mortality in patients with posterior circulation aneurysms treated with the Pipeline Embolization Device: a subgroup analysis of the international retrospective study of the Pipeline Embolization Device.** *Neurosurgery* 2018;83:488–500 CrossRef Medline

Reduced Activity of von Willebrand Factor after Flow-Diverting Stent Implantation for Intracranial Aneurysms: A Link to Acquired von Willebrand Disease?

I. Oran, C. Cinar, H. Bozkaya, M. Parildar, and S. Duman

ABSTRACT

BACKGROUND AND PURPOSE: Vascular devices generating high shear stress can cause type 2A acquired von Willebrand disease, which is characterized by low von Willebrand factor activity accompanied by hemorrhagic complications. The braided mesh structure of flow-diverting stents with a relatively small strut size can create abnormally high shear stress while arterial blood flows through the stent struts into the aneurysm, and flow-diverting stent may be associated with reduced von Willebrand factor activity.

MATERIALS AND METHODS: Aneurysmal morphologic parameters and patient data were examined retrospectively among patients who had an unruptured intracranial aneurysm treated with a flow-diverting stent. The RISTOtest (test for whole blood ristocetin-induced platelet aggregation) for von Willebrand factor activity, as well as tests for aspirin and clopidogrel/prasugrel effectiveness, were performed immediately before the endovascular procedure and 24 hours later by multiple electrode aggregometry.

RESULTS: A total of 39 patients with 56 aneurysms were recruited, and statistical analyses were performed in 32 patients with 49 aneurysms. Compared with the baseline values, von Willebrand factor activity was reduced in 16 patients but increased in 23 patients. Aneurysmal variables (eg, neck area, volume, volume-to-neck area ratio, size ratio, and morphologic index) clearly distinguished patients with reduced von Willebrand factor activity from those with nonreduced von Willebrand factor activity. The receiver operating characteristic curve showed that the morphologic index and volume had the highest discriminative power, with an area under the curve of 0.99.

CONCLUSIONS: In high-volume/large-neck aneurysms, flow-diverting stent implantation can cause reduced von Willebrand factor activity, which may be linked causally to acquired von Willebrand disease.

ABBREVIATIONS: ADP = test for clopidogrel/prasugrel responsiveness; AvWD = acquired von Willebrand disease; FDS = flow-diverting stent; LVAD = left ventricular assist device; vWD = von Willebrand disease; vWF = von Willebrand factor; RISTO = test for whole blood ristocetin-induced platelet aggregation

Reduced von Willebrand Factor (vWF) activity, secondary to quantitative and qualitative abnormalities, results in defective hemostasis known as von Willebrand disease (vWD), the most frequent hereditary hemorrhagic disease worldwide. Various cardiovascular diseases, such as aortic stenosis and several congenital heart diseases, have long been known to cause acquired von Willebrand disease (AvWD).¹ In recent decades, a considerable number of patients have also been described with AvWD, associated with vascular devices that create pathologically high shear stress in the blood. Such devices include the left ventricular assist

device (LVAD) and extracorporeal membrane oxygenation.^{2,3} vWF is synthesized normally and at normal levels in such patients, and the reduced vWF activity results from accelerated enzymatic cleavage of the factor due to device-related high shear stress.

The flow-diverting stent (FDS) is a novel endovascular device for the treatment of previously difficult-to-treat cerebral aneurysms. A unique feature of the FDS is its braided mesh structure with a relatively high pore density and small strut size. Computational fluid dynamics simulation recently showed that FDSs⁴ and even peripheral stents⁵ can create abnormally high supraphysiologic shear stress while blood flow passes through stent struts into the aneurysm.

We aimed to characterize reduced vWF activity after FDS implantation for endovascular treatment of intracranial aneurysms. We focused on the spatial characteristics of the aneurysm to identify ≥ 1 simple variable that may predict the presence of reduced vWF activity. We also assessed the current literature about the vascular device-related AvWD in the

Received August 9, 2019; accepted after revision October 20.

From the Departments of Radiology (I.O., C.C., H.B., M.P.) and Internal Medicine (S.D.), Ege University Medical School, Izmir, Turkey. Dr Oran is currently affiliated with Section of Interventional Radiology, KENT Hospital, Izmir, Turkey.

Please address correspondence to Ismail Oran, MD, EBIR, Section of Interventional Radiology, KENT Hospital, 35630, Cigli, Izmir, Turkey; e-mail: ismailoran@gmail.com; @profismailoran

<http://dx.doi.org/10.3174/ajnr.A6343>

context of our results to propose a hypothesis that links reduced vWF activity to delayed intracranial bleeding after FDS implantation, a life-threatening complication that occurs in approximately 6% of these patients.⁶

MATERIALS AND METHODS

Patients

This study was performed in accordance with the ethical standards established in the 1964 Declaration of Helsinki and its later amendments, and the study protocol was approved by our institutional review board. All patients provided written informed consent to undergo planned endovascular procedures. Data were collected retrospectively from patients who had intracranial aneurysms treated endovascularly with an FDS (Pipeline Embolization Device; Covidien, Irvine, California) (alone or in conjunction with coiling) from July 2017 to October 2018. Patients received FDS treatment if they had giant, wide-neck, fusiform, dissecting, and/or recurrent/remnant (after intrasaccular coiling) unruptured aneurysms or any unruptured aneurysms deemed unsuitable for standard (simple coiling, balloon-assisted coiling, or stent-assisted coiling) endovascular procedures. Patients with multiple aneurysms were included only if all aneurysms had received FDS treatment. Only patients treated by dual-antiaggregant loading with a single dose (at midnight the night before a morning endovascular procedure) were selected; all other loading strategies were excluded. Finally, patients who had an existing mass effect and were given intravenous and/or oral corticosteroids during/immediately after FDS implantation were also excluded from the study, due to possible distortion of the aggregometry results.

Aneurysm Characteristics

All geometric characteristics were examined on reconstructed 3D rotational angiographic images (Allura Clarity; Philips Healthcare, Best, the Netherlands) by 2 interventional neuroradiologists. The measured morphologic parameters of the aneurysms included neck width (along the long axis of the parent artery), height (perpendicular to the neck), and 2 orthogonal maximum widths, represented as N, H, W1, and W2, respectively. The diameter of the parent artery (D) was also measured at the level of the neck region. All measurements were expressed in millimeters. In patients with bifurcation aneurysms, the arithmetic mean diameters of the main trunk and 1 stented branch were calculated. In patients with fusiform aneurysms, the neck width was measured as the aneurysm length along the parent artery. Using these parameters, we calculated specific variables previously defined in the literature,⁷ including the aspect ratio (calculated as H/N), size ratio (H/D), neck area, volume of the aneurysm, and volume-to-neck area ratio. To generate rapid and user-friendly calculations, we assumed that the neck area was circular and calculated it simply as N^2 ; volume was calculated as $H \times W1 \times W2$ (for saccular aneurysms). We defined 1 novel variable (morphologic index), multiplication of the neck area and volume, represented as $N^2 \times H \times W1 \times W2$. In patients with multiple aneurysms, individual variables were calculated for each aneurysm and were then added to obtain a single value for each patient.

Medications

All endovascular procedures were performed with the patients under general anesthesia and systemic heparinization, which was typically initiated before placement of the guiding catheter to maintain the activated clotting time at 2- to 3-fold above baseline (initial heparin bolus, 5000–10,000 IU). All patients received a loading dose of 600 mg of clopidogrel or 30–60 mg of prasugrel, as well as 300 mg of aspirin, 9–12 hours before the procedure. As a maintenance dose, 75 mg/day of clopidogrel or 10 mg/day of prasugrel, combined with 100–300 mg of aspirin, was prescribed to all patients at the time of discharge. Some patients with a relatively low body mass index could not tolerate the prasugrel-aspirin dual-maintenance therapy; aspirin was discontinued in such circumstances. In patients undergoing stent implantation in the carotid artery proximal to the Willis polygon or vertebral artery, clopidogrel/prasugrel maintenance therapy was typically given for up to 3 months. In patients who underwent stent implantation in or distal to the Willis polygon or basilar artery, antiaggregant maintenance was extended by up to 6 months. After cessation of clopidogrel or prasugrel, aspirin was prescribed for at least another 6 months.

Impedance Aggregometry

Patients were assessed for platelet responsiveness by a rapid platelet function test (Multiplate Analyzer; Roche, Basel, Switzerland) performed in the angiography suite, just before the endovascular procedure. During the past 2 years, we have routinely repeated the test at 24 hours after treatment for patients treated with FDSs. We also expanded our routine test examination to include the ristocetin-induced platelet aggregation (RISTOHigh; Roche) (test for vWF activity) tests, besides the test for clopidogrel/prasugrel responsiveness (ADP), the test for aspirin responsiveness, and the test for general performance of platelets and their glycoprotein IIb/IIIa receptor. All 4 tests were performed through a single blood draw and lasted about 10 minutes. As described previously, we followed a tailored medication strategy and noted a positive clinical impact under the guidance of the rapid platelet-function test.⁸

Patients were scheduled for follow-up visits at 1, 3, and 6 months after discharge from our institution. Routine CTA was performed at 3 months, and CTA or digital subtraction angiography was performed at 6 or 12 months after discharge.

Statistical Analyses

Data were analyzed using SPSS (Version 25; IBM, Armonk, New York). Differences with $P < .05$ were considered statistically significant. Categorical data were expressed as No. (%) and were compared using the Fisher exact test. Continuous data were expressed as the mean \pm SD and were compared using the Mann-Whitney *U* test. The Wilcoxon signed rank test was used to compare dependent data. Receiver operating characteristic curve analysis was performed to determine the optimal sensitivity and specificity, as well as the cutoff points to establish the predictive ability of each variable.

RESULTS

A total of 39 patients with 56 aneurysms were recruited (patient age, 18–67 years). Of the 56 aneurysms, 42 were sidewall and 14

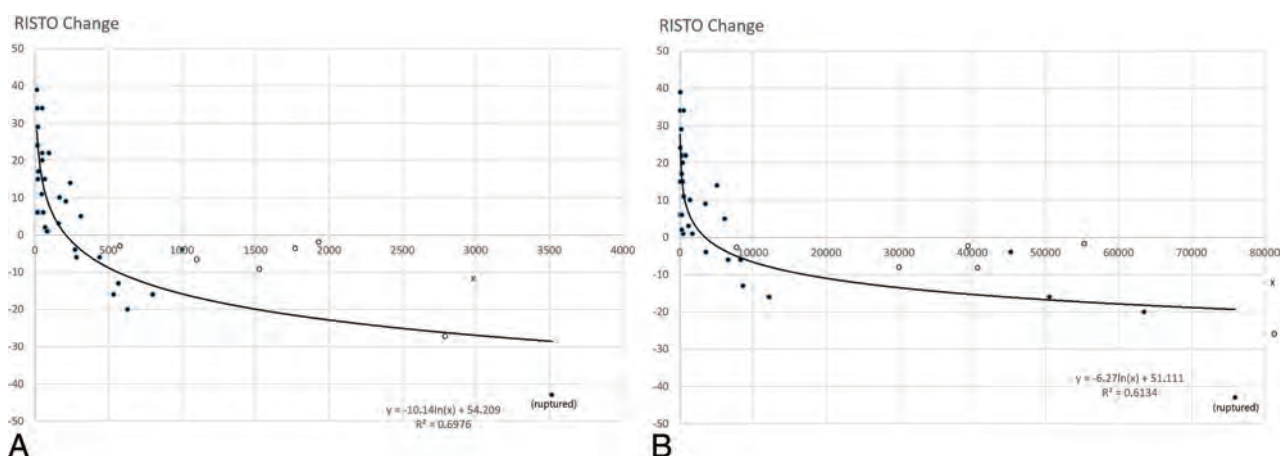


FIG 1. Scatterplots extracted from 32 patients treated by FDS only (closed circles) show a comparison of RISTO (ie, whole blood ristocetin-induced platelet aggregation) change with the volume (A) and morphologic index (B) of the aneurysm depicted on the x-axis. Open circles denote 6 patients treated by coiling + FDS, and x denotes 1 fusiform aneurysm; all have actually reduced vWF activity. The patient with delayed aneurysmal bleeding after FDS implantation is designated by (ruptured).

Table 1: Treatment variables in the reduced and nonreduced vWF groups

Characteristic	Reduced vWF (%)	Nonreduced vWF (%)	All (%)	P Value
Patient No.	9	23	32	
Mean age (yr)	59.4 ± 5.6	46.8 ± 11	50.3 ± 11.3	.003
Sex (female)	7 (77.7)	17 (73.9)	24 (75)	.869
Mean aneurysm No.	1.56 ± 0.7	1.61 ± 0.5	1.59 ± 0.6	.742
Aneurysm frequency				
1 aneurysm/patient	5 (55.6)	13 (56.5)	18 (56.3)	.559
2 aneurysms/patient	3 (33.3)	9 (39.1)	12 (37.5)	.564
3 aneurysms/patient	1 (11.1)	1 (4.4)	2 (6.2)	.826
FDS frequency				
1 stent/patient	5 (55.6)	17 (73.9)	22 (68.7)	.566
2 stents/patient	3 (33.3)	5 (21.7)	8 (25)	.581
3 stents/patient	1 (11.1)	1 (4.4)	2 (6.3)	.294

were bifurcation aneurysms; 1 aneurysm was fusiform and the remaining 55 were saccular aneurysms. Five and 37 were located on the cavernous and intradural segments of the internal carotid artery, respectively; 10, on the middle cerebral artery; 1, on the anterior cerebral artery; 2, on the vertebral artery; and 1, on the basilar artery. All patients were treated with FDSs; 6 patients (1 aneurysm each) also received suboptimal coiling before FDS implantation during the same procedure. This preceding coiling was performed for the treatment of aneurysms with relatively large sizes that exceeded 1.5–2 cm in 1 dimension.

The RISTOtest results indicated reduced vWF activity 24 hours after treatment, compared with baseline values, in 16 (41%) patients. The preceding preventive intrasaccular coiling may further change flow variables within the aneurysmal lumen and distort the RISTOtest results; thus, the 6 patients treated by coiling plus an FDS were not included in the statistical analyses. Indeed, all those 6 patients had reduced vWF activity (Fig1). One patient with fusiform aneurysms and reduced vWF activity was also excluded from the analysis. After we excluded these 7 patients, 9 of the remaining patients with 14 saccular aneurysms treated by an FDS alone were

included in the reduced-vWF group. The remaining 23 patients did not show a reduction in vWF activity and thus composed the nonreduced vWF group. The demographic data and treatment variables in the reduced and nonreduced vWF groups are summarized in Table 1. All test results and aneurysmal morphologic variables of the reduced and nonreduced vWF groups are summarized in Tables 2–4. After we compared all aneurysmal variables with the RISTOtest results, the so-called morphologic index and volume of the aneurysm provided superior

discrimination between the reduced and nonreduced vWF groups (Table 5 and Figs 1 and 2).

All patients were followed up both radiologically and clinically for at least 3 months. We encountered 2 clinical complications. First, 1 patient from the reduced vWF group with 2 aneurysms at the basilar artery fenestration and right MCA bifurcation experienced dysphasia 10 days after treatment. MR imaging showed right-sided insular cortex ischemia. At 3 months, the dysphasia had resolved completely, and both aneurysms were occluded according to CTA. Second, 1 patient from the reduced vWF group with 3 aneurysms at the anterior communicating artery and right and left MCA bifurcation experienced rupture of a large (18-mm maximum diameter) anterior communicating artery aneurysm into the ventricular system 4 weeks after treatment, which subsequently resulted in death. For anatomic reasons, preventive coiling before FDS implantation was not used for this relatively large aneurysm. No other clinical complications were observed during the 3-month follow-up period.

DISCUSSION

This study is the first to show laboratory evidence of reduced vWF activity in approximately 41% of our study population after

FDS implantation for the treatment of intracranial aneurysms. Reduced vWF activity was best predicted by the morphologic index and volume of the aneurysm, with cutoff values of 4343 and 256, respectively. This finding suggests that a FDS may reduce vWF activity after its implantation in a saccular aneurysm larger than 8–10 mm in 1 dimension, according to the results of Multiplate Analyzer. Our findings clearly link the FDS

implantation to AvWD and thus may provide a way to better explain the mechanism of delayed hemorrhagic complications because both the laboratory-verified reduced vWF activity and various hemorrhagic complications during the clinical course are 2 leading characteristics of shear-generating vascular device-related type 2A AvWD.¹⁻³

vWF mediates platelet tethering to the subendothelial matrix at sites of vascular injury to initiate hemostasis under the condition of arterial flow. Its secretion from endothelial cells is constitutive and accelerated in response to inflammation and ischemia (ie, activated endothelium). A mature vWF monomer has several domains and forms high-molecular-weight multimers (up to 100 monomers) just before entering the circulation; the A1 domain contains binding sites for the platelet glycoprotein Ib-IX receptor complex, whereas the A3 domain binds to subendothelial collagen. The A2 domain has a specific site that is cleaved by disintegrin and metalloprotease with thrombospondin type 1 repeat 13 (ADAMTS-13) normally found in the circulation. The vWF multimer circulates normally in the globular inactive form and is hemostatically active only after exposure to supraphysiologic high shear stress, which causes force-induced conformational changes (ie, elongation), which lead to brief activation of the binding domains of A1 and A3. The vWF attains a globular configuration within 1–2 seconds when the shear is stopped or normalized. This shear-induced elongation, particularly in a repetitive manner, also renders the vWF multimer accessible to the ADAMTS-13 enzyme, leading to smaller vWF multimer fragments, which globally reduce factor activity.⁹

Although many studies have used computational fluid dynamics to analyze changes in intrasaccular flow and shear stress on the aneurysm wall after FDS implantation, 1 study also examined the shear stress of blood flow through stent struts in the aneurysm.⁴ The authors of that study found ultra-high levels of blood shear stress (up to 200 Pa) through the struts, nearly equal to the shear stress created by a typical LVAD. The authors stated a possible link existed between shear stress-induced platelet activation and subsequent intrasaccular white thrombus formation after FDS. That study, however, did not refer to vWF or AvWD. Another computational fluid dynamics study, in which a bare metal stent was implanted across an aneurysm of the thoracic aorta, also yielded similar results, with a peak value of the systolic shear rate through the stent struts of up to 16,000/s (approximately 40- to 50-Pa shear stress).⁵ Of note, a critical shear rate of 3000–5000/s (approximately 5- to 8-Pa shear stress) is needed for vWF elongation (ie, activation).¹⁰

We have used the Multiplate Analyzer, a rapid automated whole-blood aggregometry test, for determination of vWF activity because all patients have already been assessed by this test for

Table 2: Multiplate aggregometry results in all 32 patients

Aggregometry	Initial (Mean)	Last (Mean)	P Value	Normal Range ^a
ADP	13.34 ± 5.4	11.97 ± 5.2	.096	53–122
ASPI	12.0 ± 5.0	12.78 ± 6.4	.537	74–136
TRAP	57.34 ± 23.6	60.0 ± 26.6	.524	94–156
RISTOtest	31.88 ± 17.9	38.66 ± 20.3	.024	90–201

Note:—ASPI indicates test for aspirin responsiveness; TRAP, test for general performance of platelet and its glycoprotein IIb/IIIa receptor; RISTO, test for whole blood ristocetin-induced platelet aggregation.

^a According to the manufacturer.

Table 3: Multiplate aggregometry results among the reduced and nonreduced vWF groups

Multiplate Aggregometry	Reduced vWF (Mean) (n = 9)	Nonreduced vWF (Mean) (n = 23)	P Value
ADPin	14.78 ± 5.5	12.78 ± 5.4	.433
ADPlast	12.33 ± 6	11.83 ± 5.1	.681
ASPIin	11.67 ± 5.6	12.13 ± 4.9	1.000
ASPIlast	14.56 ± 6.5	12.09 ± 6.4	.341
TRAPin	59.11 ± 25.3	56.65 ± 23.5	.837
TRAPlast	50.44 ± 16.2	63.74 ± 29.2	.229
RISTOin	43.44 ± 21.9	27.35 ± 14.3	.103
RISTOlast	29.22 ± 18.1	42.35 ± 20.3	.094
RISTOchange	−(14.22 ± 12.3)	+(15.0 ± 11.3)	.000
RISTOchange (range)	−43 to −4	+1 to +39	

Note:—in indicates initial; -last, last; ASPI, test for aspirin responsiveness; TRAP, test for general performance of platelet and its glycoprotein IIb/IIIa receptor; RISTO, test for whole blood ristocetin-induced platelet aggregation.

Table 4: Morphologic variables of aneurysms in the reduced and nonreduced vWF groups

Morphologic Variables	Reduced vWF (Mean) (n = 9)	Nonreduced vWF (Mean) (n = 23)	P Value
Neck area	41.35 ± 32.89	11.44 ± 6.13	.000
Volume	894.09 ± 1010.45	82.33 ± 81.37	.000
Volume-to-neck area	37.11 ± 49.4	9.65 ± 7.12	.001
Aspect ratio	1.72 ± 0.74	1.31 ± 0.43	.103
Size ratio	6.36 ± 7.15	1.68 ± 1.0	.000
Morphologic index	30,515.58 ± 28,234.38	1042.84 ± 1641.06	.000

Table 5: Cutoff values of aneurysm variables according to the ROC analysis

Morphologic Variables	AUC	Threshold Value	Sensitivity (%)	Specificity (%)	95% Confidence Intervals	P Value
Neck area	0.908	18.35	78	79	0.800–1.000	.000
Volume	0.990	256	89	96	0.966–1.000	.000
Volume-to-neck area	0.870	13.67	89	78	0.736–1.000	.001
Aspect ratio	0.691	1.47	67	65	0.486–0.895	.098
Size ratio	0.908	2.16	89	78	0.807–1.000	.000
Morphologic index	0.990	4343	89	91	0.965–1.000	.000

Note:—AUC indicates area under curve; ROC, receiver operating characteristic.

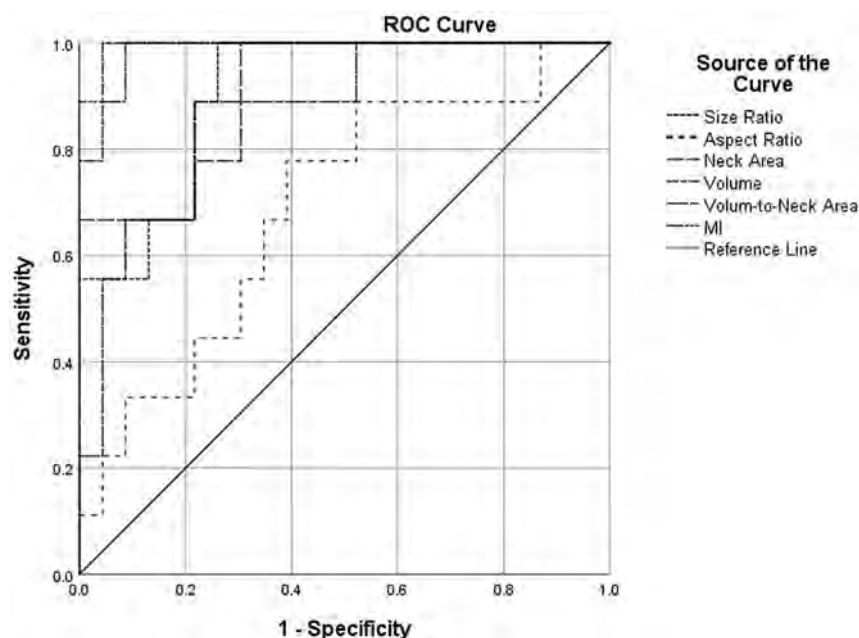


FIG 2. Receiver operating characteristic (ROC) curves for all aneurysm variables. Volume and morphologic index of the aneurysm have the highest discriminative ability. See also Table 5. MI indicates morphologic index.

clopidogrel/prasugrel and aspirin responsiveness. Recent studies using the Multiplate Analyzer have suggested that the RISTOtest may be used to rule out vWD confidently.^{11,12} The test is also reportedly effective for the diagnosis and follow-up of AvWD in patients with a LVAD.¹³

Because both the thromboxane A2 and ADP pathways are important amplification mechanisms that greatly enhance outside-in signaling of platelets via interactions between vWF and the glycoprotein Ib-IX receptor,^{9,14} high-shear-stress platelet aggregation¹⁵ and the RISTOtest¹⁶ are sensitive to aspirin and clopidogrel/prasugrel. The initial and late RISTOtest results, therefore, were below the normal limits in all our patients who underwent loading of both medications. Irreversibly suppressed thromboxane A2 (by aspirin) and ADP (by clopidogrel/prasugrel) metabolism remained stable while we took blood samples for the initial and 24-hour aggregometry tests (Table 2); thus, changes in the RISTO test during this period might be associated solely with changes in vWF activity. In the present study, the late RISTOtest results indicated reduced vWF activity in 16 patients and increased activity in 23 patients. Indeed, an increase in vWF activity in the blood is seen within 24 hours after endothelial activation (ie, injury), induced by either balloon angioplasty¹⁷ or stent implantation¹⁸ in the coronary arteries. A similar response was expected in all patients in our study population; this occurred, however, in only 23 patients with “small” aneurysms, whereas vWF activity was reduced in the remaining 16 patients with “large” aneurysms due to the predominant role of FDSs.

Because computational fluid dynamics simulations show supra-physiologic characteristics while the flow passes through stent struts across the aneurysmal neck,⁴ the total sheared blood volume (and number of shear-induced elongated vWF multimers) might

correlate with both the aneurysmal neck area and aneurysmal volume. Therefore, we established a novel variable to predict the presence of reduced vWF activity. The morphologic index of the aneurysm is determined as the aneurysmal neck area multiplied by volume. Receiver operating characteristic curve analysis showed that reduced vWF activity was best predicted equally by both the novel morphologic index and the volume of the aneurysm (Table 5 and Fig 1 and 2). As expected, 1 fusiform aneurysm was observed in the reduced vWF group due to a relatively large neck length/area.

Adjunctive coiling is the most frequently used measure to protect aneurysms from delayed rupture in patients undergoing FDS implantation. Although adjunctive coiling does not eradicate this complication,¹⁹ we applied a preventive coiling strategy in 6 of 39 patients whose aneurysms were deemed vulnerable to rupture/growth because of their relatively large

size. The morphologic indices and volumes of these patients predicted that they would be in the reduced vWF group, and this prediction was correct (Fig 1). Our results show that adjunctive suboptimal coiling may not nullify the reduction in vWF activity after FDS implantation.

One problem that continues to be encountered after FDS implantation is late aneurysm rupture, a life-threatening complication that occurs in approximately 3% of patients.⁶ The accumulation of white thrombi within the aneurysmal lumen, with subsequent lysis of and/or extravasations from the aneurysmal wall due to local vasoactive and destructive factors secreted by the recruited cells, appears to be the most acceptable explanation for late aneurysm rupture after FDS implantation.^{20,21} MR imaging findings after FDS implantation (ie, perianeurysmal edema and circumferential mural enhancement after contrast administration) further support the concept of thrombus-initiated aneurysmal wall injury.²² Moreover, approximately half of such ruptured aneurysms are larger than 2.5 cm in diameter,¹⁹ implying that a heavier thrombus load (ie, a larger aneurysm) may be a predisposing factor.

One other life-threatening complication that occurs after FDS implantation in approximately 3% of patients is delayed parenchymal bleeding.⁶ More than 80% of delayed intraparenchymal bleeding occurs within the vascular territory having that of treated aneurysms,¹⁹ supporting a deleterious role of FDS and/or its implantation procedure. In a previous study documenting MR imaging findings soon (within 2–9 days) after elective FDS implantation,²³ new DWI lesions in the brain were present in 13 of 24 patients (57%). Additionally, new susceptibility effect foci were definitively found in 8 (38%) and putatively found in 6 (28%) of 21 patients (66% overall); these foci nearly always occurred distally within the vascular territory undergoing FDS

treatment. On delayed MR imaging, all susceptibility effect foci remained unchanged in size, number, and morphology, confirming that the stable lesions represented microhemorrhages. Another recent strictly controlled clinical study²⁴ identified a temporal/causative association between DWI lesions and susceptibility effect foci (microhemorrhage) after FDS implantation. Those investigators found new DWI lesions in 27 of 30 patients (90%), whereas microhemorrhage was not detected on MR imaging at 1 day after stent placement. At 6 months, MR imaging indicated new microhemorrhagic foci in 11 of 30 patients (36%); notably, 14 of 18 (77%) microhemorrhagic foci had originated from previous ischemic DWI lesions, while the remaining 4 were de novo. Because de novo emergence of ipsilateral ischemic foci has been observed on MR imaging up to 1 year after FDS therapy,²⁵ these remaining 4 microhemorrhagic foci might also have resulted from newly generated ischemic foci during the follow-up period. Taken together, a shear-induced sustained increase in vWF activity coming from a downstream stented vessel may be responsible for the initiation of a series of events leading to microthrombus formation in the ipsilateral microcirculation of the brain with subsequent hemorrhagic transformation.

Some vascular devices can create high shear in the blood, thus deteriorating strictly controlled vWF activity balance and causing clinical and laboratory evidence of type 2A AvWD. LVAD and extracorporeal membrane oxygenation are typical examples. Neuroimaging studies of patients with these types of shear-generating vascular devices may help explain the above-mentioned MR imaging findings after FDS. An MR imaging examination conducted on patients after LVAD explantation (mean duration, 2.43 ± 1.08 years) revealed cerebral microbleeds in 97% of patients; the number of microbleeds was positively correlated with the hemorrhagic stroke episode during LVAD support.²⁶ Similarly, symmetric white matter microhemorrhagic foci have been reported on MR imaging, even after days or weeks of extracorporeal membrane oxygenation maintenance.^{27,28} These findings are consistent with previous MR imaging studies conducted on patients with FDS.^{23,24} We hypothesized that supraphysiologic shear-induced activation (ie, elongation) of vWF serves as an initiator of a cascade of events that eventually lead to delayed hemorrhagic complications after FDS implantation. Our result is the first to show the possible link between FDS implantation and AvWD.

Important limitations of this study are its retrospective design and limited number of patients. Another important limitation is that it was constructed on the basis of a single laboratory investigation. Lack of computational fluid dynamics analysis of the aneurysms is another limitation. Therefore, a prospective series supported by other vWF assays (both multimer activity and length) and computational fluid dynamics analysis would be useful to validate the present findings.

CONCLUSIONS

This is the first study to show that reduced vWF activity may occur after FDS implantation, especially in patients with relatively large intracranial aneurysms. A reduction in vWF activity was best predicted by the morphologic index and volume of the aneurysm. Because the reduced vWF activity accompanying

the hemorrhagic disorder is the typical characteristic of vascular device-related AvWD, we hypothesize by analogy that after FDS implantation, shear-induced activation of vWF may be causally linked to the initiation of a cascade of events leading to delayed hemorrhagic complications.

Disclosures: Mustafa Parildar—UNRELATED: Payment for Lectures Including Service on Speakers Bureaus: Transarterial Radioembolization Lectures and Satellite Symposium.* *Money paid to institution.

REFERENCES

1. Horiuchi H, Doman T, Kokame K, et al. **Acquired von Willebrand syndrome associated with cardiovascular diseases.** *J Atheroscler Thromb* 2019;26:303–14 CrossRef Medline
2. Nascimbene A, Neelamegham S, Frazier OH, et al. **Acquired von Willebrand syndrome associated with left ventricular assist device.** *Blood* 2016;127:3133–41 CrossRef Medline
3. Kalbhenn J, Schlagenhauf A, Rosenfelder S, et al. **Acquired von Willebrand syndrome and impaired platelet function during venovenous extracorporeal membrane oxygenation: rapid onset and fast recovery.** *J Heart Lung Transplant* 2018;37:985–91 CrossRef Medline
4. Xiang J, Ma D, Snyder KV, et al. **Increasing flow diversion for cerebral aneurysm treatment using a single flow diverter.** *Neurosurgery* 2014;75:286–94 CrossRef Medline
5. Zhang P, Liu X, Sun A, et al. **Hemodynamic insight into overlapping bare-metal stents strategy in the treatment of aortic aneurysm.** *J Biomech* 2015;48:2041–46 CrossRef Medline
6. Zhou G, Su M, Yin YL, et al. **Complications associated with the use of flow-diverting devices for cerebral aneurysms: a systematic review and meta-analysis.** *Neurosurg Focus* 2017;42:E17 CrossRef Medline
7. Zanaty M, Chalouhi N, Tjoumakaris SI, et al. **Aneurysm geometry in predicting the risk of rupture: a review of the literature.** *Neurol Res* 2014;26:308–13 CrossRef
8. Oran I, Cinar C, Bozkaya H, et al. **Tailoring platelet inhibition according to multiple electrode aggregometry decreases the rate of thrombotic complications after intracranial flow-diverting stent implantation.** *J Neurointerv Surg* 2015;7:357–62 CrossRef Medline
9. Springer TA. **Von Willebrand factor, Jedi knight of the bloodstream.** *Blood* 2014;124:1412–25 CrossRef Medline
10. Schneider SW, Nuschele S, Wixforth A, et al. **Shear-induced unfolding triggers adhesion of von Willebrand factor fibers.** *Proc Natl Acad Sci U S A* 2007;104:7899–903 CrossRef Medline
11. Schmidt DE, Bruzelius M, Majeed A, et al. **Whole blood ristocetin-activated platelet impedance aggregometry (Multiplate) for the rapid detection of von Willebrand disease.** *Thromb Haemost* 2017;117:1528–33 CrossRef Medline
12. Nummi V, Lassila R, Joutsu-Korhonen L, et al. **Comprehensive re-evaluation of historical von Willebrand disease diagnosis in association with whole blood platelet aggregation and function.** *Int J Lab Hematol* 2018;40:304–11 CrossRef Medline
13. Steinlechner B, Dworschak M, Birkenberg B, et al. **Platelet dysfunction in outpatients with left ventricular assist devices.** *Ann Thorac Surg* 2009;87:131–38 CrossRef Medline
14. Du X. **Signaling and regulation of the platelet glycoprotein Ib-IX-V complex.** *Curr Opin Hematol* 2007;14:262–69 CrossRef Medline
15. Matsumoto M, Kawaguchi S, Ishizashi H, et al. **Platelets treated with ticlopidine are less reactive to unusually large von Willebrand factor multimers than are those treated with aspirin under high shear stress.** *Pathophysiol Haemost Thromb* 2005;34:35–40 CrossRef Medline
16. Annick Ankri A, Baranger A, Martin-Toutain I, et al. **Impaired ristocetin-induced platelet aggregation in whole blood assessed with a Multiplate analyzer suggests a new mechanism of antiplatelet effect of aspirin and clopidogrel.** *Int J Lab Hem* 2011;118:3362 CrossRef

17. Hojo Y, Ikeda U, Katsuki T, et al. **Release of endothelin 1 and angiotensin II induced by percutaneous transluminal coronary angioplasty.** *Cathet Cardiovasc Interv* 2000;51:42–49 CrossRef Medline
18. Marketou M, Kochiadakis GE, Giaouzaki A, et al. **Long-term serial changes in platelet activation indices following sirolimus elution and bare metal stent implantation in patients with stable coronary artery disease.** *Hellenic J Cardiol* 2017;58:43–48 CrossRef Medline
19. Rouchaud A, Brinjikji W, Lanzino G, et al. **Delayed hemorrhagic complications after flow diversion for intracranial aneurysms: a literature overview.** *Neuroradiology* 2016;58:171177 CrossRef Medline
20. Kulcsar Z, Houdart E, Bonafe A, et al. **Intra-aneurysmal thrombosis as a possible cause of delayed aneurysm rupture after flow-diversion treatment.** *AJNR Am J Neuroradiol* 2011;32:20–25 CrossRef Medline
21. Raymond J, Darsaut TE, Kotowski M, et al. **Thrombosis heralding aneurysmal rupture: An exploration of potential mechanisms in a novel giant swine aneurysm model.** *AJNR Am J Neuroradiol* 2013;34:346–53 CrossRef Medline
22. Berge J, Tourdias T, Moreau JF, et al. **Perianeurysmal brain inflammation after flow diversion treatment.** *AJNR Am J Neuroradiol* 2011;32:1930–34 CrossRef Medline
23. McGuinness BJ, Memon S, Hope JK. **Prospective study of early MRI appearances following flow-diverting stent placement for intracranial aneurysms.** *AJNR Am J Neuroradiol* 2015;36:943–48 CrossRef Medline
24. Nakae R, Nagaishi M, Kawamura Y, et al. **Microhemorrhagic transformation of ischemic lesions on T2*-weighted magnetic resonance imaging after Pipeline Embolization Device treatment.** *J Neurosurg* 2018 May 1:1–8 [Epub ahead of print] CrossRef Medline
25. Safain MG, Roguski M, Heller RS, et al. **Flow diverter therapy with the Pipeline Embolization Device is associated with an elevated rate of delayed fluid-attenuated inversion recovery lesions.** *Stroke* 2016;47:789–97 CrossRef Medline
26. Yoshioka D, Okazaki S, Toda K, et al. **Prevalence of cerebral microbleeds in patients with continuous-flow left ventricular assist device.** *J Am Heart Assoc* 2017;6:e005955 CrossRef Medline
27. Le Guennec L, Bertrand A, Laurent C, et al. **Diffuse cerebral microbleeds after extracorporeal membrane oxygenation support.** *Am J Respir Crit Care Med* 2015;191:594–96 CrossRef Medline
28. Liebeskind DS, Sanossian N, Sapota ML, et al. **Cerebral microbleeds after use of extracorporeal membrane oxygenation in children.** *J Neuroimaging* 2013;23:75–78 CrossRef Medline

Lesion-Specific Language Network Alterations in Temporal Lobe Epilepsy

O. Foesleitner, K.-H. Nenning, L. Bartha-Doering, C. Baumgartner, E. Patariaia, D. Moser, M. Schwarz, V. Schmidbauer, J.A. Hainfellner, T. Czech, C. Dorfer, G. Langs, D. Prayer, S. Bonelli, and G. Kasprian



ABSTRACT

BACKGROUND AND PURPOSE: Temporal lobe epilepsy, structural or nonlesional, may negatively affect language function. However, little is known about the lesion-specific influence on language networks. We hypothesized that different epileptogenic lesions are related to distinct alterations in the functional language connectome detected by fMRI.

MATERIALS AND METHODS: One hundred one patients with epilepsy due to mesiotemporal sclerosis (21 left, 22 right), low-grade mesiotemporal tumors (12 left), or nonlesional temporal lobe epilepsy (22 left, 24 right) and 22 healthy subjects performed 3T task-based language fMRI. Task-based activation maps (laterality indices) and functional connectivity analysis (global and connectivity strengths between language areas) were correlated with language scores.

RESULTS: Laterality indices based on fMRI activation maps failed to discriminate among patient groups. Functional connectivity analysis revealed the most extended language network alterations in left mesiotemporal sclerosis (involving the left temporal pole, left inferior frontal gyrus, and bilateral premotor areas). The other patient groups showed less extended but also predominantly ipsilesional network changes compared with healthy controls. Left-to-right hippocampal connectivity strength correlated positively with naming function ($P = .01$), and connectivity strength between the left Wernicke area and the left hippocampus was linked to verbal fluency scores ($P = .01$) across all groups.

CONCLUSIONS: Different pathologies underlying temporal lobe epilepsy are related to distinct alterations of the functional language connectome visualized by fMRI functional connectivity analysis. Network analysis allows new insights into language organization and provides possible imaging biomarkers for language function. These imaging findings emphasize the importance of a personalized treatment strategy in patients with epilepsy.

ABBREVIATIONS: FC = functional connectivity; HC = hippocampus; LI = laterality index; MTS = mesiotemporal sclerosis; nl-TLE = nonlesional TLE; TLE = temporal lobe epilepsy

Temporal lobe epilepsy (TLE) can be triggered by various underlying pathologies with mesiotemporal sclerosis (MTS) and low-grade tumors being the most frequent.¹ In some cases, no structural alteration can be found on MR imaging, which is termed nonlesional (nl-TLE). Despite sharing the same anatomic

location and clinical picture, these conditions differ in clinical and cognitive outcomes and thus require different treatment strategies.^{2,3}

Progressive cognitive deficits are common comorbidities in patients with epilepsy.⁴ One-third of patients with TLE have impaired language function, which may further deteriorate after epilepsy surgery.^{2,5} Imaging tools that assess language organization preoperatively are therefore essential to optimize treatment decisions.

Task-based fMRI is a well-established clinical tool for noninvasive presurgical language mapping and shows good concordance with direct cortical stimulation.^{6,7} However, language processing has network properties,⁸ which cannot be fully captured by fMRI activation maps alone. Functional connectivity (FC) analysis uses fMRI data to investigate brain networks^{9,10} and thus opens new perspectives in our understanding of language function.

Received June 17, 2019; accepted after revision October 21.

From the Departments of Biomedical Imaging and Image-Guided Therapy (O.F., K.-H.N., M.S., V.S., G.L., D.P., G.K.), Neurology (E.P., D.M., S.B.), Pediatrics and Adolescent Medicine (L.B.-D.), Institute of Neurology (J.A.H.), and Neurosurgery (T.C., C.D.), Medical University of Vienna, Vienna, Austria; and General Hospital Hietzing with Neurological Center Rosenhügel (C.B.), Vienna, Austria.

Please address correspondence to Gregor Kasprian, MD, Department of Biomedical Imaging and Image-Guided Therapy, Medical University of Vienna, Waehringer Gürtel 18-20, 1090 Vienna, Austria; e-mail: gregor.kasprian@meduniwien.ac.at



Indicates article with supplemental on-line appendix and tables.



Indicates article with supplemental on-line photos.

<http://dx.doi.org/10.3174/ajnr.A6350>

Demographics

	Controls		Left nl-TLE		Right nl-TLE		Left MTS		Right MTS		Left Tumor	
	No.	Median (Range)	No.	Median (Range)	No.	Median (Range)	No.	Median (Range)	No.	Median (Range)	No.	Median (Range)
Sex												
Male	14		14		10		10		16		6	
Female	8		8		14		11		6		6	
Handedness												
Right	21		15		17		20		17		10	
Left	1		6		5		1		4		2	
Age at fMRI imaging (yr)		34 (23–52)		36 (21–55)		3 (18–60)		44 (17–64)		39 (19–52)		29 (18–54)
Age at seizure onset (yr)		NA		23 (4–54)		21 (1–35)		17 (1–41)		19 (1–42)		25 (12–46)
Duration of epilepsy (yr)		NA		9 (1–42)		10 (1–43)		21 (3–48) ^a		14 (1–44)		6 (1–29) ^a

Note:—NA indicates not applicable.

^aSignificant difference (post hoc Tukey test, $P=.04$).

In comparison with task-based fMRI, FC may be more sensitive to lesion-specific alterations of functional representations and/or network changes. In current scientific and clinical imaging practice, there is a common bias toward the anatomic location and a certain indifference regarding the etiology and type of lesion causing TLE.^{11,12} This study aimed to provide a deeper understanding of the relation among the etiology of epileptogenic lesions, the resulting language network alterations, and cognitive function.

We tested the following major hypotheses: 1) The underlying pathology causing TLE influences the organization of language function, and 2) FC analysis provides additional information compared with standard fMRI activation analysis.

MATERIALS AND METHODS

The study was approved by the local ethics committee (Medical University of Vienna, Austria; EK 1883/2016) and was conducted in accordance with the Declaration of Helsinki of 1975. All participants gave informed consent.

Participants

A flow chart listing inclusion and exclusion criteria for patient selection is provided in On-line Fig 1. One hundred one patients with TLE due to MTS (21 left, 22 right), with low-grade epilepsy-associated tumors (12 left) or without structural MR imaging alteration (22 left, 24 right), were included into this retrospective study (demographics are listed in the Table). All patients had task-based language fMRI examinations as part of their presurgical evaluation between March 2011 and June 2018. Clinical data were retrieved from the hospital information system or directly from the physician in charge. Additionally, 22 healthy subjects with no history of neurologic or psychiatric disease, no clinical evidence of neurologic dysfunction, and no structural alteration on MR imaging were scanned with the same imaging protocol as patients.

Diagnosis of unilateral TLE was based on typical seizure semiology and prolonged ictal and interictal video-electroencephalography interpreted by epileptologists. Diagnosis of MTS and nonexistence of other pathologies were confirmed by a trained neuroradiologist with 6 years of experience in epilepsy imaging.

Cases of nl-TLE were selected on the basis of no structural lesion on a 3T scan with a dedicated epilepsy protocol, which included sagittal isotropic FLAIR and T1WI, axial DWI and SWI, and coronal slices perpendicular to the long axis of the hippocampus on T2WI and inversion recovery. In cases of tumor, additional contrast-enhanced T1WI was acquired.

Low-grade TLE-associated brain tumors were included if patients fulfilled the following criteria: substantial involvement of the mesiotemporal lobe without any extratemporal impact, MR imaging features typical of a low-grade lesion, and little or no mass effect/perifocal edema (On-line Fig 2). Twelve patients with left-sided tumors fulfilled these criteria (On-line Fig 1). Because only 5 patients with right-sided lesions were eligible, they were excluded from further analysis. Six of the patients with left tumors proceeded to surgery, with histopathology defining an astrocytoma II in 2 cases, a composite/dysembryoplastic neuroepithelial tumor I in 2 cases, and a ganglioglioma I in 2 cases (grading according to the World Health Organization brain tumor classification system, Version 2007 or 2016, depending on time of reporting^{13,14}).

Epilepsy surgery was performed on 32/43 patients with MTS (15 left, 17 right), confirming hippocampal sclerosis in 31 cases and revealing an irregular neuronal architecture of the hippocampus (HC) in 1 case, reported as a mild malformation of cortical development. Nineteen of 46 patients with nl-TLE (7 left, 12 right) underwent partial temporal lobe resection with histopathologic work-up finding a focal cortical dysplasia in 11 cases, mild MTS in 4, gliosis in 2, and no abnormal findings in 2.

Neuropsychological assessment as part of presurgical evaluation was performed by 2 experienced neuropsychologists and was retrieved from the hospital information system. We focused on language scores—that is, naming ability assessed with the Boston Naming Test¹⁵ and verbal fluency assessed with the Regensburg Verbal Fluency Test.¹⁶ Because for many patients, medical reports did not provide absolute test scores, performance was dichotomized into “below average” and “average or above average.”

fMRI Acquisition

fMRI was performed on the same Achieva 3T scanner (Phillips Healthcare, Best, the Netherlands) in all subjects, using a gradient-

echo EPI sequence (section thickness, $1.8 \times 1.8 \times 4$ mm; TE, 35 ms; TR, 3000 ms; flip angle, 90° ; matrix, 128×128 ; 32 contiguous slices with no interslice gap; ascending section acquisition; bandwidth, 2280 Hz/Px). Additionally, 1-mm isotropic T1WI was acquired for anatomic coregistration. Every participant performed validated language tasks in 1–5 runs (verb generation and/or a semantic task; for task descriptions and distributions, see the On-line Appendix and On-line Table 1). The paradigms were all constructed in block design with 5 minutes per run, resulting in 100 measured time points per run. A training run before scanning and on-line processing ensured correct in-scanner performance.

Activation Analysis

First, fMRI data were converted from DICOM format to Neuroimaging Informatics Technology Initiative format (<https://nifti.nih.gov/>) using SPM 12 software (<http://www.fil.ion.ucl.ac.uk/spm/software/spm12>).¹⁷ Standard preprocessing was applied—that is, motion correction, coregistration of functional-to-anatomic images, direct spatial normalization to Montreal Neurological Institution space, and smoothing (full width at half maximum, 8 mm). First-level analysis was then performed according to the general linear model. Language-related activations were visually checked using SPM 12 (P uncorrected $< .001$). Scans were excluded from further analysis if no significant activations were seen in classic language areas (ie, in the inferior frontal gyrus and/or superior temporal gyrus bilaterally; On-line Fig 3). In second-level analysis, task-related activations were contrasted between patient and control groups for each task separately (P family-wise error–corrected $< .05$).

Additionally, a laterality index (LI) was calculated from the individual activation maps for each run using a bootstrap approach as recommended by Wilke and Lidzba.¹⁸ We used the same ROIs for further FC analysis, with language network ROIs defined as the triangular and opercular parts of the inferior frontal gyrus for the Broca area and a slightly extended region of the posterior superior temporal gyrus for the Wernicke area as well as their right-hemispheric homologs. This parcellation is based on an ICA analysis of 497 subjects from the Human Connectome Project data base and integrated in the CONN toolbox (<https://web.conn-toolbox.org/>).¹⁹ In cases of >1 run per task, a mean LI was calculated for each ROI and each task separately. Moreover, per subject an average LI for both Broca and Wernicke ROIs per task, as well as an average LI for both tasks per Broca and Wernicke ROIs, and finally, an average LI for both tasks and both Broca and Wernicke ROIs were calculated. This ultimately resulted in 9 group comparisons for the LI, allowing a multi-layered analysis of lateralization scores. Left-sided language lateralization was defined as $LI \geq 0.2$; atypical LI was accordingly set at $LI < 0.2$, as is common in the literature.²⁰

Functional Connectivity Analysis

FC was analyzed using the CONN toolbox, Version 17.f running on SPM12.¹⁹ Preprocessing of anatomic and functional data was performed using default settings (functional realignment and unwarping, centering to $[0,0,0]$ coordinates, section-timing correction, artifact detection tools-based outlier detection, direct segmentation and Montreal Neurological Institute normalization,

and smoothing with an 8-mm Gaussian kernel). Denoising included GM and WM signal, CSF signal, realignment, and scrubbing parameters. Task design and first-derivative task regression were also included in the denoising step to prevent coactivations being erroneously summarized as a network.²¹ By default, the CONN toolbox uses a principal component analysis approach to reduce motion-related artifacts.²² We included all acquired time points ($n=100$ per run) in our FC analysis in order to not introduce artificial fluctuations into the frequency spectrum by cutting and concatenating task and resting blocks.²³ Moreover, this approach should maximize the available number of time points, which is known to critically influence the reliability of connectivity measures.²⁴ After regression, a high-pass filter (0.008–infinity) was applied for denoising instead of the default bandpass filter for resting-state data, which aimed to keep potentially task-relevant low-frequency fluctuations.²⁵ Then, bivariate correlation was calculated for the 103 supratentorial atlases and for 4 (language) network ROIs defined by anatomic parcellation atlases included in the CONN toolbox (FSL Harvard-Oxford atlas; <http://neuro.debian.net/pkgs/fsl-harvard-oxford-atlases.html>). The language ROIs were congruent to the ones used in the LI analysis (On-line Fig 3). This feature resulted in Fisher z -transformed correlation coefficients for each connection.

First, we analyzed the global language network changes—that is, group differences in the FC strength between the 4 language-network ROIs and 97 anatomic ROIs (ie, disregarding the left and right triangular and opercular inferior frontal gyri and posterior superior temporal gyrus to avoid autocorrelation). For this analysis, a nonparametric approach (network-based analysis) was chosen with a combination of an ROI-to-ROI connection-correction (P uncorrected $< .01$) and a seed corrected by size (P false discovery rate–corrected $< .05$).²⁶ Second, changes in the FC between the ipsilesional HC and the 103 anatomic ROIs at P false discovery rate–corrected (analysis-level correction) $< .05$ were specifically assessed. Patient groups were each contrasted to the healthy control group on the basis of a standard unpaired t test. Finally, FC strength among the 4 language ROIs was analyzed regarding group-specific differences (ANOVA).

Statistical Analysis of Clinical and Imaging Parameters

We tested group differences regarding sex, handedness, age at fMRI scan, age at first seizure, epilepsy duration, naming, and verbal fluency performance. These clinical values were correlated with LI values (9 values as described above) and FC values (Fisher z -transform) between the language ROIs and the left or right HC. Furthermore, motion parameters (mean and maximum motion) were tested for significant group differences to rule out motion-driven false-positive results. Independent t tests or ANOVA was used for continuous variables with the Tukey test for post hoc analysis and χ^2 tests for categorical data (SPSS Statistics for Macintosh, Version 25.0, released 2017; IBM, Armonk, New York). Visual inspection of histograms determined the Gaussian distribution of metric variables and, subsequently, selection of parametric (Pearson) or nonparametric (Spearman) correlation tests. Significance was set at $\alpha = .05$ if not indicated otherwise.

RESULTS

Clinical Parameters

There were no significant group differences regarding sex ($P = .43$), handedness ($P = .2$), age at fMRI scan ($P = .78$), or age at first seizure ($P = .2$). In 4 patients, handedness was not known. The median duration of epilepsy was different between patients with left tumor and left MTS (6 versus 21 years, $P = .04$, post hoc Tukey test). Demographics are outlined in the Table.

Neuropsychological testing was performed in 68/101 patients (67.3%). Forty-three patients performed well (63.2%), and 25, below average (36.8%) on the verbal fluency test. The naming test resulted in below-average scores in 47/101 (69.1%) and good scores in 21 patients (30.9%). There was a strong correlation among test scores in the different tests ($P = .001$), while there were no significant differences in verbal fluency or naming scores between groups ($P = .6$ and $P = .67$, respectively).

fMRI Quality Assessment

From the subjects included, 27/279 fMRI runs had to be excluded due to missing language-related activations, leaving 252 fMRI scans for further analysis (On-line Table 1). There were no significant group differences in mean or maximum interscan movement; hence, group differences in activation and FC analyses are unlikely to be driven by motion artifacts (On-line Fig 4).

fMRI Activation Analysis and Language LI

There was no significant group difference in activation maps between patient groups and controls ($P \leq .05$ family-wise error-corrected for multiple comparisons). Group-level activation maps are shown in On-line Figs 5 and 6.

Calculation of laterality indices did not result in significant differences in any group (ANOVA, listed in On-line Tables 2 and 3). The mean LI for the verb-generation task was left-lateralized in all groups (mean ranging from 0.3 ± 0.4 in left nl-TLE to 0.57 ± 0.29 in right MTS, Fig 1). The semantic task achieved a slightly lower but still left-lateralized mean LI (ranging from 0.25 ± 0.41 in left nl-TLE to 0.53 ± 0.19 in left tumor, Fig 1).

Of the 19 left-handed subjects, only 1 patient with left nl-TLE had an atypical LI considering both Broca and Wernicke ROIs; 1 patient with left nl-TLE showed a bilateral language dominance, while the other 17 had a typical LI. Right-handed participants showed a typical LI considering both frontal and temporal language ROIs in 100 cases, bilateral language distribution in 19 cases, and an atypical LI in 4 cases. Handedness was not associated with language lateralization ($P = .5$).

Functional Connectivity Analysis

Distinct patterns of FC alterations could be found in the comparison between the control group and each patient group (Fig 2). Most widespread changes were seen in left and right MTS; less significant network alterations, in left and right nl-TLE; and even less, in patients with left tumor. In all except patients with right nl-TLE and left tumor, FC from frontal language areas showed impaired connectivity strength. Temporal language regions were affected in all patient groups (for anterior, left and right projections see On-line Figs 7–11). FC values among the 4 language

network ROIs alone did not show significant group differences, nor did direct comparisons among patient groups.

Regarding ipsilesional hippocampal network changes, only patients with left and right MTS showed significant FC changes between the ipsilesional HC and all other ROIs (Fig 3). In both cases, the superior frontal gyrus was bilaterally affected. In left MTS, visual areas and the right temporal pole also showed weaker FC to the ipsilesional HC. In right MTS, both frontal poles as well as the left temporal and right parietal areas were affected.

Correlation of Clinical and Imaging Parameters

Right- or left-hemispheric TLE was associated with the language LI in the verb-generation task in the Broca area and with the LI in the verb-generation task in both Broca and Wernicke areas, regardless of the underlying pathology ($P = .01$ and $P = .008$, respectively), indicating a more atypical language lateralization in left-sided TLE. Similarly, left seizure onset showed a negative correlation with interhippocampal connectivity ($P = .01$) and a positive correlation with FC between the right HC and left Wernicke area ($P = .002$) across all patients. Boxplots are shown in On-line Fig 12.

Epilepsy duration was negatively correlated with the language LI in the semantic task in Broca and Wernicke areas across all patients ($P < .02$). The longer the epilepsy duration, the more atypical was the LI (On-line Fig 13). Moreover, epilepsy duration showed a negative correlation with FC between the right HC and right Wernicke homolog ($P < .02$) and with FC between the right HC and left Broca area ($P < .04$) across all patients. The longer the epilepsy duration, the weaker were these connections.

Verbal fluency was negatively correlated with FC between the right Broca and Wernicke homologs ($P < .03$) across all patients (On-line Fig 14). Naming performance showed a positive correlation with FC between the right HC and left Broca area ($P < .02$) across all patients (On-line Fig 14). There was no significant correlation between any LI and performance in verbal fluency or naming.

DISCUSSION

Key Findings

This study evaluated the impact of different temporal lobe pathologies, grossly involving the same anatomic locations on language function, cortical representations, and networks. While fMRI activation analysis failed to find significant group differences in cortical language representations, FC analysis detected lesion-specific footprints of language connectome changes. Among all analyzed pathologies, patients with left and right MTS showed the most widespread, bilateral language network alterations. Patients with nl-TLE mainly showed FC decreases in temporal language regions, whereas patients with tumor showed the smallest language network alterations. Moreover, changes in the strength of certain connections correlated with deficits in specific language domains, independent of the underlying lesion. A normal score in verbal fluency was associated with less right hemispheric language connectivity, and naming ability correlated with FC between the right HC and left Broca area.

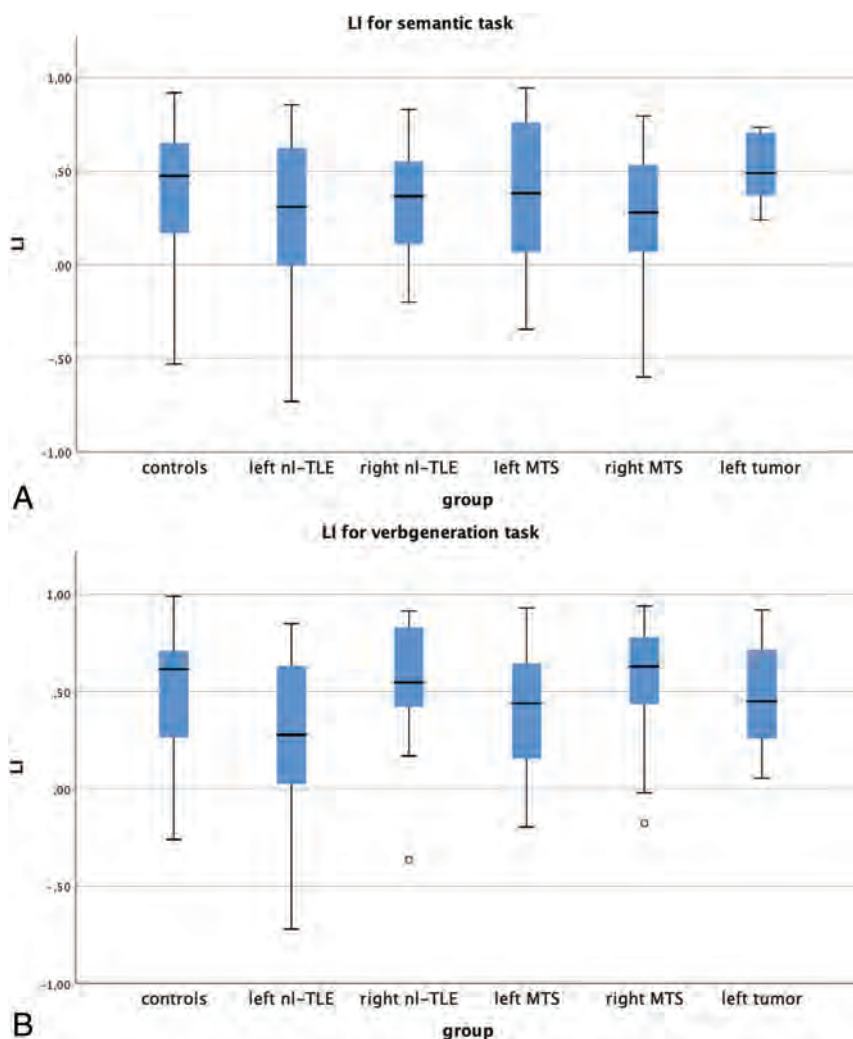


FIG 1. Group-wise boxplot of laterality indices for the verb-generation and semantic tasks. The mean LI was left-lateralized in every group, with no significant group differences at $\alpha = .05$.

Mesiotemporal Sclerosis

Histopathologic hallmarks of MTS are segmental loss of pyramidal cells accompanied by astrogliosis.²⁷ Despite MTS being a focal lesion, widespread structural alterations such as diffuse GM and WM atrophy were detected in MTS.^{28,29} Similarly, distinct functional changes were visible far beyond the seizure-onset zone.^{30,31} This finding is in line with ours in patients with MTS, who showed the most widespread language network of all patient groups, with alterations involving both hemispheres. The median epilepsy duration was higher in patients with left MTS than in those with left tumors, a finding that certainly influenced our results. However, there was no significant difference compared with the other patient groups and none at all compared with patients with right MTS.

The HC is not considered a “classic” language region, but there is evidence that it makes a pivotal contribution to language function, even more than harvesting verbal memory.³² Using resting-state fMRI, de Campos et al³¹ showed the ipsilesional HC as the “main hub of alterations” with widespread connectivity reductions in left and right MTS and, specifically, impaired connectivity of the visuo-spatial network in left MTS. Using

graph theory and resting-state data, Vaughan et al³³ found a functional segregation of the sclerotic HC and decreased FC to the frontal lobe. In our cohort, exclusively, the patients with MTS showed significant changes in FC of the ipsilesional HC, including premotor areas and the contralateral temporal pole. In left MTS, left visual areas were also affected, while right MTS showed disrupted FC to right parietal regions. Most interesting, hippocampal language connectivity was minimally affected in nl-TLE and temporal lobe tumors.

Long-Term Epilepsy-Associated Tumors

Long-term epilepsy-associated tumors are characterized by slow cell growth, rare malignant transformation, young age at epilepsy onset, and predominance for the temporal lobe (ie, proximity to the eloquent cortex).^{34,35} Besides oncologic control, seizure freedom is the main therapeutic goal. In these tumor entities, neuronal dysfunction seems to be less prominent, and functional reorganization, less exclusive compared with other epileptogenic pathologies.^{36,37} Reasons might be their slow growth and young age of onset.³⁸ Our findings are in concordance with the existing literature because functional imaging changes in our cohort of left TLE-associated tumors were the least severe. However,

our data did not show compensatory stronger FC in other brain regions, which could be too subtle for the given sample size of 12 patients.

Nonlesional TLE

With improved structural imaging (ie, 3T scanners and beyond, dedicated epilepsy protocols), MR imaging negative for TLE is increasingly seen as a distinct entity rather than a subtle form of MTS.³⁹ This is suggested by studies using advanced MR imaging techniques, both structural and functional.^{29,33} For instance, in a graph-theory study, nl-TLE showed impaired connectivity in the ipsilateral neocortical but not medial temporal lobe, contrary to MTS with severe affection of the HC.³³ Our results add to this because the extent of changes in the functional language network in our patients with nl-TLE was significantly less numerous and widespread than in MTS, possibly reflecting the severity of the impact of the pathology on the language network. Clinically, cognitive function is much less frequently impaired in patients with nl-TLE than in those with MTS, which, as a downside, puts them at higher risk of postoperative decline.³

Language Laterality

Language is one of the most critical cognitive functions in TLE because it is impaired in every third patient and may further deteriorate after epilepsy surgery.^{2,5} In the general population,

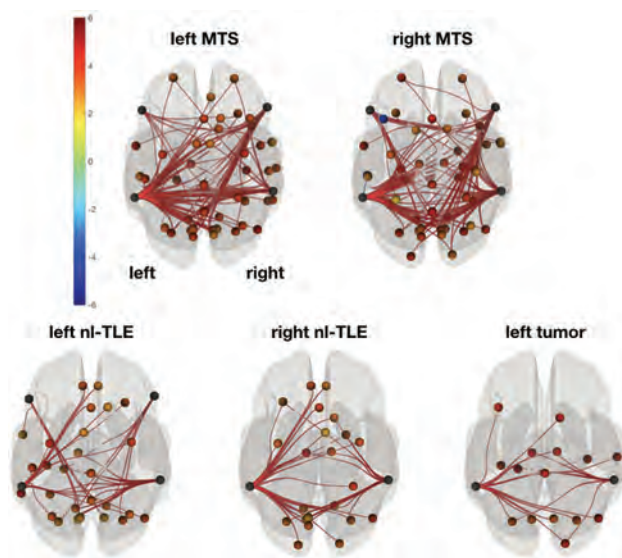


FIG 2. FC contrast between control and patient groups. Left and right MTS was associated with the most widespread, bilateral FC decreases compared with controls. Changes in both frontal and temporal language ROIs were found in left nl-TLE, while right nl-TLE and the left tumor groups showed decreases in only temporal language regions. Superior view in neurologic convention. Network based statistics, connection-corrected at $P < .01$ and seed-corrected at P false discovery rate $< .05$; seeds: 4 language network ROIs; target ROIs: supratentorial brain. Color bar shows t values (-6 ; 6), warm colors meaning decreased, cold colors increased FC strength (controls $>$ patients).

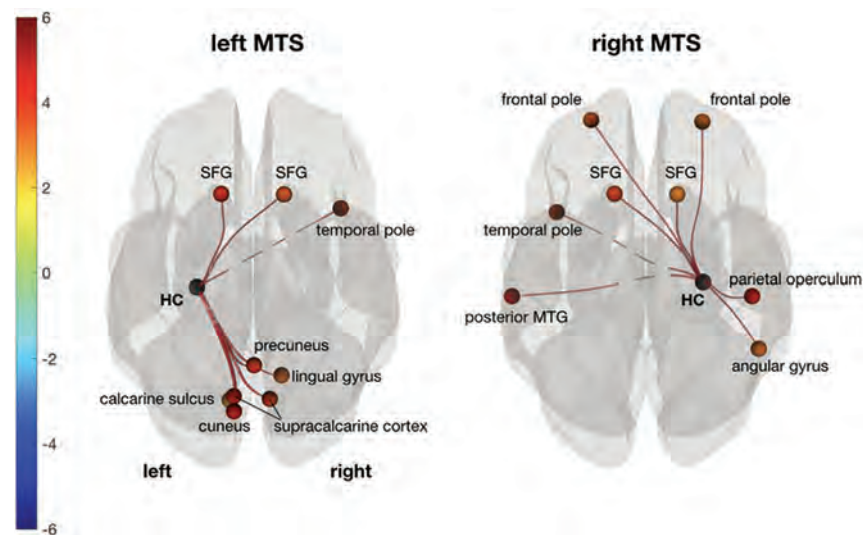


FIG 3. FC changes between the ipsilesional HC and all other supratentorial ROIs show weaker connectivity to the superior frontal gyrus (SFG) in both patients with left and right MTS compared with controls. In left MTS, visual areas and the right temporal pole are also affected. In right MTS, left temporal, right parietal, and bilateral frontal areas show significant FC decreases. Superior view in neurologic convention. P false discovery rate-corrected $< .05$. Color bar shows t values (-6 ; 6), warm colors meaning decreased, cold colors increased FC strength (controls $>$ patients). MTG indicates middle temporal gyrus.

language function is mostly left-hemisphere dominant. Especially, left-sided pathologies such as left TLE are associated with a higher prevalence of atypical (ie, bilateral or even right-dominant) language distribution.⁴⁰ Not surprisingly, left seizure onset was linked to an atypical language lateralization, regardless of the underlying pathology in our patients. Handedness is frequently seen as a predictive marker for language lateralization. However, it seems that this assumption is mainly driven by a minority of subjects ($<1\%$ of the general population) with strongly atypical language dominance who also have a strong preference for their left hand.⁴¹ Yet, left-handedness alone is not predictive of language dominance, which also applied to our participants (see “fMRI Quality Assessment”).

Activation-versus-FC Analysis

According to the current neurobiologic concept, language is built on multiple bilateral brain regions.⁸ The current clinical practice of presurgical fMRI is based on task-based activation analyses. While these are adequate to detect task-associated brain regions, they do not have the potential to provide information about the communication among these functional areas. Previous work showed that FC analysis can detect more subtle differences than standard fMRI analysis on a group level.⁴² In 2006, Briellmann et al⁴³ did not find pathology-related differences in standard fMRI laterality indices between MTS and neuroglial tumors. In a small cohort of patients with TLE with mixed etiologies, Pravata et al⁴² found a correlation between left-intrahemispheric FC and the verbal intelligence quotient in left TLE, but no such association in the task-based LI. Our findings are in line with these studies because only FC analysis found group-specific differences and a significant association between imaging and clinical parameters.

Task-Based FC

Most FC analyses are based on spontaneous fluctuations known as resting-state fMRI (ie, subjects being at wakeful rest inside the scanner) reliably revealing major functional networks (eg, sensorimotor or language). However, task-based fMRI enhances specific networks while decreasing others,⁴⁴ and the findings remain different from resting-state data, even with sophisticated postprocessing such as task-regression or concatenation of resting blocks.²³ Success in determining language lateralization in resting-state fMRI is heterogeneous, with the pitfall of showing a more bilateral language distribution.^{45,46} In terms of clinical feasibility, task-based FC offers the advantage of no additional scan time compared with a dedicated resting-state sequence. These reasons support combining standard fMRI activation analysis

for language lateralization with task-based FC for the network aspect.

Clinical Implications

Our study suggests that FC may be a potent tool to visualize side- and pathology-dependent alterations of language networks in epilepsy. First, studies showed a correlation between connectivity strength and cognitive function.⁴⁷ In our patient sample, good naming ability was correlated with stronger FC between the right HC and left Wernicke area, while better performance in verbal fluency was seen in patients with less FC in right language areas across all patients. Neuropsychological studies have linked left-sided MTS to worse performance in language testing.³ This may imply that patients with left MTS need early special support to reduce language worsening. Because longer disease duration leads to more extensive network changes, earlier surgical treatment could prevent some of these widespread functional network alterations. Furthermore, the results presented here may further help to identify the ideal patients and their optimal treatment strategy at the optimal time point. Improved presurgical imaging of the individual organization of brain functions such as language could ultimately help to better assess the individual risk profile of patients with TLE. Further studies and a longitudinal study design are needed to differentiate whether the observed changes in FC are due to effective plasticity or a mere attempt at compensation for language deficits or whether they are the result of a pathologic process interfering with language function.

Limitations

Seizure frequency recorded by patients was not considered because its accuracy may be biased due to amnesic seizures. Also, the impact of antiepileptic medication, mood/anxiety, or depression was not investigated in this study. Our selection criteria of low-grade mesiotemporal tumors were strict to keep the group as homogeneous as a tumor cohort could be, however, resulting in a modest sample size of left-sided lesions. While we found significant lesion-specific FC changes compared with the control group, the direct comparison of patient subgroups did not yield significant results. This may be due to the subtlety of alterations not detectable with our modest sample sizes and the statistical necessity of multiple comparison corrections. On the contrary, sample size limitations forced us to combine 2 different language tasks and different numbers of runs, thereby inferring a certain heterogeneity. The rationale behind the inclusion of different numbers of runs was to maximize the time points available for analysis, thus making functional connectivity analysis more robust.²⁴ Subsequent studies with larger cohorts may further refine our results.

For both the LI and FC analyses, we used the same ROIs integrated in the CONN toolbox, which are based on an independent component analysis of 497 healthy subjects from the Human Connectome Project dataset. This approach should facilitate the direct comparability between these methods but could, however, potentially “dilute” connectivity measures. Alternatively, we could have used ROIs individually defined by task-based activation maps; this process, however, is prone to bias due to thresholding. Because there is no criterion standard for brain

parcellation today,⁴⁶ we are positive that the chosen approach addresses our study aim.

CONCLUSIONS

Different types of pathologies underlying TLE cause distinct alterations of the functional language connectome. FC analysis identifies these lesion-specific footprints of epileptogenic lesions in a unique fashion. Furthermore, FC strength correlates with clinical language function in patients with TLE. Thus, FC analysis may provide a comprehensive and more global perspective on language processing compared with standard fMRI activation analysis. In summary, these functional imaging findings emphasize the importance of a personalized treatment strategy in patients with TLE.

Disclosures: Lisa Bartha-Doering—UNRELATED: Grants/Grants Pending: Austrian Science Fund, Comments: I am the Principal Investigator of the project FWF KLIF 544 “Prenatal Brain Asymmetry and Language,” funded by the Austrian Science Fund, 2016–2020. This project does not interact with the present work. Gregor Kasprian—UNRELATED: Comments: I am the principal investigator of the project FWF I3925-B27 entitled “Epigenetic control of brain wiring role of miRNAs in FASD”. This project does not interact with the present work.

REFERENCES

1. Blumcke I, Spreafico R, Haaker G, et al. **Histopathological findings in brain tissue obtained during epilepsy surgery.** *N Engl J Med* 2017;377:1648–56 CrossRef Medline
2. Helmstaedter C. **Cognitive outcomes of different surgical approaches in temporal lobe epilepsy.** *Epileptic Disord* 2013;15:221–39 CrossRef Medline
3. Helmstaedter C, Petzold I, Bien CG. **The cognitive consequence of resecting nonlesional tissues in epilepsy surgery—results from MRI- and histopathology-negative patients with temporal lobe epilepsy.** *Epilepsia* 2011;52:1402–08 CrossRef Medline
4. Oyegbile TO, Dow C, Jones J, et al. **The nature and course of neuropsychological morbidity in chronic temporal lobe epilepsy.** *Neurology* 2004;62:1736–42 CrossRef Medline
5. Bartha-Doering L, Trinka E. **The interictal language profile in adult epilepsy.** *Epilepsia* 2014;55:1512–25 CrossRef Medline
6. Austerlueh A, Cocjin J, Reynolds R, et al. **Language functional MRI and direct cortical stimulation in epilepsy preoperative planning.** *Ann Neurol* 2017;81:526–37 CrossRef Medline
7. Black DF, Vachha B, Mian A, et al. **American Society of Functional Neuroradiology-Recommended fMRI paradigm algorithms for presurgical language assessment.** *AJNR Am J Neuroradiol* 2017;38: E65–73 CrossRef Medline
8. Poeppel D. **The neuroanatomic and neurophysiological infrastructure for speech and language.** *Curr Opin Neurobiol* 2014;28:142–49 CrossRef Medline
9. Friston KJ. **Functional and effective connectivity: a review.** *Brain Connect* 2011;1:13–36 CrossRef Medline
10. Biswal B, Yetkin FZ, Haughton VM, et al. **Functional connectivity in the motor cortex of resting human brain using echo-planar MRI.** *Magn Reson Med* 1995;34:537–41 CrossRef Medline
11. Rosazza C, Ghielmetti F, Minati L, et al. **Preoperative language lateralization in temporal lobe epilepsy (TLE) predicts peri-ictal, pre- and post-operative language performance: an fMRI study.** *Neuroimage Clin* 2013;3:73–83 CrossRef Medline
12. Kaestner E, Reyes A, Macari AC, et al. **Identifying the neural basis of a language-impaired phenotype of temporal lobe epilepsy.** *Epilepsia* 2019;60:1627–38 CrossRef Medline
13. Louis DN, Ohgaki H, Wiestler OD, et al. **The 2007 WHO classification of tumours of the central nervous system.** *Acta Neuropathol* 2007;114:97–109 CrossRef Medline

14. Louis DN, Perry A, Reifenberger G, et al. **The 2016 World Health Organization Classification of Tumors of the Central Nervous System: a summary.** *Acta Neuropathol* 2016;131:803–20 CrossRef Medline
15. Kaplan E, Goodglass H, Weintraub S. *Boston Naming Test*. Philadelphia: Lea & Febiger; 1983
16. Aschenbrenner A, Tucha O, Lange K. *RWT: Regensburger Wortflüssigkeits-Test*. Göttingen: Hogrefe; 2000
17. Friston KJ, Holmes AP, Worsley KJ, et al. **Statistical parametric maps in functional imaging: a general linear approach.** *Hum Brain Mapp* 1994;2:189–210 CrossRef
18. Wilke M, Lidzba K. **LI-tool: a new toolbox to assess lateralization in functional MR-data.** *J Neurosci Methods* 2007;163:128–36 CrossRef Medline
19. Whitfield-Gabrieli S, Nieto-Castanon A. **Conn: a functional connectivity toolbox for correlated and anticorrelated brain networks.** *Brain Connect* 2012;2:125–41 CrossRef Medline
20. Seghier ML. **Laterality index in functional MRI: methodological issues.** *Magn Reson Imaging* 2008;26:594–601 CrossRef Medline
21. Fair DA, Schlaggar BL, Cohen AL, et al. **A method for using blocked and event-related fMRI data to study “resting state” functional connectivity.** *Neuroimage* 2007;35:396–405 CrossRef Medline
22. Behzadi Y, Restom K, Liu J, et al. **A component based noise correction method (CompCor) for BOLD and perfusion-based fMRI.** *Neuroimage* 2007;37:90–101 CrossRef Medline
23. Ganger S, Hahn A, Kublbock M, et al. **Comparison of continuously acquired resting state and extracted analogues from active tasks.** *Hum Brain Mapp* 2015;36:4053–63 CrossRef Medline
24. Shah LM, Cramer JA, Ferguson MA, et al. **Reliability and reproducibility of individual differences in functional connectivity acquired during task and resting state.** *Brain Behav* 2016;6:e00456 CrossRef Medline
25. Davey CE, Grayden DB, Egan GF, et al. **Filtering induces correlation in fMRI resting state data.** *Neuroimage* 2013;64:728–40 CrossRef Medline
26. Zalesky A, Fornito A, Bullmore ET. **Network-based statistic: identifying differences in brain networks.** *Neuroimage* 2010;53:1197–1207 CrossRef Medline
27. Blumcke I, Thom M, Aronica E, et al. **International consensus classification of hippocampal sclerosis in temporal lobe epilepsy: a Task Force Report from the ILAE Commission on Diagnostic Methods.** *Epilepsia* 2013;54:1315–29 CrossRef Medline
28. Bonilha L, Edwards JC, Kinsman SL, et al. **Extrahippocampal gray matter loss and hippocampal deafferentation in patients with temporal lobe epilepsy.** *Epilepsia* 2010;51:519–28 CrossRef Medline
29. Coan AC, Campos BM, Yasuda CL, et al. **Frequent seizures are associated with a network of gray matter atrophy in temporal lobe epilepsy with or without hippocampal sclerosis.** *PLoS One* 2014;9:e85843 CrossRef Medline
30. Haneef Z, Lenartowicz A, Yeh HJ, et al. **Functional connectivity of hippocampal networks in temporal lobe epilepsy.** *Epilepsia* 2014; 55:137–45 CrossRef Medline
31. de Campos BM, Coan AC, Lin Yasuda C, et al. **Large-scale brain networks are distinctly affected in right and left mesial temporal lobe epilepsy.** *Hum Brain Mapp* 2016;37:3137–52 CrossRef Medline
32. Covington NV, Duff MC. **Expanding the language network: direct contributions from the hippocampus.** *Trends Cogn Sci* 2016;20:869–70 CrossRef Medline
33. Vaughan DN, Rayner G, Tailby C, et al. **MRI-negative temporal lobe epilepsy: a network disorder of neocortical connectivity.** *Neurology* 2016;87:1934–42 CrossRef Medline
34. Blumcke I, Aronica E, Urbach H, et al. **A neuropathology-based approach to epilepsy surgery in brain tumors and proposal for a new terminology use for long-term epilepsy-associated brain tumors.** *Acta Neuropathol* 2014;128:39–54 CrossRef Medline
35. Giulioni M, Marucci G, Martinoni M, et al. **Epilepsy associated tumors: review article.** *World J Clin Cases* 2014;2:623–41 CrossRef Medline
36. Noll KR, Sullaway C, Ziu M, et al. **Relationships between tumor grade and neurocognitive functioning in patients with glioma of the left temporal lobe prior to surgical resection.** *Neuro Oncol* 2015;17:580–87 CrossRef Medline
37. Briganti C, Sestieri C, Mattei PA, et al. **Reorganization of functional connectivity of the language network in patients with brain gliomas.** *AJNR Am J Neuroradiol* 2012;33:1983–90 CrossRef Medline
38. Ghinda CD, Duffau H. **Network plasticity and intraoperative mapping for personalized multimodal management of diffuse low-grade gliomas.** *Front Surg* 2017;4:3 CrossRef Medline
39. Muhlhofer W, Tan YL, Mueller SG, et al. **MRI-negative temporal lobe epilepsy: what do we know?** *Epilepsia* 2017;58:727–42 CrossRef Medline
40. Weber B, Wellmer J, Reuber M, et al. **Left hippocampal pathology is associated with atypical language lateralization in patients with focal epilepsy.** *Brain* 2006;129:346–51 CrossRef Medline
41. Mazoyer B, Zago L, Jobard G, et al. **Gaussian mixture modeling of hemispheric lateralization for language in a large sample of healthy individuals balanced for handedness.** *PLoS One* 2014;9:e101165 CrossRef Medline
42. Pravata E, Sestieri C, Mantini D, et al. **Functional connectivity MR imaging of the language network in patients with drug-resistant epilepsy.** *AJNR Am J Neuroradiol* 2011;32:532–40 CrossRef Medline
43. Briellmann RS, Labate A, Harvey AS, et al. **Is language lateralization in temporal lobe epilepsy patients related to the nature of the epileptogenic lesion?** *Epilepsia* 2006;47:916–20 CrossRef Medline
44. Fox MD, Raichle ME. **Spontaneous fluctuations in brain activity observed with functional magnetic resonance imaging.** *Nat Rev Neurosci* 2007;8:700–11 CrossRef Medline
45. Teghipco A, Hussain A, Tivarus ME. **Disrupted functional connectivity affects resting state based language lateralization.** *Neuroimage Clin* 2016;12:910–27 CrossRef Medline
46. Doucet GE, Pustina D, Skidmore C, et al. **Resting-state functional connectivity predicts the strength of hemispheric lateralization for language processing in temporal lobe epilepsy and normals.** *Hum Brain Mapp* 2015;36:288–303 CrossRef Medline
47. Trimmel K, van Graan AL, Caciagli L, et al. **Left temporal lobe language network connectivity in temporal lobe epilepsy.** *Brain* 2018; 141:2406–18 CrossRef Medline

CT and MRI Findings of Glomangiopericytoma in the Head and Neck: Case Series Study and Systematic Review

C.H. Suh, J.H. Lee, M.K. Lee, S.J. Cho, S.R. Chung, Y.J. Choi, and J.H. Baek



ABSTRACT

SUMMARY: Glomangiopericytoma is a rare sinonasal mesenchymal tumor of borderline or low malignant potential. We reviewed the CT and MR imaging findings of head and neck glomangiopericytoma via a retrospective case series study and systematic review. Our study revealed that glomangiopericytoma is a well-defined lobulated avidly enhancing soft-tissue mass with erosive bony remodeling that is most commonly found in the sinonasal cavity. Typically, it is hyperintense on T2-weighted images with vascular signal voids, has a high mean ADC value, and a wash-in and washout pattern on dynamic contrast-enhanced MR imaging. Although the CT findings are nonspecific, typical MR imaging findings, including those on the ADC map and dynamic contrast-enhanced MR imaging, may be helpful for differentiating glomangiopericytomas from other hypervascular tumors in the head and neck.

ABBREVIATION: DCE = dynamic contrast-enhanced

Glomangiopericytoma is a rare sinonasal mesenchymal tumor demonstrating a perivascular myoid phenotype and is one of the sinonasal vascular spindle cell tumors, such as spindle cell hemangioma, kaposiform hemangioendothelioma, and Kaposi sarcoma.¹⁻³

Glomangiopericytoma, which accounts for <0.5% of all sinonasal tumors, was categorized as a borderline or low-malignant-potential tumor by the World Health Organization in 2005.¹ A previous study showed that 18 of 104 patients (17.3%) had a local recurrence and were managed by additional surgery.⁴ Glomangiopericytoma was formerly called “sinonasal hemangiopericytoma” because of a hemangiopericytomatous pattern.

To date, a number of case reports have been published describing the CT or MR imaging findings of glomangiopericytoma in the head and neck. Although these previous reports demonstrated that glomangiopericytoma is usually a well-defined and avidly enhancing soft-tissue mass with erosive remodeling mainly in the sinonasal cavity, there has been no report systematically

reviewing the CT and MR imaging findings of glomangiopericytoma in the head and neck. In addition, details on the findings on advanced MR imaging methods including DWI and dynamic contrast-enhanced (DCE)-MR imaging have not yet been published.

Therefore, the purpose of our study was to review the CT and MR imaging findings of glomangiopericytoma in the head and neck, including findings on DWI and DCE-MR imaging, via a retrospective study of a case series and a systematic review.

Case Series

Our study was approved by the institutional review board of Asan Medical Center, and the requirement for informed consent was waived due to the retrospective nature of the study. The pathology reports for January 2010 to January 2019 were electronically searched using “glomangiopericytoma,” “sinonasal hemangiopericytoma,” “sinonasal-type hemangiopericytoma,” “hemangiopericytoma-like tumor,” and “hemangiopericytoma of sinonasal origin” as keywords. Patients who underwent preoperative CT and/or MR imaging were enrolled. Clinical and demographic data including age, sex, and symptoms were acquired from the electronic medical record. The imaging findings including location, size, border, adjacent bone change, CT density, enhancement pattern, MR imaging signal intensity on T2WI, ADC value of the whole tumor, the presence of vascular signal voids, and DCE-MR imaging patterns were independently reviewed by 2 board-certified neuroradiologists (J.H.L., with

Received April 26, 2019; accepted after revision October 7.

From the Department of Radiology and Research Institute of Radiology, University of Ulsan College of Medicine, Asan Medical Center, Seoul, Republic of Korea.

Please address correspondence to Jeong Hyun Lee, MD, PhD, Department of Radiology and Research Institute of Radiology, University of Ulsan College of Medicine, Asan Medical Center, 86 Asanbyeongwon-Gil, Songpa-Gu, Seoul 05505, Republic of Korea; e-mail: jeonghlee@amc.seoul.kr



Indicates article with supplemental on-line tables.

<http://dx.doi.org/10.3174/ajnr.A6336>

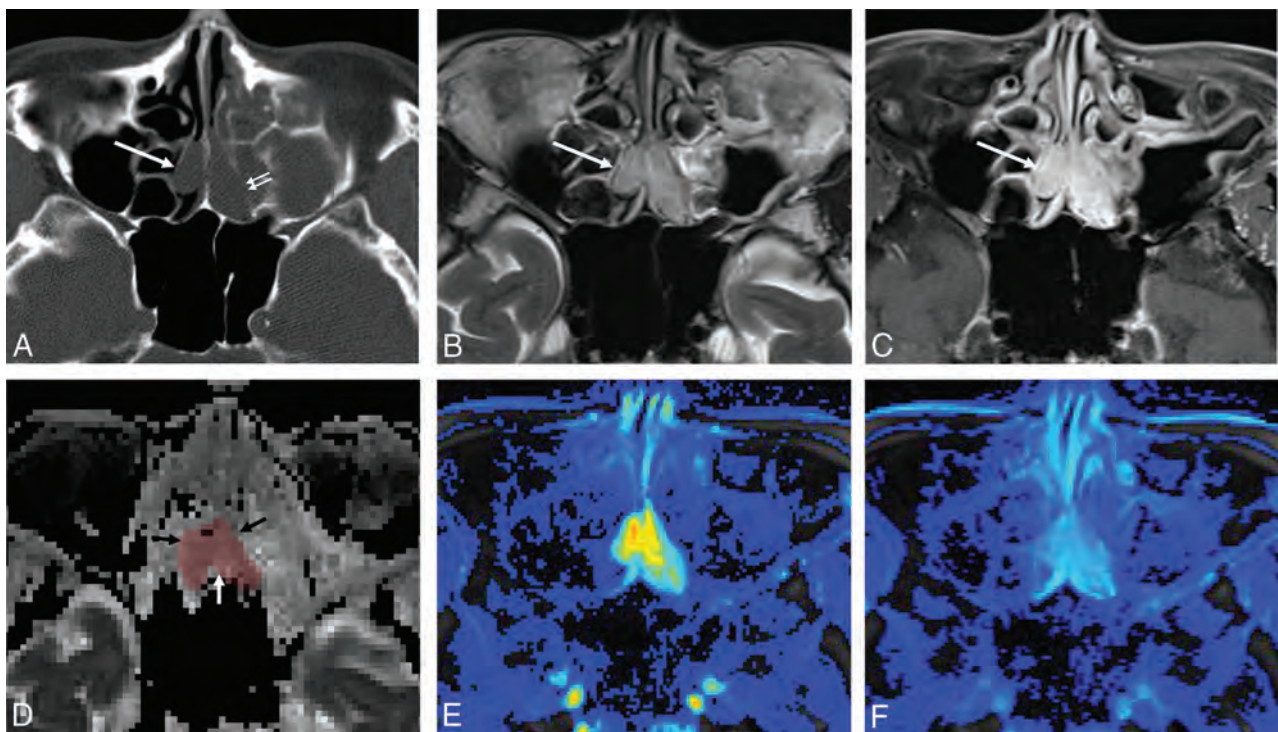


FIG 1. A 79-year-old woman with sinonasal glomangiopericytoma. A, Nonenhanced CT shows a midline bilobed soft-tissue mass (*long arrow*) overriding the permeated nasal septum with erosive remodeling on the bony wall of the left ethmoidal sinus (*short arrows*). On MR imaging, the mass (*arrow*) shows slight hyperintensity on T2WI (B) and strong and homogeneous enhancement on fat-suppressed contrast-enhanced T1WI (C). D, On the ADC map, the mass shows a high mean ADC value ($1.47 \times 10^{-3} \text{ mm}^2/\text{s}$) (*arrows*). E and F, On DCE-MR imaging, the mass reveals wash-in and washout patterns on the initial and final area under the curve maps, which were obtained by trapezoidal integration of the normalized signal intensity curve during the initial 90 seconds after the onset of contrast enhancement and during the last 90 seconds using the same enhancing voxels.

18 years of experience in head and neck neuroradiology, and C.H.S., with 6 years of experience in neuroradiology). We placed ROIs for the entire tumor to obtain a mean ADC value of the whole tumor.

Six patients satisfied the inclusion criteria (3 men and 3 women; mean age, 67 years; range, 48–79 years; On-line Table 1). Four patients had symptoms, and 2 patients were identified incidentally on imaging studies. Following initial detection, all patients underwent an operation. One patient had preoperative embolization of the tumor. Two patients had minor bleeding during resection, but the other 3 had no bleeding complication, despite no preoperative embolization. Four glomangiopericytomas were located in the sinonasal cavity; 1, in the masticator/buccal spaces, and 1, in the prevertebral space. The maximum diameters ranged from 2.9 to 5 cm (median, 3.3 cm).

All patients underwent CT, which was performed using ≥ 16 -detector row CT scanners with excellent image quality. Intravenous iodine contrast agent was used in all except 1 patient. All glomangiopericytomas were well-defined round or lobulated contoured soft-tissue masses (Fig 1). Five tumors were in direct contact with the adjacent bone, which showed erosive remodeling, while 1 tumor was surrounded by soft tissue. On contrast-enhanced CT, 2 tumors revealed avid and homogeneous enhancement patterns that were slightly lower than the adjacent vessels (Fig 2), whereas 3 tumors demonstrated heterogeneous enhancement.

Four of 6 patients underwent MR imaging, which included DWI in 1 patient and both DWI and DCE-MR imaging in 2 patients. All MR imaging was performed using a 3T scanner with excellent image quality. Detailed information about our own MR imaging parameters was the same as that published in previous articles by our group.^{5,6}

On MR imaging, 2 glomangiopericytomas showed homogeneous hyperintensity on T2WI, 1 glomangiopericytoma showed intermediate signal intensity, and 1 glomangiopericytoma showed heterogeneous intermediate-to-high signal intensity. All glomangiopericytomas revealed vascular signal voids on T2WI. The 3 patients for whom ADC maps were available demonstrated high mean ADC values ranging from 1.27 to $2.09 \times 10^{-3} \text{ mm}^2/\text{s}$ (On-line Table 1 and Figs 1 and 2). On contrast-enhanced MR imaging, 3 glomangiopericytomas in the sinonasal cavity or masticator space revealed avid and homogeneous enhancement, whereas 1 glomangiopericytoma in the prevertebral space revealed heterogeneous enhancement. On DCE-MR imaging, 2 glomangiopericytomas revealed a rapid wash-in and washout pattern (Fig 1).

For the systematic review, a systematic search of PubMed and EMBASE was performed using the following search term: ((glomangiopericytoma) OR (“sinonasal hemangiopericytoma”) OR (“sinonasal-type hemangiopericytoma”) OR (“hemangiopericytoma-like tumor”) OR (“hemangiopericytoma of sinonasal origin”)) AND (“computed tomography”) OR (CT) OR (“magnetic

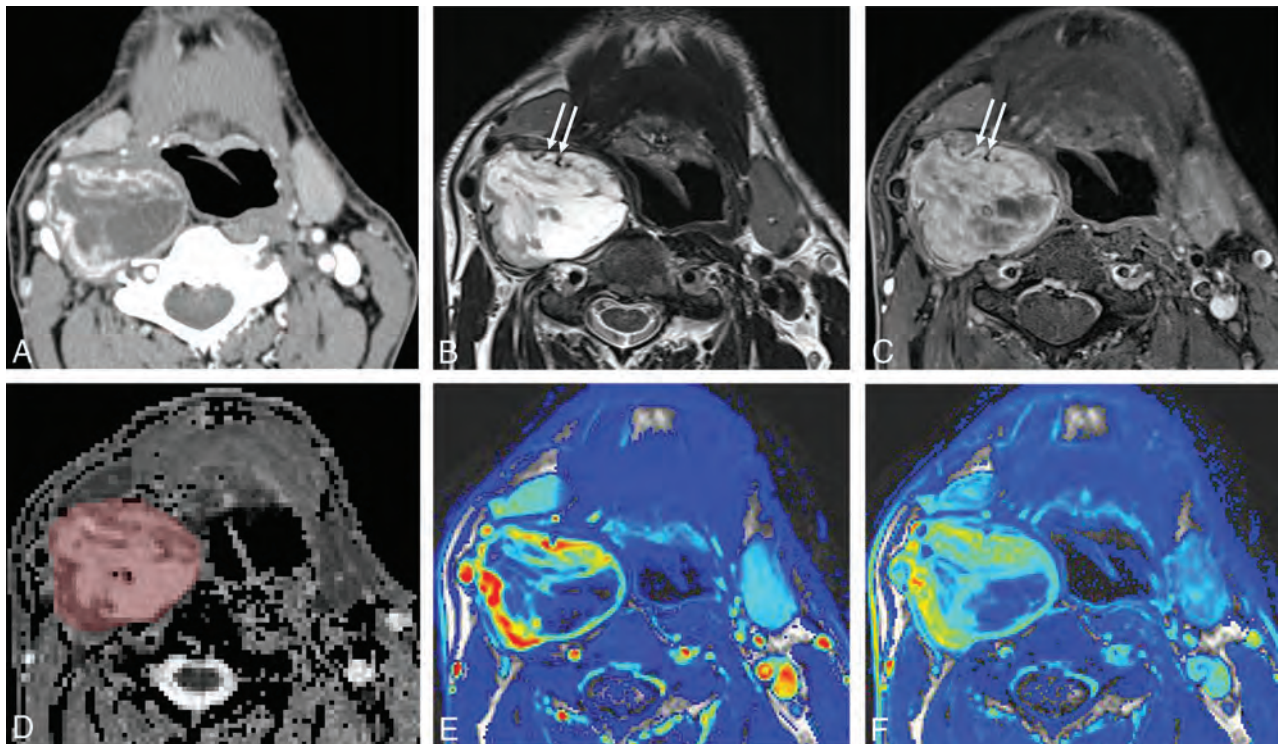


FIG 2. A 72-year-old man with glomangiopericytoma in the prevertebral space. A, Contrast-enhanced CT shows a well-defined heterogeneously enhancing mass in the right prevertebral space. The mass demonstrates iso- to hyperintensity on T2WI (B) and has heterogeneous enhancement on fat-suppressed contrast-enhanced T1WI (C). Note several vascular signal voids (arrows) at the periphery of the mass. D, On the ADC map, the mass shows a high mean ADC value ($2.09 \times 10^{-3} \text{ mm}^2/\text{s}$). E and F, On DCE-MR imaging, the mass reveals rapid wash-in and washout patterns on the initial and final area under the curve maps, which were obtained by trapezoidal integration of the normalized signal intensity curve during the initial 90 seconds after the onset of contrast enhancement and during the last 90 seconds using the same enhancing voxels.

resonance imaging”) OR (“MR imaging”) OR (MRI)). The literature search was not limited by any filters or published language. The search was updated until August 15, 2019. The literature search, study selection, and data extraction were independently performed by 2 board-certified neuroradiologists (J.H.L. and C.H.S.).

This systematic search originally yielded 59 articles (38 from PubMed and 21 from EMBASE). After removal of duplicate articles and those that were not in the field of interest, 11 case reports with 14 cases were left for inclusion in this systematic review (On-line Table 2).^{7–17} Eleven of 14 glomangiopericytomas were located in the sinonasal cavity and had maximum diameters ranging from 2.9 to 4 cm. On CT, 11 glomangiopericytomas were well-defined lobulated contoured soft-tissue masses and 7 showed erosive remodeling of adjacent bone. On contrast-enhanced CT, 6 glomangiopericytomas revealed strong and homogeneous enhancement patterns, while 2 glomangiopericytomas demonstrated heterogeneous enhancement. On MR imaging, 3 glomangiopericytomas showed hyperintensity on T2WI. These CT and MR imaging findings were similar to our findings.

DISCUSSION

Both our case series and the systematic review confirmed that glomangiopericytomas are well-defined round or lobulated,

contoured soft-tissue masses that frequently show erosive bone remodeling, especially in the sinonasal cavity. Our study also revealed that glomangiopericytomas usually show avid and homogeneous enhancement on contrast-enhanced CT or MR imaging, intermediate-to-high signal intensity on T2WI, high ADC values, and rapid wash-in and washout patterns on DCE-MR imaging. They are also accompanied by vascular signal voids on T2WI. Although the individual imaging findings might be nonspecific, a combination of these findings on CT and MR imaging, especially when DWI and DCE-MR imaging are included, may help to suggest glomangiopericytoma of borderline malignant potential, which is important in preoperative planning of the surgical approach or extent of resection.

In this study, we report on the CT and MR imaging (including DWI and DCE-MR imaging) findings of glomangiopericytoma. While the lesions are imaged in a manner similar to that of other vascular tumors, the combination of findings may help differentiate glomangiopericytoma from other hypervascular tumors. High ADC values indicate low cellularity, which reflects the low malignant potential of the tumor. Therefore, high ADC values may be a key imaging finding for differentiating glomangiopericytoma from malignant sinonasal cancer.¹⁸ The signal voids on T2WI and avid enhancement suggest a vascular tumor. Surgeons may request preoperative embolization in this category of lesion before endoscopic resection.⁹

Given the submucosal nature of glomangiopericytomas, they can be differentiated from more common mucosal tumors such as squamous cell carcinomas or inverted papillomas. The differential diagnosis for a submucosal tumor is broad and can include solitary fibrous tumor, lobular capillary hemangioma, or nasopharyngeal angiofibroma. Differentiating these entities when they occur in the head and neck can be challenging because of similar imaging findings. However, the distinction is clinically important because glomangiopericytoma has borderline or low malignant potential, unlike some of the other disease entities. Solitary fibrous tumor, formerly known as hemangiopericytoma, consists of a cellular spindle cell proliferation effacing submucosal structures with staghorn-type vessels,¹⁹ with the tumors being characterized by chromosomal translocation resulting in the formation of a *NAB2-STAT6* fusion gene; thus nuclear staining of *STAT6* is a reference standard method for diagnosing solitary fibrous tumors.²⁰ Glomangiopericytoma is most commonly confused with solitary fibrous tumor because solitary fibrous tumor is also a well-defined tumor with avid enhancement and a washout time-intensity curve pattern on DCE-MR imaging.²¹ However, solitary fibrous tumor in the sinonasal cavity shows iso- to hypointensity on T2WI because of its fibrous component.²² Although it is difficult to differentiate glomangiopericytoma from solitary fibrous tumor on CT, these signal intensity differences on T2WI may be helpful.

Lobular capillary hemangioma is another potential differential diagnosis; it has a lobular architecture with staghorn-type vessels in the interlobular stroma.²³ Although lobular capillary hemangioma is also known to be a well-defined avidly-enhancing mass with hyperintensity on T2WI and a washout time-intensity curve pattern, bony changes are not usually seen on CT or MR imaging.^{24,25} Nasopharyngeal angiofibroma has abundant stromal collagen and a prominent vascular stroma. Although angiofibroma is a similar hypervascular tumor, the typical demographic data, including age and sex and the characteristic location (ie, lateral nasopharyngeal mucosa at the sphenopalatine foramen), can help to differentiate angiofibroma from glomangiopericytoma. When glomangiopericytoma occurs outside the sinonasal cavity, neurogenic tumors can be one of the major differential diagnoses. However, neurogenic tumor can be differentiated by its location, typical shape, and heterogeneous hypoenhancement.

The main limitations of our study are the small number of enrolled cases and its retrospective nature, inevitable given the rare occurrence of glomangiopericytoma in the head and neck. We have attempted to overcome these limitations by performing a systematic review, and the results are in accord with ours. We were able to include 3 cases with advanced MR imaging techniques, and these techniques may be of assistance in generating a more focused differential diagnosis. Tissue sampling remains the standard, however. We believe that our results could provide an insight into further investigation of glomangiopericytoma with advanced MR imaging techniques.

CONCLUSIONS

Our case series and the systematic review revealed that glomangiopericytoma is a well-defined lobulated avidly-enhancing soft-tissue mass with erosive bony remodeling usually occurring in

the sinonasal cavity. It typically shows hyperintense signal on T2WI with vascular signal voids, a high mean ADC value, and a wash-in and washout pattern on DCE-MR imaging. Although the CT findings are nonspecific, typical MR imaging findings, including the ADC value and DCE-MR imaging pattern, can be helpful for differentiating glomangiopericytomas from other hypervascular tumors in the head and neck, especially in the sinonasal cavity.

Disclosures: Jung Hwan Baek—UNRELATED: Consultancy: radiofrequency ablation, Comments: consultant of 2 radiofrequency companies, StarMed and RF Medical since 2017.

REFERENCES

1. Stelow EB, Bishop JA. **Update from the 4th Edition of the World Health Organization Classification of Head and Neck Tumours: Tumors of the Nasal Cavity, Paranasal Sinuses and Skull Base.** *Head Neck Pathol* 2017;11:3–15 CrossRef Medline
2. Compagno J, Hyams VJ. **Hemangiopericytoma-like intranasal tumors: a clinicopathologic study of 23 cases.** *Am J Clin Pathol* 1976;66:672–83 CrossRef Medline
3. Marusic Z, Billings SD. **Histopathology of spindle cell vascular tumors.** *Surg Pathol Clin* 2017;10:345–66 CrossRef Medline
4. Thompson LD, Miettinen M, Wenig BM. **Sinonasal-type hemangiopericytoma: a clinicopathologic and immunophenotypic analysis of 104 cases showing perivascular myoid differentiation.** *Am J Surg Pathol* 2003;27:737–49 CrossRef Medline
5. Choi YJ, Lee JH, Kim HO, et al. **Histogram analysis of apparent diffusion coefficients for occult tonsil cancer in patients with cervical nodal metastasis from an unknown primary site at presentation.** *Radiology* 2016;278:146–55 CrossRef Medline
6. Lee JY, Cheng KL, Lee JH, et al. **Detection of local recurrence in patients with head and neck squamous cell carcinoma using voxel-based color maps of initial and final area under the curve values derived from DCE-MRI.** *AJNR Am J Neuroradiol* 2019;40:1392–1401 CrossRef Medline
7. Kono M, Bandoh N, Matsuoka R, et al. **Glomangiopericytoma of the nasal cavity with CTNNB1 p.S37C mutation: a case report and literature review.** *Head Neck Pathol* 2019;13:298–303 CrossRef Medline
8. Anschuetz L, Buchwalder M, Dettmer M, et al. **A clinical and radiological approach to the management of benign mesenchymal sinonasal tumors.** *ORL J Otorhinolaryngol Relat Spec* 2017;79:131–46 CrossRef Medline
9. Psoma E, Karkos PD, Dova S, et al. **Sinonasal glomangiopericytoma treated with preoperative embolisation and endoscopic sinus surgery.** *Eccancermedscience* 2016;10:692 CrossRef Medline
10. Kim J, Jeon J, Kim DH, et al. **Glomangiopericytoma and glomus tumor of the sinonasal tract: a report of two cases with emphasis on the differential diagnosis.** *Pathol Int* 2016;66:348–50 CrossRef Medline
11. Fox DP, Helekar BS, Gallagher KK. **Laryngeal, retropharyngeal, and cervical glomangiopericytomas: a case report.** *Otolaryngol Head Neck Surg* 2016;155:1059–60 CrossRef Medline
12. Papierska L, Cwikla JB, Misiorowski W, et al. **FGF23 producing mesenchymal tumor.** *Case Rep Endocrinol* 2014;2014:492789 CrossRef Medline
13. Arpaci RB, Kara T, Vayisoğlu Y, et al. **Sinonasal glomangiopericytoma.** *J Craniofac Surg* 2012;23:1194–96 CrossRef Medline
14. Terada T, Kato T. **Sinonasal-type hemangiopericytoma of the nasal cavity and paranasal sinus.** *Int J Clin Oncol* 2012;17:169–73 CrossRef Medline
15. Conrad GR, Sinha P, Absher KJ. **FDG PET/CT findings of a glomangiopericytoma.** *Clin Nucl Med* 2011;36:462–64 CrossRef Medline

16. Taglialatela Scafati C, D'Antonio A, Taglialatela Scafati S, et al. **Glomangiopericytoma of the pterygomandibular space: an unusual case.** *Br J Oral Maxillofac Surg* 2007;45:673–75 CrossRef Medline
17. Palacios E, Restrepo S, Mastrogiovanni L, et al. **Sinonasal hemangiopericytomas: clinicopathologic and imaging findings.** *Ear Nose Throat J* 2005;84:99–102 CrossRef Medline
18. Gencturk M, Ozturk K, Caicedo-Granados E, et al. **Application of diffusion-weighted MR imaging with ADC measurement for distinguishing between the histopathological types of sinonasal neoplasms.** *Clin Imaging* 2019;55:76–82 CrossRef Medline
19. Thompson LD. **Sinonasal tract glomangiopericytoma (hemangiopericytoma).** *Ear Nose Throat J* 2004;83:807 Medline
20. Anzai T, Saito T, Tsuyama S, et al. **A case of glomangiopericytoma at the nasal septum.** *Head Neck Pathol* 2018;12:572–75 CrossRef Medline
21. Ganly I, Patel SG, Stambuk HE, et al. **Solitary fibrous tumors of the head and neck: a clinicopathologic and radiologic review.** *Arch Otolaryngol Head Neck Surg* 2006;132:517–25 CrossRef Medline
22. Yang BT, Song ZL, Wang YZ, et al. **Solitary fibrous tumor of the sinonasal cavity: CT and MR imaging findings.** *AJNR Am J Neuroradiol* 2013;34:1248–51 CrossRef Medline
23. Higashi K, Nakaya K, Watanabe M, et al. **Glomangiopericytoma of the nasal cavity.** *Auris Nasus Larynx* 2011;38:415–17 CrossRef Medline
24. Yang BT, Li SP, Wang YZ, et al. **Routine and dynamic MR imaging study of lobular capillary hemangioma of the nasal cavity with comparison to inverting papilloma.** *AJNR Am J Neuroradiol* 2013;34:2202–07 CrossRef Medline
25. Kim JH, Park SW, Kim SC, et al. **Computed tomography and magnetic resonance imaging findings of nasal cavity hemangiomas according to histological type.** *Korean J Radiol* 2015;16:566–74 CrossRef Medline

Predicting Ischemic Risk Using Blood Oxygen Level–Dependent MRI in Children with Moyamoya

 N. Dlamini,  M. Slim,  F. Kirkham,  M. Shroff,  P. Dirks,  M. Moharir,  D. MacGregor,  A. Robertson,  G. deVeber, and  W. Logan

ABSTRACT

BACKGROUND AND PURPOSE: Moyamoya is a progressive steno-occlusive arteriopathy. MR imaging assessment of cerebrovascular reactivity can be performed by measuring the blood oxygen level–dependent cerebrovascular reactivity response to vasoactive stimuli. Our objective was to determine whether negative blood oxygen level–dependent cerebrovascular reactivity status is predictive of ischemic events in childhood moyamoya.

MATERIALS AND METHODS: We conducted a retrospective study of a consecutive cohort of children with moyamoya who underwent assessment of blood oxygen level–dependent cerebrovascular reactivity. The charts of patients with written informed consent were reviewed for the occurrence of arterial ischemic stroke, transient ischemic attack, or silent infarcts. We used logistic regression to calculate the OR and 95% CI for ischemic events based on steal status. Hazard ratios for ischemic events based on age at blood oxygen level–dependent cerebrovascular reactivity imaging, sex, and moyamoya etiology were calculated using Cox hazards models.

RESULTS: Thirty-seven children (21 female; median age, 10.7 years; interquartile range, 7.5–14.7 years) were followed for a median of 28.8 months (interquartile range, 13.7–84.1 months). Eleven (30%) had ischemic events, 82% of which were TIA without infarcts. Steal was present in 15 of 16 (93.8%) hemispheres in which ischemic events occurred versus 25 of 58 (43.1%) ischemic-free hemispheres (OR = 19.8; 95% CI, 2.5–160; $P = .005$). Children with idiopathic moyamoya were at significantly greater risk of ischemic events (hazard ratio, 3.7; 95% CI, 1.1–12.8; $P = .037$).

CONCLUSIONS: Our study demonstrates that idiopathic moyamoya and the presence of steal are independently associated with ischemic events. The use of blood oxygen level–dependent cerebrovascular reactivity could potentially assist in the selection of patients for revascularization surgery and the direction of therapy in children with moyamoya.

ABBREVIATIONS: BOLD = blood oxygen level–dependent; CVR = cerebrovascular reactivity; HR = hazard ratio; IQR = interquartile range

Moyamoya is a chronic progressive steno-occlusive arteriopathy, which typically involves the distal internal carotid artery and/or the proximal anterior cerebral and middle cerebral arteries of the circle of Willis, leading to the development of a compensatory vascular network at the base of the brain.^{1,2} In childhood, moyamoya is associated with a greater risk of recurrent ischemic

strokes and poor neurologic outcomes, which result in a substantial and sustained economic burden to the family and society.^{3,4} There is no cure for the disease, and medical therapeutic strategies are thus far inadequate at preventing the adverse outcomes associated with moyamoya. Surgical revascularization, the mainstay of treatment, has been shown to be effective in improving cerebral blood flow and reducing ischemic risk in children with moyamoya.⁵ However, multiple factors need to be considered when determining the appropriateness and timing of surgical interventions, including disease severity, risk of ischemic events, perioperative risk, technical aspects of vascular surgery, and anesthesia risk.^{6–9}

Cerebrovascular reactivity (CVR) is defined as the measurement of vessel reactivity in response to a vasoactive stimulus such as carbon dioxide. It is an important marker of cerebrovascular reserve and autoregulation through which cerebral blood flow is maintained under physiologic conditions of stress such as hypotension and anemia.^{10–12}

Received July 5, 2019; accepted after revision October 2.

From the Division of Neurology (N.D., M. Slim, M.M., D.M., A.R., G.d.V., W.L.), Department of Pediatrics, and Departments of Diagnostic Imaging (M. Shroff) and Surgery (P.D.), The Hospital for Sick Children, Toronto, Ontario, Canada; and Developmental Neurosciences Unit and Biomedical Research Centre (F.K.), University College London Great Ormond Street Institute of Child Health, London, UK.

This study was funded by the Auxilium Foundation.

G. deVeber and W. Logan are Co-Senior Authors.

Please address correspondence to Nomazulu Dlamini, MD, MSc, PhD, Division of Neurology, The Hospital for Sick Children, 555 University Ave, Toronto, ON, Canada M5G 1X8; e-mail: nomazulu.dlamini@sickkids.ca
<http://dx.doi.org/10.3174/ajnr.A6324>

Harnessing the paramagnetic properties of deoxygenated hemoglobin, blood oxygen level-dependent (BOLD) MR imaging can be used to perform in vivo assessment of cerebrovascular reactivity and reserve by measuring the change in BOLD-MR imaging signal in response to a hypercapnic-vasoactive challenge.¹³⁻¹⁵ Negative BOLD-CVR, referred to as “vascular steal”, occurs when blood flow redistributes away from the corresponding vascular territory during the global vasodilatory stimulus. Impairment of CVR and negative BOLD reactivity or steal in adults with arteriopathy are independent predictors of ischemic risk, including stroke and TIA.¹⁶⁻¹⁸ Hence, the demonstration of steal is used to identify adult patients with moyamoya who might benefit from revascularization surgery.^{19,20} However, any association between steal and ischemic risk has not been demonstrated in children. Early diagnosis of children with moyamoya before symptomatic ischemic presentation now occurs as a result of increased syndrome-specific MR imaging screening protocols. The incidence of ischemic events is reported to peak between 5 and 10 years, and the risk of recurrent ischemic events after the first ischemic presentation is high.²¹⁻²³ The need for improved risk-stratification for the direction of care forms the basis of the compelling need for a clinically useful tool for the prediction of ischemic risk in children with moyamoya. An MR imaging-based biomarker of ischemic risk using standard MR images has the potential to be such a tool and to provide a noninvasive, individualized approach to the selection of pediatric patients for revascularization surgery.

We hypothesized that negative BOLD-CVR status or steal is a predictor of ischemic risk in children with moyamoya.

MATERIALS AND METHODS

Population and Study Definitions

We conducted a retrospective study of a consecutive cohort of children with moyamoya who underwent BOLD-CVR assessment and were followed in our clinic between November 2000 and September 2017. We included children 1–18 years of age, diagnosed according to Fukui criteria and confirmed by conventional angiography.²⁴ Children with unilateral moyamoya and collaterals were included in the study. Children without a comorbid condition were diagnosed as having idiopathic moyamoya. Children with comorbid neurofibromatosis type 1, sickle cell disease, trisomy 21, other chromosomal conditions, or radiation vasculopathy were diagnosed as having moyamoya. Demographic data, clinical characteristics, and treatment modalities were reviewed for all eligible patients.

Ethics permission was obtained from the institutional research ethics board at The Hospital for Sick Children, and written informed consent was obtained from all study participants.

Study Outcomes

Our primary outcome was the occurrence or recurrence of ipsilateral ischemic events following BOLD-CVR imaging evaluation. Patient charts were reviewed for the occurrence of any of the following: arterial ischemic stroke, TIA, or silent infarcts. Arterial ischemic stroke was defined as the occurrence of a focal neurologic deficit with radiologic evidence of new focal areas of infarction on neuroimaging within a vascular territory. TIA was defined as the occurrence of transient

focal neurologic deficits lasting <24 hours, without radiologic evidence of new focal areas of infarction and which were not seizures or migraines clinically. Silent infarcts were defined as the presence of new focal areas of infarction on neuroimaging in the absence of a clinically evident focal neurologic deficit.

MR Imaging Acquisition

MR imaging was performed on a 1.5T or 3T scanner (Achieva; Philips Healthcare, Best, the Netherlands). Anatomic imaging included standard fluid-attenuated inversion recovery, diffusion-weighted imaging, and 3D time-of-flight MRA. High-resolution 3D T1-weighted structural images [160 slices; voxel size = $(0.86-1) \times (0.86-1) \times (1-2)$ mm³; FOV = 22–26 cm] were acquired for tissue classification and coregistration of the CVR maps.

Cerebrovascular Reactivity Imaging Acquisition

Vasoactive stimulation was achieved by hypercapnic challenge using breath-hold or targeted controlled delivery of carbon dioxide in children older than 7 years of age and ventilator-assisted delivery of carbon dioxide under general anesthetic in children younger than 7 years of age during CVR acquisition.^{15,25,26} CVR data were acquired using a T2*-weighted single-shot echo-planar gradient-echo sequence (25 slices; TE, 30–40 ms; TR, 2000 ms; flip angle, 90°; FOV, 22–26 cm; matrix, 64 × 64; section thickness, 5 mm; dynamics, 180–240).

Cerebrovascular Reactivity Postprocessing

Blood oxygen level-dependent MR imaging processing and the generation of CVR maps were conducted using Analysis of Functional Neuro Images (AFNI; <http://afni.nimh.nih.gov/afni/>),^{27,28} the FMRIB Software Library (FSL; <http://www.fmrib.ox.ac.uk/fsl/>),²⁹⁻³¹ and custom scripts. The first 2 volumes were dropped for scanner stabilization, and the data were section-time- and motion-corrected. The maximum displacement, which is the maximum distance for each volume from a reference volume during the registration, was calculated. The maximum distance signal was regressed from the data, and volumes with a maximum distance exceeding 1.5 mm were censored. Data were smoothed using a 7-mm full width at half maximum Gaussian kernel, normalized to a mean intensity of 10,000, and temporally filtered between 0.001 and 0.2 Hz. Patients' functional data were registered to the Montreal Neurological Institute space using each patient's high-resolution T1 image. Signal contributions from the CSF, along with the 6 motion parameters, were regressed from the data as covariates in a generalized linear model.

For CVR maps, the patient's BOLD time-series in each voxel of the brain was subjected to generalized linear model analysis using the corresponding averaged cerebellar time courses as a regressor. The regression coefficients (or the β weights) were then calculated for each voxel. Negative β weights describing an inverse relationship with the regressor are the markers of steal. CVR maps consisting of voxelwise negative and positive β weights (describing a negative and positive relationship with the regressor, respectively) were coregistered to the high-resolution T1 images in the native space for visualization.^{15,32}

Visual inspection of the BOLD-CVR maps for hemispheric negative reactivity/steal was conducted by study neurologists blinded to the clinical information (Fig 1). The interrater

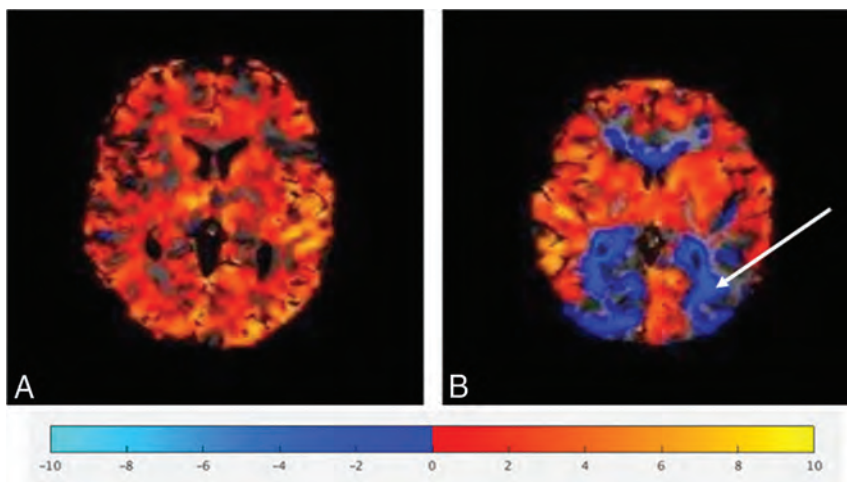


FIG 1. Representative BOLD-CVR parametric maps demonstrating normal (positive) (A) reactivity and abnormal (negative) reactivity (B, arrow).

Table 1: Baseline clinical and demographic characteristics

	Total Sample (n = 37)
Demographic characteristics	
Female (No.) (%)	21 (56.8)
Age at moyamoya diagnosis (median) (IQR, 25–75) (yr)	10 (6.3–11.8)
Age at initial CVR (median) (IQR, 25–75) (yr)	10.7 (7.5–14.7)
Time to follow-up (median) (IQR, 25–75) (mo)	20.8 (13.7–84.1)
Moyamoya classification	
Idiopathic	14 (37.8)
Syndromic	23 (62.2)
NFI	9 (24.3)
Trisomy 21/other chromosomal disorders	7 (18.9)
Sickle cell disease	5 (13.5)
Postradiation vasculopathy	2 (5.4)
Clinical presentation	
Stroke (No.) (%)	12 (32.4)
Bilateral	2 (5.4)
Right	6 (16.2)
Left	4 (10.8)
TIA (No.) (%)	8 (21.6)
Seizure (No.) (%)	3 (8)
Headaches (No.) (%)	8 (21.6)
Asymptomatic (No.) (%)	6 (16.2)
Other (No.) (%)	2 (5.4)
Radiographic findings (No.) (%)	
Parenchymal	
Not ischemic	8 (21.6)
Watershed	12 (32.4)
Deep white matter	1 (2.7)
Cortical	12 (32.4)
Cortical	3 (8.1)
Cortical ischemic and watershed	14 (37.8)
Vascular	
Moyamoya laterality (No.) (%)	
Left	8 (21.6)
Right	6 (16.2)
Bilateral	23 (62.2)
Grade of stenosis (No.) (%)	
50%–74% Occlusion	5 (13.5)
≥75% Occlusion	32 (86.5)

Note:—NFI indicates neurofibromatosis type 1.

reliability for the hemispheric scoring by visual inspection was substantial (weighted κ of 1 for the left side and 0.83 for the right side).¹⁵

Statistical Analysis

Continuous variables were presented as medians and interquartile ranges (IQRs). Qualitative variables were described using frequency distributions and proportions. Patient characteristics were compared using the Mann-Whitney *U* test or Fisher exact test, as appropriate.

The evaluation of the ischemic risk as a function of steal status was conducted per hemisphere.^{33,34} In children who had multiple BOLD-CVR assessments during the study period, the BOLD-CVR study before the occurrence of ischemic events or the end of the study follow-up was considered.

We used logistic regression to calculate the OR and 95% CI for ischemic risk based on BOLD-CVR steal status. To control for the effects of surgical interventions, we used multivariable logistic models that controlled for procedures undertaken in the corresponding hemispheres.

Hazard ratios (HRs) and the corresponding 95% CIs for ischemic events at the patient level (ie, occurring in any of 2 hemispheres) as function of age at initial BOLD-CVR imaging (dichotomized into 8 years of age and younger and older than 8 years of age),^{35,36} sex, and moyamoya etiology were calculated by using Cox proportional hazards models. The compliance with the proportional hazards assumption was assessed using the scaled Schoenfeld residuals and by visual inspection of the log (minus log) curves for the different Cox models. $P < .05$ was statistically significant. Statistical analyses were conducted using R statistical and computing software, Version 3.4.1 (<http://www.r-project.org>).

RESULTS

Population Description

Thirty-seven children (21 female; median age, 10.7 years; IQR, 7.5–14.7 years) were included in the study (Table 1). The median age at moyamoya diagnosis was 9.9 years (IQR, 6.3–11.8 years). Twelve (32%) presented with arterial ischemic stroke; 8 (22%), TIAs (without infarction); 6 (16%) were asymptomatic; 8 (21.6%) had headaches only; and 3 (8%), seizures. Twenty-eight children (76%) were treated with aspirin; 4 children were on chronic blood transfusion; 1 child had a bone marrow transplant; and another underwent radiation therapy and chemotherapy during the study period. Twenty-one children had revascularization surgery before (7; 19%) or following (14; 38%) enrollment and before the study end point.

Steal Status and Baseline Clinical and Demographic Characteristics

Twenty-five children had steal in at least 1 hemisphere on BOLD-CVR imaging. Thirty-seven of 74 hemispheres had steal:

Table 2: Comparison of clinical and demographic characteristics based on steal status^a and ischemic events

	Steal Status ^a			Ischemic Events		
	No Steal (n = 12)	Steal (n = 25)	P Value	No (n = 26)	Yes (n = 11)	P Value
Age at baseline CVR (median) (IQR, 25–75) (yr)	9.3 (5.6–14.5)	10.8 (8.3–15)	.28	10.9 (8.3–15)	10.3 (7.2–12.5)	.44
Female (No.) (%)	5 (41.7)	16 (64)	.29	14 (53.9)	7 (63.6)	.72
Moyamoya classification (No.) (%)			.69			.06
Idiopathic	4 (33.3)	10 (40)		7 (26.9)	7 (63.6)	
Syndromic ^b	8 (66.7)	15 (60)		19 (73.1)	4 (36.4)	
NFI	2 (16.7)	7 (28)		7 (26.9)	2 (18.2)	
Trisomy 21/other chromosomal disorders	3 (25)	4 (16)		6 (23.1)	1 (9.1)	
Sickle cell disease	1 (8.3)	4 (16)		4 (15.4)	1 (9.1)	
Postradiation vasculopathy	2 (16.7)	0		2 (7.7)	0	
Stroke (No.) (%)	4 (33.3)	8 (32)	1	11 (42.3)	1 (9.1)	.06
TIA (No.) (%)	2 (16.7)	6 (24)	1	5 (19.2)	3 (27.3)	.67
Seizure (No.) (%)	2 (16.7)	1 (4)	.24	2 (7.7)	1 (9.1)	1
Headaches (No.) (%)	3 (25)	5 (20)	1	6 (23.1)	2 (18.2)	1
Asymptomatic (No.) (%)	2 (16.7)	4 (16)	1	3 (11.5)	3 (27.3)	.33
Others (No.) (%)	0	2 (8.3)	.54	0	2 (18.2)	.08
Moyamoya laterality (No.) (%)			.77			.78
Left	3 (25)	5 (20)		6 (23.1)	2 (18.2)	
Right	1 (8.3)	5 (20)		5 (19.2)	1 (9.1)	
Bilateral	8 (66.7)	15 (60)		15 (57.7)	8 (72.7)	

Note:—NFI indicates neurofibromatosis type 1.

^a Steal status before ischemic event occurrence or the end of follow-up.

^b Comorbidities falling under syndromic moyamoya are shown for informative purposes only and were not included in the inferential analysis.

17 (23%) left and 20 (27%) right hemispheres. Comparisons of clinical and demographic characteristics of patients with steal in at least 1 hemisphere versus those with no steal are summarized in Table 2. Patients with steal were more likely to experience ischemic events compared with those with no steal (36% versus 16.7%). They were more likely to be female (64% versus 41.7%) and be diagnosed with idiopathic moyamoya (40% versus 33.3%) (Table 2).

Predictors of Ischemic Events

During a median follow-up of 28.8 months (IQR, 13.7–84.1 months), ischemic events were documented in 11 children: 1 with arterial ischemic stroke, 9 with TIA without infarcts, and 1 with asymptomatic silent infarction. Five children had bilateral, 4 had left-sided, and 2 had right-sided ischemic events. No significant differences in clinical and demographic characteristics were found between children who had ischemic events and those who did not (Table 2).

Between-group comparisons of hemispheric steal status by ipsilateral hemispheric ischemic event status demonstrated the presence of steal in 15 of 16 (93.8%) hemispheres in which ischemic events occurred versus 25 of 58 (43.1%) ischemic-free hemispheres (OR = 19.8; 95% CI, 2.5–160; $P = .005$). When adjusted for surgical interventions in the corresponding hemisphere, the odds of ischemic events remained significantly higher among hemispheres with steal (OR = 19.9; 95% CI, 2.45–161; $P = .005$).

Univariable analysis using the Cox proportional hazards model demonstrated that children with idiopathic moyamoya were at significantly greater risk of ischemic events (HR = 3.71; 95% CI, 1.1–12.8; $P = .03$) (Fig 2). Age as a continuous variable was not predictive of ischemic events. Older age (older than 8 years) and male sex were suggestive of a lower risk of ischemic events, though statistical significance was not reached (Fig 2). On controlling for age and sex, the association of ischemic risk with

idiopathic moyamoya remained statistically significant (HR = 3.95; 95% CI, 1.12–13.9; $P = .03$). There were no violations of the proportional hazards assumption in any of these models.

DISCUSSION

Our study suggests an association between BOLD-CVR steal status, idiopathic moyamoya and an increased risk of ischemic events in childhood moyamoya. Almost two-thirds of the children with moyamoya had steal. Children with steal were more likely to be female, diagnosed with idiopathic moyamoya, and experience ischemic events. The presence of steal was associated with an increased risk of ischemic events in the corresponding hemisphere, which is similar to findings in studies in adults with arteriopathy.^{17,18} To our knowledge, this is the first study to investigate the association between steal status and ischemic risk in children with arteriopathy.

In a large single-center study of asymptomatic children with syndromic moyamoya, radiographic progression occurred in most and typically heralded clinical progression.³⁷ Children with sickle cell disease had a higher risk of radiographic and clinical progression than children with neurofibromatosis type 1, and those with unilateral moyamoya had the lowest overall rate of progression. In our study, there were no differences in clinical characteristics between the steal and no-steal or the ischemic and no ischemic event groups, highlighting the limitations of current clinical approaches for the assessment of ischemic risk in this population. Our study showed that children with steal had significantly higher ipsilateral ischemic risk. The odds for ischemic events remained significantly elevated for children with steal after controlling for revascularization surgery conducted in the respective hemispheres.

The current understanding of the natural history and stroke risk profile of idiopathic moyamoya is mostly derived from studies in Asian populations, which describe a bimodal stroke-risk profile of ischemic stroke typically occurring in

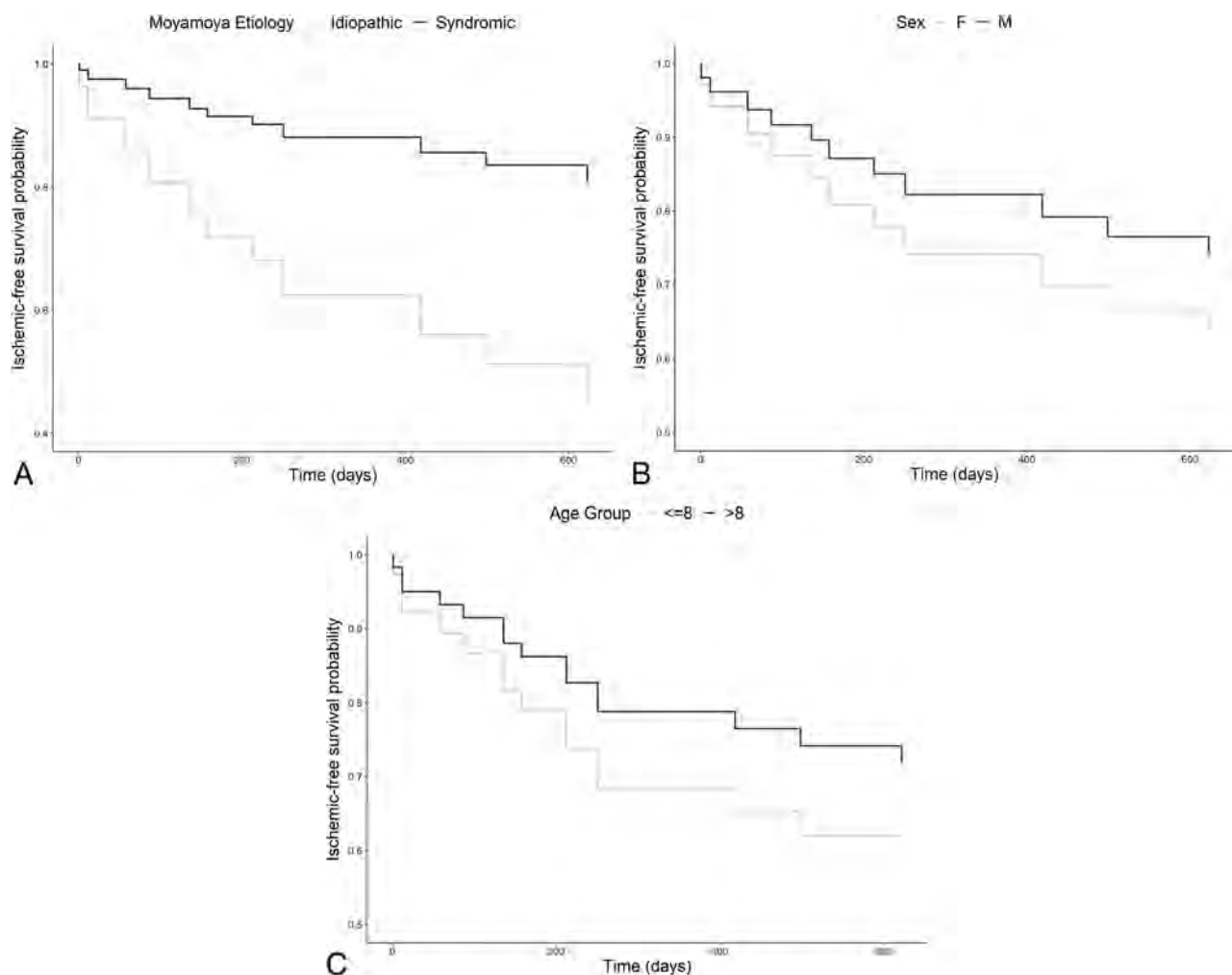


FIG 2. Direct adjusted survival curves for ischemic-free survival as a function of the moyamoya comorbidities (A) (HR for idiopathic moyamoya: 3.71; 95% CI, 1.1–12.8; $P = .03$), sex (B) (HR for males: 0.65; 95% CI, 0.19–2.23; $P = .49$), and age group (C) (HR for older than 8 years: 0.62; 95% CI, 0.18–2.1; $P = .44$). Age as a continuous variable was not predictive of ischemic events. Age is represented in years.

the first decade of childhood and hemorrhagic syndromes dominating in adulthood.²⁴ In a recently published cross-sectional study of a large international cohort of children with predominantly syndromic moyamoya, older age was also linked to a lower ischemic risk.³⁸ Similarly, in our study, older children had lower ischemic risk, but these results did not reach statistical significance. While no significant differences in the ischemic risk between patients with idiopathic or syndromic moyamoya were reported, our longitudinal analysis using Cox regression models demonstrated significantly higher ischemic risk associated with a diagnosis of idiopathic moyamoya.

Hence, BOLD-CVR studies using standard T2* gradient-echo sequences could potentially allow quantifiable clinical assessment of ischemic risk and the subsequent prediction of future ischemic events in children with moyamoya. The clinical correlates of BOLD-CVR-detected steal are pertinent to and important for an improved individualized model of care for children with moyamoya.

Limitations of our study include the small sample size, limiting our statistical analysis.³⁹ However, to our knowledge,

this is the largest single-center North American study examining a functional MR imaging technique for the prediction of ischemic risk in childhood moyamoya. BOLD-CVR studies were systematically conducted at predetermined time points according to institutional practice guidelines in most study participants. Consequently, we were unable to determine the temporal relationship between subclinical ischemic MR imaging changes and changes in steal status. However, this issue reflects real-world clinical practice. With the wider acceptance and implementation of BOLD-CVR studies in the longitudinal follow-up of children with moyamoya, future directions will include qualitative and quantitative predictive analyses of a larger prospective cohort.^{15,40} However, the purpose of this study was to evaluate whether qualitative analysis of BOLD-CVR maps could be used as a biomarker of ischemic risk in childhood moyamoya and thus be translatable for clinical use.

CONCLUSIONS

Our study demonstrated that the presence of steal was associated with significantly greater odds of developing ipsilateral ischemic

events. Furthermore, idiopathic moyamoya etiology was predictive of ischemic events. The use of hypercapnic challenge BOLD-CVR in combination with other clinical predictors in children with moyamoya represents a promising model for the clinical assessment of ischemic risk and patient selection for revascularization surgery. Larger prospective clinical studies are warranted to adequately elucidate the clinical utility of BOLD-CVR in predicting ischemic risk in this high-risk population.

Disclosures: Fenella Kirkham—UNRELATED: Consultancy: Shire Pharmaceuticals Group, Eisai, BIAL, Pharmaceuticals, Comments: for work on epilepsy; Employment: University College London Great Ormond Street Institute of Child Health Institute of Child Health, University of Southampton; Grants/Grants Pending: Action Medical Research (UK charity), Comments: for a trial of montelukast in sickle cell disease*; Royalties: MacKeith press. *Money paid to the institution.

REFERENCES

- Suzuki J, Takaku A. Cerebrovascular “Moyamoya” disease: disease showing abnormal net-like vessels in base of brain. *Arch Neurol* 1969;20:288–99 CrossRef Medline
- Fukui M, Kono S, Sueishi K, et al. Moyamoya disease. *Neuropathology* 2000;20(Suppl):S61–64 Medline
- Amlie-Lefond C, Bernard TJ, Sebire G, et al. Predictors of cerebral arteriopathy in children with arterial ischemic stroke: results of the International Pediatric Stroke Study. *Circulation* 2009;119:1417–23 CrossRef Medline
- Gardner MA, Hills NK, Sidney S, et al. The 5-year direct medical cost of neonatal and childhood stroke in a population-based cohort. *Neurology* 2010;74:372–78 CrossRef Medline
- Scott RM, Smith ER. Moyamoya disease and Moyamoya syndrome. *N Engl J Med* 2009;360:1226–37 CrossRef Medline
- Soriano SG, Sethna NF, Scott RM. Anesthetic management of children with Moyamoya syndrome. *Anesth Analg* 1993;77:1066–70 CrossRef Medline
- Imaizumi T, Hayashi K, Saito K, et al. Long-term outcomes of pediatric Moyamoya disease monitored to adulthood. *Pediatr Neurol* 1998;18:321–25 CrossRef Medline
- Kim SK, Seol HJ, Cho BK, et al. Moyamoya disease among young patients: its aggressive clinical course and the role of active surgical treatment. *Neurosurgery* 2004;54:840–44; discussion 44–46 Medline
- Heyer GL, Dowling MM, Licht DJ, et al. The cerebral vasculopathy of PHACES syndrome. *Stroke* 2008;39:308–16 CrossRef Medline
- Harper AM, Glass HI. Effect of alterations in the arterial carbon dioxide tension on the blood flow through the cerebral cortex at normal and low arterial blood pressures. *J Neurol Neurosurg Psychiatry* 1965;28:449–52 CrossRef Medline
- Kety SS, Schmidt CF. The effects of altered arterial tensions of carbon dioxide and oxygen on cerebral blood flow and cerebral oxygen consumption of normal young men. *J Clin Invest* 1948;27:484–92 CrossRef Medline
- Prohovnik I, Hurler-Jensen A, Adams R, et al. Hemodynamic etiology of elevated flow velocity and stroke in sickle-cell disease. *J Cereb Blood Flow Metab* 2009;29:803–10 CrossRef Medline
- Spano VR, Mandell DM, Poulblanc J, et al. CO₂ blood oxygen level-dependent MR mapping of cerebrovascular reserve in a clinical population: safety, tolerability, and technical feasibility. *Radiology* 2013;266:592–98 CrossRef Medline
- Pillai JJ, Mikulis DJ. Cerebrovascular reactivity mapping: an evolving standard for clinical functional imaging. *AJNR Am J Neuroradiol* 2015;36:7–13 CrossRef Medline
- Dlamini N, Shah-Basak P, Leung J, et al. Breath-hold blood oxygen level-dependent MRI: a tool for the assessment of cerebrovascular reserve in children with Moyamoya disease. *AJNR Am J Neuroradiol* 2018;39:1717–23 CrossRef Medline
- Markus H, Cullinane M. Severely impaired cerebrovascular reactivity predicts stroke and TIA risk in patients with carotid artery stenosis and occlusion. *Brain* 2001;124:457–67 CrossRef Medline
- Gupta A, Chazen JL, Hartman M, et al. Cerebrovascular reserve and stroke risk in patients with carotid stenosis or occlusion: a systematic review and meta-analysis. *Stroke* 2012;43:2884–91 CrossRef Medline
- Reinhard M, Schwarzer G, Briel M, et al. Cerebrovascular reactivity predicts stroke in high-grade carotid artery disease. *Neurology* 2014;83:1424–31 CrossRef Medline
- Schubert GA, Weinmann C, Seiz M, et al. Cerebrovascular insufficiency as the criterion for revascularization procedures in selected patients: a correlation study of xenon contrast-enhanced CT and PWI. *Neurosurg Rev* 2009;32:29–35; discussion 35–36 Medline
- Fierstra J, Maclean DB, Fisher JA, et al. Surgical revascularization reverses cerebral cortical thinning in patients with severe cerebrovascular steno-occlusive disease. *Stroke* 2011;42:1631–37 CrossRef Medline
- Smith ER, Scott RM. Moyamoya: epidemiology, presentation, and diagnosis. *Neurosurg Clin N Am* 2010;21:543–51 CrossRef Medline
- Rea D, Brandsema JF, Armstrong D, et al. Cerebral arteriopathy in children with neurofibromatosis type 1. *Pediatrics* 2009;124:e476–83 CrossRef Medline
- Adams RJ, McKie VC, Hsu L, et al. Prevention of a first stroke by transfusions in children with sickle cell anemia and abnormal results on transcranial Doppler ultrasonography. *N Engl J Med* 1998;339:5–11 CrossRef Medline
- Fukui M. Guidelines for the diagnosis and treatment of spontaneous occlusion of the circle of Willis (‘Moyamoya’ disease): Research Committee on Spontaneous Occlusion of the Circle of Willis (Moyamoya disease) of the Ministry of Health and Welfare, Japan. *Clin Neurol Neurosurg* 1997;99:S238–40 CrossRef Medline
- Slessarev M, Han J, Mardimae A, et al. Prospective targeting and control of end-tidal CO₂ and O₂ concentrations. *J Physiol* 2007;581:1207–19 CrossRef Medline
- Thomason ME, Burrows BE, Gabrieli JD, et al. Breath holding reveals differences in fMRI BOLD signal in children and adults. *Neuroimage* 2005;25:824–37 CrossRef Medline
- Cox RW, Hyde JS. Software tools for analysis and visualization of fMRI data. *NMR Biomed* 1997;10:171–78 Medline
- Gold S, Christian B, Arndt S, et al. Functional MRI statistical software packages: a comparative analysis. *Hum Brain Mapp* 1998;6:73–84 CrossRef Medline
- Jenkinson M, Beckmann CF, Behrens TE, et al. FSL. *Neuroimage* 2012;62:782–90 CrossRef Medline
- Smith SM, Jenkinson M, Woolrich MW, et al. Advances in functional and structural MR image analysis and implementation as FSL. *Neuroimage* 2004;23(Suppl 1):S208–19 CrossRef Medline
- Woolrich MW, Jbabdi S, Patenaude B, et al. Bayesian analysis of neuroimaging data in FSL. *Neuroimage* 2009;45:S173–86 CrossRef Medline
- Heyn C, Poulblanc J, Crawley A, et al. Quantification of cerebrovascular reactivity by blood oxygen level-dependent MR imaging and correlation with conventional angiography in patients with Moyamoya disease. *AJNR Am J Neuroradiol* 2010;31:862–67 CrossRef Medline
- Hallemeier CL, Rich KM, Grubb RL Jr, et al. Clinical features and outcome in North American adults with Moyamoya phenomenon. *Stroke* 2006;37:1490–96 CrossRef Medline
- Mikulis DJ, Krolczyk G, Desal H, et al. Preoperative and postoperative mapping of cerebrovascular reactivity in Moyamoya disease by using blood oxygen level-dependent magnetic resonance imaging. *J Neurosurg* 2005;103:347–55 CrossRef Medline
- Biagi L, Abbruzzese A, Bianchi MC, et al. Age dependence of cerebral perfusion assessed by magnetic resonance continuous arterial spin-labeling. *J Magn Reson Imaging* 2007;25:696–702 CrossRef Medline
- Kennedy C, Sokoloff L. An adaptation of the nitrous oxide method to the study of the cerebral circulation in children: normal values for cerebral blood flow and cerebral metabolic rate in childhood. *J Clin Invest* 1957;36:1130–37 CrossRef Medline

37. Lin N, Baird L, Koss M, et al. **Discovery of asymptomatic moyamoya arteriopathy in pediatric syndromic populations: radiographic and clinical progression.** *Neurosurg Focus* 2011;31:E6 CrossRef Medline
38. Lee S, Rivkin MJ, Kirton A, et al. **Moyamoya disease in children: results from the International Pediatric Stroke Study.** *J Child Neurol* 2017;32:924–29 CrossRef Medline
39. Vittinghoff E, McCulloch CE. **Relaxing the rule of ten events per variable in logistic and Cox regression.** *Am J Epidemiol* 2007;165:710–18 CrossRef Medline
40. Han JS, Mikulis DJ, Mardimae A, et al. **Measurement of cerebrovascular reactivity in pediatric patients with cerebral vasculopathy using blood oxygen level-dependent MRI.** *Stroke* 2011;42:1261–69 CrossRef Medline

Acute Cortical Lesions in MELAS Syndrome: Anatomic Distribution, Symmetry, and Evolution

 K.D. Bhatia,  P. Krishnan,  H. Kortman,  J. Klostranec, and  T. Krings



ABSTRACT

BACKGROUND AND PURPOSE: Mitochondrial encephalomyopathy with lactic acidosis and stroke-like episodes (MELAS) syndrome is a rare mitochondrial disorder affecting children and young adults. Stroke-like episodes are often associated with acute cortical lesions in the posterior cerebral cortex and are classically described as asymmetric and transient. In this study we assessed the anatomic distribution of acute cortical lesions, the incidence of symmetry, and the temporal evolution of lesions.

MATERIALS AND METHODS: This was a retrospective cohort study of patients who had a confirmed genetic diagnosis of a pathogenic variant associated with MELAS and MR imaging performed at our center (2006–2018). Each MR imaging study was assessed for new lesions using T1, T2, FLAIR, DWI, ADC, and SWI. The anatomic location, symmetry, and temporal evolution of lesions were analyzed.

RESULTS: Eight patients with the same pathogenic variant of MELAS (MT-TL1 m.3243A>G) with 31 MR imaging studies were included. Forty-one new lesions were identified in 17 of the studies (5 deep, 36 cortical). Cortical lesions most commonly affected the primary visual cortex, the middle-third of the primary somatosensory cortex, and the primary auditory cortex. Thirty of 36 cortical lesions had acute cortical diffusion restriction, of which 21 developed cortical laminar necrosis on subacute imaging. Six of 11 studies with multiple lesions showed symmetric cortical involvement.

CONCLUSIONS: Acute cortical lesions in MELAS most commonly affect the primary visual, somatosensory, and auditory cortices, all regions of high neuronal density and metabolic demand. The most common pattern of temporal evolution is acute cortical diffusion restriction with subacute cortical laminar necrosis and chronic volume loss. Symmetric involvement is more common than previously described.

ABBREVIATIONS: BA = Brodmann area; MELAS = mitochondrial encephalomyopathy with lactic acidosis and stroke-like episodes

Mitochondrial encephalomyopathy with lactic acidosis and stroke-like episodes (MELAS) syndrome is a rare mitochondrial disorder affecting children and young adults. MELAS typically presents between 2 and 40 years of age with stroke-like episodes (classically acute hemiparesis, hemianopia, or cortical blindness), seizures, recurrent headaches, or muscle weakness and can progress with multifocal cerebral atrophy into dementia.^{1–3} MR imaging is helpful in establishing the diagnosis through

demonstration of cortical lesions of varying ages that do not conform to typical vascular distributions.^{4,5}

Two established sets of clinical diagnostic criteria exist for the syndrome (Hirano et al,⁶ 1992, and Yatsuga et al,¹ 2012), with the latter taking into account developments in genetic diagnoses (On-line Table 1). While at least 15 different mitochondrial mutations have been associated with MELAS, a single base substitution mutation of adenine for guanine at nucleotide pair 3243 of the mitochondrial DNA molecule (MT-TL1 m.3243A>G pathogenic variant) is present in approximately 80% of cases.^{2,7} Phenotypic expression of this genotype is variable and dependent on heteroplasmy of mitochondrial DNA, which can influence the age of presentation and disease burden.^{8,9} Elevated lactate and pyruvate levels are often found on blood and CSF analysis, and muscle biopsy typically demonstrates ragged-red fibers and strongly succinate dehydrogenase–reactive vessels.^{1,2,10}

Typical MR imaging findings in an acute stroke-like episode of MELAS include gyral swelling,^{4,5} gyriform cortical diffusion restriction (previously thought not to occur in MELAS but

Received July 5, 2019; accepted after revision October 2.

From the Division of Neuroradiology (K.D.B., H.K., J.K., T.K.), Joint Department of Medical Imaging, Toronto Western Hospital, Toronto, Ontario, Canada; and Department of Diagnostic Imaging (P.K.), Hospital for Sick Children, Toronto, Ontario, Canada.

Please address correspondence to Kartik Dev Bhatia, MD, Division of Neuroradiology, Level 3, Toronto Western Hospital, 399 Bathurst St, Toronto, M5T 2S8, ON, Canada; e-mail: Kartik.bhatia@uhn.ca



Indicates article with supplemental on-line tables.

<http://dx.doi.org/10.3174/ajnr.A6325>

Table 1: Genetic testing results and clinical presentation

Patient No.	Sex	Age ^a (yr)	No. of MR Imaging Studies Available	Genetic Testing Results	Clinical Presentation: First Available MR Imaging
1 ^b	Female	20	2	MT-TL1 m.3243A>G	Stroke-like episode Right facial numbness
2 ^b	Female	27	1	MT-TL1 m.3243A>G Heteroplasmy 21%	Asymptomatic Screening MRI after sibling diagnosed
3	Male	56	1	MT-TL1 m.3243A>G	Follow-up study Childhood diagnosis
4	Female	23	10	MT-TL1 m.3243A>G	Stroke-like episode Right hemiparesis followed 1 week later by partial status epilepticus
5	Female	32	2	MT-TL1 m.3243A>G	Follow-up study Childhood diagnosis
6	Female	18	8	MT-TL1 m.3243A>G	Seizure Left upper limb paresthesia with secondary generalization
7	Male	26	6	MT-TL1 m.3243A>G	Encephalopathy Confusion and headaches
8	Female	40	1	MT-TL1 m.3243A>G	Stroke-like episode Right homonymous hemianopia

Note:—MT-TL1 m.3243A>G indicates a substitution point mutation of adenine for guanine at nucleotide pair 3243 in the *MT-TL1* mitochondrial DNA sequence (associated with 80% of all MELAS cases).

^a Age at time of first MR imaging available for review.

^b Siblings.

increasingly recognized in early imaging),^{10–13} subcortical white matter T2 FLAIR hyperintensity with elevated ADC values,^{10,11} and elevated parenchymal lactate in both acutely affected and nonaffected brain regions on MR spectroscopy.^{4,14} Lesions frequently spread to the cortex of adjacent gyri with time in a migratory fashion, resulting in large regions of cortical involvement that cross the boundaries of arterial vascular territories, often associated with seizures.^{10,15,16} In the subacute phase, cortical lesions may develop T2 hypointensity (“black toenail sign”) and T1 gyriform hyperintensity, in keeping with cortical laminar necrosis.^{17–19} In the chronic stage, gyral infarcts evolve into areas of encephalomalacia, volume loss, and progressive multifocal cerebral and cerebellar atrophy, with associated cognitive decline.³ Symmetric basal ganglia calcifications have also been described.²⁰

The anatomic distribution of acute lesions is typically in the occipital, parietal, and posterior temporal lobes as well as the cerebellar hemispheres,^{1,5,20} though involvement of the lateral temporal cortex, mesial temporal lobes, and posterior frontal cortex has been described.^{19,21,22} Classic involvement of the pericalcarine visual cortex in the medial occipital lobes is associated with episodes of hemianopia or cortical blindness.^{1,23} Cortical involvement has typically been described as asymmetric^{4–6,17}; however, cases with symmetric involvement are increasingly recognized,^{19,24} and the incidence of symmetric involvement is unknown.

In this study, we aimed to assess, in detail, the anatomic distribution of acute cortical lesions in MELAS, the incidence of symmetric involvement, and the temporal evolution of lesions.

MATERIALS AND METHODS

Ethics approval for this study was granted by the University Health Network Research Ethics Board (approval No. 13–6081). This was a retrospective cohort study of patients meeting the following inclusion criteria: 1) confirmed genetic diagnosis of a

pathogenic variant associated with MELAS, and 2) MR imaging performed at our center between 2006 and 2018.

The following data points were collected from the electronic patient records: sex, age in years at the time of first MR imaging at University Health Network, Toronto, clinical presentation for each MR imaging study performed, and results of mitochondrial DNA genetic testing. Imaging was initially assessed by a fellowship-trained diagnostic neuroradiologist (P.K.), and the findings were then confirmed with independent assessment by a fellowship-trained diagnostic and interventional neuroradiologist (K.D.B.). Disagreements were resolved by a senior reviewer (T.K.).

Each available MR imaging study (all performed on the same 3T machine, which has undergone multiple hardware and software upgrades during this 12-year period) was assessed for new cortical or deep parenchymal lesions, defined as a T2 FLAIR focal hyperintensity affecting the cortex/foia and/or juxtacortical white matter (cortical lesion) or the deep parenchymal structures and not present on the prior study (if available), and excluding cases of spread from contiguous gyri affected on the previous study. Sequence-specific imaging characteristics of each new lesion were assessed on T1, T2, FLAIR, DWI (*b* = 1000), ADC, SWI, MR spectroscopy, and, when available, gadolinium-enhanced T1 imaging. Sequence acquisition protocols have been refined on multiple occasions within the past decade and, thus, were not uniform.

The anatomic location of each lesion was identified (On-line Table 2 has a full list of brain locations assessed), and the presence of symmetric acute cortical lesions was assessed (involving symmetric gyri or cortical regions). The presence of superficial cortical T2 sparing (involvement of the middle/deep layers of the cortex only) was noted. When serial imaging was available, the evolution of lesion DWI, ADC, and T2 signal was assessed as was the presence of old infarcts and volume loss. Lesion evolution was compared between lesions that demonstrated low ADC versus normal/high ADC values on initial imaging.

Table 2: MR imaging characteristics and temporal evolution of new lesions in MELAS

Sequence	Intensity	No. of Lesions: Deep	No. of Lesions: Cortical
Acute (first week)		Total: 5	Total: 36
T1 (spin-echo)	↓	0	24
T2 (spin-echo)	↑	5	36
T2 sparing of superficial cortex			23
T2 FLAIR	↑	5	36
DWI (<i>b</i> = 1000)	↑	0	34
ADC	↓	0	30
SWI	↓	0	0
Subacute (second-to-fourth weeks)			
Prior low ADC		0	30
Follow-up imaging available		0	29
T1	↑		12
T2: black toenail sign	↓		21
SWI	↓		7
Prior normal/high ADC		5	6
Follow-up imaging available		5	6
T1	↑	0	0
T2: black toenail	↓	0	0
SWI	↓	0	0
Chronic (>3 mo)			
Prior low ADC		0	30
Follow-up imaging available		0	19
Volume loss			19
Prior normal/high ADC		5	6
Follow-up imaging available		4	4
Volume loss		2	0
¹ H-MRS performed	Doublet at 1.3 ppm	5 Patients	
Long TE (288 ms)	Elevated	5 Patients	
Intermediate TE (144 ms)	Inverted	5 Patients	
Affected white matter		5 Patients	
Nonaffected white matter		3 Patients	

Note:—↓ indicates hypointense signal; ↑, hyperintense signal.

RESULTS

Eight patients who underwent 31 MR imaging studies fulfilled the inclusion criteria (women = 6, men = 2; age, mean 26.1 years; range, 18–56 years at imaging). The demographics, clinical presentations, genetic testing findings, and number of MR imaging studies available for review are reported in Table 1. All 8 patients had the same genetic pathogenic variant—MT-TL1 m.3243A>G (the mutation that is responsible for approximately 80% of all MELAS cases). Two patients (patients 1 and 2) were siblings. Fifteen of 31 MR imaging studies were performed for assessment of an acute neurologic episode (5 for seizures, 9 for stroke-like episodes, 1 for confusion/encephalopathy), 1 study was screening of an asymptomatic individual with an affected sibling and confirmed genetic diagnosis, and 15 studies were follow-up without new acute neurologic deterioration. Lesion imaging characteristics are outlined in Table 2.

New Lesions

Across 17 MR imaging studies demonstrating new lesions, 41 new lesions were identified (Table 2). Six studies demonstrated a single new lesion, and 11 studies demonstrated multiple lesions. Fifteen studies were performed for the indication of an acute neurologic episode, and 2 studies that were performed purely for follow-up demonstrated new lesions. Six of 8 patients demonstrated old infarcts with volume loss and multifocal cerebral atrophy, 3 patients had atrophy on the baseline or only available study, and 3 patients developed progressive atrophy during serial imaging.

Three of 5 patients who underwent MR spectroscopy assessment demonstrated elevated lactate doublet peaks in both acutely affected and nonaffected regions of subcortical white matter using single-voxel long-TE ¹H-MRS (TE = 288 ms), with confirmatory peak inversion to separate lactate from lipid on intermediate TE acquisitions (TE = 144 ms).

Anatomic Distribution and Symmetry

Anatomic distribution results are detailed in On-line Table 3. In summary, the most commonly affected locations were the pericalcarine cortex of the inferior cuneus in the medial occipital lobe—primary visual cortex: Brodmann Area 17 (BA17) (*n* = 5); the middle-third of the postcentral gyrus in the parietal lobe—primary somatosensory cortex: BA3 (homunculus hand/arm region) (*n* = 5); the ventral posterolateral thalamus (*n* = 4); the posterior half of the superior temporal gyrus—primary auditory cortex: BA 41 and 42 (*n* = 3); and the cerebellar hemisphere posterior lobe folia surface (*n* = 3; two superior, 1 inferior). Four lesions crossed multiple (>2) cortical regions at initial imaging. Five new lesions were deep in location (4 thalamic, 1 red nucleus, and 36 cortical (33 cerebral, 3 cerebellar). Patients 4 and 6 (who had 10 and 8 MR imaging studies, respectively) both demonstrated a caudal-to-rostral evolution in the distribution of cortical lesions with time.

Symmetric new acute lesions were identified in 6 of the 11 studies with multiple new lesions, with symmetry of not just the gyrus involved but to the level of the cortical area/nucleus in all cases (On-line Table 3).

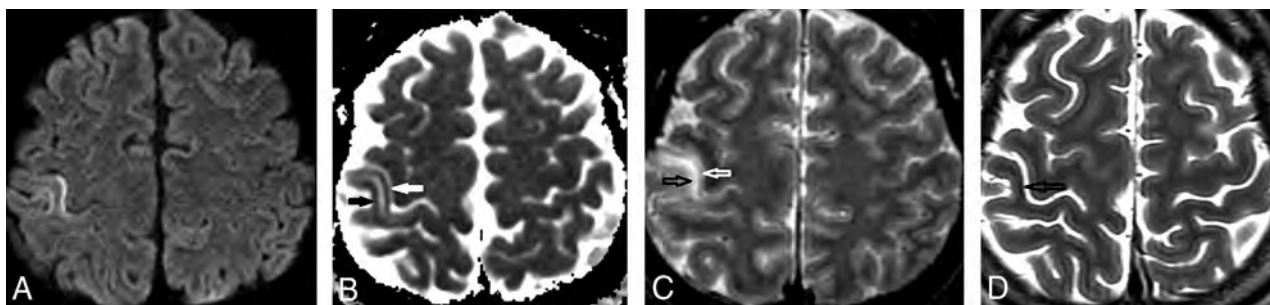


FIG 1. Axial MR imaging shows temporal evolution of an acute cortical lesion in a patient with MELAS presenting with an acute stroke-like episode with left upper limb sensory loss. A, DWI ($b = 1000$) image from the day after symptom onset shows hyperintense intracortical signal in the middle-third of the right postcentral gyrus (hand/arm region of the primary somatosensory cortex). B, ADC image shows corresponding hypointense intracortical signal in keeping with diffusion restriction (white and black arrows). C, T2-weighted spin-echo image shows T2 hyperintensity in the deeper cortical layers and juxtacortical white matter (black arrow), with sparing of the superficial cortex (white arrow). D, Progress T2-weighted spin-echo image obtained 3 weeks later shows focal intracortical hypointense signal (black arrow) and mild volume loss, in keeping with pseudolaminar necrosis (black toenail sign).

Lesion Imaging Characteristics

The 5 deep lesions all demonstrated T2 and FLAIR hyperintensity without diffusion restriction or susceptibility artifacts. Of the 36 cortical lesions, all 36 had T2 and FLAIR hyperintense cortical and subcortical white matter hyperintensity (100%), 30 had intracortical gyriform diffusion restriction (83.3%), 23 demonstrated T2 sparing of the most superficial cortical layers (63.9% of all cortical lesions, 76.7% of restricting lesions), 24 had acute T1 hypointensity (66.7% of all cortical lesions, 80% of restricting lesions), and none had susceptibility-weighted artifacts at baseline assessment (Table 2). Gadolinium-enhanced T1 imaging was available in only 2 studies with an acute lesion and subacute lesions, respectively, demonstrating adjacent leptomeningeal but no cortical enhancement in the acute lesion and mild intracortical enhancement at the sites of prior diffusion restriction in the subacute lesions.

Of 30 cortical lesions demonstrating acute diffusion restriction, follow-up imaging was available for 29 lesions: Twenty-one lesions evolved to develop T2 hypointense cortical signal on subacute follow-up (black toenail sign, 72.4%), and 12 lesions developed cortical T1 hyperintensity (41.4%). Long-term follow-up imaging (>3 months later) was available for 19 of 30 restricting lesions, all of which were associated with focal volume loss (Table 2). Temporal evolution of a typical cortical diffusion-restricting lesion is shown in Fig 1.

DISCUSSION

Pathophysiology

The pathophysiology of acute cortical lesions in MELAS is uncertain. Two major theories for their development are the cytopathic theory and the angiopathic theory.^{10,25} The cytopathic theory proposes that defects in oxidative phosphorylation resulting from the mitochondrial mutation cause neuronal and glial cellular dysfunction, potentially resulting in cell death during periods of higher metabolic activity.^{25,26} Known higher baseline metabolic activity in the occipital cortex may partially explain the posterior distribution of lesions in this theory.^{25,27} The angiopathic theory proposes that abnormal mitochondrial function in the arteriolar endothelium results in impaired autoregulation and subsequent ischemia.²⁸

Anatomic Distribution of Cortical Lesions

Preferential distribution of lesions in the posterior cortical regions is well-described in MELAS.^{1,4,16,20,21,23} The particular predominance of pericalcarine visual cortex involvement is a classic feature and explains the frequent clinical presentations with hemianopia or cortical blindness.^{1,4,10,23} The primary visual cortex (BA17) has one of the highest metabolic demands of all cortical regions.²⁷ Across the cortical sheet, neuronal density is also highest in the primary visual cortex.²⁹ Visual cortex neurons have far more extensive glutaminergic dendritic input than motor cortex neurons, with increased energy demands to maintain ionic homeostasis following excitatory depolarization.^{27,30} In addition, dendrite-rich areas of the cortex are particularly vulnerable to hypoxic damage.³¹ These considerations may support the cytopathic theory of pathogenesis.

The primary somatosensory cortex was the second most common distribution in our study, most often involving the anterior cortex in the middle-third (hand/arm region) of the postcentral gyrus (BA3) (Fig 1). The distribution of mitochondria is greatest in dendrites relative to other cell components,³² leaving the dendrite-rich sensory cortex vulnerable to the effects of dysfunctional oxidative phosphorylation. The sensory cortex is known to be particularly vulnerable to hypoxia-induced injury.³³

Primary motor cortex (BA4) involvement was seen in our study despite the known lower neuronal density,^{34,35} was frequently symmetric, and was restricted to the middle or lateral thirds with relative sparing of the medial third (identical to the somatosensory distribution). The middle and lateral aspects of the motor cortex are in charge of fine movements of the fingers, tongue, and lips, having higher neuronal density and metabolic activity than those of the more medial leg/foot regions.³⁴

The highly specific distribution of acute lesions to focal cortical areas of higher neuronal density and metabolic demand would, in our opinion, favor the cytopathic theory of pathogenesis. An additional interesting finding in 2 patients was the evolving caudal-to-rostral lesion distribution across time, beginning in the visual cortex, then involving the parietal cortex, and finally involving the motor cortex and middle frontal gyri in later studies. This caudal-rostral evolution may represent progression in

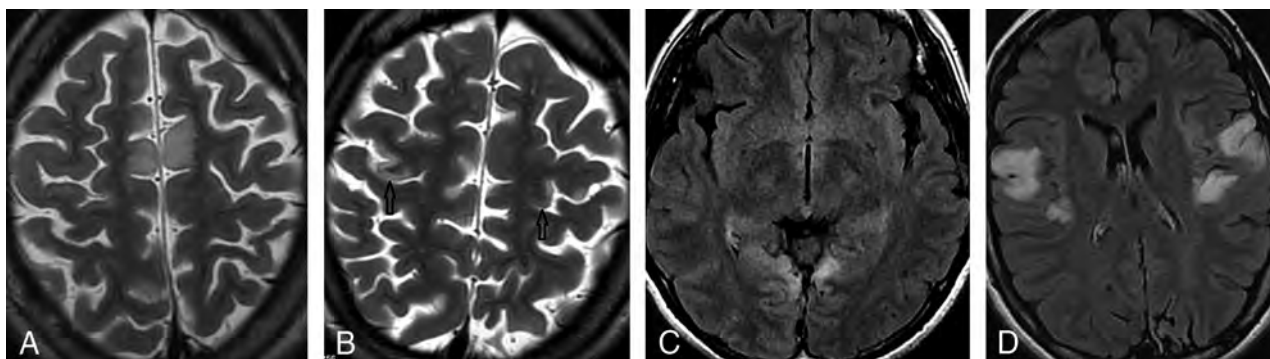


FIG 2. Axial MR imaging shows 4 examples of symmetric cortical involvement by acute lesions in patients with MELAS. A, T2-weighted spin-echo image shows symmetric hyperintense signal in the deep cortex and juxtacortical white matter of the bilateral medial frontal gyri, with sparing of the superficial cortex (typical for pseudolaminar involvement). B, T2-weighted spin-echo image shows symmetric hyperintense intracortical signal in the middle-thirds (black arrows) of the bilateral precentral gyri (hand regions of the primary motor cortex), with sparing of the superficial cortex. C, T2-FLAIR image shows symmetric cortical and subcortical hyperintense signal in the pericalcarine cortex of the bilateral medial occipital lobes (primary visual cortex). D, T2-FLAIR image shows symmetric cortical and subcortical hyperintense signal in the posterior halves of the bilateral superior temporal gyri (primary auditory cortex).

the severity of cellular dysfunction with time, which initially manifests in the most vulnerable cortex before affecting less vulnerable regions.

Symmetry

Symmetric cortical involvement was more common in our study than previously described (one-third of all studies positive for new lesions half of all studies with multiple lesions) and was more specific than lobar or gyral involvement, involving specific cortical regions (eg, the primary visual cortex, hand region of the primary sensory or motor cortices, and the primary auditory cortex) (Fig 2). There was even specificity to the anterior cortex of only the middle-third of the postcentral gyrus (BA3 rather than BA1 or 2) and posterior cortex of the middle-third of the postcentral gyrus (Fig 2B). Symmetric lesions have been previously described involving the precentral gyri in a postmortem-improved case¹⁹ and in the superior temporal gyri in a case of acute cortical deafness.²⁴

Many published descriptions^{2,4,5,10,17} state that asymmetric cortical involvement is helpful in making the diagnosis of MELAS. Our results would suggest that highly specific cortical symmetry should also raise the possibility of MELAS. In our opinion, the presence of such specific symmetry also supports the cytopathic theory of pathogenesis.

Cortical Laminar Necrosis and Temporal Evolution

Our results demonstrated 2 typical patterns of temporal evolution (Table 2). More commonly, lesions had acute diffusion restriction, with subacute cortical laminar necrosis and chronic volume loss. Less commonly, there were reversible lesions that did not restrict acutely or undergo volume loss. The reversible pattern is well-described in early MELAS imaging literature (transient “fleeting” cortical lesions),^{4-6,20,22} but our more common pattern of intracortical necrosis is increasingly recognized^{10,17-19,23,36} and may reflect earlier imaging with enhanced sequence protocols across time. Reversible lesions may represent limited neuronal

damage that does not reach the threshold for irreversible cell damage.^{10,17,21,36}

Cortical laminar necrosis (more correctly pseudolaminar necrosis) is a histopathologic finding in conditions causing cortical energy depletion such as ischemic stroke, diffuse hypoxic injury, or hypoglycaemia.³⁶⁻³⁸ It likely represents selective intracortical neuronal loss in hypoxic environments, whereas pannecrosis of the mantle may be seen with more severe thrombo-occlusion resulting in full-thickness infarction.^{39,40} Both inherited (MELAS¹⁷) and acquired (cyanide poisoning⁴¹) mitochondrial conditions are known to cause pseudolaminar necrosis. The typical subacute gyriform intracortical T1 hyperintensity with T2 hypointensity on MR imaging does not represent hemorrhage but rather lipid-laden macrophages.³⁸ The laminar nature of the necrosis preferentially spares the subpial superficial cortical layers,^{17,36,38,42} with the greatest involvement of the neuron-rich middle cortical layers (layers III–V).⁴⁰

Superficial Cortical T2 Sparing

In acute cortical lesions, 23/36 demonstrated T2 sparing of the superficial cortex, and all these lesions had diffusion restriction with subsequent volume loss (Table 2). This pattern of superficial sparing has been previously described in MELAS^{17,19,36} and likely reflects pseudolaminar necrosis with relative superficial-layer sparing (as discussed above).^{17,38}

Limitations

Our study is limited by its retrospective nature, the presence of an asymptomatic patient (though this does allow assessment across differing phenotypes), and variable MR imaging sequence protocols that evolved with time. MR spectroscopy was not performed in all patients. It is also likely that young patients imaged at our center with an acute stroke-like episode underwent follow-up and genetic testing at other centers and were not identified by our methodology. The sample size is small but has homogeneity of the genotype.

CONCLUSIONS

Acute cortical lesions in MELAS most commonly affect the primary visual, somatosensory, motor, or auditory cortices (BA 17, 3, 4, 41, and 42), corresponding to regions of increased neuronal density and metabolic demand. Diffusion restriction with cortical laminar necrosis is common and leads to volume loss. Symmetric lesions occur more frequently than previously described.










Disclosures: Timo Krings—UNRELATED: Consultancy: Stryker, Medtronic, Penumbra; Royalties: Thieme; Stock/Stock Options: Marblehead.

REFERENCES

1. Yatsuga S, Povalko N, Nishioka J, et al. **MELAS: a nationwide prospective cohort study of 96 patients in Japan.** *Biochim Biophys Acta* 2012;1820:619–24 CrossRef Medline
2. El-Hattab AW, Adesina AM, Jones J, et al. **MELAS syndrome: clinical manifestations, pathogenesis, and treatment options.** *Mol Genet Metab* 2015;116:4–12 CrossRef Medline
3. Kraya T, Neumann L, Paelecke-Habermann Y, et al. **Cognitive impairment, clinical severity and MRI changes in MELAS syndrome.** *Mitochondrion* 2019;44:53–57 CrossRef Medline
4. Castillo M, Kwok L, Green C. **MELAS syndrome: imaging and proton MR spectroscopic findings.** *AJNR Am J Neuroradiol* 1995;16:233–39 Medline
5. Valanne L, Ketonen L, Majander A, et al. **Neuroradiologic findings in children with mitochondrial disorders.** *AJNR Am J Neuroradiol* 1998;19:369–77 Medline
6. Hirano M, Ricci E, Koenigsberger MR, et al. **MELAS: an original case and clinical criteria for diagnosis.** *Neuromuscul Disord* 1992;2:125–35 CrossRef Medline
7. Goto Y, Nonaka I, Horai S. **A mutation in the tRNA(Leu)(UUR) gene associated with the MELAS subgroup of mitochondrial encephalomyopathies.** *Nature* 1990;348:651–53 CrossRef Medline
8. Jean-Francois MJ, Lertrit P, Berkovic SF, et al. **Heterogeneity in the phenotypic expression of the mutation in the mitochondrial tRNA (Leu) (UUR) gene generally associated with the MELAS subset of mitochondrial encephalomyopathies.** *Aust N Z J Med* 1994;24:188–93 CrossRef Medline
9. Grady JP, Pickett SJ, Ng YS, et al. **mtDNA heteroplasmy level and copy number indicate disease burden in m.3243A>G mitochondrial disease.** *EMBO Mol Med* 2018;10 CrossRef Medline
10. Ito H, Mori K, Kagami S. **Neuroimaging of stroke-like episodes in MELAS.** *Brain Dev* 2011;33:283–88 CrossRef Medline
11. Xu W, Wen J, Sun C, et al. **Conventional and diffusional magnetic resonance imaging features of mitochondrial encephalomyopathy, lactic acidosis, and stroke-like episodes in Chinese patients: a study of 40 cases.** *J Comput Assist Tomogr* 2018;42:510–16 CrossRef Medline
12. Sheerin F, Pretorius PM, Briley D, et al. **Differential diagnosis of restricted diffusion confined to the cerebral cortex.** *Clin Radiol* 2008;63:1245–53 CrossRef Medline
13. Wang XY, Noguchi K, Takashima S, et al. **Serial diffusion-weighted imaging in a patient with MELAS and presumed cytotoxic oedema.** *Neuroradiology* 2003;45:640–43 CrossRef Medline
14. Moller HE, Kurlmann G, Putzler M, et al. **Magnetic resonance spectroscopy in patients with MELAS.** *J Neurol Sci* 2005;229–230:131–39 CrossRef Medline
15. Iizuka T, Sakai F, Kan S, et al. **Slowly progressive spread of the stroke-like lesions in MELAS.** *Neurology* 2003;61:1238–44 CrossRef Medline
16. Hongo Y, Kaneko J, Suga H, et al. **A cluster of disseminated small cortical lesions in MELAS: its distinctive clinical and neuroimaging features.** *J Neurol* 2019;266:1459–72 CrossRef Medline
17. Valanne L, Paetau A, Suomalainen A, et al. **Laminar cortical necrosis in MELAS syndrome: MR and neuropathological observations.** *Neuropediatrics* 1996;27:154–60 CrossRef Medline
18. Whitehead MT, Wien M, Lee B, et al. **Black toenail sign in MELAS syndrome.** *Pediatr Neurol* 2017;75:61–65 CrossRef Medline
19. Miyahara H, Matsumoto S, Mokuno K, et al. **Autopsied case with MERRF/MELAS overlap syndrome accompanied by stroke-like episodes localized to the precentral gyrus.** *Neuropathology* 2019;39:212–17 CrossRef Medline
20. Sue CM, Crimmins DS, Soo YS, et al. **Neuroradiological features of six kindreds with MELAS tRNA(Leu) A2343G point mutation: implications for pathogenesis.** *J Neurol Neurosurg Psychiatry* 1998;65:233–40 CrossRef Medline
21. Cai SS, von Coelln R, Kouo TJ. **Migratory stroke-like lesions in a case of adult-onset mitochondrial encephalomyopathy, lactic acidosis, and stroke-like episodes (MELAS) syndrome and a review of imaging findings.** *Radiol Case Rep* 2016;11:425–29 CrossRef Medline
22. Kim IO, Kim JH, Kim WS, et al. **Mitochondrial myopathy-encephalopathy-lactic acidosis and stroke-like episodes (MELAS) syndrome: CT and MR findings in seven children.** *AJR Am J Roentgenol* 1996;166:641–45 CrossRef Medline
23. Bi WL, Baehring JM, Lesser RL. **Evolution of brain imaging abnormalities in mitochondrial encephalomyopathy with lactic acidosis and stroke-like episodes.** *J Neuroophthalmol* 2006;26:251–56 CrossRef Medline
24. Pittet MP, Idan RB, Kern I, et al. **Acute cortical deafness in a child with MELAS syndrome.** *J Inherit Metab Dis* 2016;39:465–66 CrossRef Medline
25. Iizuka T, Sakai F. **Pathogenesis of stroke-like episodes in MELAS: analysis of neurovascular cellular mechanisms.** *Curr Neurovasc Res* 2005;2:29–45 CrossRef Medline
26. Molnar MJ, Valikovics A, Molnar S, et al. **Cerebral blood flow and glucose metabolism in mitochondrial disorders.** *Neurology* 2000;55:544–48 CrossRef Medline
27. Wong-Riley M. **Energy metabolism of the visual system.** *Eye Brain* 2010;2:99–116 CrossRef Medline
28. Ohama E, Ohara S, Ikuta F, et al. **Mitochondrial angiopathy in cerebral blood vessels of mitochondrial encephalomyopathy.** *Acta Neuropathol* 1987;74:226–33 CrossRef Medline
29. Turner EC, Young NA, Reed JL, et al. **Distributions of cells and neurons across the cortical sheet in Old World Macaques.** *Brain Behav Evol* 2016;88:1–13 CrossRef Medline
30. Wong-Riley MT. **Cytochrome oxidase: an endogenous metabolic marker for neuronal activity.** *Trends Neurosci* 1989;12:94–101 CrossRef Medline
31. Hicks SP, Cavanaugh MC, O'Brien ED. **Effects of anoxia on the developing cerebral cortex in the rat.** *Am J Pathol* 1962;40:615–35 Medline
32. Santuy A, Turegano-Lopez M, Rodriguez JR, et al. **A quantitative study on the distribution of mitochondria in the neuropil of the juvenile rat somatosensory cortex.** *Cereb Cortex* 2018;28:3673–84 CrossRef Medline
33. Martin LJ, Brambrink A, Koehler RC, et al. **Primary sensory and forebrain motor systems in the newborn brain are preferentially damaged by hypoxia-ischemia.** *J Comp Neurol* 1997;377:262–85 CrossRef Medline
34. Young NA, Collins CE, Kaas JH. **Cell and neuron densities in the primary motor cortex of primates.** *Front Neural Circuits* 2013;7:30 CrossRef Medline
35. Collins CE, Airey DC, Young NA, et al. **Neuron densities vary across and within cortical areas in primates.** *Proc Natl Acad Sci USA* 2010;107:15927–32 CrossRef Medline
36. Finsterer J. **Laminar cortical necrosis in mitochondrial disorders.** *Clin Neurol Neurosurg* 2009;111:655–58 CrossRef Medline
37. Lee BW, Jin ES, Hwang HS, et al. **A case of hypoglycemic brain injuries with cortical laminar necrosis.** *J Korean Med Sci* 2010;25:961–65 CrossRef Medline
38. Castillo M, Scatliff JH, Kwok L, et al. **Postmortem MR imaging of lobar cerebral infarction with pathologic and in vivo correlation.** *Radiographics* 1996;16:241–50 CrossRef Medline

39. Kesavadas C, Santhosh K, Thomas B, et al. **Signal changes in cortical laminar necrosis-evidence from susceptibility-weighted magnetic resonance imaging.** *Neuroradiology* 2009;51:293–98 CrossRef Medline
40. Ferrer I, Vidal N. **Neuropathology of cerebrovascular diseases.** *Handb Clin Neurol* 2017;145:79–114 CrossRef Medline
41. Riudavets MA, Aronica-Pollak P, Troncoso JC. **Pseudolaminar necrosis in cyanide intoxication: a neuropathology case report.** *Am J Forensic Med Pathol* 2005;26:189–91 Medline
42. Yokoyama T, Hasegawa K, Obama R, et al. **MELAS with diffuse degeneration of the cerebral white matter: report of an autopsy case.** *Neuropathology* 2010;30:56–60 CrossRef Medline

Brain MR Imaging of Patients with Perinatal Chikungunya Virus Infection

 D.G. Corrêa,  T. A. L. Freddi,  H. Werner,  F.P.P.L. Lopes,  M.E.L. Moreira,  F.C.P. de Almeida Di Maio Ferreira,  J.M. de Andrade Lopes,  F.C. Rueda-Lopes, and  L.C.H. da Cruz Jr



ABSTRACT

SUMMARY: Since 2005, it has been known that mother-to-child transmission of the chikungunya virus is possible. Transmission generally occurs in the perinatal period. In the present study, we describe the brain lesions seen on MR imaging of 6 cases of perinatal chikungunya infection. Patients who underwent brain MR imaging in the acute phase presented with areas of restricted diffusion in the white matter, suggesting a perivascular distribution, whereas those in the subacute/late phase showed cystic lesions, also with a perivascular distribution, with or without brain atrophy. One patient also presented with scattered hemorrhages in the frontal and parietal lobes. Important differential diagnoses include rotavirus, Parechovirus, herpes simplex infection, and hypoxic-ischemic encephalopathy, depending on the disease phase.

ABBREVIATIONS: CHIKV = chikungunya virus; IgM = immunoglobulin M; RT-PCR = reverse transcription–polymerase chain reaction

Chikungunya is an arbovirus of the family *Togaviridae*, genus *Alphavirus*, transmitted by *Aedes* spp. mosquitos. In adults, the infection is characteristically manifest by fever, arthralgia, and/or cutaneous rash.¹ The first documented human outbreaks were in southern Asia during the 1960s. After decades of low transmission, the virus re-emerged in 2004, causing outbreaks throughout the islands of the Indian Ocean, India, and Southeast Asia. In 2013, it was first reported in the American continent, rapidly spreading throughout 48 American countries and territories.^{2,3} Additionally, there are increasing reports of coinfections with other arboviruses, such as Zika and dengue, in some patients, including pregnant women, with unknown consequences.³

Studies performed during chikungunya virus (CHIKV) outbreaks reported a 4.7%–46% prevalence of pediatric neurologic manifestations.² Perinatal transmission of the CHIKV was first reported during the 2005 outbreak on La Réunion Island. Essentially, neonates are asymptomatic at birth but begin to

present with symptoms in the first days of life.⁴ In general, clinical manifestations of CHIKV-infected neonates are similar to those of adults: febrile illness associated with exanthema and spontaneous resolution usually observed within 1–2 weeks.⁵ However, up to 40% of neonates present with complicated forms of CHIKV infection, which can manifest as hemorrhagic fever, disseminated intravascular coagulation, impaired liver function, myocarditis, respiratory distress, sepsis, necrotizing enterocolitis, myocarditis, pericarditis, or neurologic compromise.^{4,5} Neurologic manifestations are variable and include a compromised state of consciousness, meningoencephalitis, polyneuropathy, seizures, and encephalomyelitis.⁶ Long-term follow-up of patients with perinatal CHIKV infection has shown them to have an increased risk of global neurodevelopmental delay, especially in those who experienced encephalopathy during the neonatal period.⁵ However, pathogenic mechanisms of the neurologic syndromes of CHIKV infection remain unknown.⁶

Although brain MR imaging studies of perinatal CHIKV infection have been previously described, mainly in case reports and case series,^{6–10} a systematic description of the lesions is still necessary to improve the understanding of its pathophysiologic mechanisms. In this article, we describe the brain MR imaging findings of 6 established cases of perinatal CHIKV infection with neurologic complications.

MATERIALS AND METHODS

The institutional review board Clinica Perinatal approved this study. The diagnosis of maternal CHIKV infection was based on the presence of serum anti-CHIKV immunoglobulin M (IgM)

Received August 29, 2019; accepted after revision October 2.

From the Clínica de Diagnóstico por Imagem/Diagnósticos da América (D.G.C., H.W., F.P.P.L., F.C.R.-L., L.C.H.d.C.), Rio de Janeiro, RJ, Brazil; Department of Radiology (T.A.L.F.), Hospital do Coração, São Paulo, SP, Brazil; and Clínica Perinatal (M.E.L.M., F.C.P.d.A.D.M.F., J.M.d.A.L.), Rio de Janeiro, RJ, Brazil.

Please address correspondence to Diogo Goulart Corrêa, MD, Clínica de Diagnóstico por Imagem/Diagnósticos da América, Avenida das Américas, 4666, 302A, 303, 307, 325, 326, Barra da Tijuca, Rio de Janeiro, RJ, Brazil, 2640-102; e-mail: diogogoulartcorrea@yahoo.com.br



Indicates article with supplemental on-line table.



Indicates article with supplemental on-line photo.

<http://dx.doi.org/10.3174/ajnr.A6339>

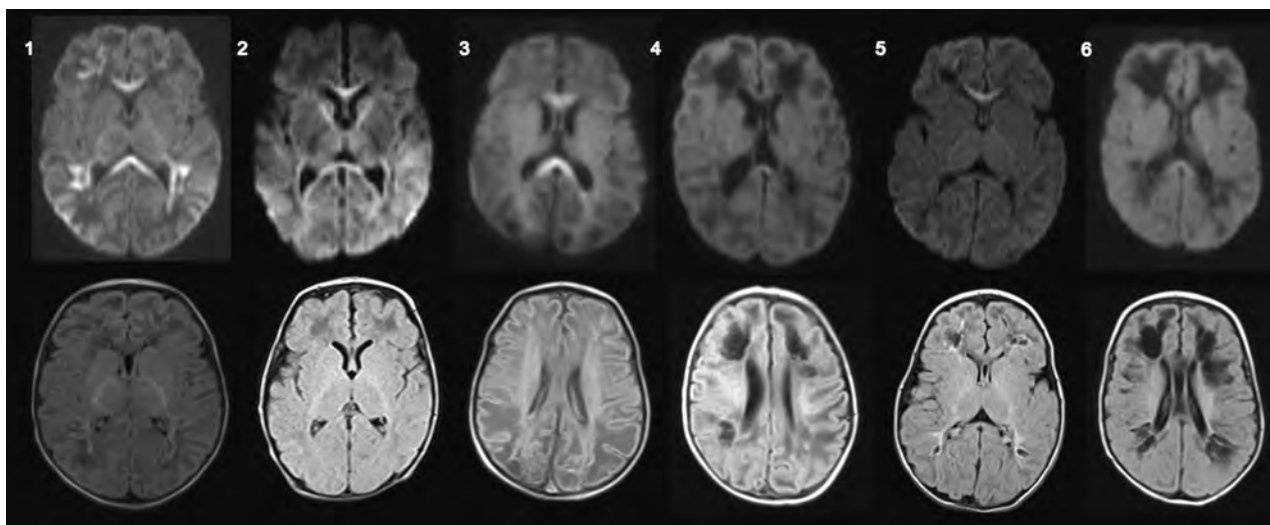


FIGURE. Brain MR imaging of 6 infants with confirmed perinatal CHIKV infection. Axial diffusion-weighted imaging (*upper row*) and axial FLAIR (*lower row*) of patients 1–6. Patients who underwent MR imaging before 14 days of symptom onset presented with restricted diffusion in the corpus callosum and/or subcortical white matter with a perivascular distribution, whereas patients who underwent MR imaging after 14 days of symptom onset presented with subcortical cystic lesions, also with a perivascular distribution with discrete restricted diffusion in the corpus callosum.

and/or serum detection of the viral genome by reverse transcription–polymerase chain reaction (RT-PCR). Mothers were screened if they presented with symptoms of CHIKV infection in the peripartum period. The diagnosis of neonatal CHIKV infection was based on the detection of serum and/or CSF anti-CHIKV IgM and/or RT-PCR positive for CHIKV in the neonate. Vertical transmission was diagnosed if the mother had a serologic test positive for CHIKV in the perinatal period in association with a confirmed infection of the symptomatic neonate within the first 21 days of life. Detection of anti-CHIKV IgM was performed by IgM capture enzyme-linked immunosorbent assay. All participants were also tested for the Zika virus, dengue virus, toxoplasmosis, cytomegalovirus, rubella, herpes virus, syphilis, and human immunodeficiency virus.

Brain MRIs were performed on 1.5T clinical scanners (Avanto, Aera, and Espree; Siemens, Erlangen, Germany). The MR imaging protocol included axial T1-weighted images with or without intravenous injection of a gadolinium-based contrast agent, axial and coronal T2-weighted images, FLAIR, axial diffusion-weighted imaging with apparent diffusion coefficient maps, and axial SWI. No participant underwent spine MR imaging.

Case Series

From 8 cases of confirmed CHIKV vertical transmission, 2 presented with normal brain MR imaging findings and 6 had brain lesions detected by MR imaging. In all cases, the mothers presented with typical symptoms of CHIKV infection in the peripartum period (On-line Table).

Case 1. A 5-day-old neonate with a reduced level of consciousness. A hemogram showed severe thrombocytopenia. Brain MR imaging on the 15th day showed areas of restricted diffusion in the entire corpus callosum and subcortical white matter of the frontal, parietal, and temporal lobes, suggesting perivascular

distribution, with discrete hyperintense signal on FLAIR (Figure and On-line Table).

Case 2. A 10-day-old neonate presented with sepsis and seizures. Brain MR imaging on the 20th day of life showed areas of restricted diffusion in the entire corpus callosum and white matter of the frontal, parietal, and temporal lobes. FLAIR, T1-, and T2-weighted imaging findings were unremarkable (Figure and On-line Table).

Case 3. A 5-day-old neonate presented with fever and a reduced level of consciousness. Brain MR imaging on the 18th day of life showed bilateral subcortical white matter lesions with hypointense signal on T1-weighted imaging and FLAIR and hyperintense signal on T2-weighted imaging, associated with restricted diffusion in the entire corpus callosum. SWI showed hemorrhage in the right frontal and parietal lobes (Figure, On-line Table, and On-line Figure).

Case 4. A 7-day-old neonate presented with fever and irritability and had 1 seizure. Brain MR imaging in the 21st day of life showed diffuse brain volume loss with enlarged ventricles and bilateral cystic lesions, suggesting a perivascular distribution, and a small area of restricted diffusion in the splenium of the corpus callosum (Figure and On-line Table).

Case 5. A 4-day-old neonate presented with fever and 2 episodes of seizures. Brain MR imaging on the 20th day of life showed small subcortical cystic lesions in the frontal and parietal lobes, suggesting a perivascular distribution, and restricted diffusion in the genu of the corpus callosum (Figure and On-line Table).

Case 6. A 4-day-old neonate presented with fever and seizures. Brain MR imaging on the 30th day of life showed brain volume loss, enlarged ventricles, as well as subcortical cystic lesions in the frontal and parietal lobes, also suggestive of perivascular

distribution, and a discrete restricted diffusion in the splenium of the corpus callosum (Figure and On-line Table).

All infants had normal findings on prenatal ultrasonography follow-up and were born without complications. All participants had serology negative for HIV and herpes and laboratory tests negative for syphilis. The participants also had IgM antibodies negative for Zika, dengue, cytomegalovirus, and rubella viruses. No participant was excluded because of coinfections. Blood and/or CSF samples of the neonates tested positive for CHIKV as assessed by RT-PCR.

DISCUSSION

We reported brain abnormalities as measured by MR imaging in 6 confirmed cases of vertical transmission of the chikungunya virus. All participants were younger than 1 month of age at the time of MR imaging, were born asymptomatic, and developed symptoms between 4 and 10 days of life. Imaging findings can be divided in 2 patterns: those imaged within 2 weeks of disease onset, here designated as the early phase, presenting with areas of restricted diffusion in the subcortical white matter of both cerebral hemispheres and in the corpus callosum; and those imaged >2 weeks after disease onset, designated as subacute/delayed phase, presenting with bilateral cystic lesions with or without brain atrophy and hemorrhage.

The mechanisms through which CHIKV affects the CNS have not been fully elucidated, and it is still unclear whether the virus acts directly by targeting neurons and glial cells or indirectly by triggering immune-mediated effects through upregulation of inflammatory and antiviral cytokines.^{3,11} In experimental studies, both ribonucleic acid and the virus itself have been isolated from CSF, suggesting direct neuroinvasion,¹² but brain postmortem examinations with histopathologic analyses were unable to detect CHIKV.^{11,13} Hence, the target cells of CHIKV in the human brain remain unknown. Studies in human cells demonstrated the susceptibility of neuroblasts and glial cells, such as astrocytes and microglia, to CHIKV invasion. The apoptosis observed in CHIKV-infected neuroblasts and astrocytes suggests a direct role of viral infection in disease pathogenesis.¹¹ On the other hand, concentrations of tumor necrosis factor- α , interferon- α , interleukin-6, and monokines induced by interferon- γ were found to be significantly higher in patients with neurologic disease secondary to CHIKV, as opposed to uncomplicated infections.³ Direct viral CNS infection is believed to be more probable in neonates and the elderly due to their weaker innate and adaptive immune responses. This belief is supported by the high rate (92%) observed of CHIKV RT-PCR positivity in infected neonates' CSF and the short latency between initial CHIKV-fever signs and encephalitic symptoms.¹⁴

In addition, microgliosis and perivascular lymphocytic infiltrates were found in the brain parenchyma of those infected by CHIKV.^{13,15} Couderc et al,¹⁶ studying mouse models with CHIKV infection, found that cells in the choroid plexus, ependymal wall, and leptomeninges, including external cells in the Virchow-Robin spaces, were strongly infected with CHIKV, whereas those in the brain parenchyma were not. Thus, in their experimental study, despite strong infection of the meninges and Virchow-Robin spaces, the barrier function of the brain

microvessels was preserved. Leptomeningeal cells form an interconnected multicellular network, which acts as a regulatory interface between CSF and the brain surface, as well as among arterioles and the surrounding neural tissue (perivascular spaces), and this tissue organization and physiology may play a role in CHIKV dissemination.¹⁶ Our study showed that regardless of the pathophysiology, CHIKV encephalitis can produce serious brain lesions with potential consequences for neural development. Furthermore, some patients presented with restricted diffusion or cystic lesions along the course of the deep medullary veins, suggesting perivascular involvement.

Although early vertical transmission has been demonstrated,¹⁷ symptomatic neonatal disease generally occurs from intrapartum maternal infections.³ Mother-to-child transmission of CHIKV is relatively rare (approximately 2.5% of exposed neonates become infected), but the intrapartum transmission rate of viremic women is close to 50%, highlighting this period as critical for disease transmission. Previous observations have suggested that the placental barrier is relatively effective in preventing antepartum CHIKV transmission. In contrast, vertical transmission is frequently observed in viremic mothers at the end of pregnancy, when the maternal blood can come into contact with placental barrier breaches resulting from uterine contractions during labor. High viral load measured in placentas from infected neonates is thus most likely a consequence of elevated maternal viremia.⁷ These data are in accordance with our results; although we did not investigate the viral presence in placentas of our participants, all neonates were born asymptomatic and developed symptoms within the first days of life. In addition, none of our participants presented with evidence of mosquito bites.

Among our cases, 4 neonates were born by cesarean delivery and 2 were born by vaginal delivery. A cesarean delivery does not appear to prevent vertical transmission; therefore, systematic performance of cesarean deliveries for infected mothers to reduce the risk of viral transmission is not recommended.^{3,18} Additionally, in a study by Torres et al,¹⁸ cesarean delivery was unrelated to mother-to-child CHIKV transmission. The ideal type of delivery and the interval between symptom onset and childbirth are still unknown.

Previous authors have found that at the acute stage (within 2 weeks of disease onset), brain MR imaging of perinatal CHIKV-infected children revealed scattered restricted diffusion in the subcortical white matter and corpus callosum, with unremarkable features on T1- and T2-weighted imaging.⁶⁻¹⁰ Restricted diffusion is related to cytotoxic edema and may be secondary to plasma leakage from capillaries and venules associated with immune-mediated allergic perivascular demyelination.¹³ In the subacute phase (15–45 days after disease onset), the areas that exhibited low signal on diffusion-weighted imaging were related to vasogenic edema. In the chronic phase (>45 days after disease onset), the lesions evolved toward cavitations and parenchymal atrophy.⁶⁻¹⁰ Foci of intraparenchymal hemorrhage scattered through white matter have also been described.^{8,10} Although we did not perform an imaging follow-up of our patients, our results show similarities to previous studies because patients who were studied early in the disease course presented with white matter- and corpus callosum-restricted

diffusion, whereas those in the late phases showed cystic lesions and brain atrophy. Most interesting, we found an association between subcortical cystic lesions and restricted diffusion in some participants. This may be because cells of the corpus callosum have a higher density of cytokine, glutamate, and other excitatory amino acid receptors, compared with other brain areas, resulting in a tendency for developing cytotoxic edema.¹⁹

The main differential diagnoses for neonatal brain CHIKV infection in the acute phase are rotavirus and parechovirus infections, which have similar imaging patterns, though most cases of rotavirus encephalitis are asymptomatic.^{20,21} In the case series of Sarma et al²¹ of neonatal parechovirus meningoencephalitis, 1 patient underwent a longitudinal follow-up at 3 months and did not present with cystic lesions. This finding is in marked contrast to those of our patients with perinatal chikungunya. However, other authors described the development of extensive cystic leukomalacia at the 4-month follow-up in a patient with parechovirus infection.²¹ Some data suggest that preterm neonates are at higher risk of severe cystic leukoencephalomalacia in parechovirus infection.²¹ Whether prematurity is also a risk factor for the development of cystic encephalomalacia in perinatal CHIKV infection needs further investigation. In the chronic phase, differential diagnoses for cystic lesions include herpes simplex infection and hypoxic-ischemic encephalopathy.²⁰⁻²² CHIKV-related lesions with perivascular dissemination could aid in the differentiation. However, the real value of this type of lesion distribution needs further research.

Our study has some limitations. First, we did not perform follow-up evaluations to confirm whether all patients who presented with restricted diffusion in the acute phase would evolve to brain cavitation and atrophy, or assess how the cavitations would evolve, or evaluate the neurologic outcome of the participants. Also, we did not perform amniocentesis or placental biopsies to search for the virus before birth. However, all participants had a confirmed diagnosis of CHIKV infection, and other coinfections or peripartum complications were excluded.

CONCLUSIONS

Neuroimaging can aid in the diagnosis of perinatal CHIKV infection. Bilateral subcortical restricted diffusion and cystic lesions with or without brain atrophy with a perivascular distribution are characteristic findings, dependent on the disease stage. However, whether this perivascular distribution can aid in the differential diagnosis needs further research.

Disclosures: Maria E.L. Moreira—UNRELATED: Employment: Fiocruz*; Payment for Manuscript Preparation: Nestle do Brasil, review article about milk osmolality.* Fernanda C. Rueda-Lopes—UNRELATED: Employment: Diagnósticos da América. *Money paid to the institution.

REFERENCES

- Contopoulos-Ioannidis D, Newman-Lindsay S, Chow C, et al. **Mother-to-child transmission of Chikungunya virus: a systematic review and meta-analysis.** *PLoS Negl Trop Dis* 2018;12:e0006510 CrossRef Medline
- Almeida Bentes A, Kroon EG, Romanelli R. **Neurological manifestations of pediatric arboviral infections in the Americas.** *J Clin Virol* 2019;116:49–57 CrossRef Medline
- Mehta R, Gerardin P, de Brito CA, et al. **The neurological complications of Chikungunya virus: a systematic review.** *Rev Med Virol* 2018;28:e1978 CrossRef Medline
- Barr KL, Vaidhyanathan V. **Chikungunya in infants and children: is pathogenesis increasing?** *Viruses* 2019;11 CrossRef Medline
- Cardona-Correa SE, Castaño-Jaramillo LM, Quevedo-Vélez A. **Vertical transmission of Chikungunya virus infection: case report.** *Rev Chil Pediatr* 2017;88:285–88 CrossRef Medline
- Bandeira AC, Campos GS, Sardi SI, et al. **Neonatal encephalitis due to Chikungunya vertical transmission: first report in Brazil.** *IDCases* 2016;5:57–59 CrossRef Medline
- Gérardin P, Barau G, Michault A, et al. **Multidisciplinary prospective study of mother-to-child Chikungunya virus infections on the island of La Réunion.** *PLoS Med* 2008;5:e60 CrossRef Medline
- Ramful D, Carbonnier M, Pasquet M, et al. **Mother-to-child transmission of Chikungunya virus infection.** *Pediatr Infect Dis J* 2007;26:811–15 CrossRef Medline
- Gérardin P, Sampériz S, Ramful D, et al. **Neurocognitive outcome of children exposed to perinatal mother-to-child Chikungunya virus infection: the CHIMERE cohort study on Reunion Island.** *PLoS Negl Trop Dis* 2014;8:e2996 CrossRef Medline
- Karthiga V, Kommu PP, Krishnan L. **Perinatal Chikungunya in twins.** *J Pediatr Neurosci* 2016;11:223–24 CrossRef Medline
- Matusali G, Colavita F, Bordi L, et al. **Tropism of the Chikungunya virus.** *Viruses* 2019;11:175 CrossRef Medline
- Tandale BV, Sathe PS, Arankalle VA, et al. **Systemic involvements and fatalities during Chikungunya epidemic in India, 2006.** *J Clin Virol* 2009;46:145–49 CrossRef Medline
- Ganesan K, Diwan A, Shankar SK, et al. **Chikungunya encephalomyelorradiculitis: report of 2 cases with neuroimaging and 1 case with autopsy findings.** *AJNR Am J Neuroradiol* 2008;29:1636–37 CrossRef Medline
- Cerny T, Schwarz M, Schwarz U, et al. **The range of neurological complications in Chikungunya fever.** *Neurocrit Care* 2017;27:447–57 CrossRef Medline
- Pinheiro TJ, Guimarães LF, Silva MTT, et al. **Neurological manifestations of Chikungunya and Zika infections.** *Arq Neuropsiquiatr* 2016;74:937–43 CrossRef Medline
- Couderc T, Chrétien F, Schilte C, et al. **A mouse model for Chikungunya: young age and inefficient type-I interferon signaling are risk factors for severe disease.** *PLoS Pathog* 2008;4:e29 CrossRef Medline
- Touret Y, Randrianaivo H, Michault A, et al. **Early maternal-fetal transmission of the Chikungunya virus.** *Presse Med* 2006;35:1656–58 CrossRef Medline
- Torres JR, Falleiros-Arlant LH, Dueñas L, et al. **Congenital and perinatal complications of Chikungunya fever: a Latin American experience.** *Int J Infect Dis* 2016;51:85–88 CrossRef Medline
- Starkey J, Kobayashi N, Numaguchi Y, et al. **Cytotoxic lesions of the corpus callosum that show restricted diffusion: mechanisms, causes, and manifestations.** *Radiographics* 2017;37:562–76 CrossRef Medline
- Yeom JS, Kim YS, Seo JH, et al. **Distinctive pattern of white matter injury in neonates with rotavirus infection.** *Neurology* 2015;84:21–27 CrossRef Medline
- Sarma A, Hanzlik E, Krishnasarma R, et al. **Human parechovirus meningoencephalitis: neuroimaging in the era of polymerase chain reaction-based testing.** *AJNR Am J Neuroradiol* 2019;40:1418–21 CrossRef Medline
- Verboon-Macielek MA, Groenendaal F, Hahn CD, et al. **Human parechovirus causes encephalitis with white matter injury in neonates.** *Ann Neurol* 2008;64:266–73 CrossRef Medline

Number Needed to Treat with Vertebral Augmentation to Save a Life

J.A. Hirsch, R.V. Chandra, N.S. Carter, D. Beall, M. Frohbergh, and K. Ong



ABSTRACT

BACKGROUND AND PURPOSE: Evidence from randomized controlled trials for the efficacy of vertebral augmentation in vertebral compression fractures has been mixed. However, claims-based analyses from national registries or insurance datasets have demonstrated a significant mortality benefit for patients with vertebral compression fractures who receive vertebral augmentation. The purpose of this study was to calculate the number needed to treat to save 1 life at 1 year and up to 5 years after vertebral augmentation.

MATERIALS AND METHODS: A 10-year sample of the 100% US Medicare data base was used to identify patients with vertebral compression fractures treated with nonsurgical management, balloon kyphoplasty, and vertebroplasty. The number needed to treat was calculated between augmentation and nonsurgical management groups from years 1–5 following a vertebral compression fracture diagnosis, using survival probabilities for each management approach.

RESULTS: The adjusted number needed to treat to save 1 life for nonsurgical management versus kyphoplasty ranged from 14.8 at year 1 to 11.9 at year 5. The adjusted number needed to treat for nonsurgical management versus vertebroplasty ranged from 22.8 at year 1 to 23.8 at year 5.

CONCLUSIONS: Both augmentation modalities conferred a prominent mortality benefit over nonsurgical management in this analysis of the US Medicare registry, with a low number needed to treat. The calculations based on this data base resulted in a low number needed to treat to save 1 life at 1 year and at 5 years.

ABBREVIATIONS: BKP = balloon kyphoplasty; NNT = number needed to treat; NSM = nonsurgical management; VCF = vertebral compression fracture; VP = vertebroplasty

Vertebral augmentation techniques became popular in the late 1990s and 2000s due to their efficacy in reducing pain and disability in patients with painful vertebral compression fractures (VCFs). Early data from large observational studies and open-label randomized controlled trials comparing vertebral augmentation with nonsurgical therapy supported the use of augmentation.^{1–3} However, since that time, evidence for the effectiveness of vertebroplasty has been made controversial by 2 randomized sham trials. These high-profile randomized controlled trials in

2009 did not demonstrate that vertebroplasty conferred benefit over active control sham.^{4,5} These findings considerably reduced the use of vertebral augmentation procedures.^{6,7} In 2016, in an attempt to control for a number of perceived methodologic limitations from those earlier trials, the authors of the Vertebroplasty for Acute Painful Osteoporotic Fractures (VAPOUR)⁸ trial selected a group of patients with severe pain from a recent fracture using advanced imaging and modified the sham procedure to a subcutaneous injection of local anesthetic. It became the first placebo-controlled randomized controlled trial of vertebroplasty to demonstrate positive results. The evidentiary landscape again changed with the 2018 publication of A Randomised Sham Controlled Trial of Vertebroplasty for Painful Chronic Osteoporotic Vertebral Fractures (VERTOS IV), another active control sham randomized controlled trial, which again failed in its primary end point to show benefit for use of vertebroplasty, primarily due to the high level of pain relief seen in the active sham group and a statistically highly controversial method of comparing the difference in pain reduction between the 2 treatment groups.⁹

Received August 25, 2019; accepted after revision October 25.

From the Neuroendovascular Program (J.A.H.), Massachusetts General Hospital, Harvard Medical School, Boston, Massachusetts; Faculty of Medicine (R.V.C., N.S.C.), Nursing and Health Sciences, and Neurointerventional Radiology (R.V.C., N.S.C.), Monash Imaging, Monash Health, Melbourne, Australia; Clinical Radiology of Oklahoma (D.B.), Edmond, Oklahoma; Exponent Inc (M.F., K.O.), Philadelphia, Pennsylvania; and Alfred Hospital (N.S.C.), Melbourne, Australia.

Please address correspondence to Nicole S. Carter, MBBS, Alfred Hospital, Commercial Rd, Melbourne, Victoria 3004, Australia; e-mail: nicolascarter4@gmail.com

<http://dx.doi.org/10.3174/ajnr.A6367>

Multiple analyses of larger datasets from national registries or insurance-based claims data have demonstrated a significant survival benefit for patients with VCFs who receive vertebral augmentation, taking research in a new direction because the sham trials were not intended to assess mortality risk.^{10,11} Most recently, Ong et al⁷ studied a cohort that included 2,077,944 patients with VCF, analyzing vertebral augmentation use and mortality risk in Medicare patients from 2005 to 2014. The use of kyphoplasty conferred a >50% 1-year mortality benefit and reduced the 10-year mortality by up to 24% compared with nonsurgical management (NSM).¹⁰ This mortality benefit has also been observed in an analysis of claims data in the German population, which found a 43% reduction in 5-year mortality in those treated by vertebral augmentation compared with NSM.¹¹ The discovery of this survival benefit that spans countries, cultures, and races would seem an important informational component on which to base treatment decisions in the population of patients with VCF. On the basis of this information and on the entire Medicare data base for a decade, our aim in this study was to calculate the number needed to treat (NNT) to save 1 life at 1 and up to 5 years after treatment.¹²

MATERIALS AND METHODS

Patient Population

Inpatient/outpatient US Medicare Fee-For-Service claims data from 2005 to 2014 were used to identify incident patients with VCFs (International Classification of Diseases, Ninth Revision, Clinical Modification [ICD-9-CM] codes 733.13, 805.0, 805.2, 805.4, 805.6, and 805.8). The first VCF diagnosed in the study period was used as the incident fracture. The patients were required to have at least a 12-month claims history before the VCF diagnosis to confirm a VCF-free period. Those without 12 months of claims history before the VCF diagnosis were excluded due to potential incompleteness in their claims history. Patients undergoing vertebral augmentation in the 12 months before the index VCF were excluded. Those younger than 65 years of age were also excluded due to potential confounding factors from their Medicare eligibility, including certain disabilities such as permanent kidney failure, amyotrophic lateral sclerosis, and other significant medical conditions that may result in Medicare enrollment. Patients enrolled in a Health Maintenance Organization plan and not residing in the 50 states were also excluded.¹⁰

Patients were stratified into NSM, balloon kyphoplasty (BKP), and vertebroplasty (VP) cohorts. Surgical treatment meant that patients underwent vertebral augmentation within the first year of the VCF diagnosis. Those who underwent fusion surgery between the VCF diagnosis and BKP/VP were excluded. The NSM cohort comprised patients who did not undergo augmentation or fusion during the study period and those who underwent augmentation or fusion only >1 year after the index VCF diagnosis. Balloon kyphoplasty was identified using ICD-9-CM code 81.66 or Current Procedural Terminology codes 22289 and 22523–22525.¹³

This study was based on publicly available datasets, did not use private health identifiable information, and did not represent

human subject research; therefore, it did not require oversight by our institutional review boards.

Calculation of NNT

The NNT for survival between BKP and NSM was evaluated from years 1 to 5 following a VCF diagnosis via a time-to-event approach. The input for this calculation was the Kaplan-Meier survival probability as an estimate of the hazard ratio, as described by Altman and Anderson¹⁴ and Bowry et al.¹⁵ To estimate the unadjusted NNT for each year following a VCF diagnosis, we first obtained the corresponding unadjusted NSM survival probabilities via the Kaplan-Meier approach from previously published data on survival of patients with VCF. These data had been stratified into groups by NSM, BKP, and VP. Using the adjusted hazard ratio for mortality risk of BKP obtained from published data from a mortality study of BKP and NSM,⁶ we calculated the survival probability for BKP at each year as the survival probability for NSM with the hazard ratio as the exponent (as per Equation 2 in Bowry et al). The unadjusted NNT was then determined from the inverse of the difference in the BKP and NSM survival probabilities. The 95% confidence interval for the NNT was obtained by replacing the hazard ratio with the 2 limits of the 95% confidence interval for the hazard ratio. To estimate the adjusted NNT, we replaced the unadjusted survival probability for NSM with the corresponding adjusted survival probability. The NNT for survival between VP and NSM used a similar approach but relied on the adjusted hazard ratio for mortality risk of VP relative to NSM, instead of BKP relative to NSM. Similarly, for the NNT between BKP and VP, the VP results were used in place of the NSM results from the previous BKP-NSM analysis.

RESULTS

BKP versus NSM

The patients with NSM had an unadjusted survival probability of 76.8% at 1 year post-VCF diagnosis, which decreased to 42.5% at 5 years post-VCF diagnosis, while the corresponding survival probabilities for patients with BKP were 84.2% and 50.9% respectively, after accounting for the relative hazard ratios between BKP and NSM (Table 1). The adjusted survival probabilities decreased from 79.1% to 41.9% at years 1–5 for patients with NSM and from 85.9% to 50.3% at years 1–5 for those with BKP. The unadjusted NNT for BKP versus NSM ranged from 13.5 patients (95% CI, 13.1–13.9 patients) at year 1 to 12.0 patients (95% CI, 11.4–12.6 patients) at year 5 (Table 2). The adjusted NNT ranged from 14.8 (95% CI, 14.4–15.2) at year 1 to 11.9 (95% CI, 11.3–12.6) at year 5.

VP versus NSM

The survival probabilities for patients with VP were 81.6% at year 1 and 46.7% at year 5, after accounting for the relative hazard ratios between VP and NSM (Table 1). The adjusted survival probabilities decreased from 83.5% to 46.1% at years 1–5 for patients with VP. The unadjusted NNT for VP versus NSM ranged from 20.8 patients (95% CI, 19.9–21.8 patients) at year 1 to 23.8 patients (95% CI, 21.8–26.3 patients) at year 5 (Table 2).

Table 1: Survival probability for BKP versus NSM, VP versus NSM, and BKP versus VP

Year	BKP vs NSM				VP vs NSM				BKP vs VP			
	Unadjusted		Adjusted		Unadjusted		Adjusted		Unadjusted		Adjusted	
	NSM	BKP	NSM	BKP	NSM	VP	NSM	VP	VP	BKP	VP	BKP
1	76.8%	84.2%	79.1%	85.9%	76.8%	81.6%	79.1%	83.5%	81.4%	84.1%	79.7%	82.6%
2	66.4%	74.2%	67.9%	75.4%	66.4%	70.9%	67.9%	72.2%	70.3%	73.6%	68.7%	72.1%
3	57.4%	65.6%	58.3%	66.4%	57.4%	62.0%	58.3%	62.9%	60.7%	64.4%	59.3%	63.1%
4	49.5%	57.8%	49.6%	57.9%	49.5%	53.9%	49.6%	54.0%	52.1%	56.0%	50.7%	54.6%
5	42.5%	50.9%	41.9%	50.3%	42.5%	46.7%	41.9%	46.1%	44.3%	48.5%	43.0%	47.2%

Table 2: Number needed to treat for BKP versus NSM, VP versus NSM, and BKP versus VP

Year	BKP vs NSM		VP vs NSM		BKP vs VP	
	Unadjusted	Adjusted	Unadjusted	Adjusted	Unadjusted	Adjusted
	(95% CI)	(95% CI)	(95% CI)	(95% CI)	(95% CI)	(95% CI)
1	13.5 (13.1–13.9)	14.8 (14.4–15.2)	20.8 (19.9–21.8)	22.8 (21.8–23.9)	36.7 (34.5–39.2)	33.9 (31.9–36.2)
2	12.9 (12.6–13.1)	13.4 (13.1–13.6)	22.2 (20.9–23.8)	23.0 (21.6–24.6)	30.3 (28.1–32.9)	29.1 (27.0–31.6)
3	12.2 (12.0–12.5)	12.4 (12.1–12.7)	21.6 (20.1–23.3)	21.9 (20.3–23.6)	26.7 (24.6–29.2)	26.1 (24.0–28.5)
4	12.1 (11.8–12.4)	12.1 (11.8–12.4)	22.9 (21.1–25.1)	23.0 (21.1–25.1)	25.8 (23.6–28.5)	25.4 (23.2–28.1)
5	12.0 (11.4–12.6)	11.9 (11.3–12.6)	23.8 (21.8–26.3)	23.8 (21.7–26.3)	24.1 (22.0–26.6)	23.9 (21.8–26.4)

The adjusted NNT ranged from 22.8 (95% CI, 21.8–23.9) at year 1 to 23.8 (95% CI, 21.7–26.3) at year 5.

BKP versus VP

Patients with VP had an unadjusted survival probability of 81.4% at 1 year post-VCF diagnosis, which decreased to 44.3% at 5 years post-VCF diagnosis, while the corresponding survival probabilities for patients with BKP were 84.1% and 48.5%, respectively, after accounting for the relative hazard ratios between BKP and VP (Table 1). The adjusted survival probabilities decreased from 79.7% to 43.0% at years 1–5 for patients with VP and from 82.6% to 47.2% at years 1–5 for patients with BKP. The unadjusted NNT for BKP versus VP ranged from 36.7 patients (95% CI, 34.5–39.2 patients) at year 1 to 24.1 patients (95% CI, 22.0–26.6 patients) at year 5 (Table 2). The adjusted NNT ranged from 33.9 (95% CI, 31.9–36.2) at year 1 to 23.9 (95% CI, 21.8–26.4) at year 5.

DISCUSSION

There is a discordance between the findings of 3 sham-controlled trials of vertebroplasty and the mortality advantage suggested by claims-based studies. There are several possible reasons for this divergence. First, NSM is not risk-free therapy.¹⁶ The combination of analgesic therapy with a period of bed rest and limitation of daily activities can be counterproductive in the geriatric population. Moreover, NSM has long included opioid medications, which are increasingly understood to be problematic in this population.¹⁷ The nonsurgical arm in the VAPOUR trial had more significant complications than the vertebroplasty cohort, including paralysis related to vertebral body collapse in 2 patients several weeks after enrollment in the trial.⁸ It has proved difficult to design a methodologically sound trial that compares vertebral augmentation against a viable alternative while still avoiding the active placebo effect. While the impact of a placebo (and nocebo) is real in pain trials, it is difficult to replicate or harness these positive effects in routine clinical practice.¹⁸ Furthermore, the sham trials that showed a robust placebo response used

needle docking in the periosteum and periosteal injection of local anesthetic, a technique that is known to produce pain relief, as opposed to the VAPOUR trial, which used a subcutaneous injection of local anesthetic.

In the 2010 VERTOS II trial, an open-label comparison of vertebroplasty and nonsurgical management, the positive clinical outcomes observed in those who had vertebroplasty were numerous and statistically robust.³ The 2 most recent sham-controlled blinded studies, VERTOS IV⁹ and VAPOUR, yielded different results regarding pain outcomes. This difference might, in part, relate to the design of the sham procedure, in particular the use of an active control (periosteal numbing) in VERTOS IV compared with a truer sham (subcutaneous numbing) in VAPOUR, because the amount of pain decrease seen immediately after the sham in VERTOS IV was a dramatic 3.1 point reduction on the numeric rating scale compared with the 1.8 point decrease seen in the VAPOUR trial. Understanding the potential for a control to have a treatment effect is critical for interpreting pain trials.¹⁹

Vertebroplasty practitioners, and thus trials of vertebroplasty, have focused on palliation of pain and improvement in functional status. In both VAPOUR and VERTOS IV, serial follow-up studies for the long term have demonstrated that augmented vertebral bodies preserve height more readily than those that are not augmented, and collapsed vertebral bodies have resulted in severe adverse events with loss of neurologic function. The preservation of sagittal alignment and vertebral body height also has intuitive benefits that perhaps contribute to the observed mortality advantage. The elevated risk of mortality for older patients with hyperkyphotic posture, specifically due to atherosclerosis, has been reported in a prospective study of >1300 patients.²⁰

Claims-based data have tended to demonstrate relative mortality advantages of kyphoplasty over vertebroplasty. While no blinded trial of kyphoplasty exists, primarily due to the ethical challenges of such a trial along with the difficulty in adequately designing a sham procedure, the findings of the 2009 vertebroplasty trials also ultimately cast some doubt on kyphoplasty.⁶ Ong et al⁷ noted a 55% mortality advantage of kyphoplasty over

nonsurgical management at 1 year. Given the relatively low 1-year mortality event rates, this equates conservatively to an NNT of <15 to save a life at 1 year using balloon kyphoplasty rather than nonsurgical management protocols. The precise reason for this notable difference in NNT between kyphoplasty and vertebroplasty when each were compared with NSM is unclear. Recent studies have demonstrated the benefit of cementation in the preservation of height, and it could be conjectured that balloon expansion leads to better sagittal reconstruction. Confounding factors may be involved in this difference in benefit. Most notably, patients with severe comorbidities and anesthetic risk may be offered vertebroplasty over kyphoplasty; hence, a difference in outcome may be attributed to underlying medical conditions.

The original use of NNT was an epidemiologic measure designed to present data in which 2 different treatments are compared with respect to incidence rates of an unfavorable event.²¹ In practice, it facilitates understanding the clinical significance of an intervention. Although the NNT was, at first, designed to be used to indicate treatment impact in randomized controlled trials, it has also been applied to observational studies. In the case of vertebral augmentation, the very salient unfavorable event is death as demonstrated in the single largest claims-based study of VCFs.⁷

To put these numbers into practical terms, we can make comparisons with known interventions. The European Cooperative Acute Stroke Study III (ECASS-III) trial studied the use of IV-tPA administered from 3 to 4.5 hours following ischemic stroke. It was found that 15 people with acute stroke symptoms needed to be treated to achieve a single favorable outcome.²² The US Preventive Services Task Force (USPSTF) trial, pooling data from 15 trials with >70,000 patients at low risk for cardiovascular disease, found that 0.4% fewer patients taking a statin died than patients taking a placebo. This equated to an NNT of 250.²³ In another study, for those taking aspirin for 1 year to prevent a first heart attack or stroke, a cardiovascular event was prevented for 1 person in a patient population of 1667, compared with 1 in 3000 for stroke.²⁴ Each of these interventions are more favorable than the use of stents for coronary artery disease, of which studies have shown that there is no number one can treat in 5 years of follow-up to achieve any benefit.²⁵

Following the publication of the 2009 sham trials of vertebroplasty, the controversy and debate were so substantial that opportunities for learning from their findings were lost. As Firanescu et al⁹ argued, clinical care pathways that focus on improvement to NSM, moving it away from the scourge of high-dose opioid anesthesia, should be considered.²⁶ The positive outcomes demonstrated in the sham-controlled groups could indicate the potential for open-label periosteal numbing and/or medial branch blocks to be used as treatment in patients thought to be at low risk of subsequent vertebral body collapse. Further study should address the risks of vertebral body collapse and the importance of preserving vertebral body height, with future studies including it as a prespecified end point.

Using large claims-based datasets inherently equates to a heterogeneous population being analyzed retrospectively. Ong et al⁷ used propensity score matching to best account for patient

covariates and reduce the bias of confounding variables. Recent advances in vertebral augmentation practices have led to discussion of the suitability of particular augmentation procedures for specific patient subgroups (eg, traumatic fractures, neoplastic fractures, patients with significant comorbidities).²⁷ Thus, there is scope for future research to analyze the utility of different techniques in different subgroups on the basis of their unique clinical conditions.²⁸ Despite these new considerations coming into focus in the discussion of vertebral augmentation, there still remains debate regarding the utility of augmentation over non-operative management.²⁹ Thus, the low NNT to save a life when offering augmentation is an important consideration in today's evidentiary landscape.

CONCLUSIONS

This NNT analysis of >2,000,000 patients with VCF reveals that only 15 patients need to be treated to save 1 life at 1 year. This is an obvious clinically significant impact, and given that all augmentation clinical trials are underpowered to detect a mortality benefit, this large dataset analysis reveals that vertebral augmentation provides a significant mortality benefit over nonsurgical management with a low NNT.

Disclosures: Joshua A. Hirsch—UNRELATED: Consultant: Medtronic, Data Monitoring Committee: Relevant, Data and Safety Monitoring Board Service, Ceranovus; Grants/Grants Pending: Neiman Health Policy Institute, Comments: health policy; I am an affiliate senior research fellow at Neiman.* Douglas Beall—UNRELATED: Board Membership: Spintec, Nocimed; Consultancy: Medtronic, Spineology, Merit Medical, Eli Lilly, Johnson & Johnson, Spintec, Imaging3, IZI, Medlantis, Techlamed; Consultant: Peterson Enterprises, Medical Metrics, Radius Pharmaceuticals, Avanos Medical, Vertiflex, Sollis Pharma, Simplify Medical, Stryker, Lenoss Medical, Spine BioPharma; Grants/Grants Pending: Medtronic, Spintec, Medical Metrics, Avanos Medical, Relevant Medsystems, Vertiflex, Stryker, Sollis Pharma, Simplify Medical, Lenoss Medical, Spine BioPharma; Payment for Lectures Including Service on Speakers Bureaus: Medtronic, Spineology, Merit Medical, Eli Lilly, Johnson & Johnson, Spintec, Imaging3, IZI, Medlantis, Techlamed; Consultant: Peterson Enterprises, Medical Metrics, Radius Pharmaceuticals, Avanos Medical, Vertiflex, Sollis Pharma, Simplify Medical, Stryker, Lenoss Medical, Spine BioPharma; Royalties: Vivex Biologics, BioPharma; Payment for Development of Educational Presentations: Medtronic, Merit, Stryker, Vertiflex; Stock/Stock Options: Artio, Sophiris, Eleven Biotherapeutics, Radius Pharmaceuticals, FlowForward Medical, Lenoss Medical, Spine BioPharma; Travel/Accommodations/Meeting Expenses Unrelated to Activities Listed: Medtronic, Spineology, Merit Medical, Eli Lilly, Johnson & Johnson, Spintec, Imaging3, IZI, Medlantis, Techlamed, Consultant: Peterson Enterprises, Medical Metrics, Radius Pharmaceuticals, Avanos Medical, Vertiflex, Sollis Pharma, Simplify Medical, Stryker, Lenoss Medical, Spine BioPharma. Michael Frohberg—UNRELATED: Employment: Exponent Inc. Kevin Ong—UNRELATED: Other: Medtronic, Stryker Orthopaedics, Sanofi, Ferring Pharmaceuticals, Paradigm Spine, Pacira Pharmaceuticals, St. Jude Medical, Relevant Medsystems, International Society for the Advancement of Spine Surgery, Zimmer Biomet, Joerns Healthcare, SpineFrontier, SI-Technology, Ethicon, DJO Global, Össur, Karl Storz Endoscopy-America, Comments: I am an employee and shareholder of Exponent, a scientific and engineering consulting firm. Exponent has been paid fees for my consulting services on behalf of such companies and suppliers.* *Money paid to the institution.

REFERENCES

1. Jha RM, Yoo AJ, Hirsch AE, et al. Predictors of successful palliation of compression fractures with vertebral augmentation: single-center experience of 525 cases. *J Vasc Interv Radiol* 2009;20:760–68 CrossRef Medline
2. Wardlaw D, Cummings SR, Van Meirhaeghe J, et al. Efficacy and safety of balloon kyphoplasty compared with non-surgical care for vertebral compression fracture (FREE): a randomised controlled trial. *Lancet* 2009;373:1016–24 CrossRef Medline

3. Klazen CA, Lohle PN, de Vries J, et al. **Vertebroplasty versus conservative treatment in acute osteoporotic vertebral compression fractures (VERTOS II): an open-label randomised trial.** *Lancet* 2010;376:1085–92 CrossRef Medline
4. Kallmes DF, Comstock BA, Heagerty PJ, et al. **A randomized trial of vertebroplasty for osteoporotic spinal fractures.** *N Engl J Med* 2009;361:569–79 CrossRef Medline
5. Buchbinder R, Osborne RH, Ebeling PR, et al. **A randomized trial of vertebroplasty for painful osteoporotic vertebral fractures.** *N Engl J Med* 2009;361:557–68 CrossRef Medline
6. Hirsch JA, Chandra RV, Pampati V, et al. **Analysis of vertebral augmentation practice patterns: a 2016 update.** *J Neurointerv Surg* 2016;8:1299–1304 CrossRef Medline
7. Ong KL, Beall DP, Frohberg M, et al. **Were VCF patients at higher risk of mortality following the 2009 publication of the vertebroplasty “sham” trials? *Osteoporos Int* 2018;29:375–83 CrossRef Medline**
8. Clark W, Bird P, Gonski P, et al. **Safety and efficacy of vertebroplasty for acute painful osteoporotic fractures (VAPOUR): a multicentre, randomised, double-blind, placebo-controlled trial.** *Lancet* 2016;388:1408–16 CrossRef Medline
9. Firanescu CE, Vries J, Lodder P, et al. **Vertebroplasty versus sham procedure for painful acute osteoporotic vertebral compression fractures (VERTOS IV): randomised sham controlled clinical trial.** *BMJ* 2018;361:k1551 CrossRef Medline
10. Edidin AA, Ong KL, Lau E, et al. **Mortality risk for operated and nonoperated vertebral fracture patients in the Medicare population.** *J Bone Miner Res* 2011;26:1617–26 CrossRef Medline
11. Lange A, Kasperk C, Alvares L, et al. **Survival and cost comparison of kyphoplasty and percutaneous vertebroplasty using German claims data.** *Spine (Phila Pa 1976)* 2014;39:318–26 CrossRef Medline
12. Martinez-Gutierrez JC, Leslie-Mazwi T, Chandra RV, et al. **Number needed to treat: a primer for neurointerventionalists.** *Interv Neuroradiol* 2019;25:613–18 CrossRef
13. Edidin AA, Ong KL, Lau E, et al. **Morbidity and mortality after vertebral fractures: comparison of vertebral augmentation and non-operative management in the Medicare population.** *Spine* 2015;40:1228–41 CrossRef Medline
14. Altman DG, Andersen PK. **Calculating the number needed to treat for trials where the outcome is time to an event.** *BMJ* 1999;319:1492–95 CrossRef Medline
15. Bowry SK, Schoder V, Apel C. **An inadvertent but explicable error in calculating number needed to treat for reporting survival data.** *J Am Soc Nephrol* 2014;25:875–76 CrossRef Medline
16. Babayev M, Lachmann E, Nagler W. **The controversy surrounding sacral insufficiency fractures: to ambulate or not to ambulate? *Am J Phys Med Rehabil* 2000;79:404–09 CrossRef Medline**
17. Manchikanti L, Kaye AM, Knezevic NN, et al. **Responsible, safe, and effective prescription of opioids for chronic non-cancer pain: American Society of Interventional Pain Physicians (ASIPP) Guidelines.** *Pain Physician* 2017;20:S3–92 Medline
18. Manchikanti L, Boswell MV, Kaye AD, et al. **Therapeutic role of placebo: evolution of a new paradigm in understanding research and clinical practice.** *Pain Physician* 2017;20:363–86 Medline
19. Manchikanti L, Knezevic NN, Boswell MV, et al. **Epidural injections for lumbar radiculopathy and spinal stenosis: a comparative systematic review and meta-analysis.** *Pain Physician* 2016;19:E365–10 Medline
20. Kado DM, Huang MH, Karlamangla AS, et al. **Hyperkyphotic posture predicts mortality in older community-dwelling men and women: a prospective study.** *J Am Geriatr Soc* 2004;52:1662–67 CrossRef Medline
21. Cook RJ, Sackett DL. **The number needed to treat: a clinically useful measure of treatment effect.** *BMJ* 1995;310:452–54 CrossRef Medline
22. Hacke W, Kaste M, Bluhmki E, et al. **Thrombolysis with alteplase 3 to 4.5 hours after acute ischaemic stroke (ECASS III).** *N Engl J Med* 2008;359:1317–29 CrossRef Medline
23. Chou R, Dana T, Blazina I, et al. **Statins for prevention of cardiovascular disease in adults: Evidence Report and Systematic Review for the US Preventive Services Task Force.** *JAMA* 2016;316:2008–24 CrossRef Medline
24. Antithrombotic Trialists Collaboration. **Aspirin in the primary and secondary prevention of vascular disease: collaborative meta-analysis of individual participant data from randomised trials.** *Lancet* 2009;373:1849–60 CrossRef Medline
25. Stergiopoulos K, Boden WE, Hartigan P, et al. **Percutaneous coronary intervention outcomes in patients with stable obstructive coronary artery disease and myocardial ischemia: a collaborative meta-analysis of contemporary randomized clinical trials.** *JAMA Intern Med* 2014;174:232–40 CrossRef Medline
26. Hirsch JA, Beall DP, Chambers MR, et al. **Management of vertebral fragility fractures: a clinical care pathway developed by a multispecialty panel using the RAND/UCLA appropriateness method.** *Spine J* 2018;18:2152–61 CrossRef Medline
27. Cianfoni A, Distefano D, Isalberti M, et al. **Stent-screw-assisted internal fixation: the SAIF technique to augment severe osteoporotic and neoplastic vertebral body fractures.** *J Neurointerv Surg* 2019;11:603–09 CrossRef Medline
28. Shah LM, Jennings JW, Kirsch CF, et al. **ACR appropriateness criteria management of vertebral compression fractures.** *J Am Coll Radiol* 2018;15:S347–64 CrossRef Medline
29. Eberling PR, Akesson K, Bauer DC, et al. **The efficacy and safety of vertebral augmentation: a second ASBMR Task Force Report.** *J Bone Miner Res* 2019;34:3–21 CrossRef Medline

Simple Fluoroscopy-Guided Transforaminal Lumbar Puncture: Safety and Effectiveness of a Coaxial Curved-Needle Technique in Patients with Spinal Muscular Atrophy and Complex Spines

J.P. Jacobson, B.C. Cristiano, and D.R. Hoss

ABSTRACT

SUMMARY: Patients with spinal muscular atrophy often have complete interlaminar osseous fusion, precluding lumbar puncture via the standard interlaminar approach. Recently, we have developed a new coaxial curved-needle variation of fluoroscopy-guided transforaminal lumbar puncture for intrathecal injections in this patient population. Between October 2017 and November 2018, fifty-nine consecutive transforaminal lumbar punctures using this technique were performed in 12 patients with spinal muscular atrophy for intrathecal nusinersen injection, with a 100% technical success rate and no C1–2 punctures required. One major complication occurred, consisting of a post-dural puncture headache, which required a therapeutic transforaminal epidural blood patch. Two minor complications occurred, both of which involved inadvertent puncture of a dorsal muscular arterial branch, without clinical sequelae. A fluoroscopy-guided curved-needle transforaminal approach is an effective technique for lumbar puncture in difficult cases, such as in this cohort of patients with spinal muscular atrophy and complete interlaminar osseous fusion undergoing intrathecal nusinersen injections.

ABBREVIATIONS: TFLP = transforaminal lumbar puncture; SMA = spinal muscular atrophy

Recently, the US Food and Drug Administration approved nusinersen (Spinraza) as the first effective therapy for spinal muscular atrophy (SMA). The medication is administered intrathecally, with a standard treatment protocol that involves 3 loading doses separated by 2 weeks, a fourth injection at 1 month, and maintenance doses every 4 months.

Patients with SMA often have severe neuromuscular scoliosis with subsequent extensive posterior spinal fusion and, frequently, complete interlaminar osseous fusion, precluding lumbar puncture via the standard interlaminar approach.¹ Fluoroscopically guided C1–2 puncture by a lateral approach is considered standard practice for intrathecal access when the posterior lumbar interlaminar approach is not possible. However, rare-but-serious risks are associated with this technique, including cervical cord puncture and vertebral artery injury.^{2,3}

We have been performing fluoroscopy-guided transforaminal lumbar puncture (TFLP) at our institution since 2007 as an

alternative to C1–2 puncture for lumbar punctures with difficult interlaminar access. The purpose of this study was to evaluate the effectiveness and safety of a novel coaxial curved-needle technique for fluoroscopy-guided TFLP in a cohort of patients with SMA and complete interlaminar osseous fusion undergoing lumbar puncture for intrathecal nusinersen injection.

Case Series

Case Selection. Following local institutional review board approval and a waiver of informed consent, a retrospective review was performed of 59 consecutive fluoroscopy-guided TFLPs using a curved-needle technique for intrathecal nusinersen injection in 12 patients between October 2017 and November 2018. TFLPs performed for other indications or using a different technique were excluded.

Patients were identified as candidates for TFLP when there was a known history of posterior spinal fusion and evidence of interlaminar osseous fusion on available imaging, most commonly radiographs (62.5%, $n = 7$). Preprocedural planning CTs were performed in only 25% ($n = 3$) of patients, 2 of which were obtained before the study period, before development of our current technique when we previously used various straight-needle techniques. The other planning CT was obtained very early in the study period. Patients were evaluated for possible complications

Received July 29, 2019; accepted after revision October 21.

From the Department of Radiology, Neuroradiology Section, Loma Linda University Medical Center, Loma Linda, California.

Paper previously presented at: Annual Meeting of the American Society of Spine Radiology, February 20–24, 2019; Miami, Florida. Our initial experience regarding transforaminal lumbar puncture using a different technique was presented at: Annual Meeting of the American Roentgen Ray Society, April 13–18, 2008; Washington, DC.

Please address correspondence to Daniel R. Hoss, MD, Loma Linda University Medical Center, 11234 Anderson St, Loma Linda, CA 92354, e-mail: dhoss@llu.edu <http://dx.doi.org/10.3174/ajnr.A6351>

before discharge, at the subsequent procedural encounter, and during clinical follow-up.

Technical success, defined by a return of CSF and complete medication delivery, was evaluated. Immediate and delayed complications, fluoroscopy time, and radiation dose were also evaluated. Fluoroscopy time was recorded for all cases. Dose-area product and air kerma were recorded for 12 procedures, which we began prospectively recording late in the study period and could not be retrospectively recovered for earlier procedures. Effective dose was calculated using a conversion coefficient of $0.21 \text{ mSv (Gy} \times \text{cm}^2)^{-1}$ and the formula: Effective Dose = Dose Conversion Coefficient \times Dose-Area Product.⁴ A Student *t* test was used to compare mean fluoroscopy times between the first 30 TFLPs and the final 29 TFLPs to assess a learning curve effect. Complications were classified as major or minor according to Society of Interventional Radiology clinical practice guidelines.⁵

RESULTS

The 12 patients ranged from 11 to 37 years of age (mean, 21.5 years) with 62.5% ($n=7$) females. All patients had spinal fusion extending from the upper thoracic spine to the sacrum. Fifty-

nine TFLPs were performed (mean, 4.9 per patient; range, 3–6) with a 100% technical success rate. The mean fluoroscopy time was 3.8 minutes (range 0.2–15.8 minutes), and the mean fluoroscopy time was shorter for the final 29 TFLPs compared with the first 30 TFLPs (2.7 minutes versus 4.8 minutes, $P < .01$). The mean air kerma was 63.1 mGy (range, 20.8–154 mGy; $n=12$), and the mean effective dose was 1.07 mSv (range, 0.29–2.7 mSv; $n=12$). Right-sided neural foramina were used for access more commonly, L3–4 was the level most often used, and procedures were typically performed with the patient under general anesthesia, as determined by the anesthesiologist (Table 1). One major complication occurred, consisting of a post-dural puncture headache, which required inpatient hospital admission and a therapeutic transforaminal epidural blood patch. Two minor complications occurred, both of which involved inadvertent puncture of a dorsal muscular arterial branch during placement of the introducer needle. In both cases, positioning of the needle was assessed by contrast injection, which showed the intra-articular tip position and no visible flow into the spinal canal. The needles were repositioned, the procedures were completed, and the patients were observed for an additional 6 hours without sequelae.

Table 1: Procedural details

Details	No. (%)
Total	59 (100)
Level of access	
L2–3	11 (18.6)
L3–4	34 (57.6)
L4–5	14 (23.7)
Laterality of foramen accessed	
Right	48 (81.4)
Anesthesia type	
General	39 (66.1)
Local	20 (33.9)

DISCUSSION

Technique

Equipment and Patient Positioning. All TFLPs were performed using biplane fluoroscopy (Axiom Artis dBA; Siemens, Erlangen, Germany). Patient positioning was determined on the basis of lumbar curvature, taking into account the unilateral dorsal presentation of 1 neural foramen in cases of rotatory scoliosis. A right-transforaminal approach was preferred due to our standard practice of placing patients in the left-lateral decubitus position for lumbar punctures. If patient anatomy required a left-transforaminal approach (left neural foramen oriented more dorsally due to rotatory scoliosis), the patient was positioned semi-prone (left side down) with the head turned to the right. In this position, a posterior oblique approach to the left neural foramen was essentially parallel to the fluoroscopy table. Procedures were performed with the patients under either general or local anesthesia according to patient and anesthesiologist preference. Conscious sedation administered by an RN was not used due to concerns for respiratory compromise in this patient population.

Procedural Technique

A coaxial technique with an inner curved needle was previously described for access to the L5–S1 disk for diskography,⁶ and we used a similar technique for access to the target neural foramen using a Pakter Curved Needle Set (Fig 1; Cook Medical, Bloomington, Indiana). For aiming of the introducer

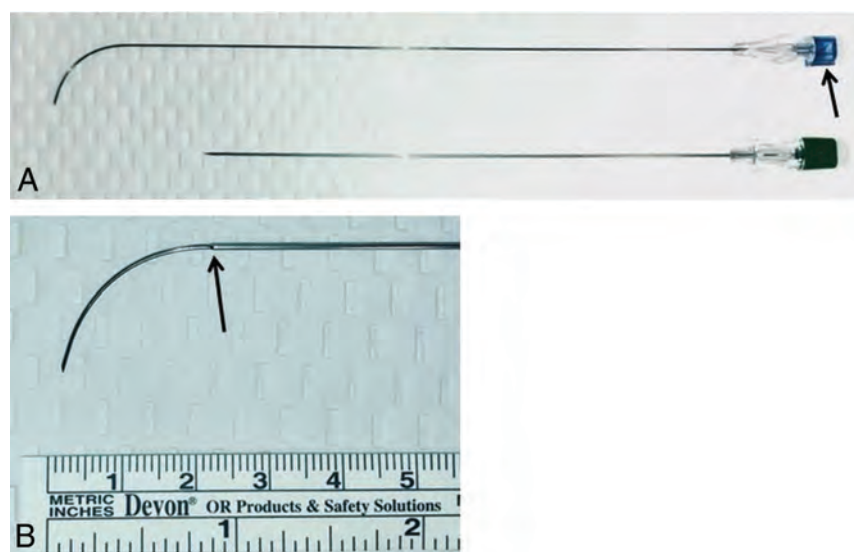


FIG 1. The Pakter Curved Needle Set. A, Unmagnified view of the outer 15-cm 21-ga introducer needle (bottom) and inner 20-cm 25-ga curved needle (top). The notch on the inner needle indicates the direction that the needle will curve as it exits the introducer needle (arrow). B, Magnified view of the curved inner needle exiting the introducer needle (arrow indicates introducer needle tip).

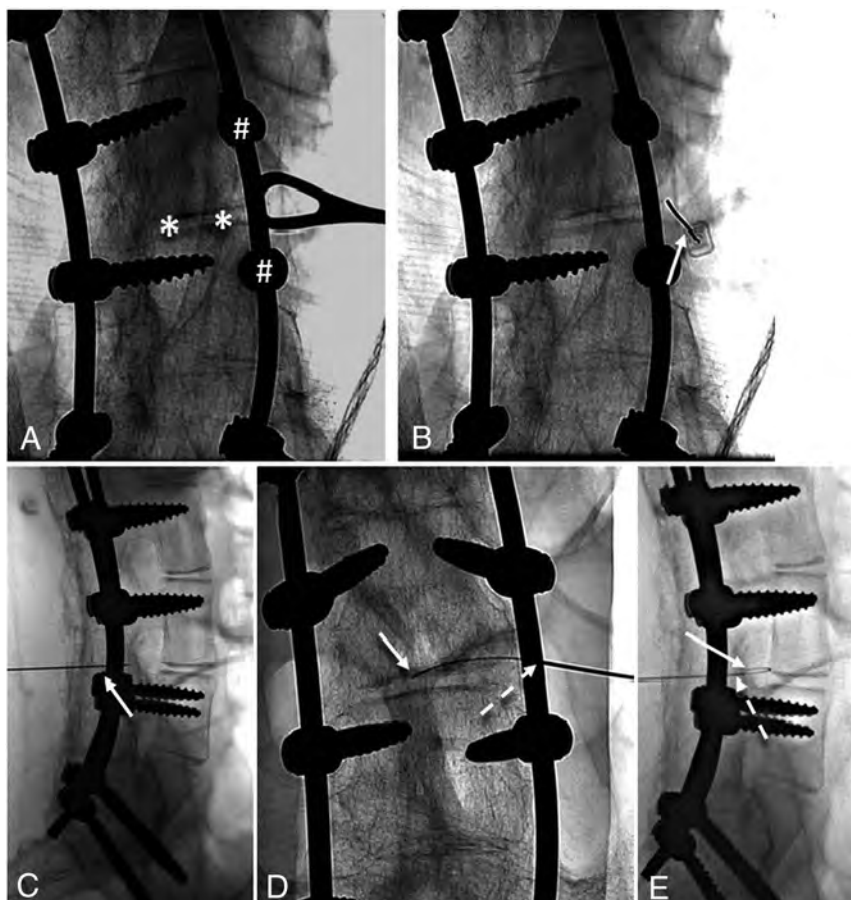


FIG 2. Spot radiographs demonstrating steps in TFLP using the curved Pakter needle. A, posterolateral oblique view along the long axis of the pedicle. A ring forceps indicates the skin entry site at the level of the disk (asterisks), just lateral to the pedicles (hashtags). B and C, posterolateral oblique and lateral views show the correct position of the outer guiding needle terminating just lateral to the posterior margin of the target neural foramen and projecting over the lateral disk margin on the posterolateral oblique view (arrow). D and E, posteroanterior and lateral views show the correct position of the outer needle (dashed arrow) and the inner curved needle (solid arrow), having passed through the target neural foramen and terminating within the thecal sac at L3–4.

needle, the B-plane fluoroscopy arm (fluoroscopy plane parallel to the floor) was initially positioned in a posterolateral oblique projection along the long axis of the pedicle inferior to the target neural foramen (approximately 15°–20° lateral from posteroanterior) (Fig 2A). For depth control, the A-plane fluoroscopy arm (fluoroscopy plane perpendicular to the floor) was positioned in a standard lateral projection, with attention paid to precise superimposition of the bilateral neural foramina at the target level (Fig 2C).

Using the posterolateral oblique view, we marked the skin overlying the target site at the lateral aspect of the disk corresponding to the target neural foramen (Fig 2A). Next, the introducer needle was advanced with biplane fluoroscopic control from the skin-entry site toward the target site at the lateral disk margin (Fig 2B) until the needle tip depth reached the posterior margin of the target neural foramen on the lateral projection (Fig 2C). This was the final position of the introducer needle.

For medial aiming and depth control of the coaxial 25-ga curved needle, the B-plane fluoroscopic arm was adjusted from

posterolateral oblique to true posteroanterior; the A-plane remained in the lateral projection. The coaxial 25-ga curved Pakter needle was then directed medially and passed through the introducer needle until both were tip-to-tip. Under live biplane fluoroscopic control, the curved needle was then advanced through the inferior neural foramen to the midline, puncturing the thecal sac (Figs 2D, -E); the puncture was confirmed by return of CSF. Five milliliters of CSF was removed, and 12 mg of nusinersen in 5-mL total volume was delivered intrathecally during 1–3 minutes.

Safety

The only noteworthy complication encountered (1.6%) was a post-dural puncture headache requiring a therapeutic transforaminal epidural blood patch. This is similar to the reported rate of blood patch both in this patient population⁷ and in a patient population⁸ without SMA via the standard interlaminar approach. Two minor complications (3.2%) also occurred, consisting of puncture of a dorsal branch of the lumbar artery during placement of the outer 21-ga needle. Branches of the lumbar artery are typically located superiorly within the neural foramen,^{9,10} but in both of our cases of arterial puncture, the needle tip was at the level of the mid-posterior foramen on the lateral view and approximately 1 cm lateral to the pedicle on the posteroanterior view (Fig 3). Although neither patient experienced an adverse event related to arterial puncture, serious hemorrhagic complications have been reported due to injury of the lumbar artery and its branches during percutaneous image-guided spine procedures, including vertebral body biopsy,¹¹ vertebroplasty,¹² and kyphoplasty¹³ and during transforaminal percutaneous endoscopic lumbar discectomy.^{10,14}

Given the potential for serious hemorrhagic complications, puncture of branches of the lumbar artery should clearly be avoided, and we now target the inferior neural foramen to avoid the dorsal branch. Although this complication has not been previously described related to TFLP, it should be kept in mind by all who perform TFLPs. Our technique differs from typical straight-needle techniques in that the stylet of the outer needle is removed when the needle tip is extraforaminal. Other straight-needle techniques likely involve removal of the stylet only when the needle tip is intrathecal; therefore, injury of an extraforaminal artery could go undetected. No patient in our cohort experienced persistent radicular symptoms.

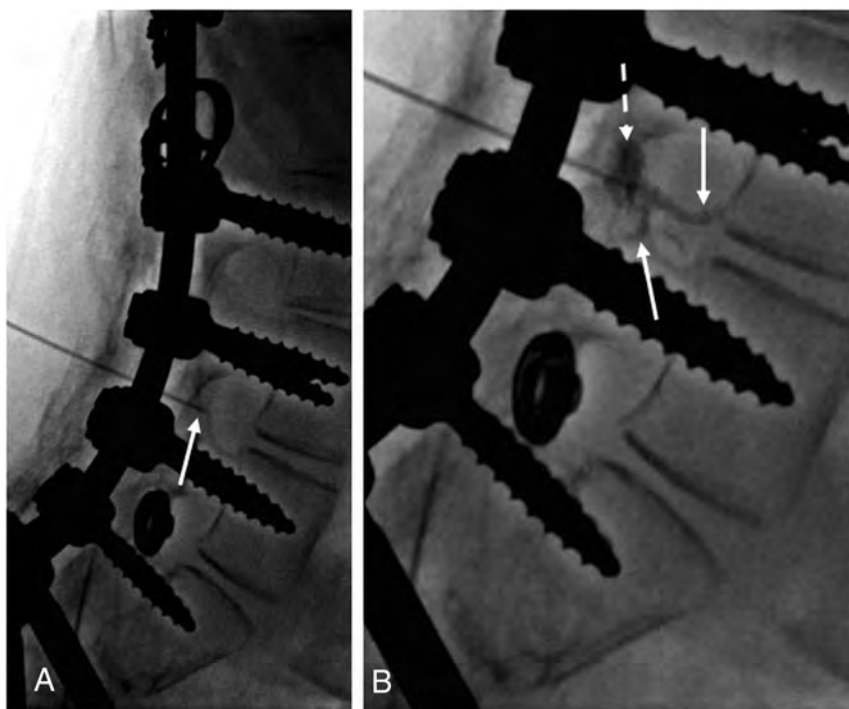


FIG 3. Lateral fluoroscopic images during TFLP. *A*, Final position of the introducer needle (arrow). Blood return was noted at the needle hub after removal of the stylet. *B*, Injection of a small volume of iodinated contrast medium demonstrates opacification of a dorsal branch of the lumbar artery (solid arrows) and contrast collecting within the soft tissues (dashed arrow).

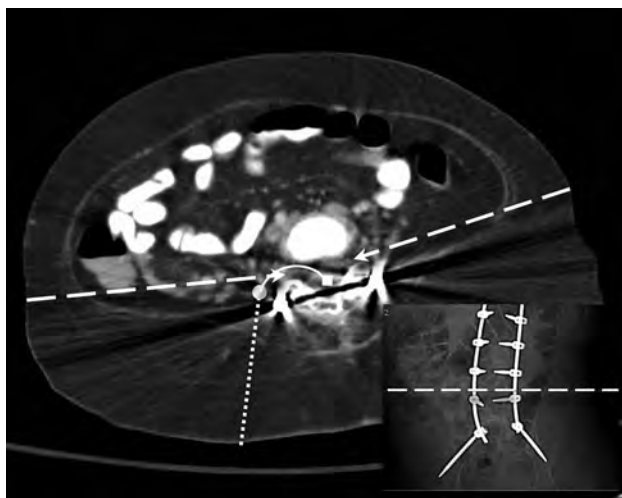


FIG 4. Axial CT obtained in the same patient depicted in Figure 2 near the time of procedure but for an unrelated indication annotated to depict approximate trajectory and ending points of the outer guiding needle and curved inner needle using curved needle technique. *Dotted line* indicates guiding needle trajectory. *Circle* indicates guiding needle termination. *Solid line* indicates curved needle trajectory. *Square* indicates curved needle termination. *Dashed arrows* indicate hypothetical right and left straight needle trajectories at this level in this patient. *Insert*: corresponding AP scout image *dashed line* indicates plane of imaging.

The transforaminal approach has been used for epidural injections for decades, with increased use of this technique in recent years. More recently, the transforaminal approach has been

described for intrathecal access, most commonly for administration of nusinersen.¹⁵⁻¹⁸ Weaver et al¹⁸ used cone-beam CT with fluoroscopic guidance overlay to perform TFLPs via a short, linear posterolateral approach in a similar patient population. In their description of their institutional protocol for intrathecal nusinersen administration in patients with SMA, Mousa et al¹⁶ also used a straight-needle TFLP technique when an interlaminar approach was deemed infeasible. In both of these studies, preprocedural lumbar spine CT was performed in all patients who had spinal hardware and osseous fusion, to assess possible interlaminar access and to determine a suitable target neural foramen if an interlaminar access was not possible. With a straight-needle transforaminal technique, cervical puncture may still be required in a small percentage of patients when retroperitoneal structures are in the expected path of the needle. With the curved-needle technique described here, retroperitoneal structures are widely avoided

(Fig 4); therefore, preprocedural CT is not performed, and no cervical puncture has been necessary.

Table 2 summarizes available publications using TFLP, which have provided radiation dose information in comparison with the current study. A conversion factor of $0.018 \text{ mSv/mGy} \times \text{cm}$ was used to calculate the effective dose for studies using CT guidance.^{15,17-21} Radiation doses in the current study are similar to the lowest doses in published literature for TFLP. However, the total radiation dose in the current study is likely lower because we do not perform a planning CT, whereas most other authors either explicitly stated that planning CTs were performed¹⁸ or described planning CT being used in some cases while not explicitly stating whether this was routine practice.^{15,17,21} The effective dose of a diagnostic lumbar spine CT is approximately 13 mSv.²² The mean effective dose for the 3 planning CTs in the present study was 12.5 mSv.

The multiplicity of recent publications and techniques indicates the ongoing challenges with intrathecal access in this patient population. The fluoroscopy-guided curve-needle transforaminal technique described here provides an attractive alternative for access. Potential benefits include the absence of a need for a surgical procedure, absence of the need for a planning CT, a low procedural radiation dose, a high technical success rate, and a low complication rate. In addition, the needle trajectory with the curved-needle technique widely avoids retroperitoneal organs, which may not always be the case with straight-needle TFLP techniques. While we use biplane fluoroscopy, this technique can be performed on single-plane equipment with minimal modification by alternating the image intensifier between the projections.

Table 2: Comparison of radiation doses associated with TFLP in the present literature

Authors	Guidance Type	Effective Dose (Mean) (mSv)	Air Kerma (Mean) (mGy)	Planning CT
Geraci et al ¹⁷	CT	9.95	NA	Not stated
Nascene et al ¹⁵	CT	1.04	NA	Not stated
Weaver et al ¹⁸	Fluoroscopy	NA	55.8	Yes
Wurster et al ²⁰	CT	1.54	NA	No
Stolte et al ²¹	CT	2.6 (<i>n</i> = 43)	NA	Not stated
	Fluoroscopy	0.55 (<i>n</i> = 13)	NA	
Current study	Fluoroscopy	1.07	63.1	No

Note:—NA indicates not applicable.

Finally, with the fluoroscopic landmarks described, even very difficult spines can be accessed by a variety of radiologists; for example, 8 radiology residents and 4 neuroradiology fellows successfully performed this technique in the reported cohort, providing evidence of its simplicity and reproducibility.

This case series has several limitations. The sample size is small and, therefore, is underpowered to detect rare complications. The sample size is even smaller when considering the number of cases in which the effective dose could be calculated. Furthermore, the cases in which the effective dose could be calculated were late in the study period, and earlier cases during the development of the technique may have had higher effective doses, particularly given the longer fluoroscopy times early in the study period. Although no patient experienced persistent radicular symptoms, occasionally patients did experience radicular symptoms during passage of the needle through the neural foramen. However, because this immediately resolved in all cases on removal of the needle, it was not always documented in the procedural notes; therefore, the true incidence is not known. The potential for unrecognized motor deficits related to nerve root injury does exist in this population due to baseline deficits related to SMA.

CONCLUSIONS

A fluoroscopy-guided curved-needle transforaminal approach is an effective technique for lumbar puncture in difficult cases, such as in this cohort of patients with spinal muscular atrophy with complete interlaminar osseous fusion undergoing intrathecal nusinersen injections. Our results suggest that this technique is safe, but the small sample size indicates that further evaluation is warranted. Additionally, the radiation dose to the patient may be decreased compared with previously described techniques, particularly if a preprocedural planning CT is avoided.

Disclosures: Brian C. Cristiano—UNRELATED: Travel/Accommodations/Meeting Expenses Unrelated to Activities Listed: sponsored travel to educational meetings unrelated to the present study; Penumbra and Stryker neuroendovascular courses. Daniel R. Hoss—UNRELATED: Payment for Lectures Including Service on Speakers Bureaus: Biogen, Comments: I have served as a consultant for Biogen, the maker of nusinersen, regarding intrathecal access in complex spines. I have also served as a speaker for Biogen regarding various aspects of nusinersen use in patients with spinal muscular atrophy; Payment for Development of Educational Presentations: Biogen, Comments: I developed an educational presentation for the Biogen staff regarding nusinersen administration in patients with spinal muscular atrophy with complex spines.

REFERENCES

- Kolb SJ, Kissel JT. **Spinal muscular atrophy.** *Neurol Clin* 2015;33:831–46 CrossRef Medline
- Katoh Y, Itoh T, Tsuji H, et al. **Complications of lateral C1-2 puncture myelography.** *Spine* 1990;15:1085–87 CrossRef Medline
- Orrison W, Eldevik O, Sackett J. **Lateral C1-2 puncture for cervical myelography, Part III: historical, anatomic, and technical considerations.** *Radiology* 1983;146:401–08 CrossRef Medline
- Hart D, Hillier MC, Wall BF. **Doses to patients from medical X-ray examinations in the UK-2000 review.** Chilton: National Radiological Protection Board; 2002. https://assets.publishing.service.gov.uk/government/uploads/system/uploads/attachment_data/file/405115/2002_NrpbW14.pdf. Accessed October 15, 2019
- Sacks D, McClenny TE, Cardella JF, et al. **Society of Interventional Radiology clinical practice guidelines.** *J Vasc Interv Radio* 2003;14(9 Pt 2):S199–202 CrossRef Medline
- Peh WCG. **Provocative discography.** In: Gangi A, Guth S, Geurmazi A, eds. *Imaging in Percutaneous Musculo-skeletal Interventions.* Berlin: Springer-Verlag; 2009:119–41
- Haché M, Swoboda KJ, Sethna N, et al. **Intrathecal injections in children with spinal muscular atrophy: nusinersen clinical trial experience.** *J Child Neurol* 2016;31:899–906 CrossRef Medline
- Özütemiz C, Köksel YK, Huang H, et al. **The efficacy of fluoroscopy-guided epidural blood patch in the treatment of spontaneous and iatrogenic cerebrospinal fluid leakage.** *Eur Radiol* 2019;29:4088–95 CrossRef Medline
- Arsalan M, Comert A, Acar HI, et al. **Surgical view of the lumbar arteries and their branches: an anatomical study.** *Neurosurgery* 2011;68(1 Suppl Operative):16–22; discussion 22 CrossRef Medline
- Ahn Y, Kim JU, Lee BH, et al. **Postoperative retroperitoneal hematoma following transforaminal percutaneous endoscopic lumbar discectomy.** *J Neurosurg Spine* 2009;10:595–602 CrossRef Medline
- Kulkarni K, Matravels P, Mehta A, et al. **Pseudoaneurysm following vertebral biopsy and treatment with percutaneous thrombin injection.** *Skeletal Radiol* 2007;36:1195–98 CrossRef Medline
- Heo DH, Cho YJ. **Segmental artery injury following percutaneous vertebroplasty using extrapedicular approach.** *J Korean Neurosurg Soc* 2011;49:131 CrossRef Medline
- Biafora SJ, Mardjetko SM, Butler JP, et al. **Arterial injury following percutaneous vertebral augmentation: a case report.** *Spine* 2006;31:E84–E87 CrossRef Medline
- Wang Y, Ai P, Zhan G, et al. **Lumbar artery injury during transforaminal percutaneous endoscopic lumbar discectomy: successful treatment by emergent transcatheter arterial embolization.** *Ann Vasc Surg* 2018;53:267.e11–67.e214 CrossRef Medline
- Nascene D, Ozutemiz C, Estby H, et al. **Transforaminal lumbar puncture: an alternative technique in patients with challenging access.** *AJNR Am J Neuroradiol* 2018;39:986–91 CrossRef Medline
- Mousa MA, Aria DJ, Schaefer CM, et al. **A comprehensive institutional overview of intrathecal nusinersen injections for spinal muscular atrophy.** *Pediatr Radiol* 2018;48:1797–1805 CrossRef Medline
- Geraci AP, Black K, Jin M, et al. **Transforaminal lumbar puncture for intrathecal nusinersen administration.** *Muscle Nerve* 2018 Jan 24. [Epub ahead of print] CrossRef Medline
- Weaver JJ, Natarajan N, Shaw DW, et al. **Transforaminal intrathecal delivery of nusinersen using cone-beam computed tomography for children with spinal muscular atrophy and extensive**

- surgical instrumentation: early results of technical success and safety.** *Pediatr Radiol* 2018;48:392–97 CrossRef Medline
19. Leng S, Christner JA, Carlson SK, et al. **Radiation dose levels for interventional CT procedures.** *AJNR Am J Roentgenol* 2011;197:W97–103 CrossRef Medline
 20. Wurster CD, Winter B, Wollinsky K, et al. **Intrathecal administration of nusinersen in adolescent and adult SMA type 2 and 3 patients.** *J Neurol* 2019;266:183–94 CrossRef Medline
 21. Stolte B, Totzeck A, Kizina K, et al. **Feasibility and safety of intrathecal treatment with nusinersen in adult patients with spinal muscular atrophy.** *Ther Adv Neurol Disord* 2018;11:1756286418803246 CrossRef Medline
 22. Shrimpton PC, Jansen JT, Harrison JD. **Updated estimates of typical effective doses for common CT examinations in the UK following the 2011 national review.** *Br J Radiol* 2016;89:20150346 CrossRef Medline

35 Years ago in AJNR

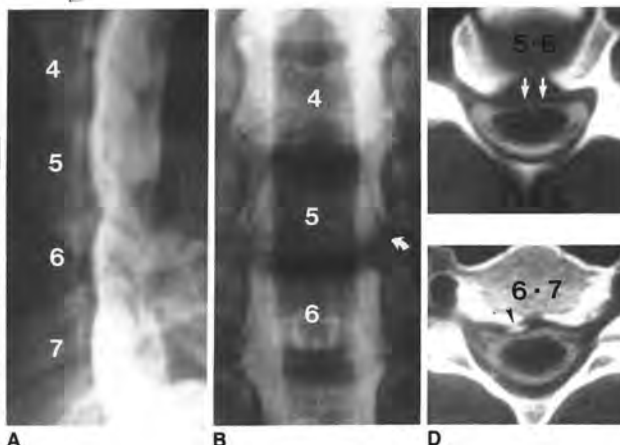
January 1985 edition

Metrizamide CT Myelography in Cervical Myelopathy and Radiculopathy: Correlation with Conventional Myelography and Surgical Findings

J. Paul Badami¹
David Norman
Nicholas M. Barbaro
Christopher E. Cann
Philip R. Weinstein
David F. Sobel

Conventional myelography, metrizamide computed tomographic (CT) myelography, and surgical findings were correlated in 30 patients with cervical radiculopathy and/or myelopathy. In 80% of patients, metrizamide CT myelography provided significant additional information including better characterization of the abnormality, lateralization if the conventional myelogram was indeterminate, more definitive demonstration of cord atrophy, foraminal narrowing not appreciated on myelography, and demonstration of abnormalities distal to a myelographic block. In no case was a myelographic abnormality not detected on metrizamide CT myelography. In patients with cervical myelopathy, a cross-sectional diameter of the cord equaling less than 50% of the subarachnoid space is predictive of poor patient response to surgical intervention.

Computed tomography (CT) has been widely accepted as an initial radiographic examination in the evaluation of lumbar radiculopathy [1-3]. The assessment of spinal pathology in patients with cervical myelopathy and/or radiculopathy has continued to consist primarily of conventional myelography. While previous studies have reported CT findings in the abnormal cervical spine [4-15], none have compared metrizamide myelography with metrizamide CT myelography and correlated the observations with surgical findings. This approach permits the development of objective criteria for the abnormal cervical metrizamide CT myelogram. The technique may in many cases eliminate the necessity for conventional myelography.



This article appears in the January/February 1985 issue of AJNR and the April 1985 issue of AJNR.

Received March 19, 1984; accepted after revision July 11, 1984.

Presented at the annual meeting of the American Society of Neuroradiology, San Francisco, June 1983.

All authors: Department of Radiology, University of California, San Francisco, CA 94143. Address reprint requests to D. Norman.

AJNR 6:55-64, January/February 1985
0195-4108/85/0601-0055\$06.00
© American Roentgen Ray Society

Acoustic Neuromas: Evaluation by Magnetic Resonance Imaging

D. P. E. Kingsley¹
G. B. Brooks²
A. W.-L. Leung²
M. A. Johnson²

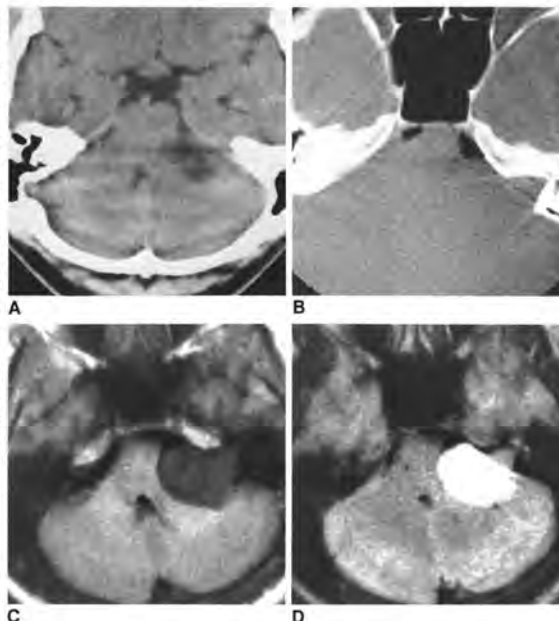
Proton magnetic resonance imaging (MRI) examinations with seven acoustic neuromas, and the results were compared with the results of conventional contrast-enhanced CT, air CT cisternography, and air CT cisternography. All tumors were identical tumors (> 1 cm diameter) looked similar to the tumors as seen on MRI in two caudal cerebellopontine angle and intracranial fat with appearances corresponding to those seen with air effects were encountered with the MRI examinations. MRI alternative to contrast-enhanced CT and air CT cisternography.

Acoustic neuromas are relatively common benign tumors of the vestibular division of the eighth cranial nerve and cerebellopontine angle and internal auditory canal. (1) diagnosis depends on the use of plain radiographs, contrast-enhanced computed tomography (CT), air or vertebral angiography. Metrizamide CT cisternography or gas CT cisternography but is associated with a higher incidence of complications. Abnormalities on plain radiographs and conventional CT are of limited value in the diagnosis of acoustic neuromas. Contrast-enhanced CT is accurate in the detection of tumors > 1 cm in size, but false negatives may occur in smaller tumors [2, 3]. Therefore, air or gas CT cisternography is more accurate [4], although false negative of arachnoid adhesions or very narrow IACs [5, 6] reserved for cases in which the surgeon needs to know the tumor.

Early reports on low-resolution proton magnetic resonance (MR) described acoustic neuroma appearances similar to enhanced CT [7-9], although intracranial extension has also been described [10]. With recent improved images, including the use of a 256 x 256 reconstruction to routinely image the normal IAC containing the seventh cranial nerve, the anatomic basis for the demonstration of acoustic neuromas on MRI as good as a potential for diagnosis as CT cisternography. We compared the results of contrast-enhanced CT, air CT cisternography, and MRI of 11 acoustic neuromas.

Subjects and Methods

Seventeen patients (four men and two women) with clinical signs



Received December 27, 1983; accepted after revision July 11, 1984.

M. A. Johnson is an Alberta Heritage Scholar.

¹Departments of Radiology and Otolaryngology, London Hospital, Whitechapel, London E1 1BB, England.

²Department of Diagnostic Radiology, Royal Postgraduate Medical School, Hammersmith Hospital, DuCane Rd., London W12 0NS, England.

Address reprint requests to M. A. Johnson.

AJNR 6:5-6, January/February 1985
0195-4108/85/0601-0001\$06.00
© American Roentgen Ray Society

Regarding “The Interpeduncular Angle: A Practical and Objective Marker for the Detection and Diagnosis of Intracranial Hypotension on Brain MRI”

We carefully read the article by Wang et al.¹ We are very interested in the method of judging intracranial hypotension by measuring the interpeduncular angle. We hope to apply this method to our clinical work, but the following questions seem to bother us: 1) Specifically, how is intracranial hypotension diagnosed? Is it by judging whether pachymeningeal enhancement or subdural collections or venous engorgement or brain stem slumping in the MR images or a combination of ≥ 2 of the above? 2) How does the brain stem slumping manifest by imaging only distinguish it from Arnold Chiari malformation? 3) How does one eliminate the influence of head displacement on the interpeduncular angle caused by the displacement of the head during plain MR imaging? If the above problems are solved, the clinical applicability of the interpeduncular angle will be greatly enhanced. We are very grateful to Wang et al for the study, which gave us a new way to evaluate intracranial hypotension on brain MR imaging.

<http://dx.doi.org/10.3174/ajnr.A6340>

REFERENCE

1. Wang DJ, Pandey SK, Lee DH, et al. **The interpeduncular angle: a practical and objective marker for the detection and diagnosis of intracranial hypotension on brain MRI.** *AJNR Am J Neuroradiol* 2019; 40:1299–1303 CrossRef Medline

 J. Zhang

 H. Wang

Department of Clinical Medicine
Dalian Medical University
Dalian Liaoning, China

 L. Dong

 Y. Li

Department of Neurosurgery
Clinical Medical College of Yangzhou University
Yangzhou, China

REPLY:

Thank you for your interest in our article and thought-provoking questions. Intracranial hypotension is diagnosed on the basis of a combination of both clinical and imaging findings. The International Classification of Headache Disorders, 3rd edition, requires a headache (typically orthostatic) that develops in temporal association with either low opening pressure on lumbar puncture or typical MRI findings for diagnosis. The MRI findings include pachymeningeal thickening or enhancement, bilateral subdural collections, venous engorgement, and/or brain stem slumping. The MRI findings complement the clinical findings and should be considered in the correct clinical context. These findings, along with a decrease in the interpeduncular angle, are thought to reflect the mass-effect interplay from low CSF volume and lack of buoyancy forces.

A different mechanism exists in the cases of Chiari malformations (ie, hypoplasia of the posterior fossa), and in the most

benign end of the pathologic spectrum, Chiari I demonstrates only low tonsils (below 5 mm from foramen magnum) without the aforementioned findings present in intracranial hypotension. In our study, we excluded such cases.

At our institution, head position is neutral in most cases (an exception includes flexion/extension views in evaluating for Hirayama disease). We did not control for head position in our study, but we are not aware of a strong association between this and brain stem/cerebellar tonsil position. We refer you to Horsburgh et al.¹

REFERENCE

1. Horsburgh A, Kirollos RW, Massoud TF. **No significant displacement of basal brain structures upon head movement: kinematic MRI morphometry relevant to neuroendoscopy.** *J Neurol Surg A Cent Eur Neurosurg* 2014;75:98–103 CrossRef Medline

D. Wang
M. Sharma

London Health Sciences Centre, Western University
London, Ontario, Canada

<http://dx.doi.org/10.3174/ajnr.A6388>

Manganese Uptake and Accumulation in the Human Brain



Sudarshana et al¹ are to be commended for their meticulous study of potential brain MR imaging in humans with use of mangafodipir (Mn dipyrdoxyl diphosphate [MnDPDP]) as a contrast agent. MnDPDP is a multifunctional chelate releasing calcium-stalking paramagnetic Mn ions for MR imaging and a catalytic antioxidant for therapy.² In healthy volunteers, MnDPDP raised the signal intensity (SI) in the exocrine glands in the head and neck, chorioid plexus, and anterior pituitary gland but not beyond the BBB. The observations are important because the infusion time (<10 minutes) and dose (5 μ mol/kg) have been standard in MR imaging of the liver and pancreas. Thus, the study confirms that a brief infusion of 1 diagnostic dose does not cause MR imaging contrast enhancement in the brains of humans with an intact BBB and normal liver function.

Concerning future brain Mn uptake studies, we find it relevant to address a patient who received MnDPDP in a total dose of 140 μ mol/kg during 8 months.³ In this patient with terminal cancer of the colon, MnDPDP (10 μ mol/kg) was administered for the protection of normal tissue during 14 cycles of chemotherapy with anticancer agents (oxaliplatin and 5-fluorouracil). The regimen was well-tolerated without the adverse effects of chemotherapy, and there was a notable relief of pain. At end of treatment, mild Parkinson-like symptoms occurred, and brain MR imaging (Fig 1), images not previously disclosed, showed high SI in the basal ganglia (caudate nucleus, globus pallidus, putamen, and thalamus). However, the SI was also high in the corpus callosum, mesencephalon, brain stem, cerebellum, and anterior pituitary gland. In this patient, the first to receive MnDPDP for therapy, an apparent palliation was at the cost of widespread brain deposition of Mn caused by a far-too-high total dose of MnDPDP, advanced liver failure, and, possibly, a BBB weakened by disease or treatment.

Most interesting, SI was maximal in the dentate nucleus and globus pallidus, sites also noted for deposition of gadolinium (Gd) ions released from linear chelates.⁴ This finding may indicate a mutual, possibly calcium-related, pathway for storage of Mn and Gd adducts in the brain.

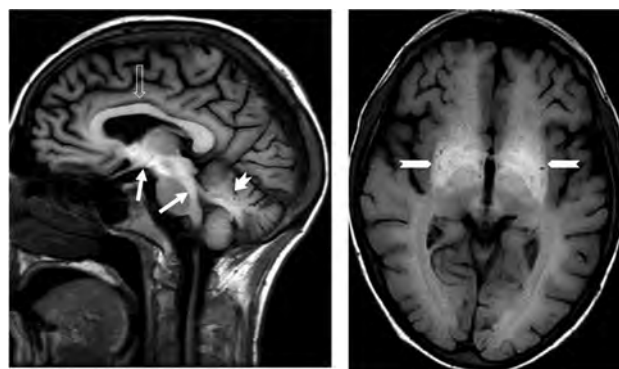


FIG 1. Sagittal (T1-weighted-FLAIR) and axial (T1-weighted spin-echo) images show high SI reflecting Mn deposition in the corpus callosum (open arrow), mesencephalon, crus cerebri, dorsal brain stem, medulla oblongata (white arrows), cerebellum (dentate nucleus) (short white arrow with cut), and basal ganglia (globus pallidus and putamen) (long arrows with cut).

REFERENCES

1. Sudarshana DM, Nair G, Dewey B, et al. **Manganese-enhanced MRI of the brain in healthy volunteers.** *AJNR Am J Neuroradiol* 2019;40:1309–16 CrossRef Medline
2. Karlsson JO, Ignarro LJ, Lundström I, et al. **Cal-mangafodipir [Ca₄Mn (DPDP)5], mangafodipir (MnDPDP) and MnPLED with special reference to their SOD mimetic and therapeutic properties.** *Drug Discov Today* 2015;20:411–21 CrossRef Medline
3. Yri OE, Vig J, Hegstad E, et al. **Mangafodipir as cytoprotective adjunct to chemotherapy: a case report.** *Acta Oncol* 2009;48:633–35 CrossRef Medline
4. Kanda T, Nakai Y, Hagiwara A, et al. **Distribution and chemical forms of gadolinium in the brain: a review.** *Br J Radiol* 2017;90:20170115 CrossRef Medline

© V. Blomlie

© R. Sivanandan

Department of Radiology
Innlandet Trust Hospital, Gjøvik Hospital
Gjøvik, Norway

© P. Jynge

Department of Radiology
Innlandet Trust Hospital, Gjøvik Hospital
Gjøvik, Norway
Norwegian University of Science and Technology
Trondheim, Norway
University of Linköping
Linköping, Sweden

Indicates open access to non-subscribers at www.ajnr.org

<http://dx.doi.org/10.3174/ajnr.A6347>

AJNR *go green*

***AJNR* urges American Society of Neuroradiology members to reduce their environmental footprint by voluntarily suspending their print subscription.**

The savings in paper, printing, transportation, and postage directly fund new electronic enhancements and expanded content.

The digital edition of *AJNR* presents the print version in its entirety, along with extra features including:

- Publication Preview
- Case Collection
- Podcasts
- The *AJNR* News Digest
- The *AJNR* Blog

It also reaches subscribers much faster than print. An electronic table of contents will be sent directly to your mailbox to notify you as soon as it publishes.

Readers can search, reference, and bookmark current and archived content 24 hours a day on www.ajnr.org.

ASNR members who wish to opt out of print can do so by using the *AJNR* Go Green link on the *AJNR* Website (<http://www.ajnr.org/content/subscriber-help-and-services>). Just type your name in the email form to stop print and spare our ecosystem.

CALL FOR AJNR EDITORIAL FELLOWSHIP CANDIDATES

ASNR and AJNR are pleased once again to join efforts with other imaging-related journals that have training programs on editorial aspects of publishing for trainees or junior staff (<5 years on staff), including Radiology (Olmsted fellowship), AJR (Figley and Rogers fellowships), JACR (Bruce J. Hillman fellowship), and Radiologia.

2020 Candidate Information and Requirements

GOALS

- Increase interest in editorial and publication-related activities in younger individuals.
- Increase understanding and participation in the AJNR review process.
- Incorporate into AJNR's Editorial Board younger individuals who have previous experience in the review and publication process.
- Fill a specific need in neuroradiology not offered by other similar fellowships.
- Increase the relationship between "new" generation of neuroradiologists and more established individuals.
- Increase visibility of AJNR among younger neuroradiologists.

ACTIVITIES OF THE FELLOWSHIP

- Serve as Editorial Fellow for one year. This individual will be listed on the masthead as such.
- Review at least one manuscript per month for 12 months. Evaluate all review articles submitted to AJNR.
- Learn how electronic manuscript review systems work.
- Be involved in the final decision of selected manuscripts together with the Editor-in-Chief.
- Participate in all monthly Senior Editor telephone conference calls.
- Participate in all meetings of the Editors during the annual meetings of ASNR and RSNA and the Radiology Editors Forum as per candidate's availability. The Foundation of the ASNR will provide \$2000 funding for this activity.
- Evaluate progress and adjust program to specific needs in annual meeting or telephone conference with the Editor-in-Chief.
- Embark on an editorial scientific or bibliometric project that will lead to the submission of an article to AJNR or another appropriate journal as determined by the Editor-in-Chief. This project will be presented by the Editorial Fellow at the ASNR annual meeting.
- Serve as liaison between AJNR and ASNR's Young Professionals Network. Participate in meetings and telephone calls with this group. Design one electronic survey/year, polling the group regarding readership attitudes and wishes.
- Recruit trainees as reviewers as determined by the Editor-in-Chief.
- Organize and host a Fellows' Journal Club podcast.
- Serve as Guest Editor for an issue of AJNR's News Digest with a timely topic.

QUALIFICATIONS

- Be a fellow in neuroradiology from North America, including Canada (this may be extended to include other countries).
- Be a junior faculty neuroradiology member (<5 years) in either an academic or private environment.
- Be an "in-training" or member of ASNR in any other category.

APPLICATION

- Include a short letter of intent with statement of goals and desired research project. CV must be included.
- Include a letter of recommendation from the Division Chief or fellowship program director. A statement of protected time to perform the functions outlined is desirable.
- Applications will be evaluated by AJNR's Senior Editors prior to the ASNR meeting. The name of the selected individual will be announced at the meeting.
- Applications should be received by March 2, 2020 and sent to Ms. Karen Halm, AJNR Managing Editor, electronically at khalm@asnr.org.